

Origin of *Homo* pushed
back 400,000 years p. 1056

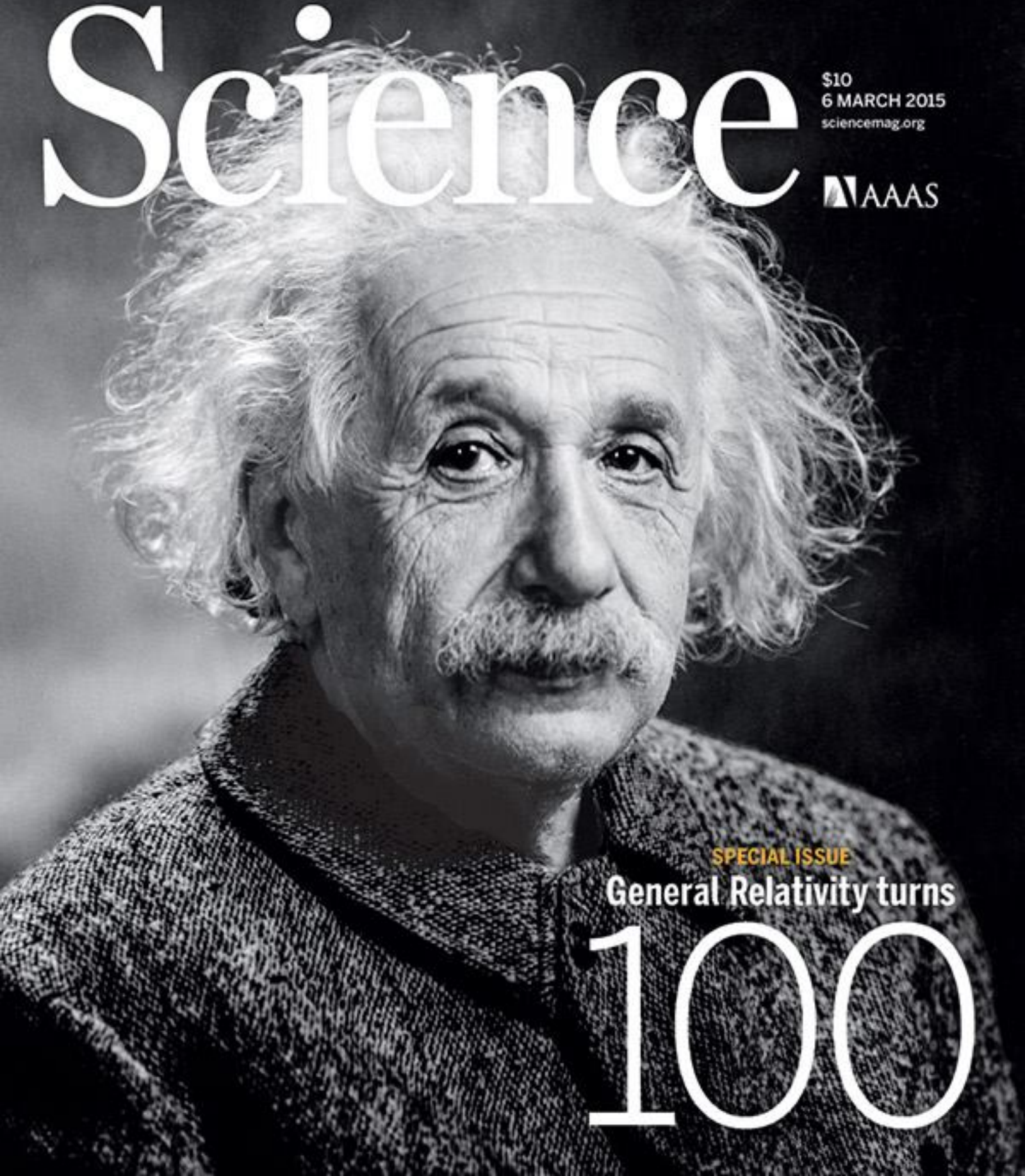
Countering antibiotic
resistance pp. 1062 & 1064

Democratic capital in
the 21st century p. 1145

Science

\$10
6 MARCH 2015
sciencemag.org

AAAS



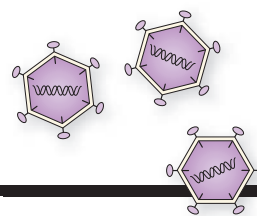
SPECIAL ISSUE

General Relativity turns

100

CONTENTS

6 MARCH 2015 • VOLUME 347 • ISSUE 6226



1069

The ups and downs of
drugging RNAi

SPECIAL SECTION

GENERAL RELATIVITY TURNS 100

INTRODUCTION

1082 Einstein's vision

NEWS

1084 To catch a wave *By A. Cho*

1089 The dark lab *By D. Clery*

1094 General Relativity: The comic book

1096 Drop test *By A. Cho*

REVIEWS

1100 The dark side of cosmology: Dark matter and dark energy *D. N. Spergel*

1103 A century of general relativity: Astrophysics and cosmology
R. D. Blandford

ON THE COVER



In 1915, Albert Einstein was a celebrity. His idea of seamlessly interwoven space and time—spacetime—had revolutionized physics and dazzled the world. Then he published his masterpiece: a short

paper describing how warped spacetime creates gravity. A century later, that “general theory of relativity” remains a pillar of physics and Einstein a peerless scientific icon. See page 1082. *Photo: Orren Jack Turner, Prints & Photographs Division, Library of Congress, LC-USZ62-60242*

SEE ALSO ► BOOKS *ET AL.* P. 1078 ► REPORT P. 1123 ► ONLINE NEWS STORY ► ANIMATION ► QUIZ
► VIDEO ► sciencemag.org/site/special/generalrelativity

NEWS

IN BRIEF

1048 Roundup of the week's news

IN DEPTH

1051 A PRISTINE AMAZON'S LAST STAND

Laboratory in the sky will sample some of the last unspoiled air on the planet *By L. Wade*

1052 MUONS PROBE FUKUSHIMA'S RUINS

Unsung imaging technique deployed to find uranium debris in reactors *By D. Normile*

1054 WHY MANY U.S. BIOLOGY TEACHERS ARE 'WISHY-WASHY'

Future science teachers lack knowledge and role models
By J. Mervis

1055 DOUBTS DISPELLED ABOUT HIV PREVENTION

New studies show remarkable efficacy and versatility of drugs for uninfected *By J. Cohen*

1056 Drug flushes out hidden AIDS virus
By J. Cohen

1056 DEEP ROOTS FOR THE GENUS *HOMO*

Fossil jawbone pushes back origins of our genus by 400,000 years *By A. Gibbons*

► REPORT BY VILLMOARE *ET AL.* 10.1126/science.aaa1343; REPORT BY DIMAGGIO *ET AL.* 10.1126/science.aaa1415

FEATURE

1058 CLEANUP CREW

Unorthodox immune proteins called natural antibodies target pathogens and remove cellular and molecular waste
By M. Leslie

INSIGHTS

PERSPECTIVES

1062 A SUSTAINABLE MODEL FOR ANTIBIOTICS

How can we foster the development of novel drugs against resistant bacteria?
By M. Perros

► PERSPECTIVE P. 1064

1064 A RETURN TO THE PRE-ANTIMICROBIAL ERA?

The effects of antimicrobial resistance will be felt most acutely in lower-income countries *By S. Baker*

► PERSPECTIVE P. 1062; PODCAST

1066 STATISTICS REQUANTITATES THE CENTRAL DOGMA

Transcription, not translation, chiefly determines protein abundance in mammals *By J. J. Li and M. D. Biggin*
► RESEARCH ARTICLE P. 1112

1068 NEW WORLD MONKEY ORIGINS

Fossils in Peru raise questions about the early evolution of monkeys in South America *By R. F. Kay*

1069 DRUGGING RNAi

RNAi therapeutics are emerging as a major drug discovery engine
By D. Haussecker and M. A. Kay

1071 VIRAL CHEMOKINE MIMICRY

How do viruses trick the human immune system? *By J. Standfuss*
► RESEARCH ARTICLES PP. 1113 & 1117

1072 SINGLE PROTEINS UNDER A DIAMOND SPOTLIGHT

A diamond nanomagnetometer is used to probe conformational changes of a single protein *By P. Hemmer and C. Gomes*

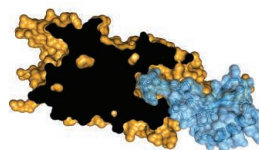
► REPORT P. 1135

1073 LOOK BUT DON'T TOUCH THE METALS

Nitrogen-vacancy defects in diamond can probe metallic conductivity at a distance
By L. P. McGuinness and F. Jelezko

► REPORT P. 1129

CONTENTS



1071, 1113, & 1117

How chemokines bind
their receptors

6 MARCH 2015 • VOLUME 347 • ISSUE 6226

1075 BEING SMART ABOUT SMART ENVIRONMENTAL TARGETS

Focus on the negotiation process, not just the end target
By S. L. Maxwell et al.

BOOKS ET AL.

1077 WHY DID THE CHICKEN CROSS THE WORLD?

By A. Lawler, reviewed by G. Larson

1078 EINSTEIN'S UNIFICATION

By J. van Dongen, reviewed by M. Janssen
► GENERAL RELATIVITY TURNS 100 P. 1082

LETTERS

1079 A BETTER WAY FORWARD FOR BRAZIL'S FISHERIES

By F. Di Dario et al.

1079 COMPLEX ECOLOGY OF CHINA'S SEAWALL

By X.-W. Huang et al.

1080 RESPONSE

By Z. Ma and B. Li

1080 TECHNICAL COMMENT ABSTRACTS

1080 ERRATA

RESEARCH

IN BRIEF

1109 From *Science* and other journals

RESEARCH ARTICLES

1112 IMMUNOGENETICS

Dynamic profiling of the protein life cycle in response to pathogens
M. Jovanovic et al.

RESEARCH ARTICLE SUMMARY; FOR FULL TEXT:
dx.doi.org/10.1126/science.1259038

► PERSPECTIVE P. 1066

STRUCTURAL BIOLOGY

1113 Structural basis for chemokine recognition and activation of a viral G protein-coupled receptor
J. S. Burg et al.

1117 Crystal structure of the chemokine receptor CXCR4 in complex with a viral chemokine *L. Qin et al.*

► PERSPECTIVE P. 1071

REPORTS

1123 ASTROPHYSICS

Multiple images of a highly magnified supernova formed by an early-type cluster galaxy lens *P. L. Kelly et al.*

► GENERAL RELATIVITY TURNS 100 P. 1082

1126 STELLAR DYNAMICS

The fastest unbound star in our Galaxy ejected by a thermonuclear supernova
S. Geier et al.

1129 QUANTUM ELECTRONICS

Probing Johnson noise and ballistic transport in normal metals with a single-spin qubit *S. Kolkowitz et al.*

► PERSPECTIVE P. 1073

1132 REPELLENT MATERIALS

Robust self-cleaning surfaces that function when exposed to either air or oil *Y. Lu et al.*

1135 PROTEIN IMAGING

Single-protein spin resonance spectroscopy under ambient conditions
F. Shi et al.

► PERSPECTIVE P. 1072

1138 BRAIN STRUCTURE

Cell types in the mouse cortex and hippocampus revealed by single-cell RNA-seq *A. Zeisel et al.*

1142 FRESHWATER ECOLOGY

Experimental nutrient additions accelerate terrestrial carbon loss from stream ecosystems
A. D. Rosemond et al.

1145 POLITICAL ECONOMY

On the endogeneity of political preferences: Evidence from individual experience with democracy
N. Fuchs-Schündeln and M. Schündeln

1148 NUCLEAR PORES

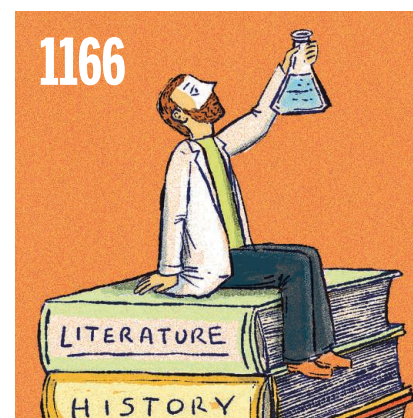
Architecture of the nuclear pore complex coat *T. Stuwe et al.*

1152 PROTEIN TARGETING

Structure of the Get3 targeting factor in complex with its membrane protein cargo *A. Mateja et al.*

1155 EVOLUTIONARY GENOMICS

Evolutionary changes in promoter and enhancer activity during human corticogenesis
S. K. Reilly et al.



DEPARTMENTS

1047 EDITORIAL

It starts with a poster
By Marcia McNutt

1166 WORKING LIFE

Oh the humanities!
By Kevin Boehnke

Science Staff1046
New Products1160
Science Careers1161

SCIENCE (ISSN 0036-8075) is published weekly on Friday, except the last week in December, by the American Association for the Advancement of Science, 1200 New York Avenue, NW, Washington, DC 20005. Periodicals mail postage (publication No. 484460) paid at Washington, DC, and additional mailing offices. Copyright © 2015 by the American Association for the Advancement of Science. The title SCIENCE is a registered trademark of the AAAS. Domestic individual membership and subscription (51 issues): \$153 (\$74 allocated to subscription). Foreign postage extra: Mexico, Caribbean (surface mail) \$55; other countries (air assist delivery) \$85. First class, airmail, student, and emeritus rates on request. Canadian rates with GST available upon request. GST #R1254 88122. Publications Mail Agreement Number 1069624. Printed in the U.S.A. Change of address: Allow 4 weeks, giving old and new addresses and 8-digit account number. Postmaster: Send change of address to AAAS, P.O. Box 96178, Washington, DC 20090-6178. Single-copy sales: \$10.00 current issue, \$15.00 back issue prepaid includes surface postage; bulk rates on request. Authorization to photocopy material for internal or personal use under circumstances not falling within the fair use provisions of the Copyright Act is granted by AAAS to libraries and other users registered with the Copyright Clearance Center (CCC) Transactional Reporting Service, provided that \$30.00 per article is paid directly to CCC, 222 Rosewood Drive, Danvers, MA 01923. The identification code for Science is 0036-8075. Science is indexed in the Reader's Guide to Periodical Literature and in several specialized indexes.

Editor-in-Chief Marcia McNutt

Executive Editor Monica M. Bradford **News Editor** Tim Appenzeller

Managing Editor, Research Journals Katrina L. Kelner

Deputy Editors Barbara R. Jasny, Andrew M. Sugden(UK), Valda J. Vinson, Jake S. Yeston

Research and Insights

SR. EDITORS Caroline Ash(UK), Gilbert J. Chin, Lisa D. Chong, Julia Fahrenkamp-Uppenbrink(UK), Pamela J. Hines, Stella M. Hurlley(UK), Paula A. Kiberstis, Marc S. Lavine(Canada), Kristen L. Mueller, Ian S. Osborne(UK), Beverly A. Purnell, L. Bryan Ray, Guy Riddihough, H. Jesse Smith, Jelena Stajic, Peter Stern(UK), Phillip D. Szuroni, Brad Wible, Nicholas S. Wigginton, Laura M. Zahn **ASSOCIATE EDITORS** Brent Grocholski, Sacha Vignieri **ASSOCIATE BOOK REVIEW EDITOR** Valerie B. Thompson **ASSOCIATE LETTERS EDITOR** Jennifer Sills **CHIEF CONTENT PRODUCTION EDITOR** Cara Tate **SR. CONTENT PRODUCTION EDITORS** Harry Jach **CONTENT PRODUCTION EDITORS** Jeffrey E. Cook, Chris Filiatreau, Cynthia Howe, Lauren Krnec, Barbara P. Ordway **SR. EDITORIAL COORDINATORS** Carolyn Kyle, Beverly Shields **EDITORIAL COORDINATORS** Ramatoulaye Diop, Joi S. Granger, Lisa Johnson, Anita Wynn **PUBLICATIONS ASSISTANTS** Aneera Dobbins, Jeffrey Hearn, Dona Mathieu, Le-Toya Mayne Flood, Shannon McMahon, Scott Miller, Jerry Richardson, Rachel Roberts(UK), Alice Whaley(UK), Brian White **EXECUTIVE ASSISTANT** Anna Bashkirova **ADMINISTRATIVE SUPPORT** Janet Clements(UK), Monika Magon(UK, Intern), Lizanne Newton(UK), Maryrose Madrid, John Wood(UK)

News

NEWS MANAGING EDITOR John Travis **INTERNATIONAL EDITOR** Richard Stone **DEPUTY NEWS EDITORS** Daniel Clery(UK), Robert Coontz, Elizabeth Culotta, David Grimm, David Malakoff, Leslie Roberts **CONTRIBUTING EDITORS** Martin Enserink(Europe), Mara Hvistendahl **SR. CORRESPONDENTS** Jeffrey Mervis, Elizabeth Pennisi **NEWS WRITERS** Adrian Cho, John Cohen, Jennifer Couzin-Frankel, Carolyn Gramling, Eric Hand, Jocelyn Kaiser, Kelly Servick, Robert F. Service, Erik Stokstad(Cambridge, UK), Emily Underwood **INTERNS** Emily Conover, David Shultz, Jia You **CONTRIBUTING CORRESPONDENTS** Pallava Bagla(South Asia), Michael Balter(Paris), John Bohannon, Ann Gibbons, Sam Kean, Richard A. Kerr, Eli Kintisch, Kai Kupferschmidt(Berlin), Andrew Lawler, Christina Larson(Beijing), Mitch Leslie, Charles C. Mann, Eliot Marshall, Virginia Morell, Dennis Normile(Tokyo), Heather Pringle, Tania Rabesandratana(Brussels), Gretchen Vogel(Berlin), Lizzie Wade(Mexico City) **CAREERS** Jim Austin(Editor), Donisha Adams, Rachel Bernstein **COPY EDITORS** Kara Estelle, Nora Kelly, Jennifer Levin **ADMINISTRATIVE SUPPORT** Scherraine Mack

Executive Publisher Rush D. Holt

Publisher Kent R. Anderson **Chief Digital Media Officer** Rob Covey

BUSINESS OPERATIONS AND ADMINISTRATION DIRECTOR Deborah Rivera-Wienhold **BUSINESS SYSTEMS AND FINANCIAL ANALYSIS DIRECTOR** Randy Yi **MANAGER OF FULFILLMENT SYSTEMS** Neal Hawkins **SYSTEMS ANALYST** Nicole Mehmedovich **ASSISTANT DIRECTOR, BUSINESS OPERATIONS** Eric Knott **MANAGER, BUSINESS OPERATIONS** Jessica Tierney **BUSINESS ANALYSTS** Cory Lipman, Cooper Tilton, Celeste Troxler **FINANCIAL ANALYST** Jeremy Clay **RIGHTS AND PERMISSIONS ASSISTANT DIRECTOR** Emilie David **PERMISSIONS ASSOCIATE** Elizabeth Sandler **RIGHTS, CONTRACTS, AND LICENSING ASSOCIATE** Lili Kiser

MARKETING DIRECTOR Ian King **MARKETING MANAGER** Julianne Wielga **MARKETING ASSOCIATE** Elizabeth Sattler **SR. MARKETING EXECUTIVE** Jennifer Reeves **SR. ART ASSOCIATE, PROJECT MANAGER** Tzeitel Sorrosa **ART ASSOCIATE** Seil Lee **ASSISTANT COMMERCIAL EDITOR** Selby Frame **MARKETING PROJECT MANAGER** Angelissa McArthur **SR. WRITER** Bill Zimmer **PROGRAM DIRECTOR, AAAS MEMBER CENTRAL** Peggy Mihelich **FULFILLMENT SYSTEMS AND OPERATIONS** membership@aaas.org **MANAGER, MEMBER SERVICES** Pat Butler **SPECIALISTS** LaToya Casteel, Javia Flemmings, Latasha Russell **MANAGER, DATA ENTRY** Mickie Napoleoni **DATA ENTRY SPECIALISTS** JJ Regan, Jaimee Wise, Fiona Giblin

DIRECTOR, SITE LICENSING Tom Ryan **DIRECTOR, CORPORATE RELATIONS** Eileen Bernadette Moran **SR. PUBLISHER RELATIONS SPECIALIST** Kiki Forsythe **PUBLISHER RELATIONS MANAGER** Catherine Holland **PUBLISHER RELATIONS, EASTERN REGION** Keith Layson **PUBLISHER RELATIONS, WESTERN REGION** Ryan Rexroth **MANAGER, SITE LICENSE OPERATIONS** Iquo Edem **FULFILLMENT ANALYST** Lana Guz **ASSOCIATE DIRECTOR, MARKETING** Christina Schlecht **MARKETING ASSOCIATES** Thomas Landreth, Minah Kim

DIRECTOR OF WEB TECHNOLOGIES Ahmed Khadr **SR. DEVELOPER** Chris Coleman **DEVELOPERS** Dan Berger, Jimmy Marks **SR. PROJECT MANAGER** Trista Smith **SYSTEMS ENGINEER** Luke Johnson **PRODUCT MANAGER** Walter Jones

CREATIVE DIRECTOR, MULTIMEDIA Martyn Green **DIRECTOR OF ANALYTICS** Enrique Gonzales **SR. WEB PRODUCER** Sarah Crespi **WEB PRODUCER** Alison Crawford **VIDEO PRODUCER** Nguyen Nguyen **SOCIAL MEDIA PRODUCER** Meghna Sachdev

DIRECTOR OF OPERATIONS PRINT AND ONLINE Lizabeth Harman **DIGITAL/PRINT STRATEGY MANAGER** Jason Hillman **QUALITY TECHNICAL MANAGER** Marcus Spiegel **DIGITAL PRODUCTION MANAGER** Lisa Stanford **ASSISTANT MANAGER DIGITAL/PRINT** Rebecca Doshi **DIGITAL MEDIA SPECIALIST** Tara Kelly **SENIOR CONTENT SPECIALISTS** Steve Forrester, Antoinette Hodal, Lori Murphy, Anthony Rosen **CONTENT SPECIALISTS** Jacob Hedrick, Kimberley Oster

DESIGN DIRECTOR Beth Rakouskas **DESIGN EDITOR** Marcy Atarod **SENIOR SCIENTIFIC ILLUSTRATORS** Chris Bickel, Katharine Sutliff **SCIENTIFIC ILLUSTRATOR** Valerie Altounian **SENIOR ART ASSOCIATES** Holly Bishop, Preston Huey **SENIOR DESIGNER** Garvin Grullón **DESIGNER** Chrystal Smith **SENIOR PHOTO EDITOR** William Douthitt **PHOTO EDITOR** Leslie Blizard

DIRECTOR, GLOBAL COLLABORATION, CUSTOM PUBLICATIONS, ADVERTISING Bill Moran **EDITOR, CUSTOM PUBLISHING** Sean Sanders: 202-326-6430 **ASSISTANT EDITOR, CUSTOM PUBLISHING** Tianna Hicklin: 202-326-6463 **ADVERTISING MARKETING MANAGER** Justin Sawyers: 202-326-7061 **science_advertising@aaas.org** **ADVERTISING MARKETING ASSOCIATE** Javia Flemmings **ADVERTISING SUPPORT MANAGER** Karen Foote: 202-326-6740 **ADVERTISING PRODUCTION OPERATIONS MANAGER** Deborah Tompkins **SR. PRODUCTION SPECIALIST/GRAPHIC DESIGNER** Amy Hardcastle **PRODUCTION SPECIALIST** Yuse Lajiminmuhip **SR. TRAFFIC ASSOCIATE** Christine Hall **SALES COORDINATOR** Shirley Young **ASSOCIATE DIRECTOR, COLLABORATION, CUSTOM PUBLICATIONS/CHINA/TAIWAN/KOREA/SINGAPORE** Ruolei Wu: +86-186 0822 9345, rwu@aaas.org **COLLABORATION/CUSTOM PUBLICATIONS/JAPAN** Adarsh Sandhu + 81532-81-5142 asandhu@aaas.org **EAST COAST/E. CANADA** Laurie Faraday: 508-747-9395, FAX 617-507-8189 **WEST COAST/W. CANADA** Lynne Stickrod: 415-931-9782, FAX 415-520-6940 **MIDWEST** Jeffrey Dembski: 847-498-4520 x3005, Steven Loerch: 847-498-4520 x3006 **UK EUROPE/ASIA** Roger Goncalves: TEL/FAX +41 43 243 1358 **JAPAN** Katsuyoshi Fukamizu (Tokyo): +81-3-3219-5777 fukamizu@aaas.org **CHINA/TAIWAN** Ruolei Wu: +86-0082-9345

WORLDWIDE ASSOCIATE DIRECTOR OF SCIENCE CAREERS Tracy Holmes: +44 (0) 1223 326525, FAX +44 (0) 1223 326532 tholmes@science-int.co.uk **CLASSIFIED** advertise@sciencecareers.org **U.S. SALES** Tina Burks: 202-326-6577 **Nancy Toerna**: 202-326-6578 **SALES ADMINISTRATOR** Marci Gallun **EUROPE/ROW SALES** Axel Gesatzki, Sarah Lecher **SALES ASSISTANT** Kelly Grace **JAPAN** Hiroyuki Mashiki(Kyoto): +81-75-823-1109 hymashiki@aaas.org **CHINA/TAIWAN** Ruolei Wu: +86-186 0082 9345 rwu@aaas.org **MARKETING MANAGER** Allison Pritchard **MARKETING ASSOCIATE** Aimee Aponte

AAAS BOARD OF DIRECTORS **RETIRING PRESIDENT, CHAIR** Phillip A. Sharp **PRESIDENT** Gerald R. Fink **PRESIDENT-ELECT** Geraldine (Geri) Richmond **TREASURER** David Evans **SHAW CHIEF EXECUTIVE OFFICER** Alan I. Leshner **BOARD** **BOONIE** L. Bessler, May R. Berenbaum, Carlos J. Bustamante, Claire M. Fraser, Laura H. Greene, Elizabeth Loftus, Raymond Orbach, Inder M. Verma

SUBSCRIPTION SERVICES For change of address, missing issues, new orders and renewals, and payment questions: 866-434-AAAS (2227) or 202-326-6417, FAX 202-842-1065. Mailing addresses: AAAS, P.O. Box 96178, Washington, DC 20090-6178 or AAAS Member Services, 1200 New York Avenue, NW, Washington, DC 20005

INSTITUTIONAL SITE LICENSES 202-326-6755 **REPRINTS**: Author Inquiries 800-635-7181 **COMMERCIAL INQUIRIES** 803-359-4578 **PERMISSIONS** 202-326-6765, permissions@aaas.org **AAAS Member Services** 202-326-6417 or <http://membercentral.aaas.org/discounts>

Science serves as a forum for discussion of important issues related to the advancement of science by publishing material on which a consensus has been reached as well as including the presentation of minority of conflicting points of view. Accordingly, all articles published in Science—including editorials, news and comment, and books reviews—are signed and reflect the individual views of the authors and not official points of view adopted by AAAS or the institutions with which the authors are affiliated.

INFORMATION FOR AUTHORS See pages 678 and 679 of the 6 February 2015 issue or access www.sciencemag.org/about/authors

SENIOR EDITORIAL BOARD

A. Paul Alivisatos, Lawrence Berkeley Nat'l Laboratory, Ernst Fehr, U. of Zürich
Susan M. Rosenberg, Baylor College of Medicine, Ali Shilatifard, Northwestern University
Feinberg School of Medicine, Michael S. Turner, U. of Chicago

BOARD OF REVIEWING EDITORS (Statistics board members indicated with \$)

Adriano Aguzzi, U. Hospital Zürich
Takuzo Aida, U. of Tokyo
Leslie Aiello, Wenner-Gren Foundation
Judith Allen, U. of Edinburgh
Sonia Altizer, U. of Georgia
Sebastian Amigorena, Institut Curie
Kathryn Anderson, Memorial Sloan-Kettering Cancer Center
Meinrat O. Andreae, Max-Planck Inst. Mainz
Paola Arlotta, Harvard U.
Johan Auwerx, EPFL
David Awschalom, U. of Chicago
Jordi Bascompte, Estación Biológica de Doñana CSIC
Facundo Batista, London Research Inst.
Ray H. Baughman, U. of Texas, Dallas
David Baum, U. of Wisconsin
Carlo Beenakker, Leiden U.
Kamran Behnia, ESPCI-ParisTech
Yasmine Belkaid, NIAID, NIH
Philip Benfey, Duke U.
Stephen J. Benkovic, Penn State U.
May Berenbaum, U. of Illinois
Gabriele Bergers, U. of California, San Francisco
Bradley Bernstein, Massachusetts General Hospital
Peer Bork, EMBL
Bernard Bourdon, Ecole Normale Supérieure de Lyon
Chris Bowler, Ecole Normale Supérieure
Ian Boyd, U. of St. Andrews
Emily Brodsky, U. of California, Santa Cruz
Ron Brookmeyer, U. of California Los Angeles (\$) **Christian Büchel**, U. Hamburg-Eppendorf
Joseph A. Burns, Cornell U.
Gyorgy Buzsaki, New York U. School of Medicine
Blanche Capel, Duke U.
Mats Carlsson, U. of Oslo
David Clapham, Children's Hospital Boston
David Clary, U. of Oxford
Joel Cohen, Rockefeller U., Columbia U.
Jonathan D. Cohen, Princeton U.
James Collins, Boston U.
Robert Cook-Deegan, Duke U.
Alan Cowman, Walter & Eliza Hall Inst.
Robert H. Crabtree, Yale U.
Roberta Croce, Vrije Universiteit
Janet Currie, Princeton U.
Jeff L. Dangl, U. of North Carolina
Tom Daniel, U. of Washington
Frans de Waal, Emory U.
Stanislas Dehaene, Collège de France
Robert Desimone, MIT
Claude Desplais, U. of Nijmegen
Ap Dijksterhuis, Radboud U. of Nijmegen
Dennis Discher, U. of Pennsylvania
Gerald W. Dorn II, Washington U. School of Medicine
Jennifer A. Doudna, U. of California, Berkeley
Bruce Dunn, U. of California, Los Angeles
Christopher Dye, WHO
Todd Ehlers, U. of Tuebingen
David Ehrhardt, Carnegie Inst. of Washington
Tim Elston, U. of North Carolina at Chapel Hill
Gerhard Ertl, Fritz-Haber-Institut, Berlin
Barry Everitt, U. of Cambridge
Ernst Fehr, U. of Zurich
Anne C. Ferguson-Smith, U. of Cambridge
Michael Feuer, The George Washington U.
Kate Fitzgerald, U. of Massachusetts
Peter Fratzl, Max-Planck Inst.
Elaine Fuchs, Rockefeller U.
Daniel Geschwind, UCLA
Andrew Gewirth, U. of Illinois
Karl-Heinz Glassmeier, TU Braunschweig
Ramon Gonzalez, Rice U.
Julia R. Greer, Caltech
Elizabeth Grove, U. of Chicago
Nicolas Gruber, ETH Zurich
Kip Guy, St. Jude's Children's Research Hospital
Taekjip Ha, U. of Illinois at Urbana-Champaign
Christian Haass, Ludwig Maximilians U.
Steven Hahn, Fred Hutchinson Cancer Research Center
Michael Hasselmo, Boston U.
Martin Heimann, Max-Planck Inst. Jena
Yia-Hai Kuo, U. of Cambridge
James A. Hendler, Rensselaer Polytechnic Inst.
Janet G. Hering, Swiss Fed. Inst. of Aquatic Science & Technology
Kai-Uwe Hinrichs, U. of Bremen
Kei Hirose, Tokyo Inst. of Technology
David Hodell, U. of Cambridge
David Holden, Imperial College
Lora Hooper, UT Southwestern Medical Ctr. at Dallas
Raymond Huey, U. of Washington
Steven Jacobsen, U. of California, Los Angeles
Kai Johnson, EPFL Lausanne
Peter Jonas, Inst. of Science & Technology (IST) Austria
Matt Kaeblerlein, U. of Washington
William Kaelin Jr., Dana-Farber Cancer Inst.
Daniel Kahne, Harvard U.
Daniel Kammen, U. of California, Berkeley
Masashi Kawasaki, U. of Tokyo
Joel Kingsolver, U. of North Carolina at Chapel Hill
Robert Kingston, Harvard Medical School
Etienne Kochlin, Ecole Normale Supérieure
Alexander Koldkin, Johns Hopkins U.
Alberto R. Kornblith, U. of Buenos Aires
Leonid Kruglyak, UCLA
Thomas Langer, U. of Cologne
Mitchell A. Lazar, U. of Pennsylvania
David Lazer, Harvard U.
Thomas Lecuit, IBDM
Virginia Lee, U. of Pennsylvania
Stanley Lemon, U. of North Carolina at Chapel Hill
Ottoline Leyser, Cambridge U.
Marcia C. Linn, U. of California, Berkeley
Jianguo Liu, Michigan State U.
Luis Liz-Marzan, CIC biomAGUNE
Jonathan Losos, Harvard U.
Ke Lu, Chinese Acad. of Sciences
Christian Lüscher, U. of Geneva
Laura Machesky, CRUK Beatson Inst. for Cancer Research
Aime Magurran, U. of St. Andrews
Oscar Marin, CSIC & U. Miguel Hernández
Charles Marshall, U. of California, Berkeley
C. Robertson McClung, Dartmouth College
Graham Medley, U. of Warwick
Yasushi Miyashita, U. of Tokyo
Mary Ann Moran, U. of Georgia
Richard Morris, U. of Edinburgh
Allison Møntsgaard-Reif, NC State U. (\$) **Sean Munro**, MRC Lab. of Molecular Biology
Thomas Murray, The Hastings Center
James Nelson, Stanford U. School of Med.
Daniel Neumark, U. of California, Berkeley
Timothy W. Nilsen, Case Western Reserve U.
Pär Nordlund, Karolinska Inst.
Heide Nowotny, European Research Advisory Board
Ben Oken, MIT
Jens Olsen, U. of California
Berkeley & Lawrence Berkeley National Lab
Harry Orr, U. of Minnesota
Andrew Oswald, U. of Warwick
Steve Palumbi, Stanford U.
Jane Parker, Max-Planck Inst. of Plant Breeding Research
Giovanni Parmigiani, Dana-Farber Cancer Inst. (\$) **Donald R. Paul**, U. of Texas, Austin
John H. J. Petrini, Memorial Sloan-Kettering Cancer Center
Joshua Plotkin, U. of Pennsylvania
Albert Polman, FOM Institute AMOLF
Philippe Poulin, CNRS
Jonathan Pritchard, Stanford U.
David Randall, Colorado State U.
Colin Renfrew, U. of Cambridge
Felix Rey, Institut Pasteur
Trevor Robbins, U. of Cambridge
Jim Roberts, Fred Hutchinson Cancer Research Ctr.
Barbara A. Romanowicz, U. of California, Berkeley
Jens Rostrup-Nielsen, Haldor Topsøe
Mike Ryan, U. of Texas, Austin
Mitinori Saitou, Kyoto U.
Shimon Sakaguchi, Kyoto U.
Miguel Salmeron, Lawrence Berkeley National Lab
Jürgen Sandkühler, Medical U. of Vienna
Alexander Schier, Harvard U.
Randy Seeley, U. of Cincinnati
Vladimir Shalae, Purdue U.
Robert Siliciano, Johns Hopkins School of Medicine
Joseph Silk, Institut d'Astrophysique de Paris
Denis Simon, Arizona State U.
Alison Smith, John Innes Centre
Richard Smith, U. of North Carolina (\$) **John Speakman**, U. of Aberdeen
Allan C. Spradling, Carnegie Institution of Washington
Jonathan Sprent, Garvan Inst. of Medical Research
Eric Steig, U. of Washington
Paula Stephan, Georgia State U. and National Bureau of Economic Research
Molly Stevens, Imperial College London
V. S. Subrahmanian, U. of Maryland
Ira Tabak, Columbia U.
Sarah Teichmann, Cambridge U.
John Thomas, North Carolina State U.
Shubha Tole, Tata Institute of Fundamental Research
Christopher Tyler-Smith, The Wellcome Trust Sanger Institute
Herbert Virgin, Washington U.
Berth Vogelstein, Johns Hopkins U.
Cynthia Volkert, U. of Göttingen
Douglas Wallace, Dalhousie U.
David Wallace, Weizmann Inst. of Science
Ian Walsmsley, U. of Oxford
David A. Wardle, Swedish U. of Agric. Sciences
David Waxman, Fudan U.
Jonathan Weissman, U. of California, San Francisco
Chris Wikle, U. of Missouri (\$) **Ian A. Wilson**, The Scripps Res. Inst. (\$) **Timothy D. Wilson**, U. of Virginia
Rosemary Wyse, Johns Hopkins U.
Jan Zaenen, Leiden U.
Kenneth Zaret, U. of Pennsylvania School of Medicine
Jonathan Zehr, U. of California, Santa Cruz
Len Zon, Children's Hospital Boston
Maria Zuber, MIT

BOOK REVIEW BOARD

David Bloom, Harvard U. Samuel Bowring, MIT, Angela Creager, Princeton U., Richard Swedner, U. of Chicago, Ed Wasserman, DuPont

It starts with a poster

Scientists frequently lament the scarcity of effective scientific communicators—those who can explain complex concepts to the public, present scientifically sound alternatives to policy-makers, and make cogent arguments for the value of science to society. A few stellar programs are designed to select and train elite articulators, but some simple steps can improve the communication skills of all scientists. Most researchers learn how to talk about science at meetings. If scientists cannot explain their work clearly and succinctly to their peers, it is highly unlikely that they can explain it effectively to nonspecialists. I recently helped to judge student papers at a large scientific meeting, an experience that brought to my attention the importance of such communication early in one's career. I offer a few tips on how to make the most of this invaluable training.

I encourage students to request a poster presentation at a large meeting. This format can be less stressful than speaking in front of a large audience. Furthermore, the student personally converses with members of the scientific community who share an interest in his or her research. The back-and-forth is good training and a reminder to students that discussing their research with experts or nonexperts should be a two-way conversation. Another advantage of presenting a poster is that the student can tailor the narrative to the interests of whoever stops by, in a Q&A exchange. I recall years ago when a graduate student was disappointed that her research would be described “only” in this format, until one of the giants in her field spent considerable time at her poster to discuss the work. As he left, he said, “I wish I had thought of that.” She was later hired into his department.

To be effective, posters need to be eye-catching as well as informative. In a convention hall lined with poster boards, scientists will bypass those with large blocks of texts and tables of impenetrable numbers.

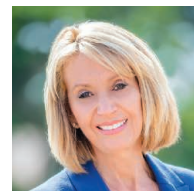
A cartoon that summarizes the model or findings, attractive displays of data, and photos that illustrate the experiment are good ways to grab attention. Creative ways to display pertinent information are a definite plus. I personally like posters that begin with the motivation for the work and end with the findings, areas for follow up, and broader implications of the results.

A 10-minute talk at a major conference is more difficult to organize and effectively deliver than an hour-long seminar. Mistakes that students often commit in preparing slides for a brief presentation are to show the same intricate multipart figures that they used in a research paper, have too much text (and in a font size too small), choose colors with insufficient contrast against the background, and use blurry images copied from the Internet. The delivery is also critical. Enthusiasm is one of the very best elements of any talk. Students should never merely recite from their slides and should never ever go over time. Recognizing who the audience is and pitching the talk appropriately are essential. Many years ago, if a scientist used unfamiliar jargon

and aimed the presentation over the heads of the audience, the speaker might just have been considered smart. No longer. Today, such a speaker is viewed as a poor communicator.

Training the next generation of scientists to communicate well should be a priority. Departments could arrange for students to hold mock presentations for other faculty, researchers, and students in advance of their presentations at conferences—a dress rehearsal before the main event. And researchers attending meetings should take some time to judge a few student papers, visit student posters, or attend student talks. This feedback to young scientists is invaluable, and the great communicators that will emerge may well trace their sharpened skills back to a moment at their poster or at the podium.

— Marcia McNutt



Marcia McNutt
Editor-in-Chief
Science Journals



“Training the next generation of scientists to communicate well should be a priority.”

“Long before being nerdy was cool,
there was Leonard Nimoy.”

President Barack Obama, in a tribute to Nimoy, who played *Star Trek*'s beloved Mr. Spock. Nimoy died last week at age 83.

IN BRIEF



China's Pearl River delta is now the world's largest urban area.

Asia's cities swell as population surges

Over the past decade, East and Southeast Asia have experienced an urbanization boom unlike any the world has ever seen. From China and Japan to the Philippines and Indonesia, the urban population of 17 countries in East and Southeast Asia increased from 738 million people in 2000 to 969 million in 2010. But the rate of expansion of urban land area—2% annually, on average, over that period—did not keep up with the rate of population change, which was about 2.8% per year, according to a 4 March report in *Environmental Research Letters*. Instead, Asia's teeming metropolises are cramming ever more humanity within existing city limits—confounding predictions that the cities will greatly expand their footprints as migrants flood in. “The assumption from past research has been that cities of all sizes will eventually decline in density,” says author Annemarie Schneider, a geographer at University of Wisconsin, Madison. “This study reveals the opposite.” The trend may seem obvious to Asian cities straining to provide basic services for burgeoning populations. But for urban planners, the findings, Schneider says, could change “how officials plan and adapt to urbanization in the future.”

AROUND THE WORLD

Push for E.U. energy bloc

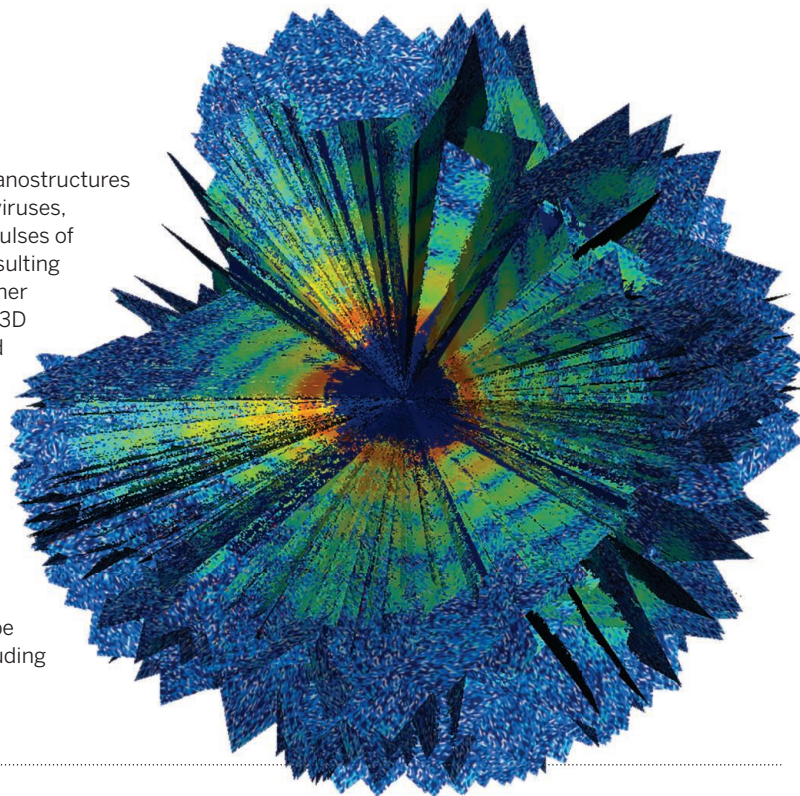
BRUSSELS | The European Commission announced a plan on 25 February to create a unified energy market, where “energy flows freely across borders,” according to the so-called Energy Union proposal. The plan calls for more research and innovation on energy efficiency and renewable energy technologies to help transform energy systems, maintain Europe's technological leadership, and boost export prospects. This would help wean the bloc from fraught gas imports, hitting Russian President Vladimir Putin “where it hurts most,” says Guy Verhofstadt, a liberal member of the European Parliament from Belgium. But green groups have criticized the plan for putting too much emphasis on fossil fuels and nuclear energy—“yesterday's instead of tomorrow's technologies,” says Rebecca Harms, a Green member of the European Parliament from Germany. The proposal will next be discussed by the European Parliament and member states.

Trials under scrutiny

MINNEAPOLIS, MINNESOTA | A damning report released last week on how the University of Minnesota protects volunteers in its clinical trials charged the university with inadequate review of research studies and failure to sufficiently protect the most vulnerable subjects. Examining protocols from 20 active trials and meeting minutes from the institutional review board (IRB), the reviewers found “little discussion of the risks and benefits” to volunteers, and noted that there were often no IRB members with expertise in a protocol present during its review. The report comes after years of complaints by academics inside and outside the school, who claimed the school failed to protect 27-year-old Dan Markinson, who died by suicide in 2004 while enrolled in a psychiatric drug trial. At press time, the Faculty Senate was preparing to meet with University President Eric Kaler and the authors of the report. Senior administrators say they hope to develop a plan to respond to the report within 60 days. <http://scim.ag/Mintrials>

Seeing a virus in 3D

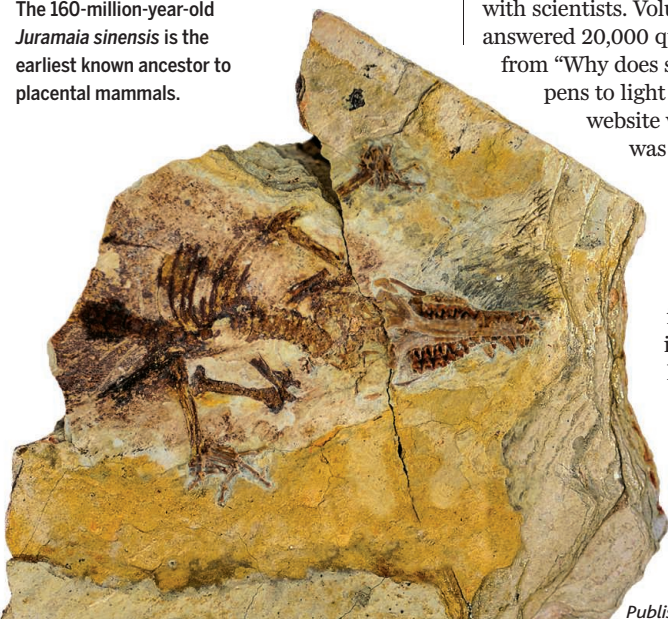
Physicists can take pictures of tiny things from chemical nanostructures to proteins to living cells. But 3D biological particles, like viruses, have proved elusive. To take a 2D image, scientists send pulses of high-energy x-rays through the particle and record the resulting diffraction patterns. Theoretically, they could stitch together multiple 2D images, each taken at a different angle, to create a 3D picture—but they'd need to know how the particle was oriented in space when each picture was taken. Now, researchers working with the Linac Coherent Light Source at SLAC National Accelerator Laboratory in Menlo Park, California, have devised an algorithm that can figure out how hundreds of such diffraction patterns fit together to form a complete 3D image of a sample—a technique, they reported this week in *Physical Review Letters*, that can reveal both the external shape and internal structure of a single particle. They tested their technique by imaging mimivirus (shown), a rather large virus that is probably not infectious. But the algorithm should be able to handle much smaller and more dangerous viruses, including influenza, herpes, and HIV. <http://scim.ag/3Dvirus>



New database for oldest fossils

GREENWICH, CONNECTICUT | Hoping to help scientists understand the origin and evolution of life on Earth, a new repository of data about the world's oldest fossils was launched last week. The Fossil Calibration Database (<http://fossilcalibrations.org/>), funded by the National Evolutionary Synthesis Center, will offer scientists a reliable anchor point from which they can accurately date new fossils and determine when species branched off from their family tree. New fossils are discovered all the time, but until now there was no centralized list of the oldest, so many estimates of evolutionary change rely on "really outdated information," says paleontologist

The 160-million-year-old *Juramaia sinensis* is the earliest known ancestor to placental mammals.



Daniel Ksepka of the Bruce Museum in Greenwich, Connecticut. He co-led the team of more than 20 paleontologists, molecular biologists, and computer programmers behind the project. To ensure the new resource remains a gold standard, new finds will be regularly added after careful vetting by specialists.

Ask A Scientist shuts down

ARGONNE, ILLINOIS | One of the Internet's oldest sources of science information for the public is closing its virtual doors. Argonne National Laboratory announced last month that they will be discontinuing their Newton – Ask A Scientist program on 1 March. Argonne created the service in 1991 as a way for students and teachers to connect with scientists. Volunteer scientists have answered 20,000 questions over the years, from "Why does steel rust?" to "What happens to light in a black hole?" But the website was outdated and its use was declining, says Meridith Bruozas, Argonne's manager of educational programs and outreach. "As technology has advanced ... it kind of doesn't serve its purpose anymore." Instead, the lab has shifted to using Twitter, Facebook, reddit, and Google Hangouts to give students a way to quiz scientists.

BY THE NUMBERS

\$41.5
million

Amount dedicated last week by the National Institutes of Health to the Human Placenta Project to study the mass of tissue that sustains a developing fetus.

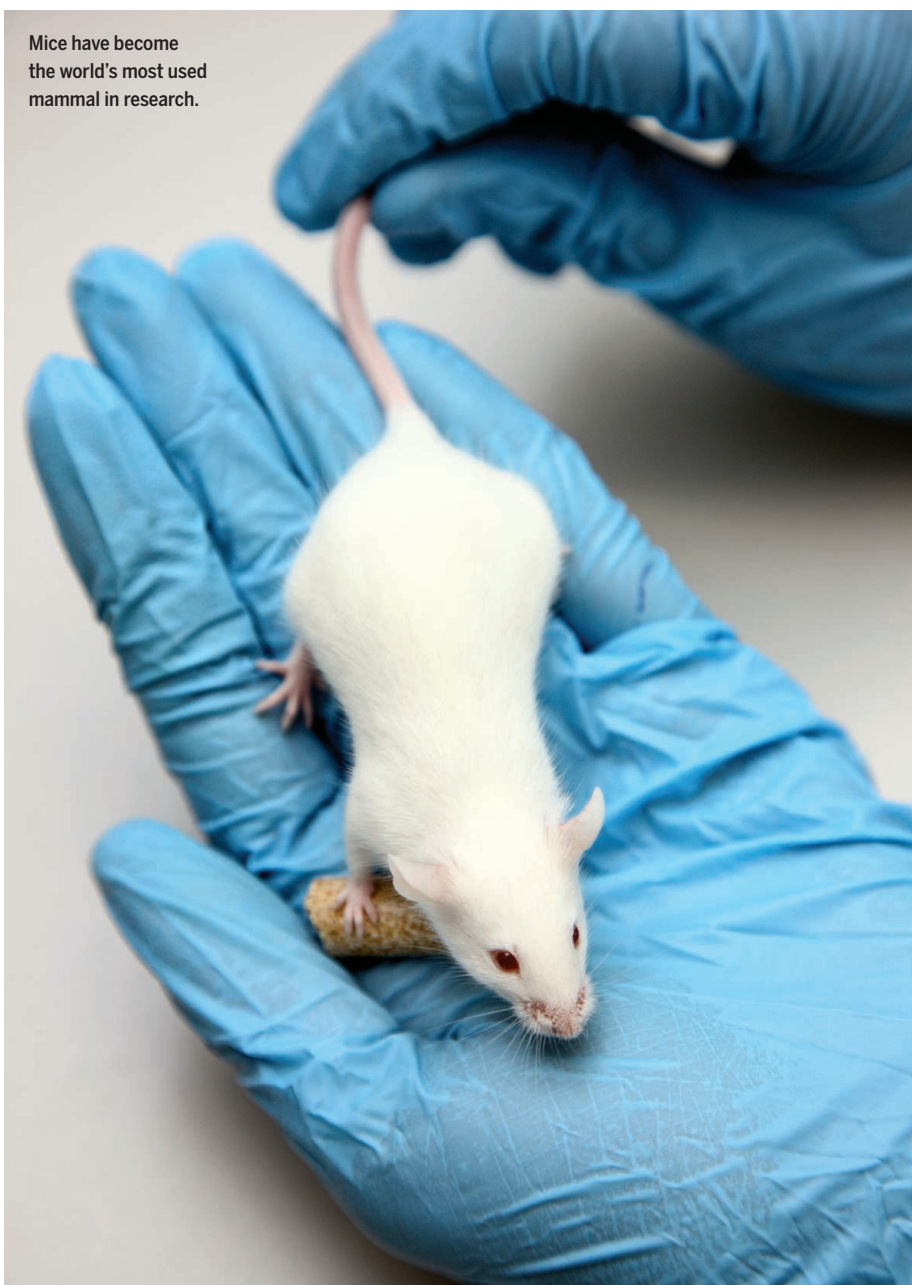
4.1

Average number of Oriental rat fleas—known to carry plague and typhus in the past—per New York City rat in a *Journal of Medical Entomology* survey. Values below 1 indicate minimal risk of epidemic disease spread.

1

Number of physicists now on the U.S. House of Representatives' science committee as of last week, when Representative Bill Foster (D-IL) joined.

Mice have become the world's most used mammal in research.



Rise in U.S. lab animals

The number of animals used by the top U.S.-funded biomedical research institutions has risen 73% over 15 years, a “dramatic increase,” according to an analysis by People for the Ethical Treatment of Animals (PETA). Although federal law requires that research labs report their use of cats, dogs, and nonhuman primates, smaller vertebrates—including rodents—are exempt. To get a sense of the trends, PETA obtained data from inventories submitted to the National Institutes of Health (NIH) every 4 years. The top 25 NIH-funded institutions housed a daily average of 74,600 animals from 1997 to 2003; that leaped to an average of 128,800 a day by 2008 to 2012, a 73% increase, PETA reports in the *Journal of Medical Ethics*. Most of the animals were mice. This parallels a rise in the use of transgenic mice internationally, PETA says. NIH cautioned that using the inventory data to track animal numbers is “inappropriate” because the data don’t show usage, but are only a “snapshot” that NIH uses to make sure institutions have adequate veterinary care. <http://scim.ag/labanimrise>

NEWSMAKERS

HIV researcher admits fraud

In an unusual turn for a scientific misconduct case, a former HIV researcher at Iowa State University (ISU) has pleaded guilty to federal fraud charges. **Dong-Pyou Han** resigned in 2013, shortly before the federal Office of Research Integrity (ORI) found he had faked data in a rabbit study of an HIV vaccine for a National Institutes of Health (NIH) grant proposal. ORI barred Han from seeking grants for 3 years, but Senator Chuck Grassley (R-IA) complained that the punishment was too light for a study that cost taxpayers millions of dollars. ISU later returned \$500,000 and NIH withheld a \$1.4 million award. Han faces up to 10 years in prison on two felony counts of making false statements; his sentencing is set for 29 May.

Three Q's

After 42 years at the Massachusetts Institute of Technology in Cambridge, including 16 years as an administrator, physicist **Marc Kastner** knows the value of basic research—and how to convince rich people to support it at a premier research



institution. Last week he announced he was leaving to become the first president of the Science Philanthropy Alliance—a job that will give him the chance to make the case on a national scale. http://scim.ag/_Kastner

Q: How will the alliance operate?

A: It will not raise any money for itself. Instead, we're trying to increase gifts to universities or help create new foundations that will fund basic research.

Q: Why is that so important today?

A: There's been a tilt in federal funding toward things that are more applied and more translational. My task is to explain to potential donors the enormous opportunities for doing exciting things in basic science and the satisfaction they will get out of that.

Q: Is it OK if the well-endowed universities simply get richer?

A: Absolutely. If foundations choose to be concerned about geography, that's their business. But my experience with these foundations is that they really want to fund the best people to do the best research. And that's fine with me.

PHOTOS: (LEFT TO RIGHT) © JOCHEN TACK/ALAMY; ALLEGRA BOVERMAN

The 325-meter-high Amazon Tall Tower Observatory, a stairway to heavenly air.

ATMOSPHERIC PHYSICS

A pristine Amazon's last stand

Laboratory in the sky will sample some of the last unspoiled air on the planet

By Lizzie Wade

Buffed by wind gusts and an unrelenting sun, Jürgen Kesselmeier spent 2 hours in January slogging up a staircase inside a skeletal, 4-meter-wide steel tower. Scents from the humid forest floor dissipated as he climbed higher, and the winds became gustier. By the time he reached the top, the Amazon rainforest canopy lay 325 meters below, a sea of green stretching to the horizon in every direction. But he wasn't there to take in the awesome view—he was there to take in the awesome air.

Kesselmeier, a botanist at the Max Planck Institute for Chemistry in Mainz, Germany, is one of the leaders of a German-Brazilian team that has just put the finishing touches on the Amazon Tall Tower Observatory (ATTO). Starting last August, the researchers shipped tower components by road and river to the remote jungle site, where the pieces were assembled like “a huge Erector set,” says Meinrat Andreae, a director at the chemistry institute. Taller than the Eiffel Tower, the \$9.4 million ATTO will

allow scientists to sample air as close to pristine as any found on Earth to learn how the rainforest shapes its own weather and influences the global carbon cycle. Meanwhile a sister project, called GoAmazon2014/5, has been using aircraft and ground stations to monitor a major threat to that unspoiled air: the pollution plume from Manaus, a metropolis of 2 million in the heart of the Amazon.

Climbing ATTO is like going back in time. Only 17% of the Amazon's 8.5 million square kilometers is inhabited, says ATTO team member and GoAmazon investigator Paulo Artaxo, an atmospheric physicist at the University of São Paulo in Brazil. “Basically, we have 82% of the forest exactly as it was 1000, 2000, 3000 years ago.” The air above that swath of the Amazon offers a window to a preindustrial world.

To sample it, the ATTO team searched for a tower site that would be unaffected by human activities such as deforestation, pollution, and construction—and hopefully would remain free of encroachment for several decades. But for a laboratory to be feasible, they needed to erect ATTO close

enough to Manaus to get there and back in a single day. The chosen location is 150 kilometers northeast—and, vitally, upwind—of the city, allowing scientists to reach the site in about 6 hours by car and boat. For the most part, the only air that reaches the tower travels from the Atlantic Ocean over 1500 kilometers of undisturbed rainforest.

One feature that sets the Amazon's pristine air apart is a dearth of aerosols—the fine particles around which water vapor can condense to form clouds. Even over relatively unpolluted stretches of North America, there are about 2000 particles per cubic centimeter of air, says Scot Martin, an environmental chemist at Harvard University and a GoAmazon investigator. Over Amazonia, there are only about 300 particles per cubic centimeter.

In most parts of the world, aerosols come from dust, smoke from wildfires, and urban and industrial pollutants. Most Amazon aerosols, on the other hand, are from the rainforest. Plants are constantly emitting microbes in the form of bacteria and spores, as well as volatile organic compounds (VOCs) like isoprene and terpene, which they use for self-defense and for communication with other plants, Kesselmeier explains. Some of those chemical signals are caught in updrafts and react with oxygen and other gases to form complex aerosol particles that seed rainclouds.

Compared with clouds that form over landmasses elsewhere, Amazonian clouds are “very peculiar,” Artaxo says. They

have relatively low tops—similar to ocean clouds—and their raindrops are exceptionally large because of the scarcity of aerosol particles around which they can form. Studying Amazonia's still pristine clouds could help scientists understand the processes that governed aerosol emission, cloud formation, and rainfall back when more of the world was forested and pollution-free, Artaxo explains.

The air washing over ATTO differs from its preindustrial state in one key sense: It is about 50% richer in carbon dioxide, because of human activity. ATTO will also study how the Amazon may be helping slow the rise in CO₂—and whether it will continue to do so in the future. The rainforest sucks vast amounts of carbon dioxide out of the air and converts it to biomass. But some fraction of carbon is released as VOCs and through anthropogenic forces such as deforestation and fires; scientists worry that if enough of the forest is lost, the region could become a net source of carbon. They don't know where the tipping point is, however, because just how much carbon the Amazon takes in and releases today is a mystery. "As long as we do not understand what is really emitted" by the Amazon, Kesselmeier

says, "it's dangerous to deal with the question of what will happen if we change the forest."

ATTO's vantage high above the canopy will allow it to measure concentrations and fluxes of greenhouse gases like carbon dioxide and methane over hundreds of kilometers. It will also be able to collect regional, rather than local, data about other interactions between the forest and the atmosphere, such as aerosol production and transport. "A person who wants to hear a concert would be ill-advised to sit right next to the trombone player," Andreae says. "Our intent [with ATTO's height] is to get away from that trombone-player tree." Antonio Ocimar Manzi, an atmospheric physicist at Brazil's National Institute of Amazonian Research in Manaus and co-coordinator of ATTO with Kesselmeier, hopes that this regional data will help improve climate models and even local

weather forecasts in the Amazon. "Different climate models project very different, contradictory scenarios for annual precipitation in the Amazon," he says. Without more data, "it's not possible to say which model is better," making the future of the Amazon something of a black box.

GoAmazon, meanwhile, is studying an area of the Amazonian atmosphere already under assault from human activity. During last year's wet and dry seasons, the Brazilian-U.S. team behind the project flew air-sampling planes straight into the pollution plume of Manaus. As Martin puts it, "You're surrounded by the year 1750, and then suddenly you're hit with the year 2014"—air rich in particulates, ozone, and oxides of sulfur and nitrogen. The team has also

sampled air from two areas downwind of Manaus, as well as from the ATTO site as a pollution-free baseline. GoAmazon wrapped up its air campaign late last year and will continue to collect ground data through December.

Among the early findings: Manaus's pollution could be changing the very nature of the rainforest. The increased concentrations of sulfates and nitrogen oxides downwind of Manaus, for example, result in smaller and more numerous

aerosol particles that are more capable of forming cloud droplets. "That implies that the clouds are different," compared with those in pristine rainforest air, Martin says. And that could mean "the rainfall is different, the hydrological cycle is different, the ecosystem is different." Changes in the Amazon's hydrological cycle could affect rainfall and drought all over the continent, including in important agricultural areas in southeastern Brazil and northeastern Argentina, Martin says—changes that could be presaged by São Paulo's devastating drought (*Science*, 20 February, p. 812).

Whereas GoAmazon took what Artaxo calls "snapshots" of a degraded Amazon, ATTO will record how long the virgin rainforest can hold out in the changing world. The tower, therefore, may also mark the last stand of the Amazon, before the great rainforest succumbs to our modern era, the Anthropocene. ■

Air assault in the Amazon

As ATTO gets ready to sample the clean Amazonian atmosphere upwind of Manaus, GoAmazon is tracking pollution downwind. Airborne pollutants alter cloud formation and rainfall patterns.



NUCLEAR DISASTER

Muons probe Fukushima's ruins

Unsung imaging technique deployed to find uranium debris in reactors

By Dennis Normile

Japan's Fukushima Daiichi Nuclear Power Station, destroyed 4 years ago in explosions and meltdowns triggered by an earthquake and tsunami, won't be truly safe until engineers can remove the reactors' nuclear fuel. But first, they have to find it. A novel way to map the scattered uranium may have come, literally, from out of the blue. Two groups of physicists plan to capture muons raining down from the upper atmosphere after they stream through the reactor wreckage, resulting in x-ray-like images that could pinpoint the uranium.

The utility that operates the station, Tokyo Electric Power Co. (TEPCO), thinks that after the tsunami knocked out the reactors' cooling systems, most of the fuel in the Unit 1 reactor melted. It burned through the reactor pressure vessel surrounding the core, dropped to the bottom of the containment vessel, and perhaps even ate its way into the concrete base. Units 2 and 3 suffered partial meltdowns, and some fuel may remain in the core. But that's as clear as the picture gets. To devise ways to safely remove the fuel, engineers need much more detail about its location and condition. Radiation levels inside the reactor buildings are too high for workers to venture in for a look. Even tethered robotic devices designed to probe inside the reactors require operators to enter areas with high radiation.

Meanwhile countless muons, generated as cosmic rays slam into the upper atmosphere, are streaming through the reactor innards. Every minute, 10,000 or so of these wispy particles, cousins of the electron, hit every square meter of Earth's surface. Most flow through solid objects unmolested. But a few get absorbed or deflected in proportion to a material's density and thickness, a phenomenon physicists first put to use in the 1950s to study the geology of an underground hydroelectric



Physicists are using muon detectors to locate the nuclear fuel that melted in the cores of three reactors at the Fukushima Daiichi Nuclear Power Station after the earthquake and tsunami of 11 March 2011.

facility in Australia and, in the 1960s, to show that no undiscovered chambers are hiding in the Pyramid of Khafre in Egypt (*Science*, 6 February 1970, p. 832).

Decades later, Kanetada Nagamine, a muon physicist at the High Energy Accelerator Research Organization (KEK) in Tsukuba, Japan, showed that detectors could snare muons spraying sideways, parallel to Earth's surface, from cosmic-ray collisions. He suggested that these muons could be used to identify magma channels in volcanoes, enhancing forecasts of eruptions. He also saw the potential for muon imaging in nuclear disaster zones.

After a reactor at the Chernobyl Nuclear Power Plant in Ukraine exploded in 1986, Nagamine threw out the idea of setting up muon detectors to map damaged fuel, but the Soviet government did not pursue it. When history's second worst nuclear disaster struck in the wake of the magnitude-9 earthquake and massive tsunami that hit Japan on 11 March 2011, Nagamine was ready. Within days of the accident, he sent a proposal to KEK's director general to use muon imaging to investigate the Fukushima reactors. The same idea occurred to Haruo Miyadera, a former student of Nagamine's, then at Los Alamos National Laboratory in New Mexico. But their approaches differ.

The KEK strategy is to flank the reactors with stacks of scintillators: rods made of a plastic that flashes when hit by a charged

particle. The team plans to map muon absorption, which depends on the density of the material it traverses. Uranium, being denser than steel or concrete, will cast a deeper muon shadow, allowing the team to distinguish fuel debris from material in the buildings and reactor vessels.

The team tested the strategy at another nuclear plant, where the plant operator "did not provide any information on the location of the fuel," says Fumihiko Takasaki, a KEK physicist heading the project. The

"How do you get these detectors mounted next to those reactors in that radiation field?"

Christopher Morris, Los Alamos National Laboratory

detectors found the fuel, revealing that it had been moved from the core to a cooling pool, and their resolution was good enough to spot a second cluster of spent fuel rods.

Last month, a TEPCO contractor installed two KEK-built detectors beside Fukushima's wrecked Unit 1 reactor. By the end of this month, Takasaki says, the detectors may have absorbed enough muons to confirm there is no fuel left in the reactor core. But these detectors, placed at

ground level outside the reactor, won't be able to map fuel that may have flowed to the bottom of the containment vessel, at basement level. That will require inspection by robots now under development.

In units 2 and 3, fuel is likely scattered throughout the core, pressure vessel, and containment vessel. For that more challenging imaging assignment, TEPCO is turning to the Los Alamos team. Work on muon detectors there began in the 1990s, when physicist Christopher Morris led a team looking for noninvasive ways to inspect nuclear weapons. They observe muons before and after they pass through an object of interest, using detectors spot muons when they ionize a gas, producing an electrical charge. The signal patterns can reveal how the particles are deflected by atomic nuclei in the material. The angle of deflection depends on the number of pro-

tons in the nucleus, identifying the element that the muon grazed, and the location of the collision.

The technology has already been commercialized to scan cargo containers and trucks for contraband nuclear material. "The detectors can spot 20 kilograms of uranium in less than a minute," Morris says. The team has tested their technique on research reactors to verify that it will also work at Fukushima, but they face a practical problem: installing their mammoth 7-by-7-meter detectors at Unit 2. "How do you get these detectors mounted next to those reactors in that radiation field?" Morris asks. Toshiba Corp., which supplied two of Fukushima's six reactors, is building the detectors and will install them later this year, says Miyadera, who joined Toshiba to oversee the project.

The KEK and the Los Alamos-Toshiba teams are both supported by the International Research Institute for Nuclear Decommissioning, established by TEPCO, Toshiba, and other public and private sector entities to develop new technologies needed for the Fukushima cleanup. The institute won't say what the muon-imaging efforts will cost. One thing is certain: The cost of pinpointing Fukushima's uranium debris will be trivial compared with that of devising a plan and the technologies for removing it. Decommissioning could take 30 to 40 years and, TEPCO says, cost at least \$8 billion. ■



EDUCATION

Why many U.S. biology teachers are 'wishy-washy'

Future science teachers lack knowledge and role models

By Jeffrey Mervis

When two political scientists asked a group of U.S. college students preparing to become biology teachers about their views on evolution, they were shocked by the answers. "I'm, you know, pretty ignorant on this topic ... is there enough of scientific evidence to say for sure?" one replied. "Evolution is one of those subjects that I'm still a bit shaky about," answered another.

Michael Berkman and Eric Plutzer of Pennsylvania State University (Penn State), University Park, knew from a previous study that more than half of the country's high school biology teachers did a poor job in their classrooms with evolution. But they didn't know why. Was the topic absent from the curriculum? Did the teachers fear a community backlash? Or were they simply choosing to avoid the subject?

Their new study suggests teachers avoid the controversial topic, and it offers a reason: Teachers lack the necessary knowledge, conviction, and role models to teach evolution properly. "Not feeling confident about your knowledge of evolution," Berkman says, "leads to being less likely to teach it."

"It absolutely makes sense," says evolutionary biologist Leslie Rissler, who this winter joined the National Science Foundation after leaving a tenured position at the University of Alabama, Birmingham, where she taught

evolution to undergraduates. Even biology majors have little opportunity to learn about the topic, says Rissler, who recently surveyed 3000 Alabama students on what they think and know about evolution and found their religious faith trumps any book learning.

The Penn State paper, which labels such future teachers "Enablers of Doubt," is one of 15 articles on "The Politics of Science" appearing this month in *The Annals of the American Academy of Political and Social Science*. The package explores why many people—regardless of their education or ideological and cultural affiliations—routinely disregard solid scientific evidence in forming their views (<http://scim.ag/scienceattitudes>).

In their earlier study, in 2007, Berkman and Plutzer surveyed a national sample of 926 high school biology teachers to better understand teachers' role in the country's long-running battle over evolution. They found that 13% were openly sympathetic to creationism, while 28% provided students with a thorough understanding of evolution. The rest, which the researchers label "the cautious 60%," spent as little time as possible teaching this most fundamental concept in modern biology.

"Where is this wishy-washiness coming from?" Berkman says they asked. Everything pointed to the teachers themselves," he says, and "we realized we didn't know much about them."

So in 2013 the researchers conducted focus

Poorly prepared science teachers often leave U.S. high school students with a shaky grounding in evolution.

groups with 35 teacher trainees at four Pennsylvania colleges—a large research university, a master's granting institution, a Catholic college, and a historically black university. What they learned deeply troubled them.

"We found that the depth of their scientific understanding is not what you'd think it would be," Berkman explains. Adds Plutzer: "These students are not the ones who were taking apart washing machines or launching rockets when they were kids. They are not driven to become scientists."

Seeing themselves as educators, the future teachers said they planned to use their pedagogical skills, rather than their knowledge of biology, to handle any conflicts over evolution that might crop up in their classrooms. "I think that education in general is probably about 90% classroom management," one student said. "You can learn content fairly easily. [But] it takes training and skill to actually be able to teach that content."

Students at the Catholic college were more comfortable discussing the potential conflict between evolution and religion than were their peers at secular institutions, the researchers found. "It struck us that they probably had been wrestling with the issue their entire lives, and they seemed to do a better job of reconciling their beliefs with what they had learned about evolution," Berkman says.

In contrast, the researchers say, students at secular institutions are unlikely to have the opportunity to explore their personal or religious views in a science or education class. "You're not going to get a Penn State professor to talk about that with their students," Berkman surmises.

The researchers admit that their small sample provides a range of views and is not representative of all U.S. science teacher-training programs. But they think the responses send up a red flag: "Young preservice teachers are already on a path that is likely to lead to evolution instruction that falls short of the expectations of leading scientific organizations," they conclude.

Reversing direction will require breaking out of a "cycle of ignorance," the researchers believe. "Many students lack good models for teaching evolution in public schools" because they weren't taught the subject well in high school or college. More trainees also need better hands-on grounding in what the researchers call "the nature of scientific inquiry," such as working in a research lab.

Faculty need to understand, Plutzer says, that "future science teachers are not junior versions of themselves. ... Getting them to understand evolution is not simply a matter of having them take more science courses." ■

INFECTIOUS DISEASES

Doubts dispelled about HIV prevention

New studies show remarkable efficacy and versatility of drugs for uninfected

By **Jon Cohen**, in Seattle, Washington

It was great news for HIV prevention, and few seemed to hear it. Five years ago, researchers showed that people likely to be exposed to HIV can cut their risk of infection with a simple pill, but the strategy has been slow to catch on. At the Conference on Retroviruses and Opportunistic Infections (CROI) here last week, a bevy of new studies quelled most remaining doubts about the real-world effectiveness of what's known as pre-exposure prophylaxis (PrEP), showed practical ways to use it, and suggested that it could help change the trajectory of the epidemic.

"This meeting is a watershed event for PrEP," said Robert Grant, a virologist at the University of California, San Francisco (UCSF), one of the pioneers of this approach. Others likened the meeting to the 1996 AIDS conference in Vancouver, which broadcast to the world that potent cocktails of antiretroviral (ARV) drugs could effectively treat the infection.

Grant led a pivotal study of PrEP that showed in 2010 how the ARV Truvada cut the rate of new infections in men who have sex with men (MSM) and transgender women by 92%—if they took the pill daily. The problem was that about half the people in the study didn't, which left the overall efficacy at a modest 44%. Later, a large study in heterosexual "discordant" couples, in which only one partner was infected, found that adherence was much better, yielding 75% protection.

But, despite approval by the U.S. Food and Drug Administration, PrEP has never gained much traction. Health workers have hesitated to prescribe it because of worries that PrEP would lead men to forgo condoms—so-called behavioral disinhibition—negating much of the benefit. Some at-risk people have not used PrEP because they fear it will brand them as promiscuous or reckless. Young, single women appear especially reluctant to use the drug. "Adherence

[is] the Achilles' heel of PrEP," said Jean-Michel Molina of Paris Diderot University.

In a study called IPERGAY, Molina and his colleagues investigated whether PrEP might work better if people did not have to take pills every day. They tested a more convenient "on-demand" regimen in 414 HIV-negative, high-risk MSM in France and Canada. The men were instructed to take pills—without knowing whether they contained Truvada or a placebo—before and after having sex. As Molina ex-

545 MSM in the United Kingdom, gave the conventional regimen of PrEP to half the participants and compared their behavior and HIV infection rates with a control group that started PrEP a year later. This design differed from the initial studies in MSM in two key ways: No one received a placebo, and participants knew that, if used, the pills offered strong protection.

PROUD was stopped early after 19 people in the deferred group became infected compared with three in the immediately

treated group—again, 86% efficacy. Other sexually transmitted infections or reported sexual behavior were no different in the treated and control groups. "Our concerns that PrEP would be less effective in the real world were unfounded," said PROUD's leader, Sheena McCormack of University College London.

A third, ongoing study led by Jared Baeten of the University of Washington, Seattle, identified a way to boost the effectiveness of PrEP in discordant couples. If an infected partner takes ARVs and fully suppresses the virus, there is little risk of transmission. But some infected people opt not to take the drugs or do not have access to them. And even in those who do start treatment, it can take several months for the drugs to reach full power, leaving a window for transmission. Baeten and colleagues explored ways to deal with those scenarios.

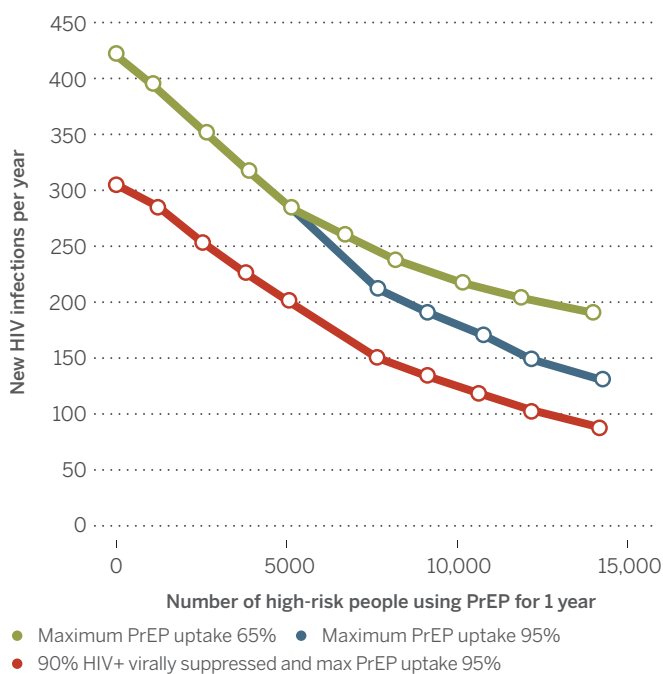
In 1013 discordant couples in Kenya and Uganda, the researchers are offering PrEP to all uninfected people to protect them for the first 6 months after their

partners start ARVs. In couples where the infected partner does not start treatment, the PrEP "bridge" is extended for as long as necessary. To date, only two people have become infected in the study, compared with 40 predicted by modeling, and neither had Truvada in their blood when transmission occurred. Baeten said that using PrEP as a bridge "is not only feasible in this higher risk population, but highly effective."

The potential payoff of widespread PrEP could be huge, UCSF's Grant showed in a

The pills that could blunt an epidemic

A model shows that widespread use of pre-exposure prophylaxis, especially when combined with increased treatment of HIV-infected people, could change the course of San Francisco's epidemic.



plained, 14 people became infected in the placebo group versus two in the treated arm—both of whom had stopped taking the drug months before their infections occurred—amounting to an 86% drop in infections. "On-demand PrEP could be a game changer in PrEP use," Molina said.

A second study found that adherence might not be as big a problem in the real world as it was in the initial studies and that behavioral disinhibition did not occur. The PROUD trial, conducted in

modeling study of the San Francisco epidemic, in which only 31% of people at high risk of infection used PrEP at some point last year. If 65% of these people used PrEP for 12 months, the number of annual new infections would be halved. That drop

could double again by aggressive use of both PrEP and treatment (see graphic). “We’re at a tipping point where PrEP was a proven concept of unknown applicability,” Grant said, “and what’s most exciting is we can now see that is feasible.” ■

Drug flushes out hidden AIDS virus

By Jon Cohen, in Seattle, Washington

HIV/AIDS researchers call it “shock and kill”—a way to obliterate the final reservoir of latent virus that stands between an infected person and a cure. Last week at a major HIV/AIDS conference here (see main story, p. 1055), a team reported new results from a monkey study that move a few steps toward that grand but elusive goal.

Strong cocktails of antiretroviral (ARV) drugs can knock down blood levels of HIV to undetectable on standard tests, but they have not cured anyone. That’s because small “reservoirs” of long-lived cells have viral DNA sleeping in their chromosomes, where it is impervious to drugs and invisible to the immune system. So cure researchers have hunted for ways to shock these cells into producing the virus, causing them to self-destruct or be killed by the immune system.

Most cure strategies have focused on the first step: waking up the virus. But virologist James Whitney of the Beth Israel Deaconess Medical Center in Boston described a drug that appears to deliver a one-two punch: It both wakes up the virus sleeping in immune cells and then, as an added bonus, revs up the immune attack against the infected cells. “It’s a magic combination effect,” says Steven Deeks, an HIV cure researcher at the University of California, San Francisco.

Gilead Sciences of Foster City,

California, is testing the drug, known as GS-9620, in people who have hepatitis B. GS-9620 works by binding to immune cell surfaces through what is known as toll-like receptor 7 (TLR7), triggering a response that includes inducing CD4 white blood cells to make copies of themselves. These are the same white blood cells that HIV favors. Because HIV-infected CD4s produce the virus when they replicate, a team at Gilead led by Romas Geleziunas wondered whether their TLR7 drug might help eliminate HIV reservoirs.

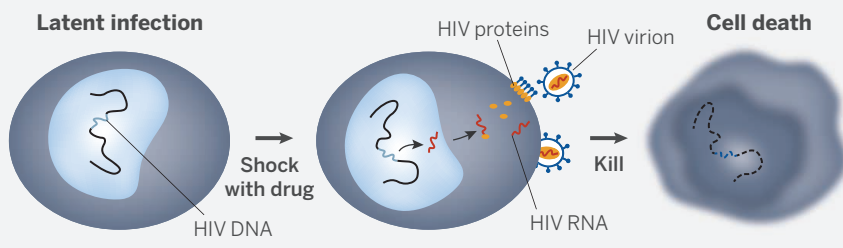
The researchers infected 10 rhesus macaques with SIV, a simian AIDS virus, and treated them with ARVs to suppress the virus to undetectable levels. Then they gave four of the animals repeated injections with an analog of GS-9620. Blood levels of SIV rose to high levels in the four treated animals, indicating that the drug had prodded reservoirs to produce virus. Other attempts to shock cells harboring latent HIV have led only to tiny blips of virus. “You don’t need binoculars to see these blips,” Geleziunas said.

The experiment did not cure the monkeys of SIV. But later analysis showed that after the shock with the drug, SIV DNA levels dropped in the blood, lymph nodes, and colons of three of four animals. That suggested the reservoir had shrunk, although the precise mechanism of cell killing is unclear.

Geleziunas says small studies of GS-9620 in HIV-infected people are about to begin. ■

Draining the reservoir

A drug that targets the TLR7 receptor shocked cells with latent HIV infections into producing the virus, setting them up for the kill.



PALEOANTHROPOLOGY

Deep roots for the genus Homo

Fossil jawbone pushes back origins of our genus by 400,000 years

By Ann Gibbons

On a hot January morning 2 years ago, Chalachew Seyoum was searching for fossils at a desolate site in Ethiopia called Ledi-Geraru, where no human ancestor had turned up in a decade of searching. But Seyoum, an Ethiopian graduate student at Arizona State University (ASU), Tempe, was upbeat after a week off. “I had a lot of energy and fresh eyes,” he says. “I was running here and there. I went up a little plateau and over the top when I spotted this specimen popping right out.”

He sat down and closed his eyes. When he opened them, he could more clearly see the gray fossil poking out of the bleached sand and mudstone, and he realized that he had found the jawbone of a hominin—a member of the human family. He called out for the ASU expedition leader: “Kaye Reece!” Reed scrambled up the steep slope on her hands and knees, saw the fossil, and yelled “Woo-hoo!”

Their excitement was justified. In two papers online this week in *Science* (<http://scim.ag/BVillmoare>; <http://scim.ag/ENDiMaggio>), the ASU team and co-authors introduce the partial lower jaw as the oldest known member of the genus *Homo*. Radiometrically dated to almost 2.8 million years ago, the jaw is a window on the mysterious time when our genus emerged. With both primitive and more modern traits, it is a bridge between our genus and its ancestors and points to when and where that evolutionary transition took place. As a transitional form “it fits the bill perfectly,” says paleontologist Fred Spoor of University College London.

Together with a reassessment of known fossils, published in *Nature* this week by Spoor and colleagues, the find is stimulating new efforts to sort out the mixed bag of early *Homo* remains and to work out which forms emerged first. “This causes us to rethink early *Homo*,” says paleoanthro-

ILLUSTRATION: ADAPTED FROM SHARON LEWIN/UNIVERSITY OF MELBOURNE

pologist Bernard Wood of George Washington University in Washington, D.C.

Researchers agree that small-brained hominins in the genus *Australopithecus* evolved into early *Homo* between 3 million and 2.5 million years ago, but the *Homo* fossil trail disappears at the crucial time. Until now, the oldest known *Homo* fossil was a 2.3-million-year-old upper jaw from Hadar, Ethiopia, that has not been classified into a species. It and other early *Homo* fossils paint a confusing picture. Some have big skulls, others small; some consist of a bit of skull, others only a jaw, resulting in a grab bag of mismatched parts. As a result, researchers have argued about whether there was a single species of early *Homo* or three. The type specimen of *H. habilis*, for example, includes a 1.8-million-year-old lower jaw called OH 7 from Olduvai Gorge in Tanzania (*Science*, 17 June 2011, p. 1370). But the type specimen of another species, *H. rudolfensis*, is a 2.1-million-year-old skull without teeth or a lower jaw.

This week's papers advance the work on two fronts. Spoor and colleagues created a virtual reconstruction of the OH 7 specimen, which was found 55 years ago, to correct for postmortem distortion. They used computed tomography and 3D imaging to digitize and reassemble pieces of the jaw in the computer. Then they compared OH 7 with other specimens and found that it has more primitive features, such as a long, narrow palate, than do the older Hadar jawbone and members of *H. rudolfensis*. Although OH 7 itself is relatively recent, their analysis suggested that *H. habilis* arose earlier than the other two species.

Meanwhile, the ASU team spent years doing targeted searches for an older ancestor. They hunted in sediments that were the right age—2.58 million to 2.84 million years old—and in an epicenter of early human evolution. Ledi-Geraru is only 30 kilometers from Hadar, home of the 2.3-million-year-old *Homo* jaw, as well as to more than 100 individuals of *Australopithecus afarensis*, the species of the famous skeleton called Lucy. The oldest known stone tools, dated to 2.6 million years ago, are only 40 km away at Gona.

The new Ledi-Geraru discovery fits best in *Homo*, says ASU paleo-anthropologist William Kimbel. Its



This partial lower jaw from Ethiopia is the oldest example of our genus *Homo*.

molars are slimmer than those of *Australopithecus*, the third molar is smaller, and the jawbone is shaped differently. The ASU team hasn't assigned the jaw to a species yet because they hope to find more parts, but say that it most closely resembles *H. habilis*.

In fact, the new jaw looks a lot like what Spoor imagined for the ancestor of OH 7. That suggests that although the two specimens are separated by almost 1 million years, they belong to the same lineage, and that the oldest *Homo* looked most like *H. habilis*, just as Spoor and others have predicted.

But the Ledi-Geraru specimen is not likely

to be a member of *H. habilis* itself, Spoor says. The jaw also has traits that link it with *A. afarensis*, such as a rounded chin region. The similarities strengthen the proposal that Lucy's species, which lived from 2.95 million to 3.8 million years ago, was the direct ancestor of *Homo*. But other types of australopiths also lived during that time, making the genealogy exercise premature.

The ASU team does rule out *A. sediba* from South Africa as the *Homo* ancestor, because at 1.9 million years old it is too recent. But its discoverer, paleoanthropologist Lee Berger of the University of the Witwatersrand in Johannesburg, South Africa, says that the known *A. sediba* skeletons might simply be late examples of the species.

The new data may help solve a puzzle: Why did so many kinds of hominins roam East Africa between 2 million and 3 million years ago? To understand this burst of evolution, the ASU team analyzed the bones of other species living at that time. As they report in the second *Science* paper, fully one-third of the Ledi-Geraru mammals were new species, not seen in older sediments at nearby Hadar.

Three million years ago, Hadar was home to monkeys, giraffes, and elephants that favored a patchwork of woods and grasslands. Ledi-Geraru hosted a different fauna just 200,000 years later, with grazers such as gazelles, zebras, wild pigs, and a baboon at home in open grasslands like the Serengeti. Climate change and the shift to more open terrain may have spurred the emergence of many species, including members of *Homo* and *Australopithecus*, Reed says. "This is a snapshot of a hominin in a landscape that's really open," agrees paleoclimatologist Peter deMenocal of Columbia University's Lamont-Doherty Earth Observatory in Palisades, New York, who has argued that climate change sparked intense periods of speciation.

Researchers often reconstruct ancient climate from clues in sediment cores. To better correlate climate and human evolution, in 2013 researchers cored lakebeds close to key fossil sites (*Science*, 2 August 2013, p. 474). "Stay tuned," deMenocal says. "We'll be answering this [climate question] within a year." ■

Homeland for *Homo*

The oldest known fossil of our genus comes from an evolutionary hotspot in Ethiopia, a place already known as the home of *Australopithecus afarensis* (Lucy's species); the oldest stone tools; and younger *Homo* specimens.



FEATURES

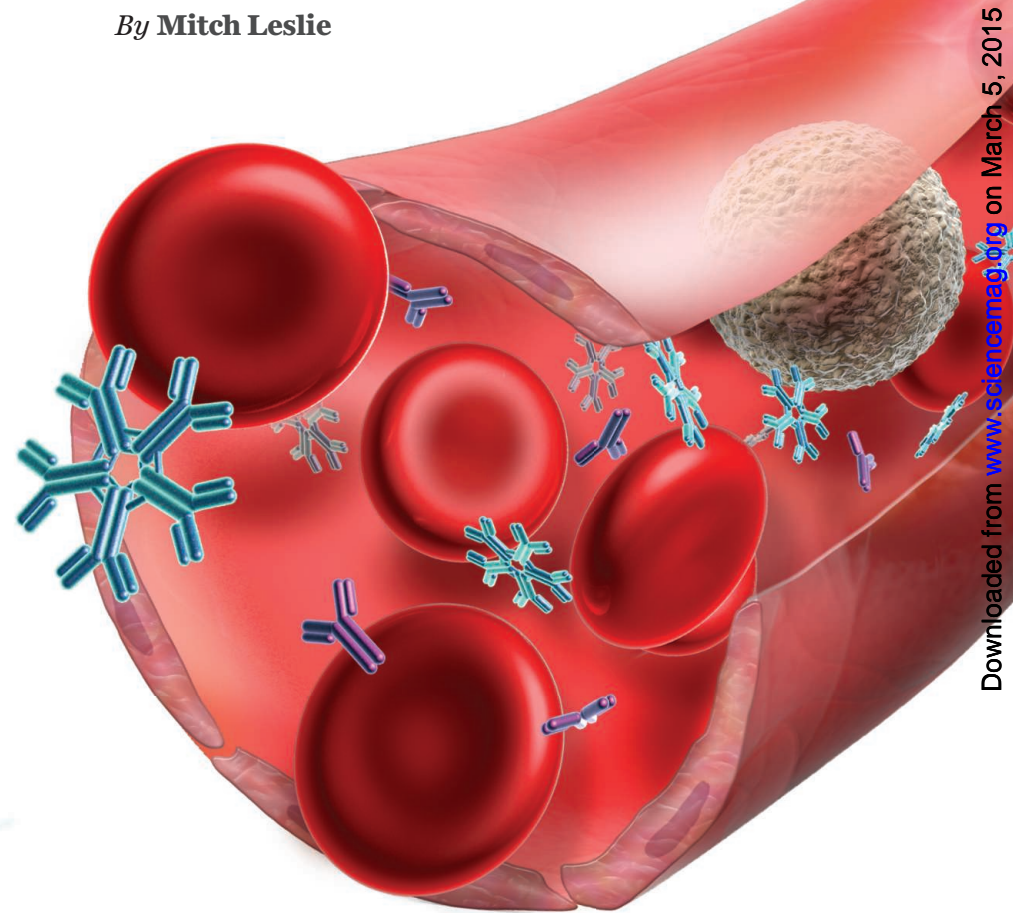
CLEANUP CREW

Unorthodox immune proteins called natural antibodies target pathogens and remove cellular and molecular waste

By Mitch Leslie

No one's fingers fell off during the clinical trial of a potential drug called rHIgM22 that wrapped up earlier this year. That may seem like a questionable measure of success, but U.S. Food and Drug Administration (FDA) reviewers were worried about this potential consequence, notes Moses Rodriguez, one of rHIgM22's discoverers. The protein, an antibody, is a possible treatment for multiple sclerosis (MS), a disease in which the body's own immune system destroys the myelin insulation around nerves. But rHIgM22 works in bunches of five, and the FDA officials fretted that those molecular clumps would jam narrow blood vessels in a person's fingers, cutting off circulation and killing tissue. This initial trial was designed to check for side effects. "I feel confident in that we accomplished the primary goal" of showing that the antibodies are safe in humans, says Rodriguez, a neuroscientist at the Mayo Clinic College of Medicine in Rochester, Minnesota.

Further studies will be needed to back up his confidence about rHIgM22's safety, but even this first trial could reveal some signs of therapeutic action. The company that conducted the trial, Acorda Therapeutics of Ardsley, New York, is now analyzing data for the 72 MS patients who received the antibody or a placebo. The results could provide tentative evidence that the antibody stimulates the regrowth of lost myelin. "If there is even a hint of efficacy there will be a big

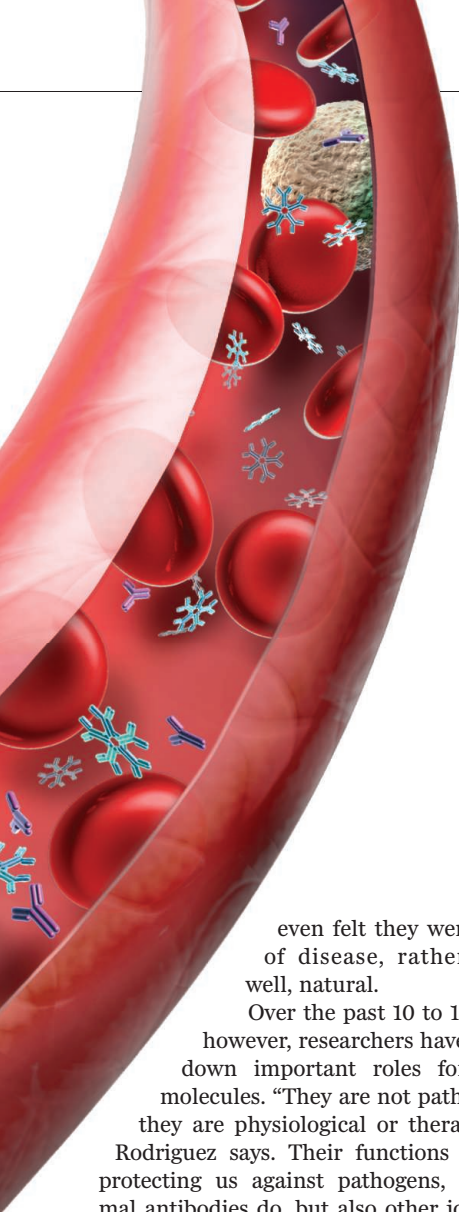


Natural antibodies like these five-armed structures break many of the immune system's rules—and are crucial for our health.

celebration," says Rodriguez, noting that no myelin-repairing treatment has received FDA approval so far.

Any suggestion of remyelination would also represent an impressive clinical debut for the unconventional group of antibodies to which rHIgM22 belongs. Although immunologists discovered so-called natural antibodies more than 100 years

ago, for decades "they were unexplainable," says immunologist Abner Notkins of the National Institutes of Health (NIH) in Bethesda, Maryland. "It was unclear what they did, where they came from, and where they fit into the greater perspective," agrees immunologist Gregg Silverman of New York University Langone Medical Center in New York City. Some researchers



even felt they were signs of disease, rather than, well, natural.

Over the past 10 to 15 years, however, researchers have nailed down important roles for these molecules. “They are not pathogenic; they are physiological or therapeutic,” Rodriguez says. Their functions include protecting us against pathogens, as normal antibodies do, but also other jobs that could turn them into useful tools for medicine. Natural antibodies help dispose of the billions of cells that die or commit suicide in our bodies every day, and they rein in inflammation-promoting immune cells such as macrophages. When they falter, disease can develop. A failure to clear cellular detritus may promote development of autoimmune illnesses. And people who’ve had strokes or heart attacks or who suffer from Alzheimer’s disease show reduced blood levels of certain natural antibodies.

The growing understanding of natural antibodies has helped reshape how researchers think about our body’s defense system. Immunologists long thought that antibodies that target the body’s own molecules, or self-antigens, are a sign of trouble—the trigger of autoimmune diseases such as systemic lupus erythematosus (SLE) and rheumatoid arthritis. The discovery that many natural antibodies react to self-antigens in order to perform beneficial functions such as cleaning up debris or damping inflammation suggests that the

immune system is more forgiving than conventional wisdom held. “The whole idea that the immune system can’t tolerate auto-reactivity is overstated,” Silverman says.

LIKE STANDARD ANTIBODIES—often known as immune antibodies—natural antibodies are made by the immune cells known as B cells. But there are some key differences. Whereas our bodies pump out immune antibodies in response to a pathogen or a vaccine, we start making natural antibodies before birth, although we typically aren’t exposed to pathogens in the womb. Even germ-free mice reared in sterile surroundings harbor natural antibodies. And in contrast to the specificity of immune antibodies, many natural antibodies are polyreactive, with each one recognizing and attaching to a range of disparate antigens.

Our bodies have many uses for these unconventional antibodies, researchers are finding. They help form a first line of protection against microbial invaders and “make a big difference to survival,” says Michael Ehrenstein, an immunologist at University College London. Researchers have discovered that mice unable to produce natural antibodies or to release them into their blood are vulnerable to an assortment of pathogens, from flu viruses to toxic fungi. Natural antibodies apparently keep an invader at bay until the body can start making specific immune antibodies against it.

How natural antibodies can mount an effective defense was a puzzle. Because they

“We have 200 billion cells that die every day, and we need to get rid of them.”

Gregg Silverman. New York University

are specific, immune antibodies bind tightly to particular pathogens, killing the invaders or stimulating other immune defenses, such as macrophages, to do the job. But the poly-reactivity of natural antibodies suggested to some researchers that they would attach to pathogens too loosely, offering limited protection. Eight years ago, NIH’s Notkins and his colleagues put those concerns to rest, showing that a particular polyreactive antibody was a killer—it directly dispatched bacteria or indirectly triggered their demise.

More recently, a research team has revealed that another type of natural antibody, known as IgG, defends the body by teaming up with other molecules. Immunologist Jeak Ding of the National University of Singapore and her colleagues have determined that natural IgG proteins pair up with

molecules called lectins. In the body, lectins recognize and fasten to pathogens but can’t kill them. “It’s a weak defense,” Ding says. But when lectins and natural IgG antibodies attach to microbes together, they trigger the pathogens’ destruction by immune cells, she and her team reported in 2013 in *The EMBO Journal*.

NATURAL ANTIBODIES TAKE ON much more than standard immune duties. Their ability to recognize self-antigens enables them to perform a vital function—clearing away cellular junk. As Silverman notes, our bodies have to cope with cellular carnage. “We have 200 billion cells that die every day, and we need to get rid of them.”

The first inkling of this function came when researchers discovered that many natural antibodies bind to molecules exposed by dead and dying cells, including DNA and damaged lipids from the cell membrane. The bound antibodies then induce janitorial cells such as macrophages and dendritic cells to consume the detritus, reducing the inflammation that cell corpses can trigger. Natural antibodies aren’t the body’s only mechanism for flagging dead cells for disposal, Silverman says, but “it’s an added safety level.” Although macrophages and dendritic cells themselves can promote inflammation, natural antibodies also bind to those cells and prevent them from spilling inflammatory molecules, Silverman and colleagues showed in a 2009 study.

rHIgM22, the antibody Rodriguez and colleagues discovered and hope to use for restoring myelin, may work in the waste disposal business. They saw the first hints of its activity nearly 30 years ago in mice infected with a virus that destroys their myelin, creating an animal model of MS. The researchers injected the mice with spinal cord material, expecting that it would spur an immune response that would increase myelin loss. But the opposite happened—the mice regrew myelin, suggesting that the spinal cord material triggered the release of factors that stimulated the insulation’s repair. Rodriguez and colleagues identified these factors as polyreactive natural antibodies.

To find human versions of the antibodies, the researchers turned to an unusual source: blood samples from people who have multiple myeloma—a cancer of the antibody producing B cells—or other illnesses that induce a surge in natural antibodies. By sifting antibodies from those blood samples and testing their ability to trigger remyelination in mice, the researchers identified two human natural antibodies with therapeutic promise. They were able to engineer cells to manufacture one of them, rHIgM22.

Exactly how the antibody triggers myelin repair is unclear. The antibody might help sweep away debris that collects around nerves. Removal of this junk might enable myelin-producing cells to move in and lay down new insulation for the nerve. Rodriguez and colleagues also suspect that it stimulates the cells to manufacture myelin.

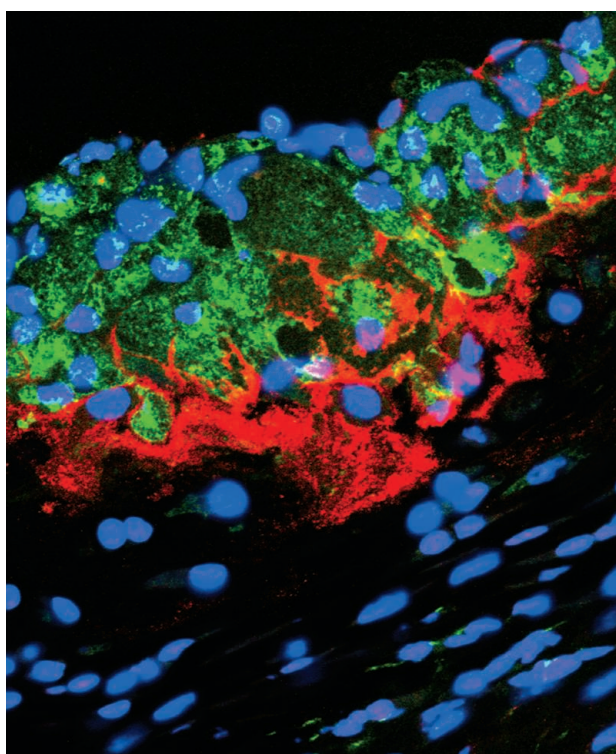
Neuroscientist Howard Weiner of Harvard Medical School in Boston, who studies myelin and isn't connected to the trial or Rodriguez's research, says he is cautiously optimistic about the antibody approach. But he notes that many multiple sclerosis patients wouldn't benefit, because their nerves are already seriously injured or even broken. Still, if the antibody does spur myelin to regenerate in humans "it would be very big," he says. The drug "wouldn't stop multiple sclerosis, but it could reverse some of the damage" caused by the disease.

RESEARCHERS HAVE FOUND

that natural antibodies' housekeeping tasks go beyond tidying up dead cells. They are part of "an endogenous waste removal system that allows us to get rid of cellular waste products that are generated all the time," says immunologist Christoph Binder of the Medical University of Vienna. He and his colleagues have determined that almost one-third of natural antibodies target molecules in the body that have been oxidized in the course of metabolism, such as low-density lipoprotein (LDL), the form of cholesterol that doctors are always nagging people to lower. Oxidized LDL drives atherosclerosis when it amasses in the lining of arteries, and natural antibodies attach to oxidized LDL, sparing the unaltered form.

Studies on mice and humans suggest that natural antibodies protect against atherosclerosis. For example, researchers found that injecting a type of natural antibody into mice slowed fat buildup in blood vessels of the animals' tails. Moreover, last year Silverman and colleagues reported that people who have the autoimmune disease SLE are more likely to develop plaques in the carotid arteries—a common complication of the disease that can lead to strokes—if they have low levels of natural antibodies.

Binder and colleagues hypothesize that natural antibodies inhibit atherosclerosis through their interactions with macrophages and oxidized LDL. Macrophages



Natural antibodies (red) that bind to oxidized LDL molecules adhere to the lower surface of an atherosclerotic plaque in a mouse's blood vessel.

gather in atherosclerotic lesions and gorge on oxidized LDL, and their diet can trigger inflammation or cause them to die. But macrophages have more than one mechanism for swallowing oxidized LDL, and natural antibodies may spur them to use a less self-destructive mechanism, in effect preventing the cells from eating themselves to death. In addition, natural antibodies might trigger removal of any macrophages that have perished. Researchers have just started to investigate whether they can use natural antibodies as atherosclerosis treatments, Binder says.

"The whole area of human natural antibodies as therapies is just beginning."

Moses Rodriguez,

Mayo Clinic College of Medicine

NATURAL ANTIBODIES MIGHT WARN of disease as well as fight it. Cell biologist Robert Nagele of the Rowan University School of Osteopathic Medicine in Stratford, New Jersey, and colleagues have found that levels of some natural antibodies were higher in patients with Alzheimer's disease or Parkinson's disease. Using measurements of only 10 natural

antibodies, Nagele and colleagues could distinguish people with Alzheimer's disease from healthy people 96% of the time. And they reported a similar success rate for people with Parkinson's disease. Large numbers of brain cells die in both diseases, and the natural antibodies might reflect rising amounts of cellular debris. Because there is no definitive test for either illness, tallying natural antibodies could afford a new approach to diagnosis, Nagele suggests.

Work by clinical immunologist Emmanuel Zorn of the Columbia University Medical Center suggests that measuring levels of natural antibodies might also predict the life span of a transplanted organ. The immune system starts attacking such an organ immediately after the patient receives it, triggering what's termed acute rejection, he notes. Thanks to drugs that suppress immune cells, "today, it is very well managed," he says. The main problem now is chronic rejection, the protracted immune attack that erodes the or-

gan over many years.

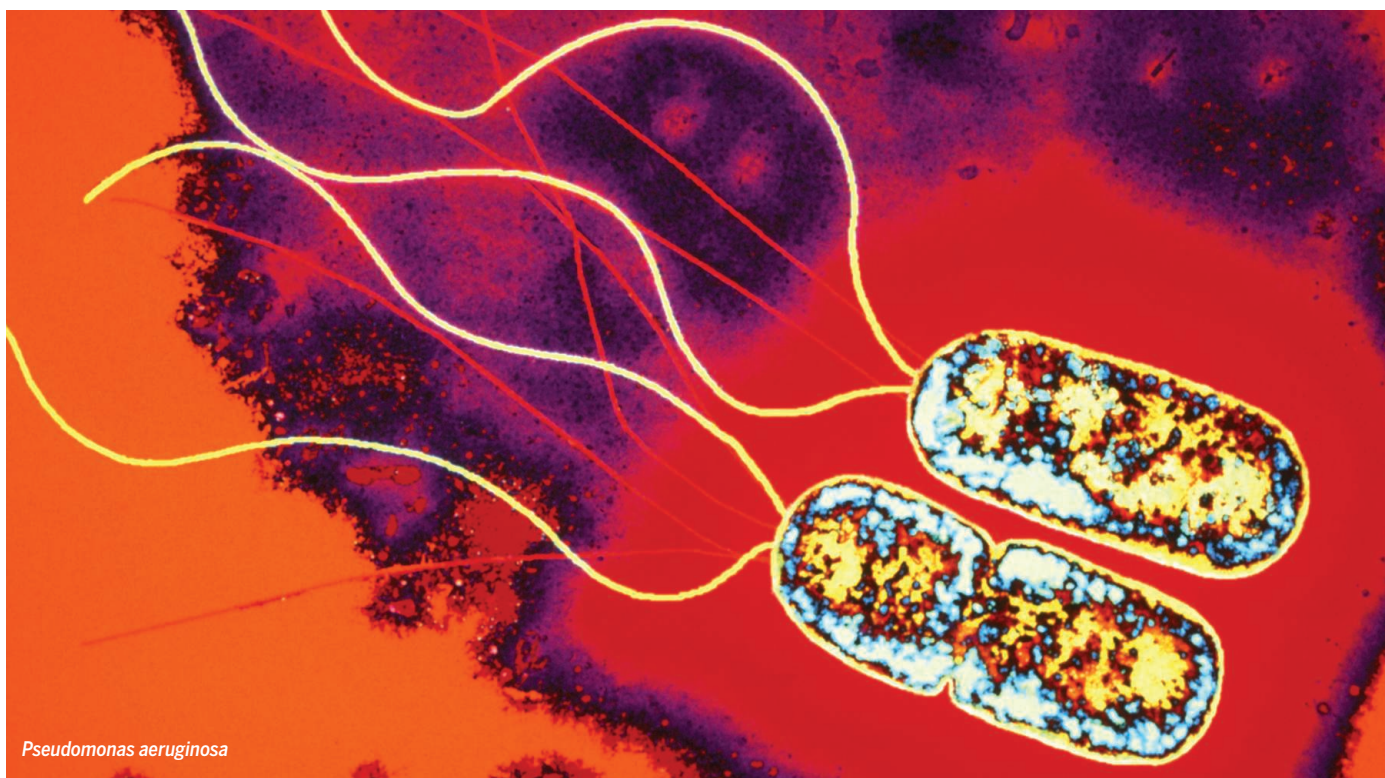
Zorn and colleagues hypothesize that natural antibodies are one of the culprits in chronic rejection—or may at least indicate when it's likely to occur. Last year in the *American Journal of Transplantation*, the researchers reported an analysis of stored blood samples—some dating as far back as 1999—taken from people before kidney transplant surgery. The higher the level of natural antibodies in the samples, the more likely a person was to have lost the transplanted kidney to chronic rejection, the researchers found.

The natural antibodies might be attacking the transplanted kidney directly. But they might also signal that the recipient's immune system will respond vigorously to the transplant and trigger its deterioration. In either case, Zorn says, evaluating potential recipients' natural antibody levels before transplantation might reveal how likely they are to reject an organ.

Any such tests are years away, however. In the meantime, Acorda Therapeutics is planning a second round of trials on rHlgM22 to judge its safety and effectiveness in people who are having MS relapses, the likely beneficiaries of the drug. Regardless of the outcome, this won't be the last clinical hope for these unconventional antibodies. "The whole area of human natural antibodies as therapies is just beginning," Rodriguez predicts. ■



PERSPECTIVES



Pseudomonas aeruginosa

INFECTIOUS DISEASE

A sustainable model for antibiotics

How can we foster the development of novel drugs against resistant bacteria?

By **Manos Perros**

Despite the alarming increase in the prevalence of drug-resistant bacterial infections, far fewer new antibiotics have been approved in the past decade than at the peak in the 1980s (1). The situation is particularly alarming for serious infections by Gram-negative bacteria, some of which are becoming untreatable by modern antibiotics (2–4). Particularly in low- and middle-income countries, untreatable infections are becoming an everyday reality in hospital and care settings (5). Increasing recognition of this

problem is spurring a number of public and private initiatives on both sides of the Atlantic (6–8). To more effectively counter the threat of emerging resistance, we must increase the number of innovative new antibiotics in development and harness advances in diagnostic technology to preserve their efficacy.

The paucity of new antibiotic approvals is the tip of the iceberg. Innovation in antimicrobial research lags behind other disease areas such as oncology, where elucidation of the signal transduction pathways has led

to more effective and better-tolerated treatments, and where, more recently, greater understanding of immunology has delivered life-saving immunotherapeutics. To foster similar breakthrough innovation in antibiotics, corrective actions are needed to rekindle basic research, provide substrate for innovative drug discovery efforts, and help evolve clinical practice.

Basic research in pathogenic bacteria has suffered a double blow of chronic underfunding and short-term focus. First, underfunding relative to other



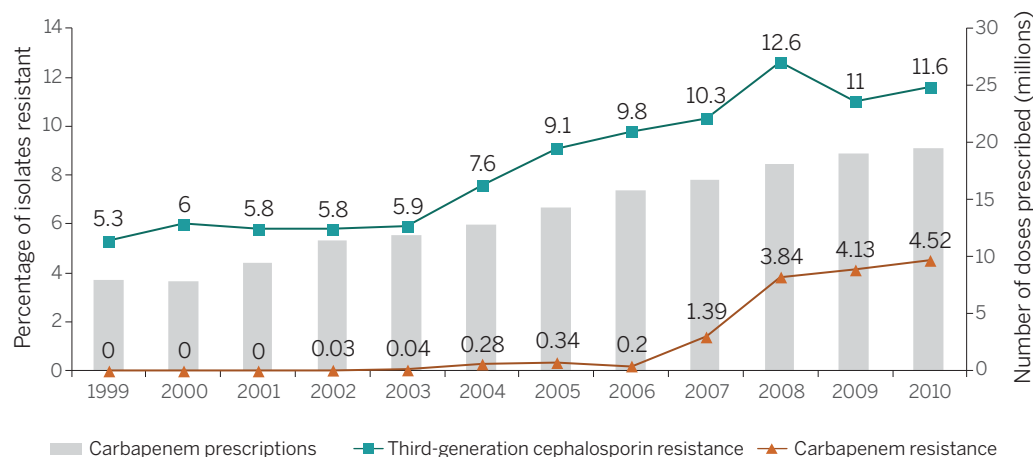
major diseases (e.g., HIV/AIDS, which is often taken as an example of how pharmaceutical innovation can transform a disease) has limited the generation of new knowledge. Second, the lack of new antibiotics being generated in biotech and pharmaceutical companies has prompted a number of academic laboratories and research institutes to engage in activities more typically associated with drug discovery, such as screening compound libraries or optimizing chemical leads for antibacterial activity and drug-like properties, funded through research grants aiming to close the gap left by companies exiting the field. This has been to the detriment of innovative, basic research required to better understand the infectious organisms so that we can develop new therapeutic modalities.

Pharmaceutical research and development has suffered from this deficit of new knowledge and technology available for antibacterial drug discovery; indeed, only two new classes of systemic antibacterial antibiotics have been brought to market in the past 30 years. The discovery of antibiotics with novel modes of action has proved to be a substantial scientific challenge, despite the effort deployed in screening both small-molecule libraries and more traditional natural products.

Our own experience at AstraZeneca is similar to but varies slightly from that described by Payne *et al.*, who found that high-throughput screening of chemical libraries was less likely to provide starting points for antibiotic drug discovery programs than for other therapeutic indications (9). Between 2001 and 2010, we performed 65 high-throughput screens using chemically diverse libraries to identify antibiotic leads. We identified attractive chemical leads against 19 distinct molecular targets. Of those, several were active against Gram-positive pathogens, but none had activity against Gram-negative bacterial cells, despite comparable levels of potency against isolated molecular targets. This is likely due to the highly effective barrier of the Gram-negative envelope and the multiple diffusion and efflux mediators that it encompasses (10).

Greater understanding of the bacterial permeability processes and insights from crystal structures of bacterial porins (11) is putting

Rising resistance



Carbapenem resistance. The percentage of *Klebsiella pneumoniae* isolates resistant to third-generation cephalosporins and carbapenems has risen in the United States between 1999 and 2010 [adapted from (13)]. Also shown are the cumulative numbers of units prescribed for the carbapenems imipenem, meropenem, ertapenem, and doripenem in the United States between 1999 and 2010 (19). Third-generation cephalosporin prescriptions have remained relatively constant at about 30 to 35 million doses prescribed per year throughout this period.

a solution to this challenge within reach. A recently launched public-private partnership initiative [Innovative Medicines Initiative's TRANSLOCATION consortium (6)] uses substantial resources from academia and industry to understand and address the challenges of making new drugs that can penetrate the envelope of Gram-negative bacteria. However, for each fundamental insight that leads to a new antibiotic, several others are likely to be dead-ends. Increased research efforts into other fundamental aspects of bacterial physiology, such as development of resistance, virulence, or the interaction with the host immune system, are thus vital. Other approaches, such as that of random screening for natural products from newly cultured bacteria (12), can produce leads against important pathogens, but antibiotics against the tougher Gram-negatives will be harder to find in this way.

At the other end of the spectrum, clinical use and prescription practices have a key role to play in the response to resistance. The practice of prescribing novel broad-spectrum antibiotics empirically, without prior knowledge of the pathogen(s) responsible for the infection, and of the drug(s) to which the pathogen(s) are sensitive, accelerates the emergence of resistance to new classes of drugs. For instance, resistance to third-generation cephalosporins is seen in only 5 to 10% of *Klebsiella pneumoniae* isolates in the United States and northern Europe, yet patients are often treated with a carbapenem on suspicion of such resistance (see the figure). This in turn leads to the emergence of highly carbapenem-resistant bacteria in intensive

care units (13). An argument could be made that because 90% of patients could be treated by a cephalosporin, carbapenems should be reserved as a second-line defense. However, in the absence of a rapid, reliable diagnostic, delaying use of this drug when resistance is suspected might cost that patient's life.

Diagnosis of bacterial infections traditionally involves culturing the organisms and testing for resistance against the drugs. Although highly accurate, such cultures require 2 to 3 days to read out; during this time, patients are treated empirically. Technologies are now available that can detect multiple pathogens and common resistance genes in primary samples, cutting down the diagnosis time to hours [see, for example, (14, 15)]. Improvements that would help wider adoption of these technologies in the clinic include further reducing time to readout, such that the diagnostic can guide the choice of the right drug(s) as early as possible; validating for different biological fluids or matrices; and adapting the technology for use in low- and middle-income countries—all technological challenges that could be solved with the right incentives and rewards to drive increased investment into this area. The United Kingdom's Longitude Prize 2014 (7) and the launch of an NIH-sponsored award for a rapid bacterial diagnostic (8) are certainly timely not only for facilitating development of those technologies, but also to raise awareness and encourage adoption of more rational prescription practices.

The greatest reward from advanced diagnostics could well lie upstream in the

discovery phase, where rapid diagnostics would enable the development and clinical adoption of pathogen-targeted antibiotics. The wide genetic diversity of pathogenic bacteria (16) has been an obstacle to the development of broad-spectrum drugs. Molecules that target individual pathogens of particular importance should be easier to identify and optimize for selectivity and toleration, and more rapid to develop in targeted patient populations. One such pathogen could be *Acinetobacter baumannii*, which is often resistant to current treatments and is associated with high mortality rates (17). Such narrowly targeted drugs should be premium priced, as they would be used to treat a small number of patients with serious, otherwise untreatable infections (18).

Rapid molecular diagnostics paired with pathogen-targeted antibiotics would usher in an era of “personalized health care” for patients suffering from bacterial infections. Most patients would continue to be treated with older, inexpensive, and still effective antibiotics. Rapid diagnostics could help identify those patients requiring new-generation drugs that target highly pathogenic or resistant strains, limiting unnecessary use and slowing the emergence of resistance; altogether, a more sustainable practice, both in terms of clinical care and antibiotic stewardship. ■

REFERENCES AND NOTES

1. H. W. Boucher et al., Infectious Diseases Society of America, *Clin. Infect. Dis.* **56**, 1685 (2013).
2. D. M. Livermore, *Int. J. Antimicrob. Agents* **39**, 283 (2012).
3. I. Karaiskos, H. Giamarellou, *Expert Opin. Pharmacother.* **15**, 1351 (2014).
4. P. M. Hawkey, A. M. Jones, *J. Antimicrob. Chemother.* **64** (suppl. 1), i3 (2009).
5. S. Baker, *Science* **347**, 1064 (2015).
6. See www.imi.europa.eu/content/translocation.
7. See <https://longitudinprize.org/>.
8. See www.nih.gov/about/director/09182014_statement_brain-amr.htm.
9. D. J. Payne et al., *Nat. Rev. Drug Discov.* **6**, 29 (2007).
10. J. M. Pagès, C. E. James, M. Winterhalter, *Nat. Rev. Microbiol.* **6**, 893 (2008).
11. S. Biswas et al., *Nat. Struct. Mol. Biol.* **14**, 1108 (2007).
12. L. L. Ling et al., *Nature* **517**, 455 (2015).
13. N. P. Braykov, M. R. Eber, E. Y. Klein, D. J. Morgan, R. Laxminarayan, *Infect. Control Hosp. Epidemiol.* **34**, 259 (2013).
14. F. C. Tenover et al., *J. Clin. Microbiol.* **51**, 3780 (2013).
15. E. Mylonakis et al., *Clin. Infect. Dis.* **10.1093/cid/ciu959** (2015).
16. N. R. Pace, *Science* **276**, 734 (1997).
17. A. Y. Peleg, H. Seifert, D. L. Paterson, *Clin. Microbiol. Rev.* **21**, 538 (2008).
18. B. Spellberg, J. H. Rex, *Nat. Rev. Drug Discov.* **12**, 963 (2013).
19. Data reproduced with permission from IMS Health International MIDAS Data 1999–2010.

ACKNOWLEDGMENTS

I thank P. Bradford for critical review. The views expressed in this article are those of the author and do not necessarily represent the views of, nor should be attributed to, AstraZeneca.

10.1126/science.aaa3048

INFECTIOUS DISEASE

A return to the pre-antimicrobial era?

The effects of antimicrobial resistance will be felt most acutely in lower-income countries

By Stephen Baker^{1,2,3}

After many years out of the limelight, antimicrobial resistance (AMR) in bacteria is firmly back on the international political and scientific agenda (1, 2). The potential impact of AMR on hospital-acquired bacterial infections such as *Staphylococcus aureus* and *Acinetobacter baumannii* in higher-income countries has created both fear and a surge of motivation aimed at providing new solutions for the problem (3, 4). The political will and momentum to tackle AMR lies in higher-income countries, but the medical, social, and economic effects of AMR are likely to be felt more in lower-income countries, particularly those in South and Southeast Asia and in sub-Saharan Africa. The identification and development of new drugs is a potential solution but is challenging and costly; any novel therapies introduced into low-income settings without a suitable infrastructure to understand and prevent the rapid development of resistance will likely be expensive and futile.

In many countries at the lower end of the global economic ladder, infections caused by multidrug resistant (MDR) and extended drug resistant (XDR) bacteria are a common reality. Variants of bacterial pathogens carrying novel AMR mechanisms disproportionately originate in lower-income countries, with downstream consequences both within and outside the region in which they appear. This phenomenon was highlighted in 2008 by the emergence of the carbapenem resistance-inducing New Delhi metallo- β -lactamase-1 (NDM-1) (5). This gene induces broad resistance against carbapenems and other β -lactams and was first identified in a *Klebsiella pneumoniae* strain isolated from a Swedish national upon returning from India. The plasmids carrying this gene have since become common and are having dramatic impact on the efficacy of carbapenems and other β -lactams in hospitals. A recent report described hospital outbreaks of *Klebsiella pneumoniae* in children on high-

dependency wards in South Asia (6). These outbreaks were caused by particularly virulent variants, which induced a rapid-onset bacteremia resulting in a 75% mortality rate in the infected children. The presence of NDM-1 within an already broadly antimicrobial-resistant and highly virulent strain severely restricted the treatment options, with a direct impact on patient mortality. This and many other studies have shown that AMR genes thrive in low-income settings and can combine effortlessly with other resistance mechanisms. Further, these wide-ranging combinations of drug resistance mechanisms can be maintained and then transferred within and between numerous bacterial species.

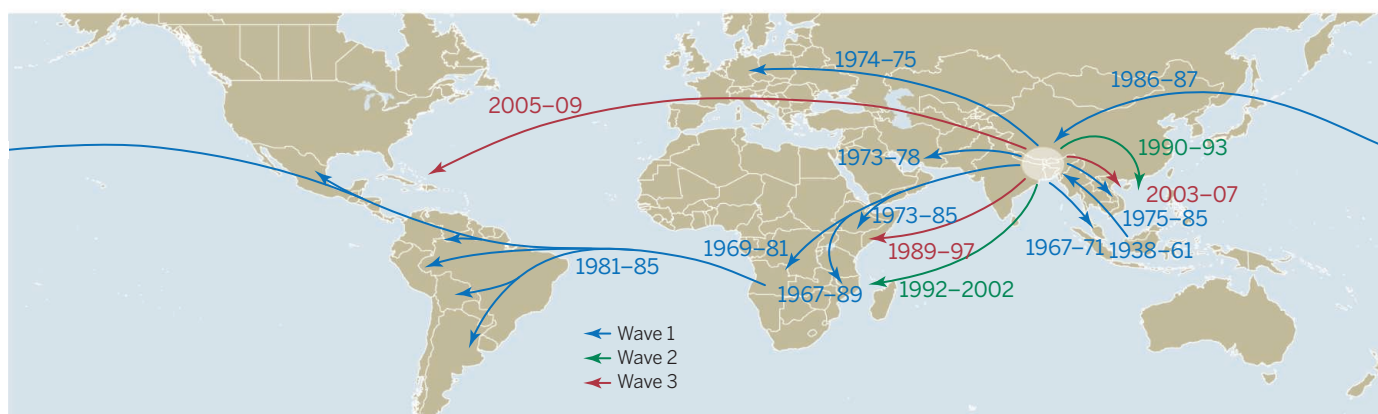
The reasons behind the apparent amplification of the current risk in AMR infections in lower-income countries are intricate and occasionally geographically driven, but there are common themes that highlight the key issues. First, the bacterial pathogens found in lower-income settings (such as typhoid fever and tuberculosis meningitis) typically cause more severe infections than those in higher-income countries. Second, antimicrobials are widely available for purchase in the community without medical consultation and without government policies restricting their use; community overuse and underdosing are common. Third, the medical treatment, range of available antimicrobials, and health care facilities are generally better in higher-income countries; the risk associated with having a poor outcome after infection with a resistant pathogen is therefore greater in lower-income countries. Fourth, very few patients receive any form of conclusive diagnostic testing before, or indeed after, they are treated with an empiric antimicrobial regime. For example, febrile infections across Asia are commonly treated with a fluoroquinolone or a



INFECTIOUS DISEASE

¹Hospital for Tropical Diseases, Wellcome Trust Major Overseas Programme, Oxford University Clinical Research Unit, Ho Chi Minh City, Vietnam. ²Centre for Tropical Medicine, Oxford University, Oxford, UK. ³London School of Hygiene and Tropical Medicine, London, UK. E-mail: sbaker@oucru.org

The three waves of pandemic *Vibrio cholerae*



The global spread of AMR genes. *Vibrio cholerae*, the bacterium that causes cholera, exemplifies how pathogenic bacteria can spread globally. Since the 1930s, the organism has spread in multiple waves from the Bay of Bengal. Waves 2 and 3 can be characterized by a SXT drug resistance-carrying gene island (9).

third-generation cephalosporin without diagnostic testing. Finally, the same classes of compounds used to treat human infections are routinely supplemented into animal feed to increase livestock production and, ultimately, agricultural profitability.

In contrast, higher-income countries have guidelines for antimicrobial usage in animals, diagnostic laboratories, antimicrobial stewardship schemes, and better health care structures on which to create sustainable AMR programs. Such infrastructures and awareness mean that AMR infections are less common in high-income countries than in low-income countries and are mainly limited to health care settings. Additionally, when an issue with a particular AMR pathogen is identified in health care settings, it can be tackled, as exemplified by the dramatic reduction through health care interventions of methicillin-resistant *Staphylococcus aureus* (MRSA)-associated infections throughout the health care structure in England and Wales (7).

Advances in genome sequencing technologies and analysis techniques have laid bare the extent of the AMR problem and have begun to explain the evolutionary mechanisms behind the maintenance and spread of AMR genes and AMR-inducing mutations. Phylogenetic reconstructions prove that the recent evolutionary histories of numerous bacterial pathogens from lower-income settings have been shaped almost exclusively by sustained antimicrobial exposure. The ability to time-stamp the emergence of specific lineages and reconstruct pivotal evolutionary events enables identification of the key drivers of new founder populations (8).

For example, genomic data have shown that *Vibrio cholerae*, the major cause of epidemic diarrhea disease in low-income settings, has radiated from the Bay of Bengal

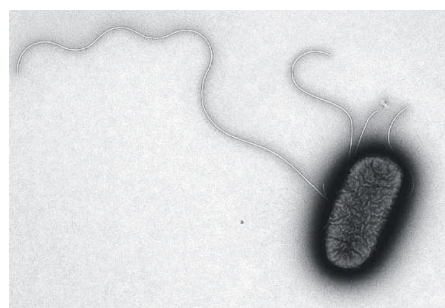
in several pandemic waves (see the map) (9). These waves have been shaped by the acquisition of an SXT (chromosomal gene island) element that encodes a whole host of AMR determinants, including those active against sulfamethoxazole, trimethoprim-sulfate, chloramphenicol, streptomycin, and β -lactams. The clinical impact of AMR in cholera is poorly defined; however, many cholera patients are treated with empirical rehydration therapy and antimicrobials. Therefore, AMR in *Vibrio cholerae* is likely to play a role in the duration of the infection and the asymptomatic transmission of the pathogen into the community after cessation of symptoms.

Typhoid fever serves as another good example. It is a common bloodstream infection caused by the bacterium *Salmonella Typhi* (see the image). Before the antimicrobial era the disease had a ~20% mortality rate, which was dramatically reduced when effective therapies were introduced. After the emergence of MDR strains, fluoroquinolones became the recommended therapy in the 1990s, but reduced susceptibility to this group of compounds emerged almost im-

mediately. Genome sequencing has shown that the mutations that catalyze resistance to fluoroquinolones emerged in numerous lineages and on several occasions; today, one lineage with reduced susceptibility to fluoroquinolones has nearly replaced all other variants (10, 11). The spread of this lineage is clinically relevant, because increasing resistance to fluoroquinolones correlates precisely with likelihood of treatment failure during fluoroquinolone therapy (12). We are on the verge of widespread resistance to fluoroquinolones in typhoid fever (13); there are few alternatives, and thus a very real possibility of a return to conditions like those in the pre-antimicrobial era.

AMR in dangerous bacterial pathogens such as *Salmonella Typhi*, *Vibrio cholerae*, and *Klebsiella pneumoniae* in low-income countries can only be tackled through a multifaceted approach that includes drug discovery programs, sustainable antimicrobial usage policies, and disease prevention strategies including immunization, improved sanitation, hospital infection control, and improved diagnostics. New-generation vaccines and diagnostics for many bacterial infections common in developing countries are under exploration, but there are currently no programs aimed at developing novel therapeutic agents specifically to treat dangerous bloodstream infections caused by pathogenic organisms such as *Salmonella Typhi* and *Klebsiella pneumoniae*.

There is an urgent need for those studying infections caused by AMR bacteria in low-income settings to establish connections with drug discovery groups and pharmaceutical companies in high-income countries (14). Examples such as the Tuberculosis Drug Accelerator program (15) and the Medicines for Malaria Venture (MMV) (16) show how such platforms can be



Electron micrograph of *Salmonella Typhi*, the agent of typhoid fever. Widespread multidrug resistance in this bacterium raises the specter of a return to conditions resembling those of the pre-antimicrobial era.

successful. These pioneering initiatives are beginning to link pharmaceutical companies, academia, and disease experts across the “gene to bedside” spectrum in the locations where these diseases have the greatest impact. The MMV provides free, open access to a range of compounds with activity against a range of pathogens for independent researchers to screen, with users requested to publish their data in the public domain, thus continuing the drug development research cycle (17).

The impact of bacterial AMR in low-income countries is severe and likely to worsen. New antimicrobial agents may provide some respite against AMR and infections caused by such drug-resistant pathogens. However, introducing novel broad-range antimicrobials into the current melee of antimicrobial use and misuse in lower-income countries would only have a short-term limited impact on infections caused by potentially life-threatening pathogens. Restricting the use of the same classes of antimicrobial compounds in animals and humans has to be an immediate priority, including a direct ban of any new antimicrobials developed for treating infections in humans. Lastly, new antimicrobial agents should only be administered to those who really need them. This means that the current capacity to perform microbial diagnostics and downstream antimicrobial susceptibility testing needs to be greatly improved, alongside the development of rational prescribing practice. ■

REFERENCES AND NOTES

1. Department of Health & Department for Environment Food & Rural Affairs, *UK Five Year Antimicrobial Resistance Strategy 2013 to 2018* (2013).
2. Centers for Disease Control and Prevention, Antibiotic Resistance Threats in the United States, 2013; www.cdc.gov/drugresistance/threat-report-2013/pdf/ar-threats-2013-508.pdf.
3. World Health Organization, “Antimicrobial resistance: Global report on surveillance” (2014).
4. M. Perros, *Science* **347**, 1062 (2015).
5. T. R. Walsh *et al.*, *Lancet Infect. Dis.* **11**, 355 (2011).
6. H. Chang The *et al.*, *EMBO Mol. Med.* **10**, 15252/emmm.201404767 (2015).
7. S. P. Stone *et al.*, *BMJ* **344**, e3005 (2012).
8. K. E. Holt *et al.*, *Proc. Natl. Acad. Sci. U.S.A.* **110**, 17522 (2013).
9. A. Mutreja *et al.*, *Nature* **477**, 462 (2011).
10. P. Roumagnac *et al.*, *Science* **314**, 1301 (2006).
11. S. Kariuki *et al.*, *J. Clin. Microbiol.* **48**, 2171 (2010).
12. C. M. Parry *et al.*, *PLOS Negl. Trop. Dis.* **5**, e1163 (2011).
13. K. D. Koirala *et al.*, *Antimicrob. Agents Chemother.* **56**, 2761 (2012).
14. M. N. Robertson *et al.*, *Parasitology* **141**, 148 (2014).
15. See www.gatesfoundation.org/What-We-Do/Global-Health/Tuberculosis.
16. See www.mmv.org.
17. K. Ingram-Sieber *et al.*, *PLOS Negl. Trop. Dis.* **8**, e2610 (2014).

ACKNOWLEDGMENTS

S. B. is a Sir Henry Dale Fellow, jointly funded by the Wellcome Trust and the Royal Society (100087/Z/12/Z).

10.1126/science.aaa2868

GENE EXPRESSION

Statistics requantitates the central dogma

Transcription, not translation, chiefly determines protein abundance in mammals

By Jingyi Jessica Li¹ and Mark D. Biggin²

Mammalian proteins are expressed at $\sim 10^3$ to 10^8 molecules per cell (1). Differences between cell types, between normal and disease states, and between individuals are largely defined by changes in the abundance of proteins, which are in turn determined by rates of transcription, messenger RNA (mRNA) degradation, translation, and protein degradation. If the rates for one of these steps differ much more than the rates of the other three, that step would be dominant in defining the variation in protein expression. Over the past decade, system-wide studies have claimed that in animals, differences in translation rates predominate (2–5). On page 1112 of this issue, Jovanovic *et al.* (6), as well as recent studies by Battle *et al.* (7) and Li *et al.* (1), challenge this conclusion, suggesting that transcriptional control makes the larger contribution.

Earlier studies used mass spectrometry, DNA microarrays, and mRNA sequencing (mRNA-Seq) to measure protein and mRNA levels for thousands of genes (2–5), and also to measure the rates of mRNA degradation, translation, and/or protein degradation (through labeling with stable isotopes) (4, 5). Some studies examined a single cell type at steady state (5), whereas others analyzed the differences between tissue types (4), between tumors (2), or between inbred mouse strains (3). Each study found a moderate to low correlation between protein and mRNA abundance data (coefficient of determination $R^2 \leq 0.4$). This was taken to suggest that no more than 40% of the variance in protein levels is explained by variance in the rates of transcription and mRNA degradation and, by implication, that the remaining variance in protein expression ($\geq 60\%$) is explained by translation and protein degradation (2–5). By employing degradation rate data for mRNAs and proteins in addition to abundance data, it was further estimated that transcription explains 34% of the variance in protein abundance, mRNA degradation 6%, translation 55%, and protein degrada-

tion 5% (5) (see the figure).

The high-throughput methods used in these studies, however, show substantial stochastic variation between replica data and also suffer systematic, reproducible biases (1, 4–6, 8, 9). For example, label-free mass spectrometry can underestimate amounts of all lower-abundance proteins by as much as a factor of 10 (1, 8), and mRNA-Seq data are biased by guanine-cytosine base pair content by a factor of up to 3 (9). Because each type of error has different causes and because RNA and protein techniques differ greatly, the errors should be uncorrelated. Thus, the correlation of protein versus mRNA as measured will be lower than that between error-free data. The papers by Jovanovic *et al.*, Battle *et al.*, and Li *et al.* used careful statistical efforts to estimate and/or reduce the impact of errors and thereby find the higher correlation expected between true protein and true mRNA levels.

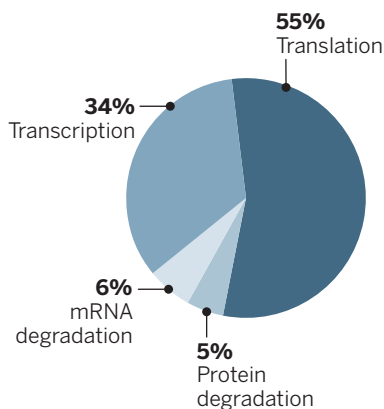
“Before gene expression can be correctly modeled, an accurate accounting of molecular abundances and expression rate constants is vital.”

Jovanovic *et al.* examined mouse bone marrow dendritic cells at steady state and during response to bacterial lipopolysaccharide (LPS) (6). They used a Bayesian model to estimate the true rates of translation and protein destruction from noisy mass spectrometry data. In addition, three independent estimates of protein abundance were made from three samples, each digested with a different protease. These three differently biased estimates were then used in separate parts of the analy-

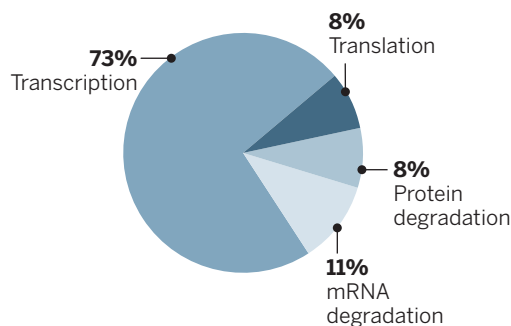
¹Department of Statistics and Department of Human Genetics, University of California, Los Angeles, CA 90095, USA. ²Genomics Division, Lawrence Berkeley National Laboratory, Berkeley, CA 94720, USA. E-mail: jjli@stat.ucla.edu; mdbiggin@lbl.gov

% Contribution to protein levels

Original data estimates



Error-corrected estimates



Control of protein expression. The charts show the percent contributions of the variance in the rates of each step in gene expression to the variance in protein abundance for 4212 genes (from a mouse cell line). The left chart shows estimates from (5); the right chart shows estimates from (1) that take into account stochastic and systematic errors in the abundance data of (5).

sis to avoid a confounding dependency on common errors that would result if a single estimate were used throughout. Filtering of unreliable data and estimates of stochastic mRNA-Seq errors, in addition, allowed Jovanovic *et al.* to calculate that at steady state, mRNA levels explain 68% of the variance in protein expression, translation rates 26%, and protein degradation rates 8%. Upon stimulation of cells with LPS, mRNA levels appear to explain 90% of the changes in protein expression, with translation and protein degradation explaining only 4% and 6%, respectively. Jovanovic *et al.* did find, though, that upon LPS treatment, translation and protein degradation rates changed more for ribosomal, mitochondrial, and other highly expressed housekeeping proteins than for other genes, indicating an important role for these two steps in the control of some processes.

Battle *et al.* took a different tack, examining human protein variation among 62 individuals from the Yoruba population of Ibadan, Nigeria (7). Genomic DNA sequences for each individual were compared to mRNA-Seq, ribosome footprinting (ribosome density per mRNA), and mass spectrometry data for lymphoblastoid cells derived from each person. Consistent with previous results (3), the variation in measured protein levels between individuals correlates poorly with the variation in measured mRNA abundances (mean $R^2 < 0.2$) (7). However, when only those differences in expression that are associated with variation in the DNA sequence of a nearby gene were considered, most gene loci showing

changes in protein levels between individuals also showed correlated differences in mRNA expression, consistent with a dominant role for transcription. In addition, there was “a scarcity” of DNA sequence changes that affected only ribosome footprint density and protein abundance, not mRNA levels. In effect, by constraining their analysis to only those differences in expression associated with DNA sequence variation, Battle *et al.* excluded much of the variation due to measurement errors to obtain a more accurate answer.

Li *et al.* (1) (our own study) reanalyzed data in (5) with two approaches to account for measurement errors. In the first, a non-linear scaling error in protein abundance estimates (from mass spectrometry data) was corrected using classic data from the literature, and a subset of the other errors in the mRNA-Seq and protein abundance data was estimated from replica and other control data. In the second approach, variance in translation rates measured directly by ribosome footprinting was substituted for a larger variance that had been inferred indirectly with a model in (5). The first approach suggests that the variance in true mRNA levels explains a minimum of 56% of the variance in true protein levels. The second implies that true mRNA levels explain 84% of the variance in true protein expression, transcription 73%, RNA degradation 11%, and translation and protein degradation each only 8%.

Most controllers of gene expression identified by classic genetic or biochemical methods are either transcription factors or proteins (such as kinases and signaling

receptors) that directly regulate the activities of proteins, not their abundances. In addition, translation and mRNA degradation rates change only modestly upon cellular differentiation or when microRNA expression is perturbed (10–12). Moreover, improved statistical analyses show that in contrast to earlier studies, mRNA levels explain most of the variance in protein abundances in yeast (13, 14). Finally, ~40% of genes in a single mammalian cell express no mRNA (1, 15); thus, for these ~8800 genes, transcriptional repression by chromatin is likely the sole determinant of the absence of protein expression.

Understanding the contributions of transcriptional versus posttranscriptional control is not simply a matter of academic interest. For example, variation in protein expression among 95 colorectal tumor samples is only poorly explained by measured mRNA abundances (2), which might imply that different responses of patients to anticancer treatments are posttranscriptional effects. If, however, most of the variation in protein levels is controlled by transcription but this fact is obscured by measurement errors, then differences in drug action could be mainly explained by variation at the transcriptional level.

Accurate quantitation of the control of gene expression is in its infancy. Experimental protocols with fewer inherent biases are needed, along with further improvements in statistical methods that can estimate and take error into account. Before gene expression can be correctly modeled, an accurate accounting of molecular abundances and expression rate constants is vital. ■

REFERENCES AND NOTES

1. J. J. Li, P. J. Bickel, M. D. Biggin, *PeerJ* **2**, e270 (2014).
2. B. Zhang *et al.*, *Nature* **513**, 382 (2014).
3. A. Ghazalpour *et al.*, *PLoS Genet.* **7**, e1001393 (2011).
4. A. R. Kristensen, J. Gspöner, L. J. Foster, *Mol. Syst. Biol.* **9**, 689 (2013).
5. B. Schwanhäusser *et al.*, *Nature* **473**, 337 (2011).
6. M. Jovanovic *et al.*, *Science* **347**, 1259038 (2015).
7. A. Battle *et al.*, *Science* **347**, 664 (2015).
8. E. Ahmri, L. Molzahn, T. Glatter, A. Schmidt, *Proteomics* **13**, 2567 (2013).
9. M. S. Cheung, T. A. Down, I. Latorre, J. Ahinger, *Nucleic Acids Res.* **39**, e103 (2011).
10. D. Baek *et al.*, *Nature* **455**, 64 (2008).
11. M. Selbach *et al.*, *Nature* **455**, 58 (2008).
12. N. T. Ingolia, L. F. Lareau, J. S. Weissman, *Cell* **147**, 789 (2011).
13. G. Csardi *et al.*, <http://biorxiv.org/content/early/2014/12/26/009472> (2014).
14. F. W. Albert, D. Muzey, J. S. Weissman, L. Kruglyak, *PLoS Genet.* **10**, e1004692 (2014).
15. D. Hebenstreit, A. Deonarine, M. M. Babu, S. A. Teichmann, *Curr. Opin. Cell Biol.* **24**, 350 (2012).

ACKNOWLEDGMENTS: J.J.L. was supported in part by the Department of Statistics at UCLA. Work at Lawrence Berkeley Laboratory National Laboratory was conducted under U.S. Department of Energy contract DEAC02-05CH11231.

10.1126/science.aaa8332



Callimico goeldii, a South American New World monkey.

ANTHROPOLOGY

New World monkey origins

Fossils in Peru raise questions about the early evolution of monkeys in South America

By Richard F. Kay

New World monkeys (Platyrrhini) appeared suddenly in South America in the middle Cenozoic. Little is certain about their origin, but theories include an African source, either by vicariance through Cretaceous rifting of South America from Africa, or an Atlantic Ocean raft crossing in the middle Cenozoic. A recent fossil discovery in Amazonian Peru reported by Bond *et al.* (1) has identified the oldest platyrrhine primate (named *Perupithecus*) at 36 million years ago (Ma), with features that suggest links to African anthropoids of similar age. Although the new fossils reinforce the African rafting source, the details of the author's origin scenario will be controversial.

The new specimens (three cheek teeth) come from Santa Rosa in Amazonian Peru and are claimed to be approximately 10 million years older than the hitherto oldest Neotropical record of monkeys, represented by ~26-Ma Bolivian *Branisella* (2, 3). The greater antiquity of Platyrrhini is consistent with molecular clock phylogenies that place the time of a cross-Atlantic monkey emigration (with their rodent fellow rafters) at

40 to 44 Ma (4, 5). The new fossils also are concordant with 37-Ma African fossils that belong to the catarrhine anthropoids (Old World monkeys, apes, and humans) establishing that the catarrhine-platyrrhine split had already occurred (6).

That *Perupithecus* is the oldest known stem platyrrhine is highly probable. The new specimens leave no doubt that platyrrhines came from Africa, and *Perupithecus* begins to span the missing 11-million-year platyrrhine lineage (from the 37-Ma catarrhine to 26-Ma *Branisella*).

Without a radiometric age, the dating of Santa Rosa is based on rodent biostratigraphy. Increases in body size and tooth crown height are common in rodent lineages. The lower tooth crowns of Santa Rosa rodents compared with those at Salla suggest that Santa Rosa is older than Salla (7). Two Santa Rosa rodent species also occur in another Amazonian Peruvian fauna at Contamana, with an estimated age of 41 Ma (8). The Santa Rosa rodents are larger than their congeners at Contamana, suggesting a younger age for Santa Rosa. Thus, though imprecise, the age of Santa Rosa is likely between 29 Ma (the age of the oldest Salla rodents) and 41-Ma Contamana (9).

The teeth of the Santa Rosa monkey are more primitive than those of any known platyrrhine, supporting Bond *et al.*'s view that *Perupithecus* was a stem platyrrhine.

More controversially, Bond *et al.* suggest that *Perupithecus* is nested within a Late Eocene (38 to 34 Ma) African anthropoid group composed of *Catopithecus*, *Proteopithecus*, and *Talahpithecus*. The details of this new phylogenetic proposal are inconsistent with what we known about early anthropoid evolution (fig. S1). Three distinct anthropoid clades were present in the African Late Eocene (Afrotarsiidae, Parapithecoidea, and Oligopithecidae). Each occupied a disparate position on the anthropoid evolutionary tree and represents several immigration events

from Asia (6). Bond *et al.* propose a very different tree of early anthropoid evolution. Solely using dental characters in their phylogenetic analysis, they join *Perupithecus* with stem taxa of two of the African clades: *Proteopithecus* is a parapithecoid and *Catopithecus* and *Talahpithecus* are oligopithecids. Bond *et al.* place these four genera together, forming an African stem platyrrhine cluster. If correct, New World monkeys would have had an African radiation before reaching South America. This radical reordering of early African anthropoids likely will be viewed skeptically by most paleoanthropologists, who will regard it as a polyphyletic pastiche requiring better supporting evidence to be considered a plausible scenario.

A key test of Bond *et al.*'s phylogenetic conclusions will be an expanded analysis beyond dental data, adding informative characters of cranial and postcranial anatomy which, although unknown in *Perupithecus*, would greatly alter the underlying tree topology. *Perupithecus* is similar dentally to Eocene African anthropoids, but cranial and postcranial evidence to date rejects a sister-group relationship of *Proteopithecus* and *Catopithecus*; *Proteopithecus* shares postcranial specializations with parapithecids. *Catopithecus* has the derived dental and postcranial characters of oligopithecids and perhaps catarrhines (10). Poorly known, *Talahpithecus* is possibly another oligopithecid.

Another test is to examine the degree to which the phylogenetic analysis of Bond *et al.* agrees with well-corroborated extant New World monkey phylogenies that are based on genomic sequences. Bond *et al.* include 15 of the 16 living platyrrhine genera for which there is a robust genetic tree (11). Their parsimony analysis of dental data

Department of Evolutionary Anthropology and Division of Earth and Ocean Sciences, Duke University, Durham, NC 27708, USA.; E-mail: richard.kay@duke.edu

differs greatly from the genetically based tree of extant species; it does not recover the extant platyrrhine family Cebidae and misplaces many extant genera within their respective families.

Although platyrrhines almost certainly rafted from Africa in the mid-Cenozoic, a precise link between Amazonian *Perupithecus* and any particular African taxon or taxa remains obscure. The fragmentary nature of the new fossils, the use of a morphological data set with only dental characters, and conflicts with genetic data raise doubt about Bond *et al.*'s conclusions. Their tree may minimize convergent evolution (homoplasy) in the dentition, but it omits cranial and postcranial characters for which their proposed topology would increase homoplasy. Likewise, gene sequence data must provide a framework for the placement of extinct taxa when analyzed in combination with living ones.

Perupithecus reveals tantalizing information that the niche of the earliest platyrrhines was very different from that of its larger, more herbivorous living relatives. Its small body size and molar structure suggest insectivory (12). Coexistence with brachyodont rodents suggests that it was a forest dweller much like Late Eocene African anthropoids. This pattern contrasts with the adaptations of the younger *Branisella*—a larger, more frugivorous, and possibly scansorial (climbing) animal (13). *Perupithecus*' presence in today's Amazon basin confirms that this region was long the center of platyrrhine development that still is largely unknown (14). ■

REFERENCES

1. M. Bond *et al.*, *Nature* 10.1038/nature14120 (2015).
2. R. F. Kay, B. J. MacFadden, R. H. Madden, H. Sandeman, F. Anaya, *J. Vertebr. Paleontol.* **18**, 189 (1998).
3. M. Takai, F. Anaya, N. Shigehara, T. Setoguchi, *Am. J. Phys. Anthropol.* **111**, 263 (2000).
4. N. S. Upham, B. D. Patterson, *Mol. Phylogenet. Evol.* **63**, 417 (2012).
5. P. Perelman *et al.*, *PLOS Genet.* **7**, e1001342 (2011).
6. E. R. Seiffert, *Evol. Anthropol.* **21**, 239 (2012).
7. C. D. Frailey, K. J. Campbell, *Nat. Hist. Mus. Los Angeles County Sci. Ser.* **40**, 71 (2004).
8. P.-O. Antoine *et al.*, *Proc. R. Soc. B Biol. Sci.* **279**, 1319 (2012).
9. O. C. Bertrand *et al.*, *Am. Mus. Novit.* **3750**, 1 (2012).
10. E. R. Seiffert *et al.*, *Science* **310**, 300 (2005).
11. D. E. Wildman, N. M. Jameson, J. C. Opazo, S. V. Yi, *Mol. Phylogenet. Evol.* **53**, 694 (2009).
12. R. F. Kay *et al.*, in *Early Miocene Paleobiology in Patagonia: High-Latitude Paleocommunities of the Santa Cruz Formation*, S. Vizcaino, R. F. Kay, M. Bargo, Eds. (Cambridge Univ. Press, Cambridge, UK, 2012), pp. 306–330.
13. R. F. Kay, B. A. Williams, F. Anaya, in *Reconstructing Behavior in the Primate Fossil Record*, J. M. Plavcan, C. van Schaik, R. F. Kay, W. L. Jungers, Eds. (Kluwer Academic/Plenum, New York, 2002), pp. 339–370.
14. R. F. Kay, *Mol. Phylogenet. Evol.* **82** (Pt. B), 358 (2015).

SUPPLEMENTARY MATERIALS

www.sciencemag.org/content/347/6226/1068/suppl/DC1
Fig. S1

10.1126/science.aaa9217

RNA INTERFERENCE

Drugging RNAi

RNAi therapeutics are emerging as a major drug discovery engine

By Dirk Haussecker¹ and Mark A. Kay²

RNA interference (RNAi)-based drugs harness endogenous posttranscriptional gene silencing pathways for therapeutic purposes. The goal is to turn down or shut off the expression of genes known to contribute to or cause disease. RNAi “triggers” are typically double-stranded RNAs (dsRNAs) of which one strand has a sequence complementary to that of a messenger RNA (mRNA), resulting in the reduction or elimination of that an mRNA and its corresponding protein product. The dsRNAs can be provided as synthetic oligonucleotides or as genetic DNA templates from which the RNAi triggers are transcribed in the target cells (vector-based transcriptional RNAi) (see the figure).

Key to the therapeutic utility of these RNAi triggers is the ability to introduce them into their target cells in the body. Such delivery is typically facilitated by formulation into nanoparticles, simple conjugates, or viral vectors (see the figure). To date, at least three delivery technologies (liposomal nanoparticles, simple conjugates, and polyconjugates) have shown highly persistent silencing of target gene expression in the liver of humans and non-human primates, suggesting therapeutic dosing frequencies as low as once-monthly or once-quarterly (1–3).

There are two lead RNAi drug candidates (ALN-TTR02 and ALN-TTRsc) in phase III trials that target the disease-causing mutant *transthyretin* (TTR) mRNA in the liver for the treatment of familial amyloid polyneuropathy. Given that deficiency of the TTR gene product is expected to be well tolerated and the mutant TTR protein causes the disease, the target risk is low, and commercialization may happen as early as 2017 (ALN-TTR02). Beyond the TTR amyloidosis candidates, there is an expanding pipeline of RNAi gene targets in the liver. These include candidates for diseases ranging from important public health issues (e.g., hepatitis B virus infection, common forms of metabolic and cardiovascular disorders, liver cancer) to the rare and severe (e.g., triglyceride-related pancreatitis, primary hyperoxaluria 1, α_1 -antitrypsin-related liver disease).

N-Acetyl-galactosamine (GalNAc) siRNA conjugates targeting the liver have emerged as an attractive delivery option offering the prospect of infrequent (once-monthly or even once-quarterly) subcutaneous dosing, making them suitable for other common chronic diseases such as type II diabetes and hypercholesterolemia (2).

Although the liver is a favored organ for delivery owing to its physiological role in removing particles from circulation, it is less clear whether new approaches aimed at nonhepatic tissues will provide therapeutic efficacy. These smaller nanoparticles, conjugates, self-delivering RNAi triggers, cationic lipoplexes, and transcriptional RNAi methods hold particular promise for targeting cancer cells, phagocytic cells, vascular endothelial cells, cell populations in the kidney, cells in the back of the eye, and the various cell types in the central nervous system (CNS) (4).

For diseases requiring life-long treatment, as well as for the hard-to-reach (e.g., CNS) tissues and/or tissues that rapidly turn over, such as blood-derived stem cells, transcriptional RNAi methods currently have a practical advantage, because of the prospect of persistent activity after single administration. In addition, transcriptional RNAi may be a better match for certain diseases where both the addition of

“Beyond the TTR amyloidosis candidates, there is an expanding pipeline of RNAi gene targets...”

a normal gene, as well as silencing of the endogenous mutated gene, are beneficial. This would include diseases such as sickle cell anemia (5) or the most common form of α_1 -antitrypsin deficiency (6). However, one disadvantage is that dosing is more difficult to control with vector-transcribed RNAi. Transcriptional RNAi candidates in clinical development today address cancer, HIV, and hepatitis C virus, as candidates for α_1 -antitrypsin deficiency and neurodegenerative disorders approach the clinic. This compares to over 20 synthetic RNAi trigger clinical candidates.

It remains to be seen how the safety profile from the largely short-term experience

¹ RNAi Therapeutics Consulting, Rastatt, Germany. ² Pediatrics and Genetics, Stanford University, Stanford, CA, USA. E-mail: dirk.haussecker@gmail.com; markay@stanford.edu

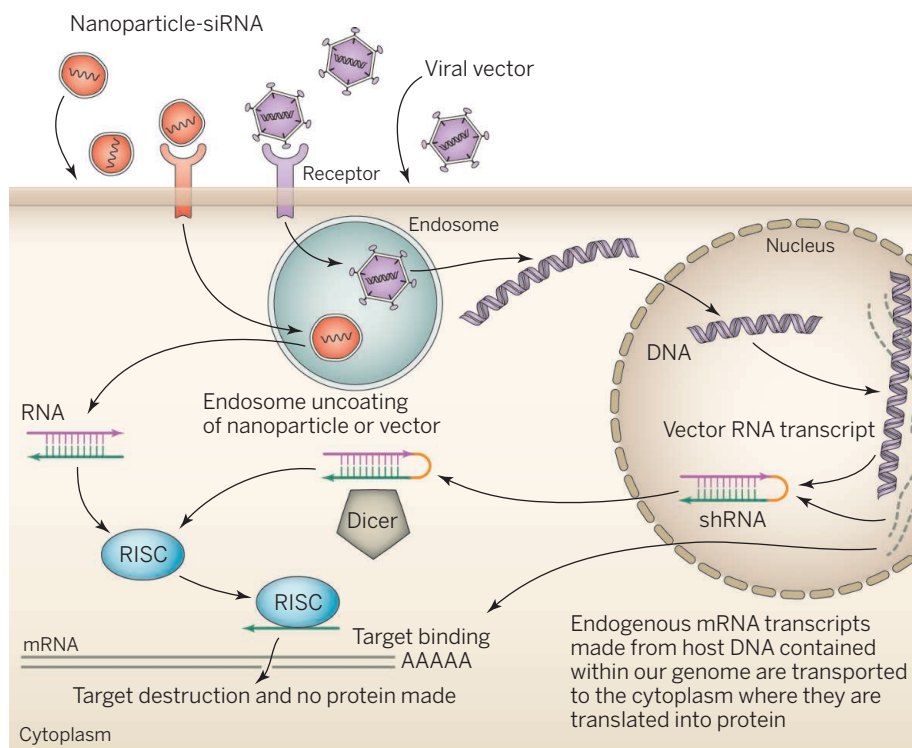
(~6 to 12 months) with the leading TTR amyloidosis candidates will hold up in the long run. So far, safety issues for the three most advanced delivery technologies (SNALP liposomal nanoparticles by Tekmira, GalNAc conjugates by Alnylam, and DPC polyconjugates by Arrowhead Research) have largely been related to the route of administration (infusion and injection site reactions) and the delivery chemistry, and not the RNAi mechanism of action per se (1, 2). In particular, the propensity of the larger nanoparticulate formulations such as liposomes to interact with the innate immune system has been a major challenge (7) and necessitated the adoption of transient immune suppression

Minimizing off-target effects at the RNAi trigger design phase relies on error-prone bioinformatic filters rather than on the iterative chemical optimization and monitoring of off-target activities in preclinical models (9).

Another long-term safety issue is whether hijacking the endogenous microRNA pathway is safe given the functions of microRNAs throughout biology. Studies involving the use of RNAi triggers generated from strong transcriptional promoters revealed that competition between therapeutic RNAi triggers and endogenous microRNAs for the same machinery can have adverse consequences given the pervasive importance of microRNAs in gene regulation (10). Nev-

pharmaceutical industry (12). This period of irrational exuberance (2005 to 2008) was preceded by initially measured investments by some large companies (Medtronic, Merck, Novartis) and the award of the Nobel Prize for the discovery of dsRNA as the efficient trigger of the RNAi gene silencing process. This exuberance culminated in bidding wars, unrealistic expectations, and misplaced investments, precipitating a considerable backlash (2008 to 2011). It was uncertain whether the industry could ever recover (12). The realization that many of the early most prominent claims for therapeutic gene silencing in animal models of human disease were in retrospect best explained by innate immunostimulatory, antiproliferative, and antiviral artifacts was a further cause of uncertainty. Important scientific breakthroughs at this time, such as the demonstration of on-target RNAi in nonhuman primates, advances in conjugate delivery, and strategies to abrogating innate immune stimulation, struggled to be appropriately recognized (12). It was only after a string of demonstrations of target gene silencing in humans that the industry started to recover (13).

There has also been competition from other nucleic acid therapeutics platforms, in particular ribonuclease H (RNase H) antisense technology and genome editing. Especially with recent advances in ligand-targeted delivery, the long-held potency advantage of RNAi has diminished relative to RNase H antisense technology (14). But competition, both among RNAi technologies and with antisense oligonucleotides, has also driven much progress in the field. With more than \$1 billion invested in RNAi-based therapeutics in the first 6 months of 2014 alone (13), together with the increased acceptance of gene therapy in general, there should be a rapidly expanding clinical pipeline of RNAi-based drugs and a maturing of delivery technologies for targeting cells and tissues outside the liver. ■



RNAi is the drug. RNAi delivery approaches include conjugates, liposomal nanoparticles (LNPs), and viral vectors. Nanoparticles deliver synthetic dsRNA, whereas viral vectors deliver a transcriptional template to the nucleus. Cellular uptake occurs nonspecifically or via receptor-mediated endocytosis. Nanoparticles deliver the RNAi trigger to the cytoplasm. The trigger enters the RNAi pathway at the RISC or Dicer processing stage. Transcriptional templates produce hairpin RNAs that enter the pathway at an earlier, nuclear stage. Ultimately, an active RISC complex is formed that cleaves the mRNA target. RISC, RNA-induced silencing complex; shRNA, short hairpin-mediated RNA.

around the time of dosing. By contrast, smaller systems such as the DPCs and GalNAc conjugates rely on the use of heavily modified RNAi triggers that may accumulate in compartments such as lysosomes, the long-term safety of which remains to be determined.

Off-target activities, a challenge shared with other drug modalities, may also influence the long-term safety experience, especially because RNAi triggers may modulate expression of dozens of off-target genes (8).

Nevertheless, improvements in RNAi trigger design to facilitate more efficient processing should lessen the burden by avoiding congestion of the RNAi pathway (11).

The history of investment in RNAi therapeutics has been something of a roller coaster ride. Initial interest in the therapeutic application of RNAi was limited to small biotechnology companies specialized in oligonucleotide therapeutics development (2002 to 2005). There followed a sudden stampede into the technology by the

REFERENCES

1. T. Coelho et al., *N. Engl. J. Med.* **369**, 819 (2013).
2. www.alnylam.com/web/assets/MASTER-RD-DAY-DECK_Capella.pdf
3. C. I. Wooddell et al., *Mol. Ther.* **21**, 973 (2013).
4. D. Haussecker, *J. Control. Release* **195**, 49 (2014).
5. S. Samakoglu et al., *Nat. Biotechnol.* **24**, 89 (2006).
6. C. Mueller et al., *Mol. Ther.* **20**, 590 (2012).
7. <http://investor.tekmirapharm.com/releasedetail.cfm?ReleaseID=857714>
8. A. L. Jackson et al., *RNA* **12**, 1179 (2006).
9. N. Vaish et al., *Nucleic Acids Res.* **39**, 1823 (2011).
10. D. Grimm et al., *Nature* **441**, 537 (2006).
11. S. Gu et al., *Cell* **151**, 900 (2012).
12. D. Haussecker, *Mol. Ther. Nucleic Acids* **1**, e8 (2012).
13. J. Maraganore, *Nature* **510**, 35 (2014).
14. T. P. Prakash et al., *Nucleic Acids Res.* **42**, 8796 (2014).

10.1126/science.1252967

Viral chemokine mimicry

How do viruses trick the human immune system?

By Jörg Standfuss

Chemokines are important regulators of the human immune system. Interactions of chemokines with their corresponding receptors guide white blood cells to the sites of infection, where they can trigger the required immune responses. Two complementary papers in this issue provide molecular details of these receptor-chemokine interactions. On page 1117, Qin *et al.* (1) report the crystal structure of the human CXCR4 receptor cross-linked to the viral chemokine vMIP-II. On page 1113, Burg *et al.* (2) describe the opposite case, the interaction of the human chemokine CX3CL1 with the viral US28 receptor (see the figure). Together, the studies provide crucial insights into the molecular mimicry that viruses use to fool the human immune system.

Chemokine receptors are members of the G protein-coupled receptor (GPCR) family of proteins. GPCRs are the largest family of signaling receptors in the human cell and are important drug targets but have long withstood structural analysis. Methodological advances—including lipidic cubic phase crystallization, conformational thermostabilization, and the use of fusion proteins or antibodies—have led to structure determination of at least 25 unique GPCRs, including those of chemokine receptors CXCR4 (3) and CCR5 (4). However, most of these structures—with the notable exception of the visual photoreceptor rhodopsin—could only be determined after heavy protein engineering. It remains unclear to what extent this engineering hampers physiological interpretation of the results. Burg *et al.*'s results will help to settle this question. The authors present the US28-CX3CL1 complex both in its fully native form and as a truncated version with bound nanobody.

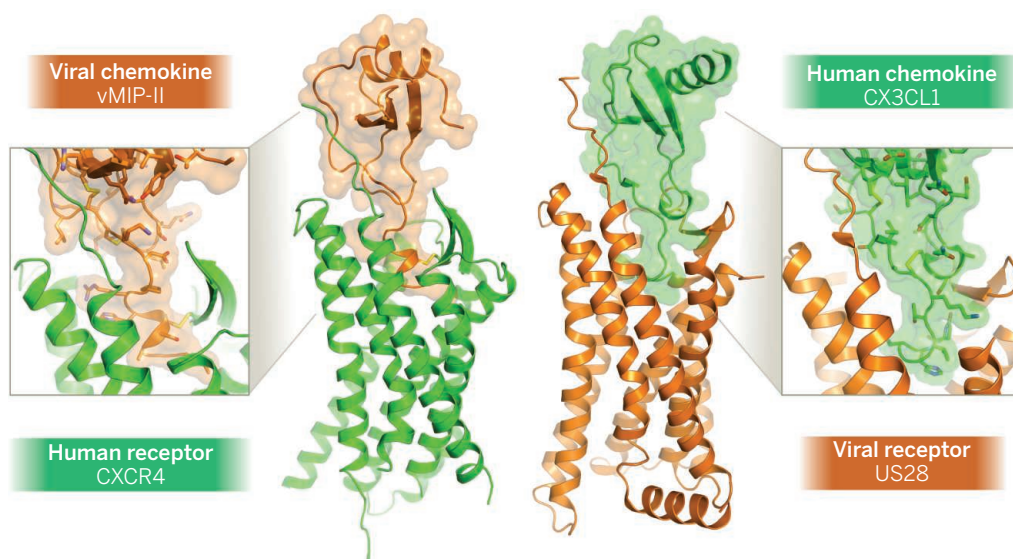
So far, most GPCR structures have been solved in complex with small-molecule ligands; only one GPCR protein complex, that

of a receptor with its main signaling partner G protein (5), has been determined. The studies of Qin *et al.* and Burg *et al.* thus fill an important hole in our understanding of GPCRs by showing how a native protein ligand can bind and activate its receptor.

The interaction interfaces between receptor and chemokine are mediated by extensive interfaces of ~1300 Å² for CXCR4-vMIP-II (1) and ~1600 Å² for US28-CX3CL1 (2). The N terminus of the two chemokines reaches

ity, likely by allowing variations in the binding mode. A third layer of complexity stems from the different conformational states of the two receptors, with CXCR4 being in the inactive and US28 in the active conformation; active and inactive states of the same receptor can differ by up to 14 Å (5). Together these points provide good reasons why both chemokines maintain the main interaction sites on their termini but vary in their positions on the extracellular loops of the receptors. The two chemokine-binding modes will provide a rich basis on which to study binding of all four chemokine classes.

Among GPCRs, chemokine receptors are particularly interesting because they are involved in inflammatory responses and host-virus interactions. CCR5 and CXCR4, for example, are important coreceptors for



Molecular mimicry. Chemokine-receptor complexes reported in (1, 2) elucidate the molecular mimicry that herpesviruses use to trick our immune system. The insets show the main interaction interfaces, with the chemokine N terminus inserted into the ligand-binding pocket of the GPCR seven-helix bundle and the receptor N terminus bound along the chemokine. In the case of CXCR4, receptor-chemokine interactions are further stabilized by an engineered disulfide bond. To allow for easy comparison, the structures have been aligned along the Cα-atoms of the receptors.

deep into the seven-helix bundle of the receptors (see the figure, insets) and binds in a position that overlaps with the small-molecule ligand-binding site of many other GPCRs. Both structures further reveal extensive interactions between the chemokines and the N terminus of the receptors. In both cases, the binding modes are in good agreement with a two-site model, with pivotal roles for the N termini of both the chemokine and its receptor (6).

Of course, the chemokine-binding modes in both studies are far from identical. This is not surprising because the two chemokines belong to two different classes, each of which typically reacts only with the same class of receptors. Furthermore, it is the core of the viral strategy to bypass chemokine specific-

HIV infections (7). The glimpses of the intermolecular cross-reaction of viral chemokine receptors and chemokines with their human counterparts provided by the two studies are thus highly relevant to understand the complex mechanisms that viruses have evolved to confound the human immune system.

The two studies cover different angles of these mechanisms. The chemokine vMIP-II that Qin *et al.* use is expressed by the Kaposi's sarcoma-associated herpesvirus to distract various human chemokine receptors (8). For this, vMIP-II has evolved characteristics that are very unusual for a chemokine. It shows promiscuous binding to a wide variety of chemokine receptors from different classes. Once bound, it acts as an antagonist to suppress receptor activation and thus helps to

Laboratory of Biomolecular Research, Paul Scherrer Institute, Villigen PSI, 5232 Switzerland. E-mail: joerg.standfuss@psi.ch

evade detection of the virus by the human immune response. The viral component in the study of Burg *et al.* is the US28 receptor, one of four chemokine receptors found in the human cytomegalovirus. This herpesvirus can persist lifelong in an asymptomatic latent form and is found in 50 to 80% of the general population. US28 helps the virus to avoid detection by binding a variety of human chemokines (9). In that sense, it follows a similar mimicry strategy as related viruses using the chemokine vMIP-II, except that in the case of US28, it is the receptor that shows promiscuous binding.

In contrast to most chemokine receptors, the viral US28 receptor signals in a ligand-independent (constitutive) manner. This further enhances pathogenicity of the virus (10) but is also of more general importance, because various diseases are attributed to activating GPCR mutations. For example, night blindness can be inherited through constitutively active mutations in rhodopsin (11). The way in which US28 stabilizes the G protein binding site with a unique residue near the conserved DRY sequence motif is remarkably similar to the effect of a constitutive active mutation in rhodopsin (12). This nicely illustrates the extent to which important interactions are conserved among GPCRs.

Future molecular dynamics simulations and structural comparisons with the inactive structures of CCR5 and CXCR4, guided by common molecular signatures of the GPCR fold (13), will teach us much of how chemokine receptors in particular and GPCRs in general are activated. GPCRs form the largest group of human drug targets with a series of antiviral and anticancer drugs specifically targeting chemokine receptors. Understanding the structural basis of viral chemokine mimicry thus has great potential to aid the development of small molecular inhibitors, not only to fight viral infections but also for treatments against a wide spectrum of inflammatory and autoimmune diseases. ■

REFERENCES

1. L. Qin *et al.*, *Science* **347**, 1117 (2015).
2. J. S. Burg *et al.*, *Science* **347**, 1113 (2015).
3. B. Wu *et al.*, *Science* **330**, 1066 (2010).
4. Q. Tan *et al.*, *Science* **341**, 1387 (2013).
5. S. G. Rasmussen *et al.*, *Nature* **477**, 549 (2011).
6. S. Thiele, M. M. Rosenkilde, *Curr. Med. Chem.* **21**, 3594 (2014).
7. E. A. Berger, P. M. Murphy, J. M. Farber, *Annu. Rev. Immunol.* **17**, 657 (1999).
8. T. N. Kiedal *et al.*, *Science* **277**, 1656 (1997).
9. H. F. Vischer, M. Siderius, R. Leurs, M. J. Smit, *Nat. Rev. Drug Discov.* **13**, 123 (2014).
10. H. F. Vischer, R. Leurs, M. J. Smit, *Trends Pharmacol. Sci.* **27**, 56 (2006).
11. A. Singhal *et al.*, *EMBO Rep.* **14**, 520 (2013).
12. X. Deupiet *et al.*, *Proc. Natl. Acad. Sci. U.S.A.* **109**, 119 (2012).
13. A. J. Venkatakrishnan *et al.*, *Nature* **494**, 185 (2013).

10.1126/science.aaa7998

PHYSICS

Single proteins under a diamond spotlight

A diamond nanomagnetometer is used to probe conformational changes of a single protein

By Philip Hemmer¹ and Carmen Gomes²

Proteins are the workhorse of life. They assemble the structural elements of the cell, catalyze metabolism, regulate cellular functions, and even transcribe and repair DNA. Many of the proteins' functions are related to their

physical shape and conformations.

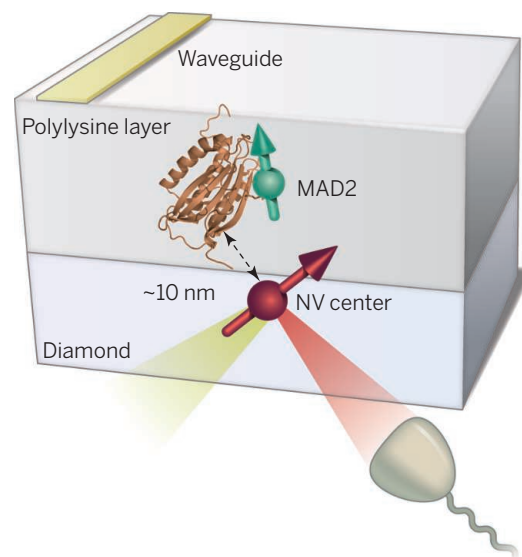
For example, protein-folding problems are responsible for a number of diseases, including Alzheimer's (1). It is no wonder that there has long been an effort to determine the structure of proteins. However, only a small fraction of protein structures have so far been determined. In most situations, results from experiments are not sufficient to build the atomic model of a protein from scratch. Even the proteins whose structures have been determined are usually purified proteins that are no longer in their functional environment, so that the key information on how the protein changes shape to perform its innate function can only be inferred. The solution is to image individual proteins in living cells in real time as they go about their business of sustaining life. An important milestone toward this goal is reported by Shi *et al.* on page 1135 of this issue (2).

They show that motions of a segment of a single protein are inferred by the magnetic signal of a nuclear spin on a nitroxide spin label located 10 nm away from a diamond nanomagnetometer.

Magnetic resonance imaging (MRI) is an established imaging modality for living systems that is scalable, in principle, down to atomic resolution. However, to achieve the resolution needed to monitor structure and motion in the critical reaction centers of proteins, a method of readout other than the usual induction coil is needed. Indeed, heroic efforts have been made over the past several decades (3). Using a custom-designed scanning magnetic probe and a technique called magnetic resonance force microscopy (MRFM), imaging of single electron spins and ensembles of nuclear spins

in a virus molecule down to a resolution of a few nanometers has been demonstrated. However, this is still far from single-atom resolution and requires cryogenic temperatures, which makes its implementation in living cells problematic.

Several years ago, a new approach to detect the magnetic fields of single nuclei has



A diamond probe. Remote nuclear spin detection using a NV center in diamond and a nitroxide reporter spin label attached to a protein, MAD2.

emerged. This involves using a laser to read out the spin state of a special nanomagnetometer probe through a process called optically detected magnetic resonance (ODMR). The first of such probes to operate at room temperature was the nitrogen vacancy (NV) color center in diamond (4, 5). Almost from the start, these NV probes have been able to see single nuclei in their local environment inside the diamond crystal. However, it took nearly a decade before they were successfully used to detect and locate single electron spins outside of the diamond lattice (6).

¹Electrical & Computer Engineering Department, Texas A&M University, College Station, TX 77843-3128, USA. ²Department of Biological and Agricultural Engineering, Texas A&M University, College Station, TX 77843-2117, USA. E-mail: prhemmer@ece.tamu.edu

Once this had been accomplished, the race was on to image single proteins with the NV center. The first major milestone on this path was the detection of small volumes of nuclear spins, close to those volumes previously achieved by MRFM, except at room temperature. This was done by two groups simultaneously (7, 8). In the latter work, the technique was pushed a step farther by interrogating the nuclear spin ensemble to give information on their local environment. By applying these techniques to single proteins, low-resolution images should be possible. However, ultimately atomic-scale resolution image of proteins are needed, at least in the reaction centers. This requires the ability to locate individual nuclei.

In the past year, detection and imaging of near-single nuclear spins outside the diamond lattice was reported (9). Here, four

clei in their immediate environment (10); a single proton bound to the diamond surface was imaged.

However, what is ultimately needed is a way to deploy reporter spins that are not limited to the diamond surface but that can be detected at long range and selectively placed at critical locations in a protein where they can sense conformation changes. It is exactly this lofty goal that has now been accomplished by Shi *et al.* (see the figures). A nitroxide spin label is anchored to a region of interest on a single protein. Each nitroxide has a single unpaired electron spin that is capable of detecting nearby nuclei by a process known as the hyperfine interaction. The nitroxide reporter spin is ~10 nm from the NV and ~5 nm beyond the diamond surface, far enough to image remote parts of the protein. Not only were Shi *et al.* able to image the

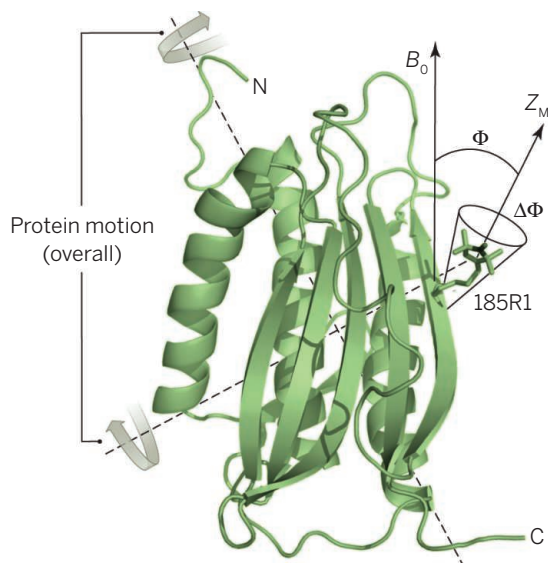
location of the reporter electron spin, they could also detect a single nuclear spin nearby. Furthermore, by analyzing the hyperfine spectrum of this nuclear spin, the approximate angle of its preferred axis relative to an applied magnetic field could be deduced [see figure 3A in (2)]. From this orientation information, they were able to infer the approximate angular range of motion of that part of the protein, which is a measure of protein flexibility and/or conformation changes. More important, the average angular motions were found to occur on time scales relevant for biological interactions.

In the future, it will be necessary to monitor far more than one nuclear spin in the protein, and so better reporter spin labels are needed. Specifically, they must have longer spin coherence

times to achieve longer-range nuclear spin imaging, and they must be photostable to the light used to interrogate the NV center. Finally, to image proteins in living cells, the bulk diamond used in these experiments must be replaced by a nanodiamond with similar NV magnetic sensitivity. ■

REFERENCES

1. J. S. Valastyan, S. Lindquist, *Dis. Model. Mech.* **7**, 9 (2014).
2. F. Shi *et al.*, *Science* **347**, 1135 (2015).
3. C. L. Degen, M. Poggio, H. J. Mamin, C. T. Rettner, D. Rugar, *Proc. Natl. Acad. Sci. U.S.A.* **106**, 1313 (2009).
4. G. Balasubramanian *et al.*, *Nature* **455**, 648 (2008).
5. J. R. Maze *et al.*, *Nature* **455**, 644 (2008).
6. B. Grotz *et al.*, *New J. Phys.* **13**, 055004 (2011).
7. T. Staudacher *et al.*, *Science* **339**, 561 (2013).
8. H. J. Mamin *et al.*, *Science* **339**, 557 (2013).
9. C. Müller *et al.*, *Nat. Commun.* **5**, 4703 (2014).
10. A. Ajoy *et al.*, *Phys. Rev. X* **5**, 011001 (2015).



See it move. Dynamics of the spin label attached to the MAD2 protein. B_0 is the external magnetic field, Z_M is the spin label quantization axis, and $\Delta\Phi$ is the angular range of motion.

silicon nuclei were observed on a specially designed glass-like coating placed on the diamond surface. This work was important because it proved that the magnetic noise produced by unpaired electrons at or near the diamond surface could be overcome, at least in principle. Until then, this magnetic noise was a roadblock that made many question whether a single external nuclear spin could ever be detected by a NV center.

Although the earlier studies proved that it is possible to greatly reduce the numbers of troublesome diamond surface spins, it has so far not been possible to eliminate them completely. However, very recently it has been shown that these few remaining surface spins can often be stable enough to use as a resource—namely, making them into “reporter” spins to image single nu-

QUANTUM MECHANICS

Look but don't touch the metals

Nitrogen-vacancy defects in diamond can probe metallic conductivity at a distance

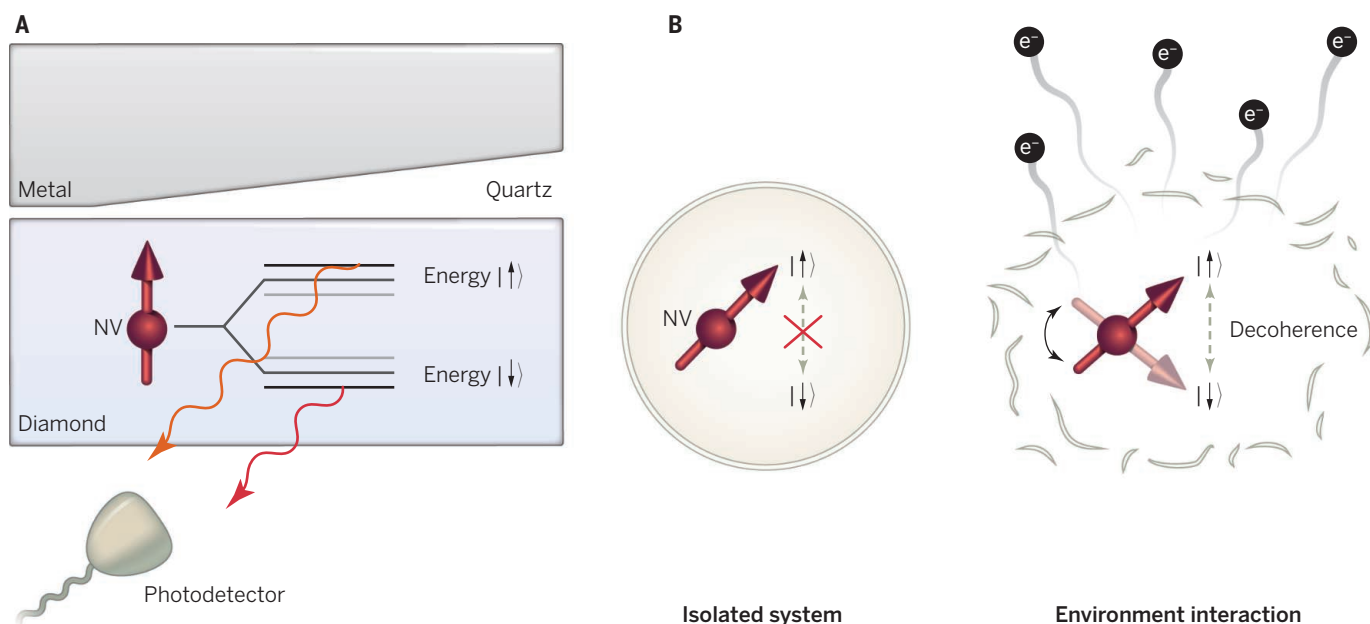
By **Liam P. McGuinness**^{1,2}
and **Fedor Jelezko**^{1,3}

Metallic conductivity is a familiar phenomenon, but metals can display surprising and exotic behavior, such as superconductivity and the quantum Hall effect. Advances in nanotechnology have led to new questions about how metallic conductivity might change in structures with dimensions approaching a few atoms. On page 1129 of this issue, Kolkowitz *et al.* (1) provide us with another tool for answering these questions: a magnetic sensor based on atomic defects in diamond.

Conductivity measurements have historically used sensors similar to an electrical multimeter, in which electrical contacts are placed across a device to measure its properties. The approach is akin to many people's first exploratory investigations of a new toy—pick it up and touch it. However, like delicate toys that can be damaged by even the most careful handling, miniaturized electrical devices are now at the point where the measuring contacts disrupt the material characteristics. For this reason, “look but don't touch” methods such as superconducting quantum interference devices (SQUIDS) and cold atomic gases have been developed. Instead of measuring resistance and conductivity via electrical contact to the sample, the magnetic field produced by electron motion is observed from a distance.

One criticism of these techniques has been their inability to measure nanometer-sized devices, because most are limited to the micrometer or millimeter scale. Recently, single dopants in diamond were proposed for experiments in nanoscale magnetic sensing (2, 3). Optically active dopants often carry ground-state spin, and for the nitrogen-vacancy (NV) color center in particular, the spin state can be coupled to photons and achieve ultrasensitive optical readout of the spin levels (4, 5). As spin en-

10.1126/science.aaa7440



A light touch. (A) Single defects in diamond known as NV centers are placed at the surface and separated from the metal layer with a gradient quartz spacer, tens of nanometers in thickness. The spin energy levels of the NV center can be monitored optically, and their response to magnetic fields (which can increase the energy gap) used as a sensitive magnetometer. (B) Rather than measuring the energy levels directly, the relaxation rate between sublevels provides information about the external environment. Well-isolated quantum systems have low relaxation rates because the environment does not provide enough energy to flip the NV spin. Bringing a noisy environment (such as moving electrons) near the NV center induces quantum decoherence and can be used to monitor dynamics in order to differentiate diffusive electron motion from ballistic motion.

ergy levels depend on the external magnetic field (known as the Zeeman effect), this technique provides a precise magnetic sensor with little more experimental setup than an optical microscope and a piece of diamond (see the figure, panel A). In (1), single NV centers were implanted in diamond with an ion beam with a well-defined energy. Careful control of the distance to the metal layer is a key point in the experiment. Kolkowitz *et al.* controlled distance by introducing a wedged quartz spacer between the diamond and metal, and boosted magnetic sensitivity by using a decoherence microscopy technique (6). Instead of measuring the energy of the spin levels directly, they monitored the relaxation rate between levels.

This approach takes advantage of the exquisite sensitivity of quantum systems to their environment. Quantum decoherence, resulting from interaction with the external environment, is the bane of many physicists' existence, and is generally avoided at all costs. Indeed, this pernicious interaction is one reason quantum computers are so difficult to build, and is also why quantum effects are not seen in everyday life. However, Kolkowitz *et al.* turn the paradigm on its head to use quantum decoherence for their benefit: Because decoherence

is caused by the environment, it can be used to provide information about the local surroundings (see the figure, panel B). Careful monitoring of the relaxation rates unraveled details of electron transport in a nearby metal layer. Clear differences for the cases of diffusive motion of electrons in polycrystalline silver (ohmic behavior) and ballistic motion of electrons in single-crystal films were demonstrated.

So how little "touch" is imparted onto the investigated metal by the team's noncontact method? Electrical isolation is ensured by the quartz layer separating the silver from the sensor, whereas physical contact can be avoided completely by fixing the diamond to a scanning tip (7). More concerning might be the unavoidable "back-action" that measurements produce in quantum physics. Kolkowitz *et al.* address this issue by measuring what is an essentially classical system, where the quantum back-action is negligible. The field produced by their single-spin sensor is completely swamped by the many thousands of electrons in the metal. However, at low temperatures, where quantum effects become relevant, quantum interaction between NV ensembles and superconducting resonators has indeed been demonstrated (8, 9).

The readout laser is perhaps the most invasive part of the measurement protocol. Illumination of metals with light can produce substantial changes in conductivity and can even lead to ejection of electrons

(the photoelectric effect). However, all of the information was gathered in the dark, when the laser was turned off and stored in the NV state. A short laser pulse was applied only at the end of the measurement to read out the sensor. Laser illumination can actually be used as a resource, in concert with diamond-based readout, to manipulate magnetic properties at the nanoscale, as shown recently (10).

The work of Kolkowitz *et al.* provides researchers with another tool for probing the importance of dimensionality, geometry, and topology on conductivity at the nanoscale. It is an important complement to well-established electrical readout techniques (11) and joins a growing repertoire of diamond sensors being applied to a diverse range of materials. As far as metals and conductivity are concerned, diamonds are nearly untouchable. ■

REFERENCES

1. S. Kolkowitz *et al.*, *Science* **347**, 1129 (2015).
2. A. Gruber *et al.*, *Science* **276**, 1202 (1997).
3. B. M. Chernobrod, G. P. Berman, *J. Appl. Phys.* **97**, 014903 (2005).
4. G. Balasubramanian *et al.*, *Nature* **455**, 648 (2008).
5. J. R. Maze *et al.*, *Nature* **455**, 644 (2008).
6. J. H. Cole, L. C. L. Hollenberg, *Nanotechnology* **20**, 495401 (2009).
7. P. Maletinsky *et al.*, *Nat. Nanotechnol.* **7**, 320 (2012).
8. Y. Kubo *et al.*, *Phys. Rev. Lett.* **105**, 140502 (2010).
9. X. Zhu *et al.*, *Nature* **478**, 221 (2011).
10. J.-P. Tetienne *et al.*, *Science* **344**, 1366 (2014).
11. A. Brenneis *et al.*, *Nat. Nanotechnol.* **10**, 135 (2015).

¹Institute of Quantum Optics, Ulm University, Ulm, D-89069 Germany. ²School of Physics, University of Melbourne, Melbourne, 3010 Australia. ³Center for Integrated Quantum Science and Technology (IQST), Ulm University, Ulm, D-89069 Germany. E-mail: fedor.jelezko@uni-ulm.de

Being smart about SMART environmental targets

Focus on the negotiation process, not just the end target

By S. L. Maxwell¹*, E. J. Milner-Gulland²,
J. P. G. Jones³, A. T. Knight²,
N. Bunnefeld⁴, A. Nuno⁵, P. Bal¹, S. Earle²,
J. E. M. Watson^{1,6}, J. R. Rhodes¹

Global progress toward meeting the Convention on Biological Diversity (CBD) Aichi targets has recently been found wanting (1). The Aichi targets were intended to be SMART (specific, measurable, ambitious, realistic, and time-bound), partly in response to the perception that failure to meet the preceding global biodiversity targets resulted from their lack of SMART-ness (2). Negotiations are building toward the September 2015 United Nations meeting on Sustainable Development Goals (SDGs), which will influence government and business development priorities for decades.

POLICY Some argue that scientists must engage with the SDG negotiation process to ensure that the environmental targets (e.g., sustainable food production and water-use efficiency) are not vague, modest, or lacking in detailed quantification (3). We caution against focusing only on ensuring that environmental targets are SMART and call for greater attention on the processes that lead to a target being set and met.

A major advantage of SMART targets is that they hold signatories to account by determining whether targets have been met. They have proven effective, for example, in guiding the successful phase-out of ozone-layer-depleting chlorofluorocarbons (CFCs) under the Montreal Protocol. However, phasing out CFC use was a politically benign topic because the ecological, social,

and economic benefits were clear and non-discriminatory (4). Many proposed SDG targets similarly address relatively noncontentious issues, including “by 2030 reduce the global maternal mortality ratio to less than 70 per 100,000 live births.” The high degree of overlap in societal, economic, and ecological values that surround noncontentious issues allow sensible SMART targets to be agreed upon and facilitates collaboration to achieve them.

It is far more difficult to set and meet SMART targets when stakeholder values are diverse and passionately defended and the costs and benefits of reaching a target are disputed. The majority of environmental issues, such as biodiversity loss and anthropogenic climate change, fall into this category. The Copenhagen climate summit in 2009 provides one example of how the interplay between lack of consensus and ineffective use of science can produce a disappointing outcome. More recently, global progress toward those CBD Aichi targets that demand collaboration between conflicting stakeholders has been slow or moving in the wrong direction (1). For example, we have failed to reduce the rate of degradation and fragmentation of natural habitats (Target 5), which conflicts with agriculture, industry, and urban development.

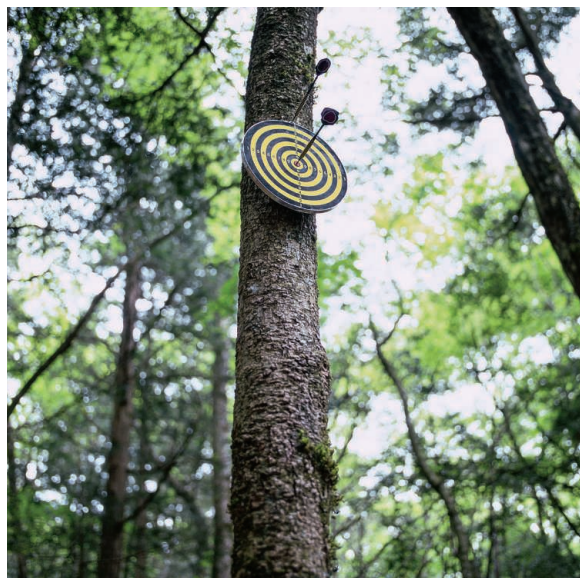
WIGGLE ROOM. A primary focus for international environmental accords should be to promote collaboration, trust, and innovation between stakeholders to enable long-term measurable action toward environmental sustainability. SMART targets provide a potential pathway for achieving this (3), but the process of building consensus and collaboration when working toward SMART targets is vital. Without this, contentious environmental issues can force environmental policy-makers to build flexibility into targets as a way to secure agreement. We identify three common pathways for providing this “wobble room”: targets that are ambiguous in definition, ambiguous in quantification, or clearly unachievable.

International signatories readily agree on targets that are ambiguous in definition because a level of increase or reduction required to meet the target is not clearly specified. For example, the 1995 United Nations Fish Stocks Agreement requires signatories to “minimize bycatch to the extent practicable” (5). It is possible to measure bycatch, but demonstrating that a nation has failed to meet the target is problematic because there is no agreed-upon level to which bycatch should be minimized, and what is practicable is not defined. The proposed SDG target to “by 2020, substantially reduce waste generation through prevention, reduction, recycling and reuse” is ambiguous in definition because, although the amount of waste generated is measurable, the specific degree of reduction is not specified.

Signatories may find it easier to agree on a target if it is difficult to measure progress toward it. The proposed SDG target to “halt the loss of biodiversity” specifies that there must be no biodiversity loss (a clearly defined level). But measuring changes in biodiversity is extremely difficult (6), so quantification is ambiguous, and signatories cannot be held accountable.

Finally, it may be easier to agree on a target so ambitious that it is clearly unachievable. Highly aspirational targets can reduce the pressure of accountability and so encourage stakeholders to become signatories. During the Ramsar Convention on Wetlands in 2002, signatories agreed to a target of “a further 55 million hectares of protected wetlands, as progress towards a global target of 250 million hectares by 2010” (7); a SMART target that seemed, and was, unachievable within the 2010 time frame.

Wobble room can enable diverse stakeholders, who are reluctant to commit to SMART targets, to agree on targets that achieve at least some



¹ARC Centre of Excellence for Environmental Decisions, School of Geography, Planning, and Environmental Management, The University of Queensland, Brisbane, QLD 4072, Australia.

²Department of Life Sciences, Imperial College London, Silwood Park, Ascot SL5 7PY, UK. ³School of Environment, Natural Resources, and Geography, Bangor University, Bangor, Gwynedd LL57 2DG, UK. ⁴School of Natural Sciences, University of Stirling, Stirling, FK9 4LA, UK. ⁵Centre for Ecology and Conservation, University of Exeter Cornwall Campus, Penryn, Cornwall TR10 9EZ, UK. ⁶Wildlife Conservation Society, Global Conservation Program, Bronx, NY 10460-1068, USA.

*Corresponding author. E-mail: smaxwell@uq.edu.au

progress toward a common goal (e.g., as achieved by the Ramsar targets—more than 208 million hectares of wetlands protected as of February 2015). However, agreeing on a target that lacks transparency and accountability can lead to failed implementation as unhappy stakeholders look to “wiggle out” of their environmental obligations [e.g., the 2010 Convention on Biological Diversity targets (2)]. For this reason, we view wiggle room as a potentially deleterious response to the symptoms of difficult target setting negotiations and not an effective solution to the underlying problems that diverse stakeholder perspectives can cause.

BUILDING CONSENSUS. To improve prospects for developing implementable and environmentally relevant targets, a sole focus on SMART-ness is not required. The strengths of natural and social science should combine, marrying ecological understanding with conflict resolution, consensus building, and negotiation tools to move toward target setting. A number of tools have demonstrated potential to increase the influence of scientific advice in negotiations, accelerate the process by reducing conflict, and lead to more effective science-driven targets.

Game theory can provide insights into why stakeholders adopt certain positions, the conditions under which they are likely to cooperate, and the likelihood that agreement can be achieved (8). Smead *et al.* (9) used a game-theoretic approach to examine failures of, and prospects for, international climate agreements. They demonstrated that very high initial demands for greenhouse gas reductions made by numerous countries led to negotiations breaking down. They suggested that future agreements are more likely to succeed if countries (particularly large emitters) reach bilateral reduction agreements before major international meetings, as happened in late 2014 between the United States and China.

Management strategy evaluation (MSE) uses socio-ecological models to test alternative management strategies under uncertain states of the world (10). For example, MSE improved management of a complex multispecies fishery in southeastern Australia. Before implementing MSE, there was little consensus in this fishery on what strategies and targets were needed to improve ecological, social, and economic performance. MSE led to substantial reduction in the time required for stakeholders to agree on a management strategy from several weeks to a few days, and improved system performance (11).

Collaborative learning (CL) is a framework that encourages joint learning, open communication, and constructive conflict

“...[V]agueness serves a political purpose that is not resolved by greater quantification alone.”

management between diverse stakeholders. Instead of demanding absolute consensus on contentious issues, CL assists stakeholders to work through issues that constrain progress toward achieving goals for the common good (12). By acknowledging conflict as inherent in most decisions, CL manages conflict so that negotiations are not soured by resentment. CL has been used in the United Kingdom to encourage biodiversity and recreation stakeholders to agree on evidence about effects of domestic dogs on bird populations, and to jointly produce a map showing areas of conflict and opportunity (13).

In both MSE and CL, rather than science being used selectively by opposing sides to support or refute arguments based on normative positions, frameworks are developed that enable stakeholders to separate factual information from normative views. This facilitates joint exploration of consequences of different actions.

PRIORITIZE THE PROCESS. The geopolitical landscape makes it very difficult to change the way targets are set. To catalyze improvements in the process for future environmental agreements, those formulating targets for negotiation should consider setting explicit targets for the improvement of trust and collaboration. This is particularly important between conflicting stakeholders, given the pivotal role that trust plays at the negotiation table. Scientists can help achieve this by applying negotiation tools that have successfully resolved contentious environmental issues at local and national levels to international negotiations. Because these tools focus on improving processes, this approach may also provide support for translating internationally set targets into national scale implementation, which can be made difficult by a lack of political support or stability or a failure to integrate biodiversity issues into other policy sectors.

There are existing conduits for enabling scientific expertise to inform international policy, such as Future Earth and the Intergovernmental Platform on Biodiversity and Ecosystem Services. With its Summary for Policymakers, the Intergovernmental Panel on Climate Change demonstrates that consensus-building approaches can produce results that are acceptable for governments while retaining scientific credibility (14).

Such initiatives could recruit researchers who study negotiation and conflict resolution and provide them a platform to support international environmental negotiations.

Science needs to inform environmental targets, to ensure their credibility and effectiveness in reducing environmental degradation. For example, Aichi Target 11—that 17% of terrestrial land area should be protected by 2020—was a negotiated compromise, rather than being based on the best available scientific advice (15). But agreeing on science-based targets requires scientists to take responsibility for ensuring that information is understood and constructively used; greater scientific engagement in improving the process of target-setting could help to achieve this. Rather than just providing ecological evidence to inform targets and monitor progress, scientists could have more of a role in supporting the processes of setting ecologically relevant targets and implementing resultant environmental policies.

It may be too late to avoid wiggle room in environmental targets within the SDGs. However, for the SDGs and other future environmental accords, simply arguing for quantified targets may be missing the point that vagueness serves a political purpose that is not resolved by greater quantification alone. Evidence from environmental negotiations suggests that failing to focus on the process of agreeing on targets will lead to stalled negotiations; targets that are ambiguous in definition or quantification or are unachievable; and a subsequent loss of momentum toward measurable environmental sustainability. ■

REFERENCES AND NOTES

1. D. P. Tittensor *et al.*, *Science* **346**, 241 (2014).
2. C. Perrings *et al.*, *Science* **330**, 323 (2010).
3. M. Stafford-Smith, *Nature* **513**, 281 (2014).
4. J. B. Skjaereth, *Glob. Environ. Change* **2**, 292 (1992).
5. Agreement for the Implementation of the Provisions of the United Nations Convention on the Law of the Sea of 10 December 1982 relating to the Conservation and Management of Straddling Fish Stocks and Highly Migratory Fish Stocks. New York, 24 July to 4 August 1995.
6. J. Bull *et al.*, *Biol. Conserv.* **178**, 2 (2014).
7. Convention on Wetlands, Resolution VIII.25: The Ramsar Strategic Plan 2003-2008, Valencia, Spain, 18 to 26 November 2002.
8. S. M. Redpath *et al.*, *Trends Ecol. Evol.* **28**, 100 (2013).
9. R. Smead *et al.*, *Nat. Climate Change* **4**, 442 (2014).
10. N. Bunnfeld *et al.*, *Trends Ecol. Evol.* **26**, 441 (2011).
11. E. A. Fulton *et al.*, *PLOS ONE* **9**, e84242 (2014).
12. S. E. Daniels, G. B. Walker, *Working Through Environmental Conflict: The Collaborative Learning Approach* (Praeger Publishers, Westport, CT, 2001).
13. R. Pouwels *et al.*, *Ecol. Soc.* **16**, 17 (2011).
14. N. K. Dubash *et al.*, *Science* **345**, 36 (2014).
15. L. M. Campbell *et al.*, *Glob. Environ. Polit.* **14**, 41 (2014).

ACKNOWLEDGMENTS

The authors thank the Australian Research Council Centre of Excellence for Environmental Decisions and Imperial College London Grand Challenges in Ecosystems and the Environment initiative for funding. They thank reviewers for comments.

10.1126/science.aaa1451

From Darwin to the dinner table, the domesticated chicken has influenced human history in a number of surprising ways.

ORNITHOLOGY

Rulers of the roost

How an unassuming bird changed the world as we know it

By Greger Larson

Like Keyser Söze, the enigmatic criminal mastermind from *The Usual Suspects*, the temporal and geographic origins of the domesticated chicken are mysterious and unresolved. In addition, although we think we understand it, we perpetually underestimate the chicken's role in human culture and history. Luckily for us, Andrew Lawler's *Why Did the Chicken Cross the World?* wakes us from our ignorant dream, detailing one surprising fact after another that ultimately reveal a grand truth: that chickens are everywhere and are inextricably linked to the emergence and maintenance of human civilization.

Although there are four closely related wild jungle fowl species, domestic chickens descend primarily from just one: the red jungle fowl. The bird's propensity to hybridize is a theme that pervades every stage of the chicken's journey across the globe. Wild populations of red jungle fowl have been subjected to such pervasive admixture with domestic fowl that some have speculated that truly wild populations may no longer exist (1).

There are now more than 20 billion chickens on Earth—more than the combined total of cats, dogs, pigs, cows, and rats. There are at least three chickens for every individual human, but as their numbers grow, “they have paradoxically become less vis-

ible.” Lawler points to the recent escalation in demand for chicken meat as one possible explanation for this phenomenon.

According to Lawler, Americans now consume four times as much chicken as they did 60 years ago. To meet our growing appetite, breeders have selected for faster growth and more rapid rates of feed conversion. Birds are now harvested only 47 days after birth—23 days earlier than chickens reared in 1950 and 2.6 pounds heavier.

The commercial poultry industry has evolved such that the average consumer interacts only with the constituent parts of the bird, either as shrink-wrapped carcasses in supermarkets or as anatomically ambiguous meat at restaurants. This disconnect between chicken as animal and chicken as food has allowed commercial producers to meet our demand for cheap protein, through questionable husbandry practices that remain exempt from animal welfare legislation.

This “cowardly reckoning,” as Proust called it (2), on the part of the consumer has also led to a shift in the way the bird is generally perceived. Idolized and venerated since their domestication (if not before), the derogatory terms “birdbrain” and “chicken shit” only entered our lexicon in the mid-20th century, when commercial poultry production began to scale up.

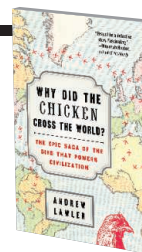
Although it's clear that we hold little regard for their intellect, chickens have influenced numerous defining events in global human history. Perhaps, then, chickens are not best equated with Keyser Söze, but with Forrest Gump.

Why Did the Chicken Cross the World?

The Epic Saga of the Bird That Powers Civilization

Andrew Lawler

Atria Books, 2014. 335 pp.



For instance, although many people know that *On the Origin of Species* opens with a chapter about domestication, few realize that Darwin spent considerable time studying the morphology and impressive color variation in chicken breeds. Chickens also played a major role in initiating and sustaining the economic independence of both slaves and women in 19th-century America. (Because the bird held so little prestige among white male farmers, blacks and women were allowed to raise flocks and sell eggs and meat.) There was even a cock-fighting pit in Shakespeare's original Globe Theatre, and proceeds from cockfighting licenses and bird sales in the 19th-century Philippines generated more revenue than tobacco, the country's biggest export. In more recent history, chicken eggs have played a crucial role in the development and production of vaccines that prevent flu viruses from erupting into pandemics.

Perhaps the clearest evidence that chickens have thoroughly infiltrated our daily lives rests in their influence on our language and humor. People are cocky and hen-pecked, and we brood and crow. We walk on eggshells, hatch ideas, rule the roost, fly the coop, get our hackles up, consider our place in the pecking order, appear cockeyed, and run around like chickens with our heads cut off. We receive French hens on the third day of Christmas, ponder the motivation of chickens to cross the road, and wonder whether the chicken or the egg arrived first.

If we are assigning fictional characters, modern humans are Jon Snow and we know nothing (3). Despite our ignorance, the chicken has experienced a recent measure of success. The prestige of an animal can be correlated with the year its genome was sequenced, and the chicken has bragging rights over the dog, pig, cow, cat, and chimp.

Lawler's book goes a long way toward restoring chickens to their respected position within human history and our modern world. Both chickens and people will benefit as a result.

REFERENCES

1. A. T. Peterson, I. L. Brisbin, *Bird Conserv. Int.* **8**, 387 (1998).
2. M. Proust, *Swann's Way* (1913).
3. G. R. R. Martin, *A Song of Ice and Fire* (Bantam Books, New York, 1996–2011).

10.1126/science.aaa4745

The reviewer is in the School of Archaeology, University of Oxford, Oxford OX1 2JD, UK. E-mail: greger.larson@arch.ox.ac.uk

THEORETICAL PHYSICS

Beyond general relativity

Einstein's quest to discover a unified field theory

By Michel Janssen

The publication of the field equations of general relativity in November 1915 was the crowning achievement of Albert Einstein's scientific career. A few years later, he embarked on a quest for a theory that would unify gravity and electromagnetism. In *Einstein's Unification*, one of the most insightful books on Einstein of the past decade, Jeroen van Dongen examines the interplay between this quest and the evolution of Einstein's views on scientific methodology.

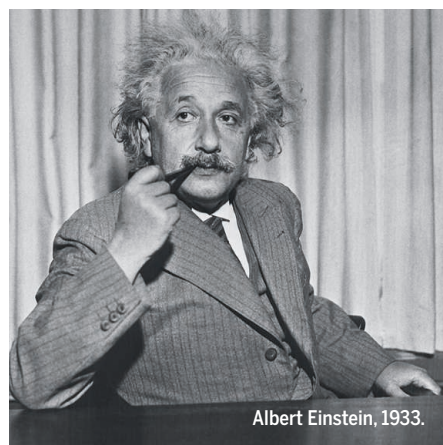
In his later years, Einstein routinely claimed that the way he had found the field equations of general relativity fundamentally changed his approach to physics. In view of this claim and drawing on studies brought together in *The Genesis of General Relativity* (1), van Dongen begins by reexamining Einstein's search for gravitational field equations from 1912 to 1915. Einstein employed two strategies in this search: either starting from a mathematically attractive candidate and then checking the physics or starting from a physically sensible candidate and then checking the mathematics. Although Einstein scholars disagree about which of these two strategies brought the decisive breakthrough of November 1915, they all acknowledge that both played an essential role in the work leading up to it. In hindsight, however, Einstein maintained that his success with general relativity had been due solely to the mathematical strategy. It is no coincidence that this is the approach he adopted in his search for a unified field theory.

Einstein famously sang the praises of the mathematical approach in his Herbert Spencer lecture in Oxford in 1933 (2), citing general relativity and the unified field theory he was working on at the time with his assistant, Walther Mayer, among its successes. The latter seemed to explain why protons and electrons have opposite charges but vastly different masses.

Ironically, Einstein's letters around this time suggest that his enthusiasm for this new theory was already waning, and a few months later a student of his colleague Wolf-

gang Pauli showed that it was mathematically flawed and did not shed any light on the mass difference between electrons and protons (pp. 121–122). The student, Valentin Bargmann, later collaborated with Einstein on a different unified field theory. In a letter recommending him to Einstein, Pauli noted that Bargmann's mathematics was stronger than his physics, adding sarcastically that Einstein might consider that a point in his favor (p. 147).

Van Dongen (p. 50) largely avoids and downplays the importance of Einstein's oft-



Albert Einstein, 1933.

cited but contentious distinction between constructive and principle theories (3). Instead, a diagram from a letter Einstein wrote to his friend Maurice Solovine in 1952 takes center stage in van Dongen's analysis of Einstein's methodology (4). This "Solovine schema," which seems to privilege principle theories, consists of three layers, with sensory data at the bottom, fundamental axioms or principles at the top, and empirical laws to be derived from these principles and then compared to the data in the middle. This last step is represented by an arrow going from the empirical laws to the data. The first and most difficult step is represented by an arrow going directly from the data to the principles. In the 1910s, Einstein insisted that this key step requires empirical intuition or, as he put it, "the intuitive grasp of the essentials of a large complex of facts" (p. 42). He later came to believe that it requires mathematical intuition instead.

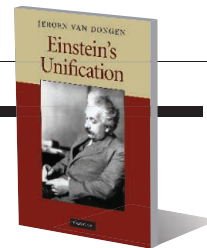
Unification introduces an additional layer to the Solovine schema, with the principles of the unified theory appearing above the prin-

Einstein's Unification

Jeroen van Dongen

Cambridge University

Press, 2010. 223 pp.



ciples of the nonunified theories for the same range of data. Einstein considered it highly improbable that a path could be found from the data through the empirical laws all the way up to the principles of the unified theory.

Van Dongen also uses the Solovine schema to explain why, later in his career, Einstein suppressed the role of the physical strategy in his work toward general relativity. The mathematical strategy corresponds to the arrow directly from data to principles. By contrast, the physical strategy, which van Dongen also describes as a constructive or bottom-up approach, would have to be represented by arrows going from data to principles indirectly through the empirical laws. There are no such arrows in the Solovine schema. By the mid-1920s, Einstein had convinced himself that these indirect paths are unreliable. Van Dongen suggests that part of the reason for Einstein's skepticism about quantum mechanics was that it had been found via such an indirect path (p. 174).

Another factor accounting for the shift in Einstein's methodology was his gradual loss of confidence in the power of experimentation to settle fundamental issues. Van Dongen highlights two 1926 experiments, proposed by Einstein and performed by Emil Rupp, to probe the nature of light. Despite strong warning signs, Einstein failed to recognize that Rupp had forged his data to match Einstein's expectations. In 1935, Rupp was forced to retract the results of several other fraudulent experiments. Even after he realized that Rupp had fabricated his data, however, Einstein stood by his theoretical considerations (p. 87).

Einstein's Unification weaves together many threads of the second half of Einstein's scientific career. It is based on an impressive array of challenging primary and secondary source material, which the author pulled together in an eminently readable book of manageable length.

REFERENCES AND NOTES

1. J. Renn, Ed. *The Genesis of General Relativity*. 4 Vols. (Springer, Berlin, 2007).
2. Reprinted in Einstein, *Ideas and Opinions* (Crown, New York, 1954; Reprint: Modern Library, New York, 1994).
3. Einstein made this distinction in 1919 in an article in the *London Times* reprinted in *Ideas and Opinions* [see (2)].
4. Van Dongen here expands on Gerald Holton, "Constructing a Theory: Einstein's Model" (1979), revised and reprinted in *The Advancement of Science and Its Burdens* (Harvard Univ. Press, Cambridge, ed. 2, 1998).

The reviewer is at the University of Minnesota and is the co-editor (with Christoph Lehner) of *The Cambridge Companion to Einstein* (2014). E-mail: janss011@umn.edu

10.1126/science.aaa7323

LETTERS

Edited by Jennifer Sills

A better way forward for Brazil's fisheries

IN DECEMBER 2014, the Brazilian Minister of the Environment released the new national red lists enumerating 2113 plants and 1173 animals threatened with extinction (1). Of the 475 aquatic species on the list, 83 are commercially exploited by fisheries, mainly as by-catch. The industrial fisheries sector is now using its political influence to persuade the government to change the contents of the list of aquatic animals or revoke it entirely. This would be an enormous setback for the conservation of Brazil's aquatic fauna. The situation is reminiscent of that of the agribusiness lobby weakening the new Forest Code, and other recent political maneuvers that could lead to the opening of mining concessions in strictly protected areas (2, 3).

The effect of the new lists on industrial fisheries is actually less disruptive than what is being purported. The ordinance that deals specifically with threatened aquatic animals provides for continued capture and trade of fishes classified as Vulnerable—the category in which most species of commercial interest fall—if they are subject to specific management plans and their fishery is regulated by federal agencies. Annual updates to the list based on new or revised information are also foreseen in the ordinance.

Therefore, instead of putting Brazil's

aquatic fauna at increased risk, the industrial fisheries sector should work with government agencies and the ministries of the Environment and Fisheries and Aquaculture to implement management strategies that have been historically lacking in Brazil (4). A permanent system to evaluate and manage stock status would eventually result in the downgrading of the extinction risk of legally protected species. Ideally, it would also prevent the overexploitation of fishing stocks that now seem to be at sustainable levels.

Fabio Di Dario,^{1*} Carlos B. M. Alves,² Harry Boos,³ Flávia L. Frédou,⁴ Rosângela P. T. Lessa,⁴ Michael M. Mincarone,¹ Marcelo A. A. Pinheiro,⁵ Carla N. M. Polaz,⁶ Roberto E. Reis,⁷ Luiz A. Rocha,⁸ Francisco M. Santana,⁹ Roberta A. Santos,³ Sonia B. Santos,¹⁰ Marcelo Vianna,¹¹ Fábio Vieira¹²

¹Núcleo em Ecologia e Desenvolvimento Socioambiental de Macaé, Universidade Federal do Rio de Janeiro, 27910-970, Macaé, RJ, Brazil. ²Projeto Manuelzão, Universidade Federal de Minas Gerais, 31270-901, Belo Horizonte, MG, Brazil. ³Centro de Pesquisa e Conservação da Biodiversidade Marinha do Sudeste e Sul, Instituto Chico Mendes de Conservação da Biodiversidade, 88301-700, Itajaí, SC, Brazil. ⁴Departamento de Pesca e Aquicultura, Universidade Federal Rural de Pernambuco, 52171-900, Recife, PE, Brazil. ⁵UNESP, Campus Experimental do Litoral Paulista (CLP), Group of Studies on Crustacean Biology (CRUSTA), 11330-900 São Vicente, SP, Brazil. ⁶Centro Nacional de Pesquisa e Conservação de Peixes Continentais, Instituto Chico Mendes de Conservação da Biodiversidade, 13630-000, Pirassununga, SP, Brazil. ⁷PUCRS, Faculdade de Biociências, Laboratory of Vertebrate Systematics, 90619-900, Porto Alegre, RS, Brazil. ⁸Institute of Biodiversity Science and Sustainability, California Academy of Sciences, San Francisco, CA 94118, USA. ⁹Unidade Acadêmica de Serra Talhada, Universidade Federal Rural de Pernambuco, 56903-970, Serra Talhada, PE, Brazil. ¹⁰Departamento de Zoologia, Universidade do Estado do Rio de Janeiro, 20550-900, Rio de Janeiro, RJ, Brazil. ¹¹Instituto de Biologia, Universidade Federal do Rio de Janeiro, CCS, bl. A. 21941-617, Rio de Janeiro, RJ, Brazil. ¹²Centro

de Transposição de Peixes/Coleção de Peixes, Universidade Federal de Minas Gerais, 31270-901, Belo Horizonte, MG, Brazil.

*Corresponding author. E-mail: didario@macae.ufrrj.br

REFERENCES

1. Brazil, Ministério do Meio Ambiente. Portarias Nos. 443, 444, 445, de 17 de Dezembro de 2014, Diário Oficial da União—Seção 1, **245**, 110 (18 December 2014); <http://pesquisa.in.gov.br/imprensa/jsp/visualiza/index.jsp?data=18/12/2014&jornal=1&pagina=110&totalArquivos=144>.
2. B. Soares-Filho *et al.*, *Science* **344**, 363 (2014).
3. J. Ferreira *et al.*, *Science* **346**, 706 (2014).
4. C. T. Elfes *et al.*, *PLOS ONE* **9**, e92589 (2014).

Complex ecology of China's seawall

IN THE POLICY Forum “Rethinking China's new great wall” (21 November 2014, p. 912), Z. Ma *et al.* demonstrated that coastal land reclamation and infrastructure construction are destroying coastal wetlands and threatening biodiversity. However, the ecological impacts of the “new Great Wall” are complex and unpredictable. With the construction of seawalls, these hard-substrate structures become “stepping stones” for rocky shore organisms (1, 2) and promote gene flow between populations in northern and southern China. Some species can rapidly occupy the “new Great Wall” and thereby extend their biogeographic ranges.

Substrate availability is one of the major factors affecting distribution of rocky intertidal species along the Chinese coastline, and there is a phylogeographic barrier to movement of rocky intertidal species at the Yangtze River estuary (3). The distribution and diversity of rocky intertidal macrobenthos (invertebrates that live on the ocean floor) have been investigated since July 2013 on the artificial seawalls along the Jangsu coastline, where a phylogeographic barrier for these species occurred before construction of large-scale artificial seawalls (4). Our preliminary observations suggest that biodiversity on the new Great Wall is showing a tendency to increase.

Xiong-Wei Huang, Wei Wang, Yun-Wei Dong*

State Key Laboratory of Marine Environmental Science, Xiamen University, Xiamen, China.

*Corresponding author. E-mail: dongyw@xmu.edu.cn

REFERENCES

1. L. Airolidi *et al.*, *Coast. Eng.* **52**, 10 (2005).
2. L. B. Firth *et al.*, *Divers. Distrib.* **19**, 10 (2013).
3. Y. Dong *et al.*, *PLOS One*, e36178 (2012).
4. Y. Dong *et al.*, World Conference on Marine Biodiversity, Qingdao, China (2014).



In January 2015, fishing boats blocked the passage of a transatlantic cruise ship at the port of Itajaí, Santa Catarina, to protest the publication of the new red lists.

PHOTO: MARCOS PORTO/AGÊNCIA RBS

Response

X.-W. HUANG *ET AL.* indicate that the seawalls constructed along the coast can help rocky shore organisms spread to and settle down in a region out of their original biogeographic range, leading to an increase in biodiversity of certain aquatic taxa in the regions where seawalls were built.

However, habitat alteration caused by human activities has profound consequences to global biodiversity (1). One of the consequences is promoting invasion of non-native species (2). In the muddy or sandy coasts, hard-substrate seawalls may create suitable habitats for organisms living in rocky shores, some of which may come from other biogeographic areas. The long-term effects of those non-native organisms on native biodiversity and local environments are unpredictable. The issue raised by Huang *et al.* highlights another potential ecological risk of seawall construction that should be monitored.

Zhijun Ma* and Bo Li

Ministry of Education Key Laboratory for
Biodiversity Science and Ecological Engineering,
Institute of Biodiversity Science, Fudan University,
Shanghai 200438, China.

*Corresponding author. E-mail: zhijunm@fudan.edu.cn

REFERENCES

1. C. Cremene *et al.*, *Conserv. Biol.* **19**, 1606 (2005).
2. T. Light, *Freshwater Biol.* **48**, 1886 (2003).

TECHNICAL COMMENT ABSTRACTS

Comment on “Stellar activity masquerading as planets in the habitable zone of the M dwarf Gliese 581”

Guillem Anglada-Escudé and Mikko Tuomi

Robertson *et al.* (Reports, 25 July 2014, p. 440) claimed that activity-induced variability is responsible for the Doppler signal of the proposed planet candidate GJ 581d. We point out that their analysis using periodograms of residual data is inappropriate and promotes inadequate tools. Because the claim challenges the viability of the method to detect exo-Earths, we encourage reanalysis and a deliberation on what the field-standard methods should be.

Full text at <http://dx.doi.org/10.1126/science.1260796>

Response to Comment on “Stellar activity masquerading as planets in the habitable zone of the M dwarf Gliese 581”

Paul Robertson, Suvrath Mahadevan, Michael Endl, Arpita Roy

Anglada-Escudé and Tuomi question the statistical rigor of our analysis while ignoring the stellar activity aspects that we present. Although we agree that improvements in multiparametric radial velocity (RV) modeling are necessary for the detection of Earth-mass planets, the key physical points we raised were not challenged. We maintain that activity on Gliese 581 induces RV shifts that were interpreted as exoplanets.

Full text at <http://dx.doi.org/10.1126/science.1260974>

ERRATA

Erratum for the Report: “Multiple nutrient stresses at intersecting Pacific Ocean biomes detected by protein biomarkers” by M. A. Saito *et al.*, *Science* **347, aaa7328 (2015). Published online 30 January 2015; 10.1126/science.aaa7328**

TECHNICAL COMMENT

EXOPLANET DETECTION

Comment on “Stellar activity masquerading as planets in the habitable zone of the M dwarf Gliese 581”

Guillem Anglada-Escudé^{1,2*} and Mikko Tuomi²

Robertson *et al.* (Reports, 25 July 2014, p. 440) claimed that activity-induced variability is responsible for the Doppler signal of the proposed planet candidate GJ 581d. We point out that their analysis using periodograms of residual data is inappropriate and promotes inadequate tools. Because the claim challenges the viability of the method to detect exo-Earths, we encourage reanalysis and a deliberation on what the field-standard methods should be.

GJ 581d was the first planet candidate of a few Earth masses reported in the circumstellar habitable zone of another star (1). It was detected by measuring the radial velocity variability of its host star using High Accuracy Radial Velocity Planet Searcher (HARPS) (1, 2). Doppler time series are usually modeled as the sum of Keplerian signals plus additional effects (e.g., correlations with activity). Detecting a planet candidate consists of quantifying the improvement of a merit statistic when one signal is added to the model. Approximate methods are often used to speed up the analyses, such as computing periodograms on residual data. Even when models are linear, correlations exist between parameters. Similarly, statistics based on residual analyses are biased quantities and cannot be used for model comparison.

A golden rule in data analysis is that the data should not be corrected but that the model is what needs improvement. The inadequacy of residual analyses can be illustrated using a simple example (Fig. 1). Assume 16 measurements of the position (x) of an object as a function of time (t) and no uncertainties. We are interested in its velocity and must decide whether a constant offset x_0 is needed to model the motion. Model A (null hypothesis) consists of $x_A(t) = vt$, where v is the only free parameter, and the alternative model B is $x_B(t) = x_0 + vt$. The question is whether including x_0 is justified, given the improvement of a statistic that we define as $\chi^2 = \frac{1}{N} \sum_{i=1}^N (x_i - x(t_i))^2$. The left panel in Fig. 1 illustrates a flawed procedure that consists of adjusting Model A and then deciding whether a constant x_0 is required to explain the residuals (bottom left panel).

Because such residuals are far from a constant shift, the reduction of χ^2 is not maximal, and the fit to a constant offset is unsatisfactory. By subtracting model A from the data, we have created a new time series that is no longer representative of the original one. A more meaningful procedure consists of comparing model A to a the global fit to all the parameters of model B (top right panel) to achieve the maximum improvement of our statistic.

Similarly, the analysis in Robertson *et al.* (3) only shows that the signal of GJ 581d is not present

in their new residual time series. Their procedure is summarized as follows: Figure 1 and figure S3 in (3) were used to suggest significant correlations between Doppler and stellar activity measurements (chromospheric emission from the H α line). After subtracting those correlations and the first three planets, periodograms (4–6) were applied to the residuals to show that GJ 581d fell below the detectability threshold. Although the semi-amplitude K of the signal of GJ 581d is large (~1.6 m/s), the apparent variability induced by the RV/H α correlations is 5 m/s peak to peak, and the scatter around the fits is at the 1.5 to 2 m/s level. Subtracting those correlations biased the residuals by removing a model that likely included contributions from real signals, and additional noise was added due to the scatter in the RV/H α relations. All things considered, the disappearance of GJ581d in such residual data is not surprising. Following Fig. 1, a simultaneous fit of the 30+ parameters involved would be needed to reach meaningful conclusions. Although there may be substantial RV/H α correlations, a global optimization analysis may not support that GJ 581d is better explained by activity. A complete analysis will be presented elsewhere.

We argue that the results of Robertson *et al.* come from the improper use of periodograms on residual data, because they implement the same flawed procedure illustrated in Fig. 1 in this Comment. Despite the utility of periodograms for providing quick-look analyses, their inadequacy to the task has been abundantly discussed in the literature (7–12). Explicitly, derived false-alarm probabilities would be representative only if a model with one sinusoid and one offset is a sufficient description of the data, measurements are uncorrelated, noise is normally distributed, and

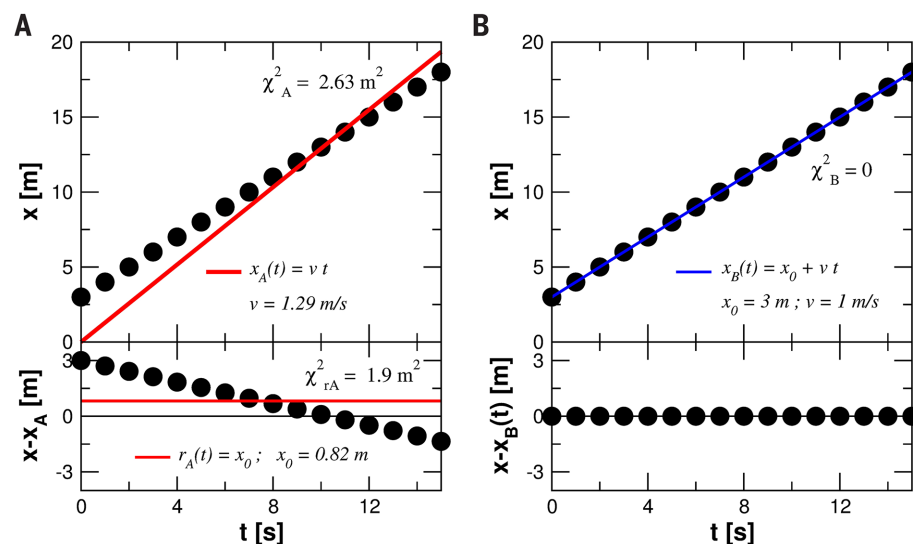


Fig. 1. This example illustrates why residual statistics must not be used to assess significance in multiparametric fits to data. We want to know if a constant x_0 is needed to model the position x of a body as a function of time t (black dots). (A) (Top) represents the fit to the null hypothesis (model A), which only includes a velocity term (red line). (A) (Bottom) shows the residuals $r_A = x - x_A(t)$ to model A. An attempt to fit a model with a constant offset to r_A is shown as a red line. (B) (Top) represents a fit adjusting all the parameters simultaneously (model B, top right panel, blue line), producing the largest possible reduction in χ^2 .

¹School of Physics and Astronomy, Queen Mary University of London, London E1 4NS, UK. ²Centre for Astrophysics Research, University of Hertfordshire, AL10 9AB, Hatfield, UK. *Corresponding author. E-mail: guillem.anglada@gmail.com

uncertainties are fully characterized (5). All of these hypotheses break down when dealing with Doppler residuals: The number of signals in not known a priori, fits to data correlate with residuals, and formal uncertainties are not realistic. Proposed alternatives, such as Monte Carlo bootstrapping of periodograms (5), do not help either, because those methods also ignore correlations. Resulting biases can lead to significance assessments off by several orders of magnitude. These issues were irrelevant when Doppler amplitudes abundantly exceeded uncertainties. For example, an amplitude larger than three times the uncertainties and more than 20 measurements easily leads to false-alarm probabilities smaller than 10^{-6} , which is much smaller than usual thresholds at 1 to 0.1%. For this reason, large biases were not problematic in the early detection of gas giants ($K \sim 50$ m/s and $\sigma \sim 5$ m/s) (13), and it is the main reason that periodograms of residual data are still widespread tools in Doppler analyses despite their inadequacy for the task.

In summary, analysis of statistical significance using residual data statistics leads to incorrect assessments. Although this has been a common practice in the past, the problem is now exacerbated

with signals closer to the noise and increased model complexity. The properties of the noise can be included in the model but can never be subtracted from the data. This discussion directly affects the viability of the Doppler method to find Earth-like planets. Although Earth causes a 0.1 m/s wobble around the Sun, the long-term stability of the most quiet stars is not better than 0.8 m/s (2). That is, activity-induced variability can be 5 to 10 times as large as the signal. Although global optimization does not provide an absolute guarantee of success, analyses based on residual statistics are bound to fail. If activity poses an ultimate barrier to the detection of small planets, strategic long-term plans concerning large projects will need serious revision (14). It is thus of capital importance that analysis and verification of multiplanet claims are properly done using global-optimization techniques and by acquiring additional observations.

REFERENCES AND NOTES

1. M. Mayor *et al.*, *Astron. Astrophys.* **507**, 487–494 (2009).
2. F. Pepe *et al.*, *Astron. Astrophys.* **534**, A58 (2011).
3. P. Robertson, S. Mahadevan, M. Endl, A. Roy, *Science* **345**, 440–444 (2014).
4. N. R. Lomb, *Astrophys. Space Sci.* **39**, 447 (1976).
5. A. Cumming, *Mon. Not. R. Astron. Soc.* **354**, 1165–1176 (2004).
6. M. Zechmeister, M. Kürster, *Astron. Astrophys.* **496**, 577–584 (2009).
7. P. C. Gregory, *Astrophys. J.* **631**, 1198G (2005).
8. R. P. Baluev, *Mon. Not. R. Astron. Soc.* **385**, 1279–1285 (2008).
9. M. Tuomi, *Astron. Astrophys.* **528**, L5 (2011).
10. G. Anglada-Escudé, M. Tuomi, *Astron. Astrophys.* **548**, A58 (2012).
11. R. D. Haywood *et al.*, *Mon. Not. R. Astron. Soc.* **443**, 2517–2531 (2014).
12. R. Baluev, *Mon. Not. R. Astron. Soc.* **393**, 969–978 (2009).
13. M. Mayor, D. Queloz, *Nature* **378**, 355–359 (1995).
14. Several instruments aimed at precision better than 1 m/s are being proposed and/or in construction (e.g., ESPRESSO/VLT at the European Southern Observatory, TPF at the Hobby-Eberly Telescope CARMENES at the Calar Alto Observatory, and SPIRou at the Canadian France Hawaii Telescope), because they are considered essential to detect any Earth-like planets or confirm/characterize those detected by next planet-hunting space missions (K2/NASA, TESS/NASA and PLATO/ESA).

ACKNOWLEDGMENTS

This work has been mostly supported by The Leverhulme Trust through grant RPG 2014-281 – PAN-Disciplinary algORithms for data Analysis. We thank H. R. A. Jones and R. P. Nelson for useful discussions and support.

3 September 2014; accepted 16 January 2015
10.1126/science.1260796

TECHNICAL RESPONSE

EXOPLANET DETECTION

Response to Comment on “Stellar activity masquerading as planets in the habitable zone of the M dwarf Gliese 581”

Paul Robertson,^{1,2*} Suvrath Mahadevan,^{1,2,3} Michael Endl,⁴ Arpita Roy^{1,2,3}

Anglada-Escudé and Tuomi question the statistical rigor of our analysis while ignoring the stellar activity aspects that we present. Although we agree that improvements in multiparametric radial velocity (RV) modeling are necessary for the detection of Earth-mass planets, the key physical points we raised were not challenged. We maintain that activity on Gliese 581 induces RV shifts that were interpreted as exoplanets.

Anglada-Escudé and Tuomi (1) raise some interesting and valid points regarding statistical analysis of radial velocity (RV) data. Although we heartily agree on the ultimate statistical desirability of fitting all RV signals simultaneously, their Comment misses the heart of the matter regarding the necessity to first find ways to discriminate stellar activity from bona fide exoplanets—i.e., our findings of stellar activity in Gliese 581 (2).

It is important to reemphasize that the primary argument of our analysis was not statistical but physical. Our work clearly established the rotation period of GJ 581 to be 130 days—twice the period of “planet d”—independently of the statistical arguments raised in the Comment. Without compelling evidence otherwise, a periodic RV signal at the stellar rotation period or its integer fractions should be assumed to be asso-

ciated with stellar activity instead of a planet [as demonstrated by (3), among others]. As recently noted by the High Accuracy Radial Velocity Planet Searcher (HARPS) team—who originally discovered “planet d”—had the rotation period of GJ 581 been previously known, it is unlikely that the 66-day RV signal would ever have been ascribed to an exoplanet (4). These authors identify an analog to GJ 581 in the GJ 3543 system and attribute the detection of an RV signal at half the rotation period to stellar activity, in the absence of definitive evidence favoring the exoplanet hypothesis.

Our analysis, although statistically and conceptually simple, strongly disfavors the planetary interpretation for GJ 581d and g. The connection between the stellar magnetic activity revealed in the H α line and the RV signals of these planets is evident using the same statistical techniques as the Gliese 581 planet discovery papers (5–7), even without an exhaustive statistical exploration of the full parameter space.

The field of RV exoplanet detection needs to make simultaneous progress on three fronts in order to detect low mass planets in the habitable zones of the nearest stars:

1) Better RV precision with new instrumentation, calibration, and reduction techniques.

2) A better understanding of stellar activity, activity indicators, and ways to ameliorate its impact. This may be done by treating the problem (e.g., this work) or by avoiding it [e.g., by using near-infrared spectra (8)].

3) Improvements in statistical techniques to not just detect signals but also to be able to disentangle Doppler RV signals from stellar activity-induced signals.

We agree that the ideal way to model RV data for multiplanet systems with stellar activity is to simultaneously model Keplerian orbits and activity signals/indicators as a single, multiparametric fit. We are well aware of these issues, as we have ourselves stated in another recent paper (9). There are a number of technical and scientific challenges to such an approach, most notably how to correctly parameterize and perform such a fit and how to best invoke the Gaussian process framework, which has been used successfully to describe stellar activity in recent work (10). The insidious impact of stellar activity—even with relatively inactive stars like Gliese 581—is only now becoming apparent, and no widely recognized or accepted framework currently exists for treating it. As a first approach, our paper relied on the same statistical techniques as used by the studies that resulted in the original discoveries of the GJ 581 planets to show that accounting for activity already explains many of the puzzling aspects of the existing RV data. We and other members of the exoplanet community are eagerly working toward developing and implementing a more complete treatment.

REFERENCES

1. G. Anglada-Escudé, M. Tuomi, *Science* **347**, 1080 (2015).
2. P. Robertson, S. Mahadevan, M. Endl, A. Roy, *Science* **345**, 440–444 (2014).
3. I. Boisse *et al.*, *Astron. Astrophys.* **528**, A4 (2011).
4. N. Astudillo-Defru *et al.*, *Astron. Astrophys.*, <http://arxiv.org/abs/1411.7048> (2014).
5. S. Udry *et al.*, *Astron. Astrophys.* **469**, L43–L47 (2007).
6. M. Mayor *et al.*, *Astron. Astrophys.* **507**, 487–494 (2009).
7. S. S. Vogt *et al.*, *Astrophys. J.* **723**, 954–965 (2010).
8. R. Marchwinski, S. Mahadevan, P. Robertson, L. Ramsey, J. Harder, *Astrophys. J.* **798**, 63 (2015).
9. P. Robertson, S. Mahadevan, *Astrophys. J.* **793**, L24 (2014).
10. R. D. Haywood *et al.*, *Mon. Not. R. Astron. Soc.* **443**, 2517–2531 (2014).

12 September 2014; accepted 16 January 2015
10.1126/science.1260974

¹Department of Astronomy and Astrophysics, The Pennsylvania State University, University Park, PA 16802, USA. ²Center for Exoplanets and Habitable Worlds, The Pennsylvania State University, University Park, PA 16802, USA. ³The Penn State Astrobiology Research Center, The Pennsylvania State University, University Park, PA 16802, USA. ⁴McDonald Observatory, The University of Texas at Austin, Austin, TX 78712-1206, USA.

*Corresponding author. E-mail: pmr19@psu.edu



EINSTEIN'S VISION

GENERAL RELATIVITY TURNS 100

By Margaret Moerchen and Robert Coontz

Sitting at a desk or toiling alone in a laboratory for years, until—eureka!—insight dawns. That's the myth of how science is done. And it's almost always wrong. In reality, scientific progress comes incrementally, most researchers work in teams, and lone geniuses do not hand the world revolutionary new theories.

But Albert Einstein did.

This 2 December will mark the 100th anniversary of the publication—in four short pages—of Einstein's general theory of relativity, to this day physicists' fundamental theory of gravity. Governing the universe on the largest scales, general relativity stands with quantum mechanics, which reigns on the smallest scales, as a foundation stone of modern physics. But whereas quantum theory was the achievement of many—de Broglie, Bohr, Heisenberg, Schrödinger, Born, Dirac—general relativity leapt fully formed from Einstein's mind.


In concocting the theory, Einstein relied on thought experiments—as he had in developing the special theory of relativity, published in 1905, which showed that space and time are fungible aspects of a single spacetime. In inventing special relativity, Einstein imagined surfing a light wave; for general relativity, he envisioned walking off a roof. Through such musings Einstein realized that gravity is merely the bending of spacetime by mass and energy.

A century later, that insight underpins cutting-edge physics: searching for gravitational waves, probing the extreme gravity near the supermassive black hole at the center of our galaxy, tracing the origin of the universe. This special issue celebrates the singular achievement that made it all possible.

Adrian Cho and Daniel Clery also edited this special issue.

Shapes of distant galaxies in this image from the Hubble Space Telescope are warped by the mass of a galaxy cluster closer to Earth—a distortion predicted by general relativity.

PHOTO: NASA, ESA, THE HUBBLE HERITAGE TEAM (STSC/AURA), J. BLAKESLEE (NRC HERZBERG ASTROPHYSICS PROGRAM, DOMINION ASTROPHYSICAL OBSERVATORY), AND H. FORD (JHU)



The twin 4-kilometer arms of LIGO Livingston embrace a working forest, where logging generates vibrations that the instrument must damp out.

TO CATCH A WAVE

After decades of work, physicists say they are a year or two away from detecting ripples in spacetime

By **Adrian Cho**, in *Livingston, Louisiana*

This patch of woodland just north of Livingston, Louisiana, population 1893, isn't the first place you'd go looking for a breakthrough in physics. Standing on a small overpass that crosses an odd arching tunnel, Joseph Giaime, a physicist at Louisiana State University (LSU), 55 kilometers west in Baton Rouge, gestures toward an expanse of spindly loblolly pine, parts of it freshly reduced to stumps and mud. "It's a working forest," he says, "so they come in here to harvest the logs." On a quiet late fall morning, it seems like only a logger or perhaps a hunter would ever come here.

Yet it is here that physicists may fulfill perhaps the most spectacular prediction of

Albert Einstein's theory of gravity, or general relativity. The tunnel runs east to west for 4 kilometers and meets a similar one running north to south in a nearby warehouselike building. The structures house the Laser Interferometer Gravitational-Wave Observatory (LIGO), an ultrasensitive instrument that may soon detect ripples in space and time set off when neutron stars or black holes merge.

Einstein himself predicted the existence of such gravitational waves nearly a century ago. But only now is the quest to detect them coming to a culmination. The device in Livingston and its twin in Hanford, Washington, ran from 2002 to 2010 and saw nothing. But those Initial LIGO instruments aimed only to prove that the experiment

was technologically feasible, physicists say. Now, they're finishing a \$205 million rebuild of the detectors, known as Advanced LIGO, which should make them 10 times more sensitive and, they say, virtually ensure a detection. "It's as close to a guarantee as one gets in life," says Peter Saulson, a physicist at Syracuse University in New York, who works on LIGO.

Detecting those ripples would open a new window on the cosmos. But it won't come easy. Each tunnel contains a pair of mirrors that form an "optical cavity," within which infrared light bounces back and forth. To look for the stretching of space, physicists will compare the cavities' lengths. But they'll have to sense that motion through the din of other vibrations. Glancing at the pave-



ment on the overpass, Giaime says that the ground constantly jiggles by about a millionth of a meter, shaken by seismic waves, the rumble of nearby trains, and other things. LIGO physicists have to shield the mirrors from such vibrations so that they can see the cavities stretch or shorten by distances 10 trillion times smaller—just a billionth the width of an atom.

IN 1915, Einstein explained that gravity arises when mass and energy warp space and time, or spacetime. A year later, he predicted that massive objects undergoing the right kind of oscillating motion should emit ripples in spacetime—gravitational waves that zip along at light speed.

For decades that prediction remained controversial, in part because the mathematics of general relativity is so complicated. Einstein himself at first made a technical error, says Rainer Weiss, a physicist at the Massachusetts Institute of Technology (MIT) in Cambridge. “Einstein had it right,” he says, “but then he [messed] up.” Some theorists argued that the waves were a mathematical artifact and shouldn’t actually exist. In 1936, Einstein himself briefly took that mistaken position.

Even if the waves were real, detecting them seemed impossible, Weiss says. At

MILESTONE: 1914

Relativity and the Great War

By Emily Conover

Albert Einstein developed his intellectual bombshell, general relativity, against a backdrop of all-too-real bombs. World War I profoundly limited scientists’ ability to share ideas and perform crucial experiments to test the theory.

The physicist Karl Schwarzschild managed to contribute while serving as an artillery officer with the German army on the Russian front. Schwarzschild’s work described the curvature of spacetime outside a spherical, nonrotating massive object—a result that later proved key to studying black holes. In a 1915 letter to Einstein, he wrote, “[T]he war treated me kindly enough, in spite of the heavy gunfire, to allow me to get away from it all and take this walk in the land of your ideas.” Schwarzschild succumbed to disease not long afterward.

Other researchers had similarly bad luck. In August 1914, the German astronomer

Erwin Freundlich led an expedition to the Crimea to take measurements during a total solar eclipse. He and colleagues hoped to test Einstein’s prediction that the sun’s gravity would deflect nearby starlight. But when war broke out before the eclipse, Russian officials seized the scientists’ equipment and detained them.

The British astronomer Arthur Eddington performed the experiment 5 years later on the island of Principe, but he too felt the shadow of the war. Eddington was a conscientious objector who nearly landed in prison for refusing conscription. His colleague, Astronomer Royal Frank Dyson, was able to obtain an exemption for Eddington on the condition that he participate in the expedition. The measurement—made in 1919, after the war ended—verified Einstein’s theory, a result Eddington saw as a tool for peace. He wrote to Einstein, “It is the best possible thing that could have happened for scientific relations between England and Germany.” ■

a time when scientists knew nothing of the cosmos's gravitational powerhouses—neutron stars and black holes—the only obvious source of waves was a pair of stars orbiting each other. Calculations showed that they would produce a signal too faint to be detected.

By the 1950s, theorists were speculating about neutron stars and black holes, and they finally agreed that the waves should exist. In 1969, Joseph Weber, a physicist at the University of Maryland, College Park, even claimed to have discovered them. His setup included two massive aluminum cylinders 1.5 meters long and 0.6 meters wide, one of them in Illinois. A gravitational wave would stretch a bar and cause it to vibrate like a tuning fork, and electrical sensors would then detect the stretching. Weber saw signs of waves pinging the bars together. But other experimenters couldn't reproduce Weber's published results, and theorists argued that his claimed signals were implausibly strong.

Still, Weber's efforts triggered the development of LIGO. In 1969, Weiss, a laser expert, had been assigned to teach general

relativity. "I knew bugger all about it," he says. In particular, he couldn't understand Weber's method. So he devised his own optical method, identifying the relevant sources of noise. "I worked it out for myself, and I gave it to the students as a homework problem," he says.

Weiss's idea, which he published in 1972 in an internal MIT publication, was slow to catch on. "It was obvious to me that this was pie in the sky and it would never work," recalls Kip Thorne, a theorist at the California Institute of Technology (Caltech) in Pasadena, California. Thorne recorded his skepticism in *Gravitation*, the massive textbook that he co-wrote and published in 1973. "I had an exercise that said 'Show that this technology will never work to detect gravitational waves,'" Thorne says.

But by 1978 Thorne had warmed to the idea, and he persuaded Caltech to put up \$2 million to build a 40-meter prototype interferometer. "It wasn't a hard sell at all," Thorne says, "which was a contrast to the

situation at MIT." Weiss says that Thorne played a vital role in winning support for a full-scale detector from the National Science Foundation in 1990. Construction in Livingston and Hanford finally began in 1994.

Now, many physicists say Advanced LIGO is all but a sure winner. On a bright Monday morning in December, researchers at Livingston are embarking on a 10-day stint that will mark their first attempt to run as if making

observations. LIGO Livingston has the feel of an outpost. Roughly 30 physicists, engineers, technicians, and operators gather in the large room that serves as the facility's foyer, auditorium, and—with a table-tennis table in one corner—rec room. "Engineering run 6 began 8 minutes ago," announces Janeen Romie, an engineer from Caltech. It seems odd that so few people can run such a big rig.

But in principle, LIGO is simple. Within the interferometer's sewer pipe-like vacuum chamber, at the elbow of the device, a laser beam shines on a beam splitter, which sends half the light down each of the inter-

ferometer's arms. Within each arm, the light builds up as it bounces between the mirrors at either end. Some of the light leaks through the mirrors at the near ends of the arms and shines back on the beam splitter. If the two arms are exactly the same length, the merging waves will overlap and interfere with each other in a way that directs the light back toward the laser.

But if the lengths are slightly different, then the recombining waves will be out of sync and light will emerge from the beam splitter perpendicular to the original beam. From that "dark port" output, physicists can measure any difference in the arms' lengths to an iota of the light's wavelength. Because a gravitational wave sweeping across the apparatus would generally stretch one arm more than the other, it would cause light to warble out of the dark port at the frequency at which the wave ripples. That light would be the signal of the gravitational wave.

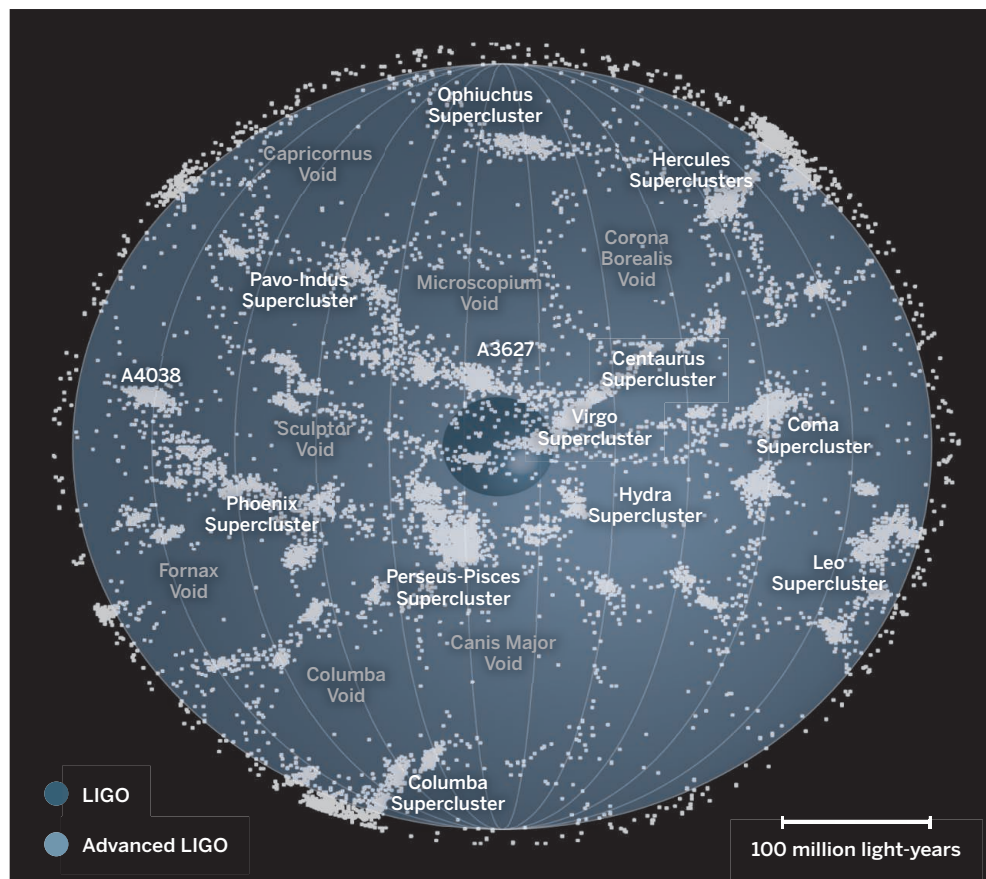
In practice, LIGO is a monumental challenge in sifting an infinitesimal signal from a mountain of vibrational noise. Sources of gravitational waves should "sing" at frequencies ranging from 10 to 1000 cycles per second, or hertz. But at frequencies of hundreds or thousands of hertz the individual photons in the laser beam produce noise as they jostle

VIDEO

Take an aerial tour of LIGO at <http://scim.ag/aerialLIGO>.

Enlarging the search

Compared with Initial LIGO, Advanced LIGO will be able to detect gravitational wave sources up to 10 times as far away, probing 1000 times as much space. Such a volume will likely yield multiple sources.



the mirrors. To smooth out such noise, researchers crank up the amount of light and deploy massive mirrors. At frequencies of tens of hertz and lower, seismic vibrations dominate, so researchers dangle the mirrors from elaborate suspension systems and actively counteract that motion. Still, a large earthquake anywhere in the world or even the surf pounding the distant coast can knock the interferometer off line.

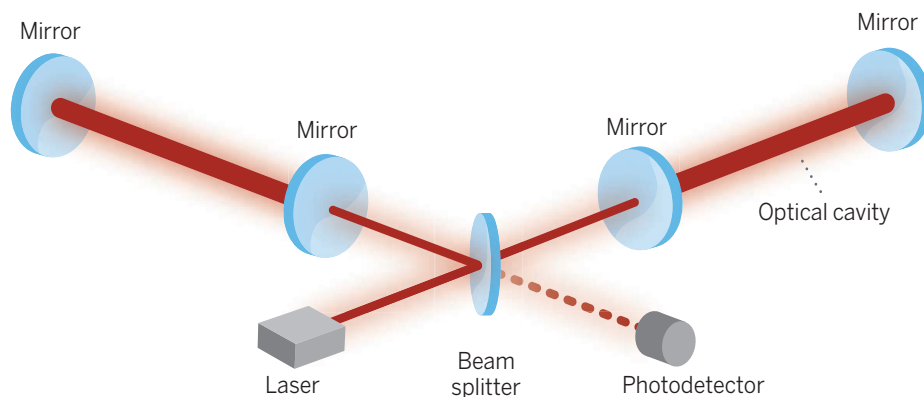
To boost the Hanford and Livingston detectors' sensitivity 10-fold, to a ten-billionth of a nanometer, physicists have completely rebuilt the devices. Each of the original 22-kilogram mirrors hung like a pendulum from a single steel fiber; the new 40-kilogram mirrors hang on silica fibers at the end of a four-pendulum chain. Instead of LIGO's original 10 kilowatts of light power, researchers aim to circulate 750 kilowatts. They will collect 100,000 channels of data to monitor the interferometer. Comparing the new and old LIGO is "like comparing a car to a wheel," says Frederick Raab, a Caltech physicist who leads the Hanford site.

The new Livingston machine has already doubled Initial LIGO's sensitivity. "In 6 months they've made equivalent progress to what Initial LIGO made in 3 or 4 years," says Raab, who adds that the Hanford site is about 6 months behind. But Valery Frolov, a Caltech physicist in charge of commissioning the Livingston detector, cautions that machine isn't running anywhere close to specs. The seismic isolation was supposed to be better, he says, and researchers haven't been able to keep the interferometer "locked" and running for long periods. As for reaching design sensitivity, "I don't know whether it will take 1 year or whether it will take 5 years like Initial LIGO did," he warns.

Still, LIGO researchers plan to make a

The ultimate motion sensor

In a LIGO interferometer, light waves leaking out of the two storage arms ordinarily interfere to send light back to the laser. By stretching the two arms by different amounts, a gravitational wave would alter the interference and send light toward a photodetector.



first observing run this year and hope to reach design sensitivity next year. "We will have detections that we will be able to stand up and defend, if not in 2016, then in 2017 or 2018," says Gabriela González, a physicist at LSU and spokesperson for the more than 900-member LIGO Science Collaboration.

That forecast is based on the statistics of the stars. LIGO's prime target is the waves generated by a pair of neutron stars—the cores of exploded stars that weigh more than the sun but measure tens of kilometers across—whirling into each other in a death spiral lasting several minutes. Initial LIGO could sense such a pair up to 50 million light-years away. Given the rarity of neutron-star pairs, that search volume was too small

to guarantee seeing one. Advanced LIGO should see 10 times as far and probe 1000 times as much space, enough to contain about 10 sources per year, González says. However, Clifford Will, a theorist at the University of Florida in Gainesville, notes that the number of sources is the most uncertain part of the experiment. "If it's less than one per year, that's not going to be too good," he says.

The hunt will be global. As well as combining data from the two LIGO detectors, researchers will share data with their peers working on the VIRGO detector, an interferometer with 3-kilometer arms near Pisa, Italy, that is undergoing upgrades, and on GEO600, one with 600-meter arms near

MILESTONE: 1915

Mercury delivers good news about a newborn theory

General relativity hit the ground running—and thrilled Albert Einstein—by explaining a decades-old puzzle regarding Mercury's orbit. According to Newtonian gravity, an isolated planet would follow exactly the same elliptical path on each orbit around its star; only the influence of neighboring planets would cause the ellipse to gradually shift, or precess, about the sun. In 1859, however, astronomer Urbain Le Verrier pointed out that Mercury was precessing slightly more than purely Newtonian gravity predicted.

Scientists proposed a slew of possible but unlikely explanations. Some insisted there must be a new planet between Mercury and the sun, which became known as Vulcan. Others proposed bands of dust near the sun, or an unseen moon around Mercury. Some tried to solve the issue by tweaking Newton's gravity. But none of these explanations withstood scrutiny.

In November 1915, Einstein finally had the solution: His new theory fully explained Mercury's extra precession. Einstein later said that the thrill of this

discovery had given him heart palpitations. "For a few days, I was beside myself with joyous excitement," he wrote.

The result immediately boosted the theory's credibility. Mathematician David Hilbert wrote to congratulate Einstein and praised him on the speed of his calculations, which Einstein had performed in only a week. What Einstein didn't let on was that his speed was the result of practice: He had done the calculations once before with an incorrect version of his theory. ■ —E.C.

MILESTONE: 1935

Battle erupts over black holes

In the 1930s, an up-and-coming physicist clashed with a distinguished member of the old guard over the cosmic implications of general relativity. Their fiery dispute enlivened scientific meetings for years.

The young rising star was the Indian-born physicist Subrahmanyan Chandrasekhar, known as Chandra; his opponent, the astronomical powerhouse Arthur Eddington (see p. 1085). Their bone of contention: the fate of aging stars. Eddington and most other scientists thought that after stars used up their fuel, they simply faded away into inert stars known as white dwarfs. But, building on the equations of general relativity and quantum mechanics, Chandra calculated that very massive stars were unstable and would collapse into nothingness at the end of their lives, producing black holes—a name coined decades later.

Chandra, then at the University of Cambridge, presented his surprising conclusions at a meeting of the Royal Astronomical Society in London in 1935. Eddington spoke immediately afterward, mercilessly pillorying Chandra's black holes as mathematical oddities that wouldn't hold up in real-world situations—"stellar buffoonery," as he later put it. "I think there should be a law of Nature to prevent a star from behaving in this absurd way!" he said. The sniping went on for years.

Eddington was well known for viciously laying into prominent physicists. The British scientists James Jeans and Chandra's mentor, Edward Arthur Milne, had both suffered similar tongue-lashings. Yet Eddington's rejection hurt Chandra both personally and professionally. He left Britain for the United States and began working on other topics.

Chandrasekhar's radical conclusions eventually did gain acceptance, as other physicists followed up on his results and astronomers began seeing hints of black holes in exotic corners of the universe. The ultimate vindication came in 1983, when he won the Nobel Prize in physics for his work. ■ —E.C.

Hannover, Germany. By comparing data, collaborators can better sift signals from noise and can pinpoint sources on the sky. Japanese researchers are also building a detector, and LIGO leaders hope to add a third detector, in India (*Science*, 14 February 2014, p. 717).

FOR THEORISTS—if not for the rest of the world—seeing gravitational waves for the first time will be something of an anticlimax. "We are so confident that gravitational waves exist that we don't actually need to see one," says Marc Kamionkowski, a theorist at Johns Hopkins University in Baltimore, Maryland. That's because in 1974 American astrophysicists Russell Hulse and

would merit science's highest accolade, physicists say. "As soon as they detect a gravitational wave, it's a Nobel Prize," Kamionkowski predicts. "It's such an extraordinary experimental accomplishment." But the prize can be shared by at most three people, so the question is who should get it.

Weiss is a shoo-in, many say, but he demurs. "I don't want to deny that there was some innovation [in my work], but it didn't come out of the blue," he says. "The lone crazy man working in a box, that just doesn't hold true." In 1962 two Russian physicists published a paper on detecting gravitational waves with an interferometer, as Weiss says he learned long after his 1972 work. In the 1970s, Robert Forward of the



Rainer Weiss of the Massachusetts Institute of Technology laid out the basic plan for LIGO 43 years ago.

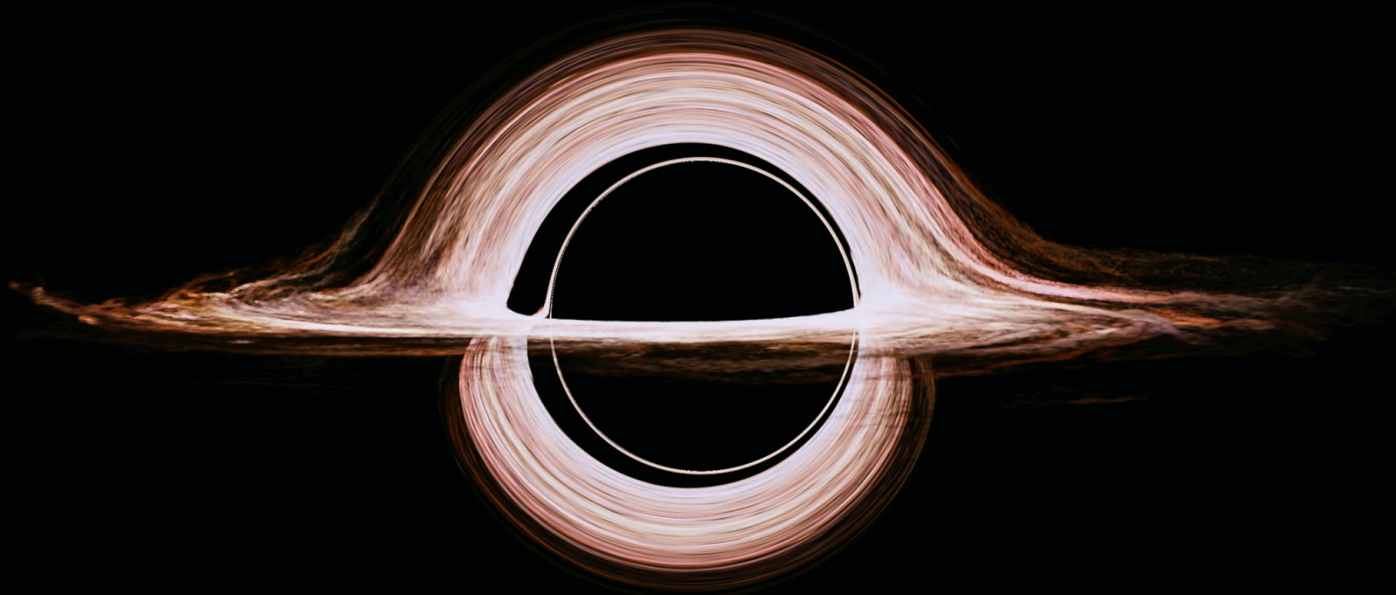
Joseph Taylor Jr. found indirect but convincing evidence of the waves. They spotted two pulsars—neutron stars that emit radio signals with clockwork regularity—orbiting each other. From the timing of the radio pulses, Hulse and Taylor could monitor the pulsars' orbit. They found it is decaying at exactly the rate expected if the pulsars were radiating energy in the form of gravitational waves.

LIGO's real payoff will come in opening a new frontier in astronomy, says Robert Wald, a gravitational theorist at the University of Chicago in Illinois. "It's kind of like after being able to see for a while, being able to hear, too," Wald says. For example, if a black hole tears apart a neutron star, then details of the gravitational waves may reveal the properties of matter in neutron stars.

All told, detecting gravitational waves

Hughes Aircraft Company in Malibu, California, ran a small interferometer. Key design elements of LIGO came from Ronald Drever, project director at Caltech from 1979 to 1987, who, Thorne says, "has to be recognized as one of the fathers of the LIGO idea."

But to make that prize-winning discovery, physicists must get Advanced LIGO up and running. At 8 a.m. on Tuesday morning, LIGO operator Gary Traylor comes off the night shift. "Last night was a total washout," he says in his soft Southern accent, swiveling in a chair in the brightly lit control room. "There's a low pressure area moving over the Atlantic that's causing 20-foot waves to crash into the coast," Traylor says, and that distant drumming overwhelmed the detector. So in the small hours, LIGO did sense waves. But not the ones everybody is hoping to see. ■



THE DARK LAB

To put general relativity to the acid test, researchers are looking inward—toward the supermassive black hole at the center of the Milky Way

By **Daniel Clery**

Like an Olympic athlete, the general theory of relativity has passed many tests in its century-long career. Its string of successes began in 1915, when Albert Einstein's picture of gravity as curved spacetime neatly explained shifts in the orbit of Mercury that had vexed astronomers for more than half a century. In recent decades it has faced more exotic and extreme tests, such as explaining why pairs of superdense neutron stars whirling around each other appear to be gradually spiraling toward collision. Here, too, general relativity triumphed: The stars are losing energy at exactly the rate expected if, as the theory predicts, they emit gravitational waves (see p. 1097).

Yet physicists remain unsatisfied. The tests so far have been too easy, they say. The gravitational fields involved have been fairly weak, coming from single stars and

bending or slowing light only very slightly. If the theory is going to show cracks, it will be under more extreme, high-field conditions. That matters because—on paper, at least—general relativity isn't the only game in town. Theorists have put forward alternative models for gravity, but in low fields they look identical to Einstein's theory. In strong fields, they begin to change.

Now, searching for a tougher test, researchers are looking toward the center of our galaxy. There, shrouded in dust, lurks a bright, compact source of radio waves known as Sagittarius A* (Sgr A*) for its position in the sky, near the edge of the constellation Sagittarius. Because of the way stars move in its vicinity, astronomers think that Sgr A* marks the dark heart of the Milky Way: a supermassive black hole weighing as much as 4 million suns but crammed into a space smaller than the distance between the sun and Mercury. That black hole produces the

A black hole distorts the image of a disk of dust and gas around it, courtesy of the special effects team for the film *Interstellar*.

most intense gravitational field in our galaxy and so provides a unique laboratory for testing the predictions of general relativity. Over the next few years, using a range of new instruments tuned to infrared light and radio waves—radiation capable of penetrating the clouds of dust and gas around the galaxy's core—astronomers are hoping to see whether Sgr A* is bending relativity beyond the breaking point.

Two teams of astronomers—one led by Andrea Ghez of the University of California, Los Angeles (UCLA), and the other by Reinhard Genzel of the Max Planck Institute for Extraterrestrial Physics (MPE) in Garching, Germany—are staring at the center of the galaxy more intently than anyone before them. They are tracking a handful of



stars that swoop close to the center—one of them to a distance equal to that between the sun and the edge of the solar system. Meanwhile, a unique new radio telescope array—still being assembled—is gearing up to carry the scrutiny right up to the edge of the putative black hole itself. In each case, the mission is the same: to spot discrepancies that Einstein's formulae cannot explain.

General relativity has “never before been tested at the high-field limit,” says astrophysicist Abraham Loeb of the Harvard-Smithsonian Center for Astrophysics (CfA) in Cambridge, Massachusetts. Elsewhere in

the galaxy, astronomers have observed stars apparently caught in the grip of smaller black holes. But the stars close to Sgr A* “are 100 times closer to the event horizon [the boundary of a black hole] and the mass scale is a million times greater,” Ghez says. “Does general relativity work down at scales 100 times closer? You’re getting into the realm of basic physics: What is gravity? That’s why people care.”

Testing general relativity in this distant laboratory isn’t easy. The black hole at Sgr A* is a small object, by galactic standards, and it emits no light. What radiation we do see is from superheated dust and gas

falling in toward the event horizon. Once material passes that boundary, no trace of it remains. All astronomers can observe is the effects of the black hole’s gravity on things around it. The UCLA and MPE teams aim to do just that.

Both groups began work in the early 1990s, when the current generation of 8- to 10-meter optical and infrared telescopes was coming online. At first, it was very difficult to pick out the movement of individual stars. The teams first determined that the stars were moving very fast (consistent with orbits around a very large mass) and then that they were

PHOTO: ESO/Y. BELETSKY



By peering through the glowing gas and dust that hides the galactic center, the Atacama Large Millimeter/submillimeter Array in Chile may help image the black hole and find pulsars around it.

accelerating around something. In 2002, the brightest of the near-in stars appeared to make its closest approach to the black hole and swing away again, essentially allowing the researchers to calculate its full orbit. It was following an ellipse so tight and so fast—5000 kilometers per second at closest approach—that it had to enclose an enormous, compact mass. “Then the community began believing in the super-massive black hole,” says astronomer Stefan Gillessen of the MPE team.

Observations stepped up a gear during the 2000s, thanks to adaptive optics: systems that rapidly deform a telescope’s mir-

ror to compensate for the blurring effect of Earth’s atmosphere. The sharper images that resulted enabled the teams to see more stars and to track them more accurately. Now the researchers could start looking for signs that relativity was making the stars’ orbits deviate from a classical Newtonian course. So far, the effects of relativity have not emerged.

Both teams expect that to change starting in 2018, when that same bright star from 2002—known as S2 in Europe and S0-2 in North America—has its next close encounter with the black hole and the gravitational field it experiences is at a

maximum. By then, both the W. M. Keck telescope in Hawaii, which the UCLA team uses, and Europe’s Very Large Telescope in Chile, used by the MPE team, will have been upgraded. “We’re trying to line up all the tools and methods ready for 2018,” says UCLA’s Gunther Witzel.

The teams will be looking for two telltale relativistic effects during and after the close approach, Ghez says. First, they expect to see the star’s light shift toward longer, redder wavelengths as the photons strain against the black hole’s intense gravity.

A more subtle effect they hope to see is precession. A star moving in a Newtonian

MILESTONE: 1936

Einstein eschews peer review

Albert Einstein was not infallible, and sometimes his pride made him slow to acknowledge mistakes. A notable example took place in 1936, when he butted heads with the editor of the journal *Physical Review* over a process that modern scientists take for granted: peer review.

Einstein, then at the Institute for Advanced Study in Princeton, New Jersey, and collaborator Nathan Rosen had submitted an article titled “Do Gravitational Waves Exist?” Their answer, surprisingly, was “no.”

At the time, peer review by anonymous outside experts was beginning to take hold among journals in the United States. Einstein, however, wasn’t used to it: Until he left Germany 3 years earlier, he had regularly published in German journals without external peer review. He was indignant when he learned that his paper had received a critical review, and he withdrew it in a huff. “We (Mr. Rosen and I) ... had not authorized you to show it to specialists before it is printed,” he wrote to the editor. “I see no reason to address the—in any case erroneous—comments of your anonymous expert.” He and Rosen submitted the paper to another journal, the *Journal of the Franklin Institute*, without change.

Yet before it was printed, Einstein revised the manuscript, retitling it “On Gravitational Waves.” It now came to the opposite conclusion: that gravitational waves were possible. The unidentified referee had pointed out a legitimate flaw in the original paper. Historians have recently confirmed that the referee was Howard Percy Robertson of Princeton University. After his anonymous criticisms were ignored, Robertson had delicately approached Einstein and convinced him of his error.

Even though peer review had helped Einstein save face, he stuck to his guns and never published another scientific paper in the *Physical Review*. ■

—E.C.

orbit would trace out an unchanging elliptical path through space, so long as no other object perturbs it. General relativity, however, predicts that after S2/S0-2’s closest approach, warped space will make the star overshoot its previous orbit very slightly, shifting the axis of its ellipse by 0.2°. The change should become apparent gradually, as the star diverges from its earlier orbit. “By 2019 we should start to see the difference,” Ghez says.

With two teams after the prize, there’s bound to be a race. “Everyone will be trying to get it. It’s a question of when do you believe your own measurements,” says Ghez, who adds that systematic errors could easily swamp the effect. But she welcomes the competition from Germany. “It’s good for getting confirmation of your results. We push each other.”

SOME OBSERVERS would like an even more stringent test of relativity. The orbiting stars don’t get *that* close to the galactic center, after all. S2/S0-2’s nearest approach is still four times the distance between the sun and the planet Neptune. If general relativity is correct, the galactic black hole’s event horizon stretches only 1/1500 that far out. An international team of researchers is preparing to look right to that edge, beyond which no photons can escape, by building a telescope array as wide as Earth itself.

The Event Horizon Telescope (EHT), as the array is called, will use short-wavelength radio waves to peer through the dust veiling the galactic center. Conventional radio telescopes can’t get a detailed image of Sgr A* because their centimeters-long wavelengths limit their resolution. But shorter radio waves, with wavelengths measured in millimeters or less, yield sharper images. Combining waves from far-apart radio telescopes can further boost the resolution. About 15 years ago, astrophysicists calculated that by combining signals from millimeter-wave observatories separated as widely as Earth allows, they could image the area around Sgr A*. Then scientists

could tackle three basic questions: Do the black hole and its event horizon really exist? If so, are they shaped the way that general relativity says they should be? Or does some other theory give a better description?

There are only a handful of millimeter-wave observatories around the world, but the EHT team is attempting to link as many as possible into a single array. The technique used, known as very-long-baseline interferometry, involves making observations with the different scopes simultaneously and recording the data with very accurate

time stamps. Later, a computer can merge the separate observations as if they were all taken at once by one huge dish. To create the planet-wide array, the EHT team has had to equip some of the individual telescopes with better receivers, recorders, and highly accurate atomic clocks. Early this year a team was doing so at the South Pole Telescope in Antarctica. “This is what gets me out of bed in the morning: fashioning a new type of telescope out of a few bits and pieces,” says team leader Shep Doeleman of the Massachusetts Institute of Technology’s Haystack Observatory in Westford and Cfa.

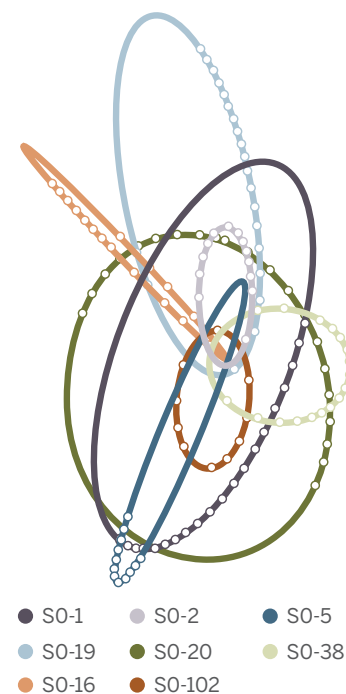
Over the past few years, the EHT team has been testing the system with just a few dishes—in Hawaii, Arizona, and California—and has seen structures

at the galactic center of about the right size but not with enough detail to probe relativity. Later this month they will try again after adding new, more distant dishes to the array: Mexico’s Large Millimeter Telescope and the Atacama Pathfinder Experiment in Chile. With this extra receiving area and longer baselines, the team hopes to see the first definitive sign of the black hole: its shadow.

The black hole should block out light from stars behind it, casting a visible shadow. Its intense gravity should also bend—or “lens”—light from stars behind it, producing a ring of distorted starlight around the edge of the shadow. That starlight is too faint to be seen from Earth. But

Invisible attractor

Stars tightly orbiting the galaxy’s central black hole may soon show relativistic effects. (Dots mark observed positions; ellipses, inferred orbits.)



Bringing general relativity down to Earth

General relativity mostly reveals itself on cosmological scales, but its effects also show up closer to home—even in our pockets. The GPS that so many smart phones use to orient and guide users would be useless if the system did not account for relativity.

According to general relativity, time slows in a gravitational field; as a result, clocks closer to a gravitational mass run slower than those farther from it—an effect known as time dilation. Time dilation results in a subtle reddening of light moving up from Earth's surface, as the weakening gravity causes the light's electromagnetic fields to oscillate at a lower frequency.

Researchers first definitively detected that “gravitational redshift” in 1959, in an experiment at a 23-meter tower at Harvard University. Physicists Robert Pound and Glen Rebka set up a source of light with a known frequency at the bottom of the tower and a detector at the top. The photons changed frequency in transit by an amount that agreed with Albert Einstein's theory. In 1977, scientists laying the foundation for GPS navigation confirmed the underlying effect, time dilation, by launching a satellite with a highly precise cesium clock. Sure enough, the clock quickly went out of sync with its Earth-bound counterparts, in agreement with Albert Einstein's theory.

For GPS to function, clocks on satellites and on the ground have to stay in sync, allowing your smart phone to measure the exact travel time of radio signals from multiple satellites. The relative timing of the signals allows the phone's GPS receiver to calculate position. If engineers failed to account for gravity's time dilation, the weaker gravity in orbit would nudge the clock in each GPS satellite ahead of ground-based clocks by tens of microseconds per day—an error that would quickly make the navigational system useless. ■ —E.C.

theorists say the EHT should see a bright ring of lensed radio waves from another source: the glowing, superheated gas and dust swirling around the black hole. A dark circle—the black hole's shadow—should blot out the very center of the glow.

Detecting the shadow, just outside the black hole's event horizon, will be a major validation of general relativity. “Just seeing the shadow as an image will be proof of the existence of a black hole,” says astrophysicist Michael Kramer of the Max Planck Institute for Radio Astronomy (MPIfR) in Bonn, Germany. It would finally give astrophysicists something more than circumstantial evidence of these objects—pure creatures of general relativity. “There is no direct evidence that [a black hole] exists; everything is from theory. First we must show it is there, and then does it deviate from general relativity,” says EHT collaborator Heino Falcke of Radboud University in Nijmegen, the Netherlands.

The shadow “would look different if there was no event horizon,” Kramer says. Theorists say that if general relativity holds, the shadow should be roughly circular; alternate theories of gravity predict slightly different shapes, such as prolate, like a cigar, or oblate, like an M&M. EHT might be able to tell the difference when it reaches full power, researchers say. The array will really come into its own when other key instruments are added in the next few years, in particular the South Pole Telescope and the Atacama Large Millimeter/submillimeter Array (ALMA). ALMA is the world's largest observatory at millimeter wavelengths; adding its 66 dishes will double EHT's resolution and boost its sensitivity 10 times, Doeleman says.

As radio astronomers sharpen their scrutiny of the galactic center, they might stumble on something that could give Einstein's theory the most stringent test of all: a pulsar, a spinning neutron star that emits clocklike radio pulses, orbiting close to the black hole. It would amount to a precise clock, probing the structure of

spacetime around the black hole with undreamed-of precision, says theorist Norbert Wex of MPIfR. By tracking variations in the pulsar's timing, Wex says, researchers could measure the black hole's mass to better than one part in a million and its spin. From those two quantities, they could calculate a quality of its gravitational field known as the quadrupole moment, predicted by general relativity. Using the pulsar again, they can then directly measure the quadrupole moment to see if relativity got it right.

For theorists, that raises a tantalizing

possibility: Even a slight difference in the two values would imply that the black hole is nonspherical. But according to general relativity, the shape of a black hole is forbidden knowledge. According to the oddly named “no-hair” theorem of relativity, the only things that it is possible to know about a black hole are its charge, its mass, and its spin. All other information about it (its “hair”) has disappeared below the event horizon, never to be seen again.

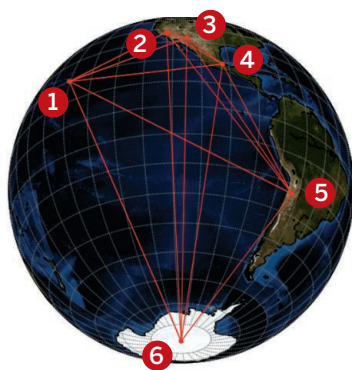
Unfortunately, despite a couple of decades of searching, the galactic center seems to be devoid of pulsars. “There should be thousands. We're completely puzzled,” Falcke says. In 2013, European radio astronomers did find one magnetar—a rare type of high-magnetic field pulsar—orbiting Sgr A*, but not close

enough to probe the black hole's spacetime. The finding did raise hopes, though, because “it shows the pulsar mechanism can work [at the galactic center] and that they are being made,” Falcke says. Bigger telescopes, like the upcoming Square Kilometer Array, or higher frequencies, such as those used by ALMA, might pierce the gloom and spot the coveted natural probe.

One way or another, researchers are looking forward to exploiting the extraordinary laboratory at the galactic center. “The next decade will be very exciting. We'll get much more data ... and hopefully an image of a black hole,” Loeb says. Says Falcke: “It's about space and time. It can't be more fundamental than this.” ■

The long view

To image the galaxy's central black hole requires a telescope array that spans the globe.



1. Submillimeter Array and James Clerk Maxwell Telescope, Hawaii
2. Combined Array for Research in Millimeter-wave Astronomy, California
3. Arizona Radio Observatory/Submillimeter-wave Telescope, Arizona
4. Large Millimeter Telescope, Mexico
5. Atacama Pathfinder Experiment, Chile
6. South Pole Telescope, Antarctica

For 100 years, the general theory of relativity has been a pillar of modern physics. The basic idea is so elegant that you don't need superpowers to understand it.



Begin with Isaac Newton's first law of motion: An object remains in uniform motion unless acted on by a force. That means if you feel no force you'll either sit still or glide forever in a straight line at a constant speed.

But Albert Einstein asked himself ...



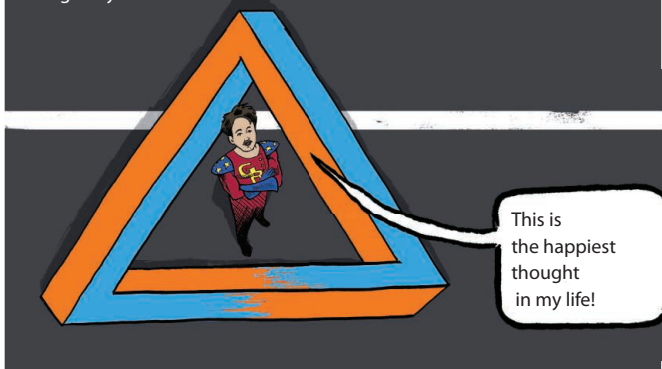
What happens if I step off a roof?

While I'm freefalling I feel weightless. I don't feel any force, even as I accelerate toward the ground!



STORY BY: ADRIAN CHO
ILLUSTRATION: NGUYEN NGUYEN
<http://scim.ag/COMICGR>

Einstein had landed inside a paradox. An object that feels no force should travel at a **constant** speed. But something **accelerating** because of gravity feels no force. Einstein realized that if he resolved the paradox, he might explain the origins of gravity.

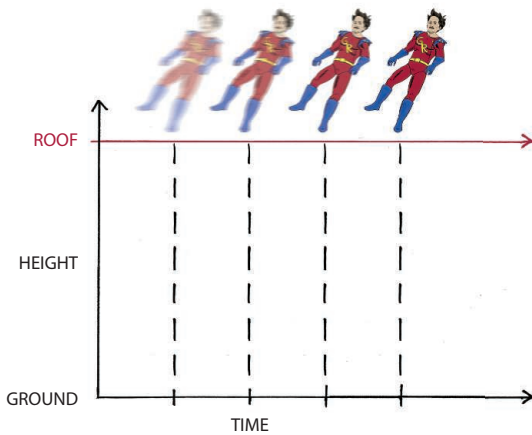


The solution:
GRAVITY IS

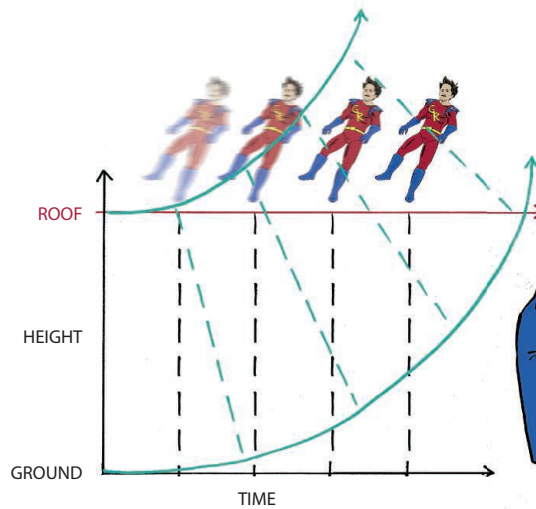
WARPED
space & time!

Einstein realized that Massive things like Earth warp spacetime. A freefalling object then follows the straightest possible path in spacetime. So—even though that path doesn't look straight to us—the object experiences no force.

"It works roughly like this. Follow me back to the roof. If we turn off gravity, I just float—tracing a straight line in this diagram."



"Now turn gravity back on. Earth's mass warps spacetime so that time on the ground ticks slower than time on the roof."



We have to stretch out the time axis nearer to the ground, so the diagram curves. Now a straight line takes me from the roof to the ground!



$$G_{\mu\nu} + g_{\mu\nu} \Lambda = 8\pi T_{\mu\nu}$$

Einstein labored for years to explain mathematically exactly how the distribution of mass and energy warps spacetime.

$$G_{\alpha\beta} = (\delta_{\alpha}^{\gamma}\delta_{\beta}^{\delta} - \frac{1}{2}g_{\alpha\beta}g^{\gamma\delta})(\Gamma_{\gamma\delta\epsilon}^{\epsilon} - \Gamma_{\gamma\epsilon\delta}^{\epsilon} + \Gamma_{\epsilon\delta\gamma}^{\epsilon} - \Gamma_{\delta\gamma\epsilon}^{\epsilon})$$

$$\Gamma_{cab} = \frac{1}{2} \left(\frac{\partial g_{ca}}{\partial x^b} + \frac{\partial g_{cb}}{\partial x^a} - \frac{\partial g_{ab}}{\partial x^c} \right)$$

$$T^{\alpha\beta} = \left(\rho + \frac{p}{c^2} \right) u^{\alpha} u^{\beta} + p g^{\alpha\beta}$$

$$\Lambda_{vac} = \frac{\Lambda c^2}{8\pi G}$$

$$ds^2 = g_{\mu\nu} dx^{\mu} dx^{\nu}$$

Today, Einstein's general relativity remains scientists' best understanding of gravity and a key to our understanding of the cosmos on the grandest scale.



DROP TEST

Physicists are challenging Einstein's theory in new versions of the most famous experiment that never happened

By Adrian Cho

About 425 years ago, legend has it, Galileo Galilei climbed the Leaning Tower of Pisa. Before a throng of scholars and students, the savant dropped pairs of balls of different weights and materials—say, wood and lead—to show that regardless of their weight or composition, all objects accelerate at the same rate under gravity's pull. About a year from now, a satellite will blast into orbit to perform the legendary test more precisely than Galileo could have imagined.

Rather than dropping things to the ground, the Drag-Compensated Micro-

Satellite for the Observation of the Equivalence Principle (MicroSCOPE) will contain two free-floating weights of different materials and will monitor whether one feels a stronger tug from Earth's gravity than the other. If so, the result would sink general relativity, Albert Einstein's theory of gravity. After more than 15 years of development, "the instrument is done, definitely done," says Pierre Touboul, a physicist at the French aerospace laboratory, ONERA, in Chatillon. "Now we cross our fingers."

Funded primarily by the French National Center for Space Studies, MicroSCOPE will test a key assumption of general relativity

called the equivalence principle, which marries two conceptions of mass. Inertial mass determines how much an object resists moving when pushed by a force—as when you shove a car. Gravitational mass determines how strongly gravity pulls on the object. According to the equivalence principle, the two masses are one and the same, regardless of how heavy a thing is or what it's made of. That explains Galileo's experiment: If the two types of mass are identical, then for all objects the pull of gravity varies in strict proportion to the resistance to motion, ensuring that all things fall at the same rate. MicroSCOPE aims to test whether the two masses



Mark Kasevich of Stanford University plans to recreate Galileo's famous tower experiment with atoms.

are the same with a precision 100 times better than any previous experiment, and other efforts could go even further.

According to general relativity, the equivalence principle must hold exactly, as acceleration and gravity are essentially the same thing. But general relativity may not be the last word on gravity, because so far it cannot be reconciled with quantum mechanics, which governs physics on the smallest scales. Efforts to bridge that gap often violate the equivalence principle, says Clifford Will, a theorist at the University of Florida in Gainesville. Spotting a violation “would definitely mean that there is some sort of physics beyond Einstein’s theory,” he says.

IRONICALLY, THE MOST FAMOUS TEST of the principle, Galileo’s demonstration at Pisa, probably never happened. “It’s a fiction,” says Alberto Martínez, a historian at the University of Texas, Austin. The first account of the event was penned long after Galileo died by his assistant Vincenzo Viviani, who said the great man wanted to show that Aristotle was wrong when he contended that heavier objects fall faster than lighter ones do.

Galileo did write about such tests in 1638 in his *Dialogues Concerning Two New Sciences*: “[T]he variation of speed in air between balls of gold, lead, copper, porphyry, and other heavy materials is so slight that ... I came to the conclusion that in a medium totally devoid of resistance all bodies would fall with the same speed.” But Galileo likely inferred the result by timing balls rolling down ramps, says John Heilbron, a historian emeritus at the University of California (UC), Berkeley. “He had a clear idea that it didn’t matter what he made the ball out of,” Heilbron says. “I think he was too lazy” to actually drag weights up a tower.

Although Galileo’s analysis jibes with the equivalence principle, he wouldn’t have understood it that way, says Domenico Bertoloni Meli, a historian of science at Indiana University, Bloomington. The concepts of inertial and gravitational mass were invented later by Isaac Newton. Newton proved that the two types of mass were equal by showing that pendulums of equal lengths but different materials swing at the same rate, as he described in *Philosophiæ Naturalis Principia Mathematica* in 1687.

The equivalence principle proved key to Einstein’s invention of general relativity. Einstein deduced that gravity arises when energy and mass bend spacetime. In that warped spacetime, freefalling objects follow the straightest possible paths, or geodesics, which to us appear as the parabolic arc of a thrown ball and the elliptical orbit of a planet. The change of the object’s speed and direction is its acceleration, which depends on the amount of warping of spacetime. If such warping is all there is to gravity, then in a given situation all things must accelerate at the same rate as they fall. That’s because for any starting position and velocity, there is only one straightest path in spacetime.

But gravity could be more complicated, says Thibault Damour, a theorist at the Institute of Advanced Scientific Studies (IHES) in Bures-sur-Yvette, France. According to Einstein’s famous equation $E = mc^2$, an object’s inertial mass measures the energy trapped inside it. So a sliver of an atom’s mass comes from the electromagnetic force that binds the electrons to the nucleus. Much more comes from the energy of the strong force that binds particles called quarks inside the nucleus’s protons and neutrons. In general relativity, all energy has the same effect regardless of its source, Damour says.

However, in some theories that aim to unify gravity and quantum mechanics, it matters how such energy arises. For example, string theory posits that every fundamental particle is an infinitesimal string rippling through a complex 10-dimensional space. In string theory a “dilaton field” acts

MILESTONE: 1974

Neutron stars show effects of gravitational waves

Forty years ago, a pair of stars locked in a cosmological dance macabre gave cosmologists a vivid glimpse of general relativity in action. One key prediction of the theory is that massive, accelerating objects send out ripples in spacetime. Scientists haven’t detected such gravitational waves directly, but the orbiting stars showed that they exist.

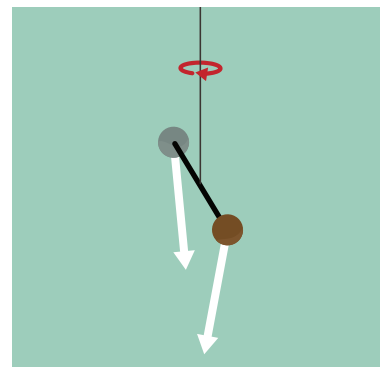
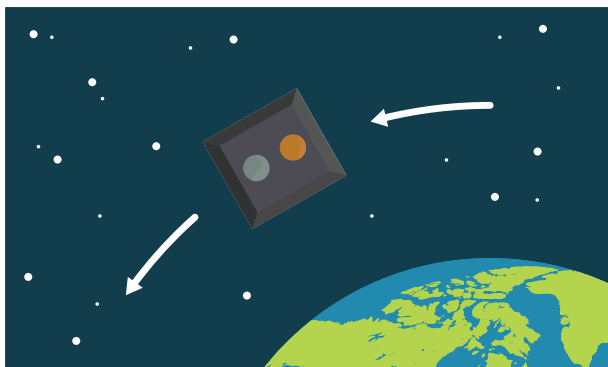
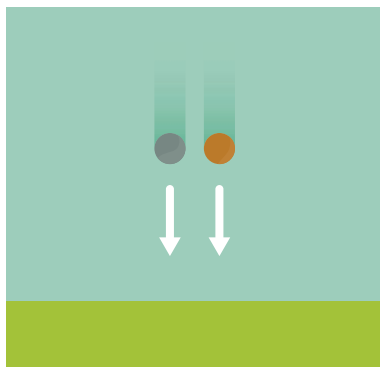
Astrophysicist Joseph Taylor Jr. and his doctoral student Russell Hulse were surveying the galaxy for pulsars: collapsed stars, or neutron stars, that sweep the universe with tight, lighthouse-like beams of energy. Using the 305-meter-wide dish of the Arecibo Observatory in Puerto Rico, Hulse and Taylor could see those beams as regular pulses of radio waves. One of their finds, known as PSR B1913+16, raised eyebrows. The intervals between pulses, about 59 milliseconds, were oddly irregular—sometimes tens of microseconds longer than expected, sometimes shorter. Apparently the pulsar was orbiting another neutron star, causing its signals to vary as it moved toward and away from Earth.

More tantalizing was what happened in the following years: The orbit of the pulsar contracted. It was shrinking exactly as Albert Einstein’s equations predicted it should if the stars were dissipating energy in the form of gravitational waves. Hulse and Taylor’s observations won them the 1993 Nobel Prize in physics. Since then, several other binary pulsars have told the same story.

In a few hundred million years, PSR B1913+16 and its companion will collide and merge, emitting a new, more powerful burst of gravitational waves. Detectors such as the Advanced Laser Interferometer Gravitational-Wave Observatory may soon detect such signals from other pairs of perishing stars—finally observing the gravitational waves that physicists are already sure are there. ■ —E.C.

Three ways to test the equivalence principle

To tell whether inertial and gravitational mass are the same, scientists can check whether objects made of different materials fall at different rates, orbit at different distances above Earth, or cause a twist in a torsional oscillator. The twist would come about if the net force produced by gravity's pull toward the center of Earth and the centrifugal force produced by Earth's rotation pointed in a different direction for each weight.



like an additional form of gravity but pulls on different types of particles with different strengths. So, two objects with the same internal energy and inertial mass may have different gravitational masses, violating the equivalence principle. The ratio of a nucleus's inertial and gravitational masses could depend on the tally of protons and neutrons in it or the difference in the numbers of protons and neutrons, Damour says.

PHYSICISTS HAVE ALREADY TESTED the equivalence principle to exquisite precision. The best test comes from Eric Adelberger, a physicist at the University of Washington, Seattle, and colleagues in the Eöt-Wash Group. "They're the gold standard right now," Will says. Eöt-Wash researchers don't drop things, but instead follow an approach pioneered in the 1800s by Hungarian physicist Loránd Eötvös, after whom the group is named.

Eötvös used a small dumbbell of weights of different materials suspended horizontally from a thin fiber. Gravity pulls each weight toward the center of Earth. But Earth also spins, so the inertia of the weights creates a tiny centrifugal force that flings them away from the planet's axis. The sum of the two forces, which align only at the equator, defines the direction "down" for each weight. If the equivalence principle holds, then the centrifugal force on each weight is locked into proportion to the gravitational one, so down is the same for both weights. Then, the dumbbell will rest pointing in any direction.

But if inertial and gravitational mass are different, then the flinging will affect the weights dif-

ferently and the net force on each one will point in a slightly different direction. "If the equivalence principle is violated, then every material has its own down," Adelberger says. That difference would cause the dumbbell to twist toward a particular orientation. In 1889, Eötvös saw no such sign and confirmed the equivalence principle to one part in 20 million.

For 25 years, Eöt-Wash researchers have refined this test. Their latest rig consists not of a dumbbell but of a nearly cylindrical shell studded on either side with weights of different materials. Instead of looking for a static twist, they slowly rotate the entire rig and look for a periodic twisting of the cylinder. Using beryllium and titanium, they found gravitational and inertial mass equal to one part in 10 trillion, as they reported in *Physical Review Letters* in 2008. That's not quite precise enough to test string theory predictions. "In principle, we could get another order of magnitude," Adelberger says. "There are difficulties, but that's the goal."

Now the MicroSCOPE team aims to

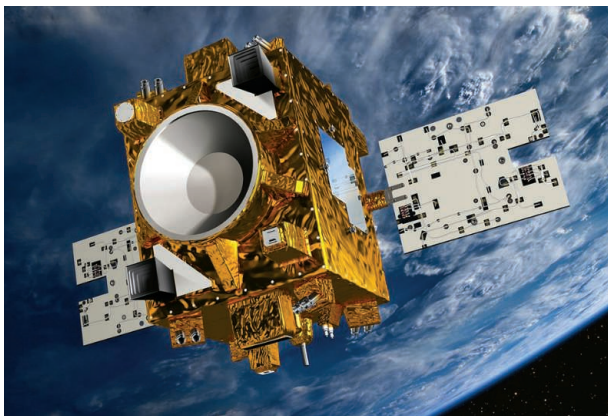
probe the equivalence principle to one part in a quadrillion. "When you have the ability to do such a test, you have to do it," says project leader Touboul. MicroSCOPE will carry aloft two cylindrical shells, one the size of a toilet paper roll and made of titanium and a smaller one inside it made of platinum-rhodium. If the equivalence principle holds, both will glide on precisely the same orbit. If not, one should slip Earthward relative to the other.

In practice, MicroSCOPE researchers will apply electrostatic forces to counteract any motion and use the force as their signal. As an extra test, they'll periodically flip the satellite so that if one cylinder does tend to circle closer to Earth, researchers will have to switch the direction of the force at the same time. MicroSCOPE will also carry a second pair of cylinders, both made of platinum-rhodium, to act as a control.

For such an ambitious experiment, MicroSCOPE is relatively cheap. The instrument cost about €20 million, Touboul says, and the entire mission less than €200 million.

Nevertheless, Damour says that according to some models MicroSCOPE has a shot at seeing a violation of the equivalence principle. "There is no sharp prediction," he says, "but there are models that say MicroSCOPE should see a strong signal."

If that sensitivity isn't enough, Mark Kasevich, a physicist at Stanford University in Palo Alto, California, thinks he can do 100 times better still. He is working on an atomic version of Galileo's drop test that will compare two different atoms: rubidium-87, which has 37 protons and 50 neutrons, and rubidium-85,



The MicroSCOPE satellite is scheduled for launch in April 2016.

which has two fewer neutrons. His 10-meter-tall vacuum chamber looks nothing like the Leaning Tower. Instead of dropping atoms from the top, Kasevich's team will toss them up from the bottom and watch them fall back down 2.3 seconds later.

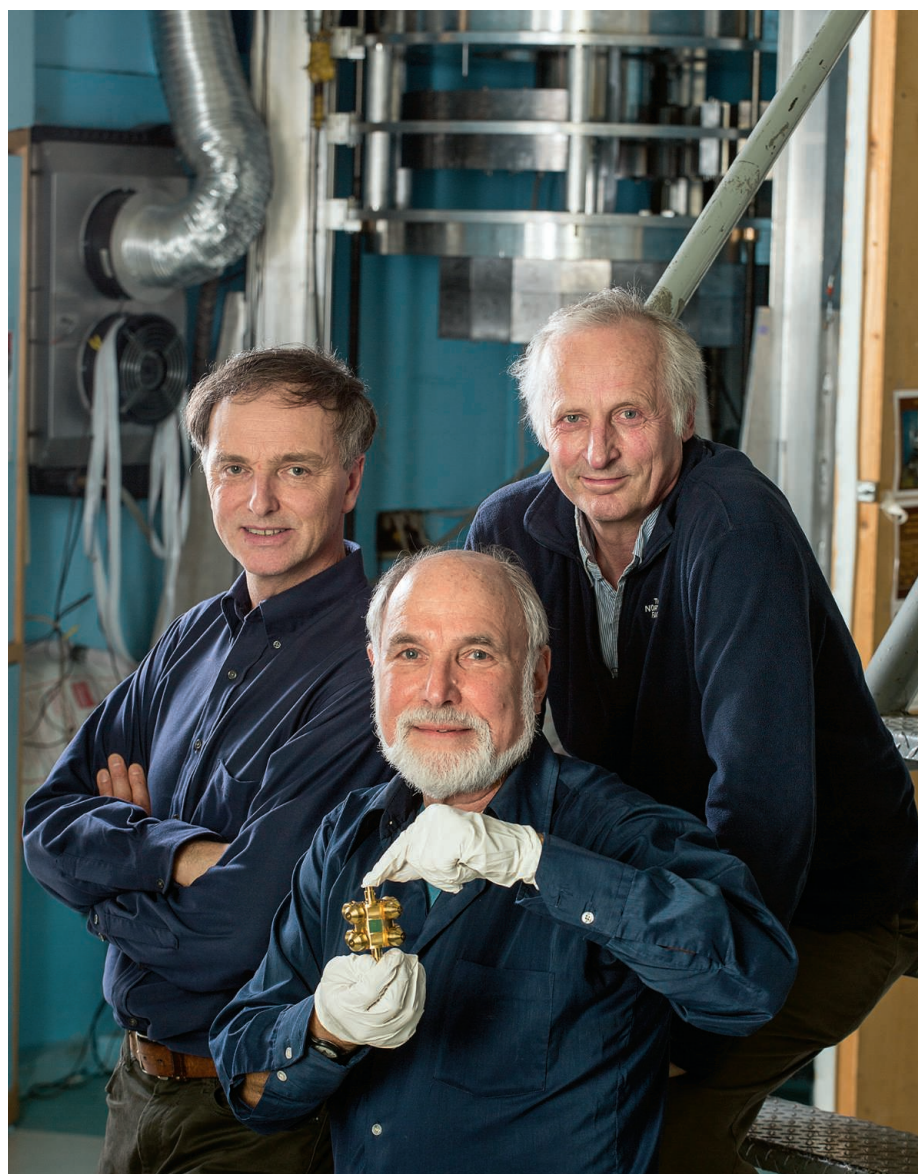
It's a tough experiment. To keep the atoms from spreading throughout the chamber, researchers must cool them to a fraction of a degree above absolute zero. "They start out as a little ball of atoms, they go up and come back down, and they're still a little ball of atoms," Kasevich says. To track the atoms, the researchers employ a technique called atom interferometry, in which pulses of laser light split the quantum wave describing the atoms in two and then bring the pieces back together, using the light waves as a ruler to measure the atoms' fall. The physicists ran the experiment with rubidium-87 alone last year and plan to run with both atoms soon. "We're optimistic that within the next year we will have our first result," Kasevich says.

Others caution that Kasevich has been promising results for some time. Reaching the sensitivity goal may be difficult, Adelberger says, as researchers will have to compensate for tiny variations in gravity throughout the tower caused by massive objects nearby. Damour also notes that the two isotopes of rubidium are not that different, which limits the experiment's ability to test the effects predicted by string theory models.

REGARDLESS OF THE SETUP—towers, pendulums, satellites—most experiments assume the test objects' gravity is too weak to contribute to their mass, so they test the so-called weak equivalence principle. But for a body the size of Earth, gravitational energy accounts for a half a billionth of its inertial mass. The strong equivalence principle states that gravitational and inertial mass remain equal even when such self-gravitation is included. To see if it holds, physicists are using the Earth and moon as test masses.

Since 1970, physicists have precisely tracked the distance to the moon by bouncing pulses of laser light off reflectors left on the surface by the Apollo astronauts and Russia's robotic rovers. The data make it possible to study how Earth and the moon—two masses of different size and composition—"fall" toward the sun. Any violation of equivalence would produce a tiny shift in the moon's orbit around Earth, toward or away from the sun, says Thomas Murphy, a physicist at UC San Diego. He heads the APOLLO project, tracking the moon with a 3.5-meter telescope at the Apache Point Observatory in New Mexico.

To search for a signal, researchers must account for many other factors that influ-



Jens Gundlach (left), Eric Adelberger (with torsion balance), and Blayne Heckel of the field-leading Eöt-Wash group.

ence the Earth-moon distance, which varies from 356,000 to 406,700 kilometers, including effects as small as the atmosphere pressing on Earth's surface. "Some people run in terror from the number of things we have to contend with," Murphy says. Researchers have shown that any shift in the orbit must be smaller than 4 millimeters, confirming the strong equivalence principle to one part in 10,000, Murphy says.

Scientists have other tests in mind. Ernst Rasel, an atomic physicist at Gottfried Wilhelm Leibniz University of Hannover in Germany, is developing a satellite known as the Space-Time Explorer and QUantum Equivalence Principle Space Test (STE-QUEST) that would run a cold-atom experiment like Kasevich's in space. There it could compare rubidium and potassium for longer times, says Naceur Gaaloul, a physicist

at Hannover. As *Science* went to press, STE-QUEST researchers were awaiting the European Space Agency's selection of projects to compete for its next mid-sized mission, to be chosen in 2018.

Then there is the Satellite Test of the Equivalence Principle (STEP), a mission proposed in the 1970s that some researchers say could cost \$300 million. STEP, conceived by Stanford's Francis Everitt and Paul Worden, is a more ambitious version of MicroSCOPE that would have 1000 times greater sensitivity. A mission like STEP is scientifically justified, says the University of Florida's Will, "but it isn't clear that such a mission is possible in the current funding climate." That climate could change, IHES's Damour notes, if MicroSCOPE spots a sign that Galileo was wrong and, after all, some balls really do fall faster than others. ■

REVIEWS

The dark side of cosmology: Dark matter and dark energy

David N. Spergel*

A simple model with only six parameters (the age of the universe, the density of atoms, the density of matter, the amplitude of the initial fluctuations, the scale dependence of this amplitude, and the epoch of first star formation) fits all of our cosmological data. Although simple, this standard model is strange. The model implies that most of the matter in our Galaxy is in the form of “dark matter,” a new type of particle not yet detected in the laboratory, and most of the energy in the universe is in the form of “dark energy,” energy associated with empty space. Both dark matter and dark energy require extensions to our current understanding of particle physics or point toward a breakdown of general relativity on cosmological scales.

John Archibald Wheeler, my academic great-grandfather, succinctly summarized “geometrodynamics,” his preferred name for the theory of general relativity (1): “Spacetime tells matter how to move; matter tells spacetime how to curve.”

Cosmologists observe the motion of atoms (either in the form of gas or stars) or follow the paths taken by light propagating across the universe and use these observations to infer the curvature of spacetime. They then use these measurements of the curvature of spacetime to infer the distribution of matter and energy in the universe. Throughout this Review I will discuss a variety of observational techniques, but ultimately they all use general relativity to interpret the observations and they all lead to the conclusion that atoms, stuff that we understand, make up only 5% of the matter and energy density of the universe.

Standard cosmological model fits, but at a price

Observations of the large-scale distribution of galaxies and quasars show that the universe is nearly uniform on its largest scales (2) and that the velocity of a distant galaxy depends on its distance (3). General relativity then implies that we live in an expanding universe that started in a big bang. Because the universe expands, light is “redshifted,” so that light from a distant galaxy appears redder when it reaches us. Hubble’s observations that found a linear relationship between galaxy redshift and distance established the basic model in the 1920s.

Our current cosmological standard model assumes that general relativity and the standard model of particle physics have been a good description of the basic physics of the universe throughout its history. It assumes that the large-scale geometry of the universe is flat: The total energy of the universe is zero. This implies that Euclidean geometry, the mathematics taught to most of us in middle school, is valid on the scale of the universe. Although the geometry of the

universe is simple, its composition is strange: The universe is composed not just of atoms (mostly hydrogen and helium), but also dark matter and dark energy.

The currently most popular cosmological model posits that soon after the big bang, the universe underwent a period of very rapid expansion. During this inflationary epoch, our visible universe expanded in volume by at least 180 *e*-foldings. The cosmic background radiation is the leftover heat from this rapid expansion. This inflationary expansion also amplifies tiny quantum fluctuations into variations in density. The inflationary model predicts that these fluctuations are “nearly scale-invariant”: The fluctuations have nearly the same amplitude on all scales.

These density variations set off sound waves that propagate through the universe and leave an imprint in the microwave sky and the large-scale distribution of galaxies. Our observations of the microwave background are a window into the universe 380,000 years after the big bang. During this epoch, electron and protons combined to form hydrogen. Once the universe became neutral, microwave background photons could propagate freely, so the sound waves imprint a characteristic scale, the distance that they can propagate in 380,000 years. This characteristic scale, the “baryon acoustic scale,” serves as a cosmic ruler for measuring the geometry of space, thus determining the density of the universe.

Observations of the temperature and polarization fluctuations in the cosmic microwave background, both from space (4–6) and from ground-based telescopes (7, 8), test this standard cosmological model and determine its basic parameters. Remarkably, a model with only six independent parameters—the age of the universe, the density of atoms, the density of matter, the amplitude of the density fluctuations, their scale dependence, and the epoch of first star formation—provides a detailed fit to all of the statistical properties of the current microwave background measurements. The same model also fits observations of the large-scale distribution of galaxies (9), measurements of the Hubble constant, and the expansion rate of the universe (10, 11), as well as distance

determinations from supernovae (12). The success comes at a price: Atoms make up less than 5% of our universe; the standard model posits that dark matter dominates the mass of galaxies and that dark energy, energy associated with empty space, makes up most of the energy density of the universe (see Fig. 1).

Astronomical observations and cosmological theory suggest that the composition of the universe is remarkably rich and complex. As Fig. 1 shows, the current best estimates of the universe’s composition (5–8) suggest that dark energy, dark matter, atoms, three different types of neutrinos, and photons all make an observable contribution to the energy density of the universe. Although black holes are an unlikely candidate for the dark matter (13), their contribution to the mass density of the universe is roughly 0.5% of the stellar density (14).

Astronomical evidence for dark matter

The evidence for dark matter long predates our observations of the microwave background, supernova observations, and measurements of large-scale structure. In a prescient article published in 1933, Fritz Zwicky (15) showed that the velocities of galaxies in the Coma cluster were much higher than expected from previous estimates of galaxy masses, thus implying that there was a great deal of additional mass in the cluster. In the 1950s, Kahn and Woltjer (16) argued that the Local Group of galaxies could be dynamically stable only if it contained appreciable amounts of unseen matter. By the 1970s, astronomers argued that mass in both clusters (17) and galaxies (18) increased with radius and did not trace light. Theoretical arguments that showed that disk stability required dark matter halos (19) buttressed these arguments. Astronomers studying the motion of gas in the outer regions of galaxies found evidence in an ever-increasing number of systems for the existence of massive halos (20–24). By the 1980s, dark matter had become an accepted part of the cosmological paradigm.

What do we know about dark matter from astronomical observations today?

Microwave background and large-scale structure observations imply that dark matter is five times more abundant than ordinary atoms (4–8). The observations also imply that the dark matter has very weak (or no) interactions with photons, electrons, and protons. If the dark matter was made of atoms today, then in the early universe, it would have been made of ions and electrons and would have left a clear imprint on the microwave sky. Thus, dark matter must be non-baryonic and “dark.”

Observations of large-scale structure and simulations of galaxy formation imply that the dark matter must also be “cold”: The dark matter particles must be able to cluster on small scales. Simulations of structure formation with cold dark matter (and dark energy) are generally successful at reproducing the observations of the large-scale distribution of galaxies (25). When combined with hydrodynamical simulations that model the effects of cooling and star formation, the

Princeton University, Princeton, NJ 08544, USA.

*Corresponding author. E-mail: dns@astro.princeton.edu

simulations can reproduce the basic observed properties of galaxies (26, 27).

Supermassive clusters are important laboratories for studying dark matter properties. These clusters are thought to be “fair samples” of the universe, as the ratio of dark matter to ordinary matter observed in the clusters is very close to the cosmological value (28). X-ray observations directly trace the distribution of ordinary (“baryonic”) matter as most of the atoms in the cluster gas have been ionized. As Zwicky (29) first discussed, observations of gravitational lensing of background galaxies directly trace the total distribution of matter in the clusters. Today, over 75 years after Zwicky’s suggestion, astronomers use large-format cameras on the Hubble Space Telescope to make detailed maps of the cluster dark matter distribution (30). These observations reveal considerable amounts of dark matter substructure in the clusters, generally consistent with the predictions of numerical simulations (31).

At much smaller scales, dwarf galaxies are another important astronomical testing ground for theories of dark matter. The gravitational potential wells of these dark matter–dominated systems are quite shallow, so the predicted properties of dwarf galaxy halos are quite sensitive to dark matter properties. Several groups (32, 33) have argued that the observed properties of dwarf galaxies do not match the predictions of numerical simulations. Although some astrophysicists argue that improved models of star-formation feedback can reconcile this discrepancy (34), others suggest that dark matter self-interactions are needed to match simulations to observations (35).

All of the astronomical arguments for the existence of dark matter assume that general relativity is valid on galactic scales. Alternative gravity theories, such as modified Newtonian dynamics (MOND) (36), obviate the need for dark matter by changing the physics of gravity. Although these models have some phenomenological success on the galaxy scale (37), they have great difficulties fitting the microwave background fluctuation observations (4–8, 38) and observations of clusters, particularly the bullet cluster (39). Most theorists also consider these alternative models as lacking motivation from fundamental physics.

What is the dark matter?

The existence of nonbaryonic dark matter implies that there must be new physics beyond the standard model of particle physics. Particle physicists have suggested a wealth of possibilities, some motivated by ideas in fundamental physics and others by a desire to explain astronomical phenomena (40).

The early universe was an incredibly powerful particle accelerator. At the high temperatures and densities of the early moments of the big bang, the cosmic background radiation created an enormous number of particles. Cosmic microwave background experiments (5–8) have detected the observational signatures of the copious number of neutrinos produced in the early first moments of the universe. These early moments could have also created the dark matter particles.

Supersymmetry, the most studied extension of our current understanding of particle physics, provides potential candidates for dark matter. Particles can be divided into two types: fermions and bosons. Fermions obey the Pauli exclusion principle: Only one particle can be found in each state. Multiple bosons can be found in the same quantum state. Electrons are fermions, while photons are bosons. Supersymmetry would be a new symmetry of nature that links each boson to a fermionic partner and vice versa. This symmetry implies a plethora of new particles: The photon would have a fermionic partner, the photino, and

seen either in deep underground experiments or through astronomical observations (40, 43). These possibilities have led to an active program of searching for dark matter. This search has had many exciting moments. There are currently a number of intriguing signals that might turn out to be the first detection of dark matter:

1) The Gran Sasso Dark Matter (DAMA) experiment has seen an annual modulation in the event rate in its detector (44) with just the theoretical predicted form (45). The interpretation of this result is controversial, as other experiments have failed to detect dark matter and

The multiple components that compose our universe

Current composition (as the fractions evolve with time)

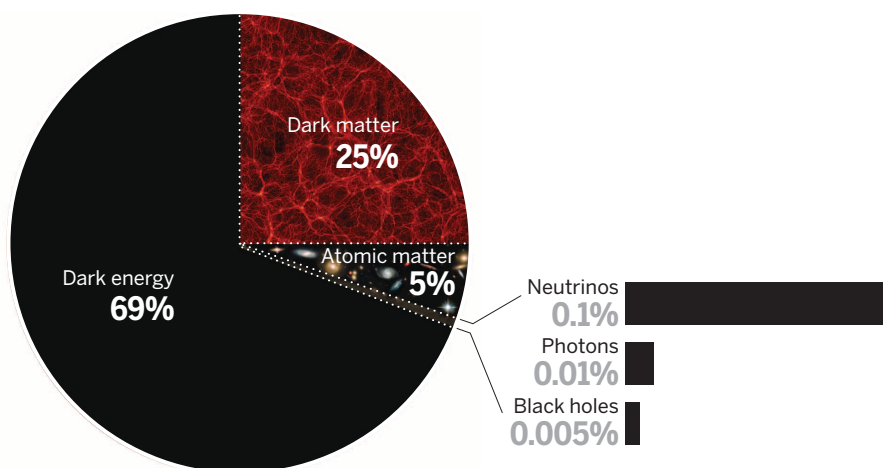


Fig. 1. The multiple components that compose our universe. Dark energy comprises 69% of the mass energy density of the universe, dark matter comprises 25%, and “ordinary” atomic matter makes up 5%. There are other observable subdominant components: Three different types of neutrinos comprise at least 0.1%, the cosmic background radiation makes up 0.01%, and black holes comprise at least 0.005%.

the electron would have a bosonic partner, the selectron. One of the goals of the Large Hadron Collider (LHC) is to search for these yet undiscovered supersymmetric particles.

The lightest supersymmetric particle (LSP) can be stable. These particles would have been produced copiously in the first moments after the big bang. For certain parameters in the supersymmetric model, the abundance of the LSP is just what is needed to explain the observed abundance of dark matter. This success is an example of the “WIMP miracle” of cosmology: A weakly interacting massive particle (WIMP), a particle that interacts through exchanging particle with masses comparable to the Higgs mass, has the needed properties to be the dark matter.

Particle physics suggests other well-motivated dark matter candidates, including the axion (41) and “asymmetric dark matter” (42), particles whose abundances are not set by their cross section but by an asymmetry between particles and antiparticles.

If WIMPs are the dark matter, then they could be detected through several different routes: Dark matter could be created at an accelerator or

seem to be in contradiction with this detection claim (46, 47).

2) There have been multiple claims of excess gamma-ray signals coming from the center of our Galaxy at a range of potential dark matter masses (48, 49). Because of the high dark matter density in the galactic center, it is potentially the brightest source of high-energy photons produced through dark matter self-annihilation. However, the galactic center also contains a wealth of astrophysical sources that emit high-energy photons. Searches in external galaxies have also suggested the existence of dark matter with yet a different mass (50). This claim is also controversial (51). Cosmologists hope that observations of nearby dwarfs could provide a less ambiguous signal (52).

3) Dark matter annihilation in our Galaxy could potentially produce positrons. Cosmic-ray experiments have been searching for these signals (53). The challenge for these experiments is to separate this signal from astrophysical sources of cosmic rays, such as pulsars and production from secondary collisions.

Hopefully, future experiments will verify one of these results.

The discovery of the dark matter particle would resolve a long-standing mystery in astronomy, provide insights into dark matter's role in galaxy formation and structure, and be the first signature of new physics beyond the Higgs.

Dark energy

When Einstein introduced his theory of general relativity, he added a cosmological constant term. This term generated a repulsive force that countered the pull of gravity and kept the universe static and stable. In the 1920s, Hubble's discoveries showed that the universe was expanding, and physicists dropped the cosmological constant term.

Motivated by observational evidence favoring a low-density universe and theoretical prejudice that favored a flat universe, enthusiasm for a cosmological constant revived in the 1970s and 1980s in the astronomy community (54–56). Physicists recognized that the value of the cosmological constant was a profound problem in fundamental physics (57).

A universe dominated by a cosmological constant is a strange place to live. We think of gravity as an attractive force. If you throw a ball upwards, gravity slows its climb out of the Earth's gravitational well. Similarly, gravity (in the absence of a cosmological constant) slows the expansion rate of the universe. Imagine your surprise if you threw a ball upwards and it started to accelerate! This is the effect that a cosmological constant has on the universe's rate of expansion.

Supernova observations provided critical evidence for the universe's acceleration. Supernovae are bright stellar explosions of nearly uniform peak luminosities (58). Thus, they serve as beacons that can be used to determine the light-travel distance to their host galaxies. By determining distance as a function of galaxy redshift, the supernova observations measure the expansion rate of the universe as a function of time. In the late 1990s, supernova observers reported the surprising result that the expansion rate of the universe is accelerating (59, 60).

Over the past 15 years, the observational evidence for cosmic acceleration has continued to grow. Measurements of the baryon acoustic scale, both in the microwave background (3–8) and in the galaxy distribution (9) as a function of redshift, traced the scale of the universe back to a redshift of 1100. Measurements of the growth rate of structure as a function of redshift also reinforced the case for cosmic acceleration.

Why is the universe accelerating? The most studied possibility is that the cosmological constant (or equivalently, the vacuum energy of empty space) is driving cosmic acceleration. Another possibility is that there is an evolving scalar field that fills space (like the Higgs field or the inflaton field that drove the rapid early expansion of the universe) (61). Both of these possibilities are lumped together in “dark energy.” Because all of the evidence for dark energy uses the equations of general relativity to interpret our observations of the universe's expansion and evolution, an alternative conclusion is that a new theory of

gravity is needed to explain the observations (38). Possibilities include modified gravity theories with extra dimensions (62).

Future observations can determine the source of cosmic acceleration and determine the nature of dark energy. Our observations can measure two different effects: the relationship between distance and redshift and the growth rate of structure (63). If general relativity is valid on cosmological scales, then these two measurements should be consistent. These measurements will also determine the basic properties of the dark energy.

Astrophysicists are currently operating several ambitious experiments that aim to use measurements of galaxy clustering and supernova observations to measure distance and gravitational lensing observations to measure the growth rate of structure (64, 65, 66). These are complemented by microwave background observations (67, 68, 69) that will provide independent measurements of gravitational lensing and more precise measurements of cosmic structure. In the next decade, even more powerful observations will map the large-scale structure of the universe over the past 10 billion years and trace the distribution of matter over much of the observable sky background (70, 71, 72). These observations will provide deeper insights into the source of cosmic acceleration.

Conclusions

Although general relativity is now a hundred-year-old theory, it remains a powerful, and controversial, idea in cosmology. It is one of the basic assumptions behind our current cosmological model: a model that is both very successful in matching observations, but implies the existence of both dark matter and dark energy. These signify that our understanding of physics is incomplete. We will likely need a new idea as profound as general relativity to explain these mysteries and require more powerful observations and experiments to light the path toward our new insights.

REFERENCES AND NOTES

1. J. A. Wheeler, K. W. Ford, *Geons, Black Holes, and Quantum Foam: A Life in Physics*. (W. W. Norton & Company, 2000). p. 153.
2. Y. Shen *et al.*, *Astron. J.* **133**, 2222–2241 (2007).
3. R. L. Barone-Nugent *et al.*, *Mon. Not. R. Astron. Soc.* **425**, 1007–1012 (2012).
4. D. N. Spergel *et al.*, *Astrophys. J. Suppl. Ser.* **148**, 175–194 (2003).
5. C. L. Bennett *et al.*, *Astrophys. J. Suppl. Ser.* **208**, 20–73 (2013).
6. Planck Collaboration *et al.*, *Astron. Astrophys.* **571**, 1–48 (2014).
7. S. Naess *et al.*, *J. Cosmol. Astropart. Phys.* **10**, 007 (2014).
8. Z. Hou *et al.*, *Astrophys. J.* **782**, 74–24 (2014).
9. L. Anderson *et al.*, *Mon. Not. R. Astron. Soc.* **441**, 24–62 (2014).
10. A. G. Riess *et al.*, *Astrophys. J.* **730**, 119 (2011).
11. W. L. Freedman *et al.*, *Astrophys. J.* **758**, 24 (2012).
12. M. Betoule *et al.*, *Astron. Astrophys.* **568**, A22 (2014).
13. F. Capela, M. Pshirkov, P. Tinyakov, *Phys. Rev. D Part. Fields Gravit. Cosmol.* **87**, 123524 (2013).
14. J. Kormendy, L. C. Ho, *Annu. Rev. Astron. Astrophys.* **51**, 511–653 (2013).
15. F. Zwicky, *Helv. Phys. Acta* **6**, 110–127 (1933).
16. F. D. Kahn, L. Woltjer, *Astrophys. J.* **130**, 705–717 (1959).
17. J. Einasto, A. Kaasik, E. Saar, *Nature* **250**, 309–310 (1974).

18. J. P. Ostriker, P. J. E. Peebles, A. Yahil, *Astrophys. J.* **193**, L1–L4 (1974).
19. J. P. Ostriker, P. J. E. Peebles, *Astrophys. J.* **186**, 467–480 (1973).
20. H. W. Babcock, *Lick Observatory Bull.* **498**, 41–51 (1939).
21. V. C. Rubin, W. K. Ford Jr., *Astrophys. J.* **159**, 379–403 (1970).
22. M. S. Roberts, A. H. Rots, *Astron. Astrophys.* **26**, 483–485 (1973).
23. A. Bosma, thesis, University of Groningen, Netherlands (1978).
24. V. C. Rubin, W. K. Ford Jr., N. Thonnard, *Astrophys. J.* **238**, 471–487 (1980).
25. V. Springel *et al.*, *Nature* **435**, 629–636 (2005).
26. M. Vogelsberger *et al.*, *Mon. Not. R. Astron. Soc.* **444**, 1518–1547 (2014).
27. J. Schaye *et al.*, *Mon. Not. R. Astron. Soc.* **446**, 521–554 (2015).
28. I. Chiu *et al.*, <http://arxiv.org/abs/1412.7823> (2014).
29. F. Zwicky, *Phys. Rev.* **51**, 290–290 (1937).
30. T. Johnston *et al.*, *Astrophys. J.* **797**, 1–31 (2014).
31. C. Grillo *et al.*, <http://arxiv.org/abs/1407.7866> (2014).
32. A. Klypin, A. V. Kravtsov, O. Valenzuela, F. Prada, *Astrophys. J.* **522**, 82–92 (1999).
33. S. Garrison-Kimmel, M. Boylan-Kolchin, J. S. Bullock, E. N. Kirby, *Mon. Not. R. Astron. Soc.* **444**, 222–236 (2014).
34. A. Brooks, A. Zolotov, *Astrophys. J.* **786**, 87–98 (2014).
35. O. D. Elbert *et al.*, <http://arxiv.org/abs/1412.1477> (2014).
36. M. Milgrom, *Astrophys. J.* **270**, 365–370 (1983).
37. B. Famaey, S. McGaugh, <http://arxiv.org/abs/1310.4009> (2013).
38. T. Clifton, P. G. Ferreira, A. Padilla, C. Skordis, *Phys. Rep.* **513**, 1–189 (2012).
39. D. Clowe *et al.*, *Astrophys. J.* **648**, L109–L113 (2006).
40. M. Kawasaki, K. Nakayama, *Annu. Rev. Nucl. Part. Sci.* **63**, 69–95 (2013).
41. K. Zurek, A. D. Matter, *Phys. Rep.* **537**, 91–121 (2014).
42. J. L. Feng, *Annu. Rev. Astron. Astrophys.* **48**, 495–545 (2010).
43. S. Arrenberg *et al.*, <http://arxiv.org/abs/1310.8621> (2013).
44. R. Bernabei *et al.*, *Nucl. Instrum. Methods Phys. Res. A* **742**, 177–180 (2014).
45. A. K. Drukier, K. Freese, D. N. Spergel, *Phys. Rev. D Part. Fields* **33**, 3495–3508 (1986).
46. E. Aprile *et al.*, *Phys. Rev. Lett.* **111**, 021301 (2013).
47. D. S. Akerib *et al.*, *Phys. Rev. Lett.* **112**, 091303 (2014).
48. M. Ackermann *et al.*, *Phys. Rev. D Part. Fields Gravit. Cosmol.* **88**, 082002 (2013).
49. T. Daylan *et al.*, <http://arxiv.org/abs/1402.6703> (2014).
50. E. Bulbul *et al.*, *Astrophys. J.* **789**, 13 (2014).
51. T. Tamura *et al.*, <http://arxiv.org/abs/1412.1869> (2014).
52. M. Ackermann *et al.*, *Phys. Rev. D Part. Fields Gravit. Cosmol.* **89**, 042001 (2014).
53. M. Aguilar *et al.*, *Phys. Rev. Lett.* **110**, 141102 (2013).
54. J. E. Gunn, B. Tinsley, *Nature* **257**, 454–457 (1975).
55. P. J. E. Peebles, *Astrophys. J.* **284**, 439–444 (1984).
56. M. S. Turner, G. Steigman, L. M. Krauss, *Phys. Rev. Lett.* **52**, 2090–2093 (1984).
57. S. Weinberg, *Rev. Mod. Phys.* **61**, 1–23 (1989).
58. M. M. Phillips, *Astrophys. J.* **413**, L105–L108 (1993).
59. A. G. Riess *et al.*, *Astron. J.* **116**, 1009–1038 (1998).
60. S. Perlmutter *et al.*, *Astrophys. J.* **517**, 565–586 (1999).
61. B. Ratra, P. J. E. Peebles, *Phys. Rev. D Part. Fields* **37**, 3406–3427 (1988).
62. C. Deffayet, G. Dvali, G. Gabadadze, *Phys. Rev. D Part. Fields Gravit. Cosmol.* **65**, 044023–044032 (2002).
63. D. H. Weinberg *et al.*, *Phys. Rep.* **530**, 87–255 (2013).
64. <https://www.sdss3.org/future/eboss.php>
65. www.darkenergysurvey.org
66. <http://sumire.ipmu.jp/en/3002>
67. www.princeton.edu/act/
68. <http://pole.uchicago.edu>
69. <http://bolo.berkeley.edu/polarbear/>
70. www.lsst.org/lsst/
71. <http://wfirst.gsfc.nasa.gov>
72. www.euclid-ec.org

ACKNOWLEDGMENTS

D.N.S. is supported by grants from the National Science Foundation and NASA.

10.1126/science.aaa0980

A century of general relativity: Astrophysics and cosmology

R. D. Blandford

One hundred years after its birth, general relativity has become a highly successful physical theory in the sense that it has passed a large number of experimental and observational tests and finds extensive application to a wide variety of cosmic phenomena. It remains an active area of research as new tests are on the way, epitomized by the exciting prospect of detecting gravitational waves from merging black holes. General relativity is the essential foundation of the standard model of cosmology and underlies our description of the black holes and neutron stars that are ultimately responsible for the most powerful and dramatic cosmic sources. Its interface with physics on the smallest and largest scales will continue to provide fertile areas of investigation in its next century.

The publication of the theory of general relativity (1, 2) by Albert Einstein in 1915 marked the culmination of a decade's serious thought—an intellectual quest that, despite much confusion and setback, was kept on track by Einstein's powerful intuition and philosophical faith that the foundational laws of physics were elegant and deterministic (3). The goal was simple: to add gravity to the theory of special relativity (4), which had explained how to modify Galilean kinematics in the presence of a fixed speed of light $c \sim 3 \times 10^8 \text{ m s}^{-1}$, as well as how to carry out physics in general in inertial frames. It did this by replacing three-dimensional Euclidean space and absolute time with a four-dimensional spacetime. It also, famously, united energy and mass.

General relativity (5) is even more radical than special relativity. It associates the motion of a body freely falling under gravity with a geodesic—a path of extremal length—in curved spacetime. (Under general relativity, in contrast to the Newtonian viewpoint, freely falling bodies are not accelerating.) According to the Einstein field equation, the spacetime curvature is described by a tensor that is proportional to a stress-energy tensor that encodes the mass-energy content. Mathematicians in the 19th century had realized that there were spaces that were not simply embedded in Euclidean space, to the consternation of some philosophers (6). They had to be studied through their internal properties. The realization that we actually inhabit such a curved space was a remarkable contribution to geometry.

The theory was quickly tested (7) and found immediate, if uncertain and incomplete, application to gravitational radiation (8), black holes (9), and cosmology (10). These topics have continued to dominate the development of classical relativity, and we consider them in turn.

Observational and experimental tests

Galileo and Newton were impressed by the apparent equality of gravitational and inertial mass

for all substances. A large cannonball falls at the same rate as a small apple under gravity in vacuo. Einstein expressed this as the Equivalence Principle, which in its weak form has been tested by millimeter-precision lunar laser ranging and torsion balances with better than $\sim 10^{-12}$ accuracy (11–13). Atom interferometry aspires to improve this limit by another two orders of magnitude (14). One astronomical affirmation is provided by the observation that neutrinos and photons from a supernova in the Large Magellanic Cloud arrived here within hours of each other (15). A stronger version of the principle that states that a body's gravitational energy experiences the same acceleration has been tested with $\sim 10^{-5}$ accuracy

by means of lunar laser ranging. A recently discovered millisecond pulsar (a spinning, magnetized neutron star with a spin period of $< 10 \text{ ms}$ and $\sim 10\%$ of its mass associated with gravitation) with two orbiting white dwarfs will be used to test this principle even more accurately by timing the pulses that it emits (16).

A simple thought experiment incorporating the conservation of energy produced the first prediction of general relativity, the relative change in the wavelength λ of light as it climbs out of a gravitational potential Φ , called the gravitational redshift (17), $\Delta\lambda/\lambda \sim \Delta\Phi/c^2$. For the Sun, this is $\sim 2 \times 10^{-6}$, but for a white dwarf star, it is ~ 0.001 , and for a neutron star, it is ~ 0.1 . The effect is most accurately measured in pulsars (below) but is also measured directly to $\sim 10^{-2}$ by using γ -ray lines and the Mössbauer effect (18) and to $\sim 10^{-4}$ by using an atomic clock carried by a rocket (19).

A more prescriptive, “classical” test is the gravitational deflection of light. Newton thought that light comprised particles and could have calculated the deflection angle α in his famous *Opticks* (20). He was prescient because the answer he would have got is $\alpha = 2GM_{\odot}/r_{\text{min}}c^2 \sim 0.9 \text{ arc sec}$, where G is the gravitational constant, M_{\odot} is the solar mass, and r_{min} is the radius of closest approach. This assumes that the space around the Sun is flat, which it is not; the curvature doubles the deflection. The “detection” of this doubling in Eddington's famous eclipse expedition of 1919 made Einstein into a household name (21). Modern measurements agree with theory at the level of ~ 0.003 at optical wavelengths and ~ 0.0003 at radio wavelengths.

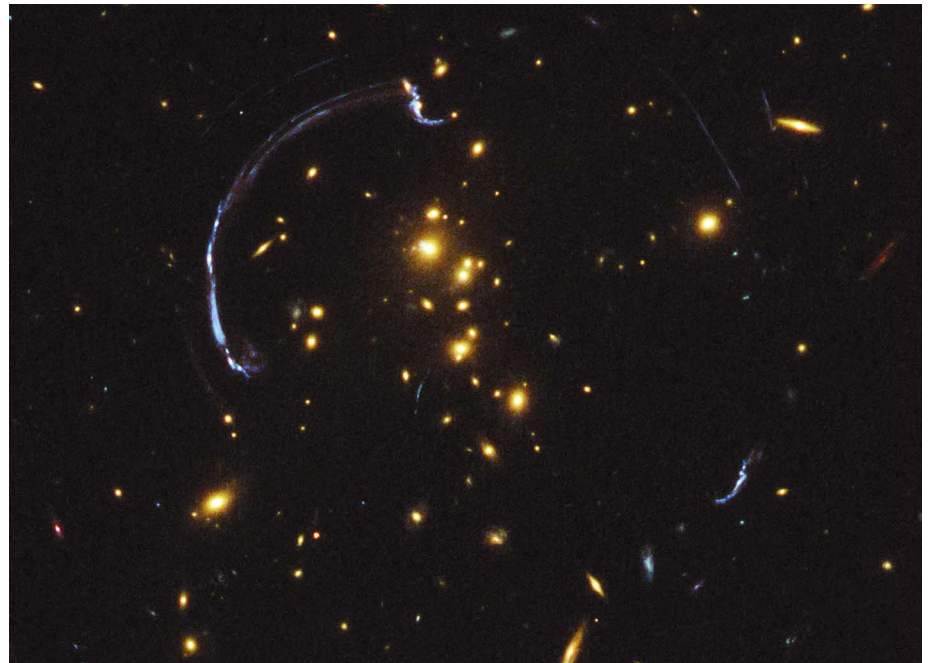


Fig. 1. Giant gravitational lens formed by a large cluster of galaxies, RCS2 032727-132623. The gravitational potential in which the (mostly yellow) cluster galaxies move produces multiple, highly sheared images of a background (blue) galaxy (with redshift $z = 1.7$). The radius of the blue arcs is $\sim 500,000$ light years. Observations such as this are used to map the dark matter and allow astronomers to infer fine detail in the source galaxy. [Image courtesy: J. Rigby, K. Sharon, M. Gladders, and E. Wuyts (104, 105)]

Kavli Institute for Particle Astrophysics and Cosmology, Stanford University, Stanford, CA, USA.

A helpful way to think about the spatial curvature is to treat the space as flat but endowed with a refractive index $1 - 2\Phi/c^2$, where Φ is the gravitational potential equal to $-GM/r$ at radius r in this case (21). The speed of light in this proxy space is now less than c , just as inside a converging glass lens. As a direct consequence, there is a gravitational delay in the time it takes a radar signal to make a round trip across the solar system. The best reported measurement involves the Cassini spacecraft with an impressive 2×10^{-5} level of agreement (22).

General relativistic light deflection is responsible for gravitational lensing (Fig. 1) (23–27). The most dramatic examples involve the deflection of light from a cosmologically distant source by an intervening galaxy ($\alpha \sim 1$ arc sec) or a cluster of galaxies ($\alpha \sim 20$ arc sec). Multiple images can be seen when the alignment is good, typically for 1 in 1000 galaxies. If the source varies, then the travel times of the light from it to us can be seen to differ from image to image by an amount $\sim \alpha^2$ times the age of the universe ~ 1 year for a galaxy lens. This has furnished competitive measurements of the size and age of the universe that have errors less than 10% (28).

On much smaller scales, foreground stars can also magnify background stars. This is known as microlensing (29). This typically happens only once in a million cases at any time. A single star lens makes two images with a varying combined magnification. The theory was first worked out correctly by Einstein before he understood general relativity, except for the missing factor of two. He did not publish his result because he doubted that it was observable. However, with giant surveys it has become a commonplace phenomenon and has been used to study exoplanets (30).

There is a third “classical” test of relativity. It explained the anomalous precession of Mercury’s perihelion, or the rotation of the line joining the sun to the point of closest approach of the planet. Einstein used general relativity to explain a $\sim 10\%$ discrepancy in the precession attributable to the gravitational pulls of the other planets ~ 43 arc sec per century. The agreement today is better than 10^{-4} (11–13).

Neutron stars are excellent clocks because they rotate at a regular and predictable rate accompanied by a beam of coherent radio emission. They exhibit many applications of general relativity and provide quantitative tests. The first example was provided by the binary pulsar PSR 1913+16 (31), which has a ~ 60 -ms pulsar period and an ~ 8 -hour orbital period. The observed pulse frequency undergoes periodic variation because of the Doppler shift and gravitational redshift. The major axis of the orbit precesses at $\sim 4^\circ$ per year. There are also the gravitational delay and some higher-order effects that are measured that can contribute to the fitting of the pulse arrival times. After solving for the neutron star masses and orbital parameters, the remaining measurements provide yet more consistency checks of general relativity (32).

Another interesting system is the “double pulsar” PSR J0737-3039 (Fig. 2) (33). This provides a

clean demonstration of geodetic precession, in which a spinning pulsar acts like a gyroscope and undergoes precession relative to the direction of distant stars owing to its companion’s space curvature. This was measured in this system until the radio beam precessed out of our line of sight. This phenomenon has also been measured in a special satellite called GP-B (34), alongside a second relativistic effect, Lense-Thirring precession, which is attributable in this case to the spin of the Earth.

Gravitational radiation

Large, moving masses radiate gravitational waves just like an oscillating guitar string radiates sound waves and an electrical charge moving back and forth in an antenna radiates electromagnetic waves. Einstein recognized soon after discovering the general theory that transverse, gravitational radiation should exist and propagate at the speed of light, but that the amplitude should be described by the perturbation to the metric tensor instead of a vector, such as with electro-

magnetic waves. The freedom to choose the coordinate system caused some technical confusion, which persisted in some quarters for 50 years. Gravitational waves carry energy and angular momentum away from their source on a time scale $\sim (c/v)^5$ orbital periods, where v is the orbital speed. In the case of PSRs 1913+16 and J0737-3039, we can compute the rate of loss of energy and the consequent rates of decrease of the orbital period. These have been measured with a precision $\sim 10^{-3}$ approaching the level at which the uncertain motion in the Galaxy precludes a more accurate test (32, 33). What is being tested here is a subtle formalism that took Einstein and others many years to get right. As such, it is a rather prescriptive test of the theory.

It is also important to detect the radiation directly in order to confirm that gravitational waves propagate as calculated and to find and explore cosmic sources. Most effort to do this has been concentrated on ground-based laser interferometers, each comprising two pairs of mirrors arranged in two perpendicular

arms. A passing wave changes the separation of these mirrors and moves interference fringes formed by combining light from the two arms. After several decades of technique refinement and removal of sources of noise, several interferometers—notably, the Advanced Laser Interferometer Gravitational Wave Observatory (LIGO) project (35)—operating in the few-hertz to few-kilohertz band should commence operation this year and eventually achieve ~ 10 times the amplitude sensitivity (a dimensionless strain of $\sim 10^{-23}$ corresponding to displacements of $\sim 10^{-20}$ m in the 4-km arms in two facilities) of their predecessors (Fig. 3).

The most secure source class for these interferometers is binary neutron stars, which should be observed in the seconds before they coalesce into black holes (36). The systems found so far enable a lower bound on the source rate, and there is confidence that if the design sensitivity is achieved, then sources of radiation will be observed. These binaries have been identified with “short” γ -ray bursts (37), which may also be seen at the same time. More speculative and rare is the source class of binaries in which both members are stellar-mass black holes, which can be seen at much greater distances. The formation of neutron stars and black holes in core collapse supernovae may also be accompanied by detectable gravitational

Studying general relativity using a double pulsar system

The masses of two neutron stars are determined by many fitted functions

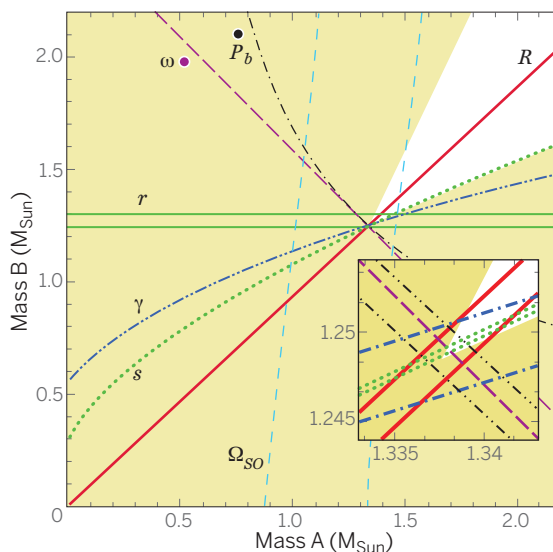


Fig. 2. Representation of the many ways to study general relativity using the double pulsar, PSR J0737-3039. The masses of the two neutron stars (“A” and “B”) are determined by many fitted functions that assume general relativity is correct. R is the mass ratio that can be determined as both pulsars were timed; γ is measured by the combined second-order Doppler shift and the gravitational redshift; r and s are measured by the gravitational delay; ω is given by the rate of advance of the major axis in the plane of the orbit, the analog of the perihelion advance of mercury; P_b is the rate of change of the orbital period due to gravitational radiation; and Ω_{SO} is the rate of geodetic precession of the pulsar spin axis. (Inset) Enlargement by a factor of 80. Every single measurement is consistent with the two neutron stars having masses $1.3381, 1.2489 \pm 0.0007$ in solar units. The remarkable concordance of these various determinations strongly limits departures from pure general relativity. [Image courtesy: M. Kramer, with data from (40)]

radiation, particularly when accompanied by “long” γ -ray bursts (37). Many of these events are potential sources of simultaneous \sim peta-electron volt neutrino bursts, which are now being detected with the IceCube facility at the South Pole (38).

Gravitational radiation in the ~ 10 to 100 nHz range can be sought by timing millisecond pulsars (39). When radio waves from the pulsar propagate through a much longer wavelength gravitational wave, there is a periodic modulation of the arrival times of the pulses. Using a network of ~ 100 pulsars, we can cross-correlate the signals and improve the sensitivity. The arrival times can now be measured to < 100 ns in the best cases, and modest improvements are anticipated (40). The associated strain sensitivity is $\sim 3 \times 10^{-14}$. Most attention has been focused on merging, massive black holes in the nuclei of galaxies. These mergers are anticipated to accompany the hierarchical merging of their host galaxies when the size of the universe was about a third of its present size (41). These mergers will lead to a background of gravitational radiation noise with a specific spectrum that could be measured soon. (If we are very lucky, then the nearest, strongest sources may be detectable individually.) Even greater sensitivity should be available after the Square Kilometer Array radio telescope (www.skatelescope.org) is completed.

The approach with arguably the greatest reach and largest number of putative sources will carry out observations at intermediate ~ 1 - to 100-mHz frequencies using a spaceborne interferometer. The sources include binary white dwarfs, smaller merging black holes, and stellar captures by individual black holes. This project, previously known as LISA (Laser Interferometer Space Antenna) (42), which would have achieved strain sensitivities of $\sim 10^{-22}$, is currently being downsized with the ambition of flying in the 2030s.

The linear (strictly, weakly nonlinear) theory of general relativity is adequate to discuss many of the sources we have described. Neutron stars merging with other neutron stars or black holes can be handled by using perturbation theory (43). However, the detection of merging black holes should provide a powerful test of general relativity in the strongly nonlinear regime. Computing the wave forms that could be seen from a suite of mass ratios, orbital configurations, and observer directions is a massive undertaking that had defeated numerical relativists for many decades. However, the problem is now solved in principle (44), several hundred wave-forms are now in hand, and the task of incorporating a complete set of wave-form templates in the observational program is well under way (45).

Black holes

Given the growing confidence that astrophysicists have developed in the general theory of relativity, it is not surprising that it has been incorporated into detailed models of cosmic objects. Foremost among these are black holes, which possess event horizons that serve as boundaries that can only be traversed in one direction, at least classically (46). The solution of the field equations under

Techniques of gravitational radiation detection

Dimensionless strain (h_c) and wave frequency (f/Hz)

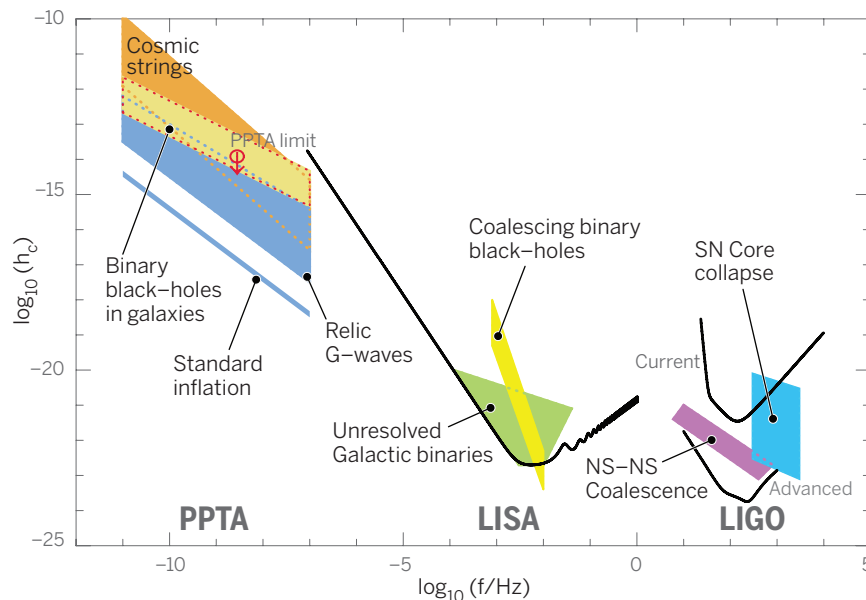


Fig. 3. Sensitivity curve for the three techniques of gravitational radiation detection mentioned in the text. The abscissa is the wave frequency, and the ordinate is the dimensionless strain. Advanced LIGO should come into operation in 2015 and should start to see neutron star coalescences. PPTA stands for the international Pulsar Timing Array, which is coming into regular operation, and SKA is the Square Kilometer Array, which should be completed in the next decade. Binary black holes are just detectable if optimistic assumptions are made. LISA is a space interferometer that has been descoped and should now fly in the 2030s. [Image courtesy: G. Hobbs and R. Manchester (106)]

spherical symmetry was published by Schwarzschild shortly before his death in 1916 (46). However, it took a very long while before the modern interpretation of this solution was developed and widely accepted. Einstein and others published misleading descriptions of gravitational collapse (47). Key steps included the analysis of the radial collapse of pressure-free particles and generic horizons (48). The moniker “black hole” is attributed to Wheeler (49, 50).

The quite remarkable discovery of the Kerr metric (51) and the subsequent realization that this was, in practice, the only solution that was needed for astrophysical applications, arrived just in time for the discovery of quasars (52). Kerr black holes are characterized by just two numbers, which can be chosen to be their mass, as would be measured by a distant orbiting and spinning satellite, and their angular momentum per mass (or equivalently, their rotational angular velocity) as measured by the precession of the spin axis of this satellite. The mass provides a scale for length, time, power, temperature, and so on; the angular momentum per mass fixes the geometry and has a maximum value proportional to the mass.

It was quickly appreciated that black holes were transformed into luminous objects when they accreted gas and that this accretion typically occurred through an orbiting accretion disk. The

relativistic theory was rapidly developed (53–56). In a “thin” disk, where pressure is ignored, the inner radius is located outside the event horizon. A proton spiraling inward through the disk under viscous friction will reach this radius having released its binding energy as heat before plunging inward to cross the event horizon. The energy released per unit mass varies from $\sim 0.06 c^2$ to $\sim 0.42 c^2$ as the hole’s angular momentum increases from zero to maximal in a prograde direction (57). These efficiencies are far greater than those associated with nuclear processes. This explains their appeal in accounting for the early observations of quasars, which could outshine their host galaxies by a factor as large as 1000.

The measurement of black hole masses is mostly Newtonian and requires measuring the speed of stars (or gas) and a distance. For example, the black hole in our galactic center has a mass of 4 million M_\odot (58, 59) and the black hole in the nucleus of the famous galaxy M87 in the Virgo cluster is 4 billion to 7 billion M_\odot (60, 61), whereas masses up to 20 billion M_\odot have been reported for other galaxy nuclei (62). Correlations of these masses with the properties of the host galaxies have been found (63). Black hole spins have been measured by using the shapes of disk iron emission line profiles broadened by Doppler motion and gravitational redshift (64). Several holes are spinning close to maximal.

In many respects, the relativistic description of accretion disks is the easy part. Ironically, it is the 19th-century subjects of thermodynamics, kinetic theory, fluid dynamics, radiative transfer, and electromagnetism that make modeling so difficult. It is now generally accepted that disks are strongly magnetized because a magnetic field will grow exponentially in a few orbital periods if it is very small initially (65). This magnetic field is thought to provide the principal torque, which leads to the disk's inflow, dissipation, and radiation (66).

Power can also be extracted from a spinning hole because it is possible for particles to cross the event horizon on orbits with negative total (including rest mass) energy (67). A variant in which magnetic field lines supported by electrical current flowing in the accretion disk thread the black hole can arise quite naturally (68), as demonstrated by three-space-plus-time general relativistic numerical simulations (Fig. 4) (69). This mechanism can account for the formation of "jets," which are relativistic outflows in antiparallel directions commonly associated with accreting black holes (66). Relativity is also very important to modeling the tidal capture and shredding of stars by black holes in galactic nuclei with mass less than $\sim 10^8$ solar masses (70).

Future observational prospects are bright. The modeling of disks and inflows is becoming more sophisticated and has been used to argue for the "observation" of event horizons (71). It is hoped to image the emitting plasma close to the massive black holes in our galactic center and in M87 by using very-long-baseline interferometry at submillimeter wavelengths (72). We may be observing oscillations of disks (73). "Reverberation mapping" by using the variation of the broad iron lines is starting to probe the curved space

outside the event horizon (74). Serious searches are also being made for radio pulsars in close orbit about the galactic center black hole (75).

General relativity is crucial in describing the structure of neutron stars, which have surface escape velocities of $\sim 0.3 c$. Given a nuclear equation of state, the star's radius, moment of inertia, and stability (as a function of the mass and spin period) can all be calculated and probed by using observations. The intent is to invert this process and derive the properties of cold nuclear matter to complement the investigations of hot nuclear matter at heavy ion colliders. Surprisingly large masses, above those permitted by softer equations of state, have been measured (76).

Cosmology

Einstein always understood that a major application of general relativity would be to the universe at large. In this connection, he noted that his field equation would remain generally covariant if he added a term directly proportional to the metric tensor (10). The coefficient of proportionality was ultimately called the cosmological constant, Λ , and is equivalent to a special energy density that was ubiquitous and eternal. Einstein allegedly came to regard this amendment as his "greatest blunder" (77), but from a modern perspective, it is looking more like his most extraordinary insight. There certainly was a blunder, and this was in the manner in which he solved the equation. He found a model for a static universe in which the repulsive character of Λ balanced the attraction of gravity. Although he could be excused for not knowing that the universe was expanding, he failed to appreciate that his solution was unstable and could not persist. As described in the accompanying article (78), the correct isotropic and homogeneous, spatially

curved and expanding solutions were found by Friedman (79), Lemaître (80), and others, and this forms the basis of the modern treatment (23–27). Observations of the cosmic microwave background (CMB) and the local universe (including the measurement of distortion of the shapes of galaxies and the microwave background by weak gravitational lensing) have combined to produce a simple, yet accurate (at roughly the 1% level) and internally consistent description of the universe today (Fig. 5). The universe is spatially flat, has an age since the "big bang" of $t_U \sim 4 \times 10^{17}$ s, and is currently accelerating under the influence of a dominant cosmological constant (69% of the universe's energy), which behaves as predicted at the $\sim 10\%$ level. It also contains 26% of "cold, dark matter," which is quite possibly one or more new elementary particles, and a mere 5% of regular or "baryonic" matter. The structure appears to derive from an almost scale-free distribution of random, Gaussian, initial fluctuations (81).

From its inception, this "big bang" cosmology posed some very deep puzzles. In particular, how could the universe be so isotropic today when the parts we can see were not in causal contact when the photons that we observe were emitted? Guth posed an ingenious mechanism, called inflation, to address this and other puzzles (82). It was suggested that the energy density in the very early universe, perhaps at $t \sim 10^{-35}$ s, was dominated by a scalar field that, like Λ , had zero enthalpy, and that this was responsible for an early phase of accelerating—in fact, exponential—expansion. Parts that were in causal contact would leave each other's influence and then come into contact, recently having carried similar contents on their separate journeys, which evolved in identical ways. The end of inflation may be a consequence of the dynamical evolution of the field and would be marked by the creation of the large entropy that we see today. The simplest version of this theory accounts for the universe's observed spatial flatness and the spectrum of its observed density fluctuations, as well as structure formation and nucleosynthesis of light elements (23–27).

Standard cosmology rests on a firm, general relativistic foundation, and much attention has been furnished on seeing how much relativity can be modified without contradicting the observations. One useful approach consists of recasting the field equations in variational form and then altering the Lagrangian density (83). It turns out to be rather hard to do this without violating tests on subcosmological scales. Another approach is to replace Λ by a dynamical field (84). This generalization is commonly called "dark energy," and there is much observational effort to see whether something like this is required (78). Planned optical and CMB studies over the next decade should put the standard cosmology to even more stringent tests.

Coda

The theory of general relativity (including Λ) provides a singular prescription for describing classical gravity per se and nongravitational physics in this environment. There seems to be no

Extracting the rotational energy of a black hole

With high efficiency and power to create observed relativistic outflows called jets

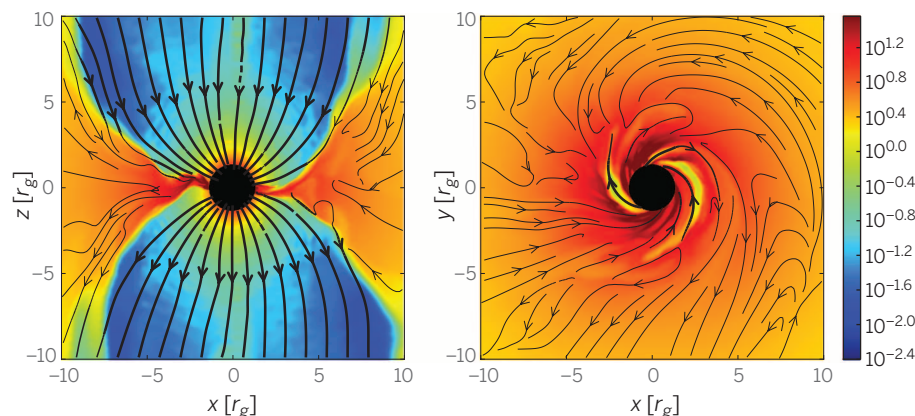


Fig. 4. Single frame from a 3D numerical simulation of relativistic magnetohydrodynamical flow around a spinning black hole. The lines with arrows represent the magnetic field lines. The blue region at left depicts an ultrarelativistic, low-density outflowing jet seen from the side. The mostly orange region at right depicts an accretion disk seen from above. Note the instability that develops in the flow. These simulations demonstrate that it is possible to extract the rotational energy of a black hole with high efficiency (69).

need for baroque variations and empirical corrections over its domain of applicability. It has grown from an essentially intuitive quest to providing the foundation for high-energy astrophysics and cosmology, in which it is routinely assumed to be correct. As this very brief Review should have made clear, astrophysical, cosmological, and laboratory investigations have subjected it to many quantitative tests, all of which it has passed, and more are on the way. This makes it a highly successful theory. Although irrefutable failures, anomalies, and disconnects may appear at any time, attention has now shifted to its interfaces with other physical investigations.

The interface of classical gravity with quantum mechanics has been extraordinarily fertile, starting with the proposal by Bekenstein (85) and Hawking (86) that black hole event horizons are endowed with entropy and temperature. (In a formal sense, this implies that the entropy of the universe is dominated by the event horizons of massive black holes in the nuclei of galaxies.) The idea that black holes can radiate has generated

enormous debates involving unitarity, information loss, and stability (87). Ongoing discussions of “firewalls” demonstrate that much remains to be understood (88). Most of this is transacted in the febrile world of theoretical physics, but there are possible connections to observation. If primordial black holes with masses of $\sim 10^{12}$ kg could ever be created, then they might evaporate and vanish in a flash of γ -rays or radio waves (89, 90). Analogous processes are thought to have occurred during inflation to form the initial gravitational potential perturbations. It is predicted that these fluctuations should be accompanied by special, spiral-like patterns in the polarization of the CMB known as “B-modes.” The modes that have been seen so far (91) are attributable to dust in our Galaxy (81). Future observations should be at least 10 times more accurate and could find these important vestiges of inflation.

Even more fundamentally, it has been suggested that the true dimensionality of our world is actually greater than four and that gravity inhabits the extra dimensions, unlike the elementary

particles and their fields. This may explain its apparent weakness and resistance to renormalization and unification (92). There may be scalar fields with long Compton wavelengths that are features of theories that attempt to unify gravity with the other fundamental forces. These have been sought on the micrometer scale as deviations from the inverse square law of gravity (93).

The ultimate interface occurs at the quantum gravity or Planck scale: a time $t_P = (G\hbar/c^5)^{1/2} \sim 10^{-43}$ s, defined by Planck’s constant \hbar , where string or M theory remains the most promising approach despite the failure so far to find evidence for supersymmetry at the Large Hadron Collider (<http://home.web.cern.ch/topics/large-hadron-collider>).

Less well developed ideas posit that the vacuum contains quantum gravity fluctuations, which could cause dispersion in the propagation of γ -rays (94). This has been constrained by using observations of distant γ -ray bursts. These fluctuations are also being sought experimentally by using a LIGO-like experiment called the

Microwave background data from the Planck satellite

Supports the application of general relativity, including the cosmological constant, on cosmological scales

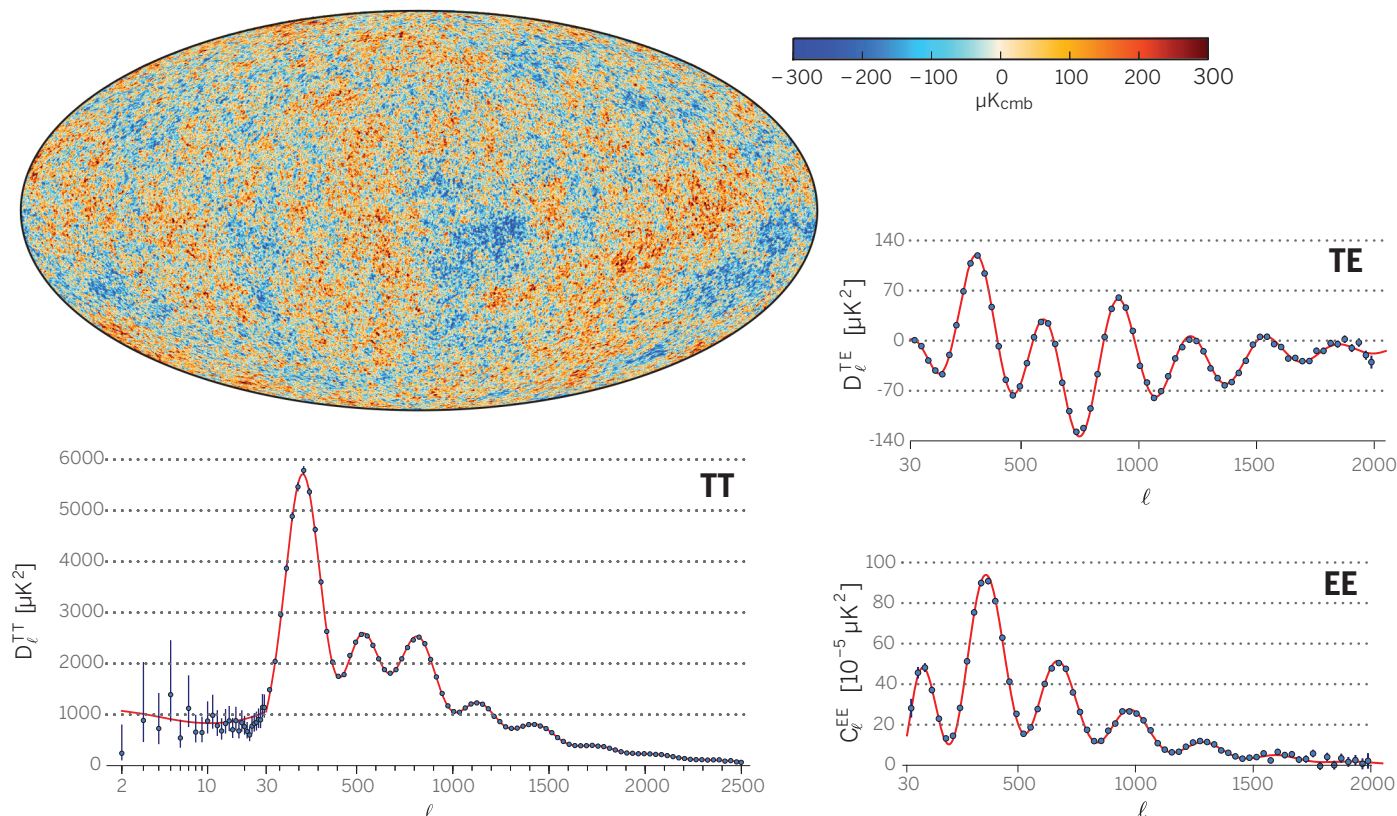


Fig. 5. Recent microwave background data from the Planck satellite. (Top left) The best fitting map of the temperature fluctuations. (Bottom left) The power in the total intensity as a function of the spherical harmonic order ℓ . It can be thought of as measuring an angular scale $\sim 180^\circ/\ell$. (Top right) The cross-correlation of the polarization with the intensity. (Bottom right) The polarization power spectrum. The fitted theoretical curves have just six free parameters, and the impressive agreement strongly supports the application of general relativity on cosmological scales. The large errors at bottom left at low ℓ are an expression of “cosmic variance,” or the limited number of independent measurements of a random process. [Map courtesy: ESA and the Planck collaboration (81); spectra courtesy: the Planck collaboration; reproduced with permission from *Astronomy & Astrophysics*, copyright ESO]

holometer (95). (The natural scale for the spectral density of these fluctuations is t_p , which is just about the sensitivity limit.)

This brings us back to Λ . Many observers have embraced it ever since it was introduced, often because it allowed the universe to be older than its contents, rather than younger. In contrast, many theorists, especially those with a particle physics background, see physics as “reductionist” and Λ as a manifestation of the vacuum. They are then challenged to explain why its magnitude, in natural or Planck units, is $\sim (t_p/t_U)^2 \sim 10^{-123}$. A second view is that Λ might be some large-scale phenomenon “emergent” from complex microphysical interaction, like waves in sand dunes (96). Such an explanation might help reconcile Einstein’s deep reservations about quantum mechanics with its modern interpretation (3).

A third approach, more appealing to those brought up in classical relativity and cosmology, is to see Λ as an independent physical quantity that gives a scale to the universe (97). The square peg of quantum field theory need not be forced into the round hole of Riemannian geometry. Λ is then “situational,” a manifestation of physics beyond our horizon, and has even less to do with the world of elementary particles than does, say, oceanography. If this is the case, we must explain why the value of Λ , as well as other physical constants and perhaps also the fundamental laws themselves, allows us to have developed and to ask these questions. The proposal here—as controversial as it is bold—is that there is an ensemble of universes ($>10^{500}$ in some formulations), almost all of which would be stillborn in this regard (98). By our very existence, we are selecting the precarious choices that allow us to be. Instead of the cause-and-effect rule of normal physics—“things are as they are because they were as they were”—we have the neo-teleological “things were as they were because we are as we are.”

That general relativity should have been so wildly successful 100 years after its birth and yet retains its freshness by stimulating such splendid debates augurs well for its continued success during its second century.

REFERENCES AND NOTES

1. A. Einstein, *Sitzungsberichte der Königlich Preussischen Akademie der Wissenschaften (Berlin)* **1915**, 778–786 (1915).
2. A. Einstein, *Sitzungsberichte der Königlich Preussischen Akademie der Wissenschaften (Berlin)* **1915**, 844–847 (1915).
3. A. Pais, *Subtle Is the Lord* (Oxford Univ. Press, Oxford, 1982).
4. A. Einstein, *Annalen der Physik* **322**, 891–921 (1905).
5. Five different approaches to teaching general relativity are represented by the textbooks in (99–103).
6. I. Kant, *Critique of Judgement* (Oxford Univ. Press, Oxford, 2007).
7. A. Einstein, *Sitzungsber. Preuss. Akad. Wiss* **47**, 831–839 (1915).
8. A. Einstein, *Sitzungsberichte der Königlich Preussischen Akademie der Wissenschaften (Berlin)* **1918**, 154–167 (1918).
9. K. Schwarzschild, *Sitzungsberichte der Königlich Preussischen Akademie der Wissenschaften (Berlin)* **1916**, 189–196 (1916).
10. A. Einstein, *Akad. Wiss. Sitz. Berlin* **1917**, 142–152 (1917).
11. Current reviews containing references to the original investigations are (12, 13).
12. C. M. Will, *Living Rev. Relativity* **17**, 4 (2014).
13. T. Baker, D. Psaltis, C. Skordis, arXiv:1412.3455 (2014).
14. S. M. Dickerson, J. M. Hogan, A. Sugarbaker, D. M. Johnson, M. A. Kasevich, *Phys. Rev. Lett.* **111**, 083001 (2013).
15. L. M. Krauss, S. Tremaine, *Phys. Rev. Lett.* **60**, 176–177 (1988).
16. S. M. Ransom et al., *Nature* **505**, 520–524 (2014).
17. A. Einstein, *Annalen der Physik* **340**, 898–908 (1911).
18. R. V. Pound, G. A. Rebka, *Phys. Rev. Lett.* **4**, 274–275 (1960).
19. R. F. C. Vessot et al., *Phys. Rev. Lett.* **45**, 2081–2084 (1980).
20. I. Newton, *Opticks* (Smith and Walford, London, 1704).
21. A. S. Eddington, *Observatory* **42**, 119–122 (1919).
22. S. G. Turyshev, *Annu. Rev. Nucl. Part. Sci.* **58**, 207–248 (2008).
23. Four different approaches to teaching cosmology (including gravitational lensing) are represented by (24–27).
24. J. A. Peacock, *Cosmological Physics* (Cambridge Univ. Press, Cambridge, 1999).
25. S. Dodelson, *Modern Cosmology* (Academic Press, New York, 2003).
26. S. Weinberg, *Cosmology* (Oxford Univ. Press, Oxford, 2008).
27. P. Schneider, *Extragalactic Astronomy and Cosmology: An Introduction* (Springer, Heidelberg, Germany, 2015).
28. S. H. Suyu et al., *Astrophys. J.* **788**, L35 (2014).
29. B. Paczynski, *Astrophys. J.* **304**, 1 (1986).
30. B. S. Gaudi et al., *Science* **319**, 927–930 (2008).
31. R. A. Hulse, J. H. Taylor, *Astrophys. J.* **195**, L51–L53 (1975).
32. J. M. Weisberg, D. J. Nice, J. H. Taylor, *Astrophys. J.* **722**, 1030–1034 (2010).
33. M. Kramer, I. H. Stairs, *Annu. Rev. Astron. Astrophys.* **46**, 541–572 (2008).
34. C. W. F. Everitt et al., *Phys. Rev. Lett.* **106**, 221101 (2011).
35. G. M. Harry, *Class. Quantum Gravity* **27**, 084006 (2010).
36. M. Dominik et al., arXiv:1405.7016 (2014).
37. C. Kouveliotou, R. Wijers, S. Woosley Eds., *Gamma-ray Bursts* (Cambridge Univ. Press, Cambridge, 2013).
38. M. G. Aartsen et al., *Phys. Rev. D Part. Fields Gravit. Cosmol.* **91**, 022001–220016 (2015).
39. R. W. Hellings, G. S. Downs, *Astrophys. J.* **265**, L39–L42 (1983).
40. M. Kramer, *Int. J. Mod. Phys. D* **23**, 1430004 (2014).
41. D. Merritt, *Dynamics and Evolution of Galactic Nuclei* (Princeton Univ. Press, Princeton, NJ, 2013).
42. K. Danzmann, *Class. Quantum Gravity* **13** (11A), A247–A250 (1996).
43. A. H. Nitz et al., *Phys. Rev. D Part. Fields Gravit. Cosmol.* **88**, 124039 (2013).
44. F. Pretorius, *Phys. Rev. Lett.* **95**, 121101–121104 (2005).
45. L. Lehner, F. Pretorius, *Annu. Rev. Astron. Astrophys.* **52**, 661–694 (2014).
46. D. Finkelstein, *Phys. Rev.* **110**, 965–967 (1958).
47. A. Einstein, *Ann. Math.* **40**, 922–936 (1939).
48. J. R. Oppenheimer, H. Snyder, *Phys. Rev.* **56**, 455–459 (1939).
49. J. A. Wheeler, *Am. Scholar* **37**, 248–274 (1967).
50. A. E. Ewing, *Sci. News Lett.* **85**, 39 (1964).
51. R. P. Kerr, *Phys. Rev. Lett.* **11**, 237–238 (1963).
52. M. Schmidt, *Nature* **197**, 1040–1041 (1963).
53. E. E. Salpeter, *Astrophys. J.* **140**, 796–800 (1964).
54. I. Novikov, Ya. B. Zel’dovich, *Uspekhi Fizicheskikh Nauk* **84**, 377–417 (1964).
55. D. Lynden-Bell, *Nature* **223**, 690–694 (1969).
56. I. D. Novikov, K. S. Thorne, in *Black Holes* (Gordon and Breach, New York, 1973), pp. 343–450.
57. J. M. Bardeen, *Nature* **226**, 64–65 (1970).
58. A. M. Ghez et al., *Astrophys. J.* **689**, 1044–1062 (2008).
59. R. Genzel, F. Eisenhauer, S. Gillessen, *Rev. Mod. Phys.* **82**, 3121–3195 (2010).
60. K. Gebhardt et al., *Astrophys. J.* **729**, 119 (2011).
61. J. L. Walsh, A. J. Barth, L. C. Ho, M. Sarzi, *Astrophys. J.* **770**, 86 (2013).
62. N. J. McConnell et al., *Astrophys. J.* **756**, 179–200 (2012).
63. T. M. Heckman, P. N. Best, *Annu. Rev. Astron. Astrophys.* **52**, 589–660 (2014).
64. C. S. Reynolds, arXiv:1302.3260 (2013).
65. S. A. Balbus, J. F. Hawley, *Rev. Mod. Phys.* **70**, 1–53 (1998).
66. D. L. Meier, *Black Hole Astrophysics* (Springer, Berlin, 2012).
67. R. Penrose, R. M. Floyd, *Nature* **229**, 177–179 (1971).
68. R. D. Blandford, R. L. Znajek, *Mon. Not. R. Astron. Soc.* **179**, 433–456 (1977).
69. J. C. McKinney, A. Tchekhovskoy, R. D. Blandford, *Mon. Not. R. Astron. Soc.* **423**, 3083–3117 (2012).
70. S. Gezari, *Phys. Today* **67**, 37–42 (2014).
71. R. Narayan, J. E. McClintock, *New Astron. Rev.* **51**, 733–751 (2008).
72. S. S. Doeleman et al., *Science* **338**, 355–358 (2012).
73. R. V. Wagoner, *Astrophys. J.* **752**, L18 (2012).
74. E. Kara et al., *Mon. Not. R. Astron. Soc.* **434**, 1129–1137 (2013).
75. V. Kaspi et al., *Astrophys. J.* **786**, 84–91 (2014).
76. J. M. Lattimer, *Annu. Rev. Nucl. Part. Sci.* **62**, 485–515 (2013).
77. G. Gamov, *My World Line* (Viking, New York, 1970).
78. D. Spergel, *Science* **347**, 1100 (2015).
79. A. Friedman, *Z. Phys.* **10**, 377–386 (1922).
80. G. Lemaître, *Proc. Natl. Acad. Sci. U.S.A.* **20**, 12–17 (1934).
81. R. Adam et al., arXiv:1502.01582 (2015).
82. A. H. Guth, *Phys. Rev.* **23**, 347–356 (1981).
83. H. A. Buchdahl, *Mon. Not. R. Astron. Soc.* **150**, 1–8 (1970).
84. S. Perlmutter, M. Turner, M. White, *Phys. Rev. Lett.* **83**, 670–673 (1999).
85. J. D. Bekenstein, *Phys. Rev. D Part. Fields* **7**, 2333–2346 (1973).
86. S. W. Hawking, *Commun. Math. Phys.* **43**, 199–220 (1975).
87. L. Susskind, *The Black Hole War: My Battle with Stephen Hawking to Make the World Safe for Quantum Mechanics* (Back Bay Books, New York, 2009).
88. A. Almheiri, D. Marolf, J. Polchinski, *J. High Energy Phys.* **2**, 1–20 (2013).
89. S. W. Hawking, *Nature* **248**, 30–31 (1974).
90. M. J. Rees, *Nature* **266**, 333–334 (1977).
91. P. A. R. Ade et al., *Phys. Rev. Lett.* **112**, 241101–241125 (2014).
92. L. Randall, R. Sundrum, *Phys. Rev. Lett.* **83**, 3370–3373 (1999).
93. D. M. Weld, J. Xia, B. Cabrera, A. Kapitulnik, *Phys. Rev. D Part. Fields Gravit. Cosmol.* **77**, 062006–062025 (2008).
94. A. A. Abdo et al., *Nature* **462**, 331–334 (2009).
95. C. J. Hogan, arXiv:1307.2283 (2014).
96. R. B. Laughlin, *A Different Universe: Reinventing Physics from the Bottom Down*. (New York: Basic Books, 2005).
97. A. Eddington, *The Nature of the Physical World: Gifford Lectures* (Cambridge Univ. Press, Cambridge, 1927).
98. A. D. Linde, *Phys. Lett. B* **108**, 389–393 (1982).
99. S. Weinberg, *Gravitation and Cosmology: Principles and Applications of the General Theory of Relativity* (J. Wiley, New York, 1972).
100. C. W. Misner, K. S. Thorne, J. A. Wheeler, *Gravitation* (Freeman, San Francisco, 1973).
101. S. Carroll, *Spacetime and Geometry: An Introduction to General Relativity* (Addison-Wesley, New York, 2003).
102. J. Hartle, *Gravity* (Addison-Wesley, New York, 2003).
103. K. S. Thorne, R. D. Blandford, *Modern Classical Physics* (Princeton Univ. Press, Princeton, NJ, 2015).
104. K. Sharon et al., *Astrophys. J.* **746**, 161 (2012).
105. <http://hubblestie.org/newscenter/archive/releases/2012/08/image>
106. R. N. Manchester, “Detection of gravitational waves using pulsar timing,” presented at the Twelfth Marcel Grossmann Meeting on General Relativity (2012), p. 226.

ACKNOWLEDGMENTS

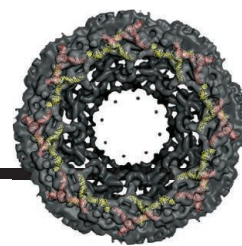
I am indebted to Y. Yuan for assistance in preparing this Review; K. Thorne, R. Wagoner, S. Ransom, and A. Graham for helpful advice; and two anonymous referees for a careful reading of the manuscript.

10.1126/science.aaa4033

RESEARCH

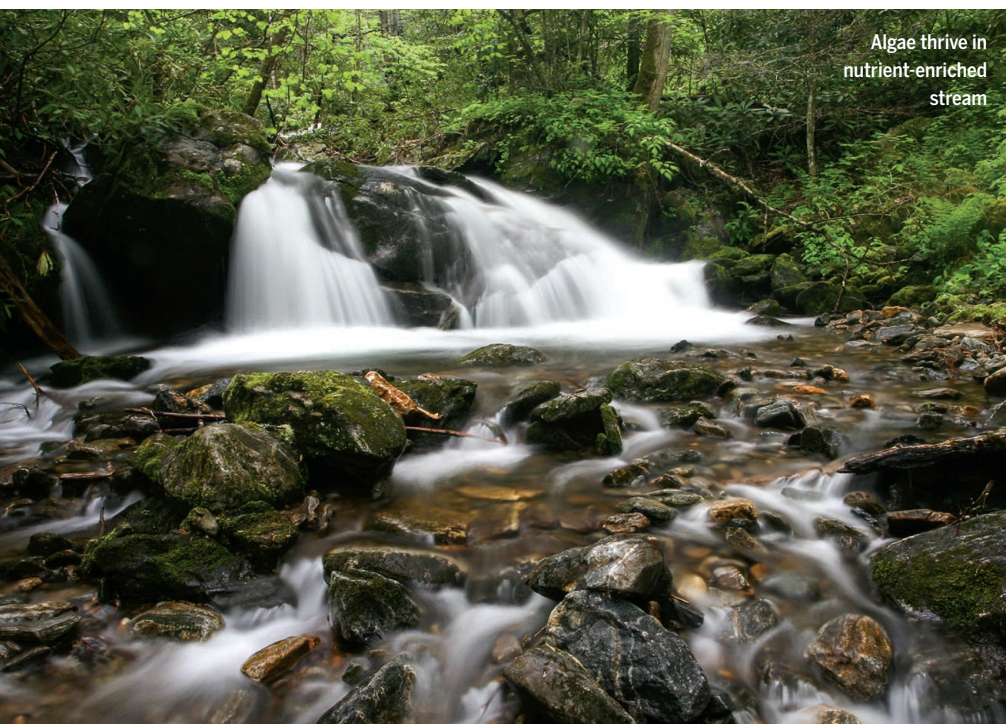
Detailed architecture of the nuclear pore complex revealed

Stuwe et al., p. 1148



IN SCIENCE JOURNALS

Edited by Stella Hurtley



Algae thrive in nutrient-enriched stream

FRESHWATER ECOLOGY

Carbon kicked out by nutrients

Excess nutrients added to streams result in net carbon loss from aquatic ecosystems. Nitrogen and phosphorus fuel the growth of algae, which take up terrestrial carbon to make biomass. More carbon is nevertheless eventually released into the atmosphere. Rosemond *et al.* monitored several multiyear experiments on headwater forest streams in the United States. Some of these streams had extra nitrogen and phosphorus added at levels that are now common in many streams and lakes. To successfully manage river ecosystems, we need to take into account both carbon loss and nutrient pollution. — NW

Science, this issue p. 1142

STRUCTURAL BIOLOGY

Molecular “go” signals reveal their secrets

Chemokines are proteins that direct how cells move within the body. For instance, chemokines help immune cells locate invading pathogens and ensure that cells position themselves correctly within a developing organ. Cells detect chemokines through G protein-coupled receptors on their surface; however, the molecular details of how these proteins interact remain unclear (see the Perspective by Standfuss). Qin *et al.* solved the crystal structure of the chemokine receptor CXCR4 bound to the viral chemokine vMIP-II. Burg *et al.* solved the crystal structure of a viral chemokine receptor bound to the chemokine domain of CX3CL1.

Given the role of chemokines in a number of diseases, these results may help in future drug design.

— KLM

Science, this issue p. 1117, p. 1113; see also p. 1071

BRAIN STRUCTURE

Cellular diversity in the brain revealed

The mammalian brain has an extraordinarily large number of cells. Although there are quite a few different cell types, many cells in any one category tend to look alike. Zeisel *et al.* analyzed the transcriptomes of mouse brain cells to reveal more than meets the eye. Interneurons of similar type were found in dissimilar regions of the brain. Oligodendrocytes that seemed

to be all of one class were differentiated by their molecular signatures into a half-dozen classes. Microglia associated with blood vessels were distinguished from look-alike perivascular macrophages. Thus, the complex microanatomy of the brain can be revealed by the RNAs expressed in its cells. — PJH

Science, this issue p. 1138

QUANTUM ELECTRONICS

Listen to the quantum art of noise

Electrons in metals are subject to thermally induced noise that can generate tiny magnetic fields. For quantum electronic applications, the noise and magnetic fields can be damaging. Kolkowitz *et al.* show that the

spin properties of single defects in diamond can be used to probe the noise. The findings provide insight into how the noise is generated, which could help to mitigate its damaging effects in sensitive quantum electronic circuits. — ISO

Science, this issue p. 1129

EVOLUTIONARY GENOMICS

Of mice, men, and macaque brains

The human brain represents a unique evolutionary trajectory. To better understand how the human brain came to be, Reilly *et al.* sought to identify changes in gene expression between mice, macaques, and humans. They compared epigenetic marks in the embryonic cortex,

which revealed changes in gene regulation in biological pathways associated with cortical development. — LMZ

Science, this issue p. 1155

ASTROPHYSICS

Finding four for the light of one

Seeing double may cause concern for some, but seeing quadruple? It's just what astronomers have been hoping for. Kelly *et al.* have now detected four images of the same distant supernova with the sharp eye of a space telescope. The supernova shines brightly from the arm of a spiral galaxy that lies far beyond another galaxy between it and us. This intervening galaxy is massive enough to bend the light from the supernova and its host galaxy into multiple images. This behavior relies on the curvature of spacetime and will provide insight into the luminous and dark matter in the lensing galaxy. — MMM

Science, this issue p. 1123

REPELLENT MATERIALS

A robust paintlike repellent coating

Superhydrophobic materials often depend on a particular surface patterning or an applied coating. However, these surfaces can be damaged by wear or fouled by oily materials. Lu *et al.* devised a suspension of coated titanium dioxide nanoparticles that can be spray-painted or dip-coated onto a range of hard and soft surfaces, including paper,

cloth, and glass. The coatings resisted rubbing, scratching, and surface contamination. — MSL

Science, this issue p. 1132

POLITICAL ECONOMY

Political preferences provide economic capital

Longer periods of democratic government favor economic growth, which in turn stabilizes democracy. But is this relationship a given? Fuchs-Schündeln and Schündeln collected individual-level data from more than 100 countries over two decades. Support for democracy did indeed increase as the length of time lived in a democratic system increased. — GJC

Science, this issue p. 1145

INFLAMMATION

Interpreting immune signals in the CNS

Mice with experimental autoimmune encephalomyelitis (EAE) provide a model of multiple sclerosis. In these mice, a subset of T helper cells that secrete the proinflammatory cytokine interleukin-17 (IL-17) are among the first immune cells to infiltrate the central nervous system (CNS). Huang *et al.* found that the kinase p38 α mediated IL-17-dependent signaling in mice with EAE (see the Focus by Gaffen and McGeachy). Disease symptoms were reduced in mice lacking p38 α in CNS cells such as astrocytes but were exacerbated in mice deficient in a phosphatase that inhibits p38 α . — JFF

Sci. Signal. **8**, ra24; see also fs5 (2015).

IN OTHER JOURNALS

Edited by **Kristen Mueller**
and **Jesse Smith**



Older female killer whales provide a fitness advantage to their kin

METABOLIC ENGINEERING

Making biofuels greener

Plant biomass, rich in hemicellulose, can be converted by microorganisms into ethanol for use as biofuel. However, some materials derived from plant cell walls, including sugars such as xylodextrin, are more difficult for microorganisms to metabolize, making the overall biofuel production process less efficient. Li *et al.* characterized a widely distributed xylodextrin consumption pathway from the fungus *Neurospora crassa* that is required for its growth on hemicellulose. Engineering this pathway into yeast produces previously unknown intermediate metabolites from xylodextrin that are then broken down to xylose and xylitol and fermented to ethanol. — NW

eLife 10.7554/eLife.05896#sthash.pkIMD1GC.dpuf (2015).

EYE DEVELOPMENT

Eye development from both sides

In vertebrates, eye development begins with the outgrowth of the optic vesicle from the brain. The optic vesicle then transforms into a bilayered structure called the optic cup after extensive morphological movements, which scientists do not completely understand. In order to visualize these events, Heermann *et al.* used four-dimensional in vivo microscopy to track the movements of cells in the eyes of developing zebrafish. They found that cells from both sides of the optic vesicle generate the neuroretinal layer of the optic cup, rather than just the side that faces the lens as previously thought. The growth factor bone morphogenic protein facilitated this process. — BAP

eLife **4**, e05216 (2015).



Superhydrophobic painting corrals water

EVOLUTION

Wisdom of the elders

Menopause is something that humans share with only two other mammal species: killer whales and pilot whales. Menopause is at odds with classic evolutionary theory, which posits that once animals stop reproducing, natural selection stops too. However, Brent *et al.* now demonstrate the importance of keeping elders around. They found that older female killer whales lead their pods to salmon feeding grounds and that this leadership is especially important in years when food is scarce. Thus, older females can act as crucial repositories of ecological knowledge, improving their own inclusive fitness and the fitness of their younger relatives. — SNV

Curr. Biol. 10.1016/j.cub.2015.01.037 (2015).



MEDICAL IMAGING

A clearer view of type 1 diabetes

Pancreatic beta cells keep blood glucose levels in check by secreting insulin, which

removes glucose from blood. In type 1 diabetes, beta cells stop functioning because the immune system destroys them. Noninvasive imaging of pancreatic inflammation—an early sign of this immune attack—could

provide scientists with new insights into how the disease begins and progresses. In a pilot study, Gaglia *et al.* used magnetic resonance imaging to generate three-dimensional high-resolution maps of pancreatic inflammation in patients with recent-onset type 1 diabetes. Key to their success was an imaging agent called ferumoxytol,

a clinically approved magnetic nanoparticle taken up by macrophages. — PAK

Proc. Natl. Acad. Sci. U.S.A. **112**, 2139 (2015).

BIOFUELS

Starting out by making the most of lignin

The woody lignin component of biomass, rich in aromatic carbon rings, ultimately could prove a cost-effective source of numerous commodity chemicals. Parsell *et al.* make a step in that direction with a zinc and palladium catalyst that transforms lignin into a tractable product stream composed predominantly of two phenol derivatives. These in turn can be further transformed by downstream chemistry. The method does not require preliminary isolation of the lignin;

rather, it works on minimally pretreated biomass and leaves behind a cellulose component that's easily broken down into fermentable sugars for biofuels production. — JSY

Green Chem. 10.1039/c4gc01911c (2014).

VIRAL SPREAD

Enteroviruses have got to hitch a ride...

Viruses are thought to come in two flavors: enveloped—surrounded with a membrane like the cells they infect, or non-enveloped—naked protein and nucleic acid particles that can invade target cells. However, it now seems that non-enveloped viruses might nevertheless sneakily co-opt host cell membranes to help them spread from cell to cell. Chen *et al.* now show that cells release clusters of newly synthesized enteroviruses, including poliovirus, coxsackievirus B3, and rhinovirus, into the extracellular environment within lipid vesicles. Compared with free viruses, the enclosed viruses do a better job of infecting new cells. — SMH

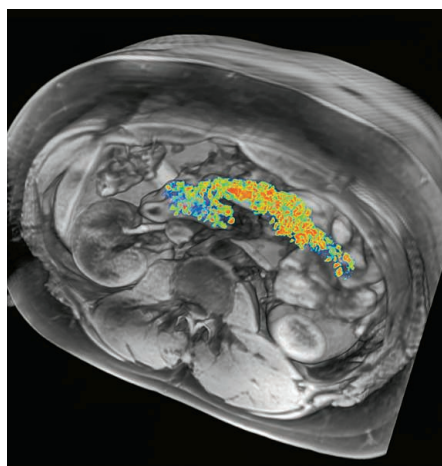
Cell **160**, 619 (2015).

CLIMATE CHANGE ECOLOGY

Long-term warming and vegetation change

How climate change specifically affects ecosystems can be difficult to sort out. To determine cause and effect, Harte *et al.* examined changes to vegetation and soil in plots of land in the U.S. Rocky Mountains that they either warmed experimentally or left untouched (ambient) over 23 years. They found that both experimental warming and the natural warming of the Rockies over that time period led to a shift from herbaceous meadow to woody shrub vegetation. Soil carbon declined, too (although in both cases more slowly in the ambient plots). These results demonstrate that climate change caused the observed vegetation and soil changes. — AMS

Global Change Biol. 10.1111/gcb.12831 (2015).



Nanoparticles help to visualize pancreatic inflammation in people with type 1 diabetes

ALSO IN SCIENCE JOURNALS

Edited by Stella Hurtley

IMMUNOGENETICS

How the immune system readies for battle

Although gene expression is tightly controlled at both the RNA and protein levels, the quantitative contribution of each step, especially during dynamic responses, remains largely unknown. Indeed, there has been much debate whether changes in RNA level contribute substantially to protein-level regulation. Jovanovic *et al.* built a genome-scale model of the temporal dynamics of differential protein expression during the stimulation of immunological dendritic cells (see the Perspective by Li and Biggin). Newly stimulated functions involved the up-regulation of specific RNAs and concomitant increases in the levels of the proteins they encode, whereas housekeeping functions were regulated posttranscriptionally at the protein level. — LMZ

Science, this issue p. 1112;
see also p. 1066

STELLAR DYNAMICS

Stars that blow up and bug out

When stars move at speeds that will launch them out of our Galaxy, eyes often turn to our core supermassive black hole as the slingshot responsible. For at least one hypervelocity star, however, the galactic center remains innocent. Geier *et al.* traced back the trajectory of a compact helium star, US 708, and deduced a different origin in a binary. In this scenario, US 708 acted as the mass donor in a type Ia supernova pair, which spun US 708 to the point of ejection. By knowing this star's exotic past, we learn both about its specific history and about the nature of all type Ia supernovae. — MMM

Science, this issue p. 1126

PROTEIN IMAGING

Single-protein spectroscopy

The spin of a single nitrogen-vacancy (NV) center in diamond is a highly sensitive magnetic-field sensor. Shi *et al.* used the NV center to detect a nitroxide-labeled protein through electron spin resonance under ambient conditions (see the Perspective by Hemmer and Gomes). The strength of the interaction and the details of the hyperfine interaction between the electron and nitrogen spin revealed the position and orientation of the spin label relative to the NV center. The findings also elucidate the dynamical motions of the protein on the diamond surface. — PDS

Science, this issue p. 1135;
see also p. 1072

PROTEIN TARGETING

How to GET to the right membrane

Membrane proteins with a hydrophobic transmembrane domain (TMD) play critical roles in virtually all aspects of cell physiology. After it has been synthesized in the cytosol, this TMD must be targeted to and inserted into the correct membrane. The GET pathway is one of two targeting pathways to the endoplasmic reticulum conserved across all eukaryotes. It is not clear how the central targeting factor, Get3, recognizes a TMD to shield it from aggregation until it is successfully inserted into the membrane. Now, Mateja *et al.* show that the functional targeting complex comprises a Get3 dimer bound to a single TMD. The helical hydrophobic TMD binds deep within a large hydrophobic groove in the Get3 dimer. This groove closes slightly upon TMD binding, forming a dynamic "lid" over the mouth of the groove. — SMH

Science, this issue p. 1152

EXOPLANETS

The search for signatures of life on exoplanets

A "terracentric" view of the likely chemical signatures of life on planets outside our solar system may be naïve. Now that we are in the early stages of characterizing exoplanets, rather than just identifying them, the question arises of how best to search for tangible evidence of life on these faraway worlds. Seager and Bains review present theory and future opportunities in the search for biosignatures in planetary atmospheres. They argue that searching for a broader range of small-molecule volatiles than those that are characteristic of biological activity on Earth may prove to be a better way forward. — KVH

Sci. Adv. 10.1126/sciadv.15 00047
(2015).

NUCLEAR PORES

A closeup view of the nuclear pore's coat

The precise molecular architecture of the nuclear pore complex (NPC), which mediates traffic between the cytoplasm and the nucleus, has been difficult to ascertain owing to the size and complexity of this subcellular structure. Now, Stuwe *et al.* describe the crystal structure of the intact ~400-kD coat nucleoporin complex (CNC) of *Saccharomyces cerevisiae* in the presence of an engineered antibody fragment. Docking the crystal structure into an electron tomography reconstruction of the human NPC established the presence of 32 copies of the CNC arranged in four stacked rings and revealed the details of higher-order CNC oligomerization at the near-atomic level. — SMH

Science, this issue p. 1148

HEART FAILURE

Taking antidepressants to heart

Drug repurposing—using drugs already approved by the Food and Drug Administration for new diseases—can save money and time. The antidepressant paroxetine, a selective serotonin reuptake inhibitor (SSRI), also inhibits GRK2, an enzyme that contributes to heart failure. Now Schumacher *et al.* report that paroxetine can block, or even reverse, the heart damage seen after myocardial infarction in mice. These effects are distinct from its SSRI action and are enhanced by β -adrenergic receptor blockers, already often used to treat heart failure. — ACC

Sci. Transl. Med. 7, 277ra31 (2015).

INFECTIOUS DISEASES

Countering antibiotic resistance

Many disease-causing bacteria are resistant to one or more antibiotics, making them difficult to treat. Yet few new antibiotics are being approved for use as medicines. In a Perspective, Perros argues that better understanding of the fundamental characteristics of Gram-negative bacteria is particularly important for the development of new antibiotics. Advances in rapid diagnostics will help to treat patients with the right medication, and also help in the development of highly targeted antibiotics. In a second Perspective, Baker chronicles how antibiotic resistance has become a daily reality in lower-income countries. Drug resistance in the bacterium causing typhoid fever, for example, is so widespread that conditions may return to those of the pre-antibiotic era. New drugs may help, but without large-scale changes in antibiotic use, their impact is likely to be short-lived. — JFU

Science, this issue p. 1062, p. 1064

RESEARCH ARTICLE SUMMARY

IMMUNOGENETICS

Dynamic profiling of the protein life cycle in response to pathogens

Marko Jovanovic,* Michael S. Rooney,* Philipp Mertins, Dariusz Przybylski, Nicolas Chevrier, Rahul Satija, Edwin H. Rodriguez, Alexander P. Fields, Schraga Schwartz, Raktima Raychowdhury, Maxwell R. Mumbach, Thomas Eisenhaure, Michal Rabani, Dave Gennert, Diana Lu, Toni Delorey, Jonathan S. Weissman, Steven A. Carr, Nir Hacohen,† Aviv Regev†

INTRODUCTION: Mammalian gene expression is tightly controlled through the interplay between the RNA and protein life cycles. Although studies of individual genes have shown that regulation of each of these processes is important for correct protein expression, the quantitative contribution of each step to changes in protein expression levels remains largely unknown and much debated. Many studies have attempted to address this question in the context of steady-state protein levels, and comparing steady-state RNA and protein abundances has indicated a considerable discrepancy between RNA and protein levels. In contrast, only a few studies have attempted to shed light on how changes in each of these processes determine differential protein expression—either relative (ratios) or absolute (differences)—during dynamic responses,

and only one recent report has attempted to quantitate each process. Understanding these contributions to a dynamic response on a systems scale is essential both for deciphering how cells deploy regulatory processes to accomplish physiological changes and for discovering key molecular regulators controlling each process.

RATIONALE: We developed an integrated experimental and computational strategy to quantitatively assess how protein levels are maintained in the context of a dynamic response and applied it to the model response of mouse immune bone marrow-derived dendritic cells (DCs) to stimulation with lipopolysaccharide (LPS). We used a modified pulsed-SILAC (stable isotope labeling with amino acids in cell culture) approach

to track newly synthesized and previously labeled proteins over the first 12 hours of the response. In addition, we independently measured replicate RNA-sequencing profiles under the same conditions. We devised a computational strategy to infer per-mRNA translation rates and protein degradation rates at each time point from the temporal transcriptional profiles and pulsed-SILAC proteomics data. This allowed us to build a genome-scale quantitative model of the temporal dynamics of differential protein expression in DCs responding to LPS.

RESULTS: We found that before stimulation, mRNA levels contribute to overall protein expression levels more than double the combined contribution of protein translation and

degradation rates. Upon LPS stimulation, changes in mRNA abundance play an even more dominant role in dynamic changes in protein levels, especially in immune response

genes. Nevertheless, several protein modules—especially the preexisting proteome of proteins performing basic cellular functions—are predominantly regulated in stimulated cells at the level of protein translation or degradation, accounting for over half of the absolute change in protein molecules in the cell. In particular, despite the repression of their transcripts, the level of many proteins in the translational machinery is up-regulated upon LPS stimulation because of significantly increased translation rates, and elevated protein degradation of mitochondrial proteins plays a central role in remodeling cellular energy metabolism.

CONCLUSIONS: Our results support a model in which the induction of novel cellular functions is primarily driven through transcriptional changes, whereas regulation of protein production or degradation updates the levels of preexisting functions as required for an activated state. Our approach for building quantitative genome-scale models of the temporal dynamics of protein expression is broadly applicable to other dynamic systems. ■

RELATED ITEMS IN SCIENCE

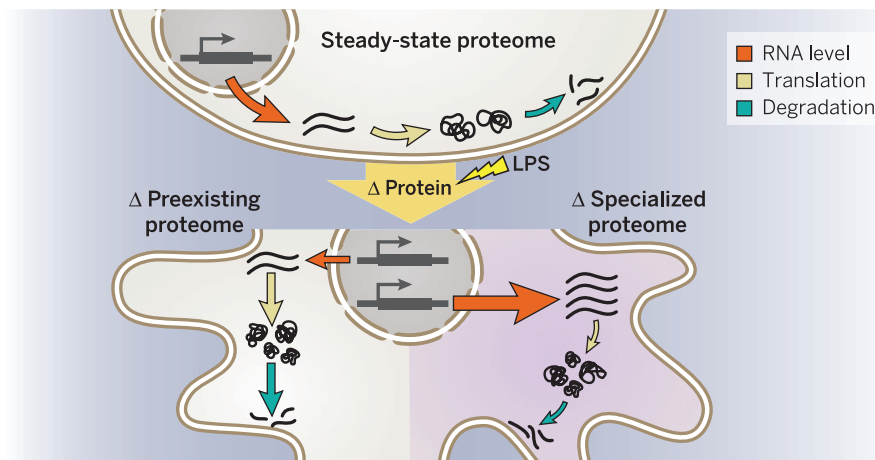
A. Battle *et al.*,
Science **347**, 664 (2015)
DOI: 10.1126/science.1260793

The list of author affiliations is available in the full article online.

*These authors contributed equally to the work.

†Corresponding author. E-mail: aregev@broad.mit.edu (A.R.); nhacohen@mgh.harvard.edu (N.H.)

Cite this article as M. Jovanovic *et al.*, *Science* **347**, 1259038 (2015). DOI: 10.1126/science.1259038



Dynamic protein expression regulation in dendritic cells upon stimulation with LPS. We developed an integrated experimental and computational strategy to quantitatively assess how protein levels are maintained in the context of a dynamic response. Our results support a model in which the induction of novel cellular functions is primarily driven through transcriptional changes, whereas regulation of protein production or degradation updates the levels of pre-existing functions.

RESEARCH ARTICLE

IMMUNOGENETICS

Dynamic profiling of the protein life cycle in response to pathogens

Marko Jovanovic,^{1,*} Michael S. Rooney,^{1,2*} Philipp Mertins,¹ Dariusz Przybylski,¹ Nicolas Chevrier,^{1,3} Rahul Satija,^{1,†} Edwin H. Rodriguez,⁴ Alexander P. Fields,⁴ Schraga Schwartz,¹ Raktima Raychowdhury,¹ Maxwell R. Mumbach,¹ Thomas Eisenhaure,^{1,5} Michal Rabani,^{1,§} Dave Gennert,¹ Diana Lu,¹ Toni Delorey,¹ Jonathan S. Weissman,^{4,6} Steven A. Carr,¹ Nir Hacohen,^{1,5,7,†} Aviv Regev^{1,8,9||}

Protein expression is regulated by the production and degradation of messenger RNAs (mRNAs) and proteins, but their specific relationships remain unknown. We combine measurements of protein production and degradation and mRNA dynamics so as to build a quantitative genomic model of the differential regulation of gene expression in lipopolysaccharide-stimulated mouse dendritic cells. Changes in mRNA abundance play a dominant role in determining most dynamic fold changes in protein levels. Conversely, the preexisting proteome of proteins performing basic cellular functions is remodeled primarily through changes in protein production or degradation, accounting for more than half of the absolute change in protein molecules in the cell. Thus, the proteome is regulated by transcriptional induction for newly activated cellular functions and by protein life-cycle changes for remodeling of preexisting functions.

Mammalian gene expression is tightly controlled through the interplay between the RNA and protein life cycles (Fig. 1A). Although studies of individual genes have shown the importance of regulating each of these processes for correct protein expression (1–4), the quantitative contribution of each process to changes in protein expression levels (Fig. 1A) remains largely unknown and much debated (5, 6). Many studies have attempted to address this question in the context of steady-state protein levels (5, 7–13), and comparing steady-state mRNA and protein abundances has indicated a considerable discrepancy between mRNA and protein levels (5, 7–13). Furthermore, protein expression is more conserved across species than is mRNA expression (11, 14, 15), both suggesting a substantial

contribution of the protein life cycle. A recent study using metabolic pulse labeling of proteins and mRNA in an asynchronously proliferating mammalian cell line (16) concluded that gene-to-gene differences in protein synthesis rates contributed most to final protein levels (~55%), followed by mRNA abundance (40%), whereas degradation of mRNA and protein played only minor roles. However, reanalysis of this data challenged some of these conclusions, arguing that the contribution of mRNA levels could be as high as 84% and that of protein synthesis as low as 8% (6).

In contrast, only a few studies (5, 12, 17–20) have attempted to shed light on how changes in each of these processes determine differential protein expression—either relative (ratios) or absolute (differences)—during dynamic responses, and only one recent report (20) has attempted to quantitate each process. However, none of these has comprehensively accounted for experimental measurement errors, nor have they deconvolved interdependencies of the data. Understanding these contributions to a dynamic response on a systems scale is essential both for deciphering how cells deploy regulatory processes to accomplish physiological changes and for discovering key molecular regulators controlling each process.

Results

A pulsed-SILAC strategy to measure protein dynamics

We assessed how protein levels are maintained in the context of the model response of mouse immune bone marrow-derived dendritic cells (DCs) (21) to stimulation with lipopolysaccharide (LPS) (22–26). This is a compelling system because DCs are mostly postmitotic, and LPS synchronizes

them (27) and causes dramatic regulatory changes from the expression of thousands of transcripts (22, 24, 25) to protein phosphorylation (26). To monitor protein production and degradation during a dynamic response, we used a modified pulsed-SILAC (stable isotope labeling with amino acids in cell culture) approach (Fig. 1B) (28, 29) to track newly synthesized and previously labeled proteins over time. We cultured DCs for 9 days in medium-heavy-labeled (M) SILAC medium then substituted the M SILAC medium with heavy-labeled (H) SILAC medium and immediately stimulated them with LPS or medium (MOCK). Newly synthesized proteins were thus labeled with heavy (H) amino acids, serving as a proxy for protein synthesis, whereas proteins with medium-heavy (M) amino acids decayed over time, reflecting cellular half lives. For normalization, we spiked in a reference sample, extracted from a mix of unstimulated and stimulated DCs grown in light (L) SILAC media. We collected biological replicate samples at 10 time points over 12 hours (0, 0.5, 1, 2, 3, 4, 5, 6, 9, and 12 hours) after LPS or mock stimulation. We quantified 6079 proteins by means of liquid chromatography–tandem mass spectrometry (LC-MS/MS) in at least one sample and 2288 proteins in all samples (time points, conditions, and replicates) (Fig. 2A and table S1). We independently measured replicate RNA-sequencing (RNA-Seq) profiles under the same conditions (Fig. 2A and table S2) (29).

A model-based estimation of protein synthesis and degradation rates

We devised a computational strategy to infer per-mRNA translation rates [$T_i(t)$] and protein degradation rates [$D_i(t)$] at each time point from the temporal transcriptional profiles [$R_i(t)$] and H/L and M/L protein ratios [$H_i(t)$ and $M_i(t)$, respectively] (Fig. 1B and fig. S1) (29). We defined a model that describes the relevant processes and associated rates (such as translation rate and protein degradation rate) and then fitted the parameters (such as rates) in the model with our mRNA and protein data. Specifically, we used an ordinary differential equations model describing, for each gene i , the changes in $M_i(t)$ and $H_i(t)$ [$dM_i(t)/dt$ and $dH_i(t)/dt$, respectively] as a function of (i) a production term, governed by mRNA abundance $R_i(t)$ and a per-mRNA molecule translation rate constant, $T_i(t)$; and (ii) a degradation term, modeled as an exponential decay function, governed by a protein degradation rate constant, $D_i(t)$. Both terms are also affected by $\gamma(t)$, the global M SILAC label recycling rate (figs. S1 and S2) (29). All rate constants are dynamic, and the mRNA levels, per-mRNA translation rate constant, and protein degradation rate constant are also gene-specific. We modeled the change over time in the per-mRNA translation rate constant [$T_i(t)$] and in the degradation rate constant [$D_i(t)$] as linear functions. This assumption reduces the number of free parameters, thus providing robustness while retaining the capacity to detect the effect of sustained changes, even if these changes do not manifest linearly in vivo (as in the case of step functions).

¹The Broad Institute of MIT and Harvard, Cambridge, MA 02142, USA. ²Division of Health Sciences and Technology, Massachusetts Institute of Technology, Cambridge, MA 02139, USA. ³Harvard Faculty of Arts and Sciences Center for Systems Biology, Harvard University, Cambridge, MA 02138, USA. ⁴Department of Cellular and Molecular Pharmacology, California Institute for Quantitative Biomedical Research, University of California, San Francisco, San Francisco, CA 94158, USA. ⁵Center for Immunology and Inflammatory Diseases, Massachusetts General Hospital, Boston, MA 02114, USA. ⁶Howard Hughes Medical Institute (HHMI), University of California, San Francisco, San Francisco, CA 94158, USA. ⁷Harvard Medical School, Boston, MA 02115, USA. ⁸Department of Biology, Massachusetts Institute of Technology, Cambridge, MA 02140, USA. ⁹HHMI, Department of Biology, Massachusetts Institute of Technology, Cambridge, MA 02140, USA.

*These authors contributed equally to the work. †Present address: New York Genome Center, New York, NY 10013, USA. ‡Present address: Center for Genomics and Systems Biology, New York University, New York, NY 10012, USA. §Present address: Department of Molecular and Cellular Biology, Harvard University, Cambridge, MA 02138, USA. ||Corresponding author. E-mail: aregev@broad.mit.edu (A.R.); nhacohen@mgh.harvard.edu (N.H.)

We fitted the different parameters in the model (fig. S1) with the RNA-Seq and MS data (29) using an empirical Bayes strategy (29), which prevents overfitting of noisy MS data by sharing information across genes. In this approach, our most differential and reliable parameter estimates correspond to the well-quantified genes (29), whereas proteins with less reliable measurements are not associated with reliable changes. This ensures a low rate of false positives (calling a change where none exists) but may result in false negatives and, hence, in some underestimation of the contribution of protein synthesis and degradation.

Fitting the parameters for 3147 genes that passed our filtering criteria (29), separately for each of our replicates (Fig. 2B, fig. S3, and table S3), we found good reproducibility of the LPS/MOCK ratios of key fitted values (Fig. 2B and fig. S4) and of the relative differences in per-mRNA translation rates [for example, $\Delta T_i(12h) = T_i(12h)_{LPS}/T_i(12h)_{MOCK}$, Pearson correlation coefficient (r) = 0.68] (fig. S5A) or degradation rates [for example, $\Delta D_i(12h) = D_i(12h)_{LPS}/D_i(12h)_{MOCK}$, r = 0.62] (fig. S5B). The robustness of these results was further supported by (i) the fair correlation of our translation and protein degradation rate estimates in resting cells (table S3 and fig. S6, A and B) with previous estimates in mouse fibroblasts (NIH3T3) based on a similar pulsed-SILAC approach $\{r[T_i(0)] = 0.35; r[D_i(0)] = 0.58\}$ (fig. S7) (16) or on estimates of translation rate efficiency (TE) values based on ribosome profiling in mouse fibroblasts (NIH3T3) $\{r[T_i(0)] = 0.37\}$ (fig. S7C) (30); (ii) a good correlation be-

tween our per-mRNA translation rates and our independent measurement of TE values in DCs using ribosome profiling at time (t) = 0 hours (r = 0.5) (table S4) (fig. S8A), which is comparable with the correlation between TE values in mouse DCs and mouse fibroblasts (r = 0.54) (fig. S8B); (iii) that strong early changes are all in immune response proteins (fig. S4A); (iv) the global increase upon LPS stimulation in protein production rates $[T_i(12h)_{LPS}$ versus $T_i(12h)_{MOCK}$; $P < 10^{-10}$, Wilcoxon rank sum test] (fig. S9A) and protein degradation rates $[D_i(12h)_{LPS}$ versus $D_i(12h)_{MOCK}$; $P < 10^{-10}$, Wilcoxon rank sum test] (fig. S9B), which is consistent with other reports (31, 32); and (v) the increase in the calculated “degradation rate”—likely reflecting depletion by secretion, or “decreased cellular half-life”—of proteins from the recently characterized secretome of LPS-stimulated mouse macrophages [$\delta D_i(12h) = D_i(12h)_{LPS}/D_i(12h)_{MOCK}$; $P < 10^{-10}$, Wilcoxon rank sum test] (fig. S9C) (33).

mRNA levels contribute the most to protein expression levels before stimulation

To determine the relative contribution of each step to steady-state protein levels in unstimulated, postmitotic DCs, we first estimated absolute protein levels from four additional MS data sets in resting DCs (0 hours) that rely on distinct peptides (29): two biological replicate samples, which were each digested in two technical replicates with LysN and AspN, respectively, rather than by trypsin, which was used for the pulsed SILAC samples (29).

Next, we assessed the contribution of each regulatory step to gene-to-gene differences in overall protein levels by comparing (with Spearman-corrected coefficients of determination) (29) the independently measured absolute protein levels to steady-state protein levels predicted by our model when setting one or more of the three regulatory steps (mRNA level, per-mRNA translation rate constant, or protein degradation rate constant) to its per-gene inferred value (at time 0 hours) and setting the remaining steps to their pan-genome median value (29). By sequentially adding to the model further per-gene values rather than pan-genome medians (such as mRNA level, translation rate, and last, degradation rate) and assessing the corresponding change in the correlation measure, we can assign additive regulatory contributions to the three steps (29). Because these three steps are not statistically independent from each other and may interact in a nonlinear manner, we explored every possible ordering of consideration.

Considering all three variables together, we account for nearly 79% of the variance of the independently measured protein levels (figs. S10 and S11A) (29). Of these 79%, mRNA levels explained 59 to 68%, per-mRNA translation rates 18 to 26%, and protein degradation rates 8 to 22% (Fig. 3A and fig. S11A) (29). We believe the unexplained variance is due to systematic errors in the measurements and modeling that could not be accounted for. In addition, we have separately estimated the variance in translation rates in the same cells under identical conditions using ribosome profiling to measure TE values [above and (29)]. Using

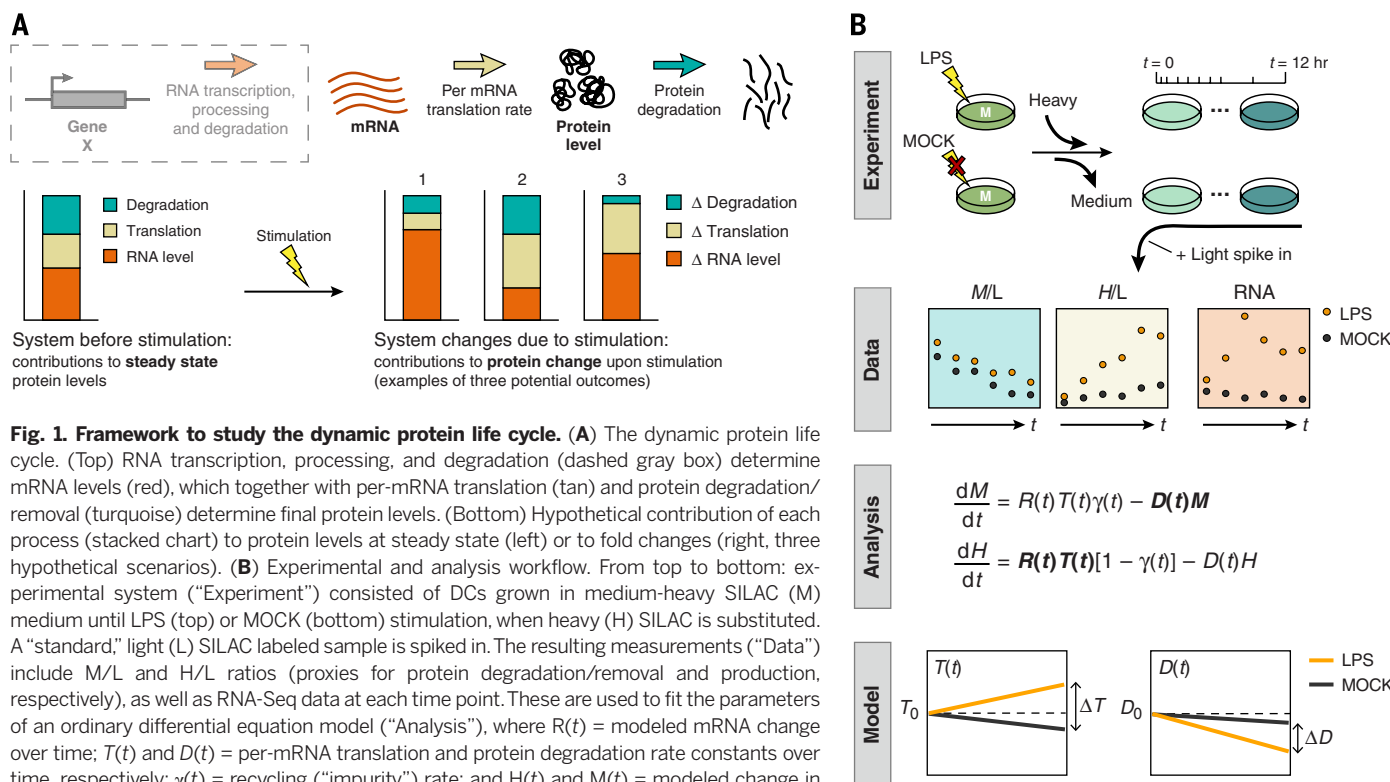


Fig. 1. Framework to study the dynamic protein life cycle. (A) The dynamic protein life cycle. (Top) RNA transcription, processing, and degradation (dashed gray box) determine mRNA levels (red), which together with per-mRNA translation (tan) and protein degradation/removal (turquoise) determine final protein levels. (Bottom) Hypothetical contribution of each process (stacked chart) to protein levels at steady state (left) or to fold changes (right, three hypothetical scenarios). (B) Experimental and analysis workflow. From top to bottom: experimental system (“Experiment”) consisted of DCs grown in medium-heavy SILAC (M) medium until LPS (top) or MOCK (bottom) stimulation, when heavy (H) SILAC is substituted. A “standard,” light (L) SILAC labeled sample is spiked in. The resulting measurements (“Data”) include M/L and H/L ratios (proxies for protein degradation/removal and production, respectively), as well as RNA-Seq data at each time point. These are used to fit the parameters of an ordinary differential equation model (“Analysis”), where $R(t)$ = modeled mRNA change over time; $T(t)$ and $D(t)$ = per-mRNA translation and protein degradation rate constants over time, respectively; $\gamma(t)$ = recycling (“impurity”) rate; and $H(t)$ and $M(t)$ = modeled change in heavy (H/L) and medium (M/L) channels, respectively. The result (“Model”) are the estimated per-mRNA translation and degradation rates over time. Details are provided in the text and (29).

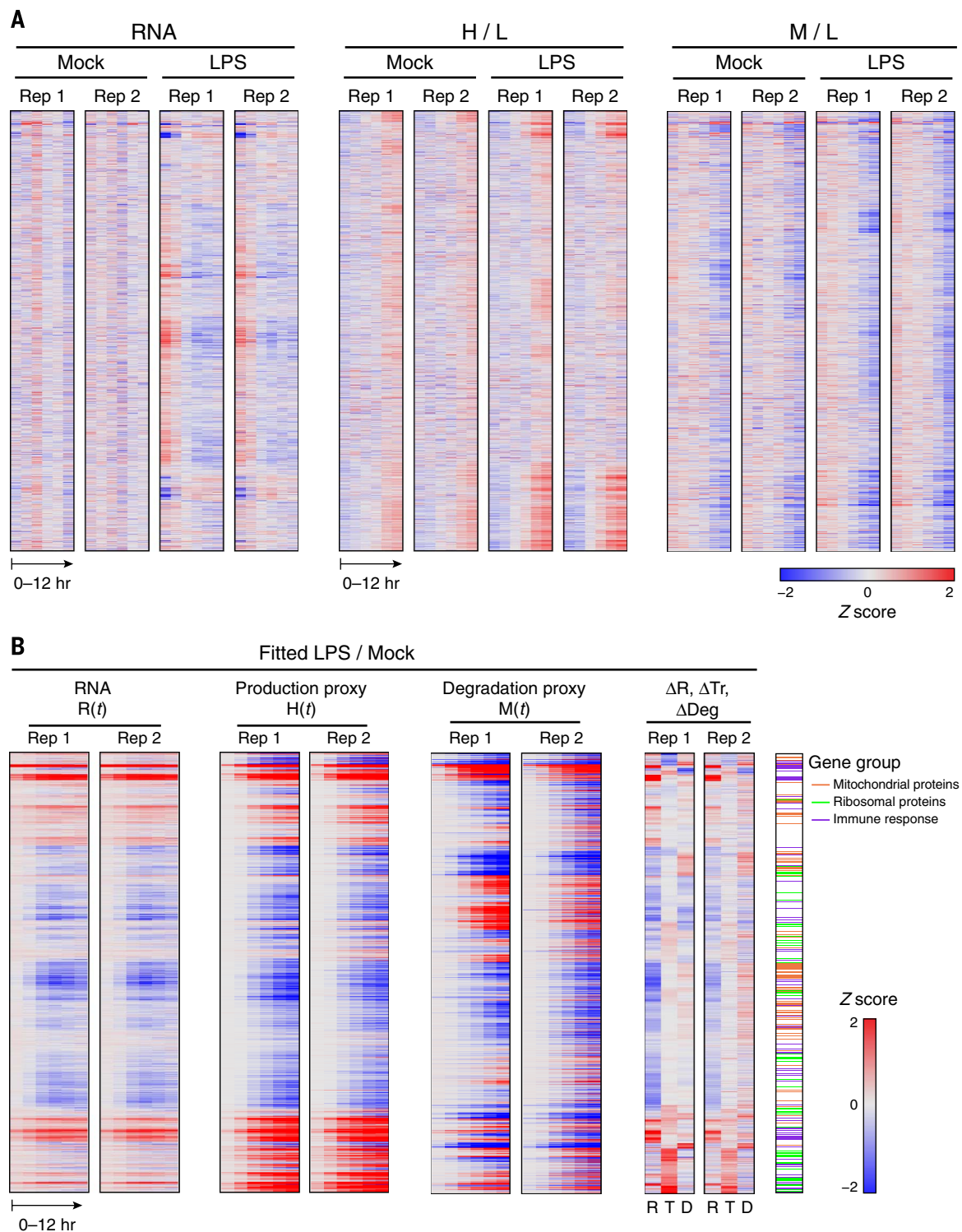


Fig. 2. The protein life cycle in LPS-stimulated DCs. (A) Shown are (left to right), for all 2288 genes (rows) that were quantified in all samples, mRNA expression, H/L protein expression, and M/L protein expression in LPS- and MOCK-stimulated DCs from each replicate (columns). Gene order is the same across all heatmaps and determined by means of hierarchical clustering of fitted fold changes in mRNA level, translation rate, and degradation rate. Values are median normalized by row, logged, and robust z-transformed per map (color scale). (B) Fitted dif-

ferential expression of the same 2288 genes (rows). Left to right: Robust z-score fitted differential expression ratios (LPS/MOCK; red/blue color scale) for $R(t)$, $H(t)$, and $M(t)$ in LPS- versus MOCK-stimulated DCs from each replicate (columns), with the \log_2 fold changes between LPS- and MOCK-stimulated DCs at 12 hours after stimulation for mRNA (ΔR), per-mRNA translation rate (ΔTr), and protein degradation rate (ΔDeg) (also z-scored). Rightmost column, immune response (purple), ribosomal (green), and mitochondrial (orange) proteins.

TE values instead of our pulsed-SILAC derived translation rates, we estimate a comparable contribution of protein synthesis (Fig. 3B and fig. S10). Thus, in postmitotic DCs, mRNA levels are contributing more to protein-to-protein variation in total protein levels than is the protein life cycle (synthesis and degradation rates combined).

mRNA abundance dynamics dominate protein changes after stimulation

Next, we determined the contribution of each regulatory step to protein fold changes at 12 hours. We used the model fit from a given replicate to

predict the protein fold change at 12 hours, when using either MOCK-estimated parameters or one or more LPS-estimated parameters for mRNA level, translation rate, and degradation rate. We then compared these predictions to the fitted fold changes from the other replicate. Starting with all parameters set to MOCK-estimated rates, we sequentially used LPS-estimated parameters for mRNA, translation rate, and degradation rate (in every possible order) and thus assessed the contribution of each step as the increase in the Spearman-corrected coefficients of determination (29).

We found that mRNA levels explain ~87 to 92%, per-mRNA translation rates ~4 to 7%, and protein degradation rates ~3 to 6% of protein fold changes after 12 hours (Fig. 3C and fig. S11B) (29). mRNA fold changes contributed at least eight times as much as did the protein life cycle combined for both induced and repressed proteins (fig. S12 and table S5) (29). However, changes in per-mRNA translation rates contributed more substantially to protein-level induction, whereas changes in protein degradation rates mostly contributed to protein-level repression (fig. S12 and table S5) (29).

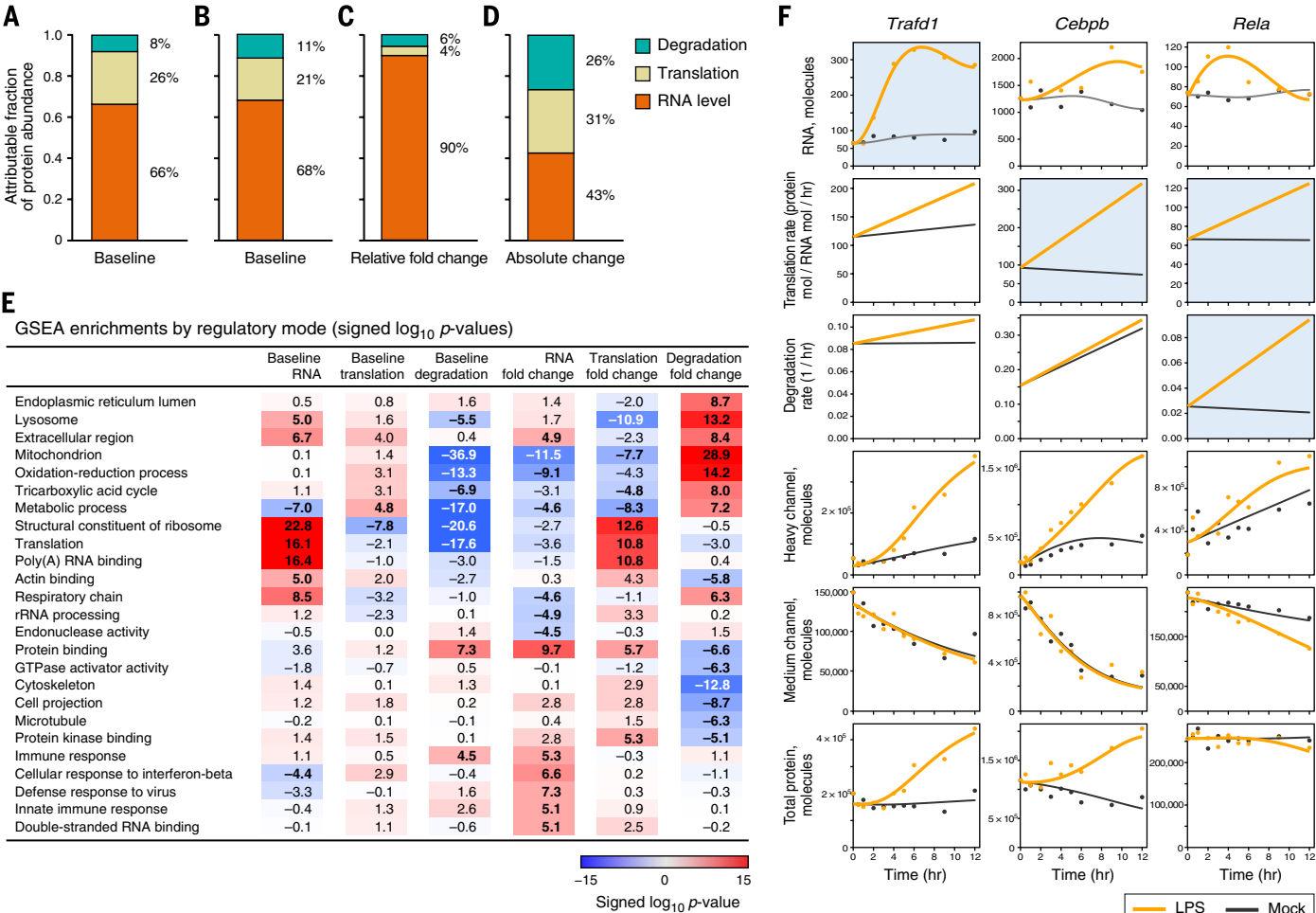


Fig. 3. Contributions of mRNA levels and the protein life cycle to steady-state and dynamic protein levels. (A to D) Global contributions of mRNA levels (orange), translation rates (tan), and protein degradation rates (turquoise) to protein levels. Translation rates were derived either from pulsed SILAC data [(A), (C), and (D)] or from TE values from ribosome profiling data [(B)]. Contributions to steady-state protein levels before LPS induction [(A) and (B)] or to the change in protein abundance between LPS-induced and mock-treated cells [(C) and (D)] are shown. The contributions to the fold change (C) and to the absolute change in protein abundances (D) after LPS stimulation are given. The contributions for steady state presented exclude the percent of the variance in measured protein levels that is not explained by the variance in mRNA, translation, or protein degradation (fig. S10). Per-gene parameter values were in the order 1, mRNA; 2, translation; 3, degradation (29). All possible orderings are provided in fig. S11. (E) Functional processes controlled by distinct regulatory steps. For each process (rows) and regulatory step (columns) shown are the magnitudes of the log₁₀(P values) for the values or

differential fold changes (LPS/MOCK at 12 hours) of mRNA levels, protein synthesis, or degradation rates of genes annotated to this process versus the background of all genes fit by the model. Values are signed according to directionality of the enrichment (Wilcoxon rank sum test). Shown are the five gene sets most enriched for increased or decreased rates for the three “fold change” columns, along with their scores in all six regulatory modes. (F) Examples of regulation of expression dynamics. For each of three genes in each of LPS (orange) and MOCK (black) condition shown are the measured values (dots) and fits (curves) for (top to bottom) mRNA levels (in mRNA molecules), per-mRNA translation rates (protein molecules/mRNA molecule/hour), degradation rates (1 per hour), $H(t)$, $M(t)$, and total protein $[(M+H)(t)]$; x axis, time; y axis, intensity or rate. Light blue indicates key regulatory mode. mRNA and protein molecules are only proxies for transcripts per million (TPM) and intensity-based absolute quantification (iBAQ) microshares, respectively, in order to help interpretation (29).

Fold changes in induced immune response proteins (29) were particularly dominated by mRNA level changes (Figs. 2B and 3E and table S6). For example, transient up-regulation of the mRNA encoding the negative immune regulator *Traf1* (Fig. 3F) (34) is the main cause of a strong increase in its protein. In *Traf1* and hundreds of other genes, a transient, strong, spiked change in mRNA, combined with a time-constant protein half-life much longer than the 12-hour time course, result in a monotonous increase in protein levels, so that global protein fold changes at 12 hours after LPS correlate best to mRNA changes at 5 hours (fig. S13). Only a handful of proteins [for example, *Tnfrsf2* (26, 35, 36)] show peaked, transient protein expression within our time scale; all have very high basal degradation rates, which typically do not increase further. Last, a few key regulators of DCs and the LPS response [such as CCAAT/enhancer-binding protein β (*Cebpb*), a pioneer transcription factor whose mRNA is already very highly expressed prestimulation, and *Rela*] (Fig. 3F) are considerably dynamically regulated at the protein level, so that increased protein degradation rates (*Rela*) and/or increased per-mRNA translation rates (*Rela* and *Cebpb*) are main drivers for protein change. These changes cannot be observed solely from total protein and transcript levels, but the corresponding rate changes are readily apparent (Fig. 3F).

Although our global model incorporates the data of only 3147 genes, several lines of evidence suggest that this did not bias our global conclusions. First, although the 3147 modeled genes are somewhat enriched for higher expressed genes (fig. S14), we do model a substantial number of lowly expressed mRNAs (fig. S14). Second, computationally correcting for this bias by recalculating the contributions of mRNA, per-mRNA translation, and protein degradation rates while proportionally up-weighting the impact of underrepresented expression bins (29) does not affect our conclusions (fig. S15). Third, the correlation between our protein translation at baseline ($t = 0$ hours), as estimated with pulsed-SILAC data or TE values, is comparable when considering only the lowest expressed 25% (Pearson $r \sim 0.52$), the highest expressed 25% ($r \sim 0.58$), or all modeled proteins ($r \sim 0.5$) (fig. S16, A and B). Last, there is no significant difference in the distribution of TE values in the (underrepresented) lowly expressed mRNA bins between those proteins we detect (in the 3147 proteins) versus those we could not include in our model ($P = 0.069$, t test) (fig. S16C); thus, it is unlikely that the lowly expressed genes that we could not model have different regulatory modes.

Protein life-cycle changes primarily affect proteins performing basic cellular functions

Although mRNA fold changes contributed most to relative changes in protein expression (ratios of LPS to MOCK-simulated protein levels), protein synthesis and degradation rates do change significantly for 357 proteins (~11% of consistently detected proteins) (tables S7 and S8) (29)

and in particular for proteins performing essential cellular functions ("housekeeping proteins") (Figs. 2B and 3E and table S6), including cytoskeletal, metabolic, ribosomal (Fig. 4A), and mitochondrial proteins (Fig. 4B). Because these are among the most abundant in the cell (13, 16, 37, 38), we reasoned that although mRNA changes may dominate the relative (fold) changes in protein levels after LPS stimulation, changes in the protein life cycle could contribute substantially more to differences in absolute cellular protein abundance than to relative changes. For example, consider two genes: Gene 1 is induced 10-fold from 10,000 to 100,000 proteins (a substantial change in relative protein abundance), whereas gene 2 is induced 1.2-fold from 1,000,000 to 1,200,000 proteins (a substantial change in absolute protein abundance). We asked whether relative and absolute changes are associated with different regulatory mechanisms. Indeed, we found that changes in translation and degradation rates together explain more of absolute protein changes than do changes in mRNA levels (mRNA, ~32 to 43% of the fit value; per-mRNA translation rates, ~22 to 41%; protein degradation rates, ~19 to 36%) (Fig.

3D and fig. S11C). Thus, posttranscriptional regulation contributes substantially more to absolute protein level changes than to relative protein level changes.

An increase in degradation rates of mitochondrial proteins is associated with mitophagy

Upon LPS stimulation, a substantial decrease in the level of mitochondrial proteins is associated with increased degradation rates, although these proteins are among the most stable in unstimulated DCs (Figs. 2B, 3E, and 4B and table S6). This increase in protein degradation is accompanied by a significant decrease ($P < 10^{-10}$, Wilcoxon rank sum test) (Fig. 3E and table S6) in mRNA levels and in per-mRNA translation rates ($P < 10^{-7}$, Wilcoxon rank sum test) (Fig. 3E and table S6), suggesting decreased production of new mitochondrial proteins and increased destruction of old ones. Both structural mitochondrial proteins and enzymes in key mitochondrial metabolic pathways have increased degradation. The increased degradation of key enzymes—such as *Suca2*, *Aldh2*, and *Aco2*—is consistent with a

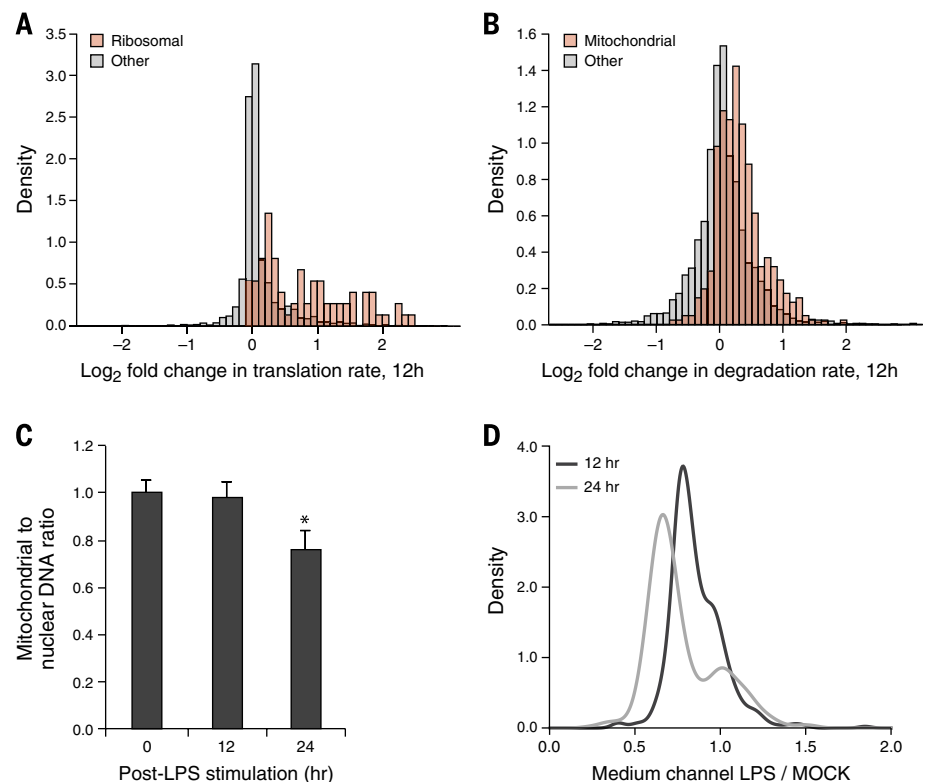


Fig. 4. Degradation of mitochondrial proteins after LPS stimulation is associated with mitophagy.

(A and B) Increased translation rates of some ribosomal proteins (A) and increased degradation rates of mitochondrial proteins (B). Shown are the distributions of \log_2 fold changes of translation rates (ΔT_i , A) or degradation rates (ΔD_i , B) between LPS- and MOCK-stimulated cells of all measured ribosomal proteins [(A), red] or mitochondrial proteins [(B), red; from MitoCarta annotations (43)] and all measured proteins (gray). (C) Evidence of mitophagy in LPS-stimulated DCs. Shown is the mitochondrial to nuclear DNA ratio (y axis) in DCs at 0, 12, and 24 hours after LPS stimulation (x axis). Values are normalized to the average mitochondrial to nuclear DNA ratio at 0 hours. Asterisk indicates a significant change relative to 0 hours ($P = 0.016$, t test, $n = 3$ independent biological replicates). (D) Distribution of raw \log_2 LPS/MOCK M/L ratios (a proxy for protein decay) for all measured mitochondrial proteins [in MitoCarta (43)] at 12 hours (black) and 24 hours (gray) after stimulation.

reported shift in LPS-stimulated DCs from oxidative phosphorylation and oxygen consumption to glycolysis, glucose consumption, and lactate production (39–42).

The increased loss of structural proteins and enzymes in the mitochondria may be due to either a targeted metabolic shift in carbon and energy metabolism through a reduction of a specific subset of the mitochondrial proteome or a more global loss of entire mitochondria through mitophagy. To experimentally distinguish between the two hypotheses, we measured the mitochondrial-to-nuclear DNA ratio in unstimulated DCs and at 12 hours and 24 hours after LPS stimulation (the latter time point was chosen to account for any delay in complete mitochondrial DNA degradation) (Fig. 4C). There was no significant change in the ratio of mitochondrial-to-nuclear DNA at 12 hours after LPS stimulation, but there was a significant (~25%; $P = 0.016$, t test) reduction at 24 hours after stimulation (Fig. 4C). Indeed, analyzing pulsed SILAC data collected at 24 hours after LPS and mock stimulation, we saw a decrease in the M/L ratios (a proxy for increased degradation) of ~80% of annotated mitochondrial proteins in LPS versus MOCK samples (Fig. 4D) and in nearly all mitochondrial proteins with a higher mitochondrial localization prediction score [from MitoCarta (43)—over 95% of the 156 proteins with a score >20 of the 472 measured mitochondrial proteins] (fig. S17). These results suggest that mitophagy is a driver of LPS-induced mitochondrial protein degradation in DCs, which is consistent with previous observations of mitophagy in virus- or bacteria-infected DCs (44) and might also contribute to epitope presentation, as previously proposed (45).

Discussion

We determined the contribution of changes in mRNA levels, protein synthesis, and protein degradation rates during a dynamic response and found that changes in mRNA levels dominate relative fold changes. When considering also absolute changes in protein molecules (abundance), our data suggest a model in which the cellular proteome is dynamically regulated through two strategies.

In the first strategy, mRNA regulation acts primarily to ensure that specific functions—here, immune response proteins—are only expressed when needed and thus explains most of the fold-change differences in protein levels, contributing to LPS-induced protein fold changes at least 8 times as much as the combined protein life cycle within the 12-hour time scale of our measurements. It is possible that protein life-cycle changes are important to turn over key regulatory and signaling proteins at later phases of the response. Although our study does not directly address which steps in mRNA regulation account for this, our related work on the RNA life cycle during the first 3 hours in LPS-stimulated DCs suggests that transcriptional changes may in turn dominate differential mRNA expression, whereas dynamic changes in RNA processing or degradation affect only a minority of genes, albeit with important

function (46). Furthermore, in contrast to previous reports in which degradation rates contributed only marginally (16, 20), but consistent with Li *et al.* (6), we see that within the protein life cycle, changes in protein degradation rates play an equal role to changes in per-mRNA translation rates. Although some of this is due to turnover from increased secretion of some proteins (figs. S9C and S18), excluding the secretome (33) from our analysis did not strongly alter this global trend (fig. S18). Last, although mRNA changes dominate changes in protein levels, it may be difficult to discern this relationship in the absence of a model-driven analysis. Thus, whereas mRNA induction is readily reflected in protein level induction (fig. S19 and table S9), albeit somewhat dampened (fig. S19 and table S9), few of the 912 repressed mRNAs (more than twofold) show matching protein changes (fig. S19 and table S9). This could be naively interpreted as substantial posttranscriptional control, but preexisting proteins, the long protein half-life, and the delay of protein changes relative to mRNA changes (fig. S13) complicate such an intuitive interpretation, and our analysis shows that mRNA changes drive protein down-regulation as well (fig. S12 and table S5) (29).

In the second strategy, regulation at the protein level primarily readjusts the preexisting proteome, especially “housekeeping” proteins, in order to meet the requirements of a new cellular state, such as change in shape or metabolism. Thus, when we consider the contribution of a change in each rate to the change in the number of proteins (rather than the relative fold change), the contribution of changes in the protein life cycle is substantially increased (Fig. 3D). We find similar patterns of contributions when we use the Spearman rank correlation rather than Pearson correlation (fig. S20) (29), suggesting that our conclusions are robust to outliers with particularly strong changes.

The extent to which this two-part strategy applies in other dynamic settings remains to be determined. Recent studies comparing protein and translation rate differences between different states (for example, differentiated versus nondifferentiated cells or between different yeast strains) suggested that translation rate differences affect differential protein expression only modestly (20, 47–51) but do affect some highly expressed proteins, including ribosomal proteins (49, 50), which are also translationally regulated in our system.

Our analysis of unstimulated (resting) postmitotic DCs refines and extends previous models of protein level regulation in steady state. In our cells, nearly two thirds of the gene-to-gene variation in total protein levels is explained by regulation of mRNA levels—a higher contribution than previously reported in dividing mammalian cells (16), possibly because of the regulatory mechanisms active in primary postmitotic, homeostatic resting cells. For example, the increased role we observed for protein degradation, in contrast to prior studies (16, 20), may be needed by postmitotic cells that cannot simply renew their protein

pool through division-coupled passive dilution. Furthermore, our analysis corrected for RNA-Seq expression reproducibility, intralibrary protein expression reproducibility, and library-dependent protein expression biases (fig. S21) (29), all of which are essential to avoid inadvertent attribution of measurement errors to modeled translation and protein degradation rates. Indeed, whereas from raw data mRNA explains 27% of the gene-to-gene variation in protein levels at baseline ($t = 0$), using modeled expression values it explains 42%, and once correcting for data reproducibility (29), it explains 52%. This compares well with a recent study (6) that found that mRNA levels explain at least 56% of the differences in protein abundance [when estimating the variances of errors with control measurements (16)] and possibly as much as ~84% [using TE values to estimate the systematic error in translation rates in (16)]. Each of these strategies highlights the importance of determining and correcting for stochastic and systematic errors in the data. Even with our conservative estimates, the protein life cycle is estimated to contribute, at minimum, about a third of the final steady-state protein expression level. Because protein expression levels span around 4 to 5 orders of magnitude (13, 16, 37, 38), differences between genes in the protein life cycle can easily cause a 10- to 100-fold change in protein expression.

Our experimental and analytical design should be broadly applicable to study similar events in diverse dynamical cell systems. Our analytical model distinguishes per-mRNA translation and protein degradation rates that were confounded in previous, model-free analyses of raw H/L and M/L ratios from dynamic pulsed-SILAC data (20) because of, for example, the contribution of mRNA and protein degradation to the H/L signal and of recycled labeled amino acids to the M/L signal (29). Our empirical Bayes strategy also handles noise in proteomics data in a principled and conservative way. Nevertheless, we make some simplifying assumptions in our model (such as linear changes in per-mRNA translation rates and degradation rates) that may be refined in the future [for example, with sigmoidal functions (22, 52, 53)], allowing us to estimate additional valuable parameters (such as time point of rate change). This would require finer-resolution data, such as from ribosome profiling (49, 54, 55), puromycin-associated nascent chain proteomics (56), or the combination of pulsed-SILAC labeling with pulse-labeling by using the methionine analog azido-homoalanine (33, 57). Such enhanced methods will provide a framework to study the contributions of the protein life cycle in diverse dynamic systems and help identify new key regulators of these responses.

REFERENCES AND NOTES

1. N. Sonenberg, A. G. Hinnebusch, Regulation of translation initiation in eukaryotes: Mechanisms and biological targets. *Cell* **136**, 731–745 (2009). doi: [10.1016/j.cell.2009.01.042](https://doi.org/10.1016/j.cell.2009.01.042); pmid: [19239892](https://pubmed.ncbi.nlm.nih.gov/19239892/)
2. M. A. Chapman *et al.*, Initial genome sequencing and analysis of multiple myeloma. *Nature* **471**, 467–472 (2011). doi: [10.1038/nature09837](https://doi.org/10.1038/nature09837); pmid: [21430775](https://pubmed.ncbi.nlm.nih.gov/21430775/)

3. A. Castello, B. Fischer, M. W. Hentze, T. Preiss, RNA-binding proteins in Mendelian disease. *Trends Genet.* **29**, 318–327 (2013). doi: [10.1016/j.tig.2013.01.004](https://doi.org/10.1016/j.tig.2013.01.004); pmid: 23415593
4. S. Komili, P. A. Silver, Coupling and coordination in gene expression processes: A systems biology view. *Nat. Rev. Genet.* **9**, 38–48 (2008). doi: [10.1038/nrg2223](https://doi.org/10.1038/nrg2223); pmid: 18071322
5. C. Vogel, E. M. Marcotte, Insights into the regulation of protein abundance from proteomic and transcriptomic analyses. *Nat. Rev. Genet.* **13**, 227–232 (2012). pmid: 22411467
6. J. J. Li, P. J. Bickel, M. D. Biggin, System wide analyses have underestimated protein abundances and the importance of transcription in mammals. *PeerJ.* **2**, e270 (2014). doi: [10.7717/peerj.270](https://doi.org/10.7717/peerj.270); pmid: 24688849
7. S. P. Gygi, Y. Rochon, B. R. Franz, R. Aebersold, Correlation between protein and mRNA abundance in yeast. *Mol. Cell. Biol.* **19**, 1720–1730 (1999). pmid: 10022859
8. R. de Sousa Abreu, L. O. Penalva, E. M. Marcotte, C. Vogel, Global signatures of protein and mRNA expression levels. *Mol. Biosyst.* **5**, 1512–1526 (2009). pmid: 20023718
9. T. Maier, M. Güell, L. Serrano, Correlation of mRNA and protein in complex biological samples. *FEBS Lett.* **583**, 3966–3973 (2009). doi: [10.1016/j.febslet.2009.10.036](https://doi.org/10.1016/j.febslet.2009.10.036); pmid: 19850042
10. C. Vogel *et al.*, Sequence signatures and mRNA concentration can explain two-thirds of protein abundance variation in a human cell line. *Mol. Syst. Biol.* **6**, 400 (2010). doi: [10.1038/msb.2010.59](https://doi.org/10.1038/msb.2010.59); pmid: 20739923
11. S. P. Schrimpf *et al.*, Comparative functional analysis of the *Caenorhabditis elegans* and *Drosophila melanogaster* proteomes. *PLOS Biol.* **7**, e48 (2009). doi: [10.1371/journal.pbio.1000048](https://doi.org/10.1371/journal.pbio.1000048); pmid: 19260763
12. S. Marguerat *et al.*, Quantitative analysis of fission yeast transcriptsomes and proteomes in proliferating and quiescent cells. *Cell* **151**, 671–683 (2012). doi: [10.1016/j.cell.2012.09.019](https://doi.org/10.1016/j.cell.2012.09.019); pmid: 23101633
13. M. Wilhelm *et al.*, Mass-spectrometry-based draft of the human proteome. *Nature* **509**, 582–587 (2014). doi: [10.1038/nature13319](https://doi.org/10.1038/nature13319); pmid: 24870543
14. M. Weiss, S. Schrimpf, M. O. Hengartner, M. J. Lercher, C. von Mering, Shotgun proteomics data from multiple organisms reveals remarkable quantitative conservation of the eukaryotic core proteome. *Proteomics* **10**, 1297–1306 (2010). doi: [10.1002/pmic.200900414](https://doi.org/10.1002/pmic.200900414); pmid: 20077411
15. Z. Khan *et al.*, Primate transcript and protein expression levels evolve under compensatory selection pressures. *Science* **342**, 1100–1104 (2013). doi: [10.1126/science.1242379](https://doi.org/10.1126/science.1242379); pmid: 24136357
16. B. Schwanhäusser *et al.*, Global quantification of mammalian gene expression control. *Nature* **473**, 337–342 (2011). doi: [10.1038/nature10098](https://doi.org/10.1038/nature10098); pmid: 21593866
17. C. Vogel, G. M. Silva, E. M. Marcotte, Protein expression regulation under oxidative stress. *Mol. Cell. Proteomics* **10**, 009217 (2011). doi: [10.1074/mcp.M111009217](https://doi.org/10.1074/mcp.M111009217); pmid: 21933953
18. M. V. Lee *et al.*, A dynamic model of proteome changes reveals new roles for transcript alteration in yeast. *Mol. Syst. Biol.* **7**, 514 (2011). doi: [10.1038/msb.2011.48](https://doi.org/10.1038/msb.2011.48); pmid: 21772262
19. T. Maier *et al.*, Quantification of mRNA and protein and integration with protein turnover in a bacterium. *Mol. Syst. Biol.* **7**, 511 (2011). doi: [10.1038/msb.2011.38](https://doi.org/10.1038/msb.2011.38); pmid: 21772259
20. A. R. Kristensen, J. Gsponer, L. J. Foster, Protein synthesis rate is the predominant regulator of protein expression during differentiation. *Mol. Syst. Biol.* **9**, 689 (2013). doi: [10.1038/msb.2013.47](https://doi.org/10.1038/msb.2013.47); pmid: 24045637
21. R. M. Steinman, J. Banachereau, Taking dendritic cells into medicine. *Nature* **449**, 419–426 (2007). doi: [10.1038/nature06175](https://doi.org/10.1038/nature06175); pmid: 17898760
22. M. Rabani *et al.*, Metabolic labeling of RNA uncovers principles of RNA production and degradation dynamics in mammalian cells. *Nat. Biotechnol.* **29**, 436–442 (2011). doi: [10.1038/nbt.1861](https://doi.org/10.1038/nbt.1861); pmid: 21516085
23. I. Mellman, R. M. Steinman, Dendritic cells: Specialized and regulated antigen processing machines. *Cell* **106**, 255–258 (2001). doi: [10.1016/S0092-8674\(01\)00449-4](https://doi.org/10.1016/S0092-8674(01)00449-4); pmid: 11509172
24. I. Amit *et al.*, Unbiased reconstruction of a mammalian transcriptional network mediating pathogen responses. *Science* **326**, 257–263 (2009). doi: [10.1126/science.1179050](https://doi.org/10.1126/science.1179050); pmid: 19729616
25. M. Garber *et al.*, A high-throughput chromatin immunoprecipitation approach reveals principles of dynamic gene regulation in mammals. *Mol. Cell* **47**, 810–822 (2012). doi: [10.1016/j.molcel.2012.07.030](https://doi.org/10.1016/j.molcel.2012.07.030); pmid: 22940246
26. N. Chevrier *et al.*, Systematic discovery of TLR signaling components delineates viral-sensing circuits. *Cell* **147**, 853–867 (2011). doi: [10.1016/j.cell.2011.10.022](https://doi.org/10.1016/j.cell.2011.10.022); pmid: 22078882
27. A. K. Shalek *et al.*, Single-cell transcriptomics reveals bimodality in expression and splicing in immune cells. *Nature* **498**, 236–240 (2013). doi: [10.1038/nature12172](https://doi.org/10.1038/nature12172); pmid: 23685454
28. F.-M. Boisvert *et al.*, A quantitative spatial proteomics analysis of proteome turnover in human cells. *Mol. Cell. Proteomics* **11**, 011429 (2012). doi: [10.1074/mcp.M11101429](https://doi.org/10.1074/mcp.M11101429); pmid: 21937730
29. Materials and methods are available as supplementary materials on Science Online.
30. A. O. Subtelny, S. W. Eichhorn, G. R. Chen, H. Sive, D. P. Bartel, Poly(A)-tail profiling reveals an embryonic switch in translational control. *Nature* **508**, 66–71 (2014). doi: [10.1038/nature13007](https://doi.org/10.1038/nature13007); pmid: 24476825
31. E. K. Schmidt, G. Clavarino, M. Ceppi, P. Pierre, SuHSET, a nonradioactive method to monitor protein synthesis. *Nat. Methods* **6**, 275–277 (2009). doi: [10.1038/nmeth.1314](https://doi.org/10.1038/nmeth.1314); pmid: 19305406
32. H. Lelouard *et al.*, Regulation of translation is required for dendritic cell function and survival during activation. *J. Cell Biol.* **179**, 1427–1439 (2007). pmid: 18166652
33. K. Eichelbaum, M. Winter, M. Berriel Diaz, S. Herzog, J. Krigsveld, Selective enrichment of newly synthesized proteins for quantitative secretome analysis. *Nat. Biotechnol.* **30**, 984–990 (2012). doi: [10.1038/nbt.2356](https://doi.org/10.1038/nbt.2356); pmid: 23000932
34. T. Sanada *et al.*, FLN2 deficiency reveals its negative regulatory role in the Toll-like receptor (TLR) and retinoic acid-inducible gene I (RIG-I)-like helicase signaling pathway. *J. Biol. Chem.* **283**, 33858–33864 (2008). doi: [10.1074/jbc.M806923200](https://doi.org/10.1074/jbc.M806923200); pmid: 18849341
35. A. P. Kuan *et al.*, Genetic control of autoimmune myocarditis mediated by myosin-specific antibodies. *Immunogenetics* **49**, 79–85 (1999). doi: [10.1007/s002510050466](https://doi.org/10.1007/s002510050466); pmid: 9887344
36. P. R. Burton *et al.*, Genome-wide association study of 14,000 cases of seven common diseases and 3,000 shared controls. *Nature* **447**, 661–678 (2007). doi: [10.1038/nature05911](https://doi.org/10.1038/nature05911); pmid: 17554300
37. M.-S. Kim *et al.*, A draft map of the human proteome. *Nature* **509**, 575–581 (2014). doi: [10.1038/nature13302](https://doi.org/10.1038/nature13302); pmid: 24870542
38. T. Geiger *et al.*, Initial quantitative proteomic map of 28 mouse tissues using the SILAC mouse. *Mol. Cell. Proteomics* **12**, 1709–1722 (2013). doi: [10.1074/mcp.M112.024919](https://doi.org/10.1074/mcp.M112.024919); pmid: 23436904
39. B. Everts *et al.*, Commitment to glycolysis sustains survival of NO-producing inflammatory dendritic cells. *Blood* **120**, 1422–1431 (2012). doi: [10.1182/blood-2012-03-419747](https://doi.org/10.1182/blood-2012-03-419747); pmid: 22786879
40. C. M. Krawczyk *et al.*, Toll-like receptor-induced changes in glycolytic metabolism regulate dendritic cell activation. *Blood* **115**, 4742–4749 (2010). doi: [10.1182/blood-2009-10-249540](https://doi.org/10.1182/blood-2009-10-249540); pmid: 20351312
41. E. L. Pearce, E. J. Pearce, Metabolic pathways in immune cell activation and quiescence. *Immunity* **38**, 633–643 (2013). doi: [10.1016/j.immuni.2013.04.005](https://doi.org/10.1016/j.immuni.2013.04.005); pmid: 23601682
42. B. Everts *et al.*, TLR-driven early glycolytic reprogramming via the kinases TBK1-IKKe supports the anabolic demands of dendritic cell activation. *Nat. Immunol.* **15**, 323–332 (2014). doi: [10.1038/ni.2833](https://doi.org/10.1038/ni.2833); pmid: 24562310
43. D. J. Pagliarini *et al.*, A mitochondrial protein compendium elucidates complex I disease biology. *Cell* **134**, 112–123 (2008). doi: [10.1016/j.cell.2008.06.016](https://doi.org/10.1016/j.cell.2008.06.016); pmid: 18614015
44. C. Lupfer *et al.*, Receptor interacting protein kinase 2-mediated mitophagy regulates inflammasome activation during virus infection. *Nat. Immunol.* **14**, 480–488 (2013). doi: [10.1038/ni.2563](https://doi.org/10.1038/ni.2563); pmid: 23525089
45. C. Bell *et al.*, Quantitative proteomics reveals the induction of mitophagy in TNF- α activated macrophages. *Mol. Cell. Proteomics* **12**, 2394–2407 (2013). doi: [10.1074/mcp.M112.025775](https://doi.org/10.1074/mcp.M112.025775)
46. M. Rabani *et al.*, High-resolution sequencing and modeling identifies distinct dynamic RNA regulatory strategies. *Cell* **159**, 1698–1710 (2014). doi: [10.1016/j.cell.2014.11.015](https://doi.org/10.1016/j.cell.2014.11.015); pmid: 25497548
47. D. Baek *et al.*, The impact of microRNAs on protein output. *Nature* **455**, 64–71 (2008). doi: [10.1038/nature07242](https://doi.org/10.1038/nature07242); pmid: 18668037
48. M. Selbach *et al.*, Widespread changes in protein synthesis induced by microRNAs. *Nature* **455**, 58–63 (2008). doi: [10.1038/nature07228](https://doi.org/10.1038/nature07228); pmid: 18668040
49. N. T. Ingolia, L. F. Lareau, J. S. Weissman, Ribosome profiling of mouse embryonic stem cells reveals the complexity and dynamics of mammalian proteomes. *Cell* **147**, 789–802 (2011). doi: [10.1016/j.cell.2011.10.002](https://doi.org/10.1016/j.cell.2011.10.002); pmid: 22056041
50. A. C. Hsieh *et al.*, The translational landscape of mTOR signalling steers cancer initiation and metastasis. *Nature* **485**, 55–61 (2012). doi: [10.1038/nature10912](https://doi.org/10.1038/nature10912); pmid: 22367541
51. F. W. Albert, D. Muzzey, J. S. Weissman, L. Kruglyak, Genetic influences on translation in yeast. *PLOS Genet.* **10**, e1004692 (2014). doi: [10.1371/journal.pgen.1004692](https://doi.org/10.1371/journal.pgen.1004692); pmid: 25340754
52. G. Chechik *et al.*, Activity motifs reveal principles of timing in transcriptional control of the yeast metabolic network. *Nat. Biotechnol.* **26**, 1251–1259 (2008). doi: [10.1038/nbt.1499](https://doi.org/10.1038/nbt.1499); pmid: 18953355
53. N. Yosef, A. Regev, Impulse control: Temporal dynamics in gene transcription. *Cell* **144**, 886–896 (2011). doi: [10.1016/j.cell.2011.02.015](https://doi.org/10.1016/j.cell.2011.02.015); pmid: 21414481
54. N. T. Ingolia, S. Ghaemmaghami, J. R. S. Newman, J. S. Weissman, Genome-wide analysis in vivo of translation with nucleotide resolution using ribosome profiling. *Science* **324**, 218–223 (2009). doi: [10.1126/science.1168978](https://doi.org/10.1126/science.1168978); pmid: 19213877
55. N. Stern-Ginossar *et al.*, Decoding human cytomegalovirus. *Science* **338**, 1088–1093 (2012). doi: [10.1126/science.1227919](https://doi.org/10.1126/science.1227919); pmid: 23180859
56. R. Aviner, T. Geiger, O. Elroy-Stein, Novel proteomic analysis (PUNCH-P) reveals cell cycle-specific fluctuations in mRNA translation. *Genes Dev.* **27**, 1834–1844 (2013). doi: [10.1101/gad.219105.113](https://doi.org/10.1101/gad.219105.113); pmid: 23934657
57. K. Eichelbaum, J. Krigsveld, Rapid temporal dynamics of transcription, protein synthesis, and secretion during macrophage activation. *Mol. Cell. Proteomics* **13**, 792–810 (2014). doi: [10.1074/mcp.M113.030916](https://doi.org/10.1074/mcp.M113.030916); pmid: 24396086

ACKNOWLEDGMENTS

We thank members of the Regev, Hacohen, and Carr groups, as well as G. Brar, N. Slavov, and E. Airolidi for constant input and discussions. We thank L. Gaffney for help with the figures and K. Lage and A. Kashani for help with some of the analyses. This work was supported by National Human Genome Research Institute Centers of Excellence in Genomics Science P50 HG006193 (A.R., N.H., S.A.C.) and Broad Institute Funds. A.R. was supported by an NIH Pioneer Award, the Klarman Cell Observatory, and HHMI. M.J. was supported by fellowships of the Swiss National Science Foundation for advanced researchers (SNF) and the Marie Skłodowska-Curie International Outgoing Fellowships. M.S.R. was supported by the NIH Training Program in Bioinformatics and Integrative Genomics training grant. S.S. was supported by a Rothschild Fellowship, a European Molecular Biology Organization fellowship, and Human Frontier Science Program fellowships. E.H.R. was supported by the Howard Hughes Medical Institute Gilliam Fellowship for Advanced Study. Data have been deposited in the Gene Expression Omnibus under accession number GSE59793. The original mass spectra may be downloaded from MassIVE (<http://massive.ucsd.edu>) using the identifier MSV000078994:a@massive.ucsd.edu. DogmaQuant is distributed under open source (BSD) license.

SUPPLEMENTARY MATERIALS

www.sciencemag.org/content/347/6226/1259038/suppl/DC1
Materials and Methods
Figs. S1 to S21
R Script for Estimation of Translation and Degradation Rates (Baseline and Fold Change)
References (58–73)
Tables S1 to S9

22 July 2014; accepted 23 January 2015
Published online 12 February 2015;
10.1126/science.1259038

RESEARCH ARTICLES

STRUCTURAL BIOLOGY

Structural basis for chemokine recognition and activation of a viral G protein-coupled receptor

John S. Burg,^{1,2,3} Jessica R. Ingram,⁴ A. J. Venkatakrishnan,^{3,5,6} Kevin M. Jude,^{1,2,3} Abhiram Dukkipati,^{1,2,3} Evan N. Feinberg,^{3,5,6} Alessandro Angelini,⁷ Deepa Waghay,^{1,2,3} Ron O. Dror,^{3,5,6} Hidde L. Ploegh,⁴ K. Christopher Garcia^{1,2,3*}

Chemokines are small proteins that function as immune modulators through activation of chemokine G protein-coupled receptors (GPCRs). Several viruses also encode chemokines and chemokine receptors to subvert the host immune response. How protein ligands activate GPCRs remains unknown. We report the crystal structure at 2.9 angstrom resolution of the human cytomegalovirus GPCR US28 in complex with the chemokine domain of human CX3CL1 (fractalkine). The globular body of CX3CL1 is perched on top of the US28 extracellular vestibule, whereas its amino terminus projects into the central core of US28. The transmembrane helices of US28 adopt an active-state-like conformation. Atomic-level simulations suggest that the agonist-independent activity of US28 may be due to an amino acid network evolved in the viral GPCR to destabilize the receptor's inactive state.

G protein-coupled receptors (GPCRs) engage a wide range of ligands, from small molecules to large proteins. The structures of GPCR complexes with small molecules and peptides have taught us much about recognition and activation mechanisms, including those of two human chemokine receptors bound to small molecules (1–4). However, proteins represent a substantial fraction of GPCR ligands for which there is currently a dearth of structural information.

Chemokines are protein GPCR ligands that function in immune modulation, wound healing, inflammation, and host-pathogen interactions, primarily by directing migration of leukocytes to inflamed or infected tissues (5, 6). One strategy that viruses use to evade the host immune response is to hijack mammalian chemokine GPCRs (7). Human cytomegalovirus (HCMV) encodes US28, a class A GPCR with 38% sequence identity to human CX3CR1 (8). An unusually promiscuous receptor, US28 binds chemokines from different families including CX3CL1 (fractalkine), which is tethered to endothelial cell membranes through an extended stalk (9).

Here we present two crystal structures of US28 in complex with the chemokine domain

of human CX3CL1. Both structures (one bound to an alpaca nanobody at a resolution of 2.9 Å and the other without a nanobody at 3.8 Å) reveal a paradigm for chemokine binding that is applicable to chemokine-GPCR interactions more generally. Furthermore, the structure of US28 in both crystal forms suggests that this viral GPCR has evolved a highly stable active state to achieve efficient agonist-independent constitutive signaling.

Overall structure of the US28-CX3CL1 complex

The structure of US28 bound to the 77-amino acid chemokine domain of CX3CL1 is essentially identical with (Fig. 1A) and without (Fig. 1B) bound nanobody 7 (Nb7), with a carbon- α root

mean square deviation (RMSD) of 0.42 Å. Nb7, which was selected from an immunized alpaca cDNA library (fig. S1), binds to the intracellular surface of US28 by projecting its three CDR loops into a central cavity between the transmembrane (TM) helices (fig. S2). The only major difference between these US28 structures is the orientation of helix 8, which runs parallel to the membrane in the nanobody-bound structure. In the nanobody-free structure, crystal packing prevents helix 8 from assuming this orientation (fig. S3).

The body of CX3CL1 sits perched above the extracellular US28 vestibule, whereas its N terminus projects deeply into the central cavity of US28 and occupies the ligand binding pocket, burying a surface area of ~1600 Å² (Fig. 1, A and B, and table S1). US28 accommodates this protein ligand by using its extracellular loops as “landing pads” upon which CX3CL1 sits. The CX3CL1 C terminus, truncated before the membrane-anchoring stalk, projects away from the complex. The globular body of CX3CL1 is less tightly constrained than its N-terminal peptide. Comparison of the two structures shows an ~2 Å wobble of CX3CL1 between the two crystal forms (fig. S4A), which may be rationalized by differences in crystal packing (fig. S4B).

Engagement of a chemokine by US28

In the structure of the US28-CX3CL1 complex, the globular chemokine body interacts with the receptor N terminus and extracellular loops (ECLs) (site 1), whereas the chemokine N terminus enters the helical core of the receptor (site 2), in accord with a two-site model (10). Site 1 is occupied by the bulkiest region of CX3CL1, with its C-terminal α helix completely outside the extracellular vestibule of the receptor (Fig. 2A). In site 2, the N-terminal peptide of CX3CL1 (residues 1 to 7) reaches to the bottom of the extracellular cavity, occupying the site that accommodates small molecules in many GPCR structures (Fig. 2A).

The site 1 interaction accounts for most of the contact between US28 and CX3CL1, burying ~775 Å²

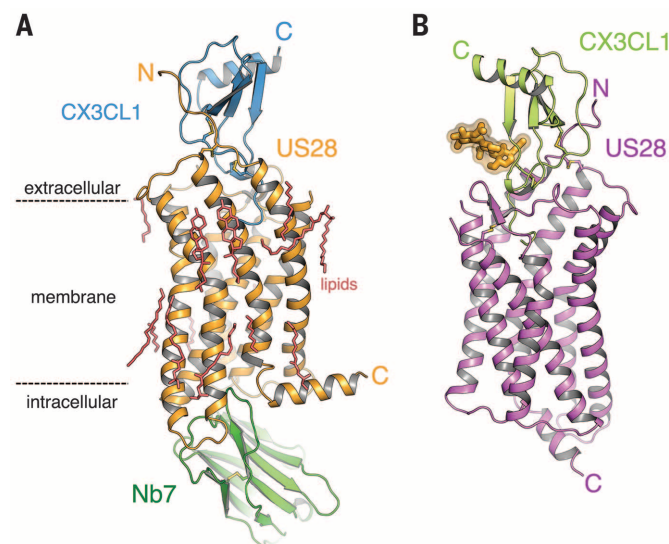


Fig. 1. Structure of US28 in complex with CX3CL1. (A) Ternary complex of CX3CL1 (blue), US28 (orange), and nanobody (green) at 2.9 Å. (B) Binary complex of US28 (magenta) bound to CX3CL1 (light green). Asn-linked glycans are shown in yellow. C, C terminus; N, N terminus.

¹Howard Hughes Medical Institute, Stanford University School of Medicine, Stanford, CA 94305, USA. ²Department of Structural Biology, Stanford University School of Medicine, Stanford, CA 94305, USA. ³Department of Molecular and Cellular Physiology, Stanford University School of Medicine, Stanford, CA 94305, USA. ⁴Whitehead Institute for Biomedical Research, 9 Cambridge Center, Cambridge, MA 02142, USA. ⁵Department of Computer Science, Stanford University, Stanford, CA 94305, USA. ⁶Institute for Computational and Mathematical Engineering, Stanford University, Stanford, CA 94305, USA. ⁷Koch Institute for Integrative Cancer Research, Massachusetts Institute of Technology, Cambridge, MA 02139, USA.

*Corresponding author. E-mail: kcgarcia@stanford.edu

with 13 hydrogen bonds and 44 van der Waals interactions (Fig. 2, B and C, fig. S5, and table S1). The principal feature of site 1 is the N terminus of US28 winding along an extended groove on the surface of CX3CL1 formed in the junction between the β sheet and the N loop (Fig. 2, B and C). A similar binding cleft is apparent in the structures of several other chemokines (fig. S6) (11). The disulfide bond from receptor Cys23 to the third extracellular loop aligns the receptor's N terminus with the chemokine's binding cleft. The preceding US28 residue, Pro22, introduces a kink in the receptor N-terminal peptide that enhances its shape complementarity to the chemokine. Contacts between the US28 N terminus and CX3CL1 involve some side chains but are primarily interactions between their peptide backbones (Fig. 2C and table S1). The extensive main-chain contacts may enhance the ligand cross-reactivity of US28. Another important site 1 contact exists between a short mini-helix of CX3CL1 and ECL2 of US28 (Fig. 2D).

Tyr16 is the second US28 N-terminal residue modeled into electron density (fig. S7B), and corresponds to the position of a sulfated tyrosine found in some chemokine receptors, although it

is unclear whether US28 Tyr16 is sulfated. Many chemokines, including CX3CL1, contain strongly basic patches that are proposed to interact with sulfotyrosine in GPCR N-termini (fig. S6) (12, 13). However, Tyr16 is poorly ordered in US28 and does not appear to make specific contacts with CX3CL1.

As with other chemokines, the CX3CL1 N terminus was found to be highly flexible in previous structural studies (14). In contrast, we find that the N terminus of receptor-bound CX3CL1 is well ordered, extending to the bottom of the US28 ligand binding pocket and burying 623 Å² of surface area (Fig. 3A and fig. S7C). Residues 1 to 4 form a hooklike conformation at the base of the pocket, with residues 5 to 7 extending outward to link the N-terminal "hook" to the globular core of CX3CL1. CX3CL1 residue Gln1 is cyclized to form pyroglutamate (pGlu1) (Fig. 3, A and B), which is apparent both in the electron density map and by mass spectrometry (figs. S7C and S8). The CX3CL1 N-terminal hook contacts residues on TM1, TM3, TM7, and ECL2, with Tyr40¹³⁹, Tyr112³³³, Thr175^{ECL2}, and Glu277⁷³⁹ of US28 participating in hydrogen bonds with pGlu1, His2, His3, and Gly4 of CX3CL1 (Fig. 3, A and B) [superscripts refer to Ballesteros-

Weinstein nomenclature (15)]. Glu277⁷³⁹ may also form a salt bridge with CX3CL1 His3. The extensive interactions of Glu277⁷³⁹ with CX3CL1 provide a structural basis for the observation that Glu⁷³⁹ is important for chemokine receptor signaling (16).

Comparison of the CX3CL1 binding mode with CXCR4 and CCR5 inhibitors

Human chemokine receptor structures have been previously reported as complexes with small-molecule (CCR5-maraviroc, CXCR4-IT1t) and peptide (CXCR4-CVX15) antagonists (2, 3). The overall helical structure of US28 superimposes closely with these structures (1.7 and 2.3 Å RMSD for CCR5 and CXCR4, respectively) (Fig. 4A). In the ligand binding pocket, maraviroc stretches across CCR5 from TM1 to TM5, whereas CX3CL1 occupies a smaller region of the ligand binding pocket concentrated toward TM1, TM2, TM3, and TM7 (Fig. 4B). The bonding chemistry of the maraviroc-CCR5 interaction grossly mimics the binding mode of CX3CL1 to US28, with the tropane and carboxamide nitrogens of maraviroc substituting for the His3 backbone amide and the His2 tau nitrogen of CX3CL1. The compact structure of CX3CL1's N-terminal hook suggests a potential pharmacophore that could be mimicked by small molecules. Several small-molecule inhibitors of US28 signaling have been developed (17, 18). One of these, VUF2274, is a four-ring structure with strong benzhydryl character that could conceivably mimic the N-terminal hook peptide of CX3CL1. The structure of CXCR4 bound to the cyclic peptide CVX15 also presents an instructive comparison with US28-CX3CL1 (3). Like CX3CL1, CVX15 fills almost the entire extracellular vestibule of its receptor and makes multiple contacts with ECL2 but leans toward the opposite side of the receptor vestibule near TM4, TM5, and TM6 (Fig. 4B, right panel).

US28 TM conformations and implications for the active state

US28 has been shown to exhibit agonist-independent activity, with CX3CL1 reportedly diminishing signaling as an inverse agonist (19). We find that both the nanobody-bound and -free US28-CX3CL1 complexes bear the structural hallmarks of an active state, as seen in previous structures (20). Nb7 appears to recognize a preformed active-state conformation of US28 present in the nanobody-free US28-CX3CL1 complex. This finding suggests that the CX3CL1-bound form of US28 is indeed active, although it may occupy an activation state distinct from unliganded US28.

The conformation of TM6 in US28 is typical of an active-state GPCR (20). Compared with the inactive-state CXCR4 and CCR5 structures, US28 exhibits an outward movement (~9 Å) at the intracellular end of TM6 (Fig. 5A). Other conserved structural motifs also display signatures of receptor activation (20). These include the DRY motif (Asp128³⁴⁹, Arg129³⁵⁰, and Tyr130³⁵¹) located at the intracellular side of TM3 and the NPXXY motif (Asn287⁷⁴⁹, Pro288⁷⁵⁰, and Tyr291⁷⁵³) in TM7. US28 Arg129³⁵⁰ of the DRY motif extends

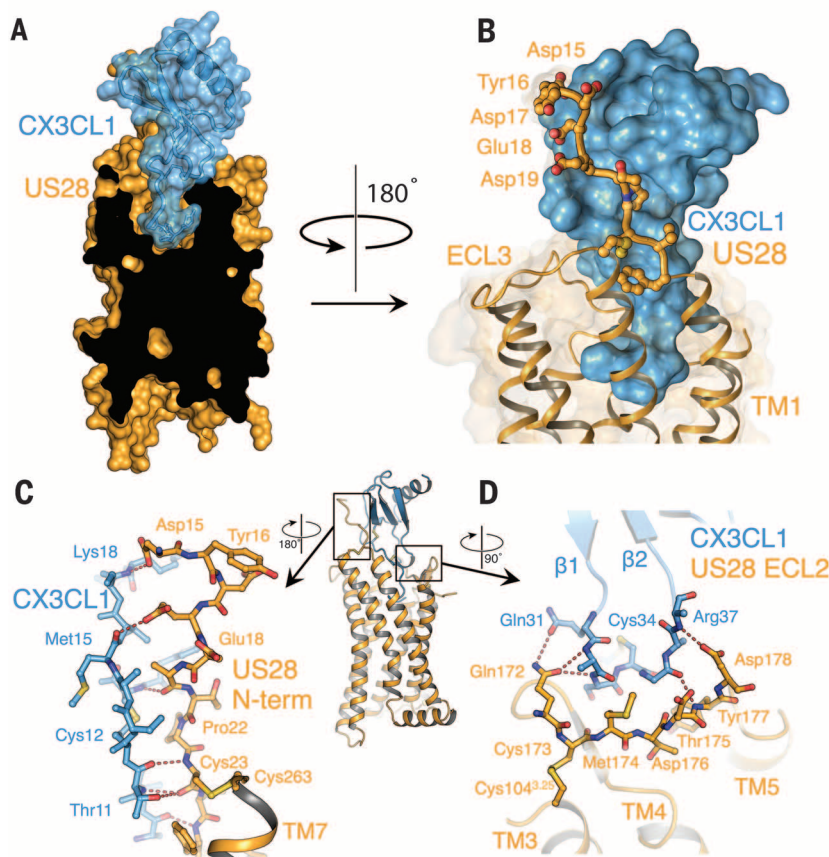


Fig. 2. Interaction of the US28 N terminus with CX3CL1 (site 1). (A) Cutaway surface representation of CX3CL1 (blue) bound to US28 (orange). (B) The N-terminal region of US28 forms a large contact surface with CX3CL1. Side chains of US28 interacting with CX3CL1 are shown as sticks. (C) Amino acid interactions between CX3CL1 and US28 at chemokine binding site 1. The entire US28-CX3CL1 complex is shown for reference with the nanobody removed for clarity. (D) Amino acid interactions between US28 ECL2 and the β 1- β 2 loop of fractalkine.

inward toward the center of the TM bundle, similar to the position seen in the active-state structure of the β_2 -adrenergic receptor (β_2 AR) and contrasting with the corresponding arginine in the inactive CCR5 structure that projects away (Fig. 5C) (2, 21). The DRY motif can stabilize the inactive conformation of some GPCRs by participating in a salt bridge between Arg^{3.50} and an acidic residue at position 6.30, in what is known as the “ionic lock” (20, 22). US28 lacks an acidic residue at position 6.30, so absence of this contact could be one factor contributing to stabilization of the active state in the absence of ligand.

Further structural evidence for the active state of US28 is demonstrated by the intracellular half of TM7, which is shifted toward the center of the TM bundle (Fig. 5A). This is seen in the active-state β_2 AR but not the inactive CCR5 structure (2, 21). The inward movement of TM7 results in Tyr291^{7.53} of the NPXXY motif shifting 7 Å toward the center of the TM bundle, which is close enough to TM5 and TM3 to form hydrogen bonds with Tyr208^{5.58} and Ile122^{3.43} through a water molecule (Fig. 5B). Tyr208^{5.58}, in turn, forms a hydrogen bond with Arg129^{3.50} of the DRY motif

(Fig. 5C). This completes a hydrogen bond network connecting TM3, TM5, and TM7 that has been seen in previously solved active-state structures (20, 21).

CX3CL1 has been shown to exhibit both agonist and inverse agonist activities in US28 signaling assays. This apparent discrepancy has been explained by CX3CL1 being a “camouflaged agonist” that signals but exhibits diminished agonist activity due to ligand-induced internalization and degradation (23). These structures support an interpretation that CX3CL1 is an agonist, not an inverse agonist, because it does not induce an inactive state of the receptor. CX3CL1 binding may either stabilize the ligand-independent active state of US28 or alter the active conformation to induce a slightly different signaling outcome from the unliganded state.

Structural basis for constitutive activity and ligand action

Constitutive activity is a common property of viral GPCRs that enhances viral pathogenesis (18) and is also seen to varying degrees in some mammalian GPCRs (24, 25). Although structures of

certain constitutively active rhodopsin mutants are available (26, 27), the mechanistic basis through which viral GPCRs have gained this evolutionarily advantageous constitutive activity has remained unclear.

To address this question, we performed atomic-level molecular dynamics (MD) simulations of US28, both with and without bound CX3CL1 (see supplementary materials and methods). Atomic-level simulations have provided mechanistic insight into important functional properties of other GPCRs (28, 29). Because the crystal structures of US28 with and without the nanobody exhibit essentially identical conformations of the TM helices, we initiated our simulations from the 2.9 Å structure but omitted the nanobody.

Using integrated analysis of sequence, structure, and simulations of US28, we uncovered molecular features of US28 that may lead to its constitutive activity. In particular, we found that US28 has evolved a distinctive structure environment around Asp128^{3.49}, near the cytoplasmic end of TM3, that probably results in a destabilization of the receptor's inactive state (Fig. 6). Asp^{3.49} is part of the conserved DRY motif, which

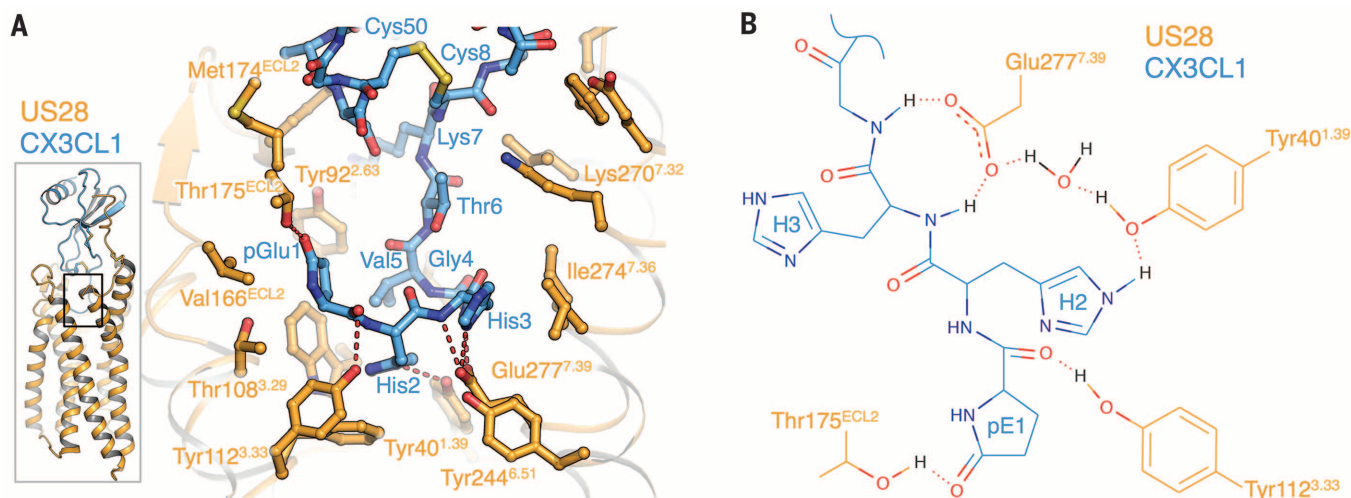


Fig. 3. Interaction of the CX3CL1 N terminus with the US28 ligand binding pocket (site 2). (A) Side chain contacts between CX3CL1 site 2 region (blue) and US28 (orange). (B) Two-dimensional plot of side-chain contacts between the CX3CL1 N-terminal hook and US28.

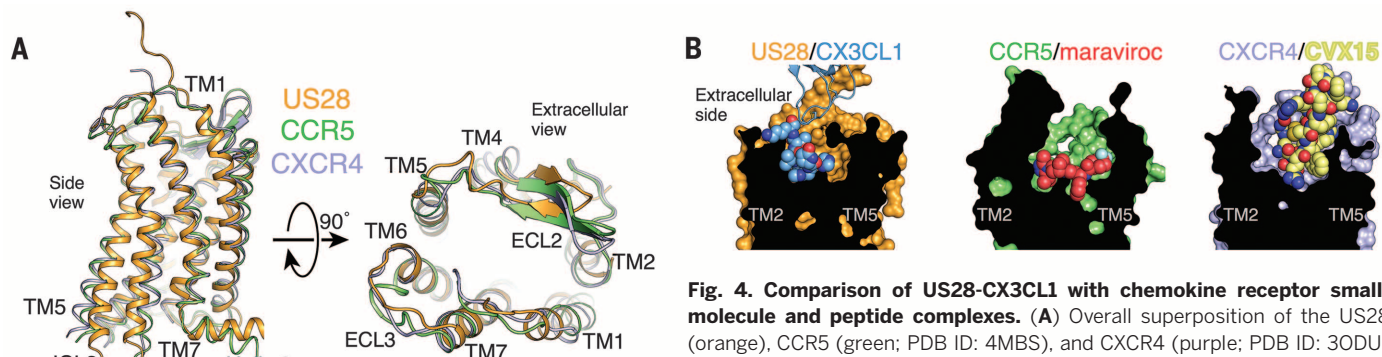


Fig. 4. Comparison of US28-CX3CL1 with chemokine receptor small-molecule and peptide complexes. (A) Overall superposition of the US28 (orange), CCR5 (green; PDB ID: 4MBS), and CXCR4 (purple; PDB ID: 3ODU) TM helices from the side (left) and as viewed from extracellular space (right). (B) Surface cutaway side views comparing ligand binding modes for US28-CX3CL1 (orange-blue), CCR5-maraviroc (green-red; PDB ID: 4MBS), and CXCR4-CVX15 (purple-yellow; PDB ID: 3OE0).

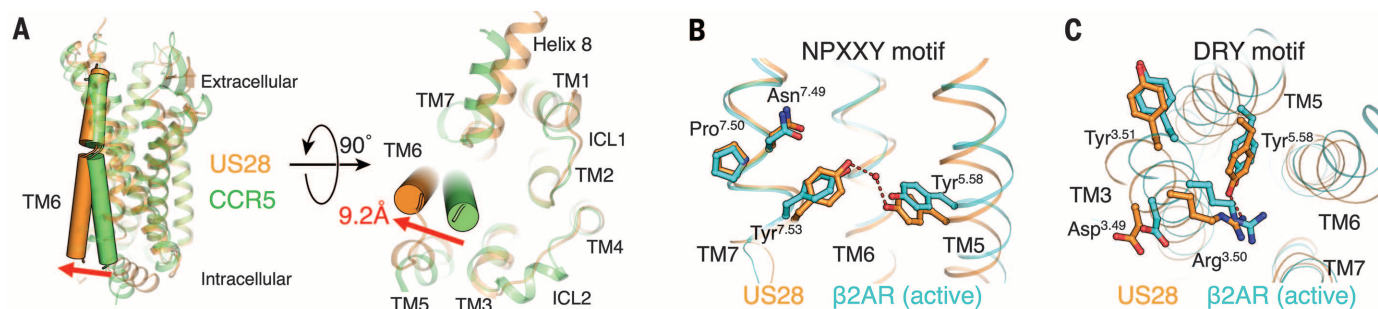


Fig. 5. Active-state hallmarks of US28 bound to CX3CL1. (A) Comparison between the TM6 conformations of US28 (orange) and CCR5 (green; PDB ID: 4MBS). (B) The NPXXY motif of US28 (orange) forms side-chain contacts resembling the active-state conformation of β_2 AR (light blue; PDB ID: 3SN6). (C) The DRY motif of US28 (orange) forms side-chain contacts resembling the active-state conformation of β_2 AR (light blue).

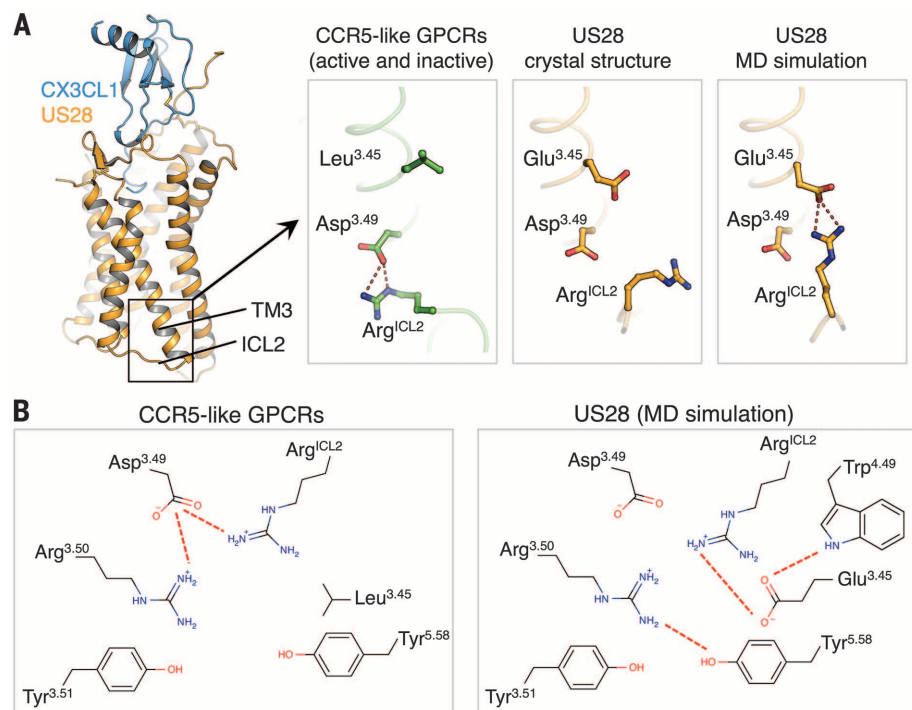


Fig. 6. Structural basis for the constitutive activity of US28. (A) Conformations of Arg^{ICL2} in CCR5 (green; PDB ID: 4MBS; left), the US28 crystal structure (orange; center) and the US28 MD simulations (orange; right). (B) Schematic diagram of the network of side-chain interactions surrounding the DRY motif in CCR5 (left panel) and US28 (MD simulation; right).

plays an important role in the conformational transition between active and inactive states of class A GPCRs (20). An ionic interaction between Asp^{3.49} and the neighboring Arg^{3.50} generally stabilizes the inactive state of these receptors and is broken upon G protein coupling (Fig. 5C).

In many previously published GPCR structures, including all those of chemokine receptors, Asp^{3.49} engages in a polar interaction with another arginine residue separate from the DRY motif on the second intracellular loop (ICL2); this arginine residue points toward the interior of the TM helical bundle (Fig. 6A, left panel). Mutation of this arginine has been associated with constitutive activity (30), suggesting that this residue is important for stabilizing the inactive state. In the US28 crystal structure, the

corresponding arginine, Arg139^{ICL2}, is pointing outward, probably as a result of the crystal lattice contacts it forms (Fig. 6A and fig. S9).

In MD simulations of US28 embedded in a lipid bilayer, Arg139^{ICL2} immediately reorients toward the center of the bundle and assumes its most favored rotamer, but instead of contacting Asp128^{3.49}, it forms an ionic interaction with Glu124^{3.45} (Fig. 6 and fig. S9B). This glutamate residue appears to function as an “ionic hook” that pulls Arg139^{ICL2} upward, preventing it from interacting with Asp128^{3.49} and, thus, potentially destabilizing the inactive state of the receptor (Fig. 6). Notably, the presence of a glutamate residue at position 3.45 is exclusive to the viral GPCR US28; it is not observed in any human class A GPCR. Together, these changes create

a different constellation of interactions centered on the DRY motif that favors the formation and stabilization of an active conformation.

Several other distinctive features of US28 may also contribute to the environment of Asp128^{3.49} and destabilization of the inactive state. First, the ionic hook Glu124^{3.45} is held in place by a hydrogen bond to Trp151^{4.49} (Fig. 6B, right panel). Like Glu124^{3.45}, the tryptophan residue at this position is also absent from all human class A GPCRs. Second, ICL2 is shorter by four residues in US28 than in most class A GPCRs, which appears to prevent the formation of an α helix in ICL2. When such an α helix does form in other GPCRs, it appropriately positions the ICL2 arginine to interact with Asp^{3.49}, so the lack of ICL2 secondary structure in US28 may be providing Arg139^{ICL2} the flexibility required to adopt different structural states. Finally, in most other class A GPCR structures, including those of chemokine receptors, Asp^{3.49} engages in a hydrogen bond with the residue at position 2.39 in TM2. In US28, this residue is replaced by a glycine, which is incapable of forming such an interaction, while a serine introduced at the neighboring position 2.38 engages in a hydrogen bond with Asp128^{3.49}; this shift appears to alter the side-chain conformation of Asp128^{3.49}.

Other viral GPCR systems might have adopted a similar strategy to achieve constitutive activity. In US27 from HCMV, the position equivalent to the US28 ionic hook Glu^{3.45} is an asparagine residue, which is also absent from human class A GPCRs. In the Kaposi's sarcoma-associated herpesvirus GPCR ORF74, Asp^{3.49} is mutated to Val^{3.49}, preventing any ionic interaction with Arg^{3.50}. Molecular tinkering with the GPCR regions important for conformational switching, such as the DRY motif and its immediate environment, may thus represent a common evolutionary strategy in viruses to achieve constitutive activity and enhance viral pathogenesis.

Summary

The structure of the human CX3CL1 chemokine domain bound to HCMV US28 serves as a model for other mammalian and viral chemokine GPCR-ligand complexes. The viral origins of US28 have allowed us to gain insight into the evolutionary strategies that viruses use to tune GPCR signaling

properties to promote their survival and propagation. Furthermore, these viral-derived structural insights shed light on the mechanisms of ligand signal-tuning and constitutive activity of mammalian GPCRs as a whole. The tunability of US28, and perhaps other viral GPCRs, suggests that chemokine ligand-engineering strategies to elicit differential and biased signaling from GPCRs may be a productive way to create new agonistic and inhibitory ligands.

REFERENCES AND NOTES

1. V. Katritch, V. Cherezov, R. C. Stevens, *Annu. Rev. Pharmacol. Toxicol.* **53**, 531–556 (2013).
2. Q. Tan *et al.*, *Science* **341**, 1387–1390 (2013).
3. B. Wu *et al.*, *Science* **330**, 1066–1071 (2010).
4. D. M. Rosenbaum, S. G. Rasmussen, B. K. Kobilka, *Nature* **459**, 356–363 (2009).
5. I. F. Charo, R. M. Ransohoff, *N. Engl. J. Med.* **354**, 610–621 (2006).
6. A. E. Proudfoot, *Nat. Rev. Immunol.* **2**, 106–115 (2002).
7. A. Sodhi, S. Montaner, J. S. Gutkind, *Nat. Rev. Mol. Cell Biol.* **5**, 998–1012 (2004).
8. M. S. Chee, S. C. Satchwell, E. Preddie, K. M. Weston, B. G. Barrell, *Nature* **344**, 774–777 (1990).
9. J. F. Bazan *et al.*, *Nature* **385**, 640–644 (1997).
10. S. Thiele, M. M. Rosenkilde, *Curr. Med. Chem.* **21**, 3594–3614 (2014).
11. M. Szpakowska *et al.*, *Biochem. Pharmacol.* **84**, 1366–1380 (2012).
12. C. J. Millard *et al.*, *Structure* **22**, 1571–1581 (2014).
13. C. T. Veldkamp *et al.*, *Sci. Signal.* **1**, ra4 (2008).
14. L. S. Mizoue, J. F. Bazan, E. C. Johnson, T. M. Handel, *Biochemistry* **38**, 1402–1414 (1999).
15. J. A. Ballesteros, H. Weinstein, *Methods Neurosci.* **25**, 366–428 (1995).
16. A. Brelot, N. Heveker, M. Montes, M. Alizon, *J. Biol. Chem.* **275**, 23736–23744 (2000).
17. P. Casarosa *et al.*, *J. Biol. Chem.* **278**, 5172–5178 (2003).
18. H. F. Vischer, M. Siderius, R. Leurs, M. J. Smit, *Nat. Rev. Drug Discov.* **13**, 123–139 (2014).
19. H. F. Vischer, R. Leurs, M. J. Smit, *Trends Pharmacol. Sci.* **27**, 56–63 (2006).
20. A. J. Venkatakrishnan *et al.*, *Nature* **494**, 185–194 (2013).
21. S. G. Rasmussen *et al.*, *Nature* **477**, 549–555 (2011).
22. K. Palczewski *et al.*, *Science* **289**, 739–745 (2000).
23. M. Waldhoer *et al.*, *J. Biol. Chem.* **278**, 19473–19482 (2003).
24. C. T. Gilliland, C. L. Salanga, T. Kawamura, J. Trejo, T. M. Handel, *J. Biol. Chem.* **288**, 32194–32210 (2013).
25. X. Han, *Adv. Pharmacol.* **70**, 265–301 (2014).
26. X. Deupi *et al.*, *Proc. Natl. Acad. Sci. U.S.A.* **109**, 119–124 (2012).
27. J. Standfuss *et al.*, *Nature* **471**, 656–660 (2011).
28. R. O. Dror *et al.*, *Proc. Natl. Acad. Sci. U.S.A.* **108**, 18684–18689 (2011).
29. R. O. Dror *et al.*, *Nature* **503**, 295–299 (2013).
30. E. S. Burstein, T. A. Spalding, M. R. Brann, *J. Biol. Chem.* **273**, 24322–24327 (1998).

ACKNOWLEDGMENTS

We thank B. Kobilka and members of the Kobilka lab for advice and discussions; S. Kim, N. Latorraca, and A. Sanborn for assistance with MD simulations and analysis; J. Spangler for helpful discussions; E. Özkan for assistance with data collection; and H. Axelrod for advice on refinement strategies. We also acknowledge beamline resources and staff of Advanced Photon Source GM/CA beamlines 23-ID-B and 23-ID-D and Stanford Synchrotron Radiation Lightsource beamline 12-2. The data in this paper are tabulated in the main manuscript and in the supplementary materials. Structure factors and coordinates have been deposited in the Protein Data Bank with identification (ID) numbers 4XT1 and 4XT3. We acknowledge support from the Cancer Research Institute (J.S.B.), Howard Hughes Medical Institute (K.C.G.), the Keck Foundation Medical Scholars Program (K.C.G.), NIH R01 GM097015 (K.C.G.), a Terman Faculty Fellowship (R.O.D.), Swiss National Science Foundation (A.A.), NIH Pioneer award (H.L.P.), and Ludwig Foundation for Cancer Research (A.A.).

SUPPLEMENTARY MATERIALS

www.sciencemag.org/content/347/6226/1113/suppl/DC1
Materials and Methods
Figs. S1 to S10
Tables S1 and S2
References (31–66)

17 December 2014; accepted 23 January 2015
10.1126/science.aaa5026

STRUCTURAL BIOLOGY

Crystal structure of the chemokine receptor CXCR4 in complex with a viral chemokine

Ling Qin,^{1*} Irina Kufareva,^{1*†} Lauren G. Holden,^{1*} Chong Wang,² Yi Zheng,¹ Chunxia Zhao,¹ Gustavo Fenalti,² Huixian Wu,² Gye Won Han,^{3,4} Vadim Cherezov,³ Ruben Abagyan,¹ Raymond C. Stevens,^{3,4†} Tracy M. Handel^{1†}

Chemokines and their receptors control cell migration during development, immune system responses, and in numerous diseases, including inflammation and cancer. The structural basis of receptor:chemokine recognition has been a long-standing unanswered question due to the challenges of structure determination for membrane protein complexes. Here, we report the crystal structure of the chemokine receptor CXCR4 in complex with the viral chemokine antagonist vMIP-II at 3.1 angstrom resolution. The structure revealed a 1:1 stoichiometry and a more extensive binding interface than anticipated from the paradigmatic two-site model. The structure helped rationalize a large body of mutagenesis data and together with modeling provided insights into CXCR4 interactions with its endogenous ligand CXCL12, its ability to recognize diverse ligands, and the specificity of CC and CXC receptors for their respective chemokines.

The chemokine receptor CXCR4 controls cell migration during immune surveillance and development of the cardiovascular, hematopoietic, and central nervous systems (1–3). Like many other chemokine receptors (CKRs), CXCR4 contributes to inflammatory diseases and cancer (4, 5). It also functions as one of two coreceptors that facilitate entry of HIV into host immune cells (6). Despite the importance of CXCR4 and CKRs in general, structural insights into CKR:chemokine recognition have been limited to nuclear magnetic resonance studies of chemokines with peptides derived from CKR N termini (7–9). This is partly due to the challenges of structure determination for full-length membrane proteins and their complexes.

Here, we present the structure of CXCR4 in complex with vMIP-II, a CC chemokine encoded by Kaposi's sarcoma-associated herpesvirus. vMIP-II functions as a broad-spectrum antagonist of many human CKRs (10) and helps the virus to escape the host immune response (11). We chose vMIP-II for structural studies because it is a high-affinity antagonist of CXCR4 [median inhibitory concentration, 6 to 15 nM (10, 12)] and, as a ligand for both CC and CXC chemokine receptors, was expected to provide insight into ligand recognition specificity.

Design of an irreversible CXCR4:vMIP-II complex

Despite high affinity in membranes, the CXCR4:vMIP-II complex was insufficiently stable in de-

tergent to justify crystallization trials. We therefore employed a strategy that uses disulfide trapping to generate an irreversible complex (13, 14). Co-expression of pairs of single cysteine mutants of CXCR4 and vMIP-II was expected to result in spontaneous formation of a disulfide bond if the disulfide was compatible with the native geometry of the CKR:chemokine complex. Guided by three-dimensional models of CXCR4:chemokine complexes (14), 37 cysteine mutant pairs were designed, and, for each pair, the abundance of disulfide-trapped complexes was evaluated (15). These pairs included seven N-terminal cysteine mutants of vMIP-II that were systematically coexpressed with two CXCR4 cysteine mutants, D97^{2.63}C or D187^{ECL2}C [superscript denotes the Ballesteros-Weinstein index (16, 17) for helical domain residues; ECL is extracellular loop]. Of all mutant pairs analyzed, CXCR4(D187C) coexpressed with vMIP-II(W5C) formed the highest percentage of trapped complex (Fig. 1A). It also showed an unfolding temperature of 63°C (Fig. 1B), which is 4° to 14°C higher than other mutant combinations, and excellent monodispersity when analyzed by size-exclusion chromatography (fig. S1). By comparison, the mutant pair with the second highest melting temperature, CXCR4(D187C):vMIP-II(H6C) (59°C), was produced in significantly lower yield and showed lower monodispersity, despite the adjacent position of the vMIP-II cysteine (fig. S1). CXCR4(D97C) formed little or no covalent complex with any of the seven vMIP-II mutants tested (Fig. 1, A and B). The observed sensitivity of several biophysical properties of the complex to precise cysteine placement suggests specificity of the disulfide-trapping approach and supports compatibility of the D187C:W5C disulfide bond with the native complex geometry. We therefore selected CXCR4(D187C):vMIP-II(W5C) for crystallization in lipidic cubic phase (LCP) (18) and determined the structure at 3.1 Å resolution. Data

¹University of California, San Diego, Skaggs School of Pharmacy and Pharmaceutical Sciences, La Jolla, CA 92093, USA. ²Department of Integrative Structural and Computational Biology, The Scripps Research Institute, 10550 North Torrey Pines Road, La Jolla, CA 92037, USA. ³Department of Chemistry, Bridge Institute. ⁴Department of Biological Sciences, Bridge Institute, University of Southern California, Los Angeles, CA 90089, USA.

*These authors contributed equally to this work. †Corresponding author. E-mail: handel@ucsd.edu (T.M.H.); stevens@usc.edu (R.C.S.); ikufareva@ucsd.edu (I.K.)

collection and refinement statistics are shown in table S1.

Overall complex geometry

In complex with vMIP-II, CXCR4 possesses the typical seven transmembrane (TM) helical topology. Whereas previous dimeric structures of CXCR4 suggested that chemokines might bind receptors in a 2:1 CKR:chemokine stoichiometry (19, 20), the present structure demonstrates that the stoichiometry is 1:1, in agreement with a recent study (14). The chemokine interacts via its globular core with the receptor N terminus [chemokine recognition site 1 (CRS1) (27)] and via its N terminus with the receptor TM pocket (CRS2) (Fig. 1C). Clear electron density is observed for the entire chemokine N terminus, including the CXCR4(D187C):vMIP-II(W5C) disulfide bond, which adopts a favorable geometry (Fig. 1D). Residues 1 to 22 of the receptor are not visible in the density, consistent with the moderate stability of the CRS1 interaction between CXCR4 and vMIP-II, as suggested by disulfide-trapping experiments (fig. S2) and previous mutagenesis studies (12).

Molecular interactions between CXCR4 and vMIP-II

The CXCR4:vMIP-II interaction is mediated by an extensive (1330 Å²) contiguous interface, with every residue in the chemokine N terminus and N loop (1-LGASCHRPDKCCLGYQ-16) contacting the receptor (Fig. 2 and table S2). Although parts of the interface can be classified as CRS1 or CRS2, the absence of a distinct boundary prompted in-

troduction of an intermediate region, CRS1.5 (Fig. 2, A and B). The CRS1 interaction involves CXCR4 N-terminal residues 23-SMKEP-27 packing against the chemokine N loop (residues 13-LGYQ-16) and its third β strand (β_3 , residues 49-QVC-51) (Fig. 2, C and D, and table S2). This interaction continues toward CRS1.5, where receptor residues 27-PCFRE-31 bind to chemokine residues 8-PDKCC-12 (Fig. 2, C and D) and form an antiparallel β sheet. In CRS2, the chemokine N terminus makes hydrogen bonds to receptor residues D97^{2,63}, D262^{6,58}, and E288^{7,39} and numerous van der Waals packing interactions (Fig. 2, C and D, and table S2). Most of the interacting CXCR4 residues are known determinants of either vMIP-II binding (table S3) or CXCL12 binding and activation (22–26). The dominant role of the vMIP-II N terminus is supported by the fact that an isolated vMIP-II(1–21) peptide binds CXCR4 with appreciable affinity [190 nM (12) versus 6 to 15 nM for wild-type (WT) vMIP-II (10, 12)], which is dramatically reduced by mutations L1A, R7A, and K10A (27) (table S3). Notably, a W5A mutation has only a moderate effect (27). Disulfide-trapping studies also support the role of the chemokine N loop (fig. S2).

Comparison of CXCR4:vMIP-II with previous structures

The conformation of the observed part of the receptor N terminus differs significantly from previous small-molecule and peptide-bound structures (19) in that it adopts an orientation almost perpendicular to the membrane to form a β -sheet interaction in CRS1.5 with chemokine residues

C11 and C12 (Fig. 3, A and B). To accommodate this change as well as binding of the chemokine N terminus in the TM pocket, the extracellular half of helix I is laterally shifted outward by ~2.4 Å, forming an extra α -helical turn and bending at the top (Fig. 3A). ECL2 forms a β hairpin as in other CXCR4 structures but is more closed onto the binding pocket (Fig. 3A), bringing D181 and D182 of CXCR4 in close proximity with K10 of vMIP-II (Fig. 2, C and D).

The binding pocket of CXCR4 is open and negatively charged (Fig. 3C) and can be separated into a major and minor subpocket (28). Similar to the small-molecule antagonist, IT1t, the chemokine N terminus makes the majority of contacts in the minor subpocket and makes polar interactions with D97^{2,63} and E288^{7,39} (Fig. 3, C and D). By contrast, the spatial overlap between the vMIP-II N terminus and CVX15 is moderate, with common recognition determinants including D187^{ECL2} and D262^{6,58} (Fig. 3, C and E). The limited overlap between CVX15 and the chemokine N terminus may enable the design of modulators that simultaneously occupy the minor and major subpockets; in fact, a series of CXCR4 ligands obtained by grafting the N terminus of CXCL12 onto a peptide analog of CVX15 (29) may bind CXCR4 in this manner.

As in five earlier structures (19), CXCR4 forms a dimer in the vMIP-II-bound form (Fig. 4A). The preservation of similar dimerization patterns in all CXCR4 structures (Fig. 4B) suggests possible physiological relevance and is consistent with numerous reports of CXCR4 homo- and heterodimerization in cells (30). The structure

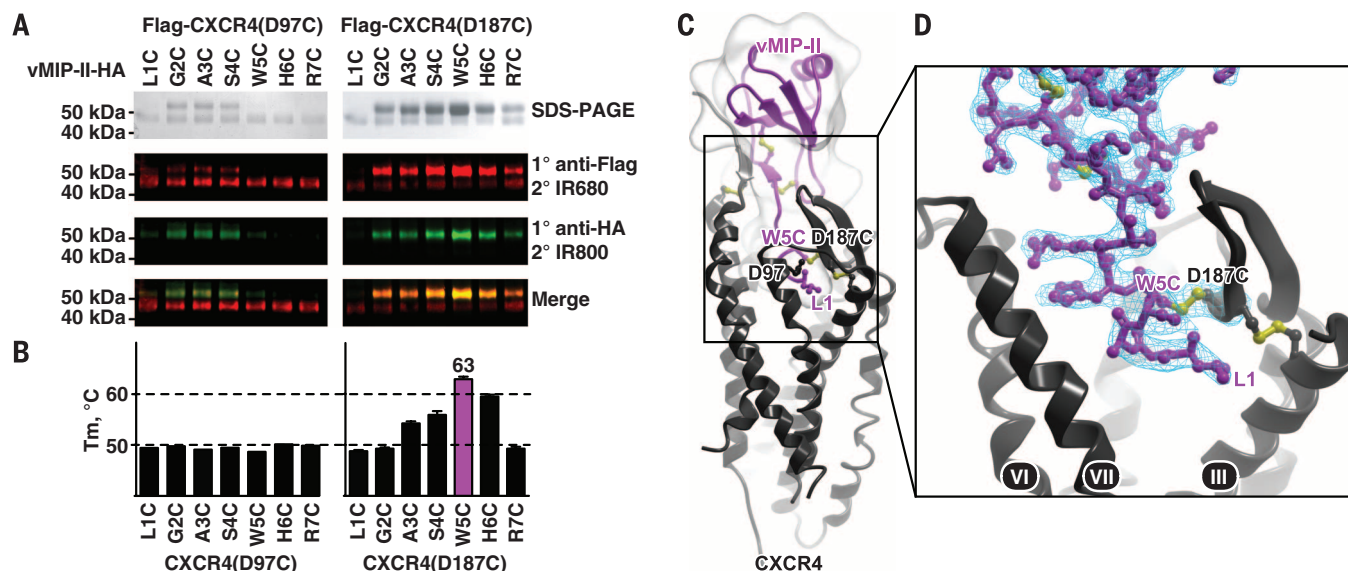


Fig. 1. Design and crystallization of a disulfide-trapped CXCR4:vMIP-II complex. (A) Nonreducing SDS-polyacrylamide gel electrophoresis and Western blot of CXCR4(D97C) (left) and CXCR4(D187C) (right) coexpressed with cysteine mutants of vMIP-II (residues 1 to 7). Uncomplexed CXCR4 and disulfide-trapped complexes have molecular weights of ~45 and 55 kD, respectively. Band identities were confirmed by Western blot using antibodies against the FLAG and hemagglutinin (HA) tags at the N and C termini of CXCR4 and vMIP-II, respectively (second and third rows). The 55-kD band was labeled by

antibodies to FLAG and HA (second to fourth rows); the band at 45 kD was only labeled by the antibody to FLAG (second and fourth rows). (B) Thermal stabilities of the complexes measured by a CPM assay (40) are shown as mean \pm SEM measurements performed in triplicate. (C) Overall structure of the CXCR4:vMIP-II complex (gray:magenta ribbon and transparent mesh). (D) Zoomed view of the vMIP-II N terminus in the CXCR4 pocket showing the CXCR4(D187C):vMIP-II(W5C) disulfide bond. The 2mF_o - DF_c electron density map around the N terminus is contoured at 1.0 σ and colored blue.

also suggests that a receptor dimer can accommodate two monomeric chemokine ligands.

Structure comparisons, bioinformatics, and homology modeling insights into the specificity of CC and CXC chemokine recognition by CKRs

With the exception of atypical CKRs, human CC and CXC chemokines generally pair exclusively with CKRs from the same subfamily. To gain insight into this specificity, as well as the non-canonical pairing of a human CXC receptor (CXCR4) with a viral CC chemokine (vMIP-II), structural and sequence analyses (fig. S4) were complemented by molecular modeling (15). A complex between CXCR4 and its endogenous CXC chemokine, CXCL12, as well as a complex between vMIP-II and another human CKR, CCR5, were chosen for analysis due to available structural and mutagenesis information.

An initial systematic analysis of chemokine structures revealed conformational differences between CC and CXC motifs of the respective chemokines: Whereas in CC chemokines, this region is straight and forms β -sheet interactions within chemokine dimers, it is bent in CXC chemokines and forms no substantial protein-protein interface contacts (fig. S4A). This difference is reflected in the CRS1.5 interactions of the struc-

ture and the modeled complexes (Fig. 5, A to C). In the CXCR4: CXCL12 model (Fig. 5A), the bend directs the chemokine N terminus toward receptor helices V/VI and enables hydrogen bonding between chemokine R8 (highly conserved as a base in CXC but not CC chemokines) (fig. S4B) and receptor D262^{6,58} (highly conserved as an acid in CXC but not CC CKRs) (fig. S4C). By contrast, in the CCR5: vMIP-II model (Fig. 5C), the straightened conformation of the chemokine CC motif directs the chemokine N terminus along the receptor N terminus toward helix I, aided by interactions with receptor K22 in position C+2 (where C is the conserved N-terminal cysteine) and with D276^{7,32}. Notably a base in position C+2 and an acid in position 7.32 are both highly conserved in CC but not CXC CKRs (fig. S4C). Furthermore, mutation of K22 or D276^{7,32} in CCR5 abrogates binding to vMIP-II, CCL3, and CCL5 (31). Interestingly, both vMIP-II and CXCR4 possess features that are atypical for their respective classes; vMIP-II has three basic residues (H6, R7, and K10) in its proximal N terminus (fig. S4B), and CXCR4 has a base (R30) at C+2 (fig. S4C), which may partially explain the unusual coupling between CXCR4 and vMIP-II.

Relevant differences between CC and CXC families are also observed in the predicted CRS1 interactions. The presence of sulfotyrosines sY14

and sY15 (32) in proximity of the conserved N-terminal cysteine in CCR5 (fig. S4C) facilitates interactions with basic residues in the vMIP-II N loop (K17 and R18) and β_2 - β_3 loop (R46 and R48) (Fig. 5C). When evaluated family-wide, high acidity and sulfotyrosine content of the proximal N terminus are characteristic of CC but not CXC receptors (fig. S4C), whereas the basic nature of N and β_2 - β_3 loops distinguishes CC from CXC chemokines (fig. S4B). It appears therefore, that even when sulfotyrosines in the N terminus of CXC receptors contribute to chemokine affinity, they do not engage the N or β_2 - β_3 loops of CXC chemokines. Consistent with this notion, CXCR4 sY21 is predicted to interact with the CXCL12 N-loop- β_1 -strand junction (Fig. 5A) instead of the neutral N and β_2 - β_3 loops, similar to positions of sulfate groups in multiple CXCL12 structures (33, 34). The cleft defined by the N and β_2 - β_3 loops of CXCL12 is occupied by the backbone of CXCR4 residues S23 to M24, which closely mimic the interaction of a small-molecule CXCR4: CXCL12 inhibitor (34). CXCR4 is a rare CXC receptor that possesses a sulfotyrosine in the proximal N terminus (position C-7) (fig. S4C), which may explain its ability to engage a CC chemokine (vMIP-II) via its basic N or β_2 - β_3 loops. This engagement is further assisted by a four-residue epitope in the chemokine β_3 -strand that is

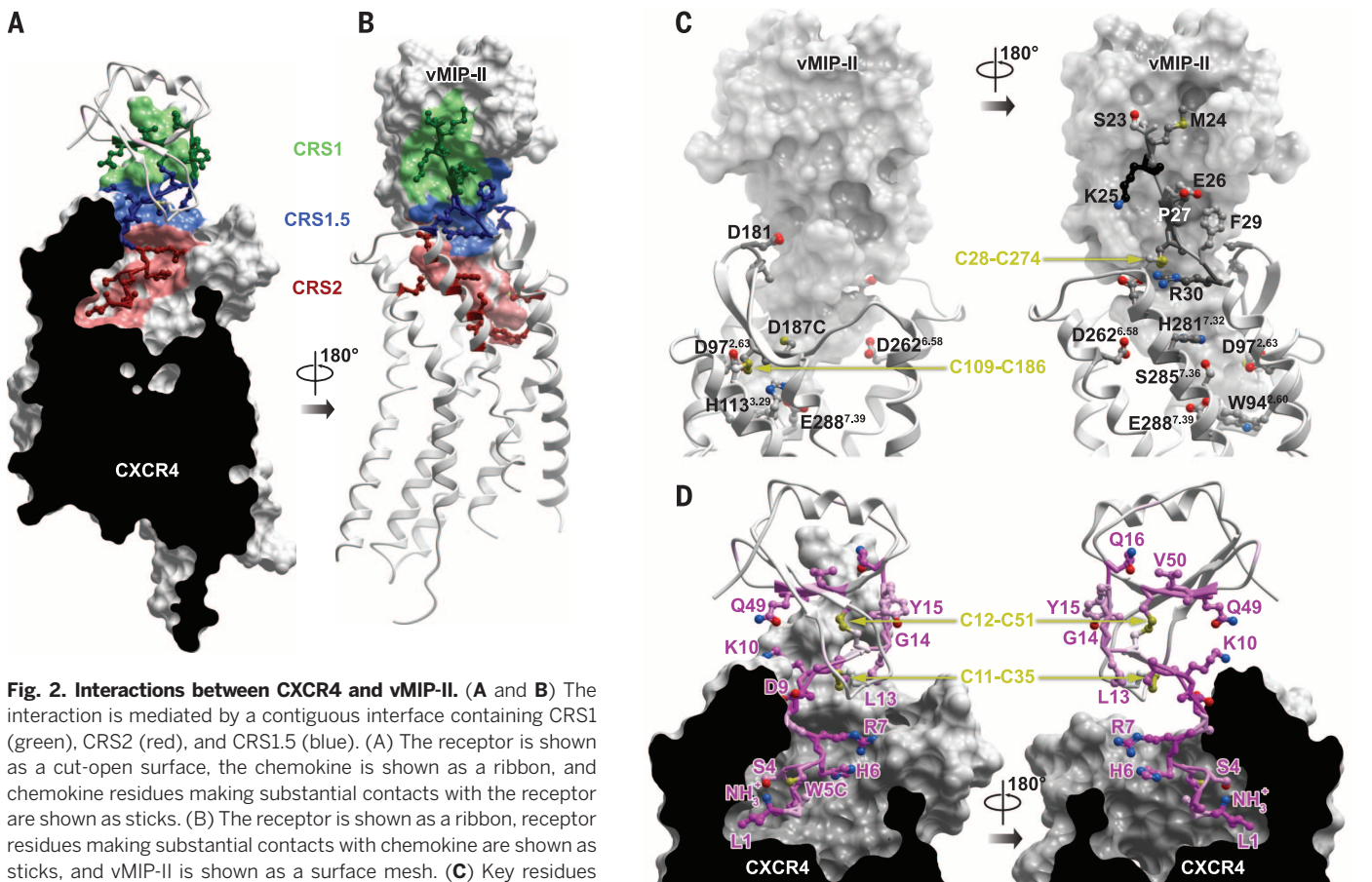


Fig. 2. Interactions between CXCR4 and vMIP-II. (A and B) The interaction is mediated by a contiguous interface containing CRS1 (green), CRS2 (red), and CRS1.5 (blue). (A) The receptor is shown as a cut-open surface, the chemokine is shown as a ribbon, and chemokine residues making substantial contacts with the receptor are shown as sticks. (B) The receptor is shown as a ribbon, receptor residues making substantial contacts with chemokine are shown as sticks, and vMIP-II is shown as a surface mesh. (C) Key residues (gray sticks) from CXCR4 (ribbon) that bind vMIP-II (surface representation). (D) Key residues (magenta sticks) from vMIP-II (white ribbon) that bind CXCR4 (cut-open surface). Noncarbon atoms are red (O), blue (N), and yellow (S); carbon stick color intensity is indicative of residue contact strength (table S2).

strictly conserved between vMIP-II (48-RQVC-51) and CXCL12 (47-RQVC-50) and that interacts with receptor D22 and E26 (Fig. 5B), both of which are important for vMIP-II and CXCL12 recognition (23, 26).

The CXCR4:vMIP-II structure can also explain why CXC (35) but not CC (36) chemokines bind and activate their receptors as dimers. CC chemokines dimerize by β -sheet interactions between the straight CC motifs and N-terminal residues (Fig. 6A). This largely coincides with the CRS1.5 interaction in the CXCR4:vMIP-II structure, making it sterically impossible for a CC chemokine to simultaneously bind its dimer partner and a receptor (Fig. 6B). By contrast, CXC chemokines dimerize by their β_1 strands (Fig. 6C), which are

not involved in receptor interactions and therefore are compatible with the geometry of the CKR: chemokine complexes (Fig. 6D). This model also suggests that CXC chemokine dimers likely bind to single receptor subunits (Fig. 6E) and not to both subunits in a dimer as previously hypothesized (37).

Modeling-based insights into agonist versus antagonist chemokine binding to CXCR4

CXCL12 can be converted into a potent antagonist of CXCR4 by as little as a single N-terminal amino-acid substitution (P2G) (38). To investigate the basis for this notable change in pharmacology, modeling of CRS2 interactions for both CXCL12

and CXCL12(P2G) with CXCR4 was performed. With both chemokine variants, the four distal N-terminal residues were predicted to bind in the minor subpocket of CXCR4 in a manner similar to vMIP-II (Fig. 5, D and E). The N-terminal and side-chain amines of chemokine K1 were predicted to form hydrogen bonds to receptor residues D97^{2.63} and E288^{7.39}, respectively, whereas chemokine residues S4 (in CXCL12) and Y7 [in both CXCL12 and CXCL12(P2G)] hydrogen-bond to D187^{ECL2}. Notably, K1 in CXCL12 and D97^{2.63}, D187^{ECL2}, and E288^{7.39} in CXCR4 are all critical for receptor interaction and activation (22, 25, 26, 38). In CXCL12, the side chain of P2 was found in proximity of receptor residue Y116^{3.32} (Fig. 5D), whose direct interaction with agonists is frequently

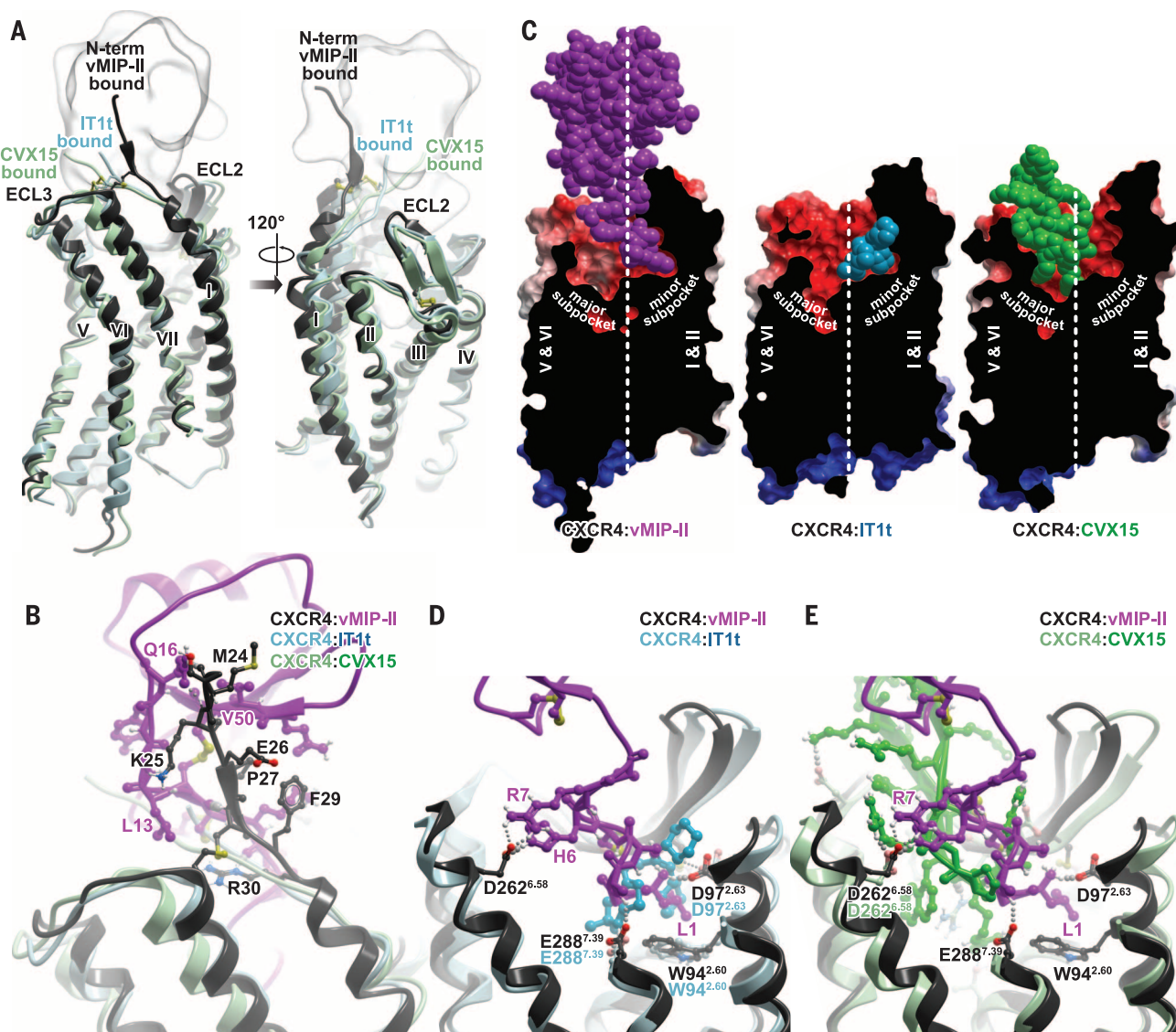


Fig. 3. Comparison between CXCR4:vMIP-II and earlier CXCR4 structures. (A) Overlay of CXCR4 in the vMIP-II complex (gray), the IT1t complex (PDB ID 3ODU; cyan), and the CVX15 complex (PDB ID 3OE0; pale green). vMIP-II is shown as a gray transparent mesh. (B) CRS1 interaction between CXCR4 (gray) and vMIP-II (magenta), in comparison with IT1t-bound (cyan) and CVX15-bound (green) structures. Key residues mediating the CXCR4:

vMIP-II interactions are shown as sticks. (C) Binding modes of vMIP-II, IT1t, and CVX15 to CXCR4. CXCR4 is shown as a cut-open surface, colored by electrostatic potential; the bound ligands are shown as spheres. The white dotted line represents the boundary between the major and minor subpockets. (D and E) Comparison of CRS2 interactions of vMIP-II (magenta) with IT1t (cyan) and CVX15 (green).

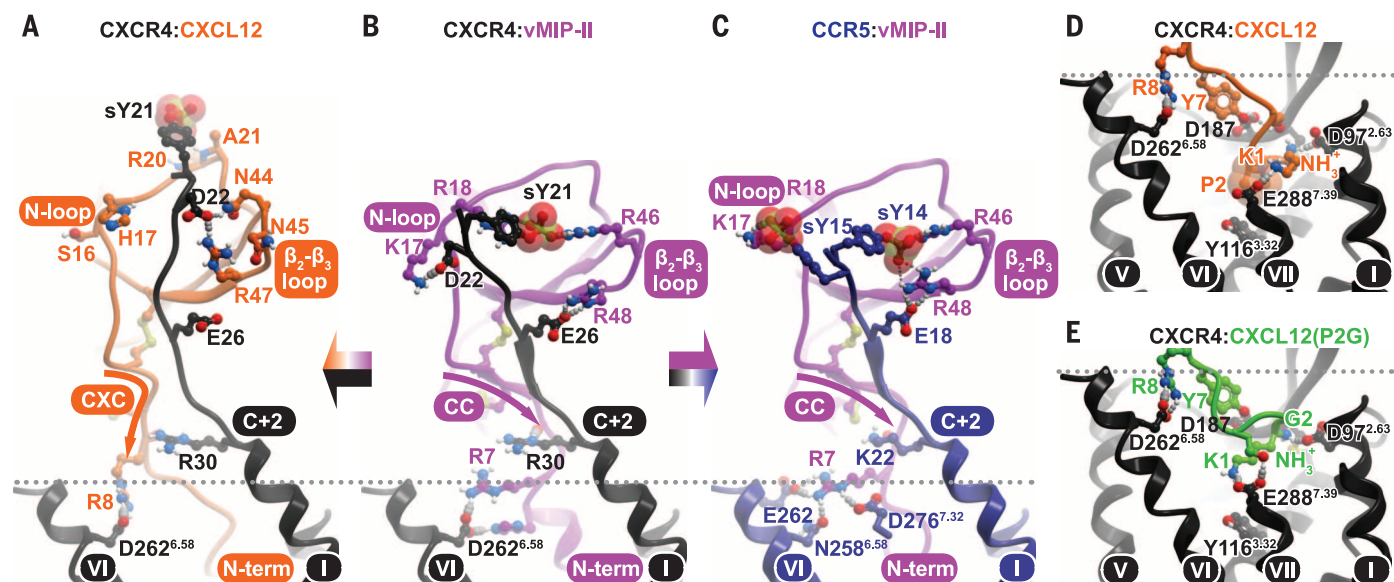
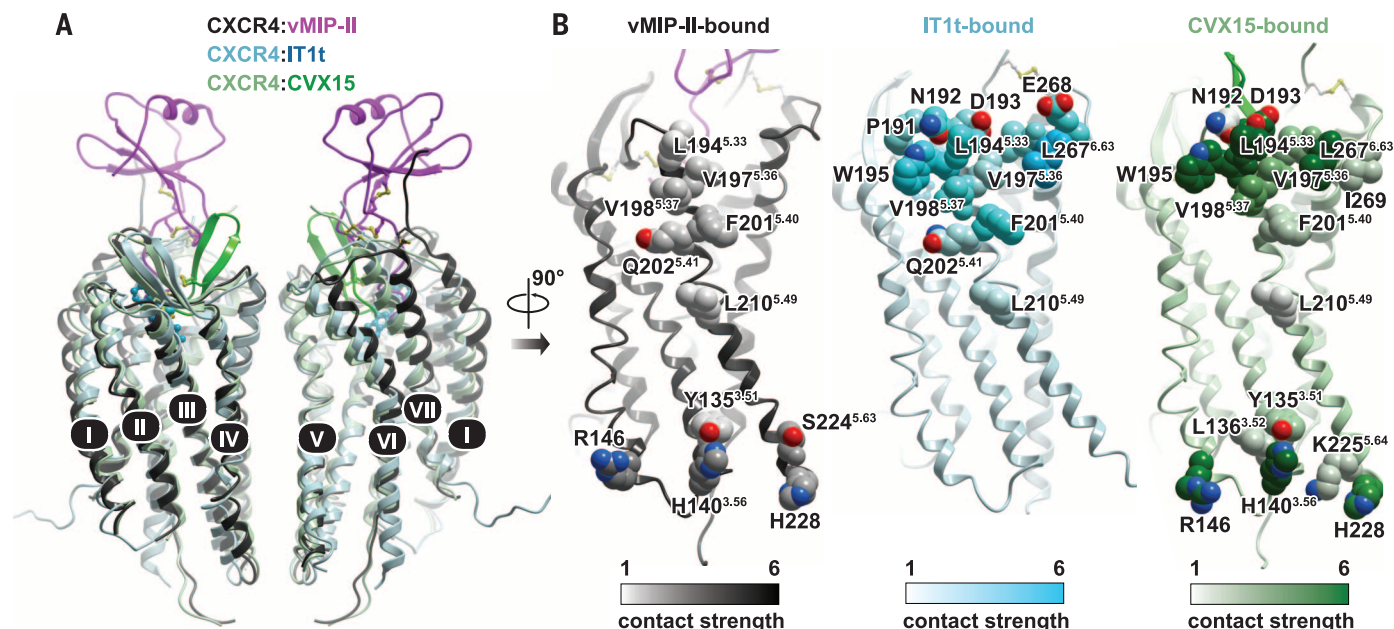
involved in activation of GPCRs (39). By contrast, due to its greater flexibility and smaller steric volume, the G2 to S4 region of CXCL12(P2G) packed differently (Fig. 5E), avoiding interaction with Y116^{3.32} and potentially explaining the inability of CXCL12(P2G) to activate CXCR4. However, because docking was performed with an inactive receptor conformation, further struc-

tural studies will be necessary to fully understand activation mechanisms.

Chemokine receptor plasticity, promiscuity, and implications for drug design

CXCR4 is remarkable in its ability to recognize multiple unrelated small molecules, peptides, and proteins. While engaging a conserved set of bind-

ing determinants, the ligands occupy different regions of the binding pocket due to receptor conformational plasticity involving receptor side-chain and backbone adjustments. Such versatility may allow the receptor to accommodate ligands of different classes, including both CC- and CXC-type chemokines as well as allosteric inhibitors. The growing number of chemokine receptor



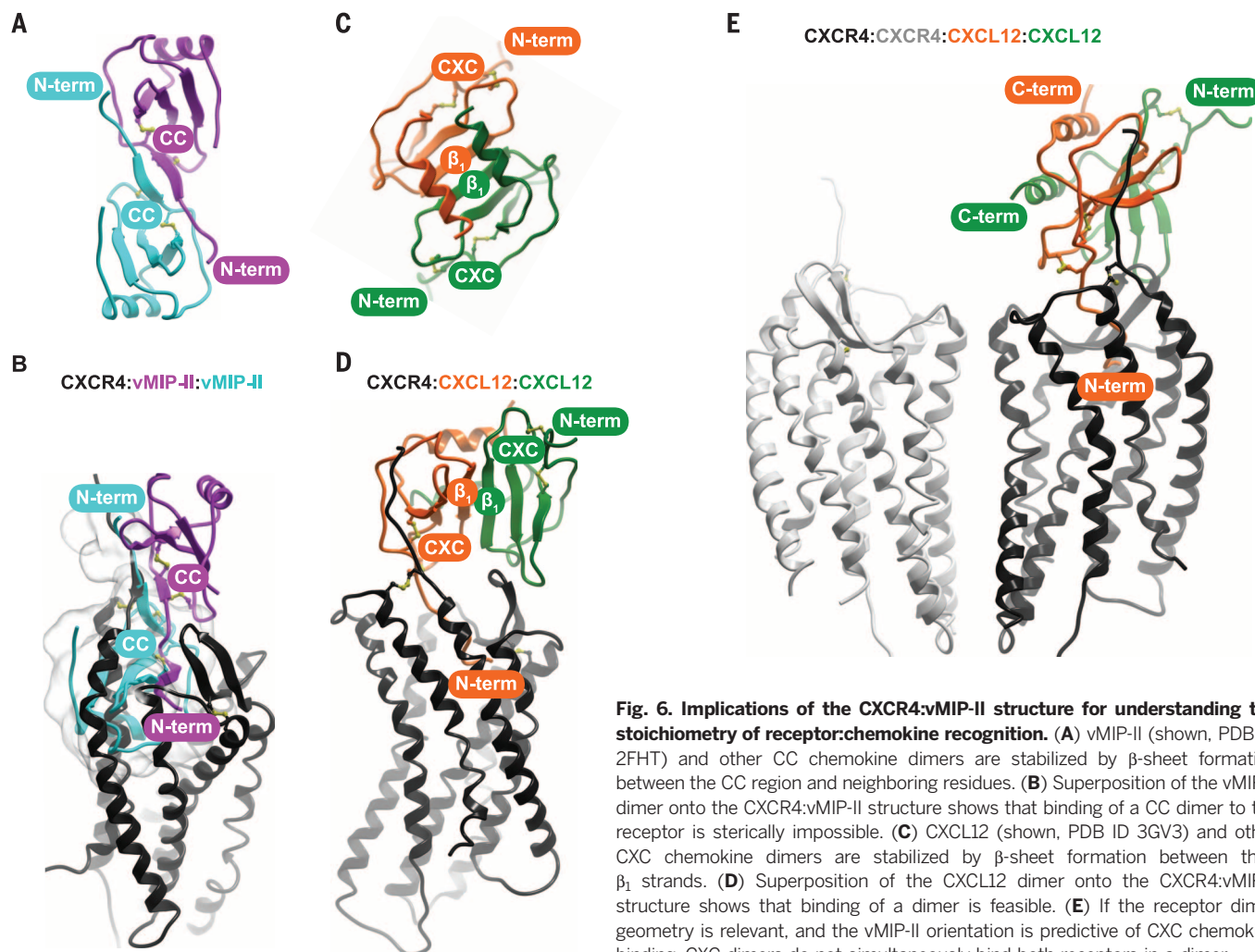


Fig. 6. Implications of the CXCR4:vMIP-II structure for understanding the stoichiometry of receptor:chemokine recognition. (A) vMIP-II (shown, PDB ID 2FHT) and other CC chemokine dimers are stabilized by β -sheet formation between the CC region and neighboring residues. (B) Superposition of the vMIP-II dimer onto the CXCR4:vMIP-II structure shows that binding of a CC dimer to the receptor is sterically impossible. (C) CXCL12 (shown, PDB ID 3GV3) and other CXC chemokine dimers are stabilized by β -sheet formation between their β_1 strands. (D) Superposition of the CXCL12 dimer onto the CXCR4:vMIP-II structure shows that binding of a dimer is feasible. (E) If the receptor dimer geometry is relevant, and the vMIP-II orientation is predictive of CXC chemokine binding, CXC dimers do not simultaneously bind both receptors in a dimer.

structures with different ligands opens possibilities for rational design of ligands that have improved inhibition profiles and mechanisms of action.

REFERENCES AND NOTES

1. T. Nagasawa et al., *Nature* **382**, 635–638 (1996).
2. Y.-R. Zou, A. H. Kottmann, M. Kuroda, I. Taniuchi, D. R. Littman, *Nature* **393**, 595–599 (1998).
3. Q. Ma et al., *Proc. Natl. Acad. Sci. U.S.A.* **95**, 9448–9453 (1998).
4. P. J. Koelink et al., *Pharmacol. Ther.* **133**, 1–18 (2012).
5. F. Balkwill, *Semin. Cancer Biol.* **14**, 171–179 (2004).
6. E. A. Berger, P. M. Murphy, J. M. Farber, *Annu. Rev. Immunol.* **17**, 657–700 (1999).
7. N. J. Skelton, C. Quan, D. Reilly, H. Lowman, *Structure* **7**, 157–168 (1999).
8. C. T. Veldkamp et al., *Sci. Signal.* **1**, ra4 (2008).
9. C. J. Millard et al., *Structure* **22**, 1571–1581 (2014).
10. T. N. Kledal et al., *Science* **277**, 1656–1659 (1997).
11. R. Yamin et al., *PLOS Pathog.* **9**, e1003568 (2013).
12. N. Zhou, Z. Luo, J. Luo, J. W. Hall, Z. Huang, *Biochemistry* **39**, 3782–3787 (2000).
13. D. M. Rosenbaum et al., *Nature* **469**, 236–240 (2011).
14. I. Kufareva et al., *Proc. Natl. Acad. Sci. U.S.A.* **111**, E5363–E5372 (2014).
15. Materials and methods are available as supplementary materials on Science Online.
16. J. A. Ballesteros, H. Weinstein, in *Methods in Neurosciences*, S. C. Sealfon, Ed. (Academic Press, San Diego, 1995), vol. 25, pp. 366–428.
17. In Ballesteros-Weinstein numbering, the most conserved residue in class A GPCRs is designated x.50, where x is the transmembrane helix number. All other residues on a given helix are numbered relative to this position, e.g., x.49, x.51 are the flanking residues.
18. M. Caffrey, V. Cherezov, *Nat. Protoc.* **4**, 706–731 (2009).
19. B. Wu et al., *Science* **330**, 1066–1071 (2010).
20. I. Kufareva, R. Abagyan, T. M. Handel, in *Chemokines* (Springer, Berlin Heidelberg, 2014), chap. 77.
21. D. J. Scholten et al., *Br. J. Pharmacol.* **165**, 1617–1643 (2012).
22. S. Tian et al., *J. Virol.* **79**, 12667–12673 (2005).
23. A. Brelot, N. Heveker, M. Montes, M. Alizon, *J. Biol. Chem.* **275**, 23736–23744 (2000).
24. J. Våbø, G. V. Nikiforovich, G. R. Marshall, *Chem. Biol. Drug Des.* **67**, 346–354 (2006).
25. W.-T. Choi et al., *J. Virol.* **79**, 15398–15404 (2005).
26. N. Zhou et al., *J. Biol. Chem.* **276**, 42826–42833 (2001).
27. Z. Luo et al., *Biochemistry* **39**, 13545–13550 (2000).
28. L. Roumen et al., *Drug Discov. Today, Technol.* **9**, e281–e291 (2012).
29. M. Lefrançois et al., *ACS Medicinal Chemistry Letters* **2**, 597–602 (2011).
30. B. Stephens, T. M. Handel, in *Oligomerization and Allosteric Modulation in G-Protein Coupled Receptors*, T. Kenakin, Ed. (Academic Press, Waltham, MA, 2013), vol. 115, chap. 9.
31. J.-M. Navenot et al., *J. Mol. Biol.* **313**, 1181–1193 (2001).
32. M. Farzan et al., *Cell* **96**, 667–676 (1999).
33. J. W. Murphy et al., *J. Biol. Chem.* **282**, 10018–10027 (2007).
34. E. W. Smith et al., *J. Med. Chem.* **57**, 9693–9699 (2014).
35. L. J. Drury et al., *Proc. Natl. Acad. Sci. U.S.A.* **108**, 17655–17660 (2011).
36. H. Jin, X. Shen, B. R. Baggett, X. Kong, P. J. LiWang, *J. Biol. Chem.* **282**, 27976–27983 (2007).
37. D. Rajasekaran et al., *Biochemistry* **51**, 5642–5654 (2012).
38. M. P. Crump et al., *EMBO J.* **16**, 6996–7007 (1997).
39. V. Katritch, V. Cherezov, R. C. Stevens, *Annu. Rev. Pharmacol. Toxicol.* **53**, 531–556 (2013).
40. A. I. Alexandrov, M. Mileni, E. Y. Chien, M. A. Hanson, R. C. Stevens, *Structure* **16**, 351–359 (2008).

ACKNOWLEDGMENTS

The authors thank H. Zhang and W. Liu for help with x-ray data collection; A. Walker for assistance with manuscript preparation; M. Gustavsson and V. Katritch for valuable discussions and critical reading of the manuscript; M. Chu for assistance with insect cell expression; E. Lolis and J. Murphy for suggesting the use of vMIP-II; and T. Kawamura, D. Hamel, and K. Wang for assistance with chemokine production. The data in this manuscript are tabulated in the main paper and in the supplementary materials. Atomic coordinates and structure factors have been deposited in the Protein Data Bank (PDB) with identification code 4RWS. This work was funded by National Institutes of Health grants R01 GM071872 (R.A.); U01 GM094612, R01 GM081763, and R21 AI101687 (T.M.H.); and U54 GM094618 (R.C.S.). L.G.H. is supported by a 2012 Postdoctoral Fellowship in Pharmacology/Toxicology from the Pharmaceutical Research and Manufacturers of America (PhRMA) Foundation. The General Medical Sciences and Cancer Institutes Structural Biology Facility at the Advanced Photon Source (GM/CA@APS) is supported by the National Cancer Institute (ACB-12002) and the National Institute of General Medical Sciences (AGM-12006).

SUPPLEMENTARY MATERIALS

www.sciencemag.org/content/347/6226/1117/suppl/DC1
Materials and Methods
Figs. S1 to S4
Tables S1 to S3
References (41–56)

10 September 2014; accepted 6 January 2015
Published online 22 January 2015;
10.1126/science.1261064

REPORTS

ASTROPHYSICS

Multiple images of a highly magnified supernova formed by an early-type cluster galaxy lens

Patrick L. Kelly,^{1*} Steven A. Rodney,² Tommaso Treu,³ Ryan J. Foley,^{4,5} Gabriel Brammer,⁶ Kasper B. Schmidt,⁷ Adi Zitrin,⁸ Alessandro Sonnenfeld,^{3,7} Louis-Gregory Strolger,^{6,9} Or Graur,^{10,11} Alexei V. Filippenko,¹ Saurabh W. Jha,¹² Adam G. Riess,^{2,6} Marusa Bradac,¹³ Benjamin J. Weiner,¹⁴ Daniel Scolnic,^{15,16} Matthew A. Malkan,³ Anja von der Linden,^{17,18} Michele Trenti,¹⁹ Jens Hjorth,¹⁷ Raphael Gavazzi,²⁰ Adriano Fontana,²¹ Julian C. Merten,⁸ Curtis McCully,^{7,22} Tucker Jones,⁷ Marc Postman,⁶ Alan Dressler,²³ Brandon Patel,¹² S. Bradley Cenko,^{24,25} Melissa L. Graham,¹ Bradley E. Tucker^{1,26}

In 1964, Refsdal hypothesized that a supernova whose light traversed multiple paths around a strong gravitational lens could be used to measure the rate of cosmic expansion. We report the discovery of such a system. In Hubble Space Telescope imaging, we have found four images of a single supernova forming an Einstein cross configuration around a redshift $z = 0.54$ elliptical galaxy in the MACS J1149.6+2223 cluster. The cluster's gravitational potential also creates multiple images of the $z = 1.49$ spiral supernova host galaxy, and a future appearance of the supernova elsewhere in the cluster field is expected. The magnifications and staggered arrivals of the supernova images probe the cosmic expansion rate, as well as the distribution of matter in the galaxy and cluster lenses.

The possibility that the light from an exploding supernova (SN) could follow more than a single path around an intervening strong galaxy lens to the observer was first explored about 50 years ago (*1*). Many decades of searches for SNe, however, have not identified an explosion visible at multiple positions around a gravitational lens. Here we report a strongly lensed supernova found in resolved multiple images, which we identified in the MACS J1149.6+2223 (2) galaxy cluster field on 11 November 2014 (Universal Time dates are used throughout this paper).

Although the apparent positions of galaxies that are multiply imaged by a foreground galaxy or cluster are now widely used to map the matter distribution within the lenses, a strongly lensed background source with a varying light curve allows distinct and powerful measurements of the lens and cosmology, because the delay between each pair of images can be measured. This difference in arrival time, owing to the difference in geometric and gravitational time delay (*3*), is directly proportional to the so-called time-delay distance and thus inversely proportional to the Hubble constant and weakly dependent on other cosmological parameters (*1, 4–6*). Conversely, for an assumed cosmological model, the time delays are a direct measurement of the difference in gravitational potential between the multiple images, and hence greatly improve the reconstruction of the mass distribution in the deflector (*7*).

After the discovery of the SBS 0957+561 A/B system 26 years ago (*8*), a handful of quasi-stellar objects (quasars) multiply imaged by an intervening galaxy lens have been identified (*9*). Quasars strongly lensed by clusters are even more rare events, with only several known (*10*). The use of lensed quasars as robust probes of the distribution of matter in the lenses and of cosmology has only become possible relatively recently, given the long time periods of monitoring needed to match their complex light curves (*6, 11–13*). In contrast, all SNe have much simpler light curves and evolve comparatively rapidly, which makes the measurement of time delays and magnification among the multiple images substantially more straightforward.

It was recently shown that a different SN, PS1-10afx (*14*) at redshift $z = 1.38$, was strongly magnified (by a factor of ~ 30) by an intervening galaxy at $z = 1.12$ (*15, 16*). The available imaging, taken from the ground, had insufficient angular resolution to separate potential multiple images of the SN, so time delays and magnifications could not be measured. In the case presented here, the four images of the SN are clearly resolved (Fig. 1), with an image separation of over $2''$, thereby presenting an ideal opportunity to carry out for the first time an experiment similar to that suggested by Refsdal (*1*), leading us to name the supernova “Refsdal.”

The Grism Lens-Amplified Survey from Space (GLASS) program [GO-13459, principal investiga-

tor (PI) T.T.] is a 140-orbit Hubble Space Telescope (HST) project that is acquiring near-infrared grism spectra of massive galaxy clusters with the primary goals of studying faint high-redshift ($z \gtrsim 6$) galaxies (*17*) and spatially resolved intermediate-redshift galaxies (*18*), as well as characterizing the cluster galaxy population. Wide-band near-infrared F105W and F140W exposures are taken using the Wide Field Camera 3 (WFC3) to align and calibrate the grism data, and we have been searching these images for transient sources.

In the F140W GLASS images acquired on 10 November 2014, we detected the component images of a quadruple lens system, which we label sources S1 to S4 (Fig. 1). Table 1 gives the coordinates of the variable sources. In Fig. 2, the color-composite image shows the red galaxy lens at $z = 0.54$ (*19*) surrounded by an Einstein ring formed by light from the distorted spiral host galaxy with $z = 1.49$ (*20*), whose nucleus is offset by $\sim 3.3''$ from the center of the lensing elliptical galaxy. Although sources S1 and S2 do not exhibit a significant change in their fluxes during the imaging taken from 3 to 20 November 2014, the light curve of S3 is consistent with a rise in brightness during this period, which corresponds to approximately a week in the rest frame (Fig. 3; see also fig. S1). The light curve of S4 is difficult to characterize with the currently available data, because it is comparatively faint.

¹Department of Astronomy, University of California, Berkeley, CA 94720-3411, USA. ²Department of Physics and Astronomy, The Johns Hopkins University, Baltimore, MD 21218, USA. ³Department of Physics and Astronomy, University of California, Los Angeles, CA 90095, USA.

⁴University of Illinois at Urbana-Champaign, 1002 West Green Street, Urbana, IL 61801, USA. ⁵Department of Physics, University of Illinois at Urbana-Champaign, 1110 West Green Street, Urbana, IL 61801, USA. ⁶Space Telescope Science Institute, 3700 San Martin Drive, Baltimore, MD 21218, USA.

⁷Department of Physics, University of California, Santa Barbara, CA 93106, USA. ⁸California Institute of Technology, MC 249-17, Pasadena, CA 91125, USA. ⁹Western Kentucky University, 1906 College Heights Boulevard, Bowling Green, KY 42101, USA. ¹⁰Center for Cosmological and Particle Physics, New York University, 4 Washington Place, New York, NY 10003, USA. ¹¹Department of Astrophysics, American Museum of Natural History, Central Park West and 79th Street, New York, NY 10024, USA. ¹²Department of Physics and Astronomy, Rutgers, the State University of New Jersey, Piscataway, NJ 08854, USA. ¹³Department of Physics, University of California, Davis, CA 95616, USA. ¹⁴Steward Observatory, University of Arizona, Tucson, AZ 85721, USA.

¹⁵Department of Physics, University of Chicago, 5720 South Ellis Avenue, Chicago, IL 60637, USA. ¹⁶Kavli Institute for Cosmological Physics, University of Chicago, 5720 South Ellis Avenue, Chicago, IL 60637, USA. ¹⁷Dark Cosmology Centre, Niels Bohr Institute, University of Copenhagen, Juliane Maries Vej 30, 2100 Copenhagen, Denmark. ¹⁸Kavli Institute for Particle Astrophysics and Cosmology, Stanford University, 452 Lomita Mall, Stanford, CA 94305, USA. ¹⁹School of Physics, University of Melbourne, VIC 3010, Australia. ²⁰Institut d'Astrophysique de Paris, 98 bis Boulevard Arago, F-75014 Paris, France.

²¹INAF-OAR, Via Frascati 33, 00040 Monte Porzio, Rome, Italy. ²²Las Cumbres Observatory Global Telescope Network, 6740 Cortona Drive Suite 102, Goleta, CA 93117, USA. ²³Carnegie Observatories, 813 Santa Barbara Street, Pasadena, CA 91101, USA. ²⁴Astrophysics Science Division, NASA Goddard Space Flight Center, MC 661, Greenbelt, MD 20771, USA. ²⁵Joint Space-Science Institute, University of Maryland, College Park, MD 20742, USA. ²⁶The Research School of Astronomy and Astrophysics, Australian National University, Mount Stromlo Observatory, via Cotter Road, Weston Creek, Australian Capital Territory 2611, Australia.

*Corresponding author. E-mail: pkelly@astro.berkeley.edu

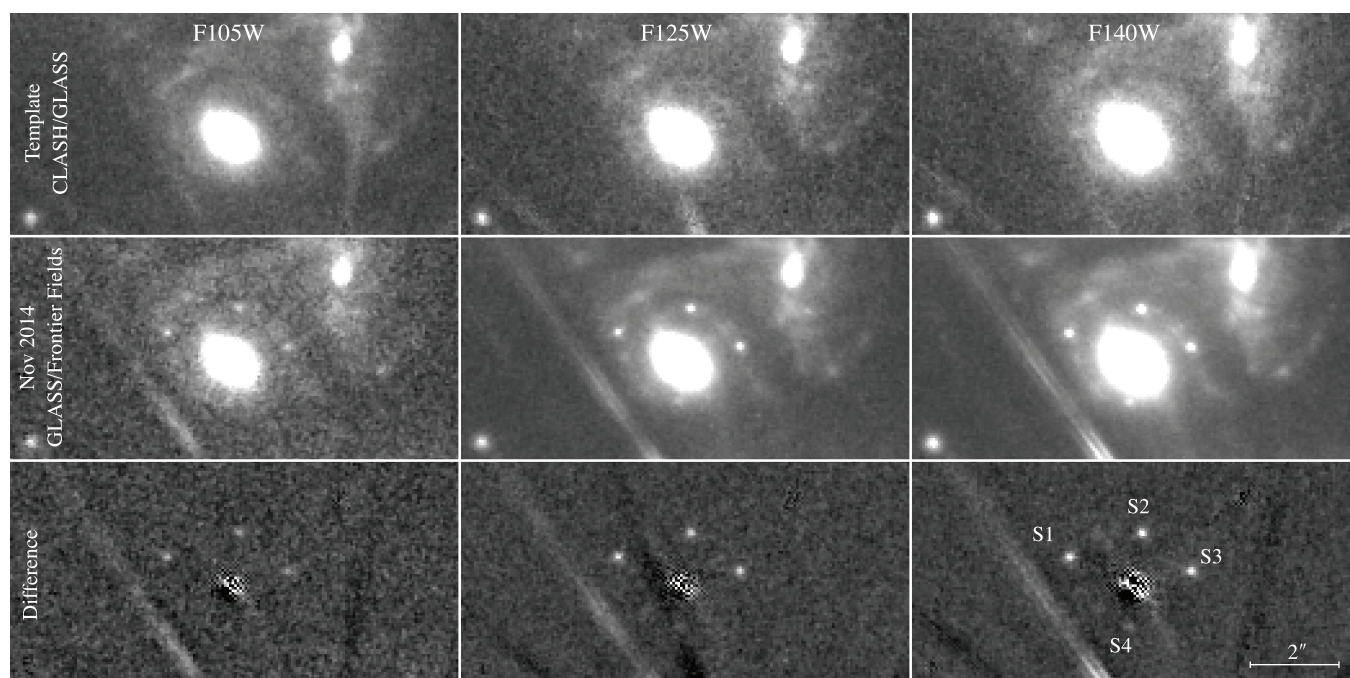


Fig. 1. HST WFC3-IR images showing the simultaneous appearance of four point sources around a cluster member galaxy. From left to right, the columns show imaging in the F105W filter (Y band), F125W (J), and F140W (H). From top to bottom, the rows show archival imaging from the Cluster Lensing And Supernova survey with Hubble (CLASH, GO-12068; PI M.P.) program, discovery epoch images from GLASS and the Hubble Frontier Fields programs, and the difference images. The template images in the top row comprise all available archival WFC3-IR imaging in these filters, collected from

5 December 2010 through 10 March 2011. The images in the middle row are the composite of all available HST imaging collected between 3 November and 11 November 2014 (for F105W, left), on 20 November 2014 (F125W, middle), and between 10 November and 20 November 2014 (F140W, right). The sources S1, S2, S3, and S4, which form an Einstein cross, are absent from all images obtained at earlier epochs but are clearly detected in the difference images along the bottom row. The line segments below S4 and in the lower right corner are diffraction spikes from a nearby bright star in the foreground.

Table 1. Coordinates of the transient point sources detected around the cluster galaxy lens, in J2000 right ascension and declination.

Name	α (J2000)	δ (J2000)
S1	11 ^h 49 ^m 35.57 ^s	+22°23'44.26"
S2	11 ^h 49 ^m 35.451 ^s	+22°23'44.84"
S3	11 ^h 49 ^m 35.369 ^s	+22°23'43.95"
S4	11 ^h 49 ^m 35.472 ^s	+22°23'42.62"

Based on the available data, we can attempt a first preliminary classification of the SN. All known type Ia SNe reach their peak brightness in fewer than 20 rest-frame days (21). The light curve for image S3 of SN Refsdal (fig. S1) through >30 days in the rest frame shows that its brightness continued to rise for a longer period than could be expected for a SN Ia, suggesting that it belongs to a different spectroscopic class.

Archival HST imaging and the configuration of the multiple images demonstrate that the source is not an active galactic nucleus (AGN) behind the galaxy and cluster lenses. A search of WFC3 F105W, F110W, F140W, and F160W images of MACS J1149.6+2223, acquired across 10 separate HST visits beginning on 4 December 2010, finds no evidence for previous variability. Several epochs of registered and coadded F140W imaging exhibit no significant variation (fig. S4); seven archival epochs of F160W imaging likewise

show no significant changes. Evidence for previous variability would have suggested that the source is a flare from an AGN instead of a SN. The transients detected in November 2014 are additionally several magnitudes above the upper limits of ~ 28.5 obtained at previous epochs (all magnitudes are in the AB system). Such a large increase in brightness would be very unusual for an AGN, whose light curves typically vary at the level of a few tenths of a magnitude over several-month time scales (22–24). Finally, the positions of the multiple images also constrain the redshift of the source to 1.1 to 1.7 with 95% confidence, consistent with the $z = 1.49$ redshift of the spiral galaxy lensed into the observed configuration (fig. S2).

The four images of SN Refsdal form an Einstein cross configuration around the massive elliptical galaxy at $z = 0.54$, which adds onto and locally perturbs the cluster potential. Because the elliptical galaxy is located close to the critical lines of the cluster lens (25), the contribution of the galaxy cluster to the gravitational potential needs to be taken into account. As a first, simple approximation of the lensing system, we construct a single isothermal ellipsoid embedded in a strong external shear (26). This yields time delays on the order of several to tens of days. S1 is generally the leading image, typically followed by S2, S3, and then S4. Magnifications are ~ 2 for the least magnified image S4 and ~ 10 for the other

images. These magnifications, however, do not include the additional contribution from the cluster, which is expected to be very substantial, especially because earlier modeling has found a relatively flat, nearly convergent central mass distribution, which is evident from the relatively undistorted shape of the magnified spiral images (25).

To account more completely for the effects of the cluster potential, we have constructed a detailed set of lens models of the entire cluster potential, including the elliptical galaxy, for several different prior probability distributions and sets of constraints. These models, which are also constrained by the positions of the SN images, generally yield magnifications of ~ 10 to 30 at the positions of the four images, and time delays on the order of days to months, in agreement with independent models (27, 28). The typical arrival sequence is consistent with the predictions of the simpler galaxy-lens model (S1, S2, and then either S3 or S4), although some models also predict different arrival orders. These time delays are also in accord with our identification of the four newly detected sources as a multiply imaged SN, because the luminosity of a SN is not expected to vary dramatically over the time scale of less than a week in the rest frame. The spiral host galaxy itself is multiply imaged by the galaxy cluster (20, 25). Consequently, our models predict both that the SN could be detected at future

Fig. 2. Color-composite image of the galaxy cluster MACSJ1149.6+2223, with critical curves for sources at the $z = 1.49$ redshift of the host galaxy overlaid.

Three images of the host galaxy formed by the cluster are marked with white labels (1.1, 1.2, and 1.3) in the left panel, and each is enlarged at right. The four current images of SN Refsdal that we detected (labeled S1 to S4 in red) appear as red point sources in image 1.1. Our model indicates that an image of the SN appeared in the past in image 1.3 and that one will appear in the near future in image 1.2. The extreme red hue of the SN may be somewhat exaggerated, because the blue and green channels include only data taken before the SN erupted. In image 1.1, both a single bright blue knot (cyan circles) and SN Refsdal are multiply imaged into four distinct locations. The image combines infrared and optical HST imaging data from the Frontier Fields and GLASS programs, along with images from the CLASH and the FrontierSN programs (GO-13790, PI S.A.R.).

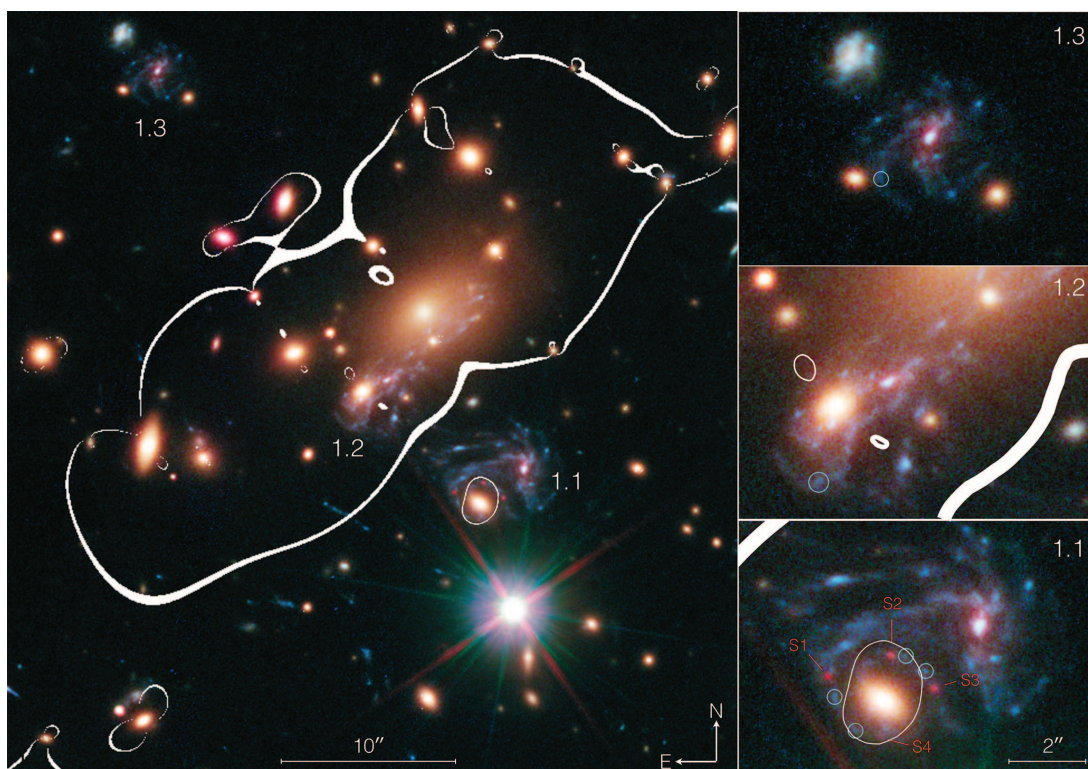
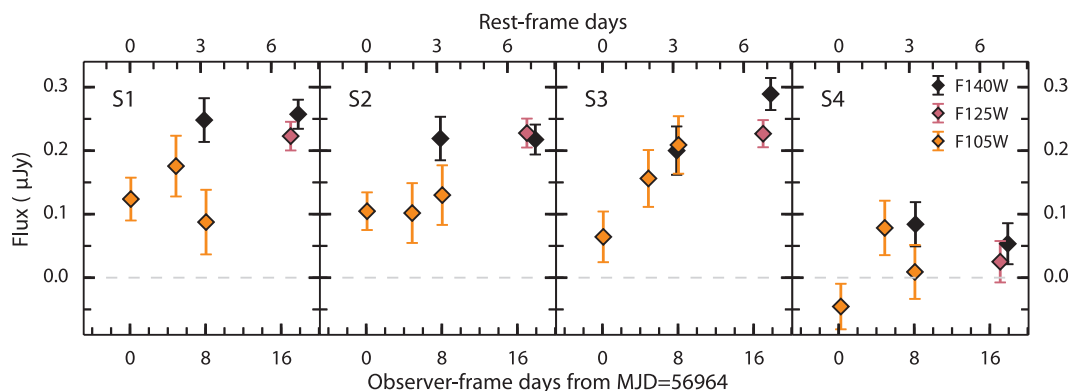


Fig. 3. Light curve of the images S1 to S4 of the strongly lensed SN taken from 3 November 2014 through 20 November 2014.

Rest-frame days assume that the SN is at the redshift of the multiply imaged spiral galaxy ($z = 1.49$). We plotted the fluxes measured in the WFC3 F105W, F125W, and F140W images of the MACSJ1149.6+2223 galaxy cluster field. The expected time delays between images of days to weeks suggest that the transient must evolve over a time scale

similar to that of a SN. Our lens models generally predict that image S3 is delayed relative to S1 and S2, which is consistent with the early photometry. Flux uncertainties are calculated by injecting a thousand point sources into the difference images and comparing the fluxes recovered using point-spread-function fitting with the input fluxes. Error bars throughout correspond to the standard deviation of a normal distribution fitted to the histogram of the difference in flux.



epochs in a different image of the spiral host galaxy and that it has already appeared elsewhere in yet another image of the spiral. A search of archival HST imaging in both the optical (F606W, F814W, and F850LP) and infrared (F105W, F125W, F140W, and F160W) at the locations of the multiple images of the presumed host galaxy has revealed no evidence for SN Refsdal when these data were taken. Our set of cluster lens models predicts that the SN will appear in the central image of the spiral host galaxy, at an approximate position of $\alpha = 11^{\text{h}}49^{\text{m}}36.01^{\text{s}}$, $\delta = +22^{\circ}23'48.13''$ (J2000.0) at a future time, within

a year to a decade from now (2015 to 2025). This is in broad agreement with independent model predictions (27, 28). The uncertainties highlight the power of a time-delay measurement to constrain lens models.

The archival HST imaging and the configuration show that this is a multiply imaged SN. This discovery demonstrates in principle the feasibility of the experiment suggested five decades ago by Refsdal (1), consisting of using the time delays between the multiple images of the SN to constrain the foreground mass distribution and eventually the geometry and content of the universe.

REFERENCES AND NOTES

1. S. Refsdal, *Mon. Not. R. Astron. Soc.* **128**, 307–310 (1964).
2. H. Ebeling, A. C. Edge, J. P. Henry, *Astrophys. J.* **553**, 668–676 (2001).
3. I. I. Shapiro, *Phys. Rev. Lett.* **13**, 789–791 (1964).
4. T. Treu, *Annu. Rev. Astron. Astrophys.* **48**, 87–125 (2010).
5. E. V. Linder, *Phys. Rev. D Part. Fields Gravit. Cosmol.* **84**, 123529 (2011).
6. S. H. Suyu et al., *Astrophys. J.* **788**, L35 (2014).
7. C. S. Kochanek et al., *Astrophys. J.* **640**, 47–61 (2006).
8. D. Walsh, R. F. Carswell, R. J. Weymann, *Nature* **279**, 381–384 (1979).
9. N. Inada et al., *Astron. J.* **143**, 119 (2012).
10. K. Sharon et al., *Astrophys. J.* **629**, L73–L76 (2005).

11. L. V. E. Koopmans, T. Treu, C. D. Fassnacht, R. D. Blandford, G. Surpi, *Astrophys. J.* **599**, 70–85 (2003).
12. M. Tewes et al., *Astron. Astrophys.* **556**, A22 (2013).
13. S. H. Suyu et al., *Astrophys. J.* **766**, 70 (2013).
14. R. Chornock et al., *Astrophys. J.* **767**, 162 (2013).
15. R. M. Quimby et al., *Astrophys. J.* **768**, L20 (2013).
16. R. M. Quimby et al., *Science* **344**, 396–399 (2014).
17. K. B. Schmidt et al., *Astrophys. J.* **782**, L36 (2014).
18. T. Jones et al., *arxiv.org/abs/1410.0967* (2014).
19. H. Ebeling et al., *Astrophys. J.* **661**, L33–L36 (2007).
20. G. P. Smith et al., *Astrophys. J.* **707**, L163–L168 (2009).
21. M. Ganeshalingam, W. Li, A. V. Filippenko, *Mon. Not. R. Astron. Soc.* **416**, 2607–2622 (2011).
22. S. Kaspi et al., *Astrophys. J.* **659**, 997–1007 (2007).
23. M. C. Bentz et al., *Astrophys. J.* **705**, 199–217 (2009).

ACKNOWLEDGMENTS

This work is based on data obtained with the NASA/ESA Hubble Space Telescope. We thank O. Fox, W. Zheng, J. Bloom, C. Keeton, J. Mauerhan, C. Steidel, and A. Strom for helpful discussions,

as well as the Space Telescope Science Institute (STScI) and Director Matt Mountain for supporting our proposal for follow-up observations. GLASS is supported by NASA through HST grant GO-13459. Support for S.A.R. was provided by NASA through Hubble Fellowship grant HST-HF-51312.01 awarded by STScI, which is operated by the Association of Universities for Research in Astronomy for NASA, under contract NAS 5-26555. Follow-up imaging through the FrontierSN program is supported by NASA through HST grant GO-13386. A.V.F.'s group at the University of California Berkeley has received generous financial assistance from the Christopher R. Redlich Fund, the TABASGO Foundation, Gary and Cynthia Bengier, and NSF grant AST-1211916. The Dark Cosmology Centre is funded by the Danish National Research Foundation. Support for A.Z. was provided by NASA through Hubble Fellowship grant HF2-51334.001-A awarded by STScI. SN research at Rutgers University is supported in part by NSF CAREER award AST-0847157 to S.W.J.. J.C.M. is supported by NSF grant AST-1313484 and by NASA HST grants GO-13343 and GO-13386; this research was carried out in part at the Jet Propulsion Laboratory, California Institute of Technology, under a contract with NASA. R.G. acknowledges the Centre National d'Etudes

Spatiales for financial support on the GLASS project. Some of the data presented here were obtained at the W. M. Keck Observatory, which is operated as a scientific partnership among the California Institute of Technology, the University of California, and NASA; the observatory was made possible by the generous financial support of the W. M. Keck Foundation. The HST imaging data used in this paper can be obtained from the Barbara A. Mikulski Archive for Space Telescopes at <https://archive.stsci.edu>, and the Keck-I LRIS spectra can be obtained at <http://hercules.berkeley.edu/database>.

SUPPLEMENTARY MATERIALS

www.sciencemag.org/content/347/6226/1123/suppl/DC1
Materials and Methods
Figs. S1 to S4
Tables S1 to S2
References (24–32)

21 November 2014; accepted 10 February 2015
10.1126/science.aaa3350

STELLAR DYNAMICS

The fastest unbound star in our Galaxy ejected by a thermonuclear supernova

S. Geier,^{1,2*} F. Fürst,³ E. Ziegerer,² T. Kupfer,⁴ U. Heber,² A. Irrgang,² B. Wang,⁵ Z. Liu,^{5,6} Z. Han,⁵ B. Sesar,^{7,8} D. Levitan,⁷ R. Kotak,⁹ E. Magnier,¹⁰ K. Smith,⁹ W. S. Burgett,¹⁰ K. Chambers,⁸ H. Flewelling,⁸ N. Kaiser,⁸ R. Wainscoat,⁸ C. Waters¹⁰

Hypervelocity stars (HVSs) travel with velocities so high that they exceed the escape velocity of the Galaxy. Several acceleration mechanisms have been discussed. Only one HVS (US 708, HVS 2) is a compact helium star. Here we present a spectroscopic and kinematic analysis of US 708. Traveling with a velocity of ~1200 kilometers per second, it is the fastest unbound star in our Galaxy. In reconstructing its trajectory, the Galactic center becomes very unlikely as an origin, which is hardly consistent with the most favored ejection mechanism for the other HVSs. Furthermore, we detected that US 708 is a fast rotator. According to our binary evolution model, it was spun-up by tidal interaction in a close binary and is likely to be the ejected donor remnant of a thermonuclear supernova.

According to the widely accepted theory for the acceleration of hypervelocity stars (HVSs) (1–3), a close binary is disrupted by the supermassive black hole (SMBH) in the center of our Galaxy, and one component is ejected as a HVS (4). In an alternative scenario, US 708 was proposed to be ejected from an ultracompact binary star by a thermonuclear supernova type Ia (SN Ia) (5). However, previous observational evidence was insufficient to put firm constraints on its past evolution. Here we show that US 708 is the fastest unbound star in our Galaxy, provide evidence for the SN ejection scenario, and identify a progenitor population of SN Ia.

In contrast to all other known HVSs, US 708 has been classified as a hot subdwarf star [subdwarf O- or B-type (sdO/B) star]. Those stars are evolved, core helium-burning objects with low masses around 0.5 times the mass of the Sun (M_{\odot}). About half of the sdB stars reside in close binaries with periods ranging from ~0.1 to ~30 days (6, 7). The hot subdwarf is regarded as

the core of a former red giant star that has been stripped of almost all of its hydrogen envelope through interaction with a close companion star (8, 9). However, single hot subdwarf stars like US 708 are known as well. Even in this case, binary evolution has been proposed, as the merger of two helium white dwarfs (He-WDs) is a possible formation channel for those objects (10).

The hot subdwarf nature of US708 poses a particular challenge for theories that aim to explain the acceleration of HVSs. Within the slingshot scenario proposed by Hills, a binary consisting of two main-sequence stars is disrupted by the close encounter with the SMBH in the center of our Galaxy. While one of the components remains in a bound orbit around the black hole, the other one is ejected with high velocity (4). This scenario explains the existence of the so-called S-stars orbiting the SMBH in the Galactic center and provides the most convincing evidence for the existence of this black hole (11). It is also consistent with the main properties of the known HVS population consisting of young main-sequence

stars (12, 13). However, more detailed analyses of some young HVSs challenge the Galactic center origin (14), and most recently, a new population of old main-sequence stars likely to be HVSs has been discovered. Most of those objects are also unlikely to originate from the Galactic center, but the acceleration mechanism remains unclear (15).

In the case of the helium-rich sdO (He-sdO) US 708, the situation is even more complicated. In contrast to all other known HVSs, which are normal main-sequence stars of different ages, this star is in the phase of shell helium burning, which lasts for only a few tens of millions of years. More importantly, it has been formed by close binary interaction. To accelerate a close binary star to such high velocity, the slingshot mechanism requires either a binary black hole (16) or the close encounter of a hierarchical triple system, where the distant component becomes bound to the black hole and the two close components are ejected (17). Similar constraints apply to the dynamical ejection out of a dense cluster, which is the second main scenario discussed to explain the HVSs.

Close binarity requires specific modifications of the canonical HVS scenarios. However, it is a necessary ingredient for an alternative scenario, in which US 708 is explained as the ejected donor

¹European Southern Observatory, Karl-Schwarzschild-Straße 2, 85748 Garching, Germany. ²Dr. Karl Remeis-Observatory and Erlangen Centre for Astroparticle Physics, Astronomical Institute, Friedrich-Alexander University Erlangen-Nuremberg, Sternwartstraße 7, 96049 Bamberg, Germany. ³Space Radiation Lab, MC 290-17 Cahill, California Institute of Technology, 1200 East California Boulevard, Pasadena, CA 91125, USA. ⁴Department of Astrophysics/Institute for Mathematics, Astrophysics and Particle Physics, Radboud University Nijmegen, P.O. Box 9010, 6500 GL Nijmegen, Netherlands. ⁵Key Laboratory of the Structure and Evolution of Celestial Objects, Yunnan Observatories, Chinese Academy of Sciences, Kunming 650011, China. ⁶Argelander-Institut für Astronomie, Universität Bonn, Auf dem Hügel 71, 53121 Bonn, Germany. ⁷Division of Physics, Mathematics, and Astronomy, California Institute of Technology, 1200 East California Boulevard, Pasadena, CA 91125, USA. ⁸Max-Planck-Institut für Astronomie, Königstuhl 17, 69117, Heidelberg, Germany. ⁹Astrophysics Research Center, School of Mathematics and Physics, Queen's University Belfast, Belfast BT7 1NN, UK. ¹⁰Institute for Astronomy, University of Hawaii at Manoa, Honolulu, HI 96822, USA.

*Corresponding author. E-mail: sgeier@eso.org

remnant of a thermonuclear SN Ia (18, 19). Underluminous SN Ia have been proposed to originate from a so-called “double detonation” of a white dwarf (WD) (20, 21). In this scenario, a massive WD is closely orbited by a low-mass helium star. Due to a tightening of the orbit, the helium star will start to transfer mass to its compact companion. After a critical amount of helium

is deposited on the surface of the WD through accretion, the helium is ignited, causing a detonation wave that triggers the explosion of the carbon-oxygen WD itself. The ultracompact sdB+WD binary CD -30° 11223 has recently been identified as progenitor candidate for such a scenario and has been linked to the putative ejected donor remnant US 708 (5, 22).

Fig. 1. Fit of model spectrum.

The fit of synthetic models to the helium and nitrogen lines of a Keck/ESI spectrum of US 708 is shown. The normalized fluxes of the single lines are shifted by constant values c for better visualization, and the most prominent lines are labeled. The weaker lines are from N III at 4634 and 4640 Å, He I at 4713 Å (spectral region in the middle), N III at 4379 Å, and He I at 4387 Å (spectral region at the bottom). The shift with respect to the rest wavelengths $\Delta\lambda$ (dashed vertical line) caused by the high radial velocity and the substantial broadening of the lines are clearly visible.

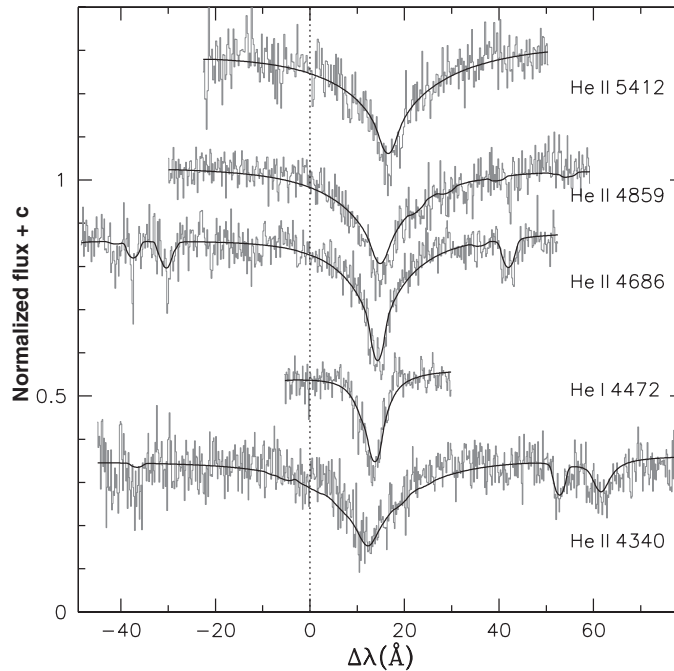


Table 1. Parameters of US 708. The uncertainty of the radial velocity is the 1σ error from a χ^2 fit, the uncertainties in the proper motion components have been propagated from the position errors by linear regression, and the uncertainties in the atmospheric parameters are bootstrap errors. The uncertainties of the other parameters have been propagated from the uncertainties of the input parameters. N/A, not applicable.

Parameter	Abbreviation	Unit	Value
Visual magnitude*	m_g	mag	18.668 ± 0.008
Proper motion	$\mu_\alpha \cos \delta$	milli-arc sec year $^{-1}$	-8.0 ± 1.8
	μ_δ	milli-arc sec year $^{-1}$	9.1 ± 1.6
Radial velocity	v_{helio}	km s $^{-1}$	917 ± 7
Galactic Cartesian coordinates	X	kpc	-14.2 ± 0.7
	Y	kpc	0.4 ± 0.1
	Z	kpc	6.2 ± 0.7
Galactic velocity components	v_X	km s $^{-1}$	-855 ± 61
	v_Y	km s $^{-1}$	643 ± 77
	v_Z	km s $^{-1}$	431 ± 58
Galactic rest-frame velocity	v_{grf}	km s $^{-1}$	1157 ± 53
Effective temperature	T_{eff}	K	47200 ± 400
Surface gravity	$\log g$	N/A	5.69 ± 0.09
Helium abundance	$\log y$	N/A	+2.0
Nitrogen abundance	$\log \frac{N(\text{N})}{N(\text{H})}$	N/A	-2.4 ± 0.2
Projected rotational velocity	$v_{\text{rot}} \sin i$	km s $^{-1}$	115 ± 8
Mass (adopted)	M_{sdB}	M_\odot	0.3
Distance	d	kpc	8.5 ± 1.0

*Taken from the Sloan Digital Sky Survey (SDSS) Data Server (das.sdss.org)

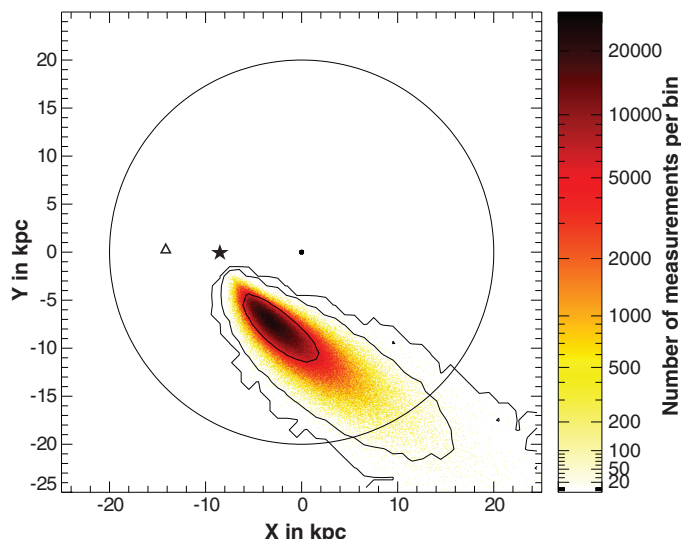
We performed a detailed spectroscopic and kinematic analysis of US 708 based on recently obtained and archival data to trace back its origin and constrain the ejection mechanism. To determine the three-dimensional motion of US 708, both the radial and tangential velocity components have to be determined. We measured the radial velocity from new spectra taken with the Keck and Palomar telescopes and compared it with archival data. We also derived atmospheric parameters and a spectroscopic distance from the new spectra (Fig. 1). In addition, we determined the proper motion by combining archival positions with new measurements from the PanSTARRS survey (fig. S2 and Table 1).

With a Galactic rest-frame velocity of 1157 ± 53 km s $^{-1}$, we find that US 708 is the fastest known unbound star in our Galaxy. Its current distance is 8.5 ± 1.0 kpc, and it is moving away from the Galactic plane into the halo. Tracing back its trajectory and assuming no further deviations, we deduced that it crossed the Galactic disc 14.0 ± 3.1 million years ago. In this way, an origin in the center of our Galaxy can be excluded with high confidence (Fig. 2), but the origin in the Galactic disc is fully consistent with the SN ejection scenario. In contrast to regular SN Ia, double-detonation SN Ia with hot subdwarf donors are predicted to happen in young stellar populations (5).

Both the current Galactic rest-frame velocity and the reconstructed ejection velocity from the Galactic disc (998 ± 68 km s $^{-1}$) are substantially higher than the value published before (~ 750 km s $^{-1}$, based on radial velocity alone) (2). This puts new constraints on the possible progenitor system, which can be derived from the observed parameters of US 708. To reach such a high ejection velocity, the progenitor binary must have been very compact and the WD companion rather massive. The likely progenitor system consists of a compact helium star with a mass of $\sim 0.3 M_\odot$ and a massive carbon-oxygen WD (1.0 to $1.2 M_\odot$) with an orbital period of ~ 10 min. We calculated the mass-transfer rate in such a binary and found that the helium is accreted by the WD at a rate suitable for the double-detonation scenario [10^{-9} to $10^{-8} M_\odot$ year $^{-1}$ (5)]. Such ultrashort-period systems with compact helium stars have indeed been observed. The eclipsing He-WD+CO-WD binary SDSS J065133+284423 has an orbital period of only 12 min (23). However, the mass of the CO-WD ($0.55 M_\odot$) is too low for a double-detonation SN Ia.

The ejection from such a close binary should leave another imprint on the remnant. We know that hot subdwarfs in compact binaries have been spun up by the tidal influence of the close companion (22, 24, 25) to projected rotational velocities ($v_{\text{rot}} \sin i$) that are substantially higher than the projected rotational velocities of single hot subdwarfs (26, 27). An ejected remnant is predicted to have a high $v_{\text{rot}} \sin i$ as well (28), and indeed we measured $v_{\text{rot}} \sin i = 115 \pm 8$ km s $^{-1}$, which is substantially higher than expected for a single He-sdO (Fig. 1) (27). However, assuming an ultracompact progenitor binary, the measured

Fig. 2. Origin of US 708. A Monte Carlo simulation (10^8 iterations) of the past trajectory of US 708 is shown. The color-coded bins mark the positions where the star crossed the Galactic disc, which is shown pole-on. The contours correspond to the 1σ , 3σ , and 5σ confidence limits. The position of the Galactic center is denoted by the black dot, the position of the Sun is given by the star symbol, and the current position of US 708 is marked by a triangle and given in Table 1.



$v_{\text{rot}} \sin i$ of the He-sdO is still slower than expected by about a factor of four. A high loss of mass and angular momentum caused by the SN impact is predicted for main-sequence companions in the standard single-degenerate SN Ia scenario, in which mass is transferred from such a companion to a WD (29–31). Though the loss of mass and angular momentum for a more compact companion like US 708 is expected to be smaller, our results indicate that it is still substantial. This puts important observational constraints on more detailed models.

Whereas the observed properties of US 708 are consistent with the SN ejection scenario, they are hardly compatible with the slingshot mechanism because an origin of the star in the center of the Galaxy is very unlikely (Fig. 2; see also the additional explanation in the supplementary materials). However, it must be stated that the SN ejection scenario is only applicable to such compact helium stars and cannot be invoked to explain the acceleration of the other HVs.

Depending on the pollution by SN material, the effect of the SN impact, and the subsequent stellar evolution, the surface abundances of US 708 might be substantially affected. Ultraviolet spectroscopy is necessary to measure the metal abundances of US 708 and put further constraints on the extreme history of this star, which witnessed a SN from a distance of less than 0.2 solar radii.

In providing evidence that US 708 is probably the donor remnant of a helium double-detonation SN Ia, we have shown an acceleration mechanism for the fastest unbound stars in our Galaxy. With that, we have also made an important step forward in understanding SN Ia explosions in general. Despite the fact that those bright events are used as standard candles to measure the expansion (and acceleration) of the universe, their progenitors are still unknown. Our results suggest that, due to the high WD masses derived for the progenitor binary, the double-detonation scenario might not only be applicable to some underluminous SN Ia (5, 21) but might also con-

tribute to the population of typical SNe Ia used as cosmic yardsticks (20).

REFERENCES AND NOTES

- W. R. Brown, M. J. Geller, S. J. Kenyon, M. J. Kurtz, *Astrophys. J.* **622**, L33–L36 (2005).
- H. A. Hirsch, U. Heber, S. J. O'Toole, F. Bresolin, *Astron. Astrophys.* **444**, L61–L64 (2005).
- H. Edelmann, R. Napiwotzki, U. Heber, N. Christlieb, D. Reimers, *Astrophys. J.* **634**, L181–L184 (2005).
- J. G. Hills, *Nature* **331**, 687–689 (1988).
- S. Geier *et al.*, *Astron. Astrophys.* **554**, A54 (2013).
- P. F. L. Maxted, U. Heber, T. R. Marsh, R. C. North, *Mon. Not. R. Astron. Soc.* **326**, 1391–1402 (2001).
- R. Napiwotzki *et al.*, *Astrophys. Space Sci.* **291**, 321–328 (2004).
- Z. Han, Ph. Podsiadlowski, P. F. L. Maxted, T. R. Marsh, N. Ivanova, *Mon. Not. R. Astron. Soc.* **336**, 449–466 (2002).
- Z. Han, Ph. Podsiadlowski, P. F. L. Maxted, T. R. Marsh, *Mon. Not. R. Astron. Soc.* **341**, 669–691 (2003).
- R. F. Webbink, *Astrophys. J.* **277**, 355–360 (1984).
- S. Gillessen *et al.*, *Astrophys. J.* **692**, 1075–1109 (2009).
- W. R. Brown, J. G. Cohen, M. J. Geller, S. J. Kenyon, *Astrophys. J.* **754**, L2 (2012).
- B. C. Bromley, S. J. Kenyon, M. J. Geller, W. R. Brown, *Astrophys. J.* **749**, L42 (2012).
- U. Heber, H. Edelmann, R. Napiwotzki, M. Altmann, R.-D. Scholz, *Astron. Astrophys.* **483**, L21–L24 (2008).
- L. E. Palladino *et al.*, *Astrophys. J.* **780**, 7 (2014).
- Y. Lu, Q. Yu, D. N. C. Lin, *Astrophys. J.* **666**, L89–L92 (2007).
- H. P. Perets, *Astrophys. J.* **698**, 1330–1340 (2009).
- B. Wang, X. Meng, X. Chen, Z. Han, *Mon. Not. R. Astron. Soc.* **395**, 847–854 (2009).
- S. Justham, C. Wolf, Ph. Podsiadlowski, Z. Han, *Astron. Astrophys.* **493**, 1081–1091 (2009).
- M. Fink *et al.*, *Astron. Astrophys.* **514**, A53 (2010).
- R. Foley *et al.*, *Astrophys. J.* **767**, 57 (2013).
- S. Vennes, A. Kawka, S. J. O'Toole, P. Németh, D. Burton, *Astrophys. J.* **759**, L25 (2012).
- W. R. Brown *et al.*, *Astrophys. J.* **737**, L23 (2011).
- S. Geier *et al.*, *Astron. Astrophys.* **464**, 299–307 (2007).
- S. Geier *et al.*, *Astron. Astrophys.* **519**, A25 (2010).
- S. Geier, U. Heber, *Astron. Astrophys.* **543**, A149 (2012).
- H. Hirsch, U. Heber, *J. Phys. Conf. Ser.* **172**, 012015 (2009).
- K.-C. Pan, P. M. Ricker, R. E. Taam, *Astrophys. J.* **773**, 49 (2013).
- K.-C. Pan, P. M. Ricker, R. E. Taam, *Astrophys. J.* **750**, 151 (2012).

30. K.-C. Pan, P. M. Ricker, R. E. Taam, *Astrophys. J.* **760**, 21 (2012).

31. Z.-W. Liu *et al.*, *Astron. Astrophys.* **554**, A109 (2013).

ACKNOWLEDGMENTS

We thank H. Hirsch for providing us with the Low Resolution Imaging Spectrometer spectra. This work is based on observations obtained at the W.M. Keck Observatory, which is operated as a scientific partnership among the California Institute of Technology, the University of California, and NASA. The W. M. Keck Observatory was made possible by the generous financial support of the W. M. Keck Foundation. We wish to recognize the important cultural role and reverence that the summit of Mauna Kea has always had within the indigenous Hawaiian community. We are most fortunate to have the opportunity to conduct observations from this mountain. This work is also based on observations at the Palomar Observatory. The Pan-STARRS1 Surveys (PS1) have been made possible through contributions from the Institute for Astronomy, the University of Hawaii, the Pan-STARRS Project Office, the Max-Planck Society and its participating institutes (the Max Planck Institute for Astronomy, Heidelberg, and the Max Planck Institute for Extraterrestrial Physics, Garching), The Johns Hopkins University, Durham University, the University of Edinburgh, Queen's University Belfast, the Harvard-Smithsonian Center for Astrophysics, the Las Cumbres Observatory Global Telescope Network, the National Central University of Taiwan, the Space Telescope Science Institute, the NASA under grant no. NNX08AR22G issued through the Planetary Science Division of the NASA Science Mission Directorate, the NSF under grant no. AST-1238877, the University of Maryland, and Eotvos Lorand University (ELTE). Z.H. is supported by the Natural Science Foundation of China (grant nos. 11390374 and 11033008). E.Z. and A.I. are supported by the Deutsche Forschungsgemeinschaft through grant HE1356/45-2. T.K. acknowledges support from the Netherlands Research School for Astronomy (NOVA). A.I. acknowledges support from a research scholarship by the Elite Network of Bavaria. R.K. acknowledges support from Science and Technologies Council UK grant no. ST/L000709/1, Queen's University Belfast's contribution to the PanSTARRS1 science consortium. K.S. acknowledges support from European Union FP7 Programme ERC grant no. 291222. F.F. acknowledges NASA contract no. NNG08FD60C for the NuSTAR mission. The data observed with the SDSS and Keck telescope are published via the SDSS and Keck data archive; the PS1 data and catalog are available upon request.

SUPPLEMENTARY MATERIALS

www.sciencemag.org/content/347/6226/1126/suppl/DC1
Materials and Methods
Supplementary Text
Figs. S1 to S7
References (32–57)

22 July 2014; accepted 29 January 2015
10.1126/science.1259063

QUANTUM ELECTRONICS

Probing Johnson noise and ballistic transport in normal metals with a single-spin qubit

S. Kolkowitz,^{1*} A. Safra,^{1*} A. A. High,^{1,2} R. C. Devlin,² S. Choi,¹ Q. P. Unterreithmeier,¹ D. Patterson,¹ A. S. Zibrov,¹ V. E. Manucharyan,³ H. Park,^{1,2†} M. D. Lukin^{1†}

Thermally induced electrical currents, known as Johnson noise, cause fluctuating electric and magnetic fields in proximity to a conductor. These fluctuations are intrinsically related to the conductivity of the metal. We use single-spin qubits associated with nitrogen-vacancy centers in diamond to probe Johnson noise in the vicinity of conductive silver films. Measurements of polycrystalline silver films over a range of distances (20 to 200 nanometers) and temperatures (10 to 300 kelvin) are consistent with the classically expected behavior of the magnetic fluctuations. However, we find that Johnson noise is markedly suppressed next to single-crystal films, indicative of a substantial deviation from Ohm's law at length scales below the electron mean free path. Our results are consistent with a generalized model that accounts for the ballistic motion of electrons in the metal, indicating that under the appropriate conditions, nearby electrodes may be used for controlling nanoscale optoelectronic, atomic, and solid-state quantum systems.

Understanding electron transport, dissipation, and fluctuations at submicrometer length scales is critical for the continued miniaturization of electronic (1, 2) and optical devices (3–5), as well as atom and ion traps (6–10), and for the electrical control of solid-state quantum circuits (11). Although it is well known that electronic transport in small samples defies the conventional wisdom associated with macroscopic devices, resistance-free transport is difficult to observe directly. Most of the measurements demonstrating these effects make use of ohmic contacts attached to submicrometer-scale samples and observe quantized but finite resistance corresponding to the voltage drop at the contact of such a system with a macroscopic conductor (12, 13). Techniques for noninvasive probing of electron transport are being actively explored (14, 15), because they can provide insights into electronic dynamics at small length scales. Our approach makes use of the electromagnetic fluctuations associated with Johnson noise close to a conducting surface, which can be directly linked to the dielectric function at similar length scales, providing a noninvasive probe of electronic transport inside the metal. Measurements of these fluctuations at micrometer length scales with cold, trapped atoms showed excellent agreement with predictions based on diffusive electron motion (7–9), whereas millimeter-length scale measurements with superconducting quantum interference devices (SQUIDs) have been demonstrated for use as an accurate, contact-free thermometer (16).

Our approach makes use of the electronic spin associated with nitrogen-vacancy (NV) defect centers in diamond to study the spectral,

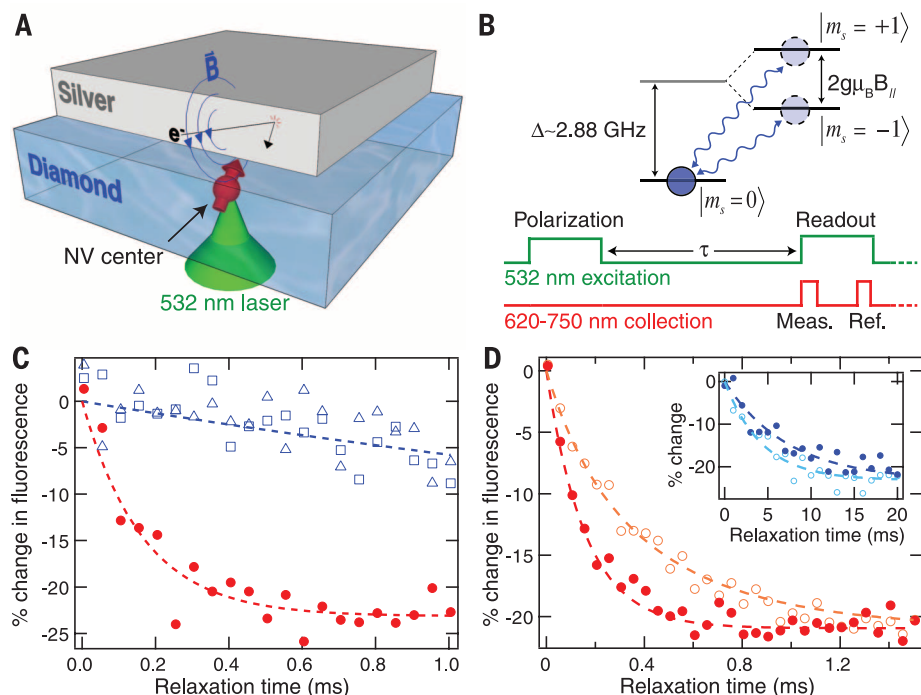


Fig. 1. Probing Johnson noise with single-spin qubits. (A) The thermally induced motion of electrons in silver generates fluctuating magnetic fields (\vec{B}), which are detected with the spin of a single NV. The NV is polarized and read out through the back side of the diamond. (B) The NV spin is polarized into the $|m_s = 0\rangle$ state using a green laser pulse. Spin relaxation into the $|m_s = \pm 1\rangle$ states is induced by magnetic field noise at ~ 2.88 GHz. After wait time τ , the population left in $|m_s = 0\rangle$ is read out by spin-dependent fluorescence. All measurements shown were performed at low magnetic fields ($\Delta \gg g\mu_B B_{||}/\hbar$). (C) Spin relaxation data for the same single shallow-implant NV before silver deposition (open blue squares), with silver deposited (red circles) and after the silver has been removed (open blue triangles). (D) Spin relaxation for a single NV close to a silver film prepared in the $|m_s = 0\rangle$ state (red circles) and in the $|m_s = -1\rangle$ state (open orange circles). (Inset) Spin relaxation for a single native NV in bulk diamond in the $|m_s = 0\rangle$ state (blue circles) and in the $|m_s = -1\rangle$ state (open light blue circles).

¹Department of Physics, Harvard University, Cambridge, MA 02138, USA. ²Department of Chemistry and Chemical Biology, Harvard University, Cambridge, MA 02138, USA. ³Department of Physics, University of Maryland, College Park, MD 20742, USA.

*These authors contributed equally to this work. †Corresponding author. E-mail: lukin@physics.harvard.edu (M.D.L.); hongkun_park@harvard.edu (H.P.)

spatial, and temperature dependence of Johnson noise emanating from conductors. The magnetic Johnson noise results in a reduction of the spin lifetime of individual NV electronic spins, thereby allowing us to probe the intrinsic properties of the conductor noninvasively over a wide range of parameters. Individual, optically resolvable NV centers are implanted ~ 15 nm below the surface of a ~ 30 - μm -thick diamond sample. A silver film is then deposited or positioned on the diamond surface (Fig. 1A). The spin sublevels $|m_s = 0\rangle$ and $|m_s = \pm 1\rangle$ of the NV electronic ground state exhibit a zero-field splitting of $\Delta = 2\pi \times 2.88$ GHz (17–20). The relaxation rates between the $|m_s = 0\rangle$ and $|m_s = \pm 1\rangle$ states provide a sensitive probe of the magnetic field noise at the transition frequencies $\omega_{\pm} = \Delta \pm 2g\mu_B B_{||}$, where $B_{||}$ is the magnetic field along the NV axis, $g \approx 2$ is the electron g -factor, and μ_B is the Bohr magneton (21, 22) (Fig. 1B).

The impact of Johnson noise emanating from a polycrystalline silver film deposited on the diamond surface (Fig. 1C) is evident when comparing the relaxation of a single NV spin below the silver (red circles) to the relaxation of the same NV before film deposition and after removal of the silver (open blue squares and triangles, respectively). At room temperature and

in the absence of external noise, the spin lifetime is limited by phonon-induced relaxation to $T_1^{\text{ph}} \approx 4$ ms. With the silver nearby, the lifetime of the $|m_s = 0\rangle$ state is reduced to $T_1 = 165$ μs , which we attribute to magnetic Johnson noise emanating from the film. To verify that the enhanced relaxation is due to magnetic noise, we compare the lifetime of the $|m_s = 0\rangle$ state, which has magnetic dipole allowed transitions to both of the $|m_s = \pm 1\rangle$ states, to that of the $|m_s = -1\rangle$ state, which can only decay directly to the $|m_s = 0\rangle$ state (Fig. 1D). As expected for relaxation induced by magnetic noise, the $|m_s = -1\rangle$ state has approximately twice the lifetime of the $|m_s = 0\rangle$ state (23). This is in contrast to the observed lifetimes when limited by phonon-induced relaxation (Fig. 1D, inset), where the $|m_s = 0\rangle$ and $|m_s = \pm 1\rangle$ states have almost identical lifetimes (24). In what follows, we define T_1 as the lifetime of the $|m_s = 0\rangle$ state.

To test the scaling of Johnson noise with distance (d) to the metal, we deposit a layer of SiO_2 on the diamond surface with a gradually increasing thickness (Fig. 2A). We characterize the thickness of the SiO_2 layer as a function of position on the sample (Fig. 2B, inset) and deposit a 60-nm polycrystalline silver film on top of the SiO_2 . The conductivity of the silver film is measured to be 2.9×10^7 S/m at room temperature. By measuring the relaxation rates $\Gamma = 1/T_1$ of individual NVs at different positions along the SiO_2 ramp, we extract the distance dependence of the noise (Fig. 2B), with the uncertainty in the distance dominated by the variation in the implanted depth of the NVs (taken to be 15 ± 10 nm). To ensure that the measured rates are Johnson noise limited, we measure the spin relaxation of 5 to 10 randomly selected NVs per location along the ramp and plot the minimum observed rate at each location (23). As expected (7–9), the magnitude of the noise increases as the NVs approach the silver surface.

To investigate the dependence of the noise on temperature and conductivity, we deposit a 100-nm polycrystalline silver film on a diamond sample and measure the T_1 of a single NV beneath the silver over a range of temperatures (~ 10 to 295 K). The measured relaxation rate for a single NV near the silver increases with temperature (red circles in Fig. 3A), as expected for thermal noise, but the scaling is clearly nonlinear. This can be understood by recognizing that the conductivity of the silver film is also a function of temperature and that the magnitude of the thermal currents in the silver depends on the conductivity. To account for this effect, a four-point resistance measurement of the silver film is performed to determine the temperature dependence of the bulk conductivity of the silver film (Fig. 3B).

To analyze the dependence of the NV spin relaxation rate on distance, temperature, and conductivity, we use the model of (6), in which an electronic spin-1/2 qubit with Larmor frequency ω_L is positioned at a distance d from the surface of a metal. For silver at room temperature,

the skin depth at ω_L is $\delta \approx 1$ μm ; consequently, when $d < 100$ nm, we are in the “quasi-static” limit $d \ll \delta$. The thermal limit $k_B T \gg \hbar \omega_L$ is valid for all temperatures in this work. In this regime, the magnetic noise spectral density perpendicular to the silver surface is given by

$$S_B^z = \frac{\mu_0^2 k_B T \sigma}{16\pi d} \quad (1)$$

where σ is the temperature-dependent conductivity of the metal as defined by the Drude model. This scaling can be intuitively understood by considering the magnetic field generated by a single thermal electron in the metal at the NV position, $B_0 = \frac{\mu_0 e v_{\text{th}}}{4\pi d^2}$, where the thermal velocity $v_{\text{th}} \propto \sqrt{k_B T/m_e}$, m_e is the effective mass of electrons in silver, and e is the electron charge. In the limit $d \ll \delta$, screening can be safely ignored, and the NV experiences the magnetic field

spectrum arising from N independent electrons in a volume V ; $S_B \propto V n(B_0)^2 \tau_c$, where n is the electron density and τ_c is the correlation time of the noise, given by the average time between electron scattering events; and $\tau_c = l/v_F$, where l is the electron mean free path and v_F is the Fermi velocity. Recognizing that the NV is sensitive to the motion of electrons within a sensing volume $V \propto d^3$, we arrive at the scaling given by Eq. 1, with $\sigma = \frac{ne^2 \tau_c}{m_e}$. Applying Fermi's golden rule and accounting for the orientation and spin-1 of the NV yields the relaxation rate for the $|m_s = 0\rangle$ state

$$\Gamma = \frac{1}{T_1} = \frac{3g^2 \mu_B^2}{2\hbar^2} S_B^z \left(1 + \frac{1}{2} \sin^2(\theta)\right) \quad (2)$$

where $g \approx 2$ is the electron g -factor, μ_B is the Bohr magneton, and $\theta \approx 54.7^\circ$ is the angle of the

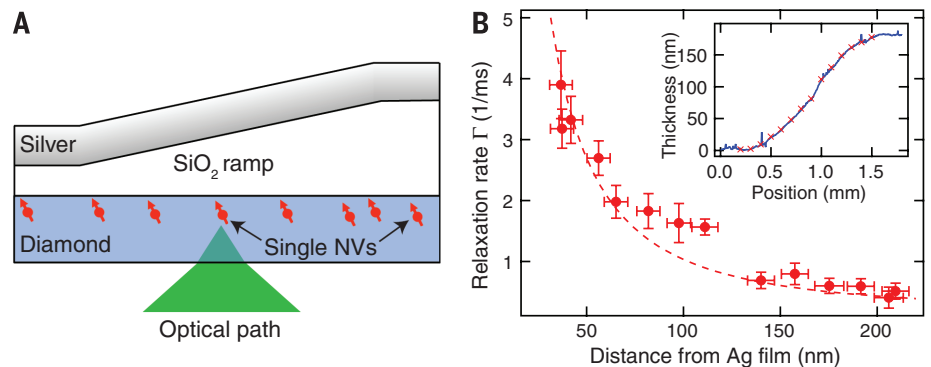


Fig. 2. Distance dependence of NV relaxation close to silver. (A) A gradual SiO_2 ramp (slope of ~ 0.2 nm/ μm) is grown on the diamond surface, followed by a 60-nm silver film. (B) The NV relaxation rate is measured as a function of position along the ramp, which is then converted to distance to the film. At each point, 5 to 10 NV centers are measured, and the minimum rate measured is plotted (red circles). The horizontal error bars reflect 1 SD in the estimated distance to the film including the uncertainty in NV depth, while the vertical error bars reflect 1 SD in the fitted relaxation rate. The red dashed line shows the expected relaxation rate with no free parameters after accounting for the finite silver film thickness. (Inset) Thickness of the ramp as a function of lateral position along the diamond sample (blue curve). The red crosses correspond to the positions along the sample where the measurements were taken.

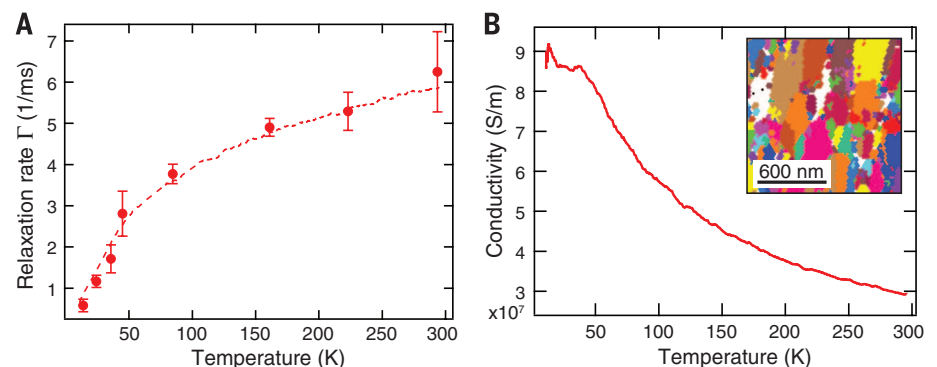


Fig. 3. Temperature dependence of NV relaxation close to polycrystalline silver. (A) The measured relaxation rate of a single NV spin under a polycrystalline silver film as a function of temperature (red data points). The error bars reflect 1 SD in the fitted relaxation rate. The conductivity of the silver film as a function of temperature shown in (B) is included in a fit to Eq. 2, with the distance to the film as the single free parameter (red dashed line). The extracted distance is 31 ± 1 nm. (B) The conductivity of the 100-nm-thick polycrystalline silver film deposited on the diamond surface is measured as a function of temperature. (Inset) Grain boundaries within the polycrystalline silver film, imaged using electron backscatter diffraction. The average grain diameter is 140 nm, with a SD of 80 nm.

NV dipole relative to the surface normal vector (23). In Fig. 2B, the inverse scaling with distance d predicted by Eq. 1 is clearly evident for NVs very close to the silver. At distances comparable to the silver film thickness, Eq. 1 is no longer valid, but we recover excellent agreement with the no-free-parameters prediction of Eq. 2 by including a correction for the thickness of the silver film (red dashed line in Fig. 2B), which is measured independently. The measured relaxation rates as a function of temperature are also in excellent agreement with the predictions of Eq. 2 (red dashed line in Fig. 3A), while the extracted distance of 31 ± 1 nm is consistent with the expected depth (23).

Notably, very different results are obtained when we replace the polycrystalline film with single-crystal silver. For this experiment, a 1.5- μm -thick single-crystal silver film grown by sputtering onto silicon (23, 25, 26) is placed in contact with the diamond surface. The measured conductivity of the single-crystal silver exhibits a much stronger temperature dependence (blue line in Fig. 4A) as compared to that of the 100-nm-thick polycrystalline film. Figure 4B

presents the measured relaxation rate as a function of temperature for an NV in a region in direct contact with the single-crystal silver (blue squares). The dashed blue line corresponds to the temperature-dependent rate predicted by Eq. 2, which strongly disagrees with the experimental results. Specifically, because the measured silver conductivity increases faster than the temperature decreases in the range from room temperature down to 40 K, Eq. 2 predicts that the relaxation rate should increase as the temperature drops, peaking at 40 K and then dropping linearly with temperature once the conductivity saturates. Instead, the T_1 of the NV consistently increases as the temperature drops, implying that at lower temperatures, the silver produces considerably less noise than expected from Eq. 2. We observe similar deviation from the prediction of Eq. 2 for all 23 NVs measured in the vicinity of the single-crystal silver (23).

To analyze these observations, we note that the conventional theoretical approach (6) resulting in Eq. 2 treats the motion of the electrons in the metal as entirely diffusive, using Ohm's law,

$\mathbf{J}(\mathbf{r}, t) = \sigma \mathbf{E}(\mathbf{r}, t)$, to associate the bulk conductivity of the metal with the magnitude of the thermal currents. While accurately describing the observed relaxation rates next to the polycrystalline material, where the resistivity of the film is dominated by electron scattering off grain boundaries (Fig. 3B, inset), this assumption is invalid in the single-crystal silver film experiments, particularly at low temperatures. Here, the measured conductivity of the single-crystal film indicates that the mean free path l is greater than 1 μm , considerably exceeding the sensing region determined by the NV-metal separation, and thus the ballistic motion of the electrons must be accounted for. Qualitatively, the correlation time of the magnetic noise in this regime is determined by the ballistic time of flight of electrons through the relevant interaction region $\tau_c \sim d/v_F$ (Fig. 4C). This results in a saturation of the noise spectral density and the spin relaxation rate Γ as either the NV approaches the silver surface or the mean free path becomes longer at lower temperatures (23), with the ultimate limit to the noise spectrum given by:

$$S_B^z = \frac{2 \mu_0^2 k_B T}{\pi} \frac{ne^2}{m_e v_F} \quad (3)$$

This regime of magnetic Johnson noise was recently analyzed theoretically (11) using the Lindhard form nonlocal dielectric function for the metal modified for finite electron scattering times (23, 27, 28). Comparison of this model (solid line in Fig. 4B) to the data, with distance again as the only free parameter, yields excellent agreement for all 23 measured NVs (23). Figure 4D shows the measured T_1 times at 103 and 27 K for each NV as a function of extracted distance (blue triangles). Of the 23 NVs measured, 15 are in a region of the diamond sample in direct contact with the silver (23). Excellent agreement between the nonlocal model (solid lines) and the data is observed for all 23 NVs at all 12 measured temperatures. Apparent in Fig. 4D is the saturation of the relaxation rate as the NV approaches the silver surface and as the mean free path becomes longer at lower temperatures (dashed black line), as predicted by Eq. 3.

Although ballistic electron motion in nanoscale structures has previously been studied and utilized (12, 13), our approach allows for non-invasive probing of this and related phenomena and provides the possibility for studying mesoscopic physics in macroscopic samples. The combination of sensitivity and spatial resolution demonstrated here enables direct probing of current fluctuations in the proximity of individual impurities, with potential applications such as imaging of Kondo states and probing of novel two-dimensional materials (29), where our technique may allow for the spatially resolved probing of edge states (12). Likewise, it could enable investigation of the origin of $1/f$ flux noise by probing magnetic fluctuations near superconducting Josephson circuits (30, 31). Finally, as Johnson noise presents an important limitation to the control of classical and quantum mechanical devices at small length scales (6–10), the present

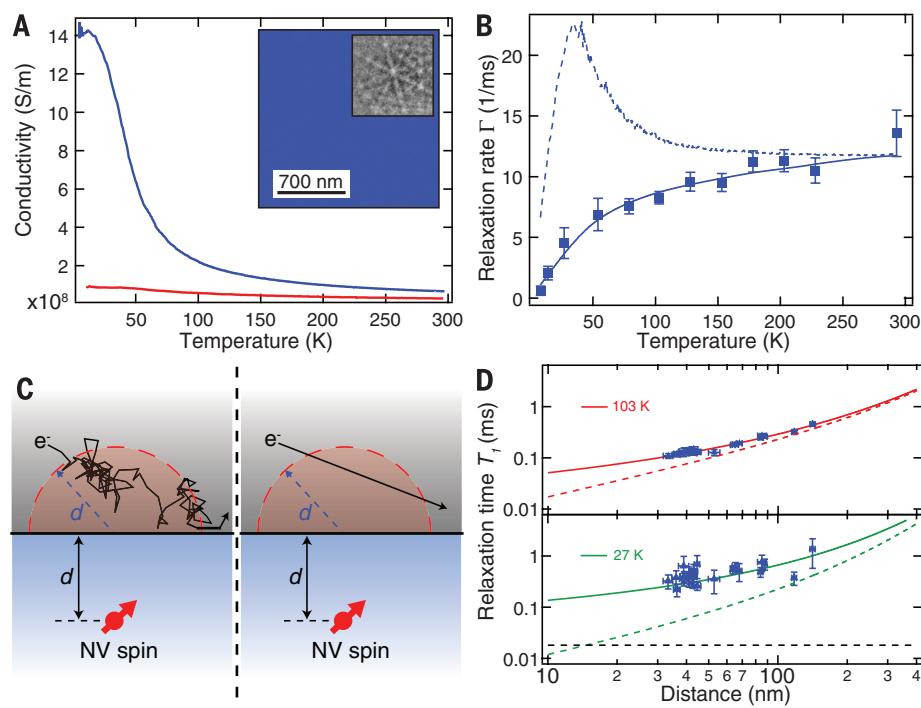


Fig. 4. Temperature dependence of NV relaxation close to single-crystal silver. (A) Measured conductivity of single-crystal (blue curve) and polycrystalline (red curve, same as Fig. 3B) silver as a function of temperature. (Inset) Electron backscatter diffraction image of the single-crystal silver film showing no grain boundaries, and the observed diffraction pattern. (B) Relaxation of a single NV spin under single-crystal silver as a function of temperature (blue squares). The error bars reflect 1 SD in the fitted relaxation rate. Equation 2 is fit to the data from 200 to 295 K (blue dashed line). A nonlocal model (23) is fit to the data (blue solid line); the extracted distance between the NV and the silver surface is 36 ± 1 nm. (C) Cartoon illustrating the relevant limits, where the noise is dominated by diffusive electron motion (left, $l \ll d$) and ballistic motion (right, $l \gg d$). (D) The same data as in (B) were taken for 23 NVs at varying distances from the film. The T_1 of each NV at 103 K (top) and 27 K (bottom) is plotted against the extracted depth (blue triangles). The horizontal error bars reflect 1 SD in the fitted distance to the film, while the vertical error bars reflect 1 SD in the fitted relaxation time. The nonlocal model (solid colored lines) saturates at a finite lifetime determined by Eq. 3 (bottom, dashed black line), whereas the local model does not (dashed colored lines).

results demonstrate that this limitation can be circumvented by operating below the length scale determined by the electron mean free path.

REFERENCES AND NOTES

1. M. Lundström, *Science* **299**, 210–211 (2003).
2. B. Weber *et al.*, *Science* **335**, 64–67 (2012).
3. Q. Xu, B. Schmidt, S. Pradhan, M. Lipson, *Nature* **435**, 325–327 (2005).
4. L. Novotny, B. Hecht, *Principles of Nano-optics* (Cambridge Univ. Press, Cambridge, 2012).
5. A. L. Falk *et al.*, *Nat. Phys.* **5**, 475–479 (2009).
6. C. Henkel, S. Pötting, M. Wilkens, *Appl. Phys. B* **69**, 379–387 (1999).
7. Y. J. Lin, I. Teper, C. Chin, V. Vuletić, *Phys. Rev. Lett.* **92**, 050404 (2004).
8. M. P. A. Jones, C. J. Vale, D. Sahagun, B. V. Hall, E. A. Hinds, *Phys. Rev. Lett.* **91**, 080401 (2003).
9. D. Harber, J. McGuirk, J. Obrecht, E. Cornell, *J. Low Temp. Phys.* **133**, 229–238 (2003).
10. M. Brownnutt, M. Kumph, P. Rabl, R. Blatt, <http://arxiv.org/abs/1409.6572> (2014).
11. L. S. Langsjoen, A. Poudel, M. G. Vavilov, R. Joynt, *Phys. Rev. A* **86**, 010301 (2012).
12. C. Beenakker, H. van Houten, *Solid State Phys.* **44**, 1–228 (1991).
13. S. Datta, *Electronic Transport in Mesoscopic Systems* (Cambridge Univ. Press, Cambridge, 1997).
14. A. C. Bleszynski-Jayich *et al.*, *Science* **326**, 272–275 (2009).
15. H. Bluhm, N. C. Koshnick, J. A. Bert, M. E. Huber, K. A. Moler, *Phys. Rev. Lett.* **102**, 136802 (2009).
16. D. Rothfuß, A. Reiser, A. Fleischmann, C. Enss, *Appl. Phys. Lett.* **103**, 052605 (2013).
17. L. Childress *et al.*, *Science* **314**, 281–285 (2006).
18. J. R. Maze *et al.*, *Nature* **455**, 644–647 (2008).
19. G. Balasubramanian *et al.*, *Nature* **455**, 648–651 (2008).
20. J. P. Tetienne *et al.*, *Science* **344**, 1366–1369 (2014).
21. E. Schäfer-Nolte, L. Schlupf, M. Ternes, F. Reinhard, K. Kern, J. Wrachtrup, <http://arxiv.org/abs/1406.0362> (2014).
22. M. Pelliccione, B. A. Myers, L. Pascal, A. Das, A. C. Bleszynski Jayich, <http://arxiv.org/abs/1409.2422> (2014).
23. Materials and methods are available as supporting material on Science Online.
24. T. H. Taminiau, J. Cramer, T. van der Sar, V. V. Dobrovitski, R. Hanson, *Nat. Nanotechnol.* **9**, 171–176 (2014).
25. A. A. Baski, H. Fuchs, *Surf. Sci.* **313**, 275–288 (1994).
26. J. H. Park *et al.*, *Adv. Mater.* **24**, 3988–3992 (2012).
27. G. W. Ford, W. Weber, *Phys. Rep.* **113**, 195–287 (1984).
28. N. W. Ashcroft, N. D. Mermin, *Solid State Physics* (Holt, Rinehart and Winston, New York, 1976).
29. P. Maher *et al.*, *Science* **345**, 61–64 (2014).
30. L. Faoro, L. B. Ioffe, *Phys. Rev. Lett.* **100**, 227005 (2008).
31. S. M. Anton *et al.*, *Phys. Rev. Lett.* **110**, 147002 (2013).

ACKNOWLEDGMENTS

We thank E. Demler, A. Bleszynski Jayich, B. Myers, A. Yacoby, M. Vavilov, R. Joynt, A. Poudel, and L. Langsjoen for helpful discussions and insightful comments. Financial support was provided by the Center for Ultracold Atoms, the National Science Foundation (NSF), the Defense Advanced Research Projects Agency Quantum-Assisted Sensing and Readout program, the Air Force Office of Scientific Research Multidisciplinary University Research Initiative, and the Gordon and Betty Moore Foundation. S.K. and A.S. acknowledge financial support from the National Defense Science and Engineering Graduate fellowship, V.E.M. from the Society of Fellows of Harvard University, and S.K. from the NSF Graduate Research Fellowship. All fabrication and metrology were performed at the Center for Nanoscale Systems (CNS), a member of the National Nanotechnology Infrastructure Network, which is supported by the NSF under award no. ECS-0335765. The CNS is part of Harvard University.

SUPPLEMENTARY MATERIALS

www.sciencemag.org/content/347/6226/1129/suppl/DC1
Materials and Methods
Figs. S1 to S7
Tables S1 to S3
References (32–34)

4 December 2014; accepted 16 January 2015
Published online 29 January 2015;
10.1126/science.aaa4298

REPELLENT MATERIALS

Robust self-cleaning surfaces that function when exposed to either air or oil

Yao Lu,¹ Sanjayan Sathasivam,¹ Jinlong Song,² Colin R. Crick,³ Claire J. Carmalt,¹ Ivan P. Parkin^{1*}

Superhydrophobic self-cleaning surfaces are based on the surface micro/nanomorphologies; however, such surfaces are mechanically weak and stop functioning when exposed to oil. We have created an ethanolic suspension of perfluorosilane-coated titanium dioxide nanoparticles that forms a paint that can be sprayed, dipped, or extruded onto both hard and soft materials to create a self-cleaning surface that functions even upon emersion in oil. Commercial adhesives were used to bond the paint to various substrates and promote robustness. These surfaces maintained their water repellency after finger-wipe, knife-scratch, and even 40 abrasion cycles with sandpaper. The formulations developed can be used on clothes, paper, glass, and steel for a myriad of self-cleaning applications.

Artificial self-cleaning surfaces work through extreme water repellence (superhydrophobicity) so that water forms near spherical shapes that roll on the surface; the rolling motion picks up and removes dirt, viruses, and bacteria (1–3). To achieve near spherical water droplets, the surfaces must be highly textured (rough) combined with extremely low water affinity (waxy) (4, 5). The big drawback of these artificial surfaces is that they are readily abraded (6–8), sometimes with little more than brushing with a tissue, and readily contaminated by oil (9–11). We report here a facile method for making superhydrophobic surfaces from both soft (cotton or paper) and hard (metal or glass) materials. The process uses dual-scale nanoparticles of titanium dioxide (TiO₂) that are coated with perfluorooctyltriethoxysilane. We created an ethanol-based suspension that can be sprayed, dipped, or painted onto surfaces to create a resilient water-repellent surface. By combining the paint and adhesives, we created a superhydrophobic surface that showed resilience and maintained its performance after various types of damage, including finger-wipe, knife-scratch, and multiple abrasion cycles with sandpaper. This method can also be used for components that require self-cleaning and lubricating such as bearings and gears, to which superamphiphobic (repels oil and water) surfaces (9–11) are not applicable.

A paint was created by mixing two different size ranges of TiO₂ nanoparticles (~60 to 200 nm and ~21 nm) in an ethanol solution containing perfluorooctyltriethoxysilane (12). Scanning electron microscopy (SEM) and transmission electron microscopy (TEM) of the constituent particles

of the paint (Fig. 1A) show the dual-scale nature of the TiO₂ nanoparticles. X-ray photoelectron spectroscopy (XPS) (Fig. 1B) showed that the titanium dioxide particles were coated with perfluorooctyltriethoxysilane.

We used many different coating methods to create the water-repellent surfaces, including an artist's spray-gun to coat hard substrates such as glass and steel, dip-coating for cotton wool, and a syringe (movie S1) to extrude the paint onto filter paper. After allowing the ethanol to evaporate for ~180 s at room temperature, the treated areas of the substrates supported water as near spherical droplets, whereas the untreated parts were readily wetted (it required ~30 min for the ethanol to fully evaporate from cotton wool and filter paper at room temperature) (fig. S1). We used x-ray diffraction (XRD) (Fig. 1C) to analyze the coatings on hard and soft substrates. The diffraction peaks show the expected patterns for nanoscaled TiO₂.

On a surface that shows water repellence, water droplets tend to bounce instead of wetting the surface (13, 14). However, for soft substrates, extreme superhydrophobicity is required to achieve the bouncing phenomenon because the water droplets tend to be trapped onto the threads of the substrates (cotton wool) (15). Shown in fig. S2 are the water dropping tests on untreated glass, steel, cotton wool, and filter paper, which were readily wetted (the contact moment of the water droplets and the solid surfaces is defined as 0). Shown in Fig. 2 is the water bouncing process on dip-coated glass, steel, cotton wool, and filter paper surfaces. Water droplets completely leave the surface without wetting or even contaminating the surfaces (the water was dyed blue to aid visualization), indicating that the surfaces were superhydrophobic. In movie S2, we compare the water-affecting behavior between untreated and treated glass, steel, cotton wool, and filter paper, respectively. The effect of artificial rain on the treated surfaces is shown in movie S3; the drop sizes varied with random impact

¹Department of Chemistry, University College London, 20 Gordon Street, London, WC1H 0AJ, UK. ²Key Laboratory for Precision and Non-traditional Machining Technology of Ministry of Education, Dalian University of Technology, Dalian, 116024, People's Republic of China. ³Department of Chemistry, Imperial College London, South Kensington Campus, London, SW7 2AZ, UK.

*Corresponding author. E-mail: i.p.parkin@ucl.ac.uk

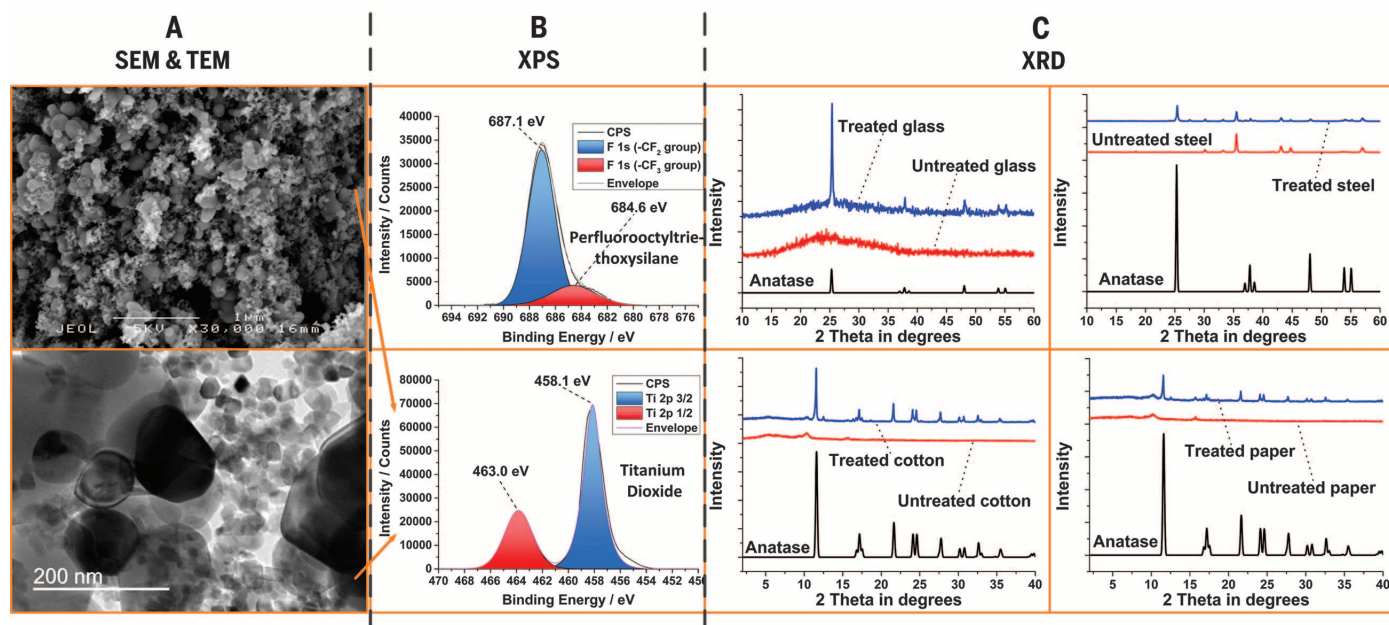


Fig. 1. Paint characterizations. (A) SEM (top) and TEM (bottom) of the constituent nanoparticles in the paint. Sizes varied from ~60 to 200 nm for the TiO₂ nanoparticles (Aldrich), whereas ~21 nm in size refers to P25. (B) XPS of the paint, where “F” refers to perfluorooctyltriethoxysilane and “Ti” refers to TiO₂. (C) XRD patterns of treated and untreated substrates compared with the respective standard patterns for TiO₂ anatase (the P25 particles had a small rutile component, as expected).

velocities, and the droplets could not wet the treated surfaces.

The paint had good self-cleaning properties when applied on various substrates, especially for soft porous materials, such as those used in making clothes and paper. The coated surfaces show water-proofing properties from the water-bouncing and artificial rain tests. Further tests on cotton wool and filter paper are shown in figs. S3 (the experimental scheme) and S4 (the experimental results). As shown in fig. S4, A and B, the dip-coated cotton wool inserted into the methylene blue-dyed water formed a negative meniscus on the solid-liquid-vapor interfaces because of hydrophobicity (16). The cotton wool was removed from the water and remained fully white with no trace of contamination by the dyed water (fig. S3). A dirt removal test when an artificial dust (MnO powder) was put on the spray-coated filter paper, which was then cleaned by pouring water, is shown in fig. S4, C and D. The untreated piece of filter paper (placed below) was wet and polluted by the dirt, whereas the treated piece stayed dry and clean (fig. S3). The self-cleaning tests on the dip-coated cotton wool and spray-coated filter paper are shown in movie S4; a time-lapsed video clip of water droplets (dyed blue) staying on the dip-coated cotton wool and syringe-coated filter paper for 10 min is shown in movie S5, and neither the cotton wool nor the filter paper had blue left after the droplets were removed. These tests indicate that the soft substrates (cotton and paper) gained the nonwetting and self-cleaning properties after treating with the paint. Dirt removal tests were also carried out on dip-coated glass and steel surfaces; as shown in fig. S4, E and F, the droplet took the dirt (MnO powder)

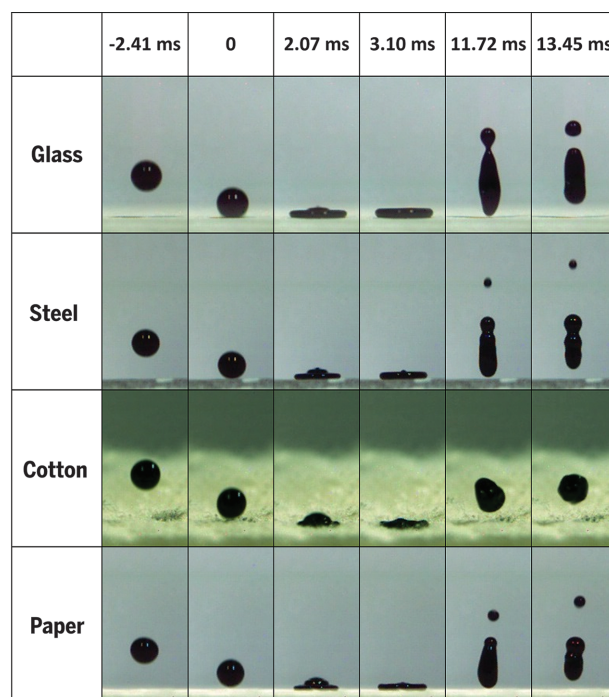


Fig. 2. Time-lapse photographs of water droplets bouncing on the treated glass, steel, cotton wool, and filter paper surfaces. Droplet sizes, ~6.3 ± 0.2 μL.

away, and the surfaces were cleaned along the path of the water droplet movement. The self-cleaning property of dip-coated glass and steel surfaces is shown in movie S6 in a high-speed motion capture.

Very few reports have shown any self-cleaning tests in oil because superhydrophobic surfaces normally lose their water repellency when even partially contaminated by oil. This is because the surface tension of the oil is lower than that of

water, resulting in the oil penetrating through the surfaces. Making superamphiphobic surfaces (that repel both water and oils) is an effective way to solve this problem (9, 10, 17). However, there are many instances that require both self-cleaning from water repellency and a smooth coating of oil, such as lubricating bearings and gears; under these conditions, superamphiphobic surfaces cannot be used because they will also repel lubricating oils.

Fig. 3. Self-cleaning tests after oil-contaminations. (A) Water droplet was repelled by the treated surface when immersed in oil (hexadecane). (B and C) The treated surface retained its water-repellent property even after being contaminated by oil (D to F) The dirt removal test in oil-solid-vapor interfaces. Dirt was put partly in oil and air, the surface was contaminated by oil, water was dropped onto the surface, and this removed the dirt both in air and oil.

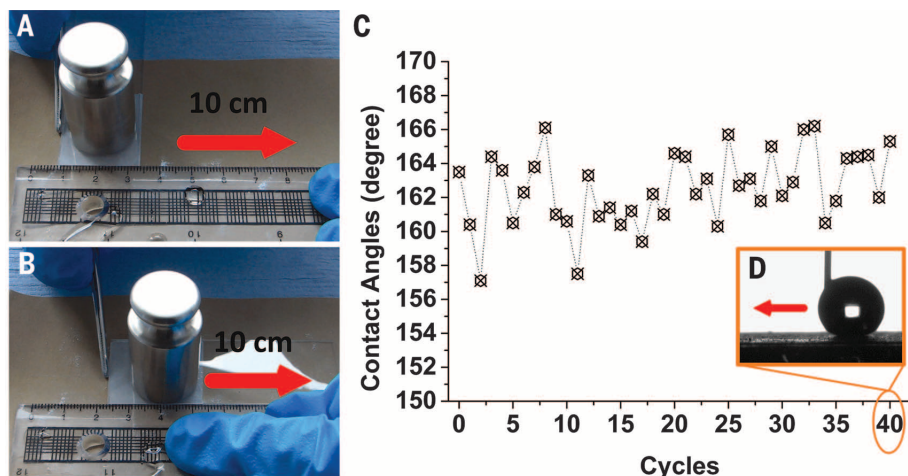
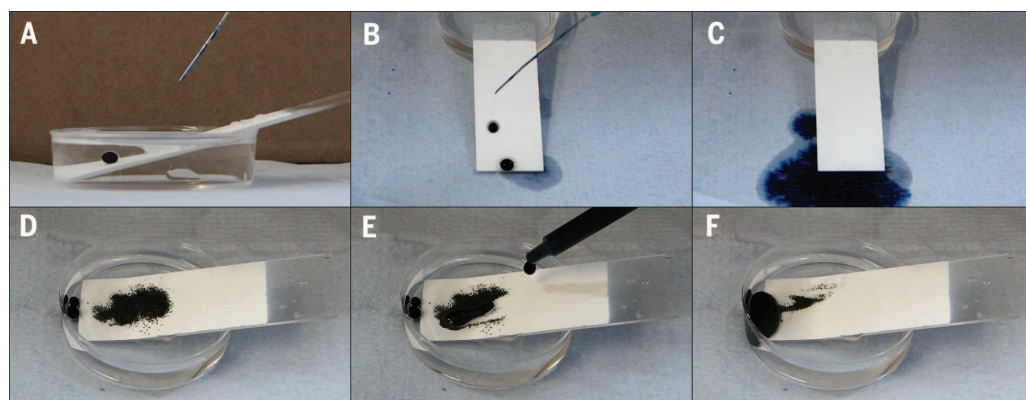


Fig. 4. Sandpaper abrasion tests. (A and B) One cycle of the sandpaper abrasion test. (C) Plot of mechanical abrasion cycles and water contact angles after each abrasion test. (D) Water droplet traveling test after 40th cycle abrasion.

The self-cleaning tests of the painted surfaces after oil (hexadecane) contamination and immersion are presented graphically in fig. S5. As shown in fig. S6, water droplets still formed “marbles” on the dip-coated surface when immersed in oil, rather than forming a two-layer system (fig. S5A), thus indicating that the surfaces will retain their self-cleaning properties after being immersed in oil. For example, on the untreated areas of a glass slide, water droplets spread and wet the surfaces. We show in movie S7 water dropped on the dip-coated and untreated surfaces immersed in oil. We show in Fig. 3A the side view of a water droplet that formed a sphere at the oil-solid interface without wetting a spray-coated surface; the droplet then rolled off from the surface. As shown in Fig. 3, B and C, the water droplets slipped off from the spray-coated surface that was contaminated by oil (hexadecane), indicating self-cleaning was retained even after oil-contamination (fig. S5B and movie S8). We show in Fig. 3, D to F, a dirt-removal test on the spray-coated surfaces both in oil and air. The treated surface was fully contaminated by oil and then partly inserted into oil; dirt (MnO powder) was also put partly in oil and air onto the surface. Water was dropped so as to remove the dirt both in air and oil (fig. S5C and movie S9). This was to test the dirt-removal pro-

perties of the oil-contaminated painted surface both in air and under oil. For further dirt-removal tests on oil-contaminated painted surfaces, we used soil, household dust, and cooking oil from actual conditions and repeated the experiments shown in fig. S5C. As shown in fig. S7, soil and dust were removed by water from the dip-coated surfaces immersed either in hexadecane or cooking oil.

When the treated surfaces were immersed in oil, the oil gradually penetrated into the surface, so the water droplets were supported by both oil and the surface structures and were still marble-shaped (fig. S6). In this condition, the self-cleaning behavior in oil is similar to that in air (18–20); thus, the treated surfaces retained the water-repellent and dirt-removal properties when immersed in oil (Fig. 3, D to F). In air, when the treated surfaces were contaminated by oil, the surface structures locked the oil as a lubricating fluid, and a slippery state was then achieved (21–24). Dirt was removed from the treated surfaces simply by passing water over the surface. For these reasons, the treated surfaces retained their self-cleaning properties when being contaminated by oil.

Low surface robustness is the main issue limiting the widespread application of superhydrophobic coatings because the surface roughness is usually at the micro- or nanoscale and is me-

chanically weak and readily abraded (25). This surface roughness is partially protected by soft substrates, such as cotton wool and filter paper, because of their inherent flexibility (6, 26) and ability to reduce direct friction between the coating and the surface. However, on hard substrates such as glass, nanostructures are easily destroyed or removed. We developed a method to bond the self-cleaning coatings to the substrates by using adhesives so as to apply more sophisticated and robust adhesive techniques and overcome the weak inherent robustness of superhydrophobic surfaces. We show in fig. S8 the “paint + adhesive (double-sided tape/spray adhesive) + substrates” sample preparation methods (fig. S8, A and B) and the relevant robustness tests, including finger-wipe (fig. S8C), knife-scratch (fig. S8D), and sandpaper abrasion (fig. S8, E and F). We show in fig. S9 and movie S10 the finger-wipe tests that compare the untreated, paint-treated, and “paint + double-sided tape”-treated (PDT) glass and steel substrates, respectively. After the finger-wipe, the paint directly coated on substrates was removed, whereas the double-sided tape-bonded paint was still left on the substrates, and the surfaces retained superhydrophobicity. Although the inherent robustness of the paint is intrinsically as weak as most superhydrophobic surfaces, it is friendly to adhesives, from which the robustness was gained. A glass substrate was used as one example for further robustness tests with double-sided tapes (knife-scratch and sandpaper abrasion tests); as shown in movie S10, the glass bonded with double-sided tape, and the paint still kept dry and clean after the knife-scratch and then water drop. The sandpaper abrasion tests were carried out on the PDT glass. The PDT glass weighing 100 g was placed face-down to sandpaper (standard glasspaper, grit no. 240) and moved for 10 cm along the ruler (Fig. 4A); the sample was rotated by 90° (face to the sandpaper) and then moved for 10 cm along the ruler (Fig. 4B). This process is defined as one abrasion cycle (movie S11), which guarantees the surface is abraded longitudinally and transversely in each cycle even if it is moved in a single direction. The water contact angles after each abrasion cycle are shown in Fig. 4C, and it was observed that the static water contact angles were between 156° and 168°, indicating superhydrophobicity was not lost by mechanical abrasion.

In order to test whether this superhydrophobicity was kept after abrasion on the whole area but not merely on some points (contact angle measuring points), water droplet was guided by a needle to travel on the PDT glass surface after the 11th, 20th, 30th, and 40th cycle's abrasion, respectively (movie S12). The water droplet traveling after the 40th cycle is shown in Fig. 4D.

To enlarge the application scale and broaden the types of substrates, the spray adhesive [EVO-STIK (Bostik, UK)] was also used to bond glass, steel, cotton wool, and filter paper substrates with the superhydrophobic paint. We show in fig. S10 and movie S13 the finger-wipe tests on untreated, paint-treated, and "paint + spray adhesive"-treated (PSAT) substrates, respectively. On hard substrates (glass and steel), PSAT surfaces retained water proofing, whereas the paint was just removed when directly applied; the case is different on soft substrates (cotton and paper), on which paint was protected by their porous structures, resulting in both paint-treated and PSAT cotton and paper being superhydrophobic after the finger-wipe. However, in a more powerful test (sandpaper abrasion of cotton), this "protection" is limited (fig. S11). As shown in fig. S12 and movie S14, the sandpaper abrasion tests on PSAT substrates and both hard and soft substrates became robust after the PSAT treatment. As shown in fig. S13 and movie S15, the PSAT substrates retained water repellency after knife-scratch tests. After different damages, the PSAT materials still remained superhydrophobic, indicating that this method could efficiently enhance the robustness of superhydrophobic surfaces on different substrates; it is believed that the idea of "superhydrophobic paint + adhesives" can be simply, flexibly, and robustly used in large-scale industrial applications.

The superhydrophobic surfaces show that a robust resistance to oil contamination and ease of applicability can be achieved by implementing straightforward coating methods such as spraying, dip-coating, or even simply extrusion from a syringe. The flexibility of the "paint + adhesives" combination enables both hard and soft substrates to become robustly superhydrophobic and self-cleaning. The surfaces can be readily implemented in harsh and oily environments where robustness is required.

REFERENCES AND NOTES

- W. Barthlott, C. Neinhuis, *Planta* **202**, 1–8 (1997).
- R. Blossley, *Nat. Mater.* **2**, 301–306 (2003).
- I. P. Parkin, R. G. Palgrave, *J. Mater. Chem.* **15**, 1689 (2005).
- T. Onda, S. Shibuichi, N. Satoh, K. Tsujii, *Langmuir* **12**, 2125–2127 (1996).
- L. Feng et al., *Adv. Mater.* **14**, 1857–1860 (2002).
- J. Zimmermann, F. A. Reiffer, G. Fortunato, L. C. Gerhardt, S. Seeger, *Adv. Funct. Mater.* **18**, 3662–3669 (2008).
- X. Zhu et al., *J. Mater. Chem.* **21**, 15793 (2011).
- Q. Zhu et al., *J. Mater. Chem. A* **1**, 5386 (2013).
- A. Tuteja et al., *Science* **318**, 1618–1622 (2007).
- X. Deng, L. Mammen, H. J. Butt, D. Vollmer, *Science* **335**, 67–70 (2012).
- Y. Lu et al., *ACS Sustainable Chem. Eng.* **1**, 102 (2013).
- Materials and methods are available as supplementary materials on Science Online.
- D. Richard, C. Clanet, D. Quéré, *Nature* **417**, 811 (2002).
- J. C. Bird, R. Dhiman, H. M. Kwon, K. K. Varanasi, *Nature* **503**, 385–388 (2013).
- Y. Lu et al., *J. Mater. Chem. A* **2**, 12177 (2014).
- D. Vella, L. Mahadevan, *Am. J. Phys.* **73**, 817 (2005).
- A. Tuteja, W. Choi, J. M. Mabry, G. H. McKinley, R. E. Cohen, *Proc. Natl. Acad. Sci. U.S.A.* **105**, 18200–18205 (2008).
- A. Nakajima et al., *Langmuir* **16**, 7044–7047 (2000).
- R. Fürstner, W. Barthlott, C. Neinhuis, P. Walzel, *Langmuir* **21**, 956–961 (2005).
- B. Bhushan, Y. C. Jung, K. Koch, *Langmuir* **25**, 3240–3248 (2009).
- T. S. Wong et al., *Nature* **477**, 443–447 (2011).
- M. Nosonovsky, *Nature* **477**, 412–413 (2011).
- A. Grinthal, J. Aizenberg, *Chem. Mater.* **26**, 698–708 (2014).
- D. C. Leslie et al., *Nat. Biotechnol.* **32**, 1134–1140 (2014).
- M. Im, H. Im, J. Lee, J. Yoon, Y. Choi, *Soft Matter* **6**, 1401 (2010).
- B. Wang et al., *ACS Appl. Mater. Interfaces* **5**, 1827–1839 (2013).

ACKNOWLEDGMENTS

We thank M. Vickers and S. Firth for XRD and TEM characterizations. Thanks to C. E. Knapp and D. S. Bhachu for ordering chemicals and the help with some experiments.

SUPPLEMENTARY MATERIALS

www.sciencemag.org/content/347/6226/1132/suppl/DC1
Materials and Methods
Supplementary Text
Figs. S1 to S13
References (27, 28)
Movies S1 to S15

16 October 2014; accepted 30 January 2015
10.1126/science.aaa0946

PROTEIN IMAGING

Single-protein spin resonance spectroscopy under ambient conditions

Fazhan Shi,^{1,2,3*} Qi Zhang,^{1,2*} Pengfei Wang,^{1,2,3*} Hongbin Sun,⁴ Jiarong Wang,⁴ Xing Rong,^{1,2,3} Ming Chen,^{1,2} Chenyong Ju,^{1,2,3} Friedemann Reinhard,^{5†} Hongwei Chen,⁴ Jörg Wrachtrup,⁵ Junfeng Wang,⁴ Jiangfeng Du^{1,2,3‡}

Magnetic resonance is essential in revealing the structure and dynamics of biomolecules. However, measuring the magnetic resonance spectrum of single biomolecules has remained an elusive goal. We demonstrate the detection of the electron spin resonance signal from a single spin-labeled protein under ambient conditions. As a sensor, we use a single nitrogen vacancy center in bulk diamond in close proximity to the protein. We measure the orientation of the spin label at the protein and detect the impact of protein motion on the spin label dynamics. In addition, we coherently drive the spin at the protein, which is a prerequisite for studies involving polarization of nuclear spins of the protein or detailed structure analysis of the protein itself.

Observing the structure and dynamics of single molecules is a long-sought goal that has inspired technical developments in a wide range of disciplines (1–4). As one of the most important techniques, electron spin resonance (ESR) finds broad application for studying basic molecular mechanisms in biology and chemistry (5). Most proteins, however, are nonparamagnetic and thus cannot be accessed by the technique. Labeling biomolecules with a small spin-bearing moiety, such as nitroxide spin labels, enables ESR to acquire a broad range of structural and dynamical information.

However, current methods need 10^{10} uniform molecules to accumulate a large enough signal-to-noise ratio. This substantially complicates efforts to compile structural and dynamical information. New methods that have tried to push the sensitivity of magnetic resonance to the single-spin level all require either a dedicated environment (6, 7) or conducting surfaces and tips (8).

A sensor that could accomplish single-protein detection under ambient conditions is a recently developed atomic-sized magnetic field sensor based on the nitrogen vacancy (NV) defect center in diamond (9–11). Because of its long coherence times (12, 13), the NV sensor can detect a single electron spin over a distance of 30 nm under ambient conditions. As proof-of-principle demonstrations, single electron spins inside diamond or on diamond surfaces have been sensed (14–16). Despite previous efforts, single-biomolecule detection and spectroscopy have not been attained. Here, we report an electron spin resonance study on a single protein, which allows us to extract the structural and dynamical properties from spectral analysis.

As the experimental sample, we chose MAD2 (mitotic arrest deficient-2), an essential spindle

¹Hefei National Laboratory for Physical Sciences at the Microscale and Department of Modern Physics, University of Science and Technology of China (USTC), Hefei 230026, China. ²Joint Laboratory of Quantum Biophysics, USTC Institute of Biophysics and Chinese Academy of Sciences. ³Synergetic Innovation Center of Quantum Information and Quantum Physics, USTC, Hefei 230026, China. ⁴High Magnetic Field Laboratory, Chinese Academy of Sciences, Hefei 230000, China. ⁵3rd Physics and Integrated Quantum Science and Technology (IQST), University of Stuttgart, 70569 Stuttgart, Germany.

*These authors contributed equally to this work. †Present address: Walter Schottky Institut, E24, Technische Universität München, 85748 Garching, Germany. ‡Corresponding author. E-mail: djf@ustc.edu.cn

checkpoint protein (17, 18). The spindle checkpoint is a major cell cycle control mechanism that prevents errors in chromosome segregation and aneuploidy, thereby ensuring the fidelity of chromosome inheritance. We chose this protein for the present study because it can be easily modified site-specifically with a single nitroxide spin label. In addition, it is reliably immobilized on the diamond surface by embedding it in a polylysine layer. We detected this spin label by its magnetic dipole interaction with a single NV center (19). In brief, the NV center consists of a nitrogen impurity and a neighboring vacancy. Its triplet ($S = 1$) ground state can be spin-polarized and read out optically. The magnetic dipole interaction between the NV spin and the spin label is conveniently measured by simultaneously driving the probe (NV) and the sample spin (spin label) (20). Single NV centers were created roughly 5 nm below the surface of diamond by ion implantation (21). We did not position MAD2 with respect to single NV centers in a controlled way, so our experiments rely on statistical proximity. For this purpose, the protein surface concentration was optimized by atomic force microscopy (AFM) (Fig. 1B and fig. S1) and various NV centers were tested for dipolar interaction with single spin labels (fig. S2).

Detecting the single-electron spin label is challenging because the coherence time of shallow NV centers is usually limited by surface noise, which obscures the coupling between the spin label and the NV center. The spin label electron spin can be reliably detected by combining the spin resonance of the NV and the spin label with dynamical decoupling. The experimental pulse

sequences are shown in Fig. 1C. Periodic XY8-NV pulses on the NV sensor were used to preserve the NV sensor coherence and to increase its magnetic field sensitivity; radio-frequency (RF) pulses on the nitroxide spin labels were used to flip the electron spin synchronously.

Denoting the spins by S_{NV} (NV sensor), S_e (electron spin of nitroxide spin labels), and I (nitrogen nuclear spin of spin labels), the combined system can be modeled by a coupling Hamiltonian:

$$H = \underbrace{\Delta S_{z,\text{NV}}^2 + \gamma_{\text{NV}} B_0 S_{z,\text{NV}}}_{H_{\text{NV}}} + \underbrace{b S_{z,\text{NV}} S_{z,e} + \gamma_e B_0 S_{z,e} + S_e A I + \gamma_I B_0 I_z + Q I^2}_{H_{\text{SL}}} \quad (1)$$

where SL denotes the spin label, B_0 is the external static field (aligned along z), Δ is the zero-field splitting of the NV, Q is the nuclear quadrupole coupling constant, and γ_{NV} , γ_e , and γ_I are the gyromagnetic ratios of the NV, target electron, and nuclear spin, respectively. The coupling between the NV and the spin label is approximated as a pure $S_{z,\text{NV}}-S_{z,e}$ interaction with coupling constant b because it is much smaller than the Zeeman and zero-field splitting of the two spins. Within this approximation, the target spin generates an effective magnetic field $B_e = b S_{z,e} / \gamma_{\text{NV}}$ at the NV center site, which depends on the quantum number $S_{z,e}$.

We addressed the effective two-level system $|0\rangle = |S_{z,\text{NV}} = 0\rangle$; $|1\rangle = |S_{z,\text{NV}} = 1\rangle$ of the NV sensor with resonant microwave pulses and performed a dynamic decoupling experiment on this system. In this measurement, an initial $\pi/2$ pulse prepared the sensor in a coherent superposition,

$$\psi(t=0) = \frac{|0\rangle + \exp(i\varphi)|1\rangle}{\sqrt{2}} \quad (2)$$

with $\varphi(t=0) = 0$. The phase φ evolved over time, was refocused by N π -pulses at $t = \tau_0/2 + n\tau_0$, and was converted into a population by the final $\pi/2$ pulse at $t = N\tau_0$. The key idea of the experiment is to map the electron spin resonance signal of the spin label S_e to a phase φ on the NV spin. This goal was accomplished by manipulation of the electron spin on the protein (Fig. 1C, “spin label”) synchronized with the dynamical decoupling period. The NV experienced an alternating field from the protein spin label and acquired a phase

$$\varphi \sim b_{\text{eff}} N \tau_0 \quad (3)$$

where b_{eff} is the effective magnetic field generated by the spin label at the location of the NV spin. In this way, the protein spin ESR signal is mapped to the signal obtained from the NV sensor.

Figure 2A shows the ESR spectrum of a single spin label. Upon cleaning the diamond surface, the signal disappeared, hence it stemmed from the spin label on the protein. The spectra in Fig. 2A were recorded at an external magnetic field $B_0 = 153.0$ G. Three spectral peaks at 356.3, 430.9, and 501.6 MHz mark the hyperfine splitting between the spin label electron spin ($S = 1/2$) and the nitrogen nuclear spin $I = 1$, similar to the ensemble results in Fig. 2B. The observation of hyperfine splitting proves that the detected spin is indeed the nitroxide spin on the protein and not, for instance, that of a substitutional nitrogen impurity inside diamond. Spectra from single

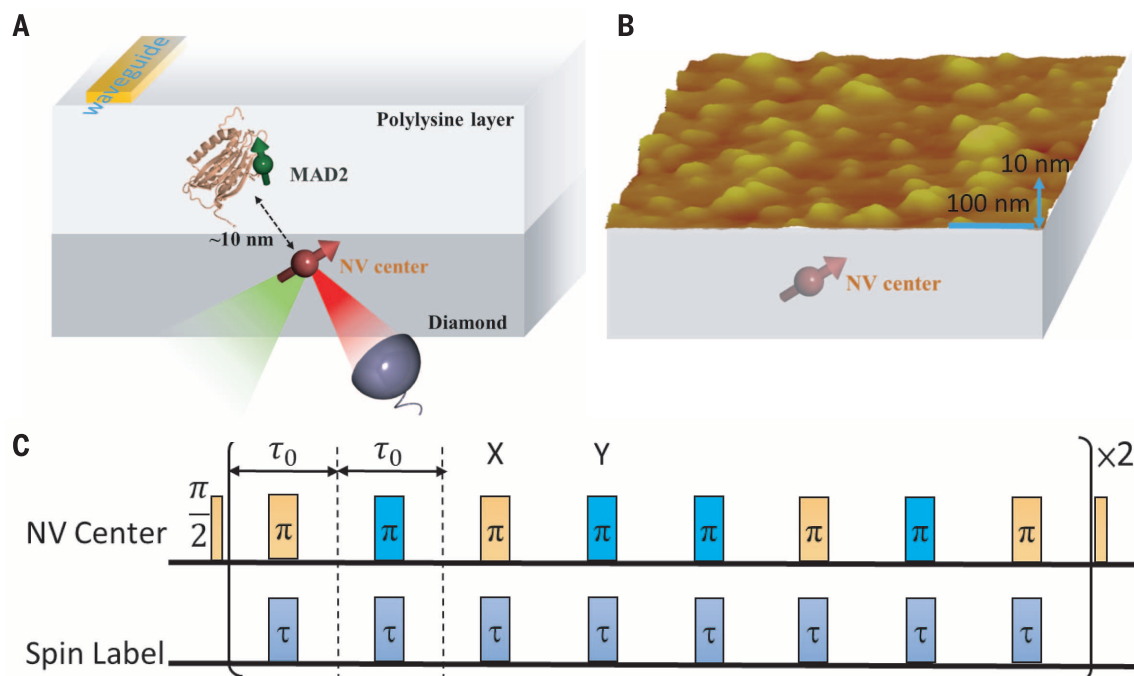


Fig. 1. Schematic of the setup and experimental method. (A) MAD2 proteins labeled with nitroxide spin labels, located on the surface of diamond, close to which NV centers were implanted. Microwaves were applied by a coplanar waveguide. (B) Distribution of freeze-dried proteins on the diamond surface measured by AFM. (C) Pulse sequence to measure the coupling of an NV sensor to the protein. The pulse sequence contains MW and RF channels, in which microwave and radio-frequency pulses were used to control the NV probe and synchronously flip the spin label (i.e., the nitroxide electron spin).

electron spins were markedly different from those measured on ensembles (22) (Fig. 2B). The ensemble ESR spectrum recorded on spin labels in fluid solution shows a spectrum with three equidistantly spaced peaks (Fig. 2B, upper panel). Here, fast tumbling of molecules averages out the anisotropic terms of the hyperfine interaction. Overall, the spectrum of a single spin label is closer to a solid-state spin ensemble (Fig. 2B, lower panel). However, for the solid-state ensemble

spectrum, the random orientation of the molecular spin principal axis causes broadening of spectral peaks (23) (Fig. 2B, lower panel) and marked side shoulders. The spectra of the single molecule, however, show three clearly resolved peaks. Figure 2 underpins one benefit of single spin ESR: The anisotropic hyperfine coupling can be determined reliably. This is important for structural and dynamical information, as shown below.

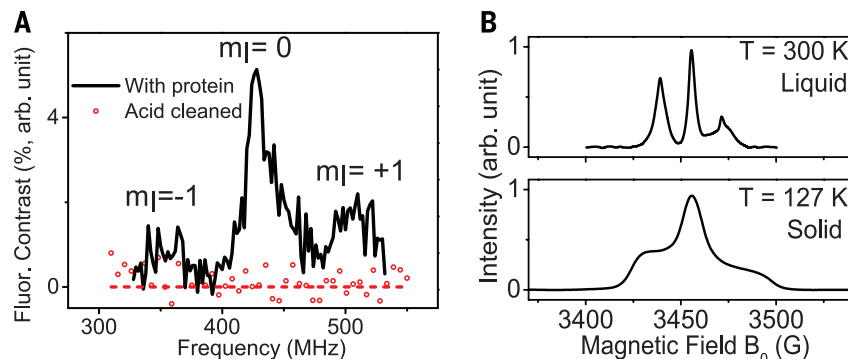


Fig. 2. Electron spin resonance spectrum of nitroxide spin labels. (A) Single spin ESR spectra under ambient conditions. The spectrum disappears after removing the protein by acid cleaning. (B) Upper curve: Ensemble ESR spectrum of $\sim 10^{16}$ protein molecules in buffer solution at room temperature. Lower curve: Ensemble ESR spectrum of protein molecules in a frozen buffer solution with glycerine at $T = 127$ K.

The polylysine matrix used to immobilize MAD2 on the diamond surface restricts protein and spin label motion. However, neither protein nor spin label dynamics is fully frozen in these matrices. Indeed, molecular dynamics is revealed by a closer analysis of the spectra (Fig. 3). Depending on the size of the molecular part undergoing dynamics, its impact on the spectra is different. In the case that only the spin label is undergoing dynamics, its motion is expected to occur on a nanosecond time scale (24), which is not captured by our method. However, overall slow protein motion or dynamics occurs on a millisecond time scale (21, 25). In our spectra, this shows up as broadening of spectral side peaks, which are indeed observed in our experiments (Fig. 3C). Without dynamics, one would expect three spectral lines for the three hyperfine levels of ^{14}N with identical intensity (Fig. 3C, upper trace). Motion specifically changing the direction of the nitrogen p orbitals (ZM in Fig. 3A) with respect to \mathbf{B}_0 causes a broadening of the $m_I = \pm 1$ peaks, as it modulates hyperfine splitting. Note that a rotation of the spin label around B_0 would not cause broadening and hence is not detected in our scheme.

To quantify protein motion, we performed a simulation of the ESR spectra using Eq. 1. The spectra are best described by a spin label, which shows a tilt angle of 46° with respect to \mathbf{B}_0 . The spectral features could only be reproduced accurately by assuming that there is an additional motion around this tilt angle of $\pm 25^\circ$. We attribute this motion to protein dynamics. The slight asymmetry of $m_I = \pm 1$ peaks, with splitting values 74.6 MHz and 70.7 MHz, is caused by the contribution of nonsecular hyperfine terms at low field. Upon reduction of the external magnetic field, the asymmetry became even more obvious (Fig. 3D, lower panel; see also table S2). The red curves in Fig. 3D are simulations using the Hamiltonian of Eq. 1, yielding an electron Zeeman factor (g-factor) of the spin label of 2.008, in good agreement with reported values (Fig. 3E).

Surprisingly, the dephasing and relaxation time of the spin label at the protein, even under ambient conditions, were long enough to generate and measure spin coherence, as shown by the Rabi oscillation of the spin label in Fig. 4A. We recorded the traces by fixing the RF frequency on the central peak of the spin label spectrum and varying the pulse duration time τ (Fig. 1C). The nutation frequency in Fig. 4A scaled with power, as expected from the Rabi oscillations (fig. S4). The method further allows us to determine the distance between the spin label and the NV probe. In Eq. 3, the phase acquired by the NV spin through the dipolar interaction with the spin label ϕ is proportional to $b_{\text{eff}} N \tau_0$. Because b_{eff} scales as d^{-3} , where d is the distance between the spin label and the NV spin, measuring the evolution of the phase thus allowed us to determine d . From a simulation of the curve in Fig. 4B, we derived a coupling strength of 90 kHz. This corresponds to $d \approx 9$ nm, with precise value depending on the orientation of the vector from the NV center to the spin label (fig. S6).

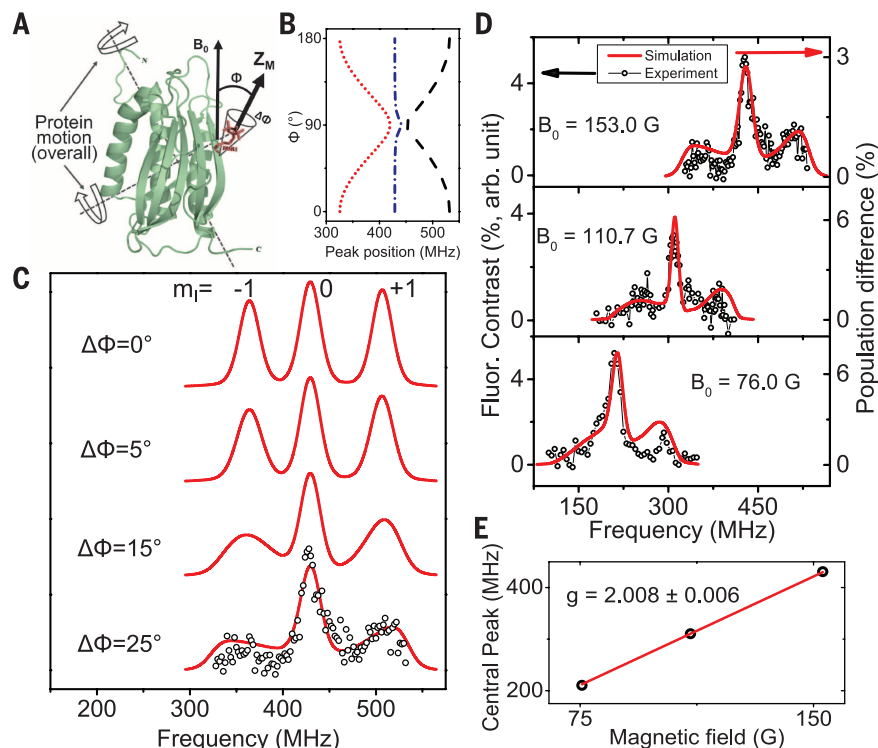


Fig. 3. Dynamics of the spin label. (A) Protein with spin label attached. \mathbf{B}_0 direction and spin label principal axis are shown. (B) Dependence of transition frequencies, corresponding to $m_I = -1, 0, +1$ transitions, on the angle Φ (between axis of spin label and external magnetic fields) and $B_0 = 153$ G. (C) Simulation of the single-protein ESR spectrum. The spectrum is best described by a tilt angle of the spin label Z_m axis of $\langle \Phi \rangle = 46^\circ$. To describe broadening of $m_I = -1, +1$ components, a variation of $\Delta \Phi = 25^\circ$ was adopted. (D) ESR spectra of single spin labels at various external magnetic fields. All three peaks shifted with the magnetic field, and the middle peak evolved at the gyromagnetic ratio of a free electron spin. (E) Resonance frequency of the central peak in (D) as a function of external magnetic field, corresponding to a gyromagnetic ratio of 2.809 ± 0.011 MHz/G and a g-factor of 2.008.

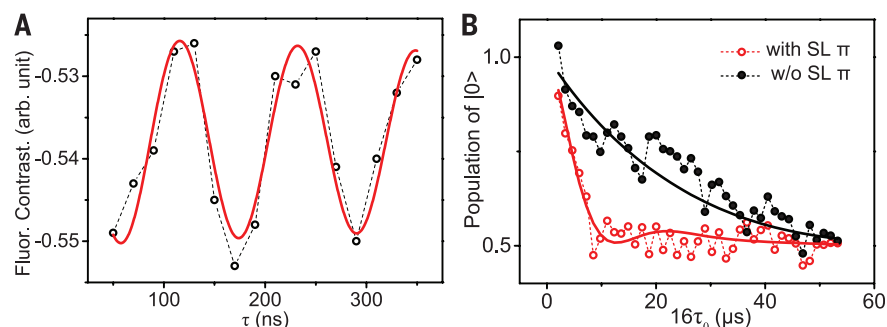


Fig. 4. Coherence and relaxation of protein spin. (A) Rabi oscillation of single spin label measured by using the sequence in Fig. 1B (fixing τ_0 and RF frequency at middle peak, varying τ). The solid curve is a fit using a sine function with exponential damping. (B) The red circles are measured by the double electron-electron resonance sequences on NV sensor and protein spin (fixing τ equal to spin label π pulse and RF frequency to the central peak, varying τ_0). The black dot is the NV center decoherence curve without protein spin flipping. The solid curves show the best simulation of both of the experimental results in (B), corresponding to a relaxation time of 4 μ s for the spin label and 90 kHz coupling between spin label and NV center.

Relaxation of the protein electron spin is an important parameter to characterize the environment, including information on molecular dynamics. Here, we deduced the longitudinal relaxation time of the spin label from Fig. 4B. The red circles denote the interaction signal between the NV center and the spin label; the black dots show the NV center decoherence curve without operation on the spin label. Simulation (solid curves) shows a relaxation time of 4 μ s. These values are compatible with those for spin labels in ensemble measurements, as the relaxation time of this kind of spin label is \sim 110 μ s at liquid nitrogen temperature (21, 24).

The ability to address single-electron spin labels on proteins adds another element to the emerging diamond sensor-based toolbox for ultra-precise structure determination. Together with the recently established nuclear magnetic resonance (NMR) detection, the present method extends the sensing range to dozens of nanometers, whereas diamond sensor-based NMR only senses nuclear spins in very close proximity (a few nanometers) to the NV center (26–29). The interaction between the spin label and the neighboring nuclei could be used to sense more distant nuclei and provide structural and dynamical information otherwise inaccessible by the sensor. In this respect, it is particularly encouraging that we find long spin relaxation times enabling coherent spin driving at the protein. This capability will allow the use of the ancillary electron spin for sophisticated coherent control (30, 31), thereby facilitating future polarization transfer experiments that could gain access to nuclear spins in proteins, including proton or ^{13}C spins. When combined with either scanning magnetometry or nanoscale magnetic resonance imaging based on magnetic field gradients, protein structure analysis under ambient conditions at the level of a single molecule is within reach (32, 33).

REFERENCES AND NOTES

1. L. Redecke et al., *Science* **339**, 227–230 (2013).
2. T. R. M. Barends et al., *Nature* **505**, 244–247 (2014).
3. M. C. Scott et al., *Nature* **483**, 444–447 (2012).
4. C. C. Chen et al., *Nature* **496**, 74–77 (2013).
5. P. P. Borbat, A. J. Costa-Filho, K. A. Earle, J. K. Moscicki, J. H. Freed, *Science* **291**, 266–269 (2001).

6. D. Rugar, R. Budakian, H. J. Mamin, B. W. Chui, *Nature* **430**, 329–332 (2004).
7. M. Xiao, I. Martin, E. Yablonovitch, H. W. Jiang, *Nature* **430**, 435–439 (2004).
8. Y. Manassen, R. J. Hamers, J. E. Demuth, A. J. Castellano Jr., *Phys. Rev. Lett.* **62**, 2531–2534 (1989).
9. G. Balasubramanian et al., *Nature* **455**, 648–651 (2008).
10. J. R. Maze et al., *Nature* **455**, 644–647 (2008).
11. J. M. Taylor et al., *Nat. Phys.* **4**, 810–816 (2008).
12. G. Balasubramanian et al., *Nat. Mater.* **8**, 383–387 (2009).
13. N. Bar-Gill, L. M. Pham, A. Jarmola, D. Budker, R. L. Walsworth, *Nat. Commun.* **4**, 1743 (2013).
14. M. S. Grinolds et al., *Nat. Phys.* **9**, 215–219 (2013).
15. B. Grotz et al., *New J. Phys.* **13**, 055004 (2011).
16. A. O. Sushkov et al., *Nano Lett.* **14**, 6443–6448 (2014).
17. L. S. Michel et al., *Nature* **409**, 355–359 (2001).

18. S. Martin-Lluesma, V. M. Stucke, E. A. Nigg, *Science* **297**, 2267–2270 (2002).
19. M. W. Doherty et al., *Phys. Rep.* **528**, 1–45 (2013).
20. F. Z. Shi et al., *Phys. Rev. B* **87**, 195414 (2013).
21. See supplementary materials on Science Online.
22. V. Gaponenko et al., *Protein Sci.* **9**, 302–309 (2000).
23. J. A. Weil, J. R. Bolton, *Electron Paramagnetic Resonance: Elementary Theory and Practical Applications* (Wiley, New York, ed. 2, 2007), pp. 316–317.
24. K. Jacobsen, S. Oga, W. L. Hubbell, T. Risse, *Biophys. J.* **88**, 4351–4365 (2005).
25. M. A. Hemminga, L. J. Berliner, *ESR Spectroscopy in Membrane Biophysics* (Springer Science and Business Media, New York, 2007), pp. 133–134.
26. T. Staudacher et al., *Science* **339**, 561–563 (2013).
27. H. J. Mamin et al., *Science* **339**, 557–560 (2013).
28. F. Z. Shi et al., *Nat. Phys.* **10**, 21–25 (2014).
29. C. Müller et al., *Nat. Commun.* **5**, 4703 (2014).
30. M. Schaffry, E. M. Gauger, J. J. L. Morton, S. C. Benjamin, *Phys. Rev. Lett.* **107**, 207210 (2011).
31. A. O. Sushkov et al., *Phys. Rev. Lett.* **113**, 197601 (2014).
32. M. S. Grinolds et al., *Nat. Nanotechnol.* **9**, 279–284 (2014).
33. L. Luan et al., <http://arxiv.org/abs/1409.5418> (2014).

ACKNOWLEDGMENTS

We thank F. Jelezko for helpful discussions. Supported by 973 Program grants 2013CB921800 and 2012CB917202, National Natural Science Foundation of China grants 11227901, 91021005, 31470835, 11275183, and 21103199, and the Chinese Academy of Sciences. J.W. was supported by the Max Planck Society and the European Union (via the ERC grants SQUITEC and DIADEMS) and by the Baden-Württemberg Stiftung.

SUPPLEMENTARY MATERIALS

www.sciencemag.org/content/347/6226/1135/suppl/DC1
Materials and Methods
Tables S1 and S2
Figs. S1 to S7
References (34–37)

3 November 2014; accepted 29 January 2015
10.1126/science.aaa2253

BRAIN STRUCTURE

Cell types in the mouse cortex and hippocampus revealed by single-cell RNA-seq

Amit Zeisel,^{1,*} Ana B. Muñoz-Manchado,^{1,*} Simone Codeluppi,¹ Peter Lönnerberg,¹ Gioele La Manno,¹ Anna Juréus,¹ Sueli Marques,¹ Hermany Munguba,¹ Liquan He,² Christer Betsholtz,^{2,3} Charlotte Rolny,⁴ Gonçalo Castelo-Branco,¹ Jens Hjerling-Lefler,^{1,†} Sten Linnarsson^{1,†}

The mammalian cerebral cortex supports cognitive functions such as sensorimotor integration, memory, and social behaviors. Normal brain function relies on a diverse set of differentiated cell types, including neurons, glia, and vasculature. Here, we have used large-scale single-cell RNA sequencing (RNA-seq) to classify cells in the mouse somatosensory cortex and hippocampal CA1 region. We found 47 molecularly distinct subclasses, comprising all known major cell types in the cortex. We identified numerous marker genes, which allowed alignment with known cell types, morphology, and location. We found a layer I interneuron expressing *Pax6* and a distinct postmitotic oligodendrocyte subclass marked by *Itpr2*. Across the diversity of cortical cell types, transcription factors formed a complex, layered regulatory code, suggesting a mechanism for the maintenance of adult cell type identity.

The brain is built from a large number of specialized cell types, enabling highly refined electrophysiological behavior, as well as fulfilling brain nutrient needs and defense against pathogens. Functional specialization

allows fine-tuning of circuit dynamics and decoupling of support functions such as energy supply, waste removal, and immune defense. Cells in the nervous system have historically been classified using location, morphology, target specificity, and

electrophysiological characteristics, often combined with molecular markers (1–5). Systematic in situ hybridization has revealed extensive regional heterogeneity (6). However, none of these properties carry enough information to result, in every case, in a definitive cell type identification (7). Single-cell RNA sequencing (RNA-seq) has been used to classify cells in spleen (8), lung epithelium (9), and embryonic brain (10). However, the adult nervous system has greater complexity and more cell types, presenting a challenge both to sample preparation methods and computational analysis.

Here, we have used quantitative single-cell RNA-seq (11) to perform a molecular census of the primary somatosensory cortex (S1) and the hippocampal CA1 region, based on 3005 single-cell transcriptomes (Fig. 1A and fig. S1, A to C). Individual RNA molecules were counted using unique molecular identifiers (UMIs) (essentially tags that identify individual molecules) (12) (figs. S1, D to J, and S2, A to E) and confirmed by single-molecule RNA fluorescence in situ hybridization (FISH) (fig. S2, G to I).

We used clustering to discover molecularly distinct classes of cells. Standard hierarchical clustering resulted in fragmented clusters (fig. S4), because most genes were not informative in most pairwise comparisons and contributed at

best only noise. Biclustering can overcome this problem by simultaneously clustering genes and cells. We developed BackSPIN (see the supplementary materials), a divisive biclustering method based on sorting points into neighborhoods (SPIN) (13), which revealed nine major classes of cells: S1 and CA1 pyramidal neurons, interneurons, oligodendrocytes, astrocytes, microglia, vascular endothelial cells, mural cells (that is, pericytes and vascular smooth muscle cells), and ependymal cells (Fig. 1, A and B, and fig. S3).

The data set allowed us to identify the most specific markers for each class, many of which are known to play a functional role in these cells (fig. S5). S1 pyramidal cells were marked by *Tbr1*, a transcription factor required for the final differentiation of cortical projection neurons; oligodendrocytes by *Hapln2*, encoding a protein required for proper formation of nodes of Ranvier; mural cells by *Acta2*, a key component of actin thin filaments; and endothelial cells by *Ly6c1* [expressed by monocytes peripherally, and endothelial cells in the brain (14)]. Some were novel, such as *Gm11549* (a long noncoding RNA specific to S1 pyramidal neurons), *Spink8* (a serine protease inhibitor specific to hippocampal pyramidal cells), and *Pnoc* (prepronociceptin, here identified as an interneuron marker).

By repeating biclustering on each of the nine major classes (Fig. 1C and figs. S5 to S8), we identified a total of 47 molecularly distinct subclasses of cells. Every subclass was detected in multiple mice (fig. S1K), arguing that cell identity was preserved across these genetically outbred (CD-1) mice. Neurons contained more RNA than glia and vascular cells and a larger number of detectable genes (Fig. 1C and fig. S1E). Mitochondrial mRNAs were less variable, although mitochondrial tRNAs were highly specifically enriched in endothelial cells (fig. S1E).

We identified seven subclasses of S1 pyramidal cells (Fig. 2A and figs. S6A and S7), which were largely layer-specific. The superficial layers II/III and IV were represented by single populations, whereas layer V showed two distinct subclasses. Layers VI and VIb were represented by single populations, but in addition we found a subclass lacking specific markers but expressing common deep-layer markers such as *Pcp4*. A distinct subclass expressed *Synpr* and *Nr4a2*, which are abundant in the adjacent claustrum, with some cells extending into S1.

We found two types of CA1 glutamatergic cells (fig. S8), plus cells derived from the adjacent CA2 (as defined by *Pcp4*) and subiculum (as defined by *Ly6g6e*). Genes highly expressed in type 2 CA1 pyramidal neurons were associated with mitochondrial function (fig. S8), which has been shown to correlate with the firing rate and length of projections in cortical neurons (15). Orthogonal to the two main classes, we found CA1 layer-specific markers (i.e., *Calb1* and *Nov*), as well as dorsoventrally patterned genes (i.e., *Wfs1* and *Grp*) (16), in both of the two main types of CA1 cells. These may correspond to functional differences between layers (17).

We found 16 subclasses of interneurons (Fig. 2B and fig. S6, C and D), but there are likely more subclasses because we achieved only shallow sampling of *Sst*- and *Pvalb*-expressing cells. In superficial layers of S1, we identified an *Htr3a*- and *Pax6*-expressing interneuron subclass, confirmed by immunohistochemistry (Fig. 2C) [$13.9 \pm 2.4\%$ of serotonin (5HT) receptor 3a-enhanced green fluorescent protein (5HT3aEGFP) cells in layer I, $n = 4$ mice, 636 cells analyzed]. These interneurons specifically expressed *Myh8*, *Fut9*, and *Manea*. In whole-cell current clamp recordings of layer I neurons, subsequently stained for PAX6, these cells exhibited intrinsic electrophysiological and

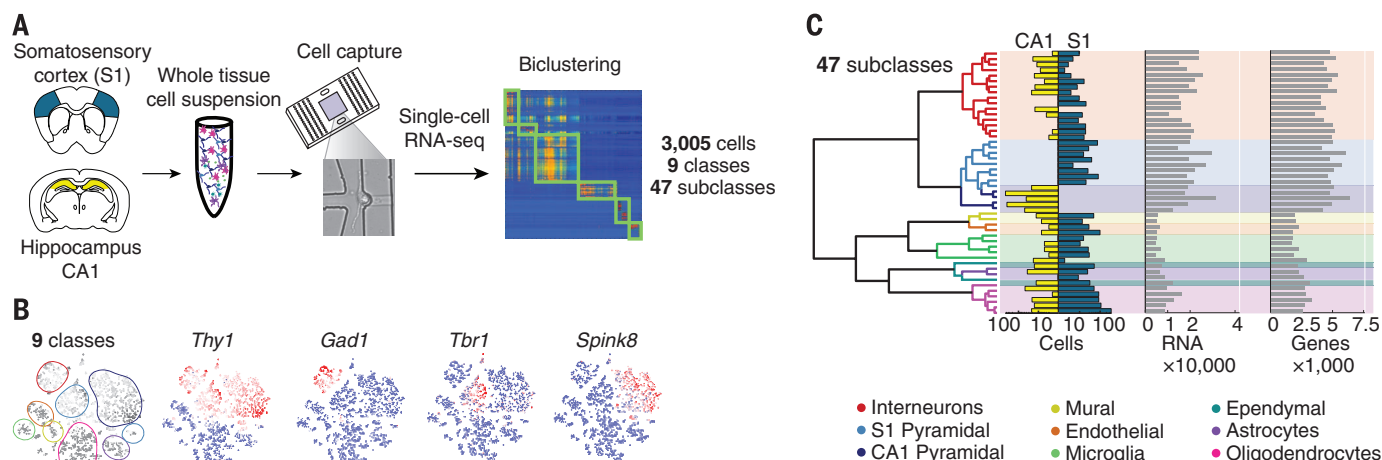


Fig. 1. Molecular census of somatosensory S1 cortex and hippocampus CA1 by unbiased sampling and single-cell RNA-seq. (A) Workflow for obtaining and analyzing single-cell RNA-seq from juvenile mouse cortical cells, from dissection to single-cell RNA-seq and biclustering. (B) Visualization of nine major classes of cells using t-distributed stochastic neighbor embedding (tSNE). Each dot is a single cell, and cells are laid out to show similarities. Colored contours correspond to the nine clusters in (A) and fig. S3. Expression of known markers is shown using the same layout (blue, no expression; white, 1% quantile; red, 99% quantile). (C) Hierarchical clustering analysis on 47 subclasses. Bar plots show number of captured cells in CA1 and S1, number of detected polyA+ RNA molecules per cell, and total number of genes detected per cell.

morphological characteristics of late-spiking neurogliaform cells (6 PAX6⁺ out of 40 recorded cells) (Fig. 2D and fig. S6E). *Pax6* is not expressed in the ventral forebrain during development, further suggesting that neurogliaform cells are developmentally heterogeneous (18).

CA1 and S1 regions both contained interneurons of almost every subclass (Fig. 2B), showing that interneurons residing in functionally distinct cortical structures are transcriptionally closely related. The two exceptions were cells expressing *Vip*, *Penk*, *Calb2*, and *Crh* (which were confined to S1) and cells expressing *Lhx6*, *Reln*, and *Gabrd* [which were confined to CA1 and may be medial ganglionic eminence-derived Ivy cells and neurogliaform cells (18)].

Astrocytes formed two subclasses (Fig. 3A and fig. S9A) distinguished by differential expression of *Gfap* (type 1) and *Mfge8* (type 2). Immunostaining showed that type 1 astrocytes were derived from

layer I, particularly from the glia limitans, a thin layer made up mostly of astrocytes that is arranged against the pia (Fig. 3B). In contrast, type 2 astrocytes were more uniformly distributed in the cortex and were smaller and less ramified.

We identified two types of immune cells: microglia (the tissue-resident macrophages of the brain) and perivascular macrophages. Although closely related, these cell types have distinct developmental origin (19). Both expressed brain macrophage markers *Aif1* and *Cx3cr1*, whereas perivascular macrophages were distinguished by expression of *Mrc1* and *Lyve1*, characteristic of pro-angiogenic perivascular type 2 macrophages (20). Immunohistochemistry for the corresponding proteins confirmed that microglia (AIF1⁺/LYVE1⁺/MRC1⁺) had a classical, ramified morphology and were located throughout the cortex (Fig. 3, D and E). In contrast, perivascular macrophages (AIF⁺/LYVE1⁺/MRC1⁺) were located

only along vessels and showed an ameboid morphology. They were distinct from mural and endothelial cells (fig. S10). Comparison with peritoneal macrophages confirmed their identity (fig. S9A). The correlation between brain and peripheral macrophages (0.67) was similar to that between neurons and glia (0.62), underscoring the functional divergence of this immune cell class.

Six subpopulations of oligodendrocytes were identified (Fig. 3F and fig. S9C), likely representing stages of maturation: immature (Oligo4), premyelinating (Oligo2), myelinating (Oligo5), and terminally differentiated postmyelination (Oligo6) oligodendrocytes. An intermediate population, Oligo3, was almost exclusively observed in somatosensory cortex and may represent a distinct cellular state specific for this tissue. The subclass Oligo1, which did not express the prototypical genes associated with oligodendrocyte precursor cells (OPCs), may represent a postmitotic cellular state, associated with the first steps of oligodendrocyte differentiation. Oligo1 cells expressed a distinct set of genes, including *Itpr2*, *Prom1*, *Gpr17*, *Tef7l2*, *9630013A20Rik*, *Idh1*, *Cnksr3*, and *Rnf122*. Single-molecule RNA FISH confirmed that *Itpr2* and *Cnksr3* were expressed in strict subsets of cells expressing *Plp1*, a pan-oligodendrocyte marker (4.5% and 7.5%, respectively) (Fig. 3G). Together, the Oligo1 to Oligo6 populations may represent sequential steps in the process of maturation from an OPC to a terminally differentiated oligodendrocyte.

Across this diverse set of cell types, we found many transcription factors with highly restricted expression patterns (Fig. 4A and supplementary materials). For example, interneurons expressed key interneuron regulators *Dlx1*, *Dlx2*, *Dlx5*, and *Arx*, and pyramidal layer II/III neurons expressed *Neurog2*, which can directly reprogram human embryonic stem cells to excitatory neurons of layer II/III phenotype with near 100% efficiency (21). *Lyl1* and *Spic* were specific to perivascular macrophages; *Spic* is essential for the maintenance of red pulp macrophages (22), suggesting that it may play a similar role in brain perivascular macrophages.

Expanding this analysis to all genes, we found extensive functional specialization between cellular subclasses. Ependymal cells (multiciliated cells lining the ventricles) expressed the largest set of subclass-restricted genes, including transcription factors *Foxj1*, *Myb*, and *Rfx2*, the master regulators of motile ciliogenesis (23) (24), and *Zmynd10*, which causes ciliopathy when mutated in humans (25). Nearly every structural component of cilia was also represented (Fig. 4B), including the 2+9 microtubule core and radial spokes, the dynein and kinesin motors, the filamentous shell, the basal body that anchors cilia to the cytoplasm, and two adenylate kinases (*Ak7* and *Ak8*) that generate adenosine triphosphate energy supporting cilia motility. Many of these structural genes are directly regulated by *Foxj1*, *Rfx2*, or *Rfx3* (23, 26) (Fig. 4B).

In summary, our findings reveal the diversity of brain cell types and transcriptomes. Across the full set of cell types, transcription factors formed a complex, layered regulatory code, suggesting a

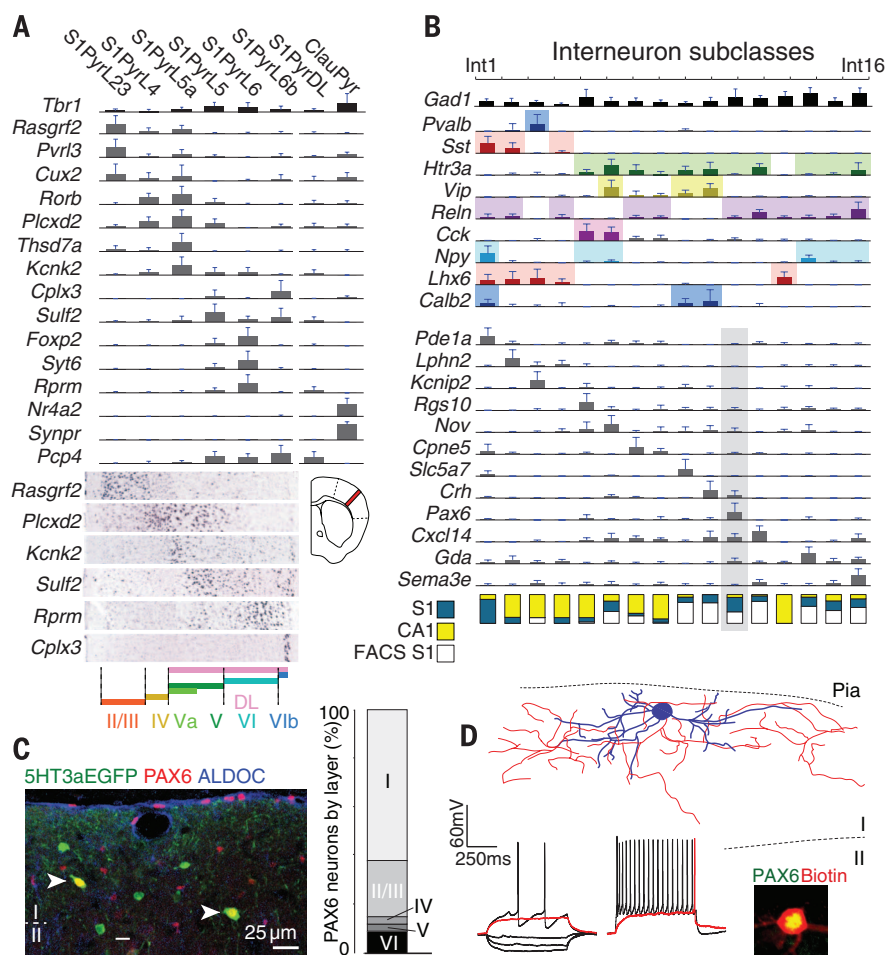


Fig. 2. Neuron subclasses in the somatosensory cortex. (A) Subclasses of pyramidal neurons in the somatosensory cortex (S1) identified by BackSPIN clustering. Bar plots show mean expression of selected known and novel markers (error bars show standard deviations). Layer-specific expression shown by in situ hybridization (Allen Brain Atlas). S1PyrL23, layer II–III; S1PyrL4, layer IV; S1PyrL5a, layer Va; S1PyrL5, layer V; S1PyrL6, layer VI; S1PyrL6b, layer Vlb; S1PyrDL, deep layers; ClauPyr, claustrum. (B) Identification of interneuron subclasses. Bar plots show selected known and novel markers. Fraction of S1/CA1 cells is depicted at bottom: blue, S1; yellow, CA1; white, flow-sorted Htr3a⁺ cells from S1. (C) Immunohistochemistry demonstrating the existence and localization of novel PAX6⁺/5HT3aEGFP⁺ interneurons, Int11. Bar plots show the layer distribution of these neurons. (D) Intrinsic electrophysiology and morphology of PAX6⁺ interneurons in S1 layer I, identified by post hoc staining.

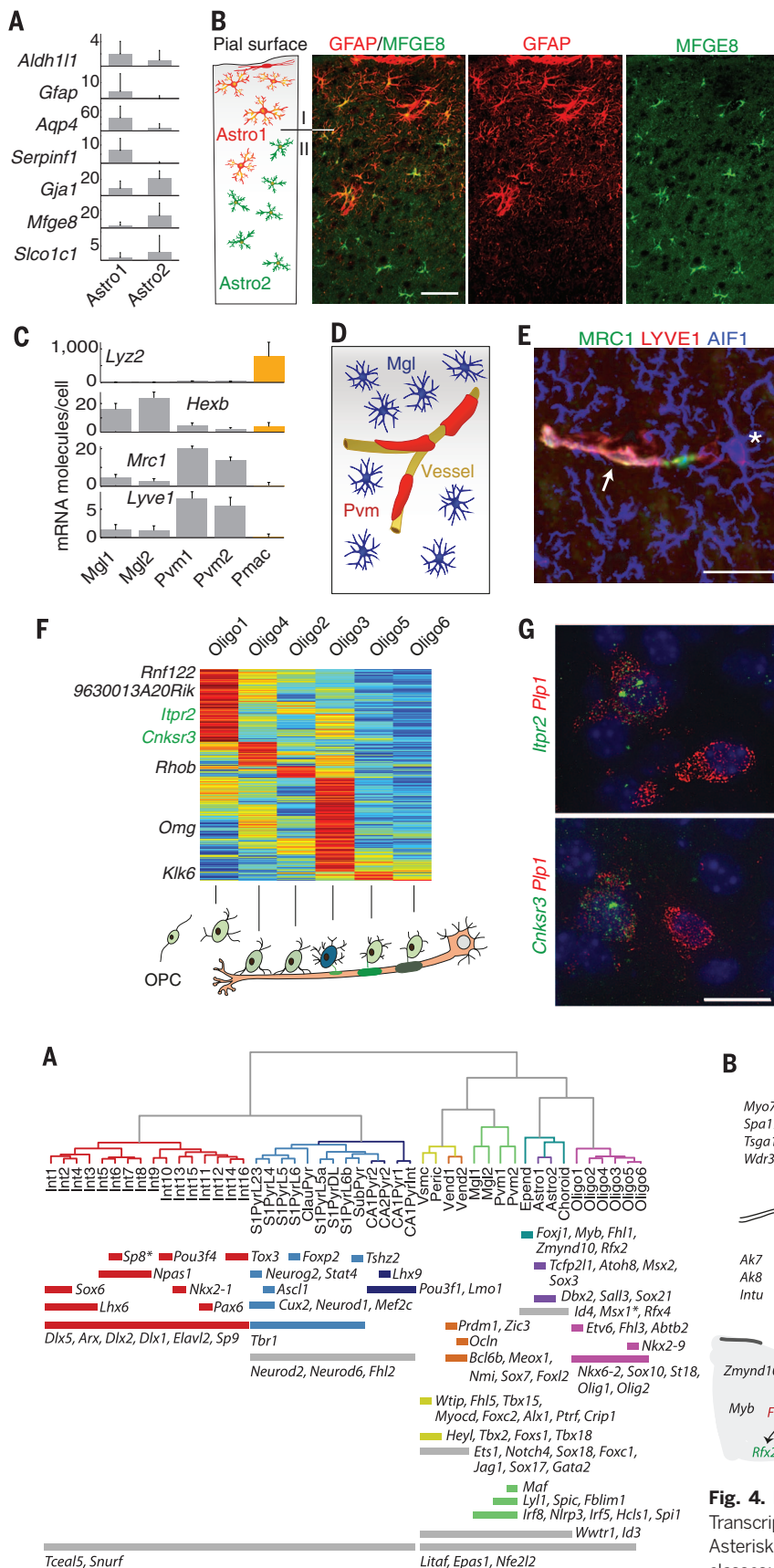


Fig. 3. Characterization of glial subclasses. (A) Two types of astrocytes (Astro1 and Astro2) identified by common and distinct markers. (B) Immunohistochemistry for glial fibrillary acidic protein (red, Astro1) and MFGE8 (green, Astro2). Scale bar, 50 μ m. (C) Genes showing expression restricted to microglia (Mgl), perivascular macrophages (Pvm), and peritoneal macrophages (Pmac). Error bars show standard deviations. (D) Cartoon illustrating the morphology and localization of microglia and perivascular macrophages. (E) Immunostaining for AIF1 (previously known as Iba-1, blue) marking microglia, and for MRC1 (green) and LYVE1 (red) marking perivascular macrophages. Asterisk, a microglia cell. Arrow, a perivascular macrophage aligned to a vessel (not stained). Scale bar, 20 μ m. (F) Heat map showing progressive changes in gene expression along oligodendrocyte differentiation, illustrated below. (G) Single-molecule RNA FISH for *Itpr2* and *Cnksr3* mark a strict subset of oligodendrocytes (as identified by *Plp1*). Scale bar, 11 μ m.

specific to ependymal cells. Transcription factors *Foxj1*, *Rfx2*, and *Rfx3* (with asterisk to indicate its wider expression) and their known targets are shown in red, green, and blue, respectively. Arrows indicate known direct interactions between transcription factors. Only genes with known ciliary function are included.

Fig. 4. Expression of regulatory genes across 47 subclasses. (A) Transcription factors showing restricted expression across cell types. Asterisks denote genes with additional expression in distinct subclasses: *Sp8* in *Int11*, *Mx1* in vascular cells and microglia. (B) Genes

plausible mechanism for the maintenance of adult differentiated cell types. More broadly, these results showcase the power of explorative single-cell RNA-seq and point the way toward future whole-brain and even whole-organism cell type discovery and characterization. Such data will deepen our understanding of the regulatory basis of cellular identity, in development, neurodegenerative disease, and regenerative medicine.

REFERENCES AND NOTES

1. B. J. Molyneaux, P. Ariotta, J. R. Menezes, J. D. Macklis, *Nat. Rev. Neurosci.* **8**, 427–437 (2007).
2. T. Klausberger, P. Somogyi, *Science* **321**, 53–57 (2008).
3. J. DeFelipe et al., *Nat. Rev. Neurosci.* **14**, 202–216 (2013).
4. K. Sugino et al., *Nat. Neurosci.* **9**, 99–107 (2006).
5. G. Fishell, B. Rudy, *Annu. Rev. Neurosci.* **34**, 535–567 (2011).
6. E. S. Lein et al., *Nature* **445**, 168–176 (2007).
7. A. Kepecs, G. Fishell, *Nature* **505**, 318–326 (2014).
8. D. A. Jaitin et al., *Science* **343**, 776–779 (2014).
9. B. Treutlein et al., *Nature* **509**, 371–375 (2014).
10. A. A. Pollen et al., *Nat. Biotechnol.* **32**, 1053–1058 (2014).
11. S. Islam et al., *Nat. Methods* **11**, 163–166 (2014).
12. T. Kivioja et al., *Nat. Methods* **9**, 72–74 (2011).
13. D. Tsafir et al., *Bioinformatics* **21**, 2301–2308 (2005).
14. C. Shi, E. G. Pamer, *Nat. Rev. Immunol.* **11**, 762–774 (2011).
15. O. Kann, C. Huchzermeyer, R. Kovács, S. Wirtz, M. Schuelke, *Brain* **134**, 345–358 (2011).
16. H. W. Dong, L. W. Swanson, L. Chen, M. S. Fanselow, A. W. Toga, *Proc. Natl. Acad. Sci. U.S.A.* **106**, 11794–11799 (2009).
17. K. Mizuseki, K. Diba, E. Pastalkova, G. Buzsáki, *Nat. Neurosci.* **14**, 1174–1181 (2011).
18. L. Tricoire et al., *J. Neurosci.* **30**, 2165–2176 (2010).
19. M. Prinz, J. Priller, *Nat. Rev. Neurosci.* **15**, 300–312 (2014).
20. I. Galea et al., *Glia* **49**, 375–384 (2005).
21. Y. Zhang et al., *Neuron* **78**, 785–798 (2013).
22. M. Kohyama et al., *Nature* **457**, 318–321 (2009).
23. J. A. Thomas et al., *Biol. Cell* **102**, 499–513 (2010).
24. E. R. Brooks, J. B. Wallingford, *Curr. Biol.* **24**, R973–R982 (2014).
25. M. A. Zarivwala et al., *Am. J. Hum. Genet.* **93**, 336–345 (2013).
26. M. I. Chung et al., *eLife* **3**, e01439 (2014).

ACKNOWLEDGMENTS

The raw data have been deposited with the Gene Expression Omnibus (www.ncbi.nlm.nih.gov/geo) under accession code GSE60361. Annotated data are available at <http://linnarssonlab.org/cortex>. We thank P. Ernfors, K. Harris, and R. Sandberg for useful comments on the manuscript; F. Ginhoux for helpful discussions on microglia and macrophages; A. Johnsson for laboratory management and support; ALM/SciLife (H. G. Blom) for technical support; and Fluidigm Inc. (R. C. Jones and M. Lynch) for generous technical and instrument support. S.L. was supported by the European Research Council (261063, BRAINCCELL) and the Swedish Research Council (STARGET); A.Z. was supported by the Human Frontier Science Program; A.B.M.-M. was supported by the Karolinska Institutet (BRECT); C.R. was supported by the Swedish Cancer Society (CAN2013/852); G.C.-B. was supported by the Swedish Research Council, the European Union (FP7/Marie Curie Integration Grant EPIOPC), the Åke Wiberg Foundation, the Karolinska Institutet Research Foundations, Svenska Läkaresällskapet, Clas Groschinskys Minnesfond, and Hjärtfonden; J.H.-L. was supported by the Swedish Research Council, the European Union (FP7/Marie Curie Actions (322304, Adolescent Development)), StratNeuro, and the Jeanssons, Åke Wibergs, and Magnus Bergvalls Foundations; C.B. was supported by the European Research Council (294556, BBBARRIER), a Knut and Alice Wallenberg Scholar Grant, the Swedish Cancer Society, and Swedish Research Council. Supplementary materials contain additional data.

SUPPLEMENTARY MATERIALS

www.sciencemag.org/content/347/6226/1138/suppl/DC1
Materials and Methods
Supplementary Text
Figs. S1 to S11
Tables S1 and S2
References (27–36)

30 October 2014; accepted 30 January 2015
Published online 19 February 2015;
10.1126/science.aaa1934

FRESHWATER ECOLOGY

Experimental nutrient additions accelerate terrestrial carbon loss from stream ecosystems

Amy D. Rosemond,^{1*} Jonathan P. Benstead,² Phillip M. Bumpers,¹ Vladislav Gulis,³ John S. Kominoski,^{1†} David W. P. Manning,¹ Keller Suberkropp,² J. Bruce Wallace¹

Nutrient pollution of freshwater ecosystems results in predictable increases in carbon (C) sequestration by algae. Tests of nutrient enrichment on the fates of terrestrial organic C, which supports riverine food webs and is a source of CO₂, are lacking. Using whole-stream nitrogen (N) and phosphorus (P) additions spanning the equivalent of 27 years, we found that average terrestrial organic C residence time was reduced by ~50% as compared to reference conditions as a result of nutrient pollution. Annual inputs of terrestrial organic C were rapidly depleted via release of detrital food webs from N and P co-limitation. This magnitude of terrestrial C loss can potentially exceed predicted algal C gains with nutrient enrichment across large parts of river networks, diminishing associated ecosystem services.

Nutrient pollution of freshwater ecosystems is pervasive and strongly affects carbon (C) cycling. Excess nutrients stimulate the production of C-rich algal biomass but can also stimulate C loss through increased organic C mineralization that releases CO₂ instead of supporting production of higher trophic levels and other ecosystem functions (1, 2). Production of aquatic life in freshwater ecosystems is based on algae and organic C of terrestrial origin. Currently, consideration of nutrient effects on C cycling in inland waters has focused on enhancement of algal C sinks in lakes and less on fates of terrestrial C that may experience accelerated loss in river networks (3–5).

The processes that lead to nutrient stimulation of algal C production and terrestrial C mineralization are fundamentally different. Algal production increases relatively predictably with the availability of growth-limiting nutrients (1, 6). In contrast, mineralization of particulate organic C (POC) is the more complex result of activity by multiple trophic levels consisting of microbial decomposers and detritivorous animals (hereafter detritivores) (7). Inputs of leaves and wood are the main sources of POC in many rivers, supporting production of animals and uptake of inorganic pollutants (8–10). Nutrients stimulate microbial processing of POC, which results in increased losses of CO₂ to the atmosphere (2, 11). Consumption of microbially colonized POC by detritivores further contributes to its breakdown and conversion to smaller particles, which affect its subsequent transport and processing downstream (7).

To determine how moderate nutrient pollution affects terrestrially derived POC at stream-

reach scales, we tested how long-term (2- to 5-year), continuous, flow-proportional nitrogen (N) and phosphorus (P) additions affected its loss rates and fates in headwater forest streams (12). We measured the response of terrestrial C loss rates in whole 70- to 150-m stream reaches (tables S1 and S2). Carbon loss rates at this spatial scale are a function of biologically driven breakdown and hydrological export and have not been previously assessed in response to human-influenced stressors (13). We conducted two manipulative experiments at large spatial and temporal scales and focused our measurements on forest-derived leaf litter, because it is the most biologically active pool of terrestrial C in forest streams and is renewed annually (7). After a pretreatment year, we enriched one stream with N and P at a set ratio for 5 years in a paired watershed design (N+P experiment; a second stream acted as a control) and used expanded N and P gradients in a second experiment in five other streams for 2 years after a pretreatment year (N×P experiment) (table S1).

Reach-scale terrestrial C loss rates increased with N and P enrichment across all the concentrations we tested (Fig. 1). Discharge, N, P, temperature, and associated random effects (stream and year) explained 83% of the variation in C loss rates across 27 annual measurements (table S3). Standardized regression coefficients indicated that our moderate additions of N and P contributed roughly three-fourths of the effect on litter loss rates as annual cumulative discharge, which varied 87-fold across streams and years (table S3). Nitrogen and P ($r = 0.79$) and discharge and temperature ($r = -0.76$) were correlated, so their effects and relative significance cannot be teased apart fully. However, roughly similar-sized effects of N and P on loss rates are strong evidence of co-limitation (Fig. 2 and table S3). Comparisons of loss rates from corresponding enriched and reference streams indicate that median C loss rates increased 1.65 times with nutrient enrichment (table S4); the range in these values (1.02 to 4.49 times) reflects variation due to N

¹Odum School of Ecology, University of Georgia, Athens, GA 30602, USA. ²Department of Biological Sciences, University of Alabama, Tuscaloosa, AL 35487, USA. ³Department of Biology, Coastal Carolina University, Conway, SC 29528, USA.

*Corresponding author. E-mail: rosemond@uga.edu †Present address: Department of Biological Sciences, Florida International University, Miami, FL 33199, USA.

and P concentrations, discharge, and temperature (table S1). Average residence time of terrestrial POC was roughly halved with nutrient

enrichment: from 167 days in reference conditions to 75 days with nutrient addition (median values were 125 and 74 days, respectively). Litter

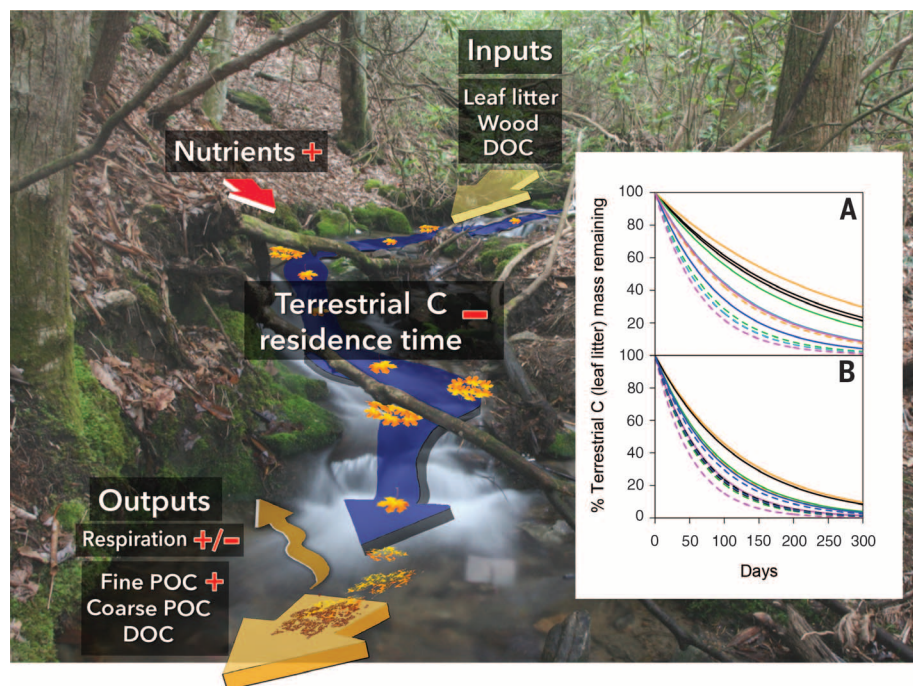
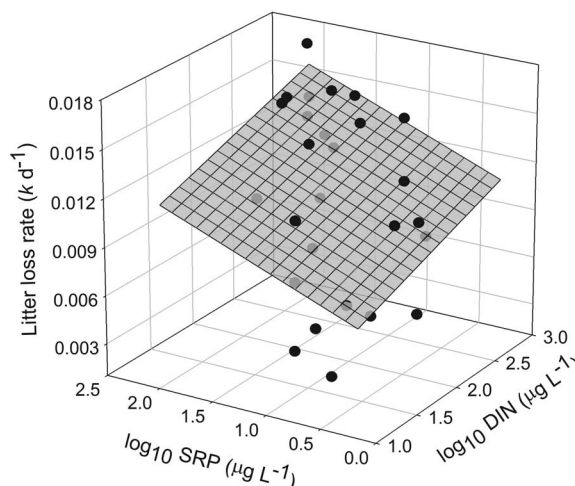


Fig. 1. Terrestrial C residence time was approximately halved with experimental nutrient enrichment. Increased nutrient inputs (+) reduced terrestrial particulate C residence time (–) and increased export of fine detrital particles (+) and respiration rates [which increased on C substrates (11) but decreased at reach scales; +/–]. Inset graph: Reach-scale leaf litter loss rates were faster in enriched (dashed lines) than in reference (solid lines) streams; the inverse of these rates is residence time. Colors correspond to the same years in (A) (reference versus enriched streams; N+P experiment; $n = 12$ annual rates) and to the same streams in (B) (pretreatment versus enriched years; N x P experiment; $n = 15$ annual rates). Data shown for litter loss are untransformed but were natural log-transformed for analyses and the calculation of loss rates (k , per day). The larger image depicts terrestrial organic C inputs, which enter as leaf litter, wood, and dissolved organic carbon (DOC), and outputs as hydrologic export (fine and coarse particles, DOC) and respired CO_2 in deciduous forest streams, using an image of one of the N x P experimental stream sites.

Fig. 2. Terrestrial C loss rates from stream reaches increased with N and P concentrations.

The surface represents the predicted loss rate (k , per day) as a function of streamwater dissolved inorganic nitrogen (DIN) and soluble reactive phosphorus (SRP) at mean discharge rate and temperature for the study period derived from the multilevel model [variance explained by fixed and random effects (conditional R^2) = 0.83; parameter estimates are in table S3]. Each data point is the estimated litter loss rate for a particular stream-year derived from the first level of our hierarchical model (12). Mean (range) annual concentrations of nutrients in micrograms per liter tested in our experiments were moderate and reflect concentrations commonly observed due to watershed land-use change: SRP reference: 6 (2 to 12), SRP-enriched: 49 (6 to 117); DIN reference: 53 (13 to 189), DIN-enriched: 347 (66 to 798).



quantity in the streambed was predicted to be 2.8 times and 7.7 times higher in reference versus nutrient-enriched streams after 6 and 12 months, respectively, based on average annual litter inputs and median loss rates in reference and enriched conditions, showing increasing differences in retained C due to nutrient enrichment over time.

Relatively large effects of nutrients on reach-scale loss rates indicated that biological processing had strong effects despite relatively large temporal variation in physical conditions in headwater streams. We further tested the importance of biological versus physical control of C loss rates by comparing the degree to which small-scale (i.e., litterbag) measurements aligned with reach-scale rates, using measurements made at the same time; relatively good alignment between reach-scale and litterbag-scale rates indicates that biological, rather than physical, processes drove reach-scale rates (table S5). Litterbag-scale loss rates of more-labile litter species tended to overestimate and those of more-refractory litter species tended to underestimate reach-scale C loss rates, due to the integration of effects from diverse litter types at the reach scale (Fig. 3). When litterbag-scale rates exceeded reach-scale rates, this suggested strong and increased biological processing of C under nutrient-enriched conditions. Higher C loss rates at the litterbag scale than the reach scale are expected, because litterbags track distinct parcels of C, whereas reaches receive additional C inputs over time. These processes probably outweigh differences due to the retention of smaller particles in litterbags that are not included in reach-scale estimates. Our results generally support the use of litterbags to measure larger-scale C dynamics, but with consideration of differences among litter species and potential divergence in rates due to the degree of biological processing (2, 14).

We quantified the potential alternative fates of terrestrial C to gain insights into the relative role of microbial decomposers that largely drive C losses as respiration, versus detritivores that largely drive C losses as POC export, in contributing to reach-scale C loss rates. Using data from our N+P experiment, we tracked all pools and losses (outputs) of terrestrial C, including litter; C pools declined, and outputs, particularly of fine (<4 mm) POC, increased with enrichment (Fig. 4 and table S6). Pretreatment conditions included higher pools of fine benthic POC and lower export of POC in the enriched stream, due to inherent morphological and hydrological differences between streams [table S6 (12)]. The first 2 years of nutrient enrichment showed that pools of benthic fine and coarse POC declined in the nutrient-enriched stream relative to the reference stream. Reach-scale outputs of C increased as fine POC export, as well as respiration (15). In subsequent years of enrichment, pools of fine and coarse benthic POC were lower in the enriched than the reference stream, as compared to pretreatment conditions, which is consistent with previous findings (15). However, relatively higher outputs from the enriched stream were due more to POC export than to respiration in later years of

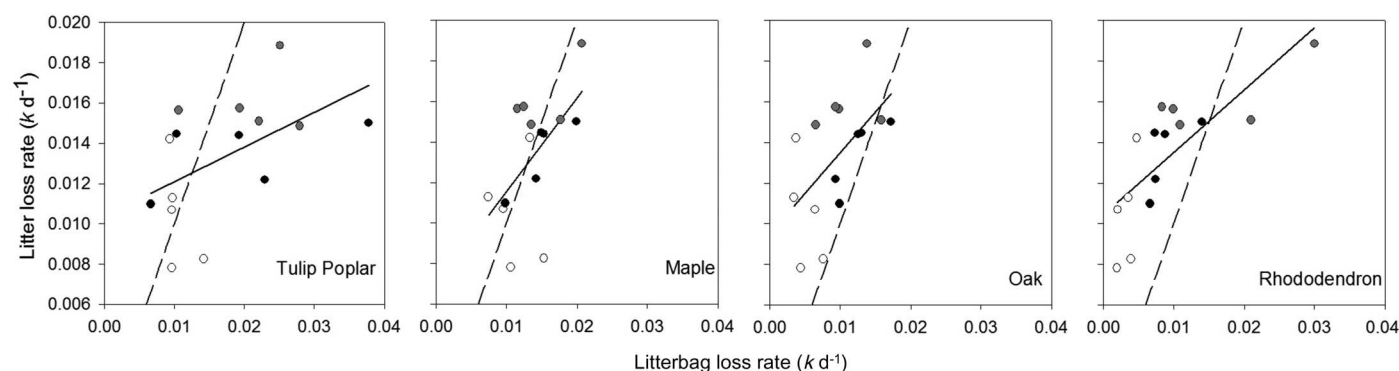
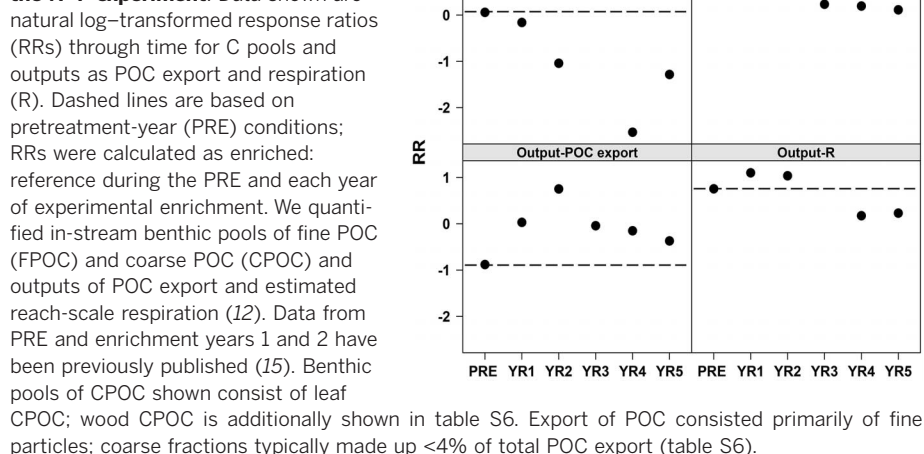


Fig. 3. Small-scale (litterbag) leaf litter loss rates can predict reach-scale leaf litter loss rates. Shown are leaf litter loss rates from equivalent streams and years for four leaf litter types across the five streams in the N+P experiment during pretreatment (open circles) and years 1 (gray circles) and 2 (black circles) of enrichment. Litterbag rates were quantified from coarse-mesh bags and represent microbial + detritivore-mediated breakdown (12). The dashed line represents a 1:1 relationship. Equations describing these relationships and those from the N+P experiment are in table S5.

Fig. 4. Nutrient enrichment affected pools and outputs of terrestrial C in the N+P experiment. Data shown are natural log-transformed response ratios (RRs) through time for C pools and outputs as POC export and respiration (R). Dashed lines are based on pretreatment-year (PRE) conditions; RRs were calculated as enriched:



reference during the PRE and each year of experimental enrichment. We quantified in-stream benthic pools of fine POC (FPOC) and coarse POC (CPOC) and outputs of POC export and estimated reach-scale respiration (12). Data from PRE and enrichment years 1 and 2 have been previously published (15). Benthic pools of CPOC shown consist of leaf CPOC; wood CPOC is additionally shown in table S6. Export of POC consisted primarily of fine particles; coarse fractions typically made up <4% of total POC export (table S6).

enrichment. Specifically, nutrient enrichment affected both outputs, but on a reach scale, POC export increased, whereas respiration declined (Fig. 4). Relatively lower reach-scale respiration despite higher substrate-specific microbial respiration rates (11) was a function of smaller pools of POC, from which the areal respiration estimates were calculated, in the enriched stream (table S6).

Increased POC export in the enriched stream was due to nutrient-stimulated particle generation from a combination of microbial decomposition and detritivore feeding (11, 16–18). These transformations alter the normal balance of the fates of C inputs to greater respiratory losses, more POC export as fine particles, and less C storage. Transport distances of POC are variable, but they are much longer for smaller than larger particles (7, 19). Thus, in a given nutrient-enriched stream reach, less C remains to contribute to annual storage and associated ecosystem services (8). Whether microorganisms or animal feeding have relatively greater influence on the processing of terrestrial C affects how much C is transported downstream or lost primarily as CO_2 . In agricultural streams with diminished abun-

dance of detritivores, nutrients stimulate largely microbial breakdown of crop residues that enter streams (20). Similarly, greater CO_2 flux than export due to increased microbial, but not detritivore, processing of terrestrial C is predicted with elevated temperature (21). When animals are reduced in streams due to biogeographic or land-use factors, nutrients or temperature accelerate losses of C, but primarily via CO_2 , not export of particles. Thus, populations of detritivores in streams play complex and important roles: They may limit terrestrial C loss as CO_2 and maintain downstream C export, but contribute to depletion of local C resources (22, 23).

Our results suggest that N and P co-limit terrestrial C loss rates in streams, for which there is a growing body of evidence (2, 24, 25). Algal C production is similarly co-limited by N and P in many systems (6, 26). The similarity in the magnitude of C loss to general patterns of C gain, despite fundamentally different processes, is significant. Average autotroph responses to N and P additions in freshwater and marine environments are roughly three times and two times higher than controls, respectively (6); however, the range in responses is highly variable (27). Organic C

pools are dominated by terrestrial sources in small streams but shift to greater contributions of autotrophic C in larger streams and rivers (28). We compared simple first approximations of the potential effects of nutrient enrichment on decreases in benthic POC relative to increases in autotrophic C across the larger river network where our studies were conducted and found a potential for terrestrial POC losses that are greater than estimated autotrophic C gains in first- through fourth-order stream channels (12) (table S7). Estimated losses for entire stream networks were greater than autotrophic C gains when summed across total streambed area in streams as large as sixth-order; nutrient-driven increases in autotrophic C production in the largest river channel (seventh-order) outweighed these losses (12). For stream ecosystems in which nutrient pollution results in net C losses, the local ecological effects of lower C availability, as well as the implications for downstream systems, may be substantial.

The mineralization of terrestrial C, similar to the production of algal C, is stimulated at nutrient concentrations that are now common across human-disturbed landscapes (2, 29). Thus, reduced retention and increased export and respiratory losses of terrestrial C are probably occurring in many aquatic systems because of increased nutrient availability, with consequences for ecosystem services. The loss of terrestrial C is not as visually obvious as increased algal biomass. Policies aimed at addressing nutrient effects on C resources, as well as efforts to determine the effects of global change on inland C balances, currently focus largely on the accrual of algal C, not losses of terrestrially derived C (30, 31). Management of nutrient effects on both of these pathways would positively affect riverine health.

REFERENCES AND NOTES

1. J. C. Finlay, G. E. Small, R. W. Sterner, *Science* **342**, 247–250 (2013).
2. G. Woodward *et al.*, *Science* **336**, 1438–1440 (2012).
3. T. J. Battin *et al.*, *Nat. Geosci.* **2**, 598–600 (2009).
4. F. S. Pacheco, F. Roland, J. A. Downing, *Inland Waters* **4**, 41–48 (2013).

5. L. J. Tranvik et al., *Limnol. Oceanogr.* **54**, 2298–2314 (2009).
6. J. J. Elser et al., *Ecol. Lett.* **10**, 1135–1142 (2007).
7. J. R. Webster et al., *Freshw. Biol.* **41**, 687–705 (1999).
8. J. B. Wallace, S. L. Eggert, J. L. Meyer, J. R. Webster, *Science* **277**, 102–104 (1997).
9. D. A. Walther, M. R. Whiles, *J. N. Am. Benthol. Soc.* **30**, 357–373 (2011).
10. J. R. Webster et al., *Verh. Int. Ver. Theor. Angew. Limnol.* **27**, 1337–1340 (2000).
11. K. Suberkropp, V. Gulis, A. D. Rosemond, J. P. Benstead, *Limnol. Oceanogr.* **55**, 149–160 (2010).
12. Materials and methods are available as supplementary materials on Science Online.
13. S. G. Fisher, G. E. Likens, *Ecol. Monogr.* **43**, 421–439 (1973).
14. M. O. Gessner, E. Chauvet, *Ecol. Appl.* **12**, 498–510 (2002).
15. J. P. Benstead et al., *Ecology* **90**, 2556–2566 (2009).
16. J. L. Greenwood, A. D. Rosemond, J. B. Wallace, W. F. Cross, H. S. Weyers, *Oecologia* **151**, 637–649 (2007).
17. V. Gulis, K. Suberkropp, *Freshw. Biol.* **48**, 123–134 (2003).
18. C. J. Tant, A. D. Rosemond, M. R. First, *Freshw. Sci.* **32**, 1111–1121 (2013).
19. S. A. Thomas et al., *Limnol. Oceanogr.* **46**, 1415–1424 (2001).
20. N. A. Griffiths et al., *Ecol. Appl.* **19**, 133–142 (2009).
21. L. Boyero et al., *Ecol. Lett.* **14**, 289–294 (2011).
22. J. B. Wallace, J. R. Webster, T. F. Cuffney, *Oecologia* **53**, 197–200 (1982).
23. J. B. Wallace, T. F. Cuffney, B. S. Goldowitz, K. Chung, G. J. Lughart, *Verh. Int. Ver. Theor. Angew. Limnol.* **24**, 1676–1680 (1991).
24. V. Ferreira et al., *Biol. Rev.* **10.1111/brv.12125** (2015).
25. J. S. Kominoski et al. (2015); available at www.esajournals.org/doi/abs/10.1890/14-1113.1.
26. D. J. Conley et al., *Science* **323**, 1014–1015 (2009).
27. J. E. Allgeier, A. D. Rosemond, C. A. Layman, *J. Appl. Ecol.* **48**, 96–101 (2011).
28. J. R. Webster, *J. N. Am. Benthol. Soc.* **26**, 375–389 (2007).
29. R. B. Alexander, R. A. Smith, *Limnol. Oceanogr.* **51**, 639–654 (2006).
30. T. J. Battin et al., *Nat. Geosci.* **1**, 95–100 (2008).
31. W. K. Dodds, *Trends Ecol. Evol.* **22**, 669–676 (2007).

ACKNOWLEDGMENTS

We thank H. Weyers, N. Taylor, R. Hilten, S. Dye, J. Coombs, and K. Norris for their assistance in maintaining the enrichments and associated data collection and analyses; C. Tant and J. Greenwood for conducting the N+P litterbag studies; and S. Eggert for assisting in data collection and analysis and helping develop sampling protocols. T. McCallister illustrated Fig. 1 (photo credit: PMB). The manuscript was improved by comments from R. Hall, E. Rosi-Marshall, F. Ballantyne, S. Altizer, A. Helton, A. Hurn, M. Paul, J. Davis, R. Sponseller, C. Song, and anonymous reviewers. J. Maerz contributed ideas and logistical help associated with the N+P experiment; S. Wenger, R. Hall, C. Song, and D. Hall provided statistical advice; D. Leigh and J. Hepinstall-Cymerman provided spatial data; and J. Webster provided site information. We are grateful to A. Helton for conducting the network-scale extrapolation. Data are available in the supplementary materials in Science Online. This research leveraged logistical support from the Coweeta Long Term Ecological Research Program at the University of Georgia, which is supported by the National Science Foundation Division of Environmental Biology (NSF DEB grant 0823293). The order of authors after the first author is alphabetical; funding for these experiments was provided in NSF grants DEB-9806610, 0318063, 0918894, 0918904, and 0919054 from the Ecosystem Studies Program to A.D.R., J.P.B., V.G., K.S., J.B.W., and others (J. Maerz, above; M. Black, University of Georgia; and P. Mulholland, Oak Ridge National Laboratory).

SUPPLEMENTARY MATERIALS

www.sciencemag.org/content/347/6226/1142/suppl/DC1
Materials and Methods
Supplementary Text
Tables S1 to S7
References (32–50)

7 November 2014; accepted 27 January 2015
10.1126/science.aaa1958

POLITICAL ECONOMY

On the endogeneity of political preferences: Evidence from individual experience with democracy

Nicola Fuchs-Schündeln*† and Matthias Schündeln*†

Democracies depend on the support of the general population, but little is known about the determinants of this support. We investigated whether support for democracy increases with the length of time spent under the system and whether preferences are thus affected by the political system. Relying on 380,000 individual-level observations from 104 countries over the years 1994 to 2013, and exploiting individual-level variation within a country and a given year in the length of time spent under democracy, we find evidence that political preferences are endogenous. For new democracies, our findings imply that popular support needs time to develop. For example, the effect of around 8.5 more years of democratic experience corresponds to the difference in support for democracy between primary and secondary education.

Popular support for democracy is critical to the success of a democracy, especially an emerging democracy (1, 2). Will support increase over time when a democracy emerges and the population gains experience with democracy? If so, how quickly? Or are democratic attitudes deeply ingrained in individuals, such that they are hard to change? The latest wave of democratizations in the world, which started in December 2010 in a movement often collectively referred to as the “Arab Spring,” and the subsequent struggles of these countries provide a recent illustration of the importance of these questions. However, a study that uses a clean identification strategy based on an experimental or quasi-experimental setup to identify the causal effect of accumulating experience with democracy on support for democracy in a broad set of countries—or more generally, a study that identifies endogenous preferences for political systems—is missing from the literature.

Indeed, recent research suggests that economic preferences are shaped by individual experiences with markets (3). In particular, preferences regarding fairness, preferences for redistribution, and other types of preferences related to economic behavior vary across societies in a way that correlates with market characteristics (4, 5). A causal interpretation of these correlations and the view that economic preferences are endogenous is founded in theoretical arguments (6–8) and is empirically supported by research based on experimental or quasi-experimental settings, such as the end of communism in Eastern Europe or the stock market return experiences accumulated over a lifetime (9–11).

Regarding the endogeneity of political preferences, research has so far shown a positive correlation between experience with political systems

and political preferences at the country level (12), a positive correlation between attitudes toward democracy and currently living under a democratic system (13), and that a longer democratic experience lowers the probability of exit from democracy and increases the probability of exit from autocracy (12). However, a causal influence of experience with democracy on the support for democracy, which would imply endogeneity of preferences, cannot be established from these correlations. The correlations could (partly) be due to reverse causality (i.e., countries have a democratic history precisely because the electorate supports democratic values); or a third, possibly unobserved, variable, such as historic events or economic conditions, could determine both individuals' support for democracy and the political system in place.

Here, we exploited within-country variation at the individual level in experience with a democratic regime to establish a plausibly causal impact of experience with democracy on preferences for democracy, and thereby contribute to a better understanding of the endogeneity of political preferences. Because we control for country-year fixed effects, the observed differences in attitudes toward democracy do not simply reflect a reaction to differences in the current quality of institutions or political environments, but, under the minimal and plausible identifying assumption that we state below, constitute a change in intrinsic preferences due to differences in the length of exposure to democracy. For example, if democratic institutions or economic conditions improve with the length of time spent under democracy, this might increase the support for democracy directly and not through intrinsic preferences, but it would be captured in our specification by the country-year fixed effects, which control for all country-level unobservables that are specific to a country in a given year. Any remaining correlation between experience with democracy and support for democracy can therefore confidently be attributed to a change in preferences.

Goethe University Frankfurt, 60320 Frankfurt, Germany.

*Both authors contributed equally to this work. †Corresponding author. E-mail: fuchs@wiwi.uni-frankfurt.de (N.F.-S.); schundeln@wiwi.uni-frankfurt.de (M.S.)

We base the analysis on two different data sets: (i) the World Values Surveys, which cover both developed and less-developed countries across the world, and (ii) the Afrobarometer Surveys, which allow us to specifically study African countries, many of which are still in the early stages of the transition from autocratic to democratic rule. Our empirical work is based on more than 380,000 individual-level observations, coming from 104 countries over the years 1994 to 2013.

We find that preferences for democracy increase as individuals experience more time living under democratic rule. This result is robust to different ways of measuring support for democracy and democracy itself, and across the different data sets. Our baseline estimates imply that 8.5 more years of continuously living under democratic rule increase support for democra-

cy by as much as going from primary to secondary education (as the highest level of education attained). For new democracies, our findings thus imply that popular support needs time to develop.

Both the World Values Surveys (WVS) and the Afrobarometer Surveys are repeated cross-sectional surveys at the individual level that cover a set of questions that is consistent across countries and over time (details, including a list of countries and years covered, are in the supplementary text and tables S1 and S2). For our purposes, the main differences between the two surveys are in the questions related to support for democracy. For the analysis based on the WVS, we mainly used the Inglehart and Welzel (IW) index introduced in (14), which is based on four different questions, where higher index numbers indicate more prodemocratic attitudes;

the index ranges from -6 to 6. The index and the four questions on which it is based are described in the supplementary materials. To demonstrate robustness, we also used all four questions individually. For the analysis based on the Afrobarometer Surveys, we created a binary variable, "support for democracy," which is coded as 1 if the individual chooses the statement "Democracy is preferable to any other kind of government" over the statements "a nondemocratic government can be preferable," "it doesn't matter," or "don't know" (15).

Our identification strategy relies on exploiting within-country variation in the length of time that individuals have experienced democracy. To this end, we first identified periods of democratic rule using the widely used Polity 2 index from the Polity IV project (16). We followed the categorization of the Polity IV

Table 1. Determinants of support for democracy. Question E117 asks whether "having a democratic political system" is "a very good, fairly good, fairly bad, or very bad way of governing this country." Question E123 asks whether the respondent agrees strongly, agrees, disagrees, or disagrees strongly with the statement "Democracy may have problems but it's better than any other form of government." Robust standard errors (in parentheses) are clustered at the country-year level. The omitted age category is older than 60 years; the omitted education category is no education. Columns 1 to 5 show coefficients from ordered probit estimations, column 6 from a probit estimation.

Determinant	Basis of support for democracy					
	World Values Survey				Afrobarometer	
	IW index (2003) (1)	IW index (2003) (2)	IW index (2003) (3)	Question E117 (4)	Question E123 (5)	Bratton (2004) (6)
Country democratic at time of survey	0.339** (0.141)	0.335** (0.142)				
Country's democratic capital	0.063** (0.030)	0.040 (0.030)				
Individual's democratic capital		0.021*** (0.005)	0.021*** (0.005)	0.018*** (0.003)	0.021*** (0.004)	0.021*** (0.006)
Age 11–20	–0.162*** (0.044)	–0.066* (0.036)	–0.053 (0.035)	–0.057** (0.024)	–0.080** (0.040)	–0.095*** (0.029)
Age 21–30	–0.101*** (0.039)	–0.023 (0.032)	–0.011 (0.032)	–0.090*** (0.020)	–0.063* (0.035)	–0.044* (0.024)
Age 31–40	–0.041 (0.031)	0.007 (0.026)	0.014 (0.026)	–0.069*** (0.017)	–0.047 (0.030)	0.049** (0.022)
Age 41–50	0.001 (0.025)	0.023 (0.023)	0.031 (0.023)	–0.039*** (0.015)	–0.022 (0.027)	0.078*** (0.021)
Age 51–60	0.038** (0.019)	0.048*** (0.018)	0.051*** (0.018)	–0.026** (0.012)	–0.001 (0.021)	0.089*** (0.020)
Male	0.049*** (0.011)	0.050*** (0.011)	0.050*** (0.011)	0.063*** (0.008)	0.042*** (0.012)	0.194*** (0.015)
Primary education	0.073** (0.033)	0.067** (0.033)	0.067** (0.034)	0.029* (0.017)	0.011 (0.031)	0.215*** (0.022)
Secondary education	0.250*** (0.043)	0.244*** (0.043)	0.233*** (0.043)	0.162*** (0.022)	0.098** (0.042)	0.448*** (0.036)
Postsecondary education	0.529*** (0.053)	0.523*** (0.052)	0.518*** (0.051)	0.374*** (0.029)	0.275*** (0.051)	0.562*** (0.045)
Country fixed effects	Yes	Yes				
Year fixed effects	Yes	Yes				
Country-year fixed effects			Yes	Yes	Yes	Yes
Observations	82,990	82,990	82,990	228,901	92,565	149,035
Number of countries	56	56	56	79	57	31
Survey waves (WVS)	3–5	3–5	3–5	3–6	3–5	
Rounds (Afrobarometer)						1–5
Years covered	1994–2006	1994–2006	1994–2006	1994–2013	1994–2006	1999–2013

* $P < 0.1$, ** $P < 0.05$, *** $P < 0.01$.

project and defined democratic countries as those with a Polity 2 index of 6 or higher (see table S4 for alternative categorizations). We then used the concept of democratic capital (12), defining democratic capital at the country level as

$$\begin{aligned} \text{democ_cap}_{jt} &= \text{democratic}_{jt} + \delta \text{democ_cap}_{jt-1} \\ &= \sum_{\tau=t_0}^t \delta^{t-\tau} \text{democratic}_{j\tau} \end{aligned} \quad (1)$$

where j and t represent the country and the year, respectively, and democratic_{jt} is an indicator variable that takes on a value of 1 if a country is democratic in year t . We set $\delta = 0.98$, which is the midpoint of the range found in (12)—that is, democratic capital depreciates at a rate of 2%. Period t_0 , at which accumulation of democratic capital starts, is defined as the year 1946, or the earliest available date after 1946 (17). Finally, to quantify experiences with political regimes at the individual level, we analogously calculated individual-specific measures of democratic capital; that is, for an individual i of age age_i , democratic capital is calculated as

$$\begin{aligned} \text{democ_cap}_{ijt} &= \text{democratic}_{ijt} + \delta \text{democ_cap}_{ijt-1} \\ &= \sum_{\tau=\max(t_0, t-\text{age}_i)}^t \delta^{t-\tau} \text{democratic}_{j\tau} \end{aligned} \quad (2)$$

Our main specification is as follows:

$$\begin{aligned} \text{support_for_democracy}_{ijt} &= \alpha_0 + \alpha_1 \text{democ_cap}_{ijt} + \\ &\alpha'_2 X_{ijt} + \text{country-year_dummies}_{jt} \\ &+ \varepsilon_{ijt} \end{aligned} \quad (3)$$

where X_{ijt} is a vector of individual characteristics (18). This specification recognizes that there are unobserved country-year-specific variables that change over time, so that country-specific fixed effects alone cannot fully account for possible reverse causality and/or omitted variables. The country-year-specific fixed effects will capture all country-level unobservables that are specific to a country in a given year, such as current democratic institutions, currently ruling parties, or current economic conditions. We are interested in α_1 , the effect of experience with democracy at the individual level. Variation in individual experience is plausibly exogenous, as it is driven by age differences.

To separate the effect of experience with democracy from the effect of age, we exploit the variation across the large number of countries whose democratic histories differ substantially in both WVS and Afrobarometer. The underlying identifying assumption of our approach is that there are no unobserved factors at the country-year-age level that are correlated with the individual democratic capital stock and support for democracy. Under this assumption, α_1 cleanly identifies the effect of the individual experience with democracy on the support for democracy. “Living

under a democracy” is the basic treatment, and the individual’s democratic capital (i.e., the “length of experience with democracy”) can be interpreted as the treatment intensity. A positive estimate for α_1 arises if the relationship between age and support for democracy is more positive in long-standing democracies than in newly formed democracies, because in the former case, older individuals have accumulated a larger democratic capital stock than younger ones, whereas in the latter case, democratic capital does not vary by age (fig. S1). For the same reason, a positive estimate for α_1 arises if the relationship between age and support for democracy is more positive in newly formed autocracies than in long-standing autocracies.

Table 1 shows the main results. The first five columns report results based on WVS. Here, the dependent variables are ordinal, and we use the ordered probit estimator. In column 6, the dependent variable is a binary index and we estimate a probit model. All standard errors are corrected for correlation within country-year observations.

Columns 1 to 3 use the IW index as the dependent variable. As a reference point, column 1 includes country and year fixed effects separately, which allows us to include a dummy for the country’s current democratic status (democratic_{jt}) and the country-level measure of democratic capital (democ_cap_{jt}). Column 2 adds individual-level democratic capital (democ_cap_{ijt}). All three variables are positively correlated with stated support for democracy. However, as noted above, the country-level variables are likely endogenous. Therefore, our main specification in column 3 includes country-year fixed effects. Because in this way we can control for country-year-specific unobservables, and under the above stated identifying assumption, we can interpret a significant coefficient on an individual’s democratic capital as the causal effect that an individual’s experience with democracy has on that individual’s support for democracy. We find a statistically highly significant positive coefficient on the democratic capital that an individual has accumulated, indicating that individual experience with democracy positively affects support for democracy. Columns 4 and 5 use as dependent variables the two individual components from the IW index that measure prodemocratic attitudes (results using the two individual components that measure antidemocratic attitudes are shown in table S5). Unlike the other questions constituting the IW index, question EI17 (column 4) is also available in the latest wave of the WVS (2010–2014) and thus leads to a much larger number of observations. The results confirm the main finding. Column 6 focuses on Africa, using Afrobarometer data. We continue to find that a higher individual-level democratic capital stock increases support for democracy.

Several robustness checks (tables S3 to S5) confirm that our main results are robust to (i) adding more individual-level controls, (ii) omitting the potentially endogenous controls for education, (iii) different assumptions about the error

structure in the regression model, (iv) controlling for a full set of age dummies, (v) controlling for interactions between age and country fixed effects and age and year fixed effects, (vi) alternative ways to use the Polity 2 index to build the democratic capital stock, (vii) using alternative depreciation parameters to calculate democratic capital, (viii) restricting the sample to current democracies, current autocracies, or countries that never experienced a regime switch, and (ix) using the two remaining subcomponents of the IW index, which measure autocratic preferences, separately. Finally, in table S6 we show that our results are robust to using the Freedom House index [see, e.g., (19)] as an alternative way of identifying democratic periods.

In sum, across data sets and across a large number of specifications, we find a statistically highly significant positive impact of individual experience with democracy on support for democracy. How big is the effect? To get some idea about this, rather than using ordered probit estimates, it is more transparent to use ordinary least-squares (OLS) estimates (table S3, column 3) for the main specification, based on the WVS. The OLS estimate for the coefficient on individual democratic capital is 0.04. Thus, to move an individual one step up in the IW index in a more prodemocratic direction would take 25 additional democratic capital units (e.g., around 35 years of continuously living under democracy). Alternatively, one can compare the coefficient on individual democratic capital to the education coefficients. For example, the difference between primary and secondary education is about 0.32 in the OLS estimates. This implies that, for an individual to achieve the same increase in support for democracy as switching from primary to secondary education, individual democratic capital needs to go up by around 8 units (for example, roughly 8.5 years of continuously living under democracy).

Our results provide evidence for the hypothesis that political preferences are shaped by the political system. Based on individual-level variation, our approach rules out potential effects of unobserved variables at the country-year level, such as the political environment or economic conditions. Of course, there are variables other than experience with the political system that affect support for democracy, many of which have been analyzed in the political science literature [e.g., (20)]. Yet the endogeneity of preferences to the actual political system is by itself an important phenomenon from both a policy and a theoretical point of view. For public policy, it means that implementing major political reforms might be a difficult task, while on the other hand individuals will increase their support for new systems over time. For the countries involved in the fresh waves of democratization movements in the Arab Spring, this gives some hope that broad support for democracy will increase over time, albeit slowly, making the new regimes more sustainable. For theoretical work, endogenous preferences pose challenges for both welfare theory and political economy.

REFERENCES AND NOTES

1. J. J. Linz, A. Stepan, *Problems of Democratic Transition and Consolidation: Southern Europe, South America, and Post-Communist Europe* (Johns Hopkins Univ. Press, Baltimore, 1996).
2. L. Diamond, *Developing Democracy: Toward Consolidation* (Johns Hopkins Univ. Press, Baltimore, 1999).
3. E. Fehr, K. Hoff, *Econ. J.* **121**, F396–F412 (2011).
4. A. Alesina, E. L. Glaeser, *Fighting Poverty in the US and Europe: A World of Difference* (Oxford Univ. Press, Oxford, 2004).
5. J. Henrich *et al.*, *Science* **327**, 1480–1484 (2010).
6. A. Alesina, G.-M. Angeletos, *Am. Econ. Rev.* **95**, 960–980 (2005).
7. R. Bénabou, J. Tirole, *Q. J. Econ.* **121**, 699–746 (2006).
8. T. Piketty, *Q. J. Econ.* **110**, 551–584 (1995).
9. A. Alesina, N. Fuchs-Schündeln, *Am. Econ. Rev.* **97**, 1507–1528 (2007).
10. E. F. P. Luttmer, M. Singhal, *Am. Econ. J. Econ. Policy* **3**, 157–179 (2011).
11. U. Malmendier, S. Nagel, *Q. J. Econ.* **126**, 373–416 (2011).
12. T. Persson, G. Tabellini, *Am. Econ. J. Macroecon.* **1**, 88–126 (2009).
13. R. Inglehart, *Polit. Sci. Politics* **36**, 51–57 (2003).
14. R. Inglehart, C. Welzel, *Comp. Polit.* **36**, 61–79 (2003).
15. M. Bratton, *J. Democracy* **15**, 147–158 (2004).
16. M. G. Marshall, K. Jaggers, *Polity IV Project: Dataset Users' Manual* (Center for Global Policy, George Mason University, Fairfax, VA, 2005).
17. A small number of deviating cases, because of data constraints, are described in the supplementary materials. Note that because we include country or even country-year fixed effects in all specifications and thus identify the coefficients only through changes within a country (or a country-year), the choice of the start year is in fact innocuous.
18. We follow standard specifications in the literature and include some basic demographic characteristics of the respondents as controls, namely variables related to age, gender, and education. Because our focus lies on establishing a causal relationship, we omit likely endogenous attitudinal variables [as analyzed in, e.g., (20)].
19. A. Karatnycky, *J. Democracy* **14**, 100–113 (2003).
20. R. Mattes, M. Bratton, *Am. J. Polit. Sci.* **51**, 192–217 (2007).

ACKNOWLEDGMENTS

Supported by the European Research Council under starting grant 262116 (N.F.-S.) and by the research cluster "Formation of Normative Orders" at Goethe University Frankfurt. Data used in the analysis are described in the supplementary materials. All data used for this study can be downloaded from publicly available websites. World Values Survey data are available from www.worldvaluessurvey.org. Afrobarometer survey data from www.afrobarometer.org. Polity IV data from www.systemicpeace.org/polity/polity4.htm, and Freedom House data from www.freedomhouse.org. Statistical programs to replicate the analysis are archived in Dataverse (doi: 10.7910/DVN/29151).

SUPPLEMENTARY MATERIALS

www.sciencemag.org/content/347/6226/1145/suppl/DC1
Materials and Methods

Fig. S1

Tables S1 to S6

References (21–24)

16 October 2014; accepted 29 January 2015
10.1126/science.aaa0880

NUCLEAR PORES

Architecture of the nuclear pore complex coat

Tobias Stuwe,^{1*} Ana R. Correia,^{1*} Daniel H. Lin,¹ Marcin Paduch,² Vincent T. Lu,² Anthony A. Kossiakoff,² André Hoelz^{1†}

The nuclear pore complex (NPC) constitutes the sole gateway for bidirectional nucleocytoplasmic transport. Despite half a century of structural characterization, the architecture of the NPC remains unknown. Here we present the crystal structure of a reconstituted ~400-kilodalton coat nucleoporin complex (CNC) from *Saccharomyces cerevisiae* at a 7.4 angstrom resolution. The crystal structure revealed a curved Y-shaped architecture and the molecular details of the coat nucleoporin interactions forming the central "triskelion" of the Y. A structural comparison of the yeast CNC with an electron microscopy reconstruction of its human counterpart suggested the evolutionary conservation of the elucidated architecture. Moreover, 32 copies of the CNC crystal structure docked readily into a cryoelectron tomographic reconstruction of the fully assembled human NPC, thereby accounting for ~16 megadalton of its mass.

The nuclear pore complex (NPC) is composed of ~34 different proteins, termed nucleoporins (Nups), that assemble in numerous copies to yield a ~120 MD transport channel embedded in the nuclear envelope (NE) (1). To facilitate the extensive membrane curvature generated in each NE pore, NPCs require a membrane-bending coat. The NPC coat is believed to be formed by an evolutionarily conserved coat Nup complex (CNC), the Nup107/160 complex in humans and the Nup84 complex in *Saccharomyces cerevisiae*, the latter of which is composed of Nup120, Sec13, Nup145C, Seh1, Nup85, Nup84, and Nup133 (1, 2).

We reconstituted a heterohexameric CNC containing the yeast Nups Nup120, Sec13, Nup145C,

Seh1, Nup85, and the Nup84 N-terminal domain (NTD) (Fig. 1, A and B). Our reconstituted CNC did not include Nup133 because this nup is conformationally flexible and loosely associated (2–4). Because the initial crystals of this reconstituted CNC diffracted poorly, we generated a series of conformation-specific, high-affinity synthetic antibodies (sABs) and tested them as crystallization chaperones (5). This approach yielded crystals of the CNC in complex with sAB-57, which allowed us to solve the structure to 7.4 Å by molecular replacement, using high-resolution crystal structures of CNC components and the sAB scaffold (figs. S1 and S2) (6–10). The inclusion of a second sAB (sAB-87) produced another crystal form, for which we collected anomalous x-ray diffraction data of Seleno-L-methionine and heavy metal-labeled crystals to confirm the placement of the CNC components (figs. S1 to S3). Because the coat Nups in both CNC•sAB complexes adopted the same arrangement, we focused our analysis on the better-ordered CNC•sAB-57 structure (figs. S4 to S6).

The CNC adopted a curved Y-shaped structure spanning ~250 Å in length and width, consistent with previous negative-stain electron microscopy (EM) analyses (Fig. 1C and movie S1) (2–4, 11). The Seh1•Nup85 pair and Nup120 constituted the upper arms of the Y, which were connected to the rest of the CNC through a central triskelion. Sec13•Nup145C•Nup84^{NTD} formed the stalk at the bottom of the triskelion and would attach the tail formed by Nup84^{CTD} and Nup133, which were absent in the structure. Both arms curved out so that the Nup120 β-propeller domain was perpendicular to the plane of the Y. Nup145C organized the CNC through four distinct interaction surfaces contacting nearly every member of the complex. sAB-57 bound at the Nup145C•Nup85 interface and formed crystal packing contacts (Fig. 2 and fig. S4).

The C-terminal domains (CTDs) of Nup145C (residues 553 to 712), Nup85 (residues 545 to 744), and Nup120 (residues 729 to 1037) converged to form the CNC triskelion. Although we observed clear electron density that revealed the connectivity of the three CTDs and their interactions (Fig. 2 and fig. S2), the sequence register in the triskelion was only approximate because of the absence of side-chain density. Nup120^{CTD} was sandwiched between Nup85^{CTD} and Nup145C^{CTD}, and no direct contacts were observed between Nup85^{CTD} and Nup145C^{CTD} (Fig. 2, A and B). The interactions between Nup85^{CTD}, Nup145C^{CTD}, and Nup120^{CTD} were mediated predominantly by their most C-terminal helices. An additional interaction was made by an N-terminal Nup145C helix bound to a groove in the Nup85^{CTD} surface ~60 Å away from the triskelion center, an interaction that was recognized by sAB-57 (Fig. 2C).

Consistent with our structural data, we reconstituted a stoichiometric complex between Nup120 and Nup85^{CTD} as monitored by size-exclusion chromatography interaction experiments (fig. S7A). Furthermore, Nup120 failed to interact with Sec13•Nup145C in the absence of Nup145C^{CTD} (fig. S7, B and C). The interaction between Seh1•Nup85 and Sec13•Nup145C depended on the presence of an N-terminal Nup145C fragment

¹Division of Chemistry and Chemical Engineering, California Institute of Technology, 1200 East California Boulevard, Pasadena, CA 91125, USA. ²Department of Biochemistry and Molecular Biology, University of Chicago, Chicago, IL 60637, USA.

*These authors contributed equally to this work.

†Corresponding author: E-mail: hoelz@caltech.edu

(residues 75 to 125) (fig. S7, D and E). Further mapping identified a region of Nup145C (residues 75 to 109) that was sufficient for Nup85^{CTD} binding (fig. S7F), confirming that this fragment bridged the two subcomplexes. Nup120^{CTD} and Nup85^{CTD} were essential for the formation of the CNC (figs. S8 and S9). These data were consistent with published CNC cross-linking data of three different species, more so than the models generated by coarse-grained analysis (3, 11, 12). Lastly, to validate their placement in the structures, we confirmed the interactions of sAB-57 and sAB-87 with Seh1•Nup85•Nup145C¹⁻¹²³ and Nup120^{NTD}, respectively (fig. S10).

Next, we compared the CNC structure to previously determined EM reconstructions of the yeast and human CNCs (3, 4). Although the EM reconstruction of the yeast CNC recapitulates its overall shape, significant deviations were apparent (fig. S11 and movie S2). No density was observed in the EM structure for the U-shaped tip of Nup85. The overall shape of the crystal structure was also consistent with the human CNC EM reconstruction, which contains the crystallized evolutionarily conserved core as well as two additional human components, Nup37 and Nup43 (Fig. 3A and movie S3). Our crystal structure did not account for additional EM density directly adjacent to the Seh1•Nup85 and Nup120 arms, which reportedly accommodate Nup43 and Nup37, respectively (Fig. 3A) (3). In the human CNC, Nup43 appears to bind to the same site as sAB-57 on the Seh1•Nup85 arm of the Y. The major difference between the CNC crystal structure and both EM reconstructions is the curvature of the arms of the Y, and thus the orientation of

the Nup120 β propeller was substantially different in the crystal structure (Fig. 3A). The flatness of both EM reconstructions suggests that these deviations may be a result of EM sample preparation. Despite this, the degree of similarity between the yeast CNC crystal structure and the human CNC EM reconstruction suggested substantial evolutionary conservation of the CNC architecture.

The higher-order arrangement of CNCs in a fully assembled NPC has been debated, with several models proposed based on various structural, biophysical, or computational approaches (3, 7, 13, 14). Given the evolutionary conservation of the CNC architecture, we tested whether our crystal structure could be docked into the ~ 32 Å-resolution tomographic reconstruction of an intact human NPC (3). Indeed, an unbiased six-dimensional search combined with a cross-correlation analysis confidently docked 32 copies of the CNC crystal structure in the tomographic reconstruction, yielding a model for the NPC coat (Figs. 3B and 4A and fig. S12). These results agreed with the stoichiometry and approximate localization previously proposed based on cross-linking mass spectrometry and the docking of the human CNC EM reconstruction (3). However, the crystal structure fit the tomographic reconstruction substantially better than the human CNC EM reconstruction (Fig. 3B).

The NPC coat was formed by 32 copies of the CNC arranged in four eight-membered rings (Fig. 4, A and B, and movie S4). The eight CNCs in each ring were oriented horizontally, with their long axis positioned parallel to the surface of the NE in a head-to-tail fashion. On each side of the

NE, a pair of inner and outer CNC rings emerged up to ~ 210 Å (Fig. 4A). These rings were separated by a ~ 280 Å gap, yielding a total height of ~ 700 Å. The diameters of the outer CNC rings were slightly larger than those of the inner CNC rings, spanning ~ 1200 Å and ~ 1050 Å, respectively (Fig. 4B). Although the CNCs in both rings were arranged with the same directionality, each CNC from the outer ring was offset from its mate in the inner ring by ~ 120 Å in a clockwise direction (Fig. 4B). Moreover, the tandem CNC rings on the nuclear and cytoplasmic side of the NE possessed the same handedness and were related by twofold rotational symmetry (Fig. 4A and fig. S12D).

The unambiguous placement and orientation of the coat Nups and their conserved surfaces allowed for an investigation into the details of their interactions in the assembled NPC coat. Each CNC was situated on top of the NE and was oriented so that the plane of the Y was nearly perpendicular to the membrane, with the Nup120 and Seh1•Nup85 arms pointed at or away from the membrane, respectively (Fig. 4A). Only two interfaces appeared to be responsible for oligomerization of individual CNCs into the NPC coat. The inner and outer rings interacted only where the top of the triskelion of each inner ring CNC met the bottom of the Nup84•Nup145C interface of each outer ring CNC (Fig. 4C). Nup120 was oriented so that its Nup133 binding site was directly adjacent to the density assigned to the N terminus of Nup133, which is consistent with our previous findings that this interaction is responsible for CNC ring formation and critical for NPC assembly (Fig. 4D) (9). This Nup120 orientation also pointed the apex of its β propeller directly toward the NE, which

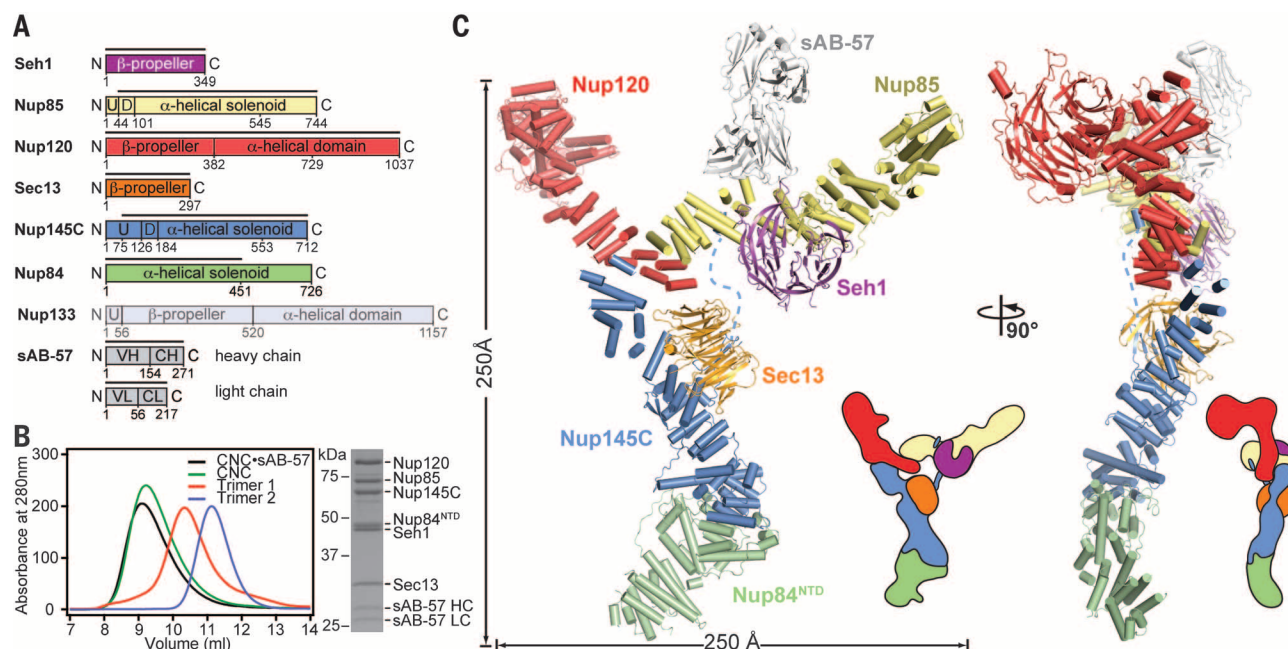


Fig. 1. Overall architecture of the CNC. (A) Domain structures of the yeast coat Nups and sAB-57. Black lines indicate the crystallized fragments. U, unstructured; D, domain invasion motif; VH, heavy chain variable region; CH, heavy chain constant region; VL, light chain variable region; CL, light chain constant region. (B) Reconstitution of the yeast CNC•sAB-57, lacking Nup133. Elution profiles from a Superdex 200 10/300 column are shown for Nup120•Seh1•Nup85 (trimer 1), Sec13•Nup145C•Nup84^{NTD} (trimer 2), CNC, and CNC•sAB-57 (left). An SDS–polyacrylamide gel electrophoresis gel of the reconstituted CNC•sAB-57 used for crystallization is shown (right). (C) Cartoon and schematic representations of the yeast CNC•sAB-57 crystal structure viewed from two sides.

Fig. 2. Architecture of the CNC triskelion. Cartoon representation of the triskelion formed by Nup120, Nup85, and Nup145C. Insets (A) to (C) depict magnified views of the interactions between (A) Nup120^{CTD}, Nup85^{CTD}, and Nup145C^{CTD}; (B) Nup120^{CTD}, Nup85^{CTD}, and the N-terminal Nup145C helix; and (C) Nup145C, Nup85^{CTD}, and sAB-57. The density-modified electron density map is contoured at 1.0 σ .

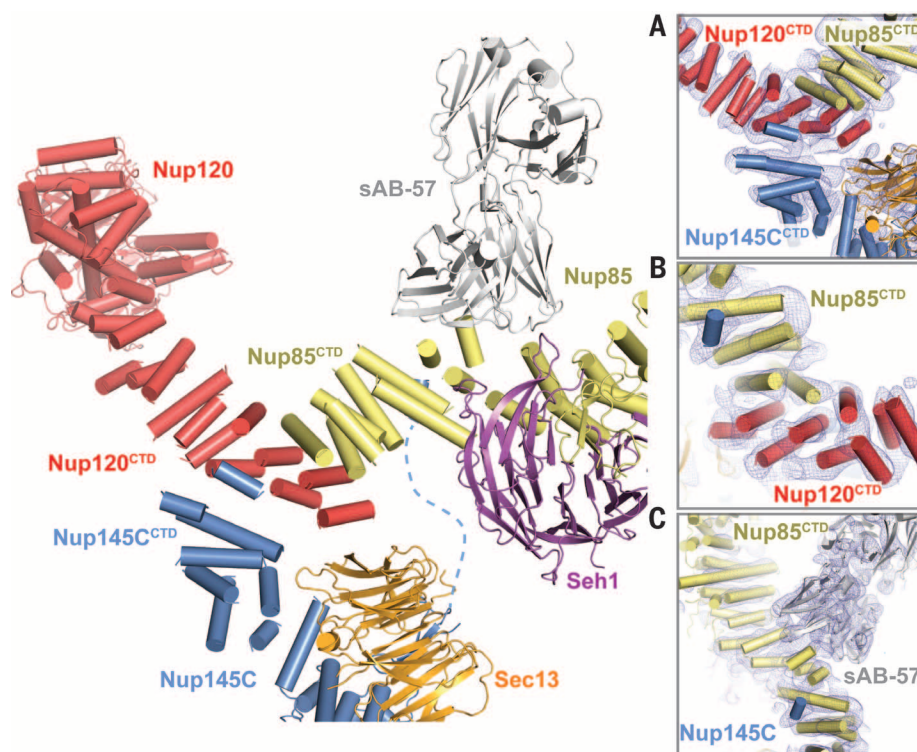
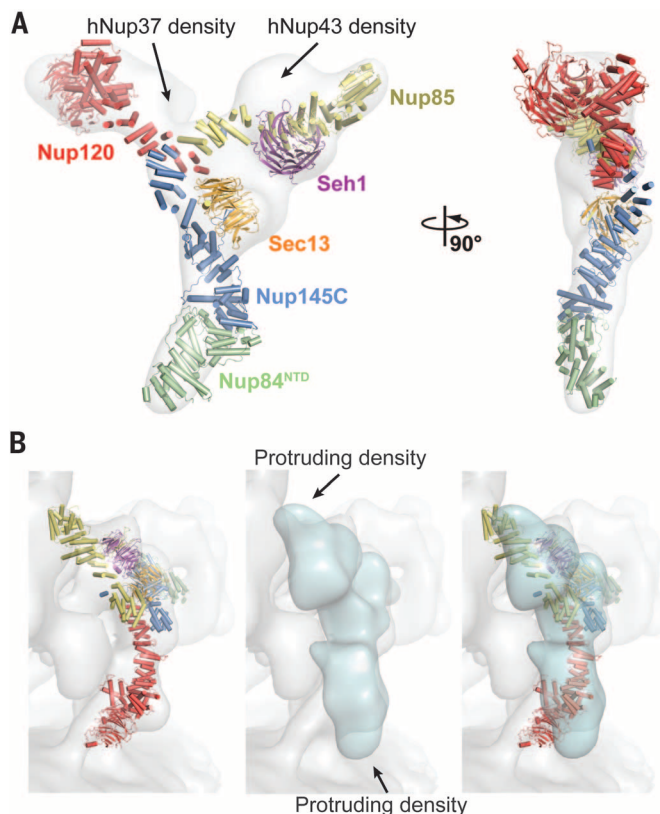


Fig. 3. Comparison of yeast and human CNCs. (A) Fit of the yeast CNC crystal structure into the human CNC negative-stain EM reconstruction (gray) (3). Arrows indicate density accounted for by the additional human coat Nups Nup37 or Nup43. (B) Comparison of the quality of fit for the yeast CNC crystal structure and human CNC EM reconstruction (cyan) into the intact human NPC cryoelectron tomographic reconstruction (gray) (3). Arrows indicate regions where the human CNC EM reconstruction protrudes from the cryoelectron tomographic reconstruction.



was the only membrane contact that we observed in our model (Fig. 4D). This region of the Nup120 β -propeller domain also contains a conserved surface patch on its side (9) that may serve as a NE anchor point for the entire NPC coat, either

through a direct interaction with the membrane or via a membrane-anchored Nup, as previously reported (15).

The NPC coat architecture is dissimilar to that of other structurally characterized membrane

coats. Whereas the latter are generated by homotypic vertex elements (16, 17), the NPC coat is formed by heterotypic interactions of its asymmetric CNC protomers. Given the location of the CNC rings above and below the NE, other Nups

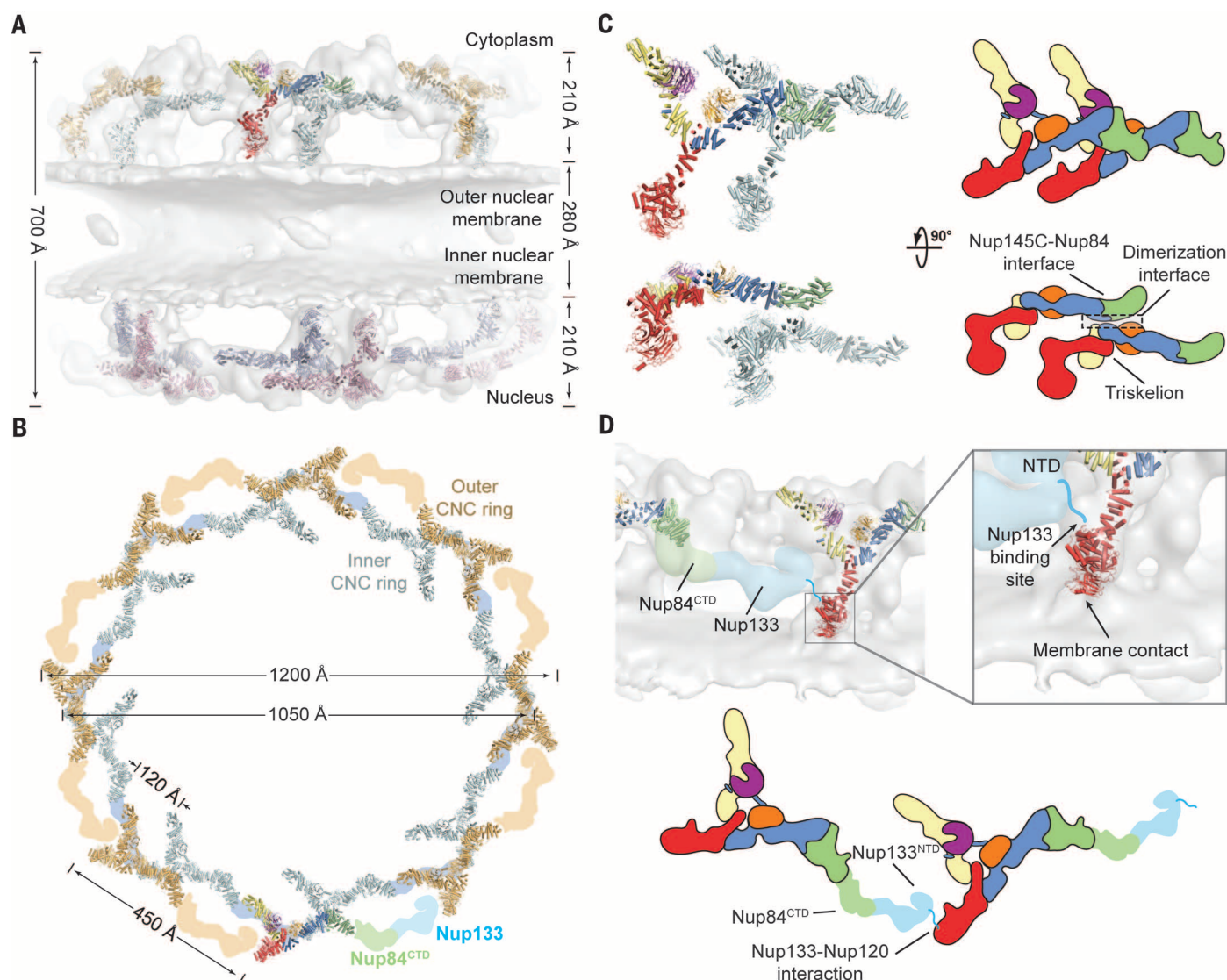


Fig. 4. Architecture of the NPC coat. (A) Thirty-two copies of the yeast CNC, shown in cartoon representation with a representative subunit colored as in Fig. 1, docked into the cryoelectron tomographic reconstruction of the intact human NPC (3), shown as a gray surface. The outer and inner cytoplasmic and nuclear CNC rings are highlighted in orange, cyan, pink, and blue, respectively. (B) Cartoon representations of 16 yeast CNC copies from the cytoplasmic side of the NPC coat. Schematics indicating the positions assigned to Nup84^{CTD} and Nup133, which were not crystallized, are shown. (C) Interface between the

inner and outer CNC rings. Two views of the yeast CNC and its mate from the inner ring are shown. (D) Orientation of the Nup120 β propeller relative to neighboring coat Nups and the membrane. Portions of two CNCs from the cytoplasmic outer ring are shown in cartoon representation. Green and cyan shading indicate the positioning of Nup84^{CTD} and Nup133, respectively. The cyan line represents the N-terminal unstructured segment of Nup133 that binds to Nup120 (9). A schematic representation of the ring-forming Nup120–Nup133 interaction is shown below.

are likely to play a role in generating the complex curvature of the NE pores. Although the placement of the CNCs in the NPC coat did not directly address the organization of the central transport channel (fig. S13), it accounted for ~16 MD of the total mass of the NPC, bridged the resolution gap between low-resolution EM analyses and high-resolution crystallographic studies, and suggested the evolutionary conservation of its architecture.

REFERENCES AND NOTES

1. A. Hoelz, E. W. Debler, G. Blobel, *Annu. Rev. Biochem.* **80**, 613–643 (2011).
2. M. Lutzmann, R. Kunze, A. Buerer, U. Aebi, E. Hurt, *EMBO J.* **21**, 387–397 (2002).
3. K. H. Bui et al., *Cell* **155**, 1233–1243 (2013).
4. M. Kampmann, G. Blobel, *Nat. Struct. Mol. Biol.* **16**, 782–788 (2009).
5. M. Paduch et al., *Methods* **60**, 3–14 (2013).
6. E. W. Debler et al., *Mol. Cell* **32**, 815–826 (2008).
7. K. C. Hsia, P. Stavropoulos, G. Blobel, A. Hoelz, *Cell* **131**, 1313–1326 (2007).
8. V. Nagy et al., *Proc. Natl. Acad. Sci. U.S.A.* **106**, 17693–17698 (2009).
9. H. S. Seo et al., *Proc. Natl. Acad. Sci. U.S.A.* **106**, 14281–14286 (2009).
10. S. S. Rizk et al., *Nat. Struct. Mol. Biol.* **18**, 437–442 (2011).
11. K. Thierbach et al., *Structure* **21**, 1672–1682 (2013).
12. Y. Shi et al., *Mol. Cell. Proteomics* **13**, 2927–2943 (2014).
13. F. Alber et al., *Nature* **450**, 695–701 (2007).
14. S. G. Brohawn, N. C. Leksa, E. D. Spear, K. R. Rajashankar, T. U. Schwartz, *Science* **322**, 1369–1373 (2008).
15. J. M. Mitchell, J. Mansfield, J. Capitanio, U. Kutay, R. W. Wozniak, *J. Cell Biol.* **191**, 505–521 (2010).
16. S. C. Harrison, T. Kirchhausen, *Nature* **466**, 1048–1049 (2010).
17. E. W. Debler, K. C. Hsia, V. Nagy, H. S. Seo, A. Hoelz, *Nucleus* **1**, 150–157 (2010).

ACKNOWLEDGMENTS

We thank C. J. Bley, W. M. Clemons, A. M. Davenport, O. Dreesen, A. Patke, D. C. Rees, S. O. Shan, P. Stavropoulos, and K. Thierbach for critical reading of the manuscript; K. Kato and K. Kato for their contributions at the initial stages of this project; L. N. Collins for technical support; D. King for mass spectrometry analysis; E. Hurt and P. Loppnau for material; S. Koide for providing the phage display library; S. Gräslund for the pSFV4 vector; P. Afonine for advice regarding structure refinement in PHENIX; and J. Kaiser and the scientific staff of Stanford Synchrotron Radiation Laboratory (SSRL) Beamline 12-2 and the National Institute of General Medical Sciences and National Cancer Institute Structural Biology Facility (GM/CA) at the

Advanced Photon Source (APS) for their support with x-ray diffraction measurements. We acknowledge the Gordon and Betty Moore Foundation, the Beckman Institute, and the Sanofi-Aventis Bioengineering Research Program for their support of the Molecular Observatory at the California Institute of Technology (Caltech). The operations at the SSRL and APS are supported by the U.S. Department of Energy and the National Institutes of Health (NIH). GM/CA has been funded in whole or in part with federal funds from the National Cancer Institute (ACB-12002) and the National Institute of General Medical Sciences (AGM-12006). T.S. was supported by a Postdoctoral Fellowship of the Deutsche Forschungsgemeinschaft.

D.H.L. was supported by a NIH Research Service Award (5 T32 GM07616). A.A.K. was supported by NIH awards U01 GM094588 and U54 GM087519 and by Searle Funds at The Chicago Community Trust. A.H. was supported by Caltech startup funds, the Albert Wyrick V Scholar Award of the V Foundation for Cancer Research, the 54th Mallinckrodt Scholar Award of the Edward Mallinckrodt Jr. Foundation, and a Kimmel Scholar Award of the Sidney Kimmel Foundation for Cancer Research. The coordinates and structure factors have been deposited with the Protein Data Bank with accession codes 4XMM and 4XMN. The authors declare no financial conflicts of interest.

SUPPLEMENTARY MATERIALS

www.sciencemag.org/content/347/6226/1148/suppl/DC1
Materials and Methods
Figs. S1 to S13
Tables S1 and S2
References (18–28)
Movies S1 to S4

18 September 2014; accepted 27 January 2015
Published online 12 February 2015;
10.1126/science.aaa4136

PROTEIN TARGETING

Structure of the Get3 targeting factor in complex with its membrane protein cargo

Agnieszka Mateja,¹ Marcin Paduch,¹ Hsin-Yang Chang,¹ Anna Szydlowska,¹ Anthony A. Kossiakoff,¹ Ramanujan S. Hegde,^{2*} Robert J. Keenan^{1,3*}

Tail-anchored (TA) proteins are a physiologically important class of membrane proteins targeted to the endoplasmic reticulum by the conserved guided-entry of TA proteins (GET) pathway. During transit, their hydrophobic transmembrane domains (TMDs) are chaperoned by the cytosolic targeting factor Get3, but the molecular nature of the functional Get3-TA protein targeting complex remains unknown. We reconstituted the physiologic assembly pathway for a functional targeting complex and showed that it comprises a TA protein bound to a Get3 homodimer. Crystal structures of Get3 bound to different TA proteins showed an α -helical TMD occupying a hydrophobic groove that spans the Get3 homodimer. Our data elucidate the mechanism of TA protein recognition and shielding by Get3 and suggest general principles of hydrophobic domain chaperoning by cellular targeting factors.

Integral membrane proteins contain hydrophobic transmembrane domains (TMDs) that must be shielded from the cytosol until their insertion into the lipid bilayer. Whereas most eukaryotic membrane proteins are cotranslationally targeted to the endoplasmic reticulum (ER) by the signal recognition particle (SRP) (1), tail-anchored (TA) membrane proteins are post-translationally targeted by the cytosolic factor Get3 (2–7). This conserved adenosine triphosphatase (ATPase) changes conformation in a nucleotide-regulated manner (8–12) to bind TMDs in the cytosol and release them at its ER membrane receptor (6, 13–16).

Assembly of the Get3-TA targeting complex requires “pretargeting” factors that mediate loading onto Get3 (17, 18). This pathway begins with TA protein in complex with the chaperone Sgt2. The Get4-Get5 scaffolding complex then recruits Sgt2 via Get5, while Get4 recruits ATP-bound Get3 (19). A hand-off reaction within this complex results in transfer of TA protein from Sgt2 to

Get3. TA substrate-loaded Get3 then dissociates from Get4 (20–22), resulting in a targeting complex whose architecture and stoichiometry have been debated (8–12, 20–23).

To define the physiologically relevant Get3 targeting complex, we recapitulated its assembly in vitro, using purified recombinant factors at in vivo concentrations (Fig. 1A). Translation of radiolabeled TA protein in the presence of SGTA (the mammalian homolog of Sgt2) produced a stable complex detectable by chemical cross-linking (fig. S1). The TA protein remained associated with SGTA upon addition of either Get4-Get5 or Get3, but released efficiently when both factors were added (Fig. 1B). Correspondingly, Get3 efficiently acquired substrate from SGTA only when Get4-Get5 was present.

The transfer reaction was rapid and unidirectional: Once substrate released from SGTA, it did not rebind (fig. S2). Likewise, substrate preloaded directly on Get3 (fig. S3) did not effectively transfer to SGTA (Fig. 1B). Structure-guided mutations disrupting either the SGTA-Get5 interaction [SGTA(C38S)] (24) or the Get4-Get3 interaction [Get3(E253R)] (20) abolished substrate release from SGTA (Fig. 1C). Targeting complex produced via Get4-Get5 supported TA protein insertion into yeast ER microsomes (Fig. 1D), while an identical

reaction containing SGTA(C38S) showed reduced insertion (Fig. 1D). Thus, the recombinant assembly system requires all factors and interactions of the early GET pathway and produces insertion-competent Get3-TA protein targeting complex.

Three lines of evidence suggested that functional targeting complex assembled via pretargeting factors consists of dimeric Get3 bound to TA protein. First, the targeting complex, containing a small (~10 kD) TA protein, had the same native size as purified Get3 dimer, and was clearly distinguishable from higher-order Get3 complexes (Fig. 1E). Such higher-order complexes, often seen when Get3 is coexpressed with TA protein in *Escherichia coli* (fig. S5) (8, 22, 23), were not observed even when the loading reaction contained 10-fold excess Get3 (fig. S4A). Second, titration of Get3 into the loading reaction showed no evidence of cooperativity (fig. S4B), arguing against its higher-order assembly during targeting complex formation. Third, size-exclusion chromatography and multiangle laser light scattering (SEC-MALLS) indicated that prior to loading, a single Get3 dimer is bound by two copies of the Get4-Get5 complex (fig. S4C). Thus, TA protein is loaded onto dimeric Get3 to form a functional targeting complex.

To gain insight into how the TA protein is shielded by Get3 in this targeting complex, we sought to determine its structure. During physiologic targeting complex assembly, Get4 preferentially recruits and stabilizes adenosine 5'-triphosphate (ATP)-bound Get3 (19, 20, 22). To mimic this during recombinant expression in *E. coli*, we biased Get3 to the ATP-bound state via the D57N hydrolysis mutant (10). Coexpression of this mutant with TA protein resulted in a targeting complex that was homogeneously dimeric for Get3 by SEC-MALLS (fig. S6A) and comigrated with in vitro-assembled targeting complex on sucrose gradients (fig. S6B).

To facilitate crystallization, we generated a high-affinity synthetic antibody fragment (sAB) (25) that recognizes the closed (ATP-bound) conformation of Get3. Kinetic analysis revealed that this sAB binds with subnanomolar affinity to nucleotide-bound Get3, both in the presence and absence of TA protein (fig. S7). Thus, rather than inducing a large conformational change in Get3, the TA protein binds to a preorganized conformation that closely resembles the closed (ATP-bound) state.

Using this sAB, we crystallized Get3(D57N) in complex with the TMD of the yeast TA protein

¹Department of Biochemistry and Molecular Biology, The University of Chicago, 929 East 57th Street, Chicago, IL 60637, USA. ²MRC Laboratory of Molecular Biology, Francis Crick Avenue, Cambridge CB2 0QH, UK.

*Corresponding author. E-mail: rhegde@mrc-lmb.cam.ac.uk (R.S.H.); bkeenan@uchicago.edu (R.J.K.)

Pep12 (table S1). The structure reveals nucleotide-bound Get3 in a closed conformation with two sABs bound to equivalent sites on opposite faces of a Get3 homodimer (Fig. 2A); no higher-order Get3 oligomers are observed in the crystal (fig. S8). The closed conformation is nearly identical to that seen in previous Get3-ADP•AlF₄⁻ structures (~0.5 Å root mean square deviation), in which two helical subdomains form a composite hydrophobic groove proposed to bind the TMDs of TA proteins (8, 10).

As is typical for the fungal Get3 crystal structures, electron density is weakest within these dynamic helical subdomains. Nevertheless, unaccounted helical density was visible within the hydrophobic groove in early unbiased maps (fig. S9). After refinement, we assigned this density to the Pep12 TMD (Fig. 2B and fig. S9), excluding the possibility that it corresponds to flexible regions of Get3 folding into the groove.

The Pep12 TMD binds to Get3 at the bottom of the composite hydrophobic groove (Fig. 2 and fig. S9), where it spans the dimer interface and stabilizes the closed conformation of Get3. The most ordered interactions are found at the ends of the TMD, where bulky hydrophobic side chains of the substrate contact groove residues

including M97 (helix 4), L126 (helix 5), M143 and M146 (helix 6), L183, L186 and F190 (helix 7), and L216 and L219 (helix 9) (Fig. 2B). Consistent with their role in TMD binding, substitution of hydrophobic residues along helices 7 and 9 with polar or charged residues abolished Get3's ability to induce TA protein release from SGTA (Fig. 3A).

The Pep12 TMD buries ~1450 Å² of hydrophobic surface area, distributed nearly evenly between the two Get3 subunits (Fig. 2C). This represents ~50% of the ordered hydrophobic surface area in the groove and is significantly greater than in the SRP54-signal peptide interaction, where ~360 Å² of hydrophobic surface area become buried upon binding (26, 27). The availability of such a large surface area likely explains how Get3 can accommodate hydrophobic sequences of differing lengths and composition.

Using the same strategies, we also solved crystal structures of Get3(D57N) in complex with unrelated TMDs from Nyy1 and Sec22 (table S1). Density for these TMDs was less defined than for the Pep12 complex, but nevertheless sufficient to place helical TMDs (fig. S9). Like Pep12, these TMDs bind at the bottom of the hydrophobic groove, spanning the dimer interface (Fig. 3B).

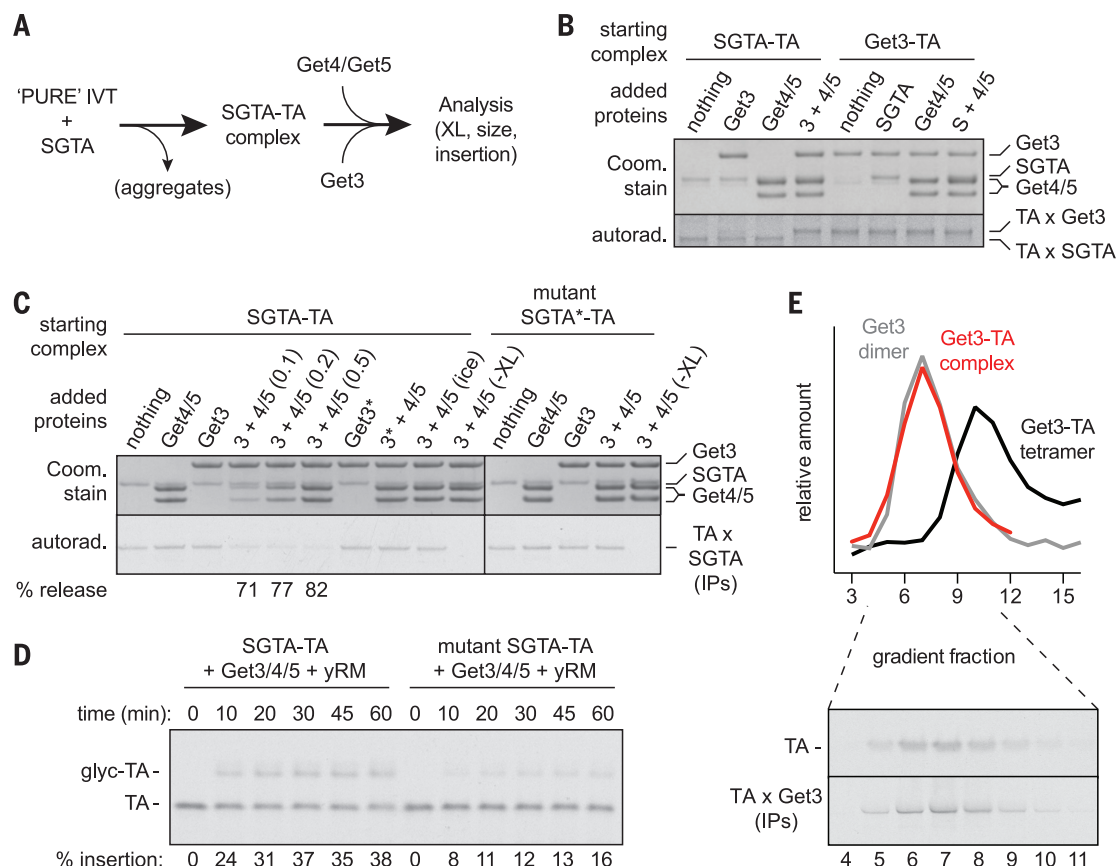
Thus, a single helix binding across the Get3 dimer represents the canonical mode of the Get3-TA substrate interaction.

Although much of the Get3 hydrophobic groove and substrate TMD are shielded in the targeting complexes, one surface of the TMD appears solvent exposed. Relative to previous closed Get3 structures, the groove in each substrate-bound complex is constricted at its apex where the ends of helix 7 curve inwards (Fig. 3B). Although the "TRC40-insert," including helix 8, is poorly defined, we found by site-specific photo-cross-linking that this region (and residues in helix 6 and 7) directly contact the TA substrate (Fig. 3C and fig. S10). Thus, helix 8 likely functions as a dynamic "lid," protecting the TMD from aggregation, while still allowing substrate release after recruitment to Get1 (Fig. 3D) (13, 14).

Our biochemical and structural analyses define the functional targeting complex as a Get3 homodimer bound to a single TA protein. Although higher-order Get3 assembly has been postulated to promote ATP hydrolysis (22), this appears unnecessary because dimeric targeting complex was functional for TA protein insertion, indicating that it had hydrolyzed its ATP (Fig. 1D). Consistent with this, the catalytic machinery

Fig. 1. Reconstitution of physiologic TA protein targeting complex assembly. (A) Experimental strategy. (B) SGTA-TA or Get3-TA complexes (figs. S1 and S3) at 1 μM were incubated with 1 μM of the indicated proteins, followed by amine-reactive cross-linking.

Reactions were analyzed by SDS-polyacrylamide gel electrophoresis and Coomassie blue staining to detect the input proteins (top) or autoradiography to detect the ³⁵S-labeled TA protein cross-links (bottom). (C) Reactions as in (B) were monitored by sulfhydryl-reactive cross-linking for TA protein release from SGTA (bottom). Reactions contained 0.5 μM of each factor, except lanes 4 and 5, which contained Get4-Get5 at 0.1 and 0.2 μM, respectively. Asterisks next to Get3 or SGTA indicate point mutants that disrupt interactions with Get4 or Get5, respectively. (D) Products of the indicated transfer reactions were incubated with yeast rough microsomes (yRM) and analyzed for insertion. (E) Sucrose gradient size analysis of Get3-TA complex formed by Get4-Get5-dependent loading from SGTA (red). Free, dimeric Get3 (gray) and *E. coli*-produced tetrameric Get3-TA substrate complex (black) are shown for comparison (fig. S5). Peak fractions containing substrate (red) were analyzed directly or after cross-linking and immunoprecipitation for Get3 to specifically detect Get3-TA complexes (bottom panel).



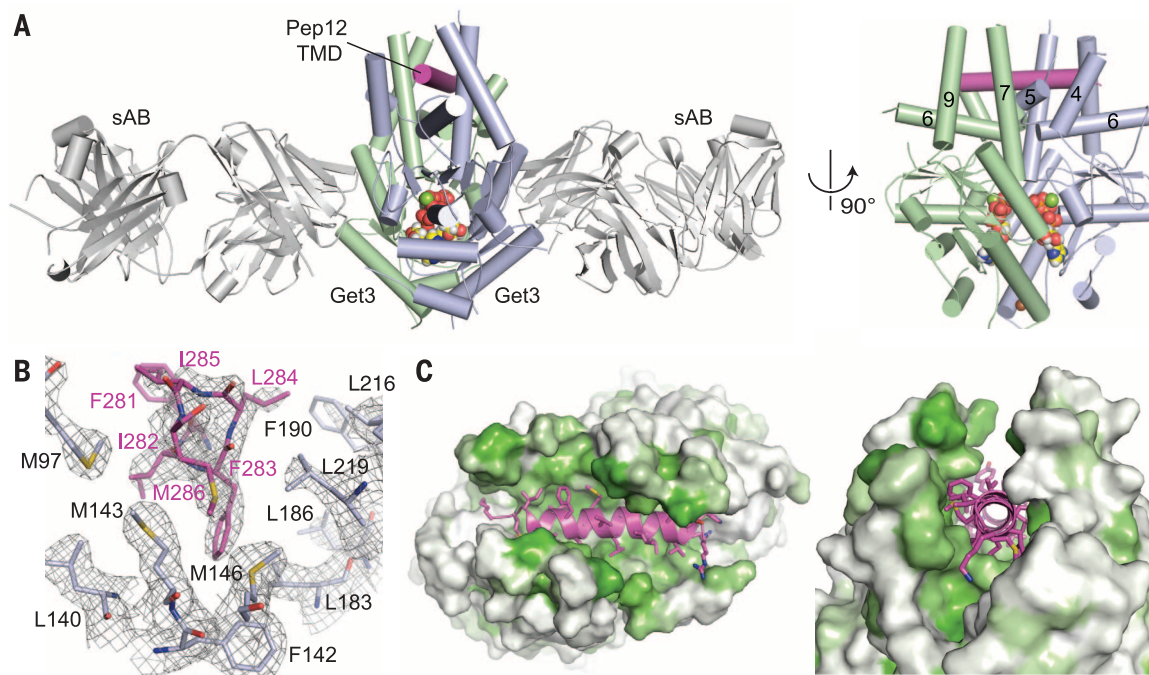
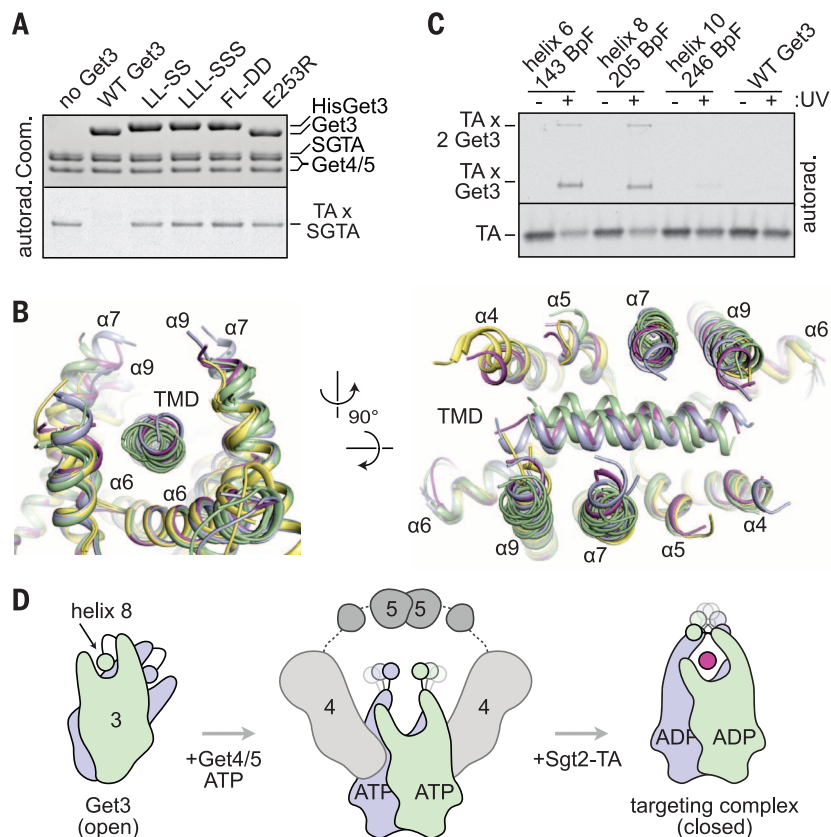


Fig. 2. The helical TMD of a TA substrate binds deep within the composite hydrophobic groove of dimeric Get3. (A) Overview of dimeric *Saccharomyces cerevisiae* Get3 bound to a truncated Pep12 TA substrate (magenta) and nucleotide (spheres), and sandwiched between two copies of an engineered sAB (gray). At right, a “side” view of the complex is shown with sABs removed for

clarity. (B) Details of the interaction between the Pep12 TMD C terminus and a methionine-rich cluster at one end of the hydrophobic groove. Electron density is from a $2.05 \text{ \AA } 2F_o - F_c$ map contoured at 1.0σ . (Amino acid abbreviations: F, Phe; I, Ile; L, Leu; and M, Met.) (C) Surface representations of the TA substrate-binding site, colored from least (white) to most (green) hydrophobic.

Fig. 3. Dynamic shielding of the TMD. (A) SGTA-TA complexes were prepared and subjected to transfer reactions with wild-type (WT) and mutant Get3 proteins as in Fig. 1C. LL-SS (L183S/L186S), LLL-SSS (L183S/L186S/L219S), and FL-DD (F190D/L216D) are hydrophobic groove mutants; E253R is a mutation that disrupts interaction with Get4. (Amino acid abbreviations: D, Asp; E, Glu; F, Phe; L, Leu; R, Arg; and S, Ser.) (B) “Top” and “side” views of Pep12 (magenta), Nyv1 (blue), and Sec22 (green) complexes superimposed on the free Get3 closed dimer structure (yellow; PDB code: 2woj). Relative to free Get3, the end of helix 7 extends and begins to curve inward over the substrate. (C) WT or benzophenone-containing (at the indicated positions) Get3-TA complexes were prepared as in fig. S3, and the dimer peak was subjected to ultraviolet (UV) cross-linking. Uncrosslinked TA protein and its adducts to one or two Get3 proteins are indicated. (D) “Side” views of the Get3 dimer, looking into the groove. In its transient empty state, Get3 is played apart, with two hydrophobic “half-sites” occupied by the helix 8 region. ATP binding drives Get3 into a closed conformation, which is captured by two copies of the Get4-Get5 complex. In this state, helix 8 is displaced, and the composite hydrophobic groove is now preorganized for substrate binding. After substrate transfer from Sgt2, the targeting complex is released. The helix 8 region now dynamically shields the substrate during transit to the ER membrane.



is organized for hydrolysis in the targeting complex structures (fig. S11). The higher-order Get3 oligomers that form during oxidative stress (28) are structurally and functionally distinct.

The structure of the Get3-TA substrate targeting complex illustrates a common strategy for binding to hydrophobic cargo. Like Get3, the signal sequence-binding subunit of SRP (SRP54) captures substrates within a hydrophobic, methionine-rich groove presented on a helical scaffold (26, 27, 29). These scaffolds provide a large and intrinsically dynamic binding site that is not appreciably ordered by substrate capture. This likely confers the ability of Get3 and SRP54 to bind a variety of hydrophobic sequences—an essential property of both targeting systems. It will be of interest to determine whether these principles are shared by other TMD-binding factors, including SGTA and Bag6.

REFERENCES AND NOTES

1. D. Akopian, K. Shen, X. Zhang, S. O. Shan, *Annu. Rev. Biochem.* **82**, 693–721 (2013).
2. J. W. Chartron, W. M. Clemons Jr., C. J. Suloway, *Curr. Opin. Struct. Biol.* **22**, 217–224 (2012).
3. V. Denic, V. Dötsch, I. Sinning, *Cold Spring Harb. Perspect. Biol.* **5**, a013334 (2013).
4. R. S. Hegde, R. J. Keenan, *Nat. Rev. Mol. Cell Biol.* **12**, 787–798 (2011).
5. V. Favalaro, M. Spasic, B. Schwappach, B. Dobberstein, *J. Cell Sci.* **121**, 1832–1840 (2008).
6. M. Schuldiner *et al.*, *Cell* **134**, 634–645 (2008).
7. S. Stefanovic, R. S. Hegde, *Cell* **128**, 1147–1159 (2007).
8. G. Bozkurt *et al.*, *Proc. Natl. Acad. Sci. U.S.A.* **106**, 21131–21136 (2009).
9. J. Hu, J. Li, X. Qian, V. Denic, B. Sha, *PLOS ONE* **4**, e8061 (2009).
10. A. Mateja *et al.*, *Nature* **461**, 361–366 (2009).
11. C. J. Suloway, J. W. Chartron, M. Zaslaver, W. M. Clemons Jr., *Proc. Natl. Acad. Sci. U.S.A.* **106**, 14849–14854 (2009).
12. A. Yamagata *et al.*, *Genes Cells* **15**, 29–41 (2010).
13. S. Stefanovic *et al.*, *Science* **333**, 758–762 (2011).
14. M. Mariappan *et al.*, *Nature* **477**, 61–66 (2011).
15. F. Wang, C. Chan, N. R. Weir, V. Denic, *Nature* **512**, 441–444 (2014).
16. F. Wang, A. Whynot, M. Tung, V. Denic, *Mol. Cell* **43**, 738–750 (2011).
17. F. Wang, E. C. Brown, G. Mak, J. Zhuang, V. Denic, *Mol. Cell* **40**, 159–171 (2010).
18. M. Mariappan *et al.*, *Nature* **466**, 1120–1124 (2010).
19. J. W. Chartron, C. J. Suloway, M. Zaslaver, W. M. Clemons Jr., *Proc. Natl. Acad. Sci. U.S.A.* **107**, 12127–12132 (2010).
20. H. B. Gristick *et al.*, *Nat. Struct. Mol. Biol.* **21**, 437–442 (2014).
21. M. E. Rome, U. S. Chio, M. Rao, H. Gristick, S. O. Shan, *Proc. Natl. Acad. Sci. U.S.A.* **111**, E4929–E4935 (2014).
22. M. E. Rome, M. Rao, W. M. Clemons, S. O. Shan, *Proc. Natl. Acad. Sci. U.S.A.* **110**, 7666–7671 (2013).
23. C. J. Suloway, M. E. Rome, W. M. Clemons Jr., *EMBO J.* **31**, 707–719 (2012).
24. J. W. Chartron, D. G. VanderVelde, W. M. Clemons Jr., *Cell Reports* **2**, 1620–1632 (2012).
25. M. Paduch *et al.*, *Methods* **60**, 3–14 (2013).
26. T. Hainzl, S. Huang, G. Meriläinen, K. Brännström, A. E. Sauer-Eriksson, *Nat. Struct. Mol. Biol.* **18**, 389–391 (2011).
27. C. Y. Janda *et al.*, *Nature* **465**, 507–510 (2010).
28. W. Voth *et al.*, *Mol. Cell* **56**, 116–127 (2014).
29. R. J. Keenan, D. M. Freymann, P. Walter, R. M. Stroud, *Cell* **94**, 181–191 (1998).

ACKNOWLEDGMENTS

We thank S. Shao for help with assay development; S. Koide for the phage library; S. Sidhu for the sAB expression vector; M. Kivlen for plasmids; F. Bezanilla, E. Perozo, and J. Piccirilli for instrumentation; members of the Keenan, Hegde, and

Koskiakoff labs for support; and the NE-CAT (24-ID-C) beamline staff at Advanced Photon Source for technical assistance. NE-CAT is supported by NIH grant P41 GM103403 and U.S. Department of Energy contract DE-AC02-06CH11357. Additional support was from the UK Medical Research Council (MC_UP_A022_1007 to R.S.H.), the NIH (U01 GM094588 and U54 GM087519 to A.A.K.; R01 GM086487 to R.J.K.), and the Searle Funds at The Chicago Community Trust for the Chicago Biomedical Consortium (to A.A.K. and R.J.K.). The Protein Data Bank (PDB) accession codes are 4XTR (Pep12), 4XVU (Nry1), and 4XWO (Sec22).

SUPPLEMENTARY MATERIALS

www.sciencemag.org/content/347/6226/1152/suppl/DC1
Materials and Methods
Supplementary Text
Figs. S1 to S12
Table S1
References (30–37)

23 September 2014; accepted 30 January 2015
10.1126/science.1261671

EVOLUTIONARY GENOMICS

Evolutionary changes in promoter and enhancer activity during human corticogenesis

Steven K. Reilly,^{1,*} Jun Yin,^{1,*} Albert E. Ayoub,^{2,3} Deena Emera,¹ Jing Leng,^{1,†} Justin Cotney,¹ Richard Sarro,¹ Pasko Rakic,^{2,3} James P. Noonan^{1,2,4,‡}

Human higher cognition is attributed to the evolutionary expansion and elaboration of the human cerebral cortex. However, the genetic mechanisms contributing to these developmental changes are poorly understood. We used comparative epigenetic profiling of human, rhesus macaque, and mouse corticogenesis to identify promoters and enhancers that have gained activity in humans. These gains are significantly enriched in modules of coexpressed genes in the cortex that function in neuronal proliferation, migration, and cortical-map organization. Gain-enriched modules also showed correlated gene expression patterns and similar transcription factor binding site enrichments in promoters and enhancers, suggesting that they are connected by common regulatory mechanisms. Our results reveal coordinated patterns of potential regulatory changes associated with conserved developmental processes during corticogenesis, providing insight into human cortical evolution.

The massive expansion and functional elaboration of the neocortex underlies the advanced cognitive abilities of humans (1). Although the overall process of corticogenesis is broadly conserved across mammals, humans exhibit differences that emerge within the first 12 weeks of gestation. Among these are an increased duration of neurogenesis, increases in the number and diversity of progenitors, modification of neuronal migration, and introduction of new connections among functional areas (2, 3). The genetic changes responsible for these evolutionary novelties are largely unknown.

Changes in gene regulation are hypothesized to be a major source of evolutionary innovation during development (1, 3, 4). Critical events in corticogenesis, including the specification of cortical areas and differentiation of cortical layers, rely on the precise control of gene expression (4).

The evolution of distinctly human cortical features required changes in many of these early developmental processes, which may have been driven by modifications in the gene regulatory programs that govern them. However, identifying such regulatory changes and linking them to relevant biological processes has proven to be challenging. Previous efforts have relied on comparative genomics or on gene expression comparisons at later developmental and adult stages (5–7). Further progress has been hindered by the lack of genome-wide maps of regulatory function during corticogenesis.

Genome-wide profiling of posttranslational histone modifications associated with regulatory functions has been used to compare regulatory element activities across species (8–12). In this work, we profiled H3K27ac and H3K4me2 to map active promoters and enhancers during human, rhesus macaque, and mouse corticogenesis, as well as to identify increases in their activity in humans. We examined biological replicates of whole human cortex at 7 postconception weeks (p.c.w.) and 8.5 p.c.w. and primitive frontal and occipital tissues from 12 p.c.w. (Fig. 1A). These stages span the appearance of the transient embryonic zones that generate cortical neurons from the deep to the superficial layers, when distinctly human features of the cortex begin to emerge

¹Department of Genetics, Yale School of Medicine, New Haven, CT 06510, USA. ²Kavli Institute for Neuroscience, Yale School of Medicine, New Haven, CT 06510, USA. ³Department of Neurobiology, Yale School of Medicine, New Haven, CT 06510, USA. ⁴Program in Computational Biology and Bioinformatics, Yale University, New Haven, CT 06511, USA.

*These authors contributed equally to this work. †Present address: Illumina, 499 Illinois Street, San Francisco, CA 94158, USA.

‡Corresponding author. E-mail: james.noonan@yale.edu

(13–15). Homologous rhesus and mouse time points were selected on the basis of cross-species studies of cortical development (13–16). The mouse cortex develops over the course of 1 week [embryonic day 11.5 (E11.5) to E17.5], adhering to the same general developmental processes observed in primates during this homologous time frame (16).

We identified 22,139 promoters (34% of genes in Gencode version 10) and 52,317 enhancers active in the human cortex during at least one developmental stage (Fig. 1B). H3K27ac and H3K4me2 are highly concordant at promoters, with 85% of sites marked by both histone modifications. Histone modification signatures were less concordant at enhancers, with 45% of all

sites marked by both H3K27ac and H3K4me2. This is consistent with studies suggesting that H3K27ac and H3K4me2 identify both overlapping and distinct sets of enhancers (11). We identified 16,473 enhancers most strongly marked by H3K27ac in the cortex relative to seven other human tissues (fig. S1A) (17). These enhancers are significantly enriched near genes associated with cortical development, such as positive regulation of neurogenesis (binomial test, $P \leq 1 \times 10^{-53}$) and neural precursor cell proliferation (binomial test, $P \leq 1 \times 10^{-29}$) (fig. S1B) (18). Both marks also significantly enrich for enhancers active in the developing cortex versus other tissues (Fisher's exact test, $P \leq 1 \times 10^{-15}$), identifying more than 80% of known forebrain enhancers (fig. S2, A

to F) (17, 19, 20). We also identified 74,189 promoters and enhancers active in the rhesus macaque genome and 74,809 in the mouse genome, generating a dense map of regulatory function during corticogenesis across species.

In principal component analysis (PCA), H3K27ac signals clustered first by embryonic tissue type, then by evolutionary distance (fig. S3A) (17). H3K27ac signals in human and mouse cortex were also more similar by PCA than signatures from homologous human and mouse adult tissues or embryonic stem cells (fig. S3B) (17). Spearman correlation analysis of H3K27ac and H3K4me2 cortex signals supported strong replicate reproducibility in all data sets, as well as higher correlations between rhesus and human

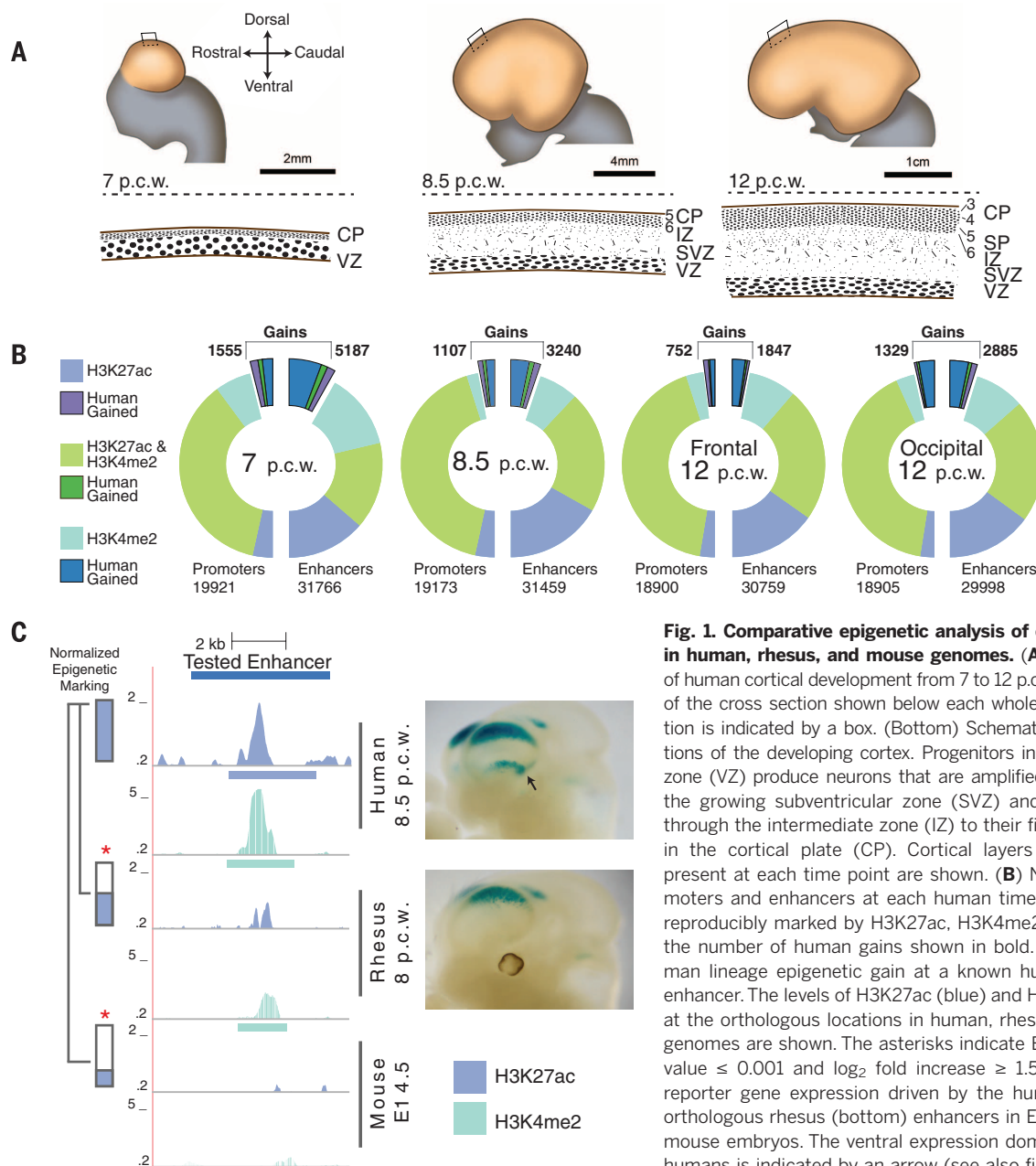


Fig. 1. Comparative epigenetic analysis of corticogenesis in human, rhesus, and mouse genomes. (A) (Top) Stages of human cortical development from 7 to 12 p.c.w. The location of the cross section shown below each whole-cortex illustration is indicated by a box. (Bottom) Schematized cross sections of the developing cortex. Progenitors in the ventricular zone (VZ) produce neurons that are amplified in number in the growing subventricular zone (SVZ) and then migrate through the intermediate zone (IZ) to their final destination in the cortical plate (CP). Cortical layers (e.g., L5, L6) present at each time point are shown. (B) Number of promoters and enhancers at each human time point that are reproducibly marked by H3K27ac, H3K4me2, or both, with the number of human gains shown in bold. (C) (Left) Human lineage epigenetic gain at a known human forebrain enhancer. The levels of H3K27ac (blue) and H3K4me2 (teal) at the orthologous locations in human, rhesus, and mouse genomes are shown. The asterisks indicate BH-corrected P value ≤ 0.001 and \log_2 fold increase ≥ 1.5 . (Right) LacZ reporter gene expression driven by the human (top) and orthologous rhesus (bottom) enhancers in E11.5 transgenic mouse embryos. The ventral expression domain specific to humans is indicated by an arrow (see also fig. S7).

cortex compared with mouse cortex (fig. S4, A and B).

To identify promoters and enhancers showing quantitative epigenetic gains in the human genome versus both the rhesus and mouse genomes, we compared the level of H3K27ac or H3K4me2 signal in replicating human peaks to the signals at corresponding orthologous sites in the other two species (9, 17) (fig. S5). Human gains were called on the basis of an increase in H3K27ac or H3K4me2 signal compared with all rhesus and mouse data sets for each mark (17). It is possible that we may be overestimating gains at 7 p.c.w., due to the lack of an early developmental stage in rhesus. However, this concern is mitigated by our inclusion of a comparable mouse time point and our requirement that each human site exhibit an epigenetic gain compared with all mouse and rhesus time points and tissues. In total, 8996 nonoverlapping enhancers and 2855 promoters show epigenetic gains in humans (Fig. 1B). To assess the robustness of these gains, we compared epigenetic signals at the orthologous human and mouse genomic locations for 77 human gains by chromatin immunoprecipitation (ChIP)-quantitative polymerase chain reaction using additional biological replicates (fig. S6, A and B).

Sixty-seven of these sites (87%) showed a gain in humans, supporting the reproducibility of the epigenetic gain calls from our genome-wide analysis (17). We then explored this high-confidence set of gains to obtain insight into their origins and relevance to human cortical evolution.

We first considered whether epigenetic gains could be attributed to human-specific sequence changes. Forty-eight highly conserved noncoding regions displaying accelerated evolution in humans exhibit increased H3K27ac or H3K4me2 in the human cortex (table S1) (5, 6). However, gains in general do not show increased rates of human-specific sequence change, suggesting that the majority of our gains cannot be identified by sequence acceleration alone (table S1).

In light of this result, we examined epigenetic gains at known human enhancers active in the embryonic forebrain to determine whether gains reveal changes in regulatory function (19) (table S1). In a proof-of-principle experiment, we compared the activities of a human forebrain enhancer exhibiting a gain and its rhesus ortholog using a mouse embryonic transgenic enhancer assay (20). The human enhancer drove reproducible reporter gene expression in two telencephalon domains: a wide caudal-dorsal domain and a

caudal-ventral stripe (Fig. 1C). The rhesus ortholog drove qualitatively weaker reporter gene expression in a similar caudal-dorsal domain but did not drive reproducible activity in the human caudal-ventral domain. Upon sectioning, we determined that the dorsal domain was restricted to the neocortex, whereas the human ventral domain corresponded to the caudal ganglionic eminence (fig. S7C).

We also searched for genomic regions with a high density of enhancers or promoters exhibiting gains. We used previously defined maps of long-range genomic interactions to demarcate putative regulatory domains maintained across tissues and species (17, 21). This analysis revealed genes within topologically delimited domains that are hotspots of epigenetic gains (fig. S8, A to D, and table S2). We identified 301 genes within a gain-enriched hotspot that included at least one gene with a promoter gain, notably *TGF β 3*, *COL3A1*, *EPHA2*, and *LMX1B*.

To obtain global insights into biological pathways associated with human lineage epigenetic gains, we integrated gains with gene coexpression network analyses (22). We generated a coexpression network using public RNA sequencing data from multiple neocortical areas spanning 8 to 15 p.c.w., which includes the periods of corticogenesis in which we mapped H3K27ac and H3K4me2 signatures (Fig. 2A, fig. S9A, and table S3) (23). This network consists of 96 modules, each of which is a set of genes showing highly correlated expression across multiple neocortical regions and developmental stages. Genes in each module may be co-regulated and may participate in related biological processes. Hub genes are defined as genes with connectivity values in the top 5% for each module, suggesting that they include important regulators that drive correlated gene expression. Epigenetic gains at promoters were directly assigned to their target genes, whereas gains at enhancers were assigned on the basis of their proximity to annotated genes (17, 18).

We used permutation analysis to identify modules significantly enriched in human lineage gains at enhancers or promoters (fig. S9, B and C) (17). Seventeen modules are enriched for H3K27ac or H3K4me2 gains in at least one human developmental stage. Overall, gains are consistently enriched in modules containing genes associated with biological processes crucial for cortical development (table S4). For example, module 3 (Fig. 2B) is enriched for human lineage H3K27ac enhancer gains that are associated with genes implicated in neuronal progenitor proliferation. Gene ontology categories showing significant enrichment include neuronal differentiation (binomial test, $P = 2.13 \times 10^{-4}$) and neuron fate commitment (binomial test, $P = 3.67 \times 10^{-4}$) (Fig. 2D). Epigenetic gains in this module are associated with genes critical for cortical development, including *PAX6*, *GLI3*, and *FGFR1*. Each of these is a hub gene, consistent with their known contributions to fundamental processes in corticogenesis. Notably, *PAX6* controls cortical cell number by regulating cell cycle exit of neural progenitor cells, and *Pax6*-null mice have a depleted progenitor

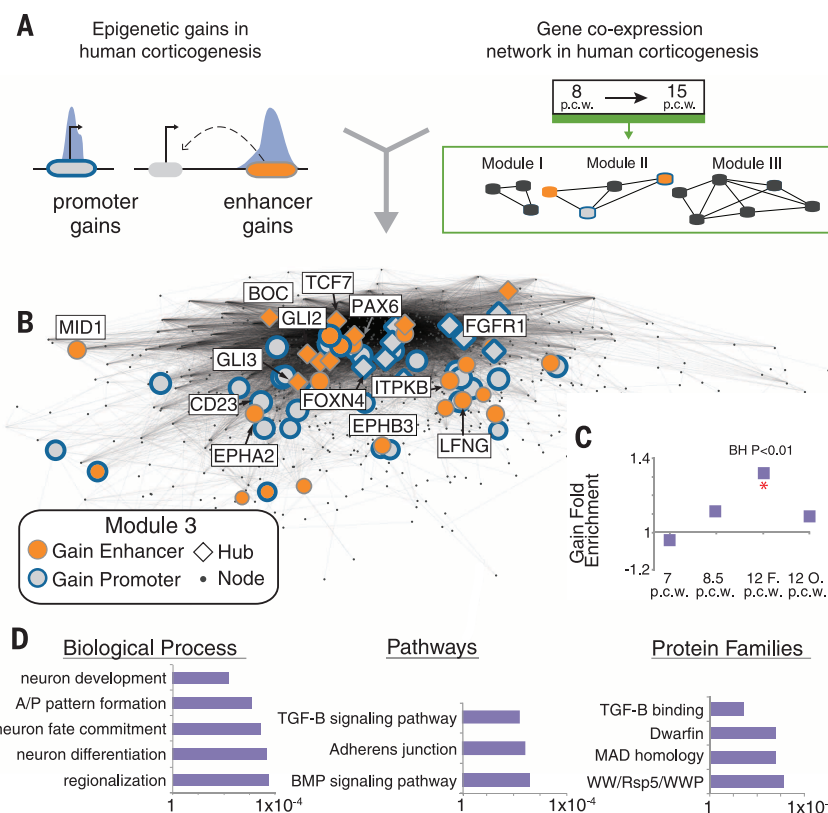
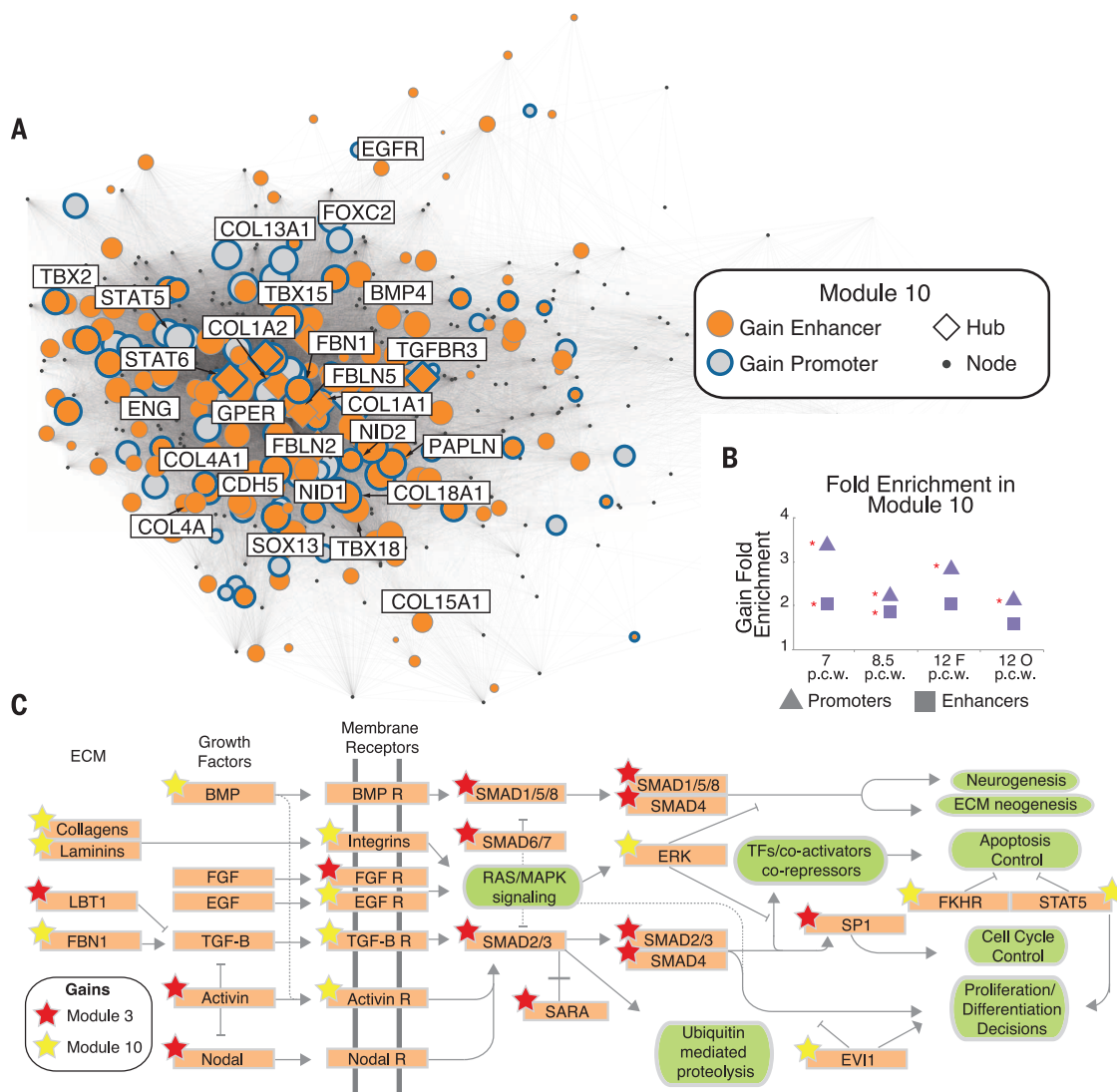


Fig. 2. Identifying modules of coexpressed genes enriched for epigenetic gains in human corticogenesis. (A) Schematic illustrating integration of epigenetic gains into coexpression networks. (B) Co-expression module enriched for H3K27ac enhancer gains. Genes associated with gains are highlighted, and genes representative of the biological enrichments associated with the module are labeled. The module was rendered using multidimensional scaling (17). (C) Fold enrichment of H3K27ac enhancer gains at each human time point in this module. $*P < 0.01$ (BH-corrected permutation). (D) Gene ontology enrichments for genes associated with gains in this module. P values were calculated using a binomial test in DAVID (the Database for Annotation, Visualization and Integrated Discovery) (17).

Fig. 3. Enrichment of epigenetic gains in module 10.

(A) Epigenetic gains mapped onto module 10; genes associated with gains are highlighted as in Fig. 2B. **(B)** Fold enrichment of H3K27ac promoter or enhancer gains at each human time point in this module. $*P < 0.01$ (BH-corrected permutation). **(C)** Genes in the related FGF, TGF β , bone morphogenetic protein (BMP), and ECM signaling pathways are associated with gains from module 10 (yellow stars) and module 3 (red stars). Genes or gene families are highlighted in orange; associated biological processes are in green. The pathway shown is derived from KEGG pathway annotations.



pool and a reduced cortical neuron number (24). Heightened signaling through *FGFR1* during rat corticogenesis increases the neuron number by more than 80% (25).

Module 15 is enriched in human H3K27ac and H3K4me2 promoter gains [Benjamini-Hochberg (BH)-corrected permutation, $P = 0.003$] (fig. S10A) associated with cortical-patterning ontologies such as regionalization (binomial test, $P = 7.53 \times 10^{-4}$) and forebrain development (binomial test, $P = 1.63 \times 10^{-5}$) (fig. S10B). Homeobox genes are notably enriched among genes associated with gains in this module (binomial test, $P = 1.18 \times 10^{-8}$).

Module 10 shows the strongest enrichment of human lineage H3K27ac and H3K4me2 promoter and enhancer gains in the network (Fig. 3, A and B). Genes implicated in extracellular matrix (ECM) functions are significantly overrepresented among gain-associated genes in this module (binomial test, $P = 2.26 \times 10^{-7}$) (table S5). The ECM contributes to the maintenance of human progenitor cell self-renewal and neuronal migration (26). Module 10 gain-associated genes are also enriched

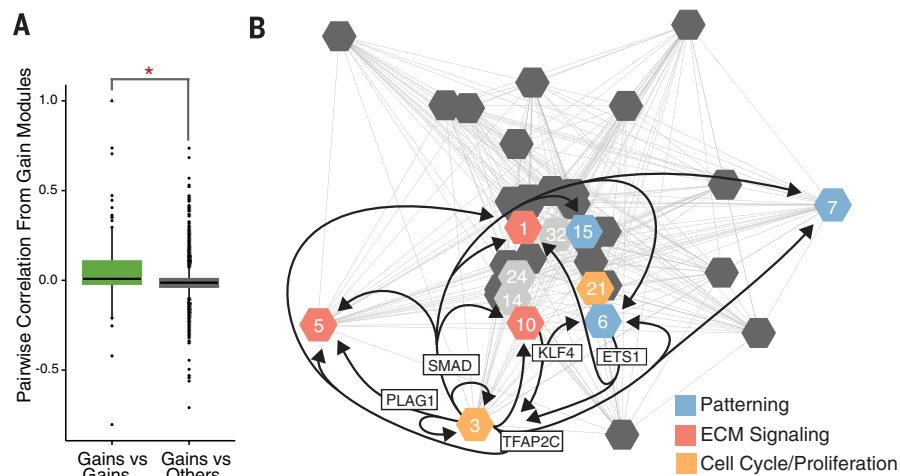


Fig. 4. Modules enriched for epigenetic gains converge on common biological processes. **(A)** Gain-enriched modules exhibit significantly higher gene expression correlation values with each other than with modules not enriched for gains. $*P < 1.1 \times 10^{-15}$ (Wilcoxon rank sum test). **(B)** Eigengene expression correlations among the top 35 modules (as ranked by number of genes). Modules enriched in gains are numbered. Ontologies associated with gains in each module are highlighted. Arrows connect modules that include each transcription factor shown with modules that are enriched for that factor's binding motif.

for transforming growth factor- β (TGF β) and fibroblast growth factor (FGF) pathway members (binomial test, $P = 2.42 \times 10^{-3}$). Notably, both module 10 and module 3 include gain-associated genes belonging to the TGF β and FGF pathways (Fig. 3C). The association of gains with biologically related genes across multiple enriched modules suggests that there may be regulatory coordination and potential transcription factor (TF) cross-talk among these modules.

Consistent with this hypothesis, gain-enriched modules exhibited significantly higher gene expression correlations with each other than with other modules in the network (Wilcoxon rank sum test, $P < 1 \times 10^{-15}$) (Fig. 4A). Moreover, gain-associated genes in enriched modules converge on related biological functions (Fig. 4B). To identify regulatory signatures underlying the correlation of these modules, we predicted transcription factor binding sites in all active promoters and enhancers in our data set, including human lineage gains. We then identified enriched TF motifs in enhancers or promoters assigned to each module. Many motifs were enriched in promoters and enhancers assigned to the same module as the transcription factor itself. Surprisingly, we also identified TF motifs enriched across multiple modules. For example, *SMAD* binding motifs were enriched in active promoters in module 10, although *SMAD* transcription factors are not included in this module (BH permutation test, $P = 7.92 \times 10^{-3}$) (table S5). The observed transcription factor binding site enrichment patterns suggest regulatory cross-talk among gain-enriched modules that may contribute to their highly correlated expression.

Our results reveal a marked convergence of human lineage epigenetic gains on common biological processes and regulatory pathways in corticogenesis. Epigenetic gains are enriched in modules important for neuronal proliferation, cortical patterning, and the ECM. Moreover, gain-associated genes in each module are enriched for similar conserved biological functions as all genes in the entire module (table S4). These findings suggest that many human lineage regulatory changes operate within, and have potentially modified, older regulatory mechanisms and developmental processes essential for building the mammalian cortex.

The epigenetic changes associated with these conserved biological pathways also predominantly occur at sequences with ancestral regulatory activity. The majority of human lineage gains involve potential modification of promoters or enhancers marked by H3K27ac in rhesus or mouse cortex (fig. S11) (10). A smaller proportion of gains may arise from co-option of ancestral regulatory sequences active in noncortical tissues. Human gains not marked in any of the 2 rhesus or 20 mouse tissues we examined may include de novo regulatory functions arising on the human lineage. We note that epigenetic gains may be due to genetic changes in humans that directly altered regulatory functions, or they may reflect coordinated changes in cellular composition in the human cortex compared with rhesus and mouse cortex. Distinguishing between these two modalities of evolutionary change will require functional analysis of the sequences underlying epigenetic gains using mouse transgenic assays and humanized mouse models. Such studies would also provide insight into the biological relevance of the molecular changes described here.

The convergence of human regulatory innovations on developmentally related functions is also consistent with the biological complexity of the cortex. Neocortical development requires the orchestration of spatially and temporally distinct but biologically interconnected mechanisms. In the context of this interdependency, it has been postulated that human cortical evolution involved coordinated changes in multiple processes during corticogenesis (3). For example, changes in progenitor proliferation probably required concomitant changes in patterning and connectivity to generate novel cortical functions (1). The inventory of human lineage regulatory changes that we identified provides the means to evaluate this hypothesis and dissect the genetic mechanisms underlying the evolution of the human cortex.

REFERENCES AND NOTES

1. D. H. Geschwind, P. Rakic, *Neuron* **80**, 633–647 (2013).
2. M. L. Schwartz, P. Rakic, P. S. Goldman-Rakic, *Proc. Natl. Acad. Sci. U.S.A.* **88**, 1354–1358 (1991).
3. P. Rakic, *Nat. Rev. Neurosci.* **10**, 724–735 (2009).
4. P. Rakic, A. E. Ayoub, J. J. Breunig, M. H. Dominguez, *Trends Neurosci.* **32**, 291–301 (2009).
5. S. Prabhakar, J. P. Noonan, S. Pääbo, E. M. Rubin, *Science* **314**, 786–786 (2006).

6. J. A. Capra, G. D. Erwin, G. McKinsey, J. L. R. Rubenstein, K. S. Pollard, *Philos. Trans. R. Soc. London Ser. B* **368**, 20130025 (2013).
7. G. Konopka et al., *Neuron* **75**, 601–617 (2012).
8. J. Cotney et al., *Genome Res.* **22**, 1069–1080 (2012).
9. J. Cotney et al., *Cell* **154**, 185–196 (2013).
10. A. Rada-Iglesias et al., *Nature* **470**, 279–283 (2011).
11. J. Ernst et al., *Nature* **473**, 43–49 (2011).
12. T. S. Mikkelsen et al., *Cell* **143**, 156–169 (2010).
13. P. Rakic, *Science* **183**, 425–427 (1974).
14. P. Rakic, *Science* **241**, 170–176 (1988).
15. P. Rakic, R. L. Sidman, *J. Neuropathol. Exp. Neurol.* **27**, 240–276 (1968).
16. T. Takahashi, T. Goto, S. Miyama, R. S. Nowakowski, V. S. Caviness Jr., *J. Neurosci.* **19**, 10357–10371 (1999).
17. See supplementary materials and methods on Science Online.
18. C. Y. McLean et al., *Nat. Biotechnol.* **28**, 495–501 (2010).
19. A. Visel, S. Minovitsky, I. Dubchak, L. A. Pennacchio, *Nucleic Acids Res.* **35** (suppl. 1), D88–D92 (2007).
20. A. Visel et al., *Cell* **152**, 895–908 (2013).
21. J. R. Dixon et al., *Nature* **485**, 376–380 (2012).
22. P. Langfelder, S. Horvath, *BMC Bioinformatics* **9**, 559 (2008).
23. BrainSpan Atlas of the Developing Human Brain; www.brainspan.org.
24. J. C. Quinn et al., *Dev. Biol.* **302**, 50–65 (2007).
25. F. M. Vaccarino et al., *Nat. Neurosci.* **2**, 246–253 (1999).
26. A. L. Pearlman, A. M. Sheppard, *Prog. Brain Res.* **108**, 119–134 (1996).

ACKNOWLEDGMENTS

This work was supported by NIH grants GM094780 (to J.P.N.), DA023999 (to P.R.), NS014841 (to P.R.), and F32 GM106628 (to D.E.); a Brown Coxie Fellowship in the Medical Sciences (to J.Y.); and an NSF Graduate Research Fellowship (to S.K.R.). Human tissue was provided by the Joint Medical Research Council (UK)/Wellcome Trust (grant 099175/Z/12/Z) Human Developmental Biology Resource (HDBR) (<http://hdb.org>). The human tissues used in this study are covered by a material transfer agreement regarding their transfer, but tissues may be requested directly from the HDBR. We thank S. Mane, K. Bilguvar, S. Umlauf, and A. Lopez at the Yale Center for Genome Analysis for sequencing data; the members of the BrainSpan consortium for providing human brain transcriptome data to the research community; N. Carriero and R. Bjornson at the Yale University Biomedical Performance Computing Center for computing support; T. Nottoli and C. Pease at the Yale Animal Genomics Service for generating transgenic mice; and S. Wilson and M. Horn for veterinary care of nonhuman primates. All ChIP-seq data are available through the Gene Expression Omnibus under accession number GSE63649.

SUPPLEMENTARY MATERIALS

www.sciencemag.org/content/347/6226/1155/suppl/DC1
Materials and Methods
Figs. S1 to S12
Tables S1 to S5
References (27–44)

8 September 2014; accepted 4 February 2015
10.1126/science.1260943

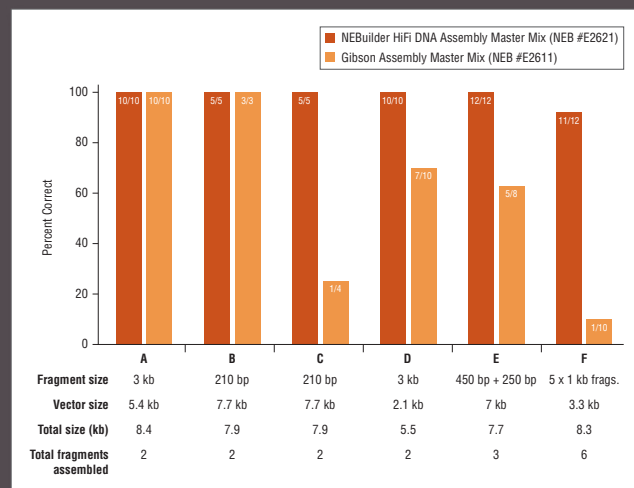
The Next Generation of DNA Assembly and Cloning

NEBuilder[®] HiFi DNA Assembly

The next generation of DNA assembly and cloning has arrived. With NEBuilder HiFi DNA Assembly, you'll enjoy virtually error-free joining of DNA fragments. More efficient assembly is now possible, even with larger fragments, low inputs, or 5'- and 3'-end mismatches. Additionally, use NEBuilder HiFi to bridge two dsDNA fragments with a ssDNA oligo. Save time with less screening or re-sequencing, and benefit from no licensing fee requirements from NEB when choosing NEBuilder products.

Request a free sample*
at www.NEBuilderHiFi.com

NEBuilder HiFi DNA Master Mix offers improved fidelity over Gibson Assembly Master Mix



Fidelity of assembled products was compared between NEBuilder HiFi DNA Assembly Master Mix (NEB #E2621) and Gibson Assembly Master Mix (NEB #E2611). Experiments were performed using the various fragment and vector sizes, following suggested protocols. Experiments B and C vary because sequences of fragments are different. Experiments D and F were performed with fragments containing 3'-end mismatches.

* While supplies last. Offer valid in the US only. Limit one sample per customer.

NEW ENGLAND BIOLABS[®], NEB[®] and NEBUILDER[®] are registered trademarks of New England Biolabs, Inc.
GIBSON ASSEMBLY[®] is a registered trademark of Synthetic Genomics, Inc.

Regional Focus: Japan

March 27, 2015

Reserve ads by March 10 to guarantee space

THERE'S A SCIENCE TO REACHING SCIENTISTS.

For recruitment in science, there's only one

Science

Regional Focus: Japan

This feature focuses on growing areas of basic and applied research at different academic institutions and provides advice for scientists building a career in Japan, including new funding initiatives that are enhancing opportunities.

Why you should advertise in this issue of *Science*:

Reach: Your job ad is seen by 570,400 readers around the globe from varied backgrounds and it sits on special bannered pages promoting opportunities in Japan. 60% of our weekly readers work in academia and 67% are Ph.D.s.

Results: Hire top scientific talent, raise the global profile of your organisation or highlight your research with this special advertising opportunity.



SCIENCECAREERS.ORG

Science Careers

FROM THE JOURNAL SCIENCE  AAAS

To book your ads, contact: advertise@sciencecareers.org

The Americas

202 326 6582

Europe/RoW

+44 (0) 1223 326500

Japan

+81 3 3219 5777

China/Korea/Singapore/Taiwan

+86 186 0082 9345

**eppendorf
& Science**
**PRIZE FOR
NEURO
BIOLOGY**



2014 年获奖者
艾曼·阿齐姆博士
哥伦比亚大学
专注精确控制肢体运动的研究

Call for Entries

申请截止日期
2015年6月15日

Eppendorf & Science 神经生物学奖

每年一度的 Eppendorf & Science 神经生物学奖是一项国际性奖项，授予用分子与细胞生物学方法在神经生物学领域取得非凡成就的青年科学家。所有奖项的获得者均是由《Science》杂志高级编辑 Peter Stern 博士领衔的独立科学家所组成的委员会评出。参选者必须是年龄在 35 岁（含）以下的青年科学家。

您可能就是下一位获奖者并获得：

- > 25,000 美元奖金
- > 获奖论文发表在《Science》杂志上
- > 得以全额资助参与美国神经科学协会年会和颁奖仪式
- > 获邀参观 Eppendorf 位于德国汉堡的总部

申请就是这么容易！

详情登陆：www.eppendorf.com/prize

eppendorf **Science**
AAAS

**eppendorf
& Science**

**PRIZE FOR
NEURO
BIOLOGY**



2014年の優勝者
Eiman Azim博士
コロンビア大学
四肢の巧緻運動に関する
研究

Call for Entries

応募期限
2015年6月15日

Eppendorf & Science Prize for Neurobiology

毎年開催される国際コンクール、エッペンドルフ&サイエンス神経生物学賞は分子・細胞生物学の方法論に基づく神経生物学研究に優秀な貢献があった若手科学者を称えるものです。受賞者および最終審査対象者はサイエンスの編集長ピーター・スターン博士が議長を務める独立科学者委員会により選定されます。応募資格は35歳以下です。

次の受賞者はあなたかも知れません

- > 賞金25,000 USドル
- > Science誌への論文掲載
- > 米国神経科学学会年次総会に並行して開催される授賞式典への全額支援
- > ドイツ ハンブルグのエッペンドルフ本社へご招待

応募は簡単です!

Learn more at: www.eppendorf.com/prize

eppendorf **Science**
AAAS



2014 Winner
Eiman Azim, Ph.D.
Columbia University
For research on skilled
limb movement

Call for Entries

Application Deadline
June 15, 2015

Eppendorf & Science Prize for Neurobiology

The annual Eppendorf & Science Prize for Neurobiology is an international award which honors young scientists for their outstanding contributions to neurobiological research based on methods of molecular and cell biology. The winner and finalists are selected by a committee of independent scientists, chaired by Science's Senior Editor, Dr. Peter Stern. To be eligible, you must be 35 years of age or younger.

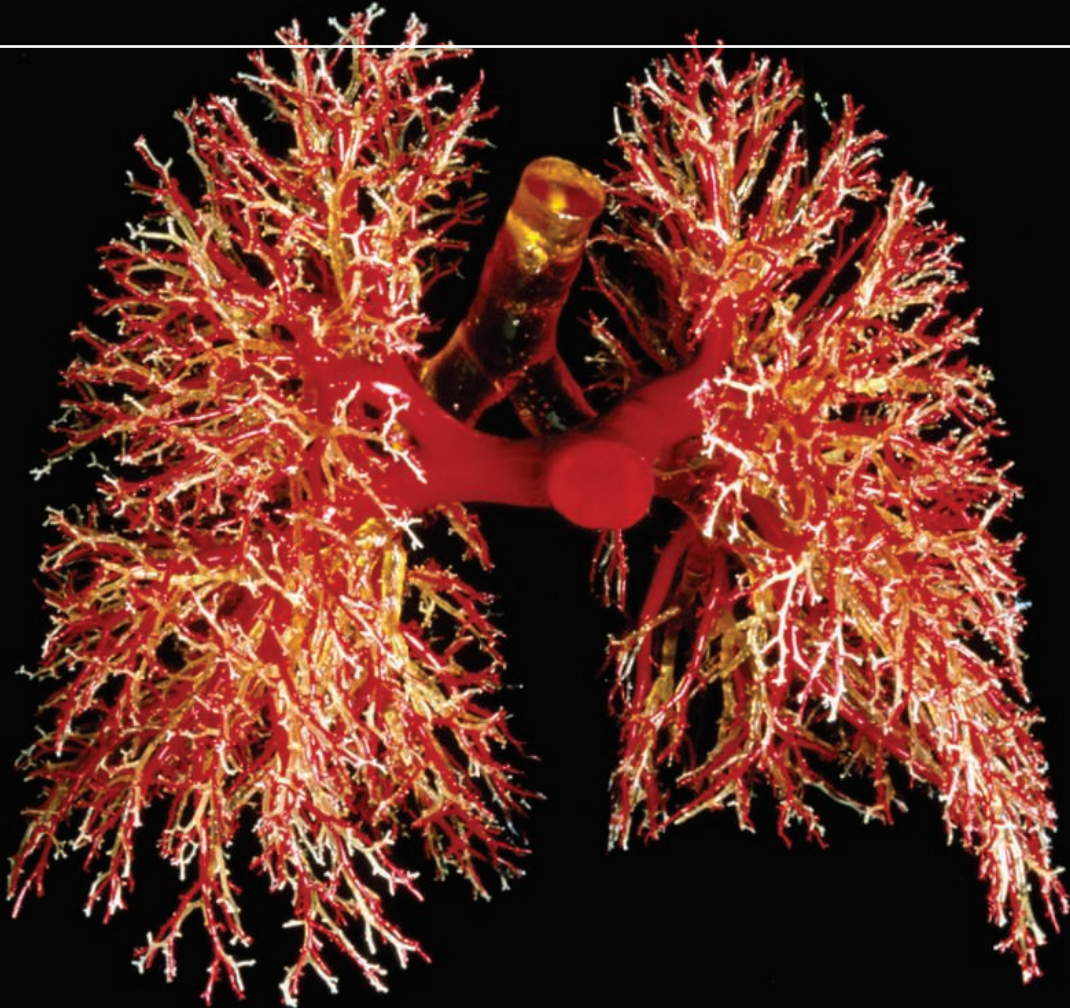
You could be next to win this prize and to receive

- > Prize money of US\$25,000
- > Publication of your work in Science
- > Full support to attend the Prize Ceremony held in conjunction with the Annual Meeting of the Society for Neuroscience in the USA
- > An invitation to visit Eppendorf in Hamburg, Germany

It's easy to apply!

Learn more at: www.eppendorf.com/prize

WILL YOUR RESEARCH LEAD TO BETTER LIVES FOR PATIENTS?



Gopinath Sutendra and Evangelos D. Michelakis, "Pulmonary Arterial Hypertension: Challenges in Translational Research and a Vision for Change", *Sci. Transl. Med.* 5, 208sr5 (2013) Credit: Science Source

Science Translational Medicine |  AAAS

INTEGRATING SCIENCE, ENGINEERING, AND MEDICINE

Find out more about the scope of the journal and submit your research today!

ScienceTranslationalMedicine.org

Full-Height Liquid Handling Pump

The new Hamilton Precision Syringe Drive 6 (PSD/6) is a compact, full-height pump for precision dispensing of small to large volumes. The PSD/6 performs all standard liquid handling functions including dispensing, serial dispensing, and diluting and offers the largest range of compatible syringes sizes. Enhanced flow stability and increased dispense times make it ideal for applications like flow cytometry and microfluidics. Designed for simple integration, a variety of mounting configurations are possible for a single unit or a daisy chain of up to 16 pumps. With selectable communication protocols and flexible programming options, every detail of the pump's performance can be adjusted to accommodate even the most challenging applications. The PSD/6 syringe and valve drive movements are optimized to extend the life and time between product maintenance. By manufacturing all the fluid path components in house, Hamilton can ensure the fluid sub-system will provide superior performance, even in harsh conditions or under heavy duty cycles.

Hamilton Company

For info: 800-648-5950
www.hamiltoncompany.com

Patient-Derived Xenograft Models

The collection of Patient-Derived Xenograft (PDX) models of breast cancer allows the study of human tumors in an in vivo model system. PDX models are a key tool in the development of personalized medicines. The lines accurately model real patient tumors, enabling researchers to discover important genetic differences, develop biomarkers to distinguish them, and ultimately develop patient-specific therapies. The new collection includes 10 triple negative lines as well as several ER+ (estrogen receptor positive) lines. Whole genome sequencing has been performed on the originating tumors, early and late passages of PDX, as well as metastases, demonstrating striking similarity and faithful modeling of the original tumor, with all contaminating mouse signal removed. Using SAGE Labs' PDXplorer, customers can access a wealth of data on the PDX models, including comprehensive patient histories, estradiol responsiveness, RNAseq profiles, DNA microarrays, and phosphoprotein profiles, and can handpick the models that best support their research.

Horizon Discovery

For info: +44-(0)-1223-655580
www.horizondiscovery.com



Dry Reagent Cocktails

DuraClone IM premixed dry reagent cocktails standardize and streamline workflow for high-content flow cytometry in translational research studies involving identification of cellular subpopulations of the human immune system. These optimized, easy-to-use panels provide worry-free compensation to minimize labor and reduce variability and errors when characterizing alterations of immune status through detection of human blood-cell subpopulations. Dried down using a proprietary process that ensures high structural stability, DuraClone IM panels are stable for up to one year at room temperature. Simple, single-step resuspension of DuraClone cocktails by the addition of a cell suspension or whole blood minimizes variability, allowing generation of comparable data across geographies and institutions. DuraClone IM panels comprising basic phenotype, B cells, T cell subsets and dendritic cells are offered for "Research Use Only" in 25-test packages containing three complete compensation kits with a single-color set of compensation reagents specific for each panel.

Beckman Coulter Life Sciences

For info: 800-361-7780
www.beckmancoulter.com

Simplified Liquid Extraction Sorbent

Novum Simplified Liquid Extraction (SLE) is a novel, synthetic alternative to traditional diatomaceous earth SLE (also known as supported liquid extraction) products and a simplified approach to traditional liquid-liquid extraction (LLE). Extraction techniques used prior to liquid and gas chromatography can improve results and reduce wear and tear on the instrument. As the first of its kind, the synthetic Novum SLE sorbent can be used with the same procedure as traditional SLE sorbents while delivering improved lot-to-lot reproducibility. Because it is a lab-manufactured sorbent, supplies are readily available, compared to diatomaceous earth, which is a natural resource that must be mined. Novum SLE simplifies the liquid-liquid extraction process by eliminating manual steps and it reduces solvent consumption. SLE also delivers higher sample recovery than liquid-liquid extraction methods by eliminating analyte loss due to emulsions that can form at the interface of the two liquid phases.

Phenomenex

For info: 310-212-0555
www.phenomenex.com/novum

Multichannel Peristaltic Pump

Maximizing available bench-top space is important for many laboratories and a new design of peristaltic pump which provides up to four fluidic channels in a single pump will help technicians to eliminate the clutter of multiple pumps. The Ismatec Reglo ICC (Independent Channel Control) peristaltic pump expands the power of laboratory and life-science pumping by providing individual control of each fluidic channel as well

as allowing users to solve application complexity in a single pump. Most importantly, independent channel calibration minimizes the tube-to-tube differences and this results in optimum accuracy for a multichannel peristaltic pump. Easy-to-use tubing cassettes also provides for quick, convenient changeovers. The Reglo ICC pump is self-priming, not sensitive to dry-running and can handle flow rates from 0.002 up to 35 mL/min and differential pressures up to 1 bar, while an easy-to-use USB interface means connections can be made quickly.

Michael Smith Engineers

For info: 800-316-7891
www.michael-smith-engineers.co.uk

Electronically submit your new product description or product literature information! Go to www.sciencemag.org/products/newproducts.dtl for more information.

Newly offered instrumentation, apparatus, and laboratory materials of interest to researchers in all disciplines in academic, industrial, and governmental organizations are featured in this space. Emphasis is given to purpose, chief characteristics, and availability of products and materials. Endorsement by *Science* or AAAS of any products or materials mentioned is not implied. Additional information may be obtained from the manufacturer or supplier.

want new technologies?

antibodies

apoptosis

biomarkers

cancer

cytometry

data

diseases

DNA

epigenetics

genomics

immunotherapies

medicine

microbiomics

microfluidics

microscopy

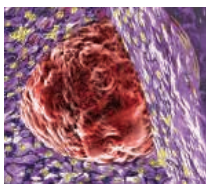
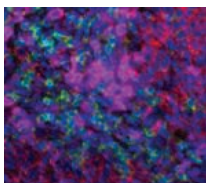
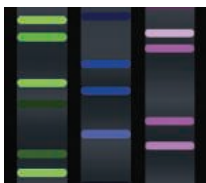
neuroscience

proteomics

sequencing

toxicology

transcriptomics



watch our **webinars**

Learn about the latest breakthroughs, new technologies, and ground-breaking research in a variety of fields. Our expert speakers explain their quality research to you and answer questions submitted by live viewers.

VIEW NOW!

webinar.sciencemag.org

Science
AAAS

Brought to you by the Science/AAAS
Custom Publishing Office



@SciMagWebinars

Introducing

bio-techne®

HIGHEST QUALITY PRODUCT PORTFOLIO



TRUSTED GLOBAL BRANDS

R&D systems

NOVUS™
BIOLOGICALS

TOCRIS

bio-techne®		LEARN MORE		bio-techne.com/launch	
	Building Innovation Opportunities	bio-techne.com info@bio-techne.com techsupport@bio-techne.com	North America TEL 800 343 7475	Europe • Middle East • Africa TEL +44 (0)1235 529449	China info.cn@bio-techne.com TEL +86 (21) 52380373
		Rest of World bio-techne.com/find-us/distributors TEL +1 612 379 2956			

Bio-Techne is a trading name for R&D Systems



There's only one **Science**

Science Careers Advertising

For full advertising details, go to ScienceCareers.org and click For Employers, or call one of our representatives.

Tracy Holmes

Worldwide Associate Director
Science Careers
Phone: +44 (0) 1223 326525

THE AMERICAS

E-mail: advertise@sciencecareers.org
Fax: 202 289 6742

Tina Burks

Phone: 202 326 6577

Nancy Toema

Phone: 202 326 6578

Marci Gallun

Sales Administrator
Phone: 202 326 6582

Online Job Posting Questions

Phone: 202 312 6375

EUROPE / INDIA / AUSTRALIA / NEW ZEALAND / REST OF WORLD

E-mail: ads@science-int.co.uk
Fax: +44 (0) 1223 326532

Axel Gesatzki

Phone: +44 (0) 1223 326529

Sarah Lelarge

Phone: +44 (0) 1223 326527

Kelly Grace

Phone: +44 (0) 1223 326528

JAPAN

Katsuyoshi Fukamizu (Tokyo)

E-mail: kfukamizu@aaas.org
Phone: +81 3 3219 5777

Hiroyuki Mashiki (Kyoto)

E-mail: hmashiki@aaas.org
Phone: +81 75 823 1109

CHINA / KOREA / SINGAPORE / TAIWAN / THAILAND

Ruolei Wu

Phone: +86 186 0082 9345
E-mail: rwu@aaas.org

All ads submitted for publication must comply with applicable U.S. and non-U.S. laws. *Science* reserves the right to refuse any advertisement at its sole discretion for any reason, including without limitation for offensive language or inappropriate content, and all advertising is subject to publisher approval. *Science* encourages our readers to alert us to any ads that they feel may be discriminatory or offensive.

Science Careers

FROM THE JOURNAL SCIENCE **MAAAS**

ScienceCareers.org



NASA seeks a new **Director** for the NASA Astrobiology Institute (NAI). The ideal candidate will be an internationally recognized scientist with proven experience in leading or managing large interdisciplinary research programs or projects, possessed with a vision for leading the Institute into the future. Applicants for this position should have a broad scientific perspective on astrobiology, experience in conducting interdisciplinary scientific research, and demonstrated skills needed to harness the strengths of disparate research communities towards a greater goal. S/he should understand how to grow a research endeavor and respond to changing budget climates while focusing on maximizing the scientific return on NASA's investments in astrobiology. S/he should have experience in leading a diverse staff ranging from established scientists to support personnel, resource planning, and executing budgets and schedules. S/he should be comfortable with modern information technologies and distributed research teams. NASA is particularly interested in applicants who will find ways to infuse astrobiology into NASA flight missions.

The NAI Director is both the senior scientific officer and chief operating officer of the NAI. The Director coordinates scientific activities of the Institute's member teams and is responsible and held accountable for all operational aspects of the NAI, including the administration of personnel, budget and NASA policies. The Director will lead the NAI in fulfilling its mission to perform, support, and catalyze collaborative interdisciplinary astrobiology research; train the next generation of astrobiologists; provide scientific and technical leadership for astrobiology space mission investigations; develop new information technology approaches for collaborations among widely distributed investigators; and support K-12 education and public outreach programs.

Established in 1998 as part of NASA's Astrobiology Program, the NAI is a virtual, distributed organization of competitively-selected teams that conduct and integrate astrobiology research and training programs in concert with the national and international science communities. The Institute has 12 teams including ~600 researchers distributed across ~100 organizations as well as 13 international partner organizations. Headquartered at NASA Ames Research Center in the heart of California's Silicon Valley, the NAI links researchers across the US and around the globe using modern information technologies.

The NAI serves a vital role in advancing the goals of the larger NASA Astrobiology Program, with a focus on seeking the answers to these fundamental questions: How does life begin and evolve? Is there life beyond Earth and, if so, how can we detect it? What is the future of life on Earth and beyond?

U.S. citizenship is required for the NAI Director.

Interested individuals should apply directly to **USAJobs** at www.usajobs.gov. In the keyword search box, type vacancy number "AR15S0001". Select "Director, NASA Astrobiology Institute", then click "Apply Online".

NASA Ames Research Center does not discriminate in employment on the basis of race, color, religion, sex, national origin, political affiliation, sexual orientation, gender identity, marital status, disability and genetic information, age, membership in an employee organization, or other non-merit factor.

LSU Health
NEW ORLEANS

School of Medicine

WILLIAM & SARAH JANE PELON ENDOWED CHAIR DEPARTMENT OF MICROBIOLOGY, IMMUNOLOGY & PARASITOLOGY

LSU Health Sciences Center School of Medicine is initiating a search for a senior researcher to join the Department of Microbiology, Immunology and Parasitology. Candidates will be considered for appointment as Professor on the tenure track and should have a strong record of research accomplishment, lead an active, nationally funded research program, and have a commitment to developing collaborative translational research programs. This position is associated with the endowed William and Sarah Jane Pelon Chair, designed to enhance the scholarly productivity of the incumbent.

The ideal candidate will have a Ph.D. and/or M.D., demonstrated team-building ability, and a strong track record of developing translational research from basic scientific observations. Expertise in all areas of host/pathogen interaction will be considered, but special consideration will be given to those complementing existing core departmental strengths in HIV, HIV-related infections, and sexually transmitted diseases.

LSU Health Sciences Center School of Medicine offers a highly interactive and collegial environment, with a strong history of collaborative research programs and state-of-the-art infrastructure, including core laboratories in genomics, proteomics, bioinformatics, imaging, and flow cytometry. Excellent opportunities exist for interaction with clinical departments, and with research Centers of Excellence in Vaccine Development, Cancer, Alcohol and Drug Abuse, Cardiovascular Biology, and Neuroscience. Anticipated duties and responsibilities will include sustaining an exceptional research program, mentoring graduate students and postdoctoral fellows, and participation in departmental and school graduate and undergraduate teaching programs. The institution offers competitive start-up packages and salaries.

Qualified applicants with a substantial record of scientific achievement should send a single PDF document containing their curriculum vitae including details of publications, previous and current research funding, teaching experience, a statement of research plans, and the names of at least three referees to: SOM-Recruits@lsuhsc.edu with **Professor - MIP** in subject line.

LSUHSC is an Equal Opportunity Employer for females, minorities, individuals with disabilities and protected veterans.



Seaver Autism
Center for Research
and Treatment



Tenure Track Positions at the Seaver Autism Center at Mount Sinai

The Seaver Autism Center is seeking researchers at the Assistant, Associate, or Full Professor levels who focus on patient-based research in autism spectrum disorder (ASD). Up to three positions are available, with at least one position prioritized for a clinician-scientist (MD or clinical psychologist) who would help manage the clinical research program. Successful applicants will have a very competitive track record in publications, and, for more senior applicants, in federal funding. Generous startup packages are available. Applicants will be members of one or more relevant Departments and Institutes at Mount Sinai.

About the Seaver Autism Center: The Seaver Autism Center integrates research at all levels. The Center includes clinical and research genetics, model systems research, controlled trials for behavioral and pharmacological interventions, biomarker development, development of assessments and screeners, large scale epidemiological studies of ASD risk factors, and neuroimaging, as well as clinical services for ASD. Psychiatrists, psychologists, neurologists, pediatricians, and clinical geneticists carry out comprehensive assessments for families and for research. The Center has a commitment to more severely affected individuals, and has taken a unique genetics-first approach to ASD research. Exceptional applicants working in any of these areas, or in additional areas of importance in ASD, are encouraged to apply.

Contact Us: Interested applicants should send a CV, a three-page summary of future research plans, and contact information for three references to:

Joseph D. Buxbaum, PhD
Director, Seaver Autism Center for Research and Treatment
Department of Psychiatry
Icahn School of Medicine at Mount Sinai
New York, NY
theseavercenter@mssm.edu

About Mount Sinai Health System: Internationally regarded for its dedication to medical science, Mount Sinai is home to an array of leading research institutes, centers, and laboratories, all of which work toward rapidly translating advances in basic science into innovative patient care. With a history rich in clinical milestones and an unequaled passion for patient-focused research, Mount Sinai has pioneered breakthroughs benefiting untold numbers of lives. The Mount Sinai Health System is also committed to providing compassionate patient care by recruiting the most skilled professionals for our patients. Join us if you share our vision of collaborative problem solving and help to shape the future of research and health care. In addition to taking the best care of our patients, we offer our employees a highly competitive compensation and benefits package, including medical, dental, vision, prescription drug coverage, a 403(b) retirement plan, and much more.

Formed in September 2013, Mount Sinai Health System combines the excellence of the Icahn School of Medicine at Mount Sinai with seven premier hospital campuses, including Mount Sinai Beth Israel, Mount Sinai Beth Israel Brooklyn, The Mount Sinai Hospital, Mount Sinai Queens, New York Eye and Ear Infirmary of Mount Sinai, Mount Sinai Roosevelt, and Mount Sinai St. Luke's.

The Mount Sinai Health System is committed to the tenets of diversity and workforce that are strengthened by the inclusion of and respect for our differences. We offer our employees a highly competitive compensation and benefits package, a 403(b) retirement plan, and much more. The Mount Sinai Health System is an Equal Opportunity Employer. We promote recognition and respect for individual and cultural differences, and we work to make our employees feel valued and appreciated, whatever their race, gender, background, or sexual orientation. EOE Minorities/Women/Disabled/Veterans

Universität
Konstanz



The University of Konstanz, belongs to the universities in Germany whose "future concepts for top-class research at universities" is promoted within the framework of the Excellence Initiative of the German federal and state governments.

The *Zukunftskolleg* of the University of Konstanz is offering:

up to five ZIF Marie Curie 5-year Research Fellowships

in any discipline represented at the University of Konstanz for the development and implementation of individual research projects (Salary Scale 14 TV-L).

Fellowships will begin on March 1, 2016, and end on February 28, 2021.

Reference number 2015 / 031

Applications, supporting materials, and two letters of reference should be submitted in English **by May 18, 2015, 17:00 h (Konstanz time)** using the **Online Application Platform:**

www.zukunftskolleg.uni-konstanz.de/online-application.

Details concerning the application, required documents, and information about the *Zukunftskolleg* are available on our website:
<http://www.zukunftskolleg.uni-konstanz.de>.

Contact: Help Desk, zukunftskolleg-application@uni-konstanz.de,
Anda Lohan, e-mail: a.lohan@uni-konstanz.de.



Universität
Konstanz



The University of Konstanz, belongs to the universities in Germany whose "future concepts for top-class research at universities" is promoted within the framework of the Excellence Initiative of the German federal and state governments.

The *Zukunftskolleg* of the University of Konstanz is offering:

up to six ZIF Marie Curie 2-year Postdoctoral Fellowships

in any discipline represented at the University of Konstanz for researchers in the early stage of their career, so as to enable them to develop and implement individual and independent research projects (Salary Scale 13 TV-L).

Fellowships will begin on February 1, 2016, and end on January 31, 2018.

Reference number 2015 / 032

Applications, supporting materials, and two letters of reference should be submitted in English **by May 18, 2015, 17:00 h (Konstanz time)** using the **Online Application Platform:**

www.zukunftskolleg.uni-konstanz.de/online-application.

Details concerning the application, required documents, and information about the *Zukunftskolleg* are available on our website:
<http://www.zukunftskolleg.uni-konstanz.de>.

Contact: Help Desk, zukunftskolleg-application@uni-konstanz.de,
Anda Lohan, e-mail: a.lohan@uni-konstanz.de.



The German Cancer Research Center (DKFZ) in Heidelberg, Germany, a foundation under public law financed by the Federal Government of Germany and the State of Baden-Württemberg, is a member of the Hermann von Helmholtz Association of German Research Centres (HGF).

We invite applications for the position of

Scientific Director and Chairman (m/f) of the Management Board of the DKFZ Foundation

(Ref.no. 30/2015)

Effective as of 1 September 2015.

The DKFZ is among the world's leading centers of cancer research and the largest biomedical research institute in Germany. From its founding in 1964, the DKFZ has pursued a threefold mission: to investigate the mechanisms leading to the development of cancer, to identify and study cancer risk factors and to develop new approaches for the diagnosis, treatment and prevention of cancer diseases. Building on its excellent basic research, the DKFZ has in recent years considerably expanded its activities in the area of translational research.

Together with the University of Heidelberg, the Heidelberg University Clinic and the German Cancer Aid, the DKFZ has established the National Center for Tumor Diseases (NCT), which has become one of the most influential institutions of translational cancer research in Europe. A new branch of the NCT will shortly be established in Dresden.

The DKFZ is the parent organization of the German Consortium for Translational Cancer Research (DKTK), a joint initiative launched by the German Federal Government and the German States with the aim of ensuring the comprehensive transfer of research results from the laboratory into clinical practice at seven partner sites throughout Germany.

The DKFZ employs around 2,750 staff members, including 1,250 scientists. The total annual budget (institutional funding, project funding and own revenues) amounts to around 250 million Euros.

The Chairman of the Management Board as the scientific representative of the foundation is jointly responsible, together with the Administrative Member of the Management Board, for overseeing the DKFZ.

The scientific departments and research groups of the DKFZ as well as the central scientific core facilities report directly to the Chairman of the Management Board. In particular, his/her responsibilities include the strategic research orientation, the oversight of the quality of the research results in conjunction with the supervisory bodies and the Board of Trustees, and the scientific development and strategic positioning of the DKFZ, both nationally and internationally. In his/her capacity as Scientific Director of the DKFZ, he/she is also spokesperson for the German Consortium for Translational Cancer Research (DKTK).

The size and scope of research carried out at the DKFZ as well as its many close collaborations with universities, research institutions and industry partners require a candidate who combines exceptional leadership qualities, international stature and outstanding scientific expertise, who is capable of providing visionary leadership to guide the strategic development of complex research structures in basic and clinical biomedical research. He/she should demonstrate an established record of management experience leading large, distinguished scientific or medical institutions. Further requirements include strategic vision, an authoritative personality, and a talent for inspiring people to work together effectively. He/she should have the stature and communicative skills to represent the DKFZ convincingly – with regard to both internal bodies and external partners. The continuous development of relations with representatives of political bodies, science, industry and relevant societal groups are of particular importance for the DKFZ. An excellent knowledge of German and English is required.

The appointment will be for a period of 5 years with the possibility of renewal. The remuneration is based on the compensation scheme for higher-level university professorships and will be the subject of individual negotiations.

The members of the Helmholtz Association actively seek to promote women in positions of leadership with managerial responsibilities in science and research. Applications from qualified women candidates are therefore particularly welcome.

Please send your application both electronically (by email) and by mail by **March 31, 2015** to:

MinDir'in Bärbel Brumme-Bothe
Chairwoman of the DKFZ Board of Trustees
and Chairwoman of the Search Committee
–Confidential/personal –

Federal Ministry for Education and Research (BMBF)
Kapelle-Ufer 1
D-10117 Berlin
baerbel.brumme-bothe@bmbf.bund.de



u^b

**UNIVERSITÄT
BERN**

ARTORG CENTER
BIOMEDICAL ENGINEERING RESEARCH

Faculty Position (ausserordentliche Professur) in Biomedical Engineering

The Medical Faculty of the University of Bern invites applications for a faculty position in the field of Biomedical Microfluidics and Organs-on-Chip Systems dedicated for biomedical applications research. The position will be established at the ARTORG Center for Biomedical Engineering Research. The professorship will be heading the existing Lung Regeneration Technologies Group, a joint technological and clinical research effort of the ARTORG Center together with the departments of Pneumology and Thoracic Surgery at the University hospital Bern, Inselspital.

The successful candidate should have a PhD in biomedical engineering or similar fields and a proven track record in at least two of the following research areas: microfluidics, microtechnologies, cell biology, micro-fabrication and thin film technologies, material sciences and in the domain of cells-on-chip and organs-on-chip technologies, particularly lung-on-chip as well as advanced in-vitro models for personalized medicine applications.

The candidate is expected to continue and further strengthen the internationally recognized, interdisciplinary research program of the existing Lung Regeneration Technologies group. The focus of the research should be on organs-on-chip technologies that allow the investigation of the pathomechanisms of specific diseases as well as the testing of efficiency and toxicity of drug candidates or other chemical substances. Furthermore, a specific focus of the work should be the development of novel pharmaceutical testing methods specifically for lung diseases. However, future collaboration schemes beyond this topic shall be envisioned.

Additional prerequisites are a strong motivation and an undisputable commitment to undergraduate and graduate student education. The professorship will be embedded in the Graduate School for Cellular and Biomedical Sciences of the University of Bern and the specialized Master's program in Biomedical Engineering, bridging the fields of engineering and clinical science and in the Master's program in Biomedical Sciences.

Candidates should demonstrate a successful track record in the acquisition of competitive third party funding. Experience in professional leadership, budgeting and administration of at least a medium-sized research group is essential. In order to assure high socio-economic impact of research program, the candidate should provide expertise in technology transfer to clinics and industry and in the planning and conducting of clinical trials evaluating novel technologies.

Collaboration with other groups within the ARTORG Center of the University of Bern as well as with other academic institutions, nationally and internationally are expected. In particular he/she is expected to continue the existing intensive collaboration with the associated clinical departments.

With a view towards increasing the proportion of female professors, the University of Bern specifically encourages female candidates to apply.

For more information, please contact Professor Aurel Perren, president of the electoral committee, e-mail: aurel.perren@pathology.unibe.ch. Applications with the usual documents are to be sent until 07 April 2015 electronically to the Dean's Office (bewerbungen@meddek.unibe.ch).

Information regarding the required documents can be found under: http://www.medin.unibe.ch/content/akademische_laufbahn/vorgehen_bewerbungen/.

The Dean's Office, Faculty of Medicine, University of Bern,
Murtenstrasse 11, CH-3010 Bern



The **Neuroscience Institute at Georgia State University (GSU)** invites applications for a **tenure track position** at the rank of **Assistant Professor**. The ideal candidate will establish a research program that synergizes with existing key strengths in the Neuroscience Institute in behavioral neuroscience, computational neuroscience, neuroendocrinology, and neuroplasticity. Preference will be given to researchers with expertise and a publication record using state-of-the art methodologies. Candidates must hold a Ph.D. or M.D. in a discipline related to neuroscience and should demonstrate the ability to establish a vigorous, externally funded research program and to mentor Ph.D. graduate students. Excellence in teaching at undergraduate and graduate levels is also expected. Candidates should have an outstanding record of accomplishment and a strong desire for research collaboration. The successful candidate would become a core member of the Neuroscience Institute, which is a thriving department housed in the Petit Science Center that provides world-class facilities and an interdisciplinary and collaborative research environment (see <http://neuroscience.gsu.edu>). A highly competitive salary, start-up funds and laboratory space will be provided.

Applications should include a full *curriculum vitae*, names and contact information for three references, and statements of research interests and teaching philosophy. Applications can be submitted either electronically in PDF format to ni-selection-committee@gsu.edu or in hard copy to: **Chair of the Neuroscience Institute Faculty Search Committee, Neuroscience Institute, PO Box 5030, Georgia State University, Atlanta, GA 30302-50310**. Application processing will begin immediately and the search will remain open until the positions are filled.

Georgia State University, a Research University of the University System of Georgia, is an EEO/AA Employer and encourages applications from women and under-represented minority groups. Offers of employment will be conditional upon background verification. This position is contingent on budgetary approval.



Open-Rank, Tenure-Track Faculty Position in the Department of Genetics, Genomics and Informatics

The Department of Genetics, Genomics and Informatics at the University of Tennessee, College of Medicine seeks outstanding candidates for open-rank, tenure-track faculty positions with a research focus in translational genomics, genome informatics, or systems genetics. Investigators working at the interface between genetics, neuroscience, human development, and pharmacogenetics are particularly encouraged to apply. Applicants should demonstrate the ability to conduct high quality research, secure extramural funding, teach relevant courses, and advise students in degree programs. Rank of appointment and seed funds will match experience, productivity, and support history. Applicants should possess a doctoral degree (PhD, MD,) in genetics, genomics, bioinformatics, or a related discipline at the time of appointment.

The new Department of Genetics, Genomics and Informatics is made up of a small group of basic science faculty with research interests in the genetics of complex diseases using murine models. A larger group of faculty with expertise in human genetics (and potential collaborators) are housed in other departments and colleges at UTHSC and affiliated institutions—including the Oak Ridge National Laboratory, St Jude Children's Research Hospital, and the University of Memphis. UTHSC is a research hub for the field of systems genetics and has been responsible for the creation of new models and novel statistical genetic approaches (see www.genenetwork.org).

Review of applicants will begin on **April 1, 2015** and will continue until the positions are filled. The anticipated start date is July 1, 2015. Please forward by email your complete curriculum vitae, a brief statement of research (ongoing and planned), and names and email addresses of three professional references. Address material to: genetics@uthsc.edu, attention of **Robert W. Williams, Chair, UTHSC, 855 Monroe Ave, Suite 501 Memphis TN 38163**.

The University of Tennessee is an EEO/AA/Title VI/Title IX/Section 504/ADA/ADEA/V institution in the provision of its education and employment programs and services.

May 26 - 31, 2015

Poster Abstract Deadline: April 5

Topics:

- **Chromosome Biology**
- **Nuclear Structure**
- **Chromatin & Epigenetics**
- **Gene Regulation & Control**
- **Developmental Regulation**
- **RNA as Controlling Elements**
- **Maintenance of Genome Stability**
- **Nuclear Receptors, Clocks & Aging**
- **Evolution**
- **Editing & Manipulation**

Speakers:

Karen Adelman, National Institute of Environmental Health Sciences
Genevieve Almouzni, Institut Curie / CNRS, France
Angelika Amon, Massachusetts Institute of Technology
Shelley Berger, University of Pennsylvania
Wendy Bickmore, MRC Human Genetics Unit, UK
Gerd Blobel, Children's Hospital of Philadelphia
Jef Boeke, NYU Langone Medical Center
Julius Brennecke, Institute of Molecular Biotechnology, Austria
Anne Brunet, Stanford University
Emmanuelle Charpentier, Helmholtz Center for Infection Research, Germany
Xavier Darzacq, University of California, Berkeley
Titia de Lange, The Rockefeller University
Job Dekker, University of Massachusetts Medical School
Jennifer Doudna, University of California, Berkeley / HHMI
Denis Duboule, University Geneva & EPFL, Switzerland
Stephen Elledge, Harvard Medical School
Ronald Evans, Salk Institute for Biological Studies
Anne Ferguson-Smith, University of Cambridge, UK
Susan Gasser, Friedrich Miescher Institute, Switzerland
David Gilbert, Florida State University
Christopher Glass, University of California, San Diego
Shiv Grewal, National Cancer Institute
Gregory Hannon, Cancer Research UK Cambridge Institute

Organizers:

Terri Grodzicker, David Stewart & Bruce Stillman,
Cold Spring Harbor Laboratory

Speakers (continued):

Edith Heard, Curie Institute / CNRS, France
Steve Jacobsen, University of California, Los Angeles
Rudolf Jaenisch, Whitehead Institute for Biomedical Research
Alexander Johnson, University of California, San Francisco
James Kadonaga, University of California, San Diego
Scott Keeney, Memorial Sloan-Kettering Cancer Center
David Kingsley, Stanford University
Mitch Lazar, University of Pennsylvania
Jeannie Lee, Massachusetts General Hospital
Arnold Levine, Simons Center for Systems Biology
Michael Levine, University of California, Berkeley
Susan Lindquist, Whitehead Institute for Biomedical Research
Dan Littman, NYU School of Medicine / HHMI
Susanne Mandrup, University of Southern Denmark
Tom Maniatis, Columbia University Medical Center
Robert Martienssen, Cold Spring Harbor Laboratory
Thomas Mistelli, National Cancer Institute
Richard Morimoto, Northwestern University
Huck-Hui Ng, Genome Institute of Singapore
Svante Paabo, Max-Planck Institute, Germany
David Page, Whitehead Institute for Biomedical Research / HHMI
David Pellman, Dana-Farber Cancer Institute
Nicholas Proudfoot, University of Oxford, UK
Wolf Reik, The Babraham Institute, UK
Danny Reinberg, NYU School of Medicine / HHMI
Bing Ren, University of California, San Diego
Gary Ruvkun, Massachusetts General Hospital
Mitunori Saitou, Kyoto University, Japan
Ulrich Schibler, University of Geneva, Switzerland
Robert Singer, Albert Einstein College of Medicine
Davor Solter, Max-Planck Institute of Immunobiology & Epigenetics, Germany
David Spector, Cold Spring Harbor Laboratory
Alexander Tarakhovsky, The Rockefeller University
Robert Tjian, University of California, Berkeley / HHMI
Maria-Elena Torres-Padilla, IGBMC, France
Didier Trono, EPFL, Switzerland
Bas Van Steensel, Netherlands Cancer Institute
Stephen West, London Research Institute, UK
Joanna Wysocka, Stanford University
Richard Young, Whitehead Institute for Biomedical Research
Virginia Zakian, Princeton University
Kenneth Zaret, University of Pennsylvania
Feng Zhang, Massachusetts Institute of Technology



Oh the humanities!

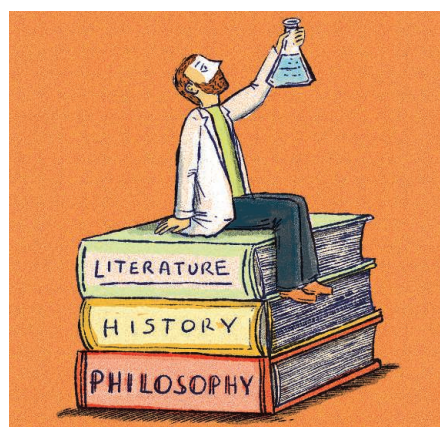
Throughout my science education, I have dutifully memorized facts: the stages of photosynthesis, the enzymes involved in the Krebs cycle, how to balance equations in chemical reactions. In contrast, the focus of my ancient history classes was on answering big, open-ended questions: Why did historical figures act in certain ways? How did the assassination of Julius Caesar affect the Roman Empire? Would our world be different had he not been murdered? There were other questions, too, related not just to historical events but to the nature of knowledge, to what we know and how we know it. What's the evidence? How reliable is it? Does the conventional explanation account for all the available information (including competing ideas) and the broader context?

Eventually, I tried applying a similar thought process to my scientific interests. I found that approach to science much more appealing—and also useful. I took it with me as I became a scientist.

Brushes with waterborne illness and professional experiences with water filtration inspired me to pursue a Ph.D. in public health, focusing on the waterborne transmission of *Helicobacter pylori* in Lima. I chose it because it's a big-picture project, a collaboration between public health officials, scientists, and doctors with the shared goal of providing data-driven advice to policymakers.

I rapidly discovered that new data, or a new technical approach, won't solve access to clean water. After all, the technology to improve water quality is already available, and water-treatment infrastructure is known to be cost-effective. The problem persists because the challenge of clean water ties into complex political and social issues: culture, economics, science, emotion, ideology. You can't solve such problems without accounting for the bigger picture. Narrow thinking can even lead to strategies that do harm, like privatization efforts in Peru that modestly improved water infrastructure but priced the poor out of the market. As our challenges become more complex, even strictly scientific problems require a broader perspective, akin to that embraced by historians, philosophers, and other humanist scholars.

I have benefited from studying history in other ways. I learned to think critically and to write rigorous, compelling qualitative arguments. Slashed research budgets make writing about broader impacts more crucial than ever. Academic scientists must defend their work against competing political and economic priorities, not just in grant proposals but also in public and political spheres. Scientists are increas-



"I encourage my peers to think about science in this larger context."

ingly involved with governments and policymakers: Every year, we've had to justify our research project to a new Peruvian minister of health in order to legally continue.

As stable academic science positions stagnate, a growing proportion of scientists seek employment outside academia. Private-sector and governmental careers usually require thinking that encompasses regulatory and cultural concerns—and pragmatic concerns like profits. The ability to consider and weigh diverse arguments and to communicate clearly with various stakeholders is essential.

Science's inherently reductive approach and its acute attention to the finest details have yielded great benefits. But the scope of science is changing. In addition to practicing

the traditional craft, today's scientists need to be prepared to tackle complex challenges in a globalized (and multi-disciplinary) world, to think critically about how we solve problems, and to communicate persuasively with diverse audiences. More than my science classes did, studying history taught me these skills. Scientists can be too eager to write off other disciplines as "soft," subjective, and therefore inferior to science and its rigorous approach. Those other fields, though, can enhance the practice and understanding of science, among scientists and the public. I encourage my peers to think about science in this larger context, as a liberal art intrinsically tied to its cousins and aimed at illuminating, improving, and adding meaning to the human experience. ■

Kevin Boehnke is a doctoral candidate at the University of Michigan School of Public Health in Ann Arbor. For more on life and careers, visit sciencecareers.org. Send your story to SciCareerEditor@aaas.org.